Topic Reprint

Green Mining

Edited by
Kun Du and Jianping Sun

mdpi.com/topics

MDPI

Green Mining

Green Mining

Topic Editors

Kun Du
Jianping Sun

Topic Editors

Kun Du
Central South University
Changsha
China

Jianping Sun
Nanyang Technological
University
Singapore
Singapore

This is a reprint of the Topic, published open access by the journals *Energies* (ISSN 1996-1073), *Minerals* (ISSN 2075-163X), *Remote Sensing* (ISSN 2072-4292) and *Sustainability* (ISSN 2071-1050), freely accessible at: https://www.mdpi.com/topics/green_mining.

For citation purposes, cite each article independently as indicated on the article page online and using the guide below:

Lastname, A.A.; Lastname, B.B. Article Title. *Journal Name* **Year**, *Volume Number*, Page Range.

Contents

Editorial

Sustainable Development in Green Mining and Geotechnical Engineering—An Overview

Jianping Sun [1,2]

1   School of Civil and Environmental Engineering, Nanyang Technological University,
     Singapore 639798, Singapore; sunj0030@e.ntu.edu.sg
2   CHECC(Singapore) Pte. Ltd., 38 Cleantech Loop, #01-31, (Tower 6 Level 1), Singapore 636741, Singapore

1. Introduction

The sustainable development of green mining and geotechnical engineering has become a crucial area of study in light of the increasing global efforts toward environmental conservation and responsible resource extraction. This Editorial synthesizes the findings of the 20 research papers published in this Special Issue, which offer significant contributions to the advancement of sustainable development practices within geotechnical and mining engineering. These studies address challenges such as groundwater preservation, carbon sequestration, and the mitigation of environmental damage caused by resource extraction, etc.

2. Special Issue Content

Longwall backfill mining helps to preserve groundwater by limiting the height of the water-conductive fractured zone (HWCFZ), but faces challenges related to filling time, space, and coordination with mining activities. A new method called continuous extraction and partial backfill (CEPB) has been proposed by Xu et al. [1] to address these issues. The analytic hierarchy process (AHP) used in their study identified five key factors affecting HWCFZ: the hard-rock lithology ratio, mining height, mining depth, and the widths of protective blocks and the blocks used in the Wongawilli method. Applied in a colliery in the Yu-Shen mining area, the model's results closely matched field measurements. This model was further generalized to the whole mining area, resulting in a thematic map of the HWCFZ including the protective zone thickness. A water-preserving mining criterion based on the equivalent permeability coefficient of the protective zone was proposed to optimize the CEPB mining parameters.

Red mud (RM), a byproduct of the Bayer process, poses several environmental risks due to its large production volume. However, its high iron content makes iron recovery a promising solution by reducing RM waste while generating economic benefits. Kong et al. [2] reviewed three methods to recover iron from RM: physical, chemical, and emerging approaches. The physical methods (e.g., gravity separation and magnetic separation) are energy-efficient but offer low iron recovery rates and produce concentrates with a low iron content (TFe). Chemical methods include hydrometallurgy (acid leaching) and pyrometallurgy (thermochemical reactions). Hydrometallurgy yields high recovery rates but is complex and costly due to the use of acid. Pyrometallurgy, particularly the reduction of Fe_3O_4 in fluidized beds, has lower energy consumption and reaction times but results in lower-TFe concentrates, requiring further research. Emerging methods are environmentally friendly but are still being tested at the lab scale, requiring further studies into process efficiency, cost assessment, and scalability. While they are promising in the long term, significant research is needed for their application within the industry.

The water-conducting fracture zone (WCFZ) is vital for preventing roof water damage in mines. Yin et al. [3] used data from 52 boreholes in the Ordos Basin to identify four key factors influencing WCFZ height: mining thickness, hard rock proportion, working

width, and mining depth. Unitary function models were developed for each factor, with mining thickness being the most significant. A multiple regression model was created using the gray correlation and fuzzy comparison methods, with an error margin below 10%. The model was applied to the Qingshuiying Coalfield to predict the height of the WCFZ based on borehole data, revealing an increasing trend from southeast to northwest. A 3D hydrogeological model was also developed to visualize the spatial distribution of the WCFZ and its relationship with overlying aquifers. This method effectively predicts WCFZ height, helping to mitigate risks from water gushing in mines while improving ecological protection.

The multicomponent transient electromagnetic method (TDEM) offers significant advantages for exploration. Through simulation and field experiments in a copper–nickel mining area, Wang et al. [4] found that the horizontal component effectively points to the center of low-resistivity ore bodies, while the vertical component has strong coupling with the ore body, aiding in quantitative inversion. Both components provide consistent results, reducing the limitations of the traditional method for interpreting a single vertical component and improving field efficiency. Although terrain variations led to some errors in measuring the inversion depth, the interpretation remains accurate. The horizontal component's zero-contour intersection consistently points to the ore body's center, enabling a faster identification of anomaly orientation and reducing field data acquisition costs. The multicomponent analysis improves reliability and overcomes the limitations of using just the vertical component for interpretation. This approach enhances the accuracy and efficiency of exploration in complex terrains.

Zhang et al. [5] addresses the intertwined challenges of ecological damage from coal mining and greenhouse gas emissions in large coal power plants. Focusing on a coal power base in northwest China, the authors propose a green mining model that captures carbon dioxide in goafs (abandoned mine voids) using backfill strips made from solid mine waste. These strips, composed of gray bricks made from aeolian sand and fly ash, are strengthened through carbonization curing, which enhances their bearing strength. The researchers analyzed surface subsidence within and the overburden stability of mines with different backfill strip configurations. The results indicate that increasing the strip width and decreasing the spacing between strips significantly improves surface subsidence, fracture propagation, and gas tightness, facilitating carbon dioxide sequestration. This research offers a promising model for environmentally friendly mining practices and the low-carbon utilization of coal resources.

Pang et al. [6] address the uneven deformation of gangue-filled walls and other challenges in providing large-scale roadway support to mining areas. A failure mechanics model of bagged gangue was developed, and uniaxial compression tests showed that gangue particles between 0 and 20 mm offer strong support, meeting technical requirements for gob-side entry. Wet shotcrete demonstrated superior deformation capacity compared to dry shotcrete, providing greater toughness under load. Additionally, the optimal spray layer thickness for flexibility and support was determined to be around 80 mm. The research offers solutions for cost-effective, environmentally friendly coal mine waste disposal while also improving structural integrity.

The governance of abandoned mines is a critical issue in China, where utilizing these sites offers a solution that aligns with the country's goals of ecological protection and carbon reduction. Du et al. [7] reviews global advancements in abandoned mine utilization, focusing on four primary models: energy storage, waste treatment, ecological restoration, and CO_2 sequestration. Applications include pumped storage, gas/oil storage, CO_2 storage, radioactive waste disposal, and the development of tourism. Despite the potential of China's abandoned mines, most utilization technologies are still in the research phase due to complex geological challenges. Learning from developed countries like the U.S., Germany, and the U.K., China must invest in key technologies and establish industrial demonstration projects. By addressing rock mechanics issues and creating sustainable business models,

China can advance the reuse of abandoned mines to contribute to ecological civilization and meet its carbon goals.

Li et al. [8] introduces a novel strain of *Acidithiobacillus ferrooxidans* (YQ-N3) that was isolated from river sediment that was polluted by acid mine drainage (AMD) from an abandoned mine in Shanxi, China. Genome sequencing revealed that YQ-N3 has a 3.2 million base pair genome, comprising one circular chromosome and five plasmids, including a newly discovered plasmid that has not been recorded in any of the major databases. YQ-N3 shares close evolutionary ties with *A. ferrooxidans* ATCC23270 and *A. ferridurans* JCM18981 and contains multiple genes related to iron and sulfur metabolism. Laboratory experiments demonstrated YQ-N3's ability to significantly enhance Fe^{2+}, S^0, and FeS_2 oxidation, improving the hydrophilicity of sulfur. In biological desulfurization tests, it achieved a 62.25% sulfur removal rate in coal by removing pyrite and organic sulfur. This strain offers promising applications in industrial desulfurization, biometallurgy, and AMD treatment, providing a foundation for future research and environmental management strategies.

Pan et al. [9] analyzes the stability of the Tongling tailings impoundment during the re-mining process, focusing on the impact of recovery height and various working conditions. Using a combination of engineering surveys, laboratory tests, and 2D and 3D numerical simulations, their study examines how dam stability can evolve. Key findings include the following: (1) Lower recovery heights improve dam stability by lowering the infiltration line, but poor drainage increases risks, particularly during floods. (2) As mining height decreases, the dam's safety factor improves, maintaining overall stability. (3) Extreme conditions, such as floods or earthquakes, reduce safety by increasing shear stress and displacements. (4) The research underscores the effectiveness of advanced simulations using 2D and 3D software to model the dam's behavior and predict risks. This approach has significant global implications for safely managing tailings dams, emphasizing the need for regular maintenance of drainage systems to ensure stability during recovery operations.

Chen et al. [10] examine the impact of wetting–drying cycles on the deterioration of cemented paste backfill (CPB) used in open-pit coal mines. CPB samples, made with marl particles, Portland cement, sulfoaluminate cement, and gypsum, were tested under various wetting–drying cycles. The results showed that the CPB underwent shear and tensile coalescence in the early cycles and shear coalescence in the later cycles. Both unconfined compressive strength (UCS) and elastic modulus (EM) decreased with increasing cycles and porosity, with EM being more sensitive to the gypsum content. The deterioration process was divided into initial and secondary stages, with the evolution of damage following an 'S' curve. This research proposes a highwall filling mining method to improve resource recovery and promote sustainable coal resource exploitation by utilizing solid waste. It also provides valuable insights into CPB design for open-pit mines.

Aeromagnetic measurements are key in mineral exploration, but unmanned aerial vehicles (UAVs) produce maneuvering noise that affects data accuracy. To address this, aeromagnetic compensation is essential. Traditional compensation models based on linear regression face multicollinearity, leading to inconsistent results across different flight directions. Bi et al. [11] introduce an adaptive model-based method to suppress UAV aeromagnetic noise by assigning model variables based on flight heading characteristics, reducing multicollinearity's impact. By automatically selecting significant variables with lower multicollinearity, the optimal compensation model is developed, improving accuracy. Testing on a UAV platform in Ma'anshan demonstrated that this adaptive algorithm outperformed traditional methods, yielding fewer errors and a higher improvement ratio. This research effectively solves the multicollinearity issue, enhancing the robustness and accuracy of aeromagnetic data compensation. This method has proven to be valuable for precise magnetic anomaly detection, aiding further inversion and interpretation in mineral exploration.

Wang et al. [12] explore the impact of open-pit coal mining on surrounding vegetation in arid and semi-arid regions, focusing on vegetation phenology. Using high-frequency time series data from Landsat 8 and Sentinel-2, the study quantifies several key phenological

phases: the Start of Season (SOS), the End of Season (EOS), and the Length of Season (LOS). The results show exponential changes in these phases as the distance from the mining areas increases. Mining causes delayed greening, early senescence, and shorter growth cycles. The disturbance range varies by mine, with HDG-HEWS, MX, and XD affecting SOS up to 1625 m and EOS up to 825 m. Mineral dust is a major factor in these disruptions. Overlapping mining areas intensify the disturbance, increasing the impact on vegetation cycles. These findings provide valuable insights for dust control and ecological restoration, helping to mitigate mining's environmental effects.

Wang et al. [13] employ three-dimensional resistivity and chargeability tomography using a distributed data acquisition system to explore new ore bodies in the Huaniushan region of China. Utilizing expanding-gradient and pole–dipole arrays, the research established a high-resolution geoelectric model that correlates well with known geological formations, indicating potential mineralization in low-resistivity and high-chargeability zones. The study emphasizes the advantages of true 3D tomography over quasi-3D methods, highlighting the importance of varied transmitter directions and vector signal collection for accurate modeling. While the true 3D inversion yielded better results, it also highlighted limitations associated with using isotropic inversion algorithms in anisotropic conditions, suggesting the need for further algorithm development. The research advocates for a balanced approach to designing acquisition schemes, weighing spatial resolution, signal quality, and cost-effectiveness, to enhance early-stage exploration and detailed investigations in mineral exploration.

Bai et al. (Contribution 1) examine mining fractures that are critical for water conservation in mining and the stability of coal mining subsidence areas, as well as the restoration of surface ecosystems. Using the key strata theory and analyzing overburden failure, their research reveals the formation mechanisms of "saddle-shaped" water-conducting fracture zones and they identify that permanent mining fractures concentrate at the working face boundaries. Through shear testing of sandstone, it was found that rock damage correlates positively with shear stress, indicating structural stability in the overburden. The fracture zone can be categorized into original fractures, tensile fractures, structural voids, and void compaction areas, with the structural void area showing the greatest deformation. A regional division method based on overburden critical failure was applied and validated through surface movement monitoring, demonstrating that subsidence near the working face boundaries exceeds that in the middle, emphasizing the long-term nature of residual surface deformation and its significance for safe mining and ecological restoration.

The novel continuous extraction and partial backfill (CEPB) mining method effectively addresses the issues associated with traditional longwall backfill mining by reducing the height of the water-conductive fractured zone (HWCFZ) and conserving groundwater. Xu et al. (Contribution 2) utilize the Analytic Hierarchy Process (AHP) to identify five key factors affecting HWCFZ: the hard-rock lithology ratio, mining height and depth, and the widths of Wongawilli and protective blocks. A numerical model was developed to simulate HWCFZ variations, leading to a predictive model validated with field measurements. The model was generalized for broader application within the Yu-Shen mining area, producing thematic maps of the HWCFZ including protective zone characteristics. Additionally, a criterion based on the equivalent permeability coefficient of the protective zone was established to guide mining parameter optimization for water-conservation efforts in Northwest China; as such, future studies should focus on mining-induced permeability changes.

Li et al. (Contribution 3) investigate the performance evaluation of green mining (GM) in underground gold mines, focusing on achieving a balance between mineral resource exploitation and environmental protection. An evaluation criteria system tailored towards underground gold mines is developed in their study, comprising four key criteria and twenty indicators. The integrated gray DEMATEL and ANP methods are employed to assess the green mining performance (GMP), accounting for the correlations between indicators. Case studies of six underground gold mines reveal significant differences between traditional and pilot green mines, highlighting areas for improvement. The study identifies

the integral elements of GM, such as safety, resource utilization, environmental protection, and mining efficiency, while analyzing the weaknesses and strengths of each mine. A cause–effect analysis further categorizes the indicators based on their prominence and relationships, guiding targeted improvements. The study acknowledges limitations, such as the need for additional evidence to validate the proposed methods, but overall the evaluation framework provides valuable insights for mining management and government policy, with potential applicability to similar underground metal mines and broader evaluation contexts.

Wu et al. (Contribution 4) address the critical need for appropriate development strategies for the mining industry's green transition by introducing a novel integrated decision support model. It employs a combined SWOT analysis and PEST framework to evaluate the internal and external factors influencing green mining. The fuzzy analytic hierarchy process (AHP) quantitatively assesses factor weights, while the fuzzy Measurement of Alternatives and Ranking according to Compromise Solution (MARCOS) method ranks development strategies. The optimal strategy identified is to "grasp the trend of green development and improve the protection and exploitation level of mineral resources". A comprehensive analysis led to the identification of four main criteria and sixteen sub-criteria, from which eight macro strategies were formulated. The methodology's robustness is confirmed through comparative and sensitivity analyses. This study is pioneering in its quantitative approach to SWOT-PEST analysis, providing a systematic framework for selecting green mining strategies. Its implications extend beyond mining, offering insights for strategic decision-making in various industries. Future research may explore extending these fuzzy analysis methods further.

The mining industry has severely impacted land and ecological environments, prompting a surge in literature focused on land reclamation and ecological restoration (LRER). Shao et al. (Contribution 5) analyze 2357 articles from the Web of Science database using the Bibliometrix R-package to evaluate LRER research from 1990 to 2022. Their key findings indicate a gradual increase in both the number of publications and citations over this period. Their high-frequency keyword analysis reveals that heavy metal pollution remediation is a prominent research area, while the cluster analysis identifies two main themes: heavy metal pollution and the ecological restoration of mining areas. A study of the thematic evolution of the field highlights ongoing research in mine drainage treatment, soil reconstruction, and vegetation restoration. Future research directions should include exploring the links between ecological restoration, carbon sequestration, and biodiversity, alongside enhancing international cooperation and technological exchanges. The analysis indicates that countries such as China, the USA, Australia, Canada, and Germany lead LRER research efforts, with a significant number of collaborations between them being present. This study provides a comprehensive overview of the LRER literature, offering valuable insights for future research.

Artisanal gold mining (AGM) is essential yet often overlooks operational efficiency and financial analyses, focusing primarily on environmental and social impacts, particularly the use of mercury. Marin et al. (Contribution 6) investigates the sustainability of mercury-free AGM operations by examining various parameters, including company interactions, production logistics, and geological planning. The findings reveal that AGM remains unsustainable even without mercury, primarily due to inadequate planning and operational inefficiencies. While much research emphasizes the health effects of mercury and the need to formalize operations, this study underscores the significance of operational efficiency and comprehensive mine planning. For AGM to be sustainable, it must simultaneously address social, economic, and environmental factors and implement a robust mine planning cycle that incorporates geological knowledge. By enhancing these strategies, AGM operations can achieve greater stability, similar to that of medium or large mining enterprises, providing insights for governments and communities to improve AGM sustainability through effective planning and operational enhancements.

To support economic growth, ecological protection, and carbon neutrality goals, green mine construction has become crucial in China. Du et al. (Contribution 7) review the significance of mineral resources and summarize the experiences of and sustainable development directions for green mines, providing insights for the global mining sector. Their study introduces the management processes currently used in China and outlines four green mine models: green technology mining, operation modernization, stability mining, and ecological restoration. Key construction elements include resource utilization, energy conservation, and technological innovation. Despite the establishment of over 1250 national green mines and notable advancements, challenges such as regional imbalances and inadequate policies persist. Future efforts require collaboration between governments, enterprises, and society, emphasizing tailored policies and the development of low-carbon technologies to achieve sustainable mining practices and enhance the quality of the industry's development.

3. Closing Remarks

The studies reviewed in this Editorial represent significant advancements in the field of sustainable geotechnical and mining engineering. Through innovative methods such as continuous extraction and continuous backfill (CECB), carbon sequestration, and advanced numerical modeling, these research efforts contribute to reducing the environmental impact of mining while ensuring operational efficiency and safety. By integrating water-preserving techniques, carbon sequestration, and structural stability measures, these studies pave the way for more sustainable and responsible resource extraction practices. As these methods are further refined and implemented on a larger scale, they have the potential to revolutionize the mining industry, making it more environmentally friendly and economically viable. The findings presented in these 20 papers serve as a foundation for future research and development on sustainable geotechnical and rock engineering.

List of Contributions

1. Bai, E.; Guo, W.; Tan, Y.; Guo, M.; Wen, P.; Liu, Z.; Ma, Z.; Yang, W. Regional Division and Its Criteria of Mining Fractures Based on Overburden Critical Failure. *Sustainability* **2022**, *14*, 5161. https://doi.org/10.3390/su14095161.
2. Xu, Y.; Ma, L.; NGO, I.; Zhai, J. Prediction of the Height of Water-Conductive Fractured Zone under Continuous Extraction and Partial Backfill Mining Method—A Case Study. *Sustainability* **2022**, *14*, 6582. https://doi.org/10.3390/su14116582.
3. Li, Y.; Zhao, G.; Wu, P.; Qiu, J. An Integrated Gray DEMATEL and ANP Method for Evaluating the Green Mining Performance of Underground Gold Mines. *Sustainability* **2022**, *14*, 6812. https://doi.org/10.3390/su14116812.
4. Wu, P.; Zhao, G.; Li, Y. Green Mining Strategy Selection via an Integrated SWOT-PEST Analysis and Fuzzy AHP-MARCOS Approach. *Sustainability* **2022**, *14*, 7577. https://doi.org/10.3390/su14137577.
5. Shao, Y.; Xu, Q.; Wei, X. Progress of Mine Land Reclamation and Ecological Restoration Research Based on Bibliometric Analysis. *Sustainability* **2023**, *15*, 10458. https://doi.org/10.3390/su151310458.
6. Marin, T.; Seccatore, J.; Cheng, Y. Mapping the Reality of Hg-Free Artisanal Small-Scale Gold Mining. *Sustainability* **2023**, *15*, 13207. https://doi.org/10.3390/su151713207.
7. Du, K.; Xie, J.; Xi, W.; Wang, L.; Zhou, J. Construction Practices of Green Mines in China. *Sustainability* **2024**, *16*, 461. https://doi.org/10.3390/su16010461.

References

1. Xu, Y.; Ma, L.; NGO, I.; Zhai, J. Continuous Extraction and Continuous Backfill Mining Method Using Carbon Dioxide Mineralized Filling Body to Preserve Shallow Water in Northwest China. *Energies* **2022**, *15*, 3614. [CrossRef]
2. Kong, H.; Zhou, T.; Yang, X.; Gong, Y.; Zhang, M.; Yang, H. Iron Recovery Technology of Red Mud—A review. *Energies* **2022**, *15*, 3830. [CrossRef]
3. Yin, H.; Dong, F.; Zhang, Y.; Cheng, W.; Zhai, P.; Ren, X.; Liu, Z.; Zhai, Y.; Li, X. Height Prediction and 3D Visualization of Mining-Induced Water-Conducting Fracture Zone in Western Ordos Basin Based on a Multi-Factor Regression Analysis. *Energies* **2022**, *15*, 3850. [CrossRef]
4. Wang, X.; Zhi, Q.; Wu, J.; Deng, X.; Huang, Y.; Yang, Q.; Wang, J. Multicomponent Transient Electromagnetic Exploration Technology and Its Application. *Minerals* **2022**, *12*, 681. [CrossRef]
5. Zhang, Z.; Liu, H.; Su, H.; Zeng, Q. Green Mining Takes Place at the Power Plant. *Minerals* **2022**, *12*, 839. [CrossRef]
6. Pang, D.; Zhou, Y.; Niu, X.; He, K.; Li, C.; Chen, Z. Research on the Mechanical Properties of Flexible Material Backfilling Wall in Gob-Side Entry Retaining. *Minerals* **2022**, *12*, 1020. [CrossRef]
7. Du, K.; Xie, J.; Khandelwal, M.; Zhou, J. Utilization Methods and Practice of Abandoned Mines and Related Rock Mechanics under the Ecological and Double Carbon Strategy in China—A Comprehensive Review. *Minerals* **2022**, *12*, 1065. [CrossRef]
8. Li, W.; Feng, Q.; Li, Z. Isolation and Characterization of A Novel Iron–Sulfur Oxidizing Bacterium Acidithiobacillus Ferrooxidans YQ-N3 and its Applicability in Coal Biodesulfurization. *Minerals* **2023**, *13*, 95. [CrossRef]
9. Pan, Y.; Chen, J.; Zuo, X.; Zhang, C.; Wu, S. The Stability of Dams with Different Stoping Elevations in the Tongling Valley-Type Tailings Impoundment: A Case Study in Yunnan China. *Minerals* **2023**, *13*, 1365. [CrossRef]
10. Chen, T.; Shu, J.; Han, L.; Tan, Z.; Lyu, J. The Effect of Wetting–Drying Cycles on the Deterioration of the Physical and Mechanical Properties of Cemented Paste Backfill in Open-Pit Coal Mines. *Minerals* **2024**, *14*, 296. [CrossRef]
11. Bi, F.; Yu, P.; Jiao, J.; Zhou, L.; Zeng, X.; Zhou, S. An Adaptive Modeling-Based Aeromagnetic Maneuver Noise Suppression Method and Its Application in Mine Detection. *Remote Sens.* **2023**, *15*, 4590. [CrossRef]
12. Wang, B.; Li, P.; Zhu, X. Quantification of Vegetation Phenological Disturbance Characteristics in Open-Pit Coal Mines of Arid and Semi-Arid Regions Using Harmonized Landsat 8 and Sentinel-2. *Remote Sens.* **2023**, *15*, 5257. [CrossRef]
13. Wang, M.; Wang, J.; Lin, P.; Meng, X. Three-Dimensional Resistivity and Chargeability Tomography with Expanding Gradient and Pole–Dipole Arrays in a Polymetallic Mine, China. *Remote Sens.* **2024**, *16*, 186. [CrossRef]

Article

Construction Practices of Green Mines in China

Kun Du [1], Junjie Xie [1], Wenqin Xi [1], Liang Wang [2,*] and Jian Zhou [1]

[1] School of Resources and Safety Engineering, Central South University, Changsha 410083, China; dukuncsu@csu.edu.cn (K.D.); 215511032@csu.edu.cn (J.X.); xwqcsu@csu.edu.cn (W.X.); j.zhou@csu.edu.cn (J.Z.)

[2] Zhongguancun Green Mining Industry Alliance, Beijing 100191, China

* Correspondence: zlm@greenmine.org.cn

Abstract: To maintain high-level economic development, protect the ecological environment, and achieve carbon peaking and carbon neutrality goals, the construction of green mines has become a critical issue in China. In this study, the importance of mineral resources to human society is discussed, and the construction experiences and sustainable development directions of green mines are summarized, which can provide valuable references for the global mining industry. The entry and management process in China was introduced to help understand green mines' construction objectives and tasks. Moreover, based on the successful construction cases of green mines, four typical green mine models are concluded: the green technology mining model, operation modernization mining model, stability mining model, and ecological restoration mining model. In addition, the key construction elements of green mines are concluded, for example, the mining environment, mining methods, comprehensive utilization of resources, energy conservation, emission reduction, scientific and technological innovation and intelligence, and enterprise-land stability, which provided the directions and guidance for green mine construction.

Keywords: mineral resource; green mine; directory management; construction model

1. Introduction

More than 95% of energy, 80% of industrial raw materials, and 70% of agricultural means of production globally come from mineral resources [1]. Thus, mineral resources are important material foundations for the survival and development of human society. The utilization of mineral resources destroys the ecological environment and increases carbon emissions to varying degrees in different countries, leading to a series of environmental problems, e.g., solid waste, exhaust gas, liquid waste, ground collapse, and a decrease in biodiversity. According to the Annual Report of the China Geological Survey in 2016, the coal mines in the Greater Khingan Mountains and Hulunbuir Grassland had destroyed and occupied a total of 2772.77 hectares of grassland due to mining operations. Six waste rock yards with a total area of 19.355 hectares and a total volume of 1.07875 m^3 and five tailing sand dumps with a total area of 25.90 hectares and a stacked volume of 943,000 m^3 of Shizhuyuan multi-metal mine have greatly impacted the environments around the Xiangjiang River [2]. The subsidence area of Yangquan coal mines near the Fenhe River in North China is about 406.73 km^2, accounting for 27.56% of the mining area [3]. Figure 1 illustrates the main geo-environmental problems of the mines. As can be seen from Figure 1, pit drainage is more severe in the central region. The highest cumulative amount of solid waste is mainly located in the provinces of Xinjiang, Inner Mongolia, and Yunnan. Higher wastewater discharges are mainly found in coastal areas. More serious land destruction is mainly in the eastern and western regions. Areas with more serious landslides and mudslides are Yunnan, Sichuan and Chongqing, and Inner Mongolia. Ground subsidence is a more serious problem in Guizhou, Anhui, and other regions. In addition, the transition from shallow mining to deep mining poses a more severe safety production situation,

and the threat of dynamic geological disasters such as water inrush, rock bursts, and high temperatures will continue to increase. From 2001 to 2021, there were 629 mine floods, resulting in 3730 deaths and the highest economic losses among all types of mining accidents [4]. In addition, the environmental problems and carbon emissions caused by mines are particularly prominent. According to the China Carbon Accounting Database (CEADs), China's cumulative carbon emissions in 2022 reached 11 billion tons, accounting for approximately 28.87% of global carbon emissions [5]. Among them, industrial emissions amounted to 4.2 billion tons, accounting for 38.18% of the national emissions, second only to the electricity industry's emissions of 5.1 billion tons, accounting for 46.37% [6]. The main types of energy sources for carbon emissions from China's mining industry are electricity and coal. China's coal-fired power generation accounts for about 50% of the global total [7]. In September 2020, at the 75th United Nations General Assembly, China proposed the "dual carbon" goal of peaking carbon emissions by 2030 and achieving carbon neutrality by 2060, which greatly promoted the green and low-carbon development of mining.

I. Main geological issues

- Drainage of mine pits
- Stock of solid waste
- Wastewater discharge
- Land destruction
- Avalanches, landslides, mudslides
- Ground subsidence

II. Main geological types and scale tables

	Small	medium	Large	None
	<1500 hm²	1500~6000 hm²	>6000 hm²	None
	<2500×10⁴ m³	(2500~8000)×10⁴ m³	>8000×10⁴ m³	None
	<2000×10⁴ t	(2000~8000)×10⁴ t	>8000×10⁴ t	None
	<2000×10⁴ m³	(2000~8000)×10⁴ m³	>8000×10⁴ m³	None
	<2000 hm²	(2000~10,000) hm²	>10,000 hm²	None

Figure 1. Distribution map of major environmental problems in mines (adapted from [8]).

In response to the challenges of mining, the Chinese government has implemented a national strategy of green mining. The specific connotation of green mining is to implement scientific and regulated mining throughout the life cycle of mines, to control mining disturbances and the surrounding ecological environment within a controllable range, to keep environmental ecology, scientific mining, efficient resource utilization, standardized

enterprise management, standardization of production safety, and stable mining communities harmonious [9,10]. The construction of green mines has become an important issue for the sustainable development of the mining industry in China. The green mine concept was first proposed in 2007 and has since undergone conceptual proposals, road exploration, and pilot demonstrations. Nowadays, it is advancing towards a new stage of standardized construction [11]. China has gained valuable experience and remarkable results in green mine construction over the past decade. To propel the development of the mining industry and support the achievement of dual carbon goals, promote the sustainable development of the mining economy, and promote the green and high-quality development of the mining industry, this paper summarizes the experience of green mine construction. It identifies the problems during green mine construction, providing direction and guidance for mine enterprises building green mines.

2. Mineral Resources and Green Mines

2.1. Global Distribution and Utilization

Figure 2 shows that the distribution of mineral resources globally has distinct regional patterns. The Middle East holds 57% of the world's oil reserves, while Eastern Europe, Russia, and the Middle East contain 72% of the global natural gas reserves [12]. Regarding coal reserves, 53% are concentrated in the United States, China, and Australia [13]. Among non-ferrous metals, 56% of copper reserves are in Chile, Peru, Mexico, the United States, and Canada. Regarding lead reserves, 57.5% are concentrated in Australia, China, the United States, and Kazakhstan. Finally, 48% of zinc reserves are distributed in Australia, China, and the United States [14].

Figure 2. Global distribution map of mineral resources (adapted from [15]).

Mineral resources are essential materials for all industries, significantly impacting socioeconomic development and national security. Figure 3 presents the change in total global production of mineral resources from 2009 to 2022. Figure 4 shows the share of energy, metal, and non-metal production in 2022. In 2022, 1/3 of countries were mining countries, and their ratio of mining output value to GDP was larger than the global average [16]. The mining industry provided 22.7 billion tons of energy, metals, and important non-metallic minerals, with a total output value of USD 5.9 trillion, equivalent to 6.9% of the global GDP [17]. Chinese mining companies account for approximately 12% of the global top 50 mining companies in terms of market value [18]. More than 80% of the natural resources

consumed by humans are mineral resources, with an average of three tons of mineral resources consumed per year per capita [19]. China's energy and mineral consumption accounts for approximately 30% globally [18]. Currently, developing countries, such as those in Asia, Africa, and Latin America, are focusing on the construction in the mining industry to support industrialization, while developed countries, such as those in Europe and North America, are increasing their support for the mining industry to develop the high-end manufacturing industry, further increasing the mining industry's contribution to global economic development [16].
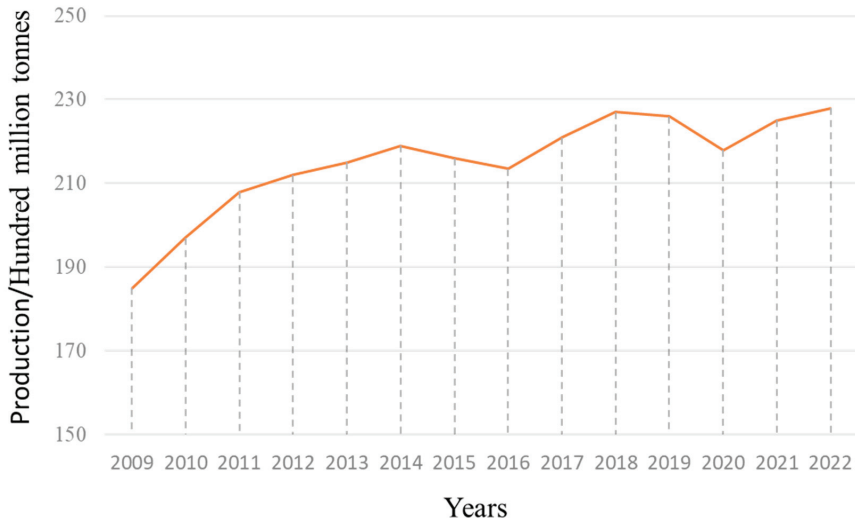
Figure 3. Global production of mineral resources, 2009–2022 (data from [17,18]).
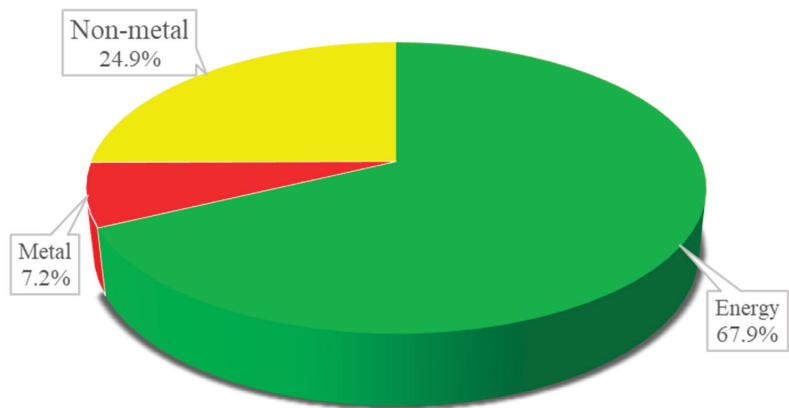
Figure 4. Global proportion of different mineral productions in 2022 (data from [18]).

2.2. Mineral Resource Exploitation and Utilization in China

China is one of the largest countries in terms of resource production, consumption, and trade. Field mining is the main method for obtaining mineral resources, and mineral resources are primarily divided into energy mineral, metal mineral, and non-metallic mineral resources in China. The revenue, income, and the proportion of the mining industry in GDP in China are reflected in Figures 5 and 6.
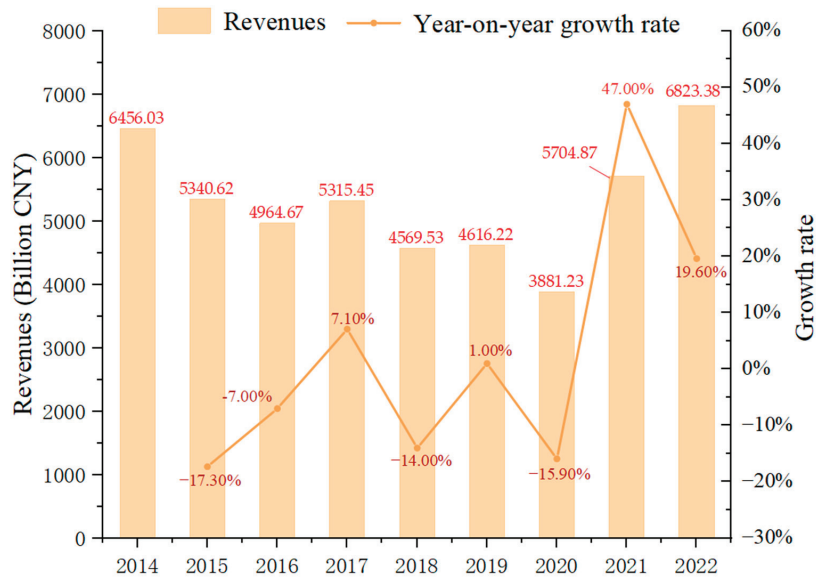
Figure 5. Revenue statistics and revenue growth ratio of China's mining industry from 2014 to 2022 (adapted from [20,21]).

Figure 6. Operating incomes of mining enterprises in different industries above the designated size in 2022 (adapted from [20,21]).

Compared to 2020, China's consumption of 28 mineral resources increased in 2021, while the consumption of 15 mineral resources decreased. The total consumption of 36 mineral resources in China, including coal, paste, manganese, chromium, vanadium, titanium, and copper, ranked first in the world. Figure 7 displays the ratio between China's mineral consumption and that of the world in 2021.
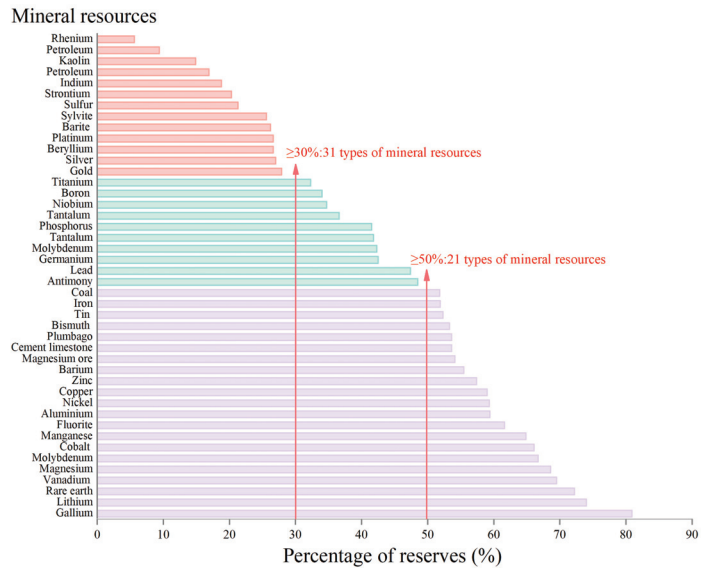
Figure 7. Global proportions of mineral resource consumption for China in 2021 (data from [22]).

Long-term, high-intensity, and large-scale development of mineral resource exploitation has created enormous pressure on the ecological environment. The National Mining Geo-Environmental Survey Report (2016) shows that from 2002 to 2015, mineral resource mining damaged more than 3.03 million hectares of land, and only about 810,000 hectares have been repaired and treated [23]. The accumulated volume of solid waste generated by mining activities is 48.31 billion tons, e.g., 38.69 billion tons of waste rock (soil), 5.48 billion tons of tailings, and 4.09 billion tons of coal gangue. Solid waste has caused several ecological and environmental problems, such as encroaching on cultivated land [24], causing geological disasters, soil and water environmental pollution, etc. In addition, the total output of mining wastewater has been 11.48 billion cubic meters, and mining pit drainage has led to a drop in regional groundwater levels, a reduction in spring flow, and even dryness in many areas [25].

2.3. Construction Mechanisms of Green Mines

Protecting the ecological environment, addressing climate change, and maintaining energy and resource security simultaneously are common global challenges. Promoting mining transformation and realizing green development are the construction goals of green mines. Since 2007, great efforts have been made, and significant progress has been achieved in constructing green mines in China. Figure 8 lists the key nodes for the development of green mines in China [26–28].

In 2007, the initiative was proposed to fundamentally transform the development mode and economic growth mode, truly realizing the coordinated development of rational resource utilization and environmental protection, which has become an inevitable choice for the development of mining enterprises. This is also the first time that China has proposed the concept of "green mining". In 2008, the China Mining Circular Economy Forum was held in Nanning, Guangxi. The China Mining Federation and 11 large mining enterprises advocated for the signing of the "Green Mining Convention", which received recognition and a positive response from many mining enterprises. In 2009, "The National Miner-al Resources Plan (2008–2015)" jointly released by the National Development and Reform Commission and the former Ministry of Land and Resources, put forward clear requirements for the development of "green mining" for the first time, and set the strategic

goal of "basically establishing a green mining pattern by 2020". This also marked the beginning of the comprehensive promotion of green mining construction at the government level. In 2010, the former Ministry of Land and Resources issued the Guiding Opinions on Implementing "The National Mineral Resources Planning, Developing Green Mines, and Building Green Mines". This was the first time that clear requirements for building "green mines" had been put forward in the form of official documents, and the basic conditions for national-level green mines had been listed. In 2011, the former Ministry of Land and Resources announced the first batch of pilot units for "green mines", marking the official launch of China's national green mine pilot work. In 2015, "The Opinions of the Central Committee of the Communist Party of China and the State Council on Accelerating the Construction of Ecological Civilization" officially included green mines in the document. This marks the shift of this work from corporate self-discipline to departmental advocacy, elevating it to a national strategy. In 2016, the Ministry of Land and Natural Resources issued "The National Mineral Resources Plan (2016–2020)", which proposed improving the quality and efficiency of mining development and accelerating the green transformation and up-grading of mining. In 2017, the former Ministry of Land and Resources, in conjunction with the Ministry of Finance and six other ministries, issued "The Implementation Opinions on Accelerating the Construction of Green Mines (Land and Resources Regulations (2017) No. 4)", marking the transition of China's green mining construction from the "pilot exploration" stage to the "comprehensive promotion" stage. In 2020, the Ministry of Natural Resources issued the "Green Mine Evaluation Indicators", which clarified the prerequisites for selecting green mines and unified the evaluation indicator standards.
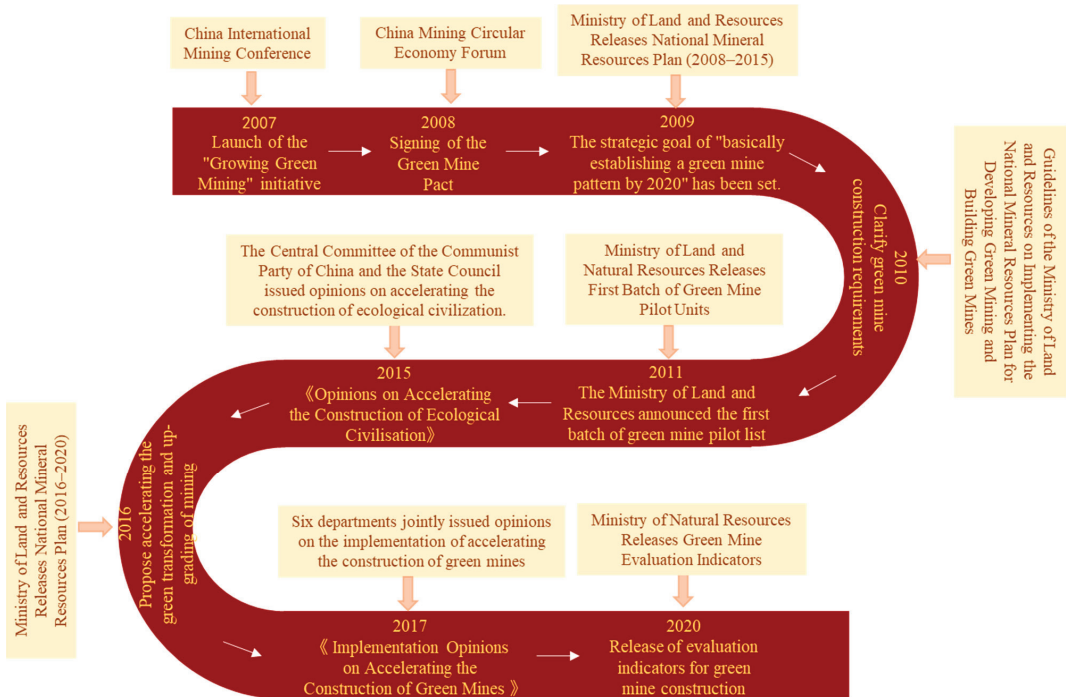
Figure 8. Development history of green mine construction in China.

2.3.1. Theoretical Basis of Green Mines

The creation of green mines is interdisciplinary and influenced by multiple factors. It is necessary to consider not only the efficient utilization of resources but also the safety of

mining and resource utilization, as well as environmental damage and ground stability in mining areas. Therefore, the creation of green mines should be informed by the theories shown in Figure 9.
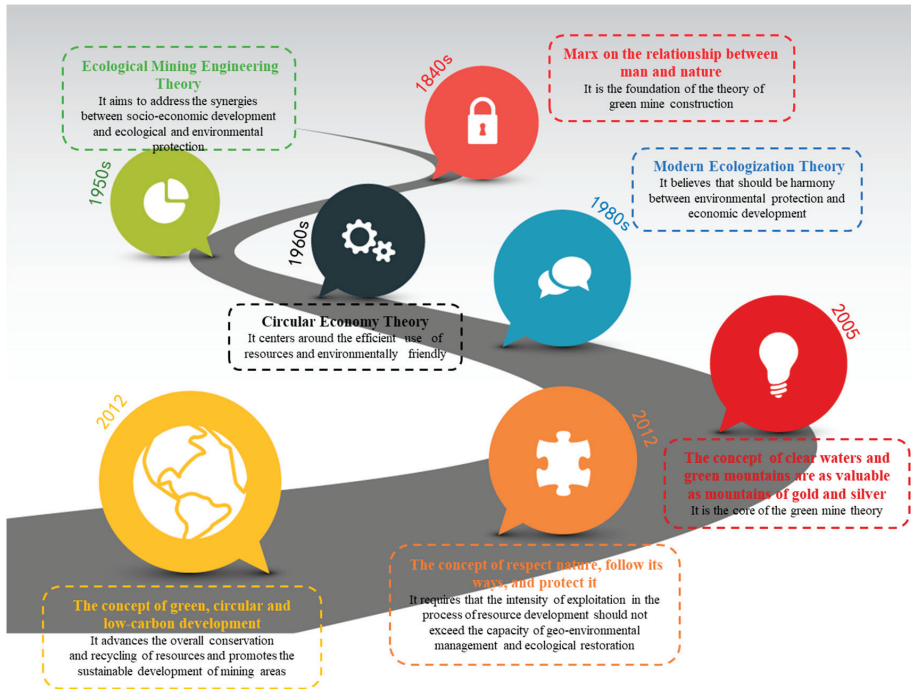
Figure 9. Basic theories for the construction of green mines.

2.3.2. Policy Support for Green Mines

To accelerate the construction process of green mines, the relevant departments and provinces (autonomous regions and municipalities) have put forward a series of policies related to green mines. In 2009, the Ministry of Land and Natural Resources issued Regulations of Geological Environment Protection in Mines, which stipulated the responsibilities, rights, and interests of protecting the geological environment in mines. It also provided for the prevention and restoration of damage to the terrain and landscape caused by mineral resource exploration and other activities [29]. In 2010, to speed up the construction of green mines, the Ministry of Land and Resources in China released the Guiding Opinions on Implementing the National Mineral Resource Planning for the Development of Green Mining and Construction of Green Mines [30]. In 2017, six ministries of China, including the Ministry of Land and Resources, issued the Guidance on Accelerating Green Mine Construction, which implemented incentive policies in four aspects: land use, mine use, finance, and funding [31]. In 2021, the National Development and Reform Commission, the Ministry of Finance, and the Ministry of Natural Resources issued the 14th Five-Year Plan for Promoting the High-Quality Development of Resource-Based Regions, which suggested that we should strongly promote green mine construction and all new and expanded mines should meet the requirements [32]. In addition, the provinces answered the call and introduced relevant policies. In 2020, Shandong Province issued the Shandong Province Green Mine Construction Management Approach [33]. In 2022, Shanxi Province released a notice titled the Guiding Opinions on the Comprehensive Promotion of Green Mine Construction [34].

2.3.3. Green Mine Selection Process and Directory Management

The mines with construction levels meeting the green mine standards can be included in the National Green Mine List of China. The incentive policies on the list have been implemented for the green mines, which can urge them to fulfill their obligations better [35]. The selection process and list management of green mines are shown in Figure 10.
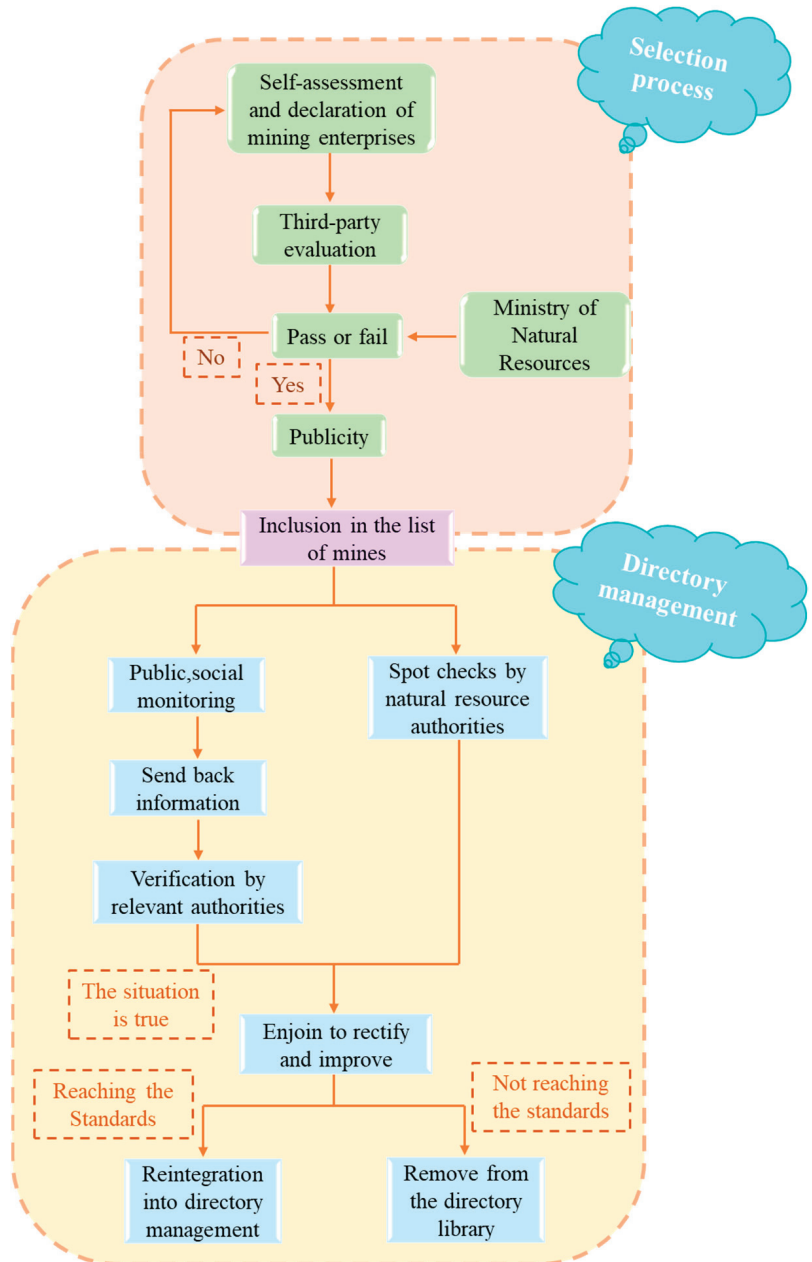
Figure 10. Entry process and list management of green mines in China.

(1)   Selection process [35,36]

According to the selection notice of green mines in 2020 issued by the General Office of the Ministry of Natural Resources in China, the main creation procedures are as follows.

i.   Application online. The mining enterprises log into the National Green Mine Directory Management Information System and fill out the relevant application information.

ii.   Self-assessment of mining enterprises. The mining enterprises conduct self-assessments and create self-assessment reports according to green mines' construction requirements and industry standards. Then, the mining enterprises fill out the self-assessment report through the directory system.

iii.   Third-party assessment. In the form of government-purchased services, third-party assessment agencies are commissioned to conduct the on-site green mine construction level assessments. The third-party assessment report is created according to the requirements of unified evaluation indicators. The department in charge of natural resources selects mines and performs field verification.

iv.   Publicity. The green mine candidates are publicly announced online, in newspapers, and through other channels. After publicity, and should there be no objection or dissent, the candidates are included on the national list of green mines.

(2)   Directory management

To reward mines included on the green mine list and urge them to sequentially fulfill their obligations, the management of the green mine list is implemented by the Land and Resource Management Departments. It mainly includes supervision mechanisms, incentive policies, and degradation mechanisms [14].

i.   Supervision mechanisms. The green mines on the national list are open to the public and subject to supervision. The Natural Resource Regulatory Department conducts on-site inspections of the green mines. If the construction levels of mines do not meet the green mine standards, the mines will be ordered to rectify the matter and excluded from the list. Meanwhile, each province's natural resource management departments conduct spot checks on green mines per the requirements of "double random and one disclosed inspection" [37].

ii.   Incentive policy. The green mines on the list can enjoy corresponding incentive policy support, and the green mines ordered to rectify cease to enjoy incentive policies.

iii.   Degradation mechanisms. The relevant departments will re-include the mines that passed the rectification process on the green mine list. The mines with unqualified rectification are removed from the list and no longer enjoy incentive policies.

2.3.4. Evaluation and Certification of Green Mine Levels

In general, the green mines on the national list have experienced self-assessment and third-party evaluations during the declaration process. Self-assessment refers to the preparation of self-assessment reports by mining enterprises or relevant evaluation institutions entrusted by mines to meet the related construction standards for green mines. Units recognized by the commission can also be invited to certify the construction levels of mining enterprises [35]. Once certified, the mine continues to implement green mine construction based on its deficiencies. After submitting the green mine application, the government department will purchase a third-party assessment service to rate whether the mine meets the green mine construction specifications in accordance with the "Implementing Opinions on Accelerating the Construction of Green Mines", "nine industry standards", "The Green Evaluation Indicator System", and other specifications [38]. The assessment process is shown in Figure 11.
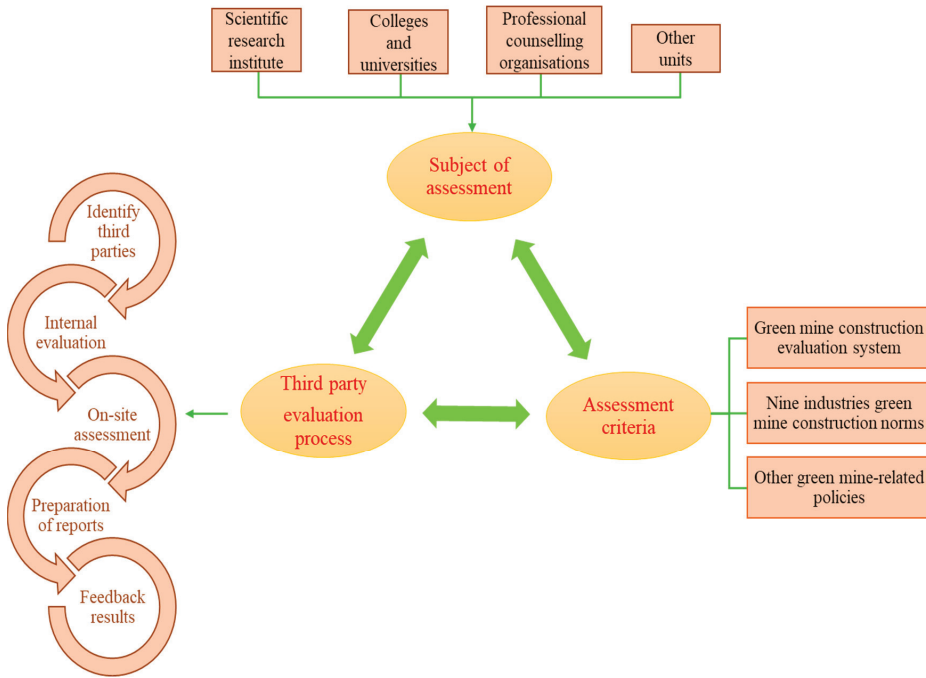
Figure 11. Third-party evaluation flow chart.

3. Parameters of Green Mines

To improve the level of comprehensive utilization of mine resources, reduce energy consumption and emissions, increase scientific and technological innovation and intelligent mine construction, and explore the stability of the mining area, the concept of green development and safety in production exists throughout the whole construction process of green mines to create safe, efficient, economical, and environmentally-friendly mines. The key points for the construction of green mines [39] are shown in Figure 12.
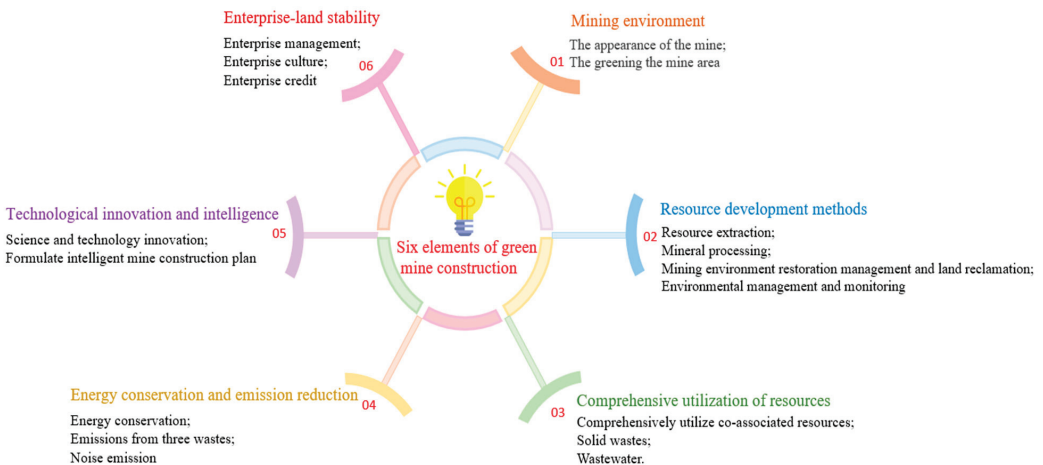
Figure 12. Key points of construction of green mines.

3.1. Mining Environment

Nearly 53,000 square kilometers of geological environment have been damaged in China, of which the seriously damaged areas account for 50% to 60% of the total area [40]. In addition, the types of mines in China are complex, and the mining methods are diverse, with different degrees of damage to the environment. Therefore, it is necessary to reasonably choose the governance measures according to the actual situation, which will not only improve the quality of mining but also promote the restoration of the mining environment. The main starting point is the appearance of the mine and the greening of the mine area.

For the appearance of the mine, combined with safety, environmental protection, practicality, and other factors, the function of the mine is a standardized layout. For example, the living area and production area are arranged in the safety zone, not less than 300 m away from the mine; the production area has set up the corresponding signboards, and the management of materials, equipment, and wastes is standardized [41]. The facilities in the mining area, such as water, roads, sanitation, etc., are fully equipped to ensure an orderly life. In addition, the living garbage is properly treated and utilized. And there are no private buildings on the mine site. The greening of the mining area should be in harmony with the original ecological environment and not affect the overall harmony of the natural environment of the surrounding area. The greening of the mine area is fully covered, a greening guarantee mechanism has been established, and the mine area is beautified based on local conditions [42]. More importantly, a systematic assessment and monitoring of geological hazards, terrain and landscape impacts, aquifer damage, soil and water environmental pollution, and land damage caused by mining should be conducted. Based on the evaluation and monitoring, corresponding land reclamation measures should be taken, and the mining area environment should be coordinated with the local natural landscape after treatment.

3.2. Resource Development Methods

The detailed demands for the construction of green mines in four aspects. i.e., resource extraction, mineral processing, mining environment restoration and management, land reclamation, and environmental management and monitoring, are described as follows [27].

(1)   Resource extraction

To meet the quality requirements of the mining face for green mining construction, a reasonable mining scale, mining sequence, mining technology, and equipment are selected based on the geological conditions of the ore body and the characteristics of the ecological environment. During the mining process, solid, liquid, and gas waste is disposed of in a timely and standardized manner [43]. Adopting mining methods can effectively reduce large-scale surface subsidence or uniform subsidence, such as backfill mining, water conservation mining, and other mining processes. To achieve intelligent production and control of various production links and the entire production process indicators, mechanized mining equipment with low energy consumption, low noise, low dust generation, and complete and effective safety protection devices is used. By adopting advanced technology and equipment such as unmanned mining vehicles and intelligent coal mining machines, mines are gradually realizing the mechanization of mining transportation systems, greening mining methods, and improving safety in mining operations.

(2)   Mineral processing

To minimize pollution to the environment, efficient, low energy consumption and low pollution equipment and processes should be selected. In addition, according to the characteristics of water quality, mining enterprises should design the wastewater treatment system, and mine water and domestic sewage treatment stations should have complete treatment functions. The appropriate dust removal and dust reduction equipment should be installed.

(3)   Mining environment restoration management and land reclamation

The designated areas should be treated and reclaimed to achieve the restoration of ecosystem functions and coordination with the surrounding environment according to the mining geological environment restoration and land reclamation project.

(4) Environmental management and monitoring

Mining enterprises should obtain environmental management system certification, ensure that environmental protection facilities are complete, and establish emergency response mechanisms. In addition, it is necessary to establish an environmental monitoring mechanism in accordance with the relevant regulations of environmental monitoring to dynamically monitor the geological environment, reclamation area, noise, and pollutants in the mining area so as to have a comprehensive understanding of the situation of environmental pollution in mines and take timely measures.

3.3. Comprehensive Utilization of Resources

The comprehensive utilization of resources varies across different industries. Referring to the Mineral Resources Development and Utilization Program or other standards, the mines choose appropriate processing technology to comprehensively utilize co-associated resources, solid wastes, and wastewater. Low-grade ores that are complex and difficult to process are utilized to improve technical and economic indexes by adopting combined processing and metallurgical processes. Enterprises should practically dispose of topsoil and recover valuable elements or useful minerals from solid waste. The solid waste that cannot be recycled is fully utilized through backfilling, paving, and other ways, striving to achieve zero resource discharge [44]. In addition, tailings containing mainly calcite and quartz can be used as raw materials for cement [45]; tailings containing mainly quartz or feldspar can be used as raw materials for ceramics [46]; tailings containing Fe, Zn, Cu, Mo, B, and other trace elements can be used as soil conditioner [47]; tailings that cannot be recovered can be used as underground filling material. Wastewater disposal and comprehensive utilization need to be equipped with corresponding wastewater treatment facilities and recycling systems [48]. Currently, the treatment of acidic wastewater from mines can be categorized into chemical, physicochemical, microbiological, and wetland methods. According to the nature and output characteristics of different mine wastewater, its treatment process and reuse methods are also different.

3.4. Energy Conservation and Emission Reduction

It mainly includes energy conservation, emissions from three wastes, and noise emissions.

(1) Energy conservation

The enterprise establishes a whole-process energy consumption management system and obtains energy management system certification. The energy consumption of each process should be analyzed according to the actual situation of the extraction process. Mining enterprises can optimize the equipment and simplify the process line of those processes whose energy consumption does not meet the standard. In terms of energy consumption in mines, carbon emissions from electricity and transportation consumption account for a large proportion. Therefore, mines should rationally utilize clean energy and adopt unmanned driving to reduce carbon emissions. It is necessary to increase scientific research investment in mining technology and equipment to reduce energy loss through new equipment and technologies [49].

(2) Emissions from three wastes

A list of major dust-producing points is created, and drainage pipes and drains are properly installed. The dust generated in the mining process is processed through appropriate dust removal measures, and wastewater from the extraction process is discharged after treatment. For solid wastes that cannot be completely utilized, they are graded and classified or disposed of according to the corresponding regulations.

(3) Noise emission

Noise emissions should be sorted and analyzed according to the process to form a noise control list. The noise generated in the extraction process is treated with noise reduction and discharged after meeting the standards.

3.5. Technological Innovation and Intelligence

It mainly includes technological innovation and intelligent mining.

(1)   Science and technology innovation

The enterprise establishes a research and development team of full-time technical personnel and formulates a technology research and development management system. A collaborative innovation system between the industry, academia, research, and utilization is established, and workers are encouraged to participate in their enterprise's scientific and technological innovation. It is imperative to summarize the scientific and technological achievements, support technological transformation, and select the mining processes, technologies, and equipment that the country encourages, supports, and promotes.

(2)   Formulate an intelligent mine construction plan

Build a centralized automation control platform. Implement the processes of three-dimensional reserve management. Develop a production automation system, remote video monitoring system, intelligent working face or unmanned mining vehicle system, and online monitoring system for the mining environment [50].

With the arrival of the 5G era, a number of mining enterprises have introduced the Internet of Things, big data, artificial intelligence, and other advanced technologies to build a dynamic visual three-dimensional geological model, intelligent truck scheduling, all-round video surveillance, real-time monitoring of dust, automation and intelligent distribution of six systems, so that the enterprise production is safer, more efficient use of resources, more environmentally friendly mining methods. For example, loaders, excavators, and other parts of the product line have been mechanized and electrified with a 5G remote control, which improves mining efficiency, reduces carbon emissions, and lowers noise [51].

3.6. Enterprise-Land Stability

The establishment of a practical green mine management system is an indispensable guarantee to maintain order at a mine. At the same time, mining enterprises should improve the production safety responsibility system and establish all production safety management procedures and safety operation procedures to guarantee the safety standardization of the production process. For slope disasters caused by open-pit mining, surface displacement monitoring, internal rock displacement monitoring, and water pressure monitoring are used to control the internal structure of the rock mass and groundwater permeability and increase slope stability. Retaining walls, anchors, anti-slip piles, grouting, and reinforcement methods are adopted to prevent landslides, minimize damage to the surrounding land, and improve the stability of the slopes [52]. The underground mining goaf is mainly treated by setting up isolation walls and observation points, filling them with waste rocks, and collapsing surrounding rocks to reduce disturbance and damage to the land [53]. Among them, waste rock filling can also reduce the occupation of land by waste rock. Enterprises should establish a mining equipment management system, functional area management system, occupational health management system, and environmental protection system. In accordance with the green mine training system and plan, regular training is organized for mine personnel. The dress code for those who enter the site must meet safety requirements. The enterprise must care for its employees, organize regular medical checkups for them, and conduct cultural activities to promote the construction of a green mine culture for the mining enterprise. In addition, the mine pays taxes according to the law, fulfills relevant obligations, cooperates with neighboring residents, and participates in public welfare activities.

4. Discussions

4.1. Construction Achievements

Over the past decade, various regions have promoted policies and regulations, gradually improving upon them, which has led to significant achievements in green mine construction and the overall image of the mining industry. In 2017, six ministries, including the former Ministry of Land and Resources, promulgated the Implementation Opinions on Accelerating Green Mine Construction, officially marking the beginning of China's journey into green mine construction. It symbolizes the transformation of green mine construction with Chinese characteristics from point to surface [54]. Concurrently, a preliminary framework of policies and regulations related to green mines has been established, such as the Regulations on the Protection of Geological Environment in Mines [55], the National Green Mine Construction Standards, and the Green Mine Construction Standards for Nine Major Industries [56]. In accordance with the China Mineral Resources Report (2022) issued by the Ministry of Natural Resources, more than 1100 national-level green mines and 50 green mining development demonstration areas will be constructed by the end of 2021. In 2020, 301 mines were included in the National List of Green Mines [57]. These 301 mines were determined based on their locations and mine types. Xinjiang had the highest number of selected mines, totaling 20. The western region had the highest number of mines on the list. Non-metallic mineral resources account for the largest proportion. Figure 13 displays the number of national green mines by province. Figure 14 analyzes the national green mines in 2020 by mine type and location.
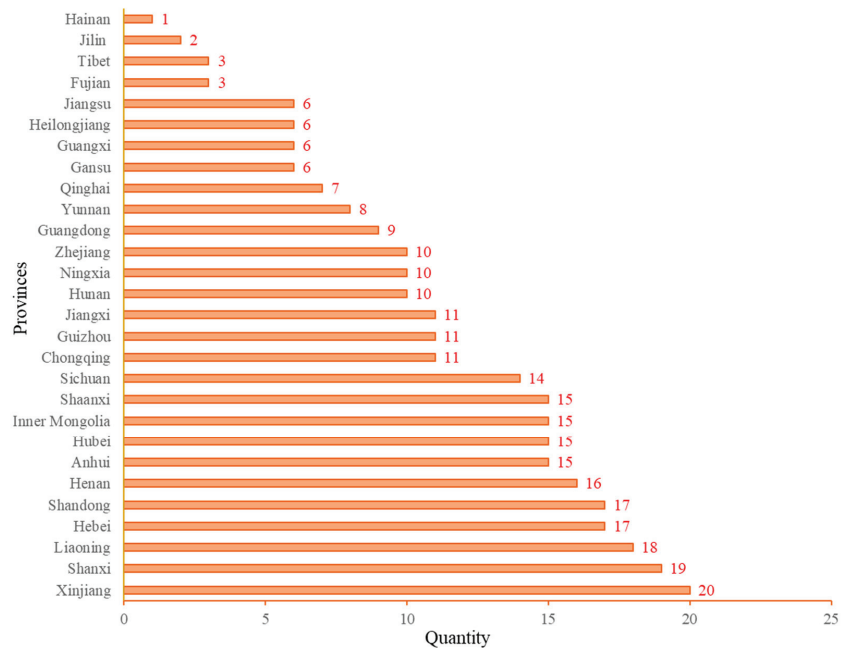
Figure 13. Number of mines included in the National List of Green Mines in 2020 by province (data from [57]).
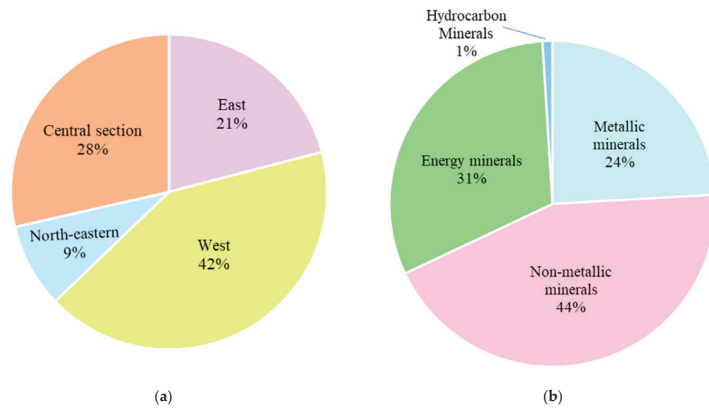
Figure 14. Structural analysis of the 2020 National List of Green Mines (data from [57]). (**a**) Regional analysis; (**b**) Mineral analysis.

4.2. Developing Directions of Green Mines

Since the creation of green mines, green mine models have emerged in China, mainly including green technology mining, modern mining operations, stable mining areas, and the ecological restoration of mines [58,59].

(1) Green technology mining

The core of the green mining model is to realize efficient and intensive mining of resources and the maximum protection of the ecological environment with green technology so that resource extraction and the environment can achieve a unified green mining development mode. Green mining technologies include fill mining, water retention mining, clean mining, etc. [60]. Figure 15 shows the tailings filling system of the green mining.
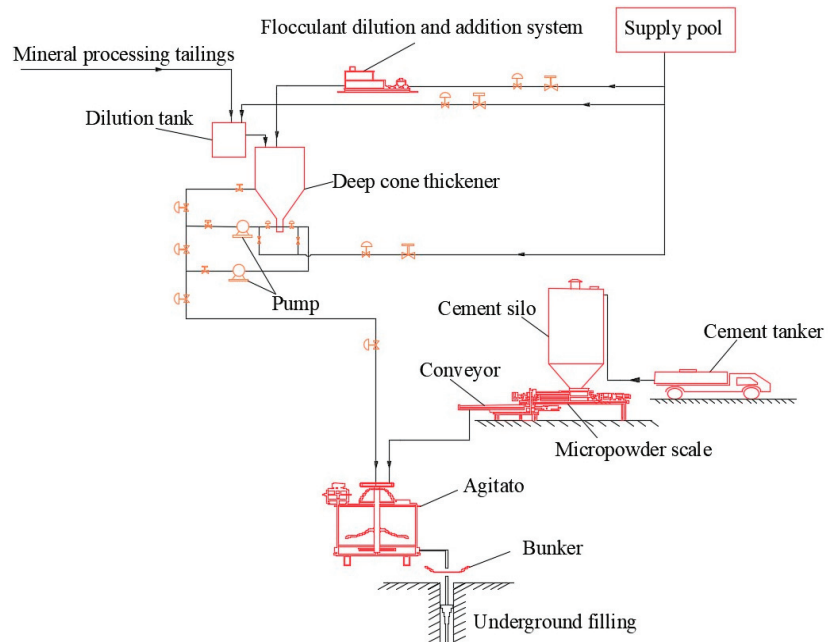
Figure 15. Flow diagram of the filling process (adapted from [61]).

(2)   Modernization of mining operations

Among the 661 pilot units, over 90% of them integrate modern network technology and automatic control technology throughout the entire production and operation process, achieving a beneficial situation for both the economy and the environment. For example, building a smart mine platform allows for equipment to be automated remotely to create smart mines and smart mining areas [62–64].

(3)   Stability in mining areas

Stability in a mining area means that mining enterprises should fulfill their social responsibilities in the pursuit of development, realizing the coexistence between the mining enterprises and surrounding communities, the promotion of mining development and regional economic development, the coordination of mineral extraction and environmental protection [65]. The paradigm is the Yunnan Phosphatization Hanying model. Figure 16 shows the stable development of economic, environmental, and cultural construction between the Yunnan Phosphorus Chemical Group and Hanying Village through the "321" working mechanism [66].
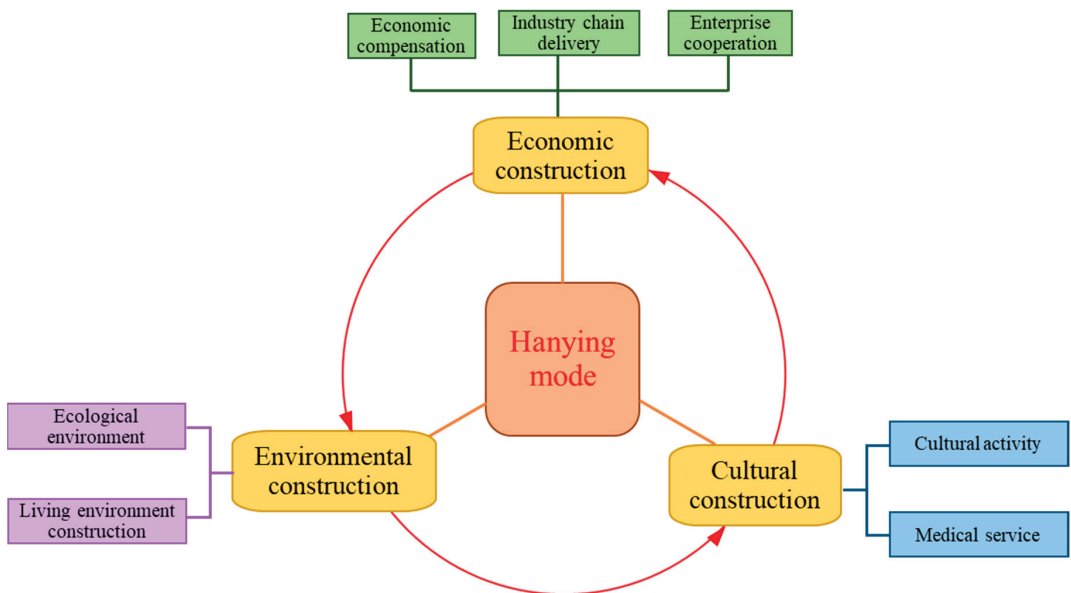
Figure 16. Schematic diagram of Hanying "321" model (adapted from [66]).

(4)   Ecological restoration of mines

Mine ecological restoration refers to the optimal restoration of the original appearance or value of the damaged land and environment around the mining area through a series of restoration technologies. The ecological restoration models of mining areas include the re-greening model, the mine park model, and the tourism landscape model [67,68].

4.3. Future Goals for Green Mine Construction

(1)   High-quality development contributes to green mining

Currently, problems exist in green mine construction in China, e.g., insufficient enthusiasm for some mines, inadequate evaluation criteria systems, and a low proportion of small-scale mines [14]. Therefore, the mines that are close to profitability should optimize the industrial structure and take the road of intensification. Small mines are intensive into medium-sized mines, while medium-sized mines should be concentrated into large mines.

It is necessary to vigorously promote technological innovation, transform the development model of mining, and breakthrough key technologies that present bottlenecks [69]. Advanced mining and beneficiation processes should be adopted, novel equipment should be used to improve the utilization rate of resources, energy consumption during mining operations should be reduced, and a beneficial relationship between the mine and nature should be achieved.

(2)   Promoting green mine construction overall with a focus on points and areas

The green mine construction is the "point", and green mine demonstration areas are the "surface". Mines with remarkable results in green mine construction are selected as demonstration sites. The government actively guides and promotes institutional innovation, management innovation, institutional innovation, point driven areas and achieves centralized integration through the process, thus promoting the development of green mines across the entire region [70].

4.4. Main Measures for Green Mine Development and Construction

(1)   Mining enterprises

The mining enterprises should fully recognize the necessity of developing green mines, take active measures to establish green mines, and practice the concept of green development. Mines should try their best to increase scientific and technological innovation to promote the transformation and upgrading of the mining industry. In addition, according to existing policy norms, the enterprises design the green mine construction plans and conduct self-assessments according to green mine standards [14]. Then, the mining enterprises make timely corrections to improve their deficiencies.

(2)   Government

    i.   Improve the policies and formulate the standards for green mines. The nine industry standards and specifications of green mines released in 2018 do not cover aquatic minerals, radioactive minerals, and other types of minerals [71]. Meanwhile, the issued standards are not applicable to different mines; therefore, it is indispensable for the government to improve the standard construction policies of green mines. Differentiated standards and detailed requirements should be formulated for mines with different scales, stages, and locations [38].

    ii.   Improve the guarantee system for the execution of green mine policies. The government should implement incentive policies for green mining enterprises in terms of land usage, mining, finance, and funding [70]. The mines that meet the relevant green mine requirements should be exempted from taxes.

    iii.   Strengthen publicity and implement regulatory responsibilities. Enterprises actively convene green mine construction exchanges and training sessions to promote mutual learning and progress in various places. Relevant departments implement regulatory responsibilities, conduct random spot checks, guide, and urge mines to rectify problems on time. The mines that do not meet the requirements are promptly removed from the list of green mines.

5. Conclusions

With the environmental impacts of mining, including three-waste emissions, ground deformation, geological disasters. Occupation and destruction of land, pollution of groundwater resources. It is important to note that, at the same time, as a traditional high-energy consuming industry, mining consumes a large amount of energy. It emits greenhouse gases, so the construction of green mines has become an inevitable trend in the development of the mining industry under the impetus of the dual-carbon target. Over the decade of pushing forward, from pilot exploration to comprehensive promotion, from demonstration sites to demonstration zones, more than 1250 national green mines have been constructed, and four typical green mine models have been developed, achieving significant achievements in

the construction of green mines. However, there are still some problems, e.g., unbalanced regional development, insufficient understanding of green mine construction by some enterprises, imperfect policies and standard systems, etc. Therefore, the construction of green mines in the future requires the joint efforts of enterprises, governments, and society, in accordance with the development model of "government-led, enterprise-oriented, association support, policy guarantee, and market operation", to promote the continuous exploration and innovation of technologies and methods for green mine construction. The government should perfect the policies and standard system, increase the financial support, and strengthen the supervision and management of existing green mines. Enterprises should formulate the construction plan of "one policy for one place and one policy for one mine", provide positivity and initiative, speed up the upgrading and transformation in line with local conditions, and gradually meet the standards of green mine construction. In addition, to achieve breakthroughs in low-carbon technology and efficient resource utilization, promote green and low-carbon development of mines, and reduce carbon emissions, enterprises should carry out research and development of "energy-saving, low-carbon key technologies" and ecological restoration of mines and implement the "two mountains" theory throughout the entire process of mining development, so that sustainable development of China's mines can be promoted. With the joint efforts of the government, enterprises, and others, we will promote the high-quality development of the mining industry and realize a new situation in the development of the mining industry.

References

1. Yang, S.S. Current situation of China's mineral resources and countermeasures. *Sci. Technol. Innov. Her.* **2010**, 70. [CrossRef]
2. He, W.P.; Mei, J.H.; Li, J. Characterization of heavy metal content and environmental impact of tailings from tailings ponds in Kakizhuyuan mine area in southern Hunan. *Land Resour. Guide* **2016**, *13*, 22–26.
3. Zhou, Q.; Li, C.Z. Evaluation of the effectiveness of comprehensive management of coal mining subsidence area in Shanxi Province. *Chem. Manag.* **2021**, *29*, 9–10.
4. Yuan, S.; Sun, B.; Han, G.; Duan, W.; Wang, Z. Application and Prospect of Curtain Grouting Technology in Mine Water Safety Management in China: A Review. *Water* **2022**, *14*, 4093. [CrossRef]
5. Yang, H.H.; Wu, D. International Energy Agency releases report on global carbon dioxide emissions in 2022. *World Oil Ind.* **2023**, *30*, 80–81.
6. Liu, X.H. New Answer Sheet for Green Development of Mining Industry under the Target of "Double Carbon", China Geological Survey. [EB/OL]. Available online: https://www.cgs.gov.cn/ddztt/jdqr/dqr54/jsdwhd/202304/t20230421_729878.html (accessed on 21 April 2023).
7. Wang, C.; Zhang, Y.X. Pathways and policy systems for realizing the vision of carbon neutrality. *China Environ. Manag.* **2020**, *12*, 58–64. [CrossRef] [PubMed]
8. Geologic Cloud. Available online: https://geocloud.cgs.gov.cn/ (accessed on 19 December 2023).
9. Liu, Y.Q. *Connotation, Development Status and Future of Green Mines in China*; China Cement Green Mining Advanced Workshop: Beijing, China, 2013.

10. Chen, J.; Zhao, K. Analysis of the conceptual connotation of green mine and its system composition points. *World Nonferrous Met.* **2019**, *17*, 260+263.
11. Sun, Y.X. Overview and reflection on the current situation of green mine construction research in China. *China Land Resour. Econ.* **2020**, *33*, 35–40+85.
12. Oil and Gas Exploration and Development in the Context of Major Changes [EB/OL]. Available online: http://center.cnpc.com.cn/sysb/system/2023/03/29/030097196.shtml (accessed on 30 March 2023).
13. Global Coal Supply and Demand Pattern Analysis in 2020 China's Coal Storage and Production Ratio Is Far Lower than Other Countries. [EB/OL]. Available online: https://www.qianzhan.com/analyst/detail/220/201010-8d8a4178.html (accessed on 10 October 2020).
14. Li, S.T. Prospects for China's economic growth from the 12th Five-Year Plan period to 2030. *Econ. Res. Ref.* **2010**, 2–27. [CrossRef]
15. An Article to Read the Characteristics of the Distribution of the World's Mineral Resources [EB/OL]. Available online: http://www.58188.com/new/2017/3-2/112999.html (accessed on 2 March 2017).
16. China releases its first global mining development report. *Gold Sci. Technol.* **2019**, *27*, 658. Available online: https://cn.chinadaily.com.cn/a/201910/11/WS5da01abaa31099ab995e4b45.html (accessed on 27 December 2023).
17. 2019 Global Mining Development Report (Excerpt). *Geogear* **2020**, *21*, 43–48.
18. Global Mining Development Report 2023 released. *Gold Sci. Technol.* **2023**, *31*, 793.
19. China is Steadily Becoming the World's Largest Producer and Consumer of Mineral Resources [EB/OL]. Available online: https://news.gmw.cn/2019-10/19/content_33246594.htm (accessed on 19 October 2019).
20. National Bureau of Statistics. Available online: https://www.stats.gov.cn/english/ (accessed on 25 August 2023).
21. Co-Research Network. Available online: https://www.gonyn.com/ (accessed on 25 August 2023).
22. Ministry of Natural Resources of the People's Republic of China. Available online: https://m.mnr.gov.cn/dt/ywbb/202209/t20220921_2759600.html (accessed on 21 September 2023).
23. Mines Blowing Green Wind—China's Green Mine Construction Tour [EB/OL]. Available online: https://www.cgs.gov.cn/gzdt/dzhy/201606/t20160628_334568.html (accessed on 21 April 2016).
24. National Green Mine Policy Interpretation [EB/OL]. Available online: https://www.sohu.com/a/260544306_99986028 (accessed on 20 October 2018).
25. Guan, F.J. Strengthening mining geological environmental protection and promoting the construction of ecological civilization. *China Environ.* **2014**, *1*, 47–50.
26. Green Mining Events [EB/OL]. Available online: https://www.mnr.gov.cn/dt/ywbb/201910/t20191009_2470066.html (accessed on 9 October 2019).
27. Ministry of Natural Resources releases green mine evaluation index. *Gold Sci. Technol.* **2020**, *28*, 449.
28. National Mineral Resources Plan (2016–2020) released. *China Min.* **2017**, *26*, 151.
29. Provisions on geological environmental protection of mines. *Bull. State Counc. People's Repub. China* **2009**, *7*, 32–35.
30. Guidelines of the Ministry of Land and Resources on the Implementation of the National Mineral Resources Plan for the Development of Green Mining and the Construction of Green Mines. *Land Resour. Newsl.* **2010**, 29–32. Available online: https://baike.baidu.com/item/%E5%9B%BD%E5%9C%9F%E8%B5%84%E6%BA%90%E9%83%A8%E5%85%B3%E4%BA%8E%E8%B4%AF%E5%BD%BB%E8%90%BD%E5%AE%9E%E5%85%A8%E5%9B%BD%E7%9F%BF%E4%BA%A7%E8%B5%84%E6%BA%90%E8%A7%84%E5%88%92%E5%8F%91%E5%B1%95%E7%BB%BF%E8%89%B2%E7%9F%BF%E4%B8%9A%E5%BB%BA%E8%AE%BE%E7%BB%BF%E8%89%B2%E7%9F%BF%E5%B1%B1%E5%B7%A5%E4%BD%9C%E7%9A%84%E6%8C%87%87%E5%AF%BC%E6%84%8F%E8%A7%81/10237886?fr=aladdin (accessed on 21 April 2016).
31. Six Departments Jointly Issue Opinions on Implementing Opinions on Accelerating the Construction of Green Mines. *Rare Earth Inf.* **2017**, *5*, 37.
32. The "14th Five-Year Plan for Promoting High-Quality Development of Resource-Based Regions" was released to increase the exploration of strategic mineral resources such as oil and rare earths. *Rare Earth Inf.* **2021**, *6*, 30–34.
33. Department of Natural Resources of Shandong Province, Department of Finance of Shandong Province, Department of Ecology and Environment of Shandong Province, Shandong Province Market Supervision Administration, Shandong Supervision Bureau of China Banking and Insurance Regulatory Commission, Shandong Supervision Bureau of China Securities Regulatory Commission on the issuance of the notice on the management measures for the construction of green mines in Shandong Province. *Bull. People's Gov. Shandong Prov.* **2019**, 7–10. Available online: http://jnxdn.jining.gov.cn/Article/ArticeDetail/bd4ffff98bf04fd3820f5f03d8f23a02 (accessed on 21 April 2016).
34. Notice of the Natural Resources Department of Shanxi Province on the Issuance of the Guiding Opinions on Comprehensively Promoting the Construction of Green Mines in Shanxi Province [EB/OL]. Available online: https://zrzyt.shanxi.gov.cn/ztzx/jjhy/gcls/202301/t20230118_7819527.shtml (accessed on 27 January 2022).
35. Dong, Y.; Hou, H.L.; Sun, Y.X. Research on the management of green mine list. *Economist* **2020**, *9*, 17–19.
36. Journal. Green mine selection for 2020 kicks off on June 1. *Stone* **2020**, *6*, 31.
37. Circular of the General Office of the Ministry of Natural Resources on the Field Sampling and Verification of Green Mines in 2023 [EB/OL]. Available online: http://gi.mnr.gov.cn/202306/t20230606_2790383.html (accessed on 2 June 2023).
38. Zhang, Y.L.; Chen, L.P.; Chen, J. Policies, Challenges and Suggestions for Green Mine Construction in China. *Land Resour. Intell.* **2018**, *10*, 48–60.

39. Wang, L.; Hu, T.T.; Deng, J.S. Research on green mine evaluation index practice. *Mod. Min. Ind.* **2023**, *39*, 255–260.
40. Fan, Y.P. Discussion on the current situation and change strategy of mining geo-environmental management. *China Met. Bull.* **2023**, *239*, 210–212.
41. Zhang, X.D. Improvement and upgrading of green mine construction in Zhaokou. *Shandong Metall.* **2023**, *45*, 56–57+62.
42. Liu, J.; Sun, L.; Chen, J. Research on the green mine construction planning of Sinohydro Huaian Salt Chemical Manganite Mine. *Jiangsu Sci. Technol. Inf.* **2023**, *40*, 68–70.
43. Miao, Y.C. *Research on the Way of Green Mine Construction in Daye Iron Mine*; Hubei University: Wuhan, China, 2013.
44. Chen, M. Research on the current situation of solid waste utilization and management countermeasures. *Agric. Technol.* **2013**, *33*, 228–231.
45. Zhang, X.; Wang, J.Q.; Wang, D.M. Research progress on the preparation of cement and concrete from gold tailings. *Silic. Bull.* **2022**, *41*, 3121–3128.
46. Wang, Z.M.; Du, M.Y.; Yao, G.; Wang, Q.; Zhao, W.; Xia, C.B.; Liu, Q.; Sun, S.K.; Jia, Z.; Lu, X.J. Study on the influencing factors of pore structure and crystal phase in the synergistic preparation of porous ceramics using alkali slag and gold tailings. *J. Shandong Univ. Sci. Technol. (Nat. Sci. Ed.)* **2022**, *41*, 65–74.
47. Chen, Z.L.; Xi, F.M.; Yin, Y.; Wang, J.; Bing, L.; Hu, Q. Direction and benefit assessment of resource utilization of iron tailings in Anshan. *Chem. Miner. Process.* **2022**, *51*, 43–47.
48. Chinese Academy of Geological Sciences, China Cement Association, Helo Cement Group Co. *Specification for Green Mine Construction of Hydraulic Limestone*; Ministry of Natural Resources of the People's Republic of China: Beijing, China, 2018.
49. Wang, Y.H. Measures for energy-saving mine construction. *Min. Equip.* **2022**, *5*, 184–185.
50. Yang, X. Intelligent Mines Need to Be carefully Plowed. *China Natural Resources News*, 7 February 2023.
51. Chen, D.Y. "Intelligent" Transformation for Mining Development—Excerpts from Experts' Opinions in China-ASEAN Green Mining Enterprise Development Seminar. *South Nat. Resour.* **2023**, *6*, 21–23.
52. Li, X.; Li, X.D. Research on factors affecting slope stability and prevention measures of open pit mining. *Sci. Technol. Wind.* **2017**, *25*, 114.
53. Zhang, X.H.; Niu, J.P.; Cheng, X.H. Research and application of the management and monitoring program of a copper mine in Xinjiang. *China Min. Ind.* **2022**, *31*, 78–83.
54. Li, D.X. Research on the construction of small-scale green mines: A case study of a small-scale gold mine in Henan Province. *China Min. Ind.* **2022**, *31*, 68–74.
55. New version of Provisions on Geological Environmental Protection of Mines released. *China Nonferrous Met.* **2019**, *10*, 24.
56. The Ministry of Natural Resources (MNR) Releases Green Mine Construction Specifications for Nine Industries [EB/OL]. Available online: https://www.mnr.gov.cn/dt/kc/201807/t20180702_2322536.html (accessed on 2 July 2018).
57. Announcement of the Ministry of Natural Resources on the Inclusion of Mines Such as Caijiaying Zinc Mine of Hebei Hua'ao Mining Development Co. into the National Green Mine List [EB/OL]. Available online: http://gi.mnr.gov.cn/202101/t20210111_2597719.html (accessed on 11 January 2021).
58. Ma, L. *Research on the Evaluation of the Development Level of Green Mines in China and the Development Mode and Long-Term Mechanism*; China University of Mining and Technology: Xuzhou, China, 2019.
59. Summary of Green Mine Construction Mode, Green Information, Zhong Guancun Green Mine Industry Alliance [EB/OL]. Available online: http://www.greenmine.org.cn/index.php/shows/31/9485.html (accessed on 10 November 2018).
60. Wang, Y.J. On the Resource Science Basis of Green Development of Mining Resources. *Resour. Sci.* **2005**, *27*, 14–19.
61. Huang, J.J.; Chen, A.M.; Liang, S.Y. Design practice of full tailing paste filling system for a copper mine in Yunnan. *Nonferrous Met. Des.* **2022**, *49*, 1–5+21.
62. "Underground World" 3D Presentation! Kaos Helps Jinding Mining Build Digital Twin Intelligent Brain_China.com [EB/OL]. Available online: https://baijiahao.baidu.com/s?id=1742462487070777054&wfr=spider&for=pc (accessed on 29 August 2022).
63. Shang, H.T.; Song, T.; Zhou, D.Y. Intelligent transformation of No.1 coal processing plant of Huangling Mining. *Manuf. Upgrad. Today* **2022**, *8*, 29–31.
64. Zibo City, Green Mine Construction again Received Good News: Shandong Jinding Mining Co., Ltd. Was Selected by the Ministry of Natural Resources, Intelligent Mine Construction Specification through the Standard Pilot Unit-Member Activities-Zhongguancun Green Mining Industry Alliance [EB/OL]. Available online: https://www.163.com/dy/article/HI7HHGL20530JPVV.html (accessed on 26 September 2022).
65. Wang, J. *Research on Community Relations of Mining Enterprises in China*; China University of Geosciences (Beijing): Beijing, China, 2017.
66. Wang, J.; Huang, H.; Hu, K.; Cui, Z.; Li, X. Research on corporate community relations and corporate community participation—Taking the "Hanying model" as an example. *Manag. Case Study Rev.* **2017**, *10*, 247–261.
67. Wu, J.X.; Zhang, X.; Li, X. Research on ecological restoration mode and technology of mine waste land. *Mod. Commer. Ind.* **2015**, *36*, 83–84.
68. Guo, X.F. Geological environmental impact assessment and ecological restoration of abandoned mines. *Reg. Gov.* **2019**, *14*, 116–118.

69. Liu, L.S.; Yu, B.; Wu, C.P.; Cui, S.; Hou, G.; Guo, L. Current situation and case analysis of green mine construction in China. *Nonferrous Met. Eng.* **2020**, *10*, 98–103.

70. The person in charge of the Ministry of Land and Resources interprets the Implementation Opinions on Accelerating the Construction of Green Mines. *Land Resour.* **2017**, *6*, 28–29.

71. Li, X.R.; Shen, W.J.; Li, R.J.; Yu, C.; Liu, Y. Reflections on the standardization work of green mine construction. *China Land Resour. Econ.* **2020**, *33*, 35–39.

Article

Regional Division and Its Criteria of Mining Fractures Based on Overburden Critical Failure

Erhu Bai [1,2,3], Wenbing Guo [1,2,3], Yi Tan [1,2,3,*], Mingjie Guo [1], Peng Wen [1], Zhiqiang Liu [1], Zhibao Ma [1] and Weiqiang Yang [1]

[1] School of Energy Science and Engineering, Henan Polytechnic University, Jiaozuo 454003, China; baieh@hpu.edu.cn (E.B.); guowb@hpu.edu.cn (W.G.); 111702010008@home.hpu.edu.cn (M.G.); wenpengcumt@126.com (P.W.); liuzhiqiang@hpu.edu.cn (Z.L.); 111902010009@home.hpu.edu.cn (Z.M.); 211902010009@home.hpu.edu.cn (W.Y.)

[2] Henan Key Laboratory for Green and Efficient Mining & Comprehensive Utilization of Mineral Resources, Henan Polytechnic University, Jiaozuo 454003, China

[3] State Collaborative Innovative Centre of Coal Work Safety and Clean-Efficiency Utilization, Jiaozuo 454003, China

* Correspondence: tanyi@hpu.edu.cn; Tel.: +86-134-5317-7787

Abstract: Mining fracture is the key factor in realizing water-conservation mining, stability evaluation of coal mining subsidence areas, and accurate restoration of the surface eco-environment. To clarify, the evolution and distribution of mining fractures, based on the key strata theory and the mining degree of overburden failure, the contact state of rock stratum after overburden critical failure was analyzed, the formation mechanism of "saddle shaped" water conducting fracture zone was revealed, and the permanent mining fractures were determined to be primarily concentrated in the overburden structure at the boundary of the working face. According to the shear test of sandstone in the fracture zone, the damage degree of the rock sample was positively correlated with shear stress, and the overburden structure exhibited no instability. Based on the distribution of mining fractures, the fracture zone was divided into the original fracture, tensile fracture, structural void, and void compaction areas in the horizontal direction. The structural void area had the largest residual deformation in the goaf. A regional division method based on overburden critical failure was proposed and applied in engineering by using surface movement monitoring. The results showed that the surface subsidence near the boundary of working face was greater than that in the middle, and the residual surface deformation in the goaf was closely related to the mining time, which has long-term characteristics. The rationality of the regional division method of mining fractures was also verified.

Keywords: overburden critical failure; mining fractures; overburden structure; regional division; strata movement

1. Introduction

Underground coal mining produces disturbances equivalent to its mining volume, causing varying degrees of damage to the overburden in the form of the changing fracture field. Then, it might cause problems, such as soil and water loss, surface collapse, landslides, vegetation degradation, and debris flows, affecting the eco-environment and the safe mining [1–3], especially in coal mining areas with dense population, developed economy, resources depletion, and fragile eco-environment [4–6]. The effective control of overburden failure height is the key factor for realizing safe coal mining under water-bodies, water conservation mining, and effective protection of the water eco-environment. Its essence lies in overburden fracture distribution and evolution induced by coal mining [7–9]. Meanwhile, the overburden void is also the main reason for the surface residual subsidence, which plays an important role in revealing the formation mechanism of the surface residual

deformation and the rational utilization of the mining subsidence area. Therefore, the study of mining fractures based on overburden critical failure is vital for the development of green mining technology, efficient gas drainage, accurate stability evaluation, and efficient ecological restoration of subsidence areas.

The mining overburden failure is a result of the combined effect of geological, mechanical, and engineering disturbance [10,11]. Combined with the overburden movement and failure characteristics, Qian et al. indicated that the characteristics of overburden movement depended on the breaking of hard strata, and proposed the key strata theory and masonry beam structure model, which suggested the direction for strata movement and ground control [12]. Based on the location of key strata, Xu et al. proposed a method to predict the height of overburden failure, a potential indicator of water diversion fracture zone height [13]. Rezaei et al. established a time-independent analytical model to determine the height of water conduction fracture zone, which incorporates both possible influencing geometrical and geo-mechanical parameters [14]. Li et al. established a mechanical model to describe the rotational motion of the masonry beam structure formed in the key stratum, and obtained the angular velocity equation of the rotational motion of the wedge beam structure in the key stratum [15]. Compared with field measurement, simulation analysis and geophysical methods can more intuitively observe and study the whole dynamic change process of overburden deformation and failure [16,17]. Ghabraie et al. used the physical models to investigate the subsidence mechanisms, and pointed out that the incremental subsidence and substrata movement profiles after lower seam extraction can be separated into three different zones [18]. Ju et al. studied the physical simulation of overburden failure based on sand particle size, providing effective guidance for the design of coal mining parameters [19]. Asaue et al. used the MT method to clarify the overburden structure in a coal-mining area in Kushiro, Japan [20]. Yu et al. analyzed and clarified the relationship between the overburden failure height and advancing distance of the working face, and put forward a formula for predicting the maximum overburden failure height of an ultra-thick coal seam in longwall mining [21]. Mills et al. measured shear movements in the overburden strata ahead of longwall mining by inclinometers [22]. Based on the time-space settlement model of overburden movement established by Han et al. [23], the movement of overburden under an advancing speed was clarified, and the mining stress characteristics under different advancing speed were explained. Combined with the variation of expansion coefficient, Xu et al. clarified the relationship between fracture path parameters, fracture angle, panel width, and mining height, establishing the trapezoidal fracture model of overburden failure to study the overburden collapse mode [24]. According to the division of water diversion fractures, Cao et al. analyzed their seepage mechanical characteristics, and constructed the main channel distribution model of a water conduction fracture zone based on the breaking size of key strata at the panel boundary [25]. Karacan and Goodman (2009) presented the results of downhole monitoring studies performed to estimate the changes in hydraulic conductivity (mainly horizontal permeability) [26]. By employing the combination of the full view borehole photography and seismic CT scanner techniques, Li et al. studied the deformation and failure of overlying strata of a fully mechanized caving face in a shallow coal seam and determined the failure development of the overburden [27]. Based on the two-block voussoir beam, Hu et al. revealed the strain distribution at the voussoir beam joint using a digital image correlation system and obtained the relationship between the transverse load and midspan displacement of the voussoir beam [28]. Shi and Zhang used physical modeling, numerical simulation and field observation to analyze the distribution characteristics of the overburden fracture rate in goaf and determined that the rock fracture rate decreased logarithmically with the increase of the distance from the coal seam [29]. Majdi et al. presented five mathematical approaches for estimating the height of the destressed zone and argued that while the short-term height of the destressed zone ranges from 6.5 to 24 times the mining height, it is 11.5 to 46.5 times the mining height in the long term [30]. He et al. systematically studied the height of the water conduction fracture zone in the layered overburden through similarity simulation,

theoretical analysis, and engineering verification, and reflected on whether water inrush occurred in the coal mine by fracture penetration criterion value and compression tension ratio (i.e., the ratio of compressive to tensile stress) [31]. Guo et al. analyzed the relationship between the height of the water conduction fracture zone and the mining degree of the working face, proposed the definition of overburden critical failure, and put forward a prediction method of failure height based on overburden failure transfer theory [32].

Therefore, based on the key strata theory and the definition of overburden critical failure, combined with the overburden failure characteristics, with the mining fractures within the fracture zone as the research object, the overburden failure and structure formation conditions were analyzed in this study. Then, the regional division method of mining fractures was proposed, and its rationality was verified through surface movement and deformation monitoring, which provides a theoretical basis for safe mining under water-bodies, efficient gas drainage, and accurate ecological restoration of subsidence areas.

2. Overburden Critical Failure and Mining Fracture Distribution

The overburden failure height is the main index for realizing water-conservation mining, surface eco-environment protection, and green mine construction. The calculation accuracy lies in the development and distribution of overburden mining fractures [33–35], and the overburden mining fracture height depends on the mining degree of overburden failure. To accurately determine the mining degree of the overburden, the mining degree and characteristics of overburden failure must be analyzed.

2.1. Mining Degree of Overburden Failure

In recent years, the mining depth of coal mines in China extend downward by 8–12 m/year. For the strike longwall mining method, with the increase of mining depth, the ratio of panel size to mining depth gradually decreases. When it was less than 1.2–1.4, the mining degree of the working face changed from supercritical mining to subcritical mining. The surface movement and deformation did not generally reach the critical mining, which was the essence of realizing water-conservation mining, safe coal mining under buildings, and reduction of surface ecological environment damage. Based on the difference in the height of the water conduction fracture zone and the definition of mining degree, Guo and Lou defined overburden critical mining as the stage when the height of overburden failure reached the maximum under its geological conditions and did not increase with the increase of mining size [36]. Moreover, the theoretical discrimination method of overburden critical failure in longwall mining was proposed [37]. To further analyze the development characteristics and evolution of overburden failure height, combined with the definition of overburden critical failure (Figure 1), the characteristics of overburden mining degree were analyzed.
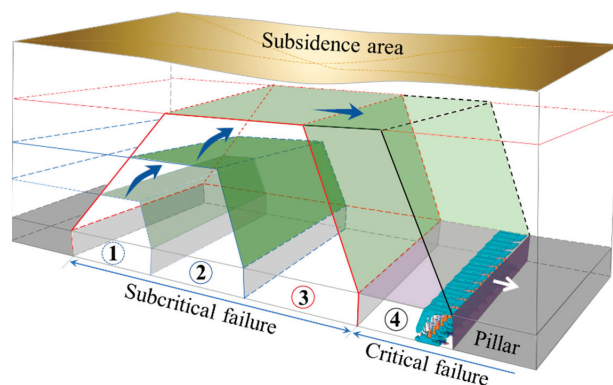
Figure 1. Diagram of overburden critical failure.

The above figure shows that when the overburden reaches critical failure, there will be a stable separation space at the junction of the fracture and bending zones. With continuous mining of the panel, the contact state of the rock interface in the middle of the goaf will change from no contact to point–surface, line–surface, and surface–surface contacts, and the separation space will gradually decrease under the load of the bending zone. At this time, the failure height of overburden reaches the maximum.

Based on the equivalent substitution principle and the definition of a surface subsidence basin, when the overburden reaches critical failure, there is only one maximum subsidence point at the top of the fracture zone. With the continuous advancement of the working face, the subsidence of the top rock stratum does not increase and has a flat bottom shape. The fracture shape in the water conduction fracture zone is similar to that of a subsidence basin, which is in line with the saddle shape of high at both ends and low in the middle (Figure 2). Therefore, the maximum separation height is equivalent to the mining height at the same location, and the mining impact will continue to transfer upward.
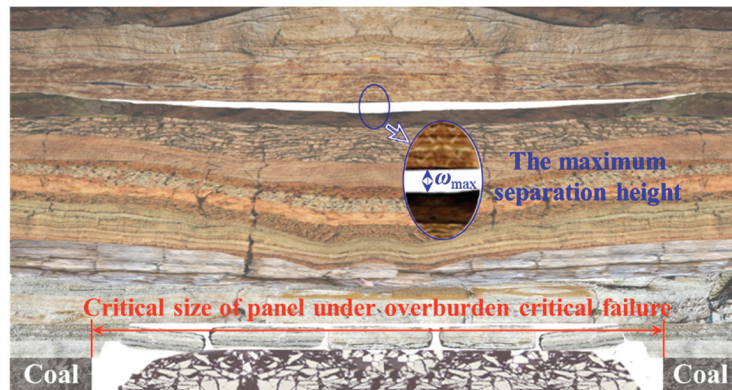
Figure 2. Separation height of the overburden critical failure.

Therefore, for the working face where the height of the water conduction fracture zone does not reach the surface, when the overburden reaches critical failure, the surface has not reached critical mining; that is, the overburden reaches critical mining earlier than the surface. Combined with the characteristics of the bending zone, when the overburden failure height is taken as the research object, the overburden bending zone is equivalent to the homogeneous load applied on the top of the fracture zone, so as to analyze the mechanical characteristics of the masonry beam structure and crack development in the fracture zone. In addition, for coalmines with different geological and mining conditions, the number and location of overburden key strata and the height of water conduction fracture zone are different. It is necessary to determine the fracture angle according to overburden lithology and similar simulation methods. For working faces with different mining widths, when the mining size is small, the overburden damage does not reach critical mining, and there will be no void compaction area in the area of water conduction fracture zone, such as strip mining or other partial mining methods. Therefore, when gas drainage is carried out in the mining process, the drainage boreholes shall be arranged in the upper part of the structural void area as far as possible, so as to realize safe mining of the working face more efficiently.

2.2. Characteristics of Overburden Failure and Fracture Distribution

Based on the geological and mining conditions of Liangbei coalmine in Xuchang City, Henan Province, China, the characteristics of overburden failure and mining fracture distribution were analyzed by physical simulation test. Coal seam 21# of the Shanxi formation was mainly mined in the mining area, where the overlying strata were medium

hard lithology. The coal seam dips at 5°, and the longwall panels were laid out along the strike. The panel length was 1200 m and panel width was 136 m with a mining height of 3 m under an average overburden depth of 580 m. The strike longwall coal mining caving method was used to manage the roof.

According to the regulations for mining under buildings, water-bodies, and railways, the calculation for the height of water conduction fracture zone is as shown in Formula (1):

$$H_{li} = \frac{100M}{1.6M + 3.6} \pm 5.6 \tag{1}$$

where H_{li} is the height of the water conduction fracture zone, m; and M is the mining height, m.

From the above formula, the height of water conduction fracture zone is calculated as 30.1–41.3 m, i.e., it ranges from 10 to 14 times the mining height. To analyze the impact of coal mining on overburden more intuitively, the coal seam is leveled. Combined with the dimensions of the working face and physical simulation test-bed (long × wide × high = 2.5 m × 0.2 m × 1.2 m), the rock strata 63.2 m above the coal seam are simulated with a geometric ratio of 1:50, a time ratio of 1:10, bulk density ratio of 3:5, Poisson's ratio of 1, strength and elastic modulus ratio of 0.012, external force ratio of 2×10^{-6}. Meanwhile, the remaining rock strata are uniformly applied on the top of the model with a load of 0.3 MPa. The physical simulation material selects fine sand as aggregate and calcium carbonate and gypsum as cementitious materials, borax as retarder, mica powder as weak surface between rock layers, and water as solvent. By changing the different ratio of materials, the rock layers with different strength in overburden are simulated. The mechanical parameters of each rock stratum in the model are shown in Table 1.

Table 1. Rock mechanics parameters of the physical model.

No.	Rock Stratum	Thickness (m)	Density (kN/m³)	Elastic Modulus (GPa)	Tensile Strength (MPa)	Internal Friction Angle (°)	Poisson's Ratio
1	Mudstone	7.6	2560	10.90	1.68	30	0.23
2	Medium sandstone	7.4	2630	36.18	5.13	36	0.26
3	Sandy mudstone	4.9	2580	18.53	3.05	32	0.27
4	Mudstone	4.5	2560	10.90	1.68	30	0.23
5	Siltstone	6.8	2660	29.77	3.84	38	0.2
6	Mudstone	2.7	2560	10.90	1.68	30	0.23
7	Sandy mudstone	6.2	2580	18.53	3.05	32	0.27
8	Fine sandstone	7.6	2750	38.45	6.75	37	0.18
9	Sandy mudstone	4.7	2580	18.53	3.05	32	0.27
10	Coal seam	3.0	1400	2.30	1.03	24	0.31

Based on the overburden failure under the mining influence, the relationship between overburden structure and periodic pressure after mining 87 m of the working face is shown in Figure 3.

Figure 3 shows that there are overburden structures and through cracks when the overburden fracture is under periodic pressure, and the overburden failure is trapezoidal distribution (36.4 m from the coal seam roof). In the vertical direction, when the height of the caved zone is reached, the overburden in the fracture zone forms a triangular spatial structure with different shapes at the breaking position. This is primarily due to the different fracture distances of each sub-key layer. With periodic pressure, the overburden structure periodically develops in the form of "formation–stability–instability–stability" as the panel advances. The average breaking angle in the advancing direction is 62–65°, which is less than 67° of the overburden at the setup room, showing a typical skewness phenomenon [38]. The overburden structure at the boundary of goaf is usually a permanent structure and is one of the sources of residual surface deformation in goaf. Moreover, it

is also the main research object of water conservation mining, gas drainage and goaf stability evaluation.
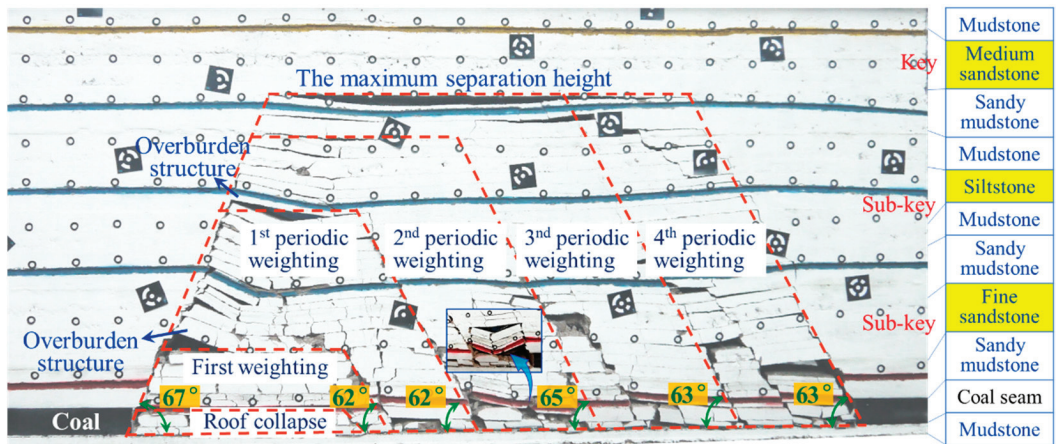
Figure 3. Overburden structure and periodic weighting.

Combined with the overburden failure characteristics under the mining influence, taking the fracture zone as the research area, the mining fractures in this area display obvious zoning characteristics in the horizontal direction, as follows:

1. Only tensile or fine fractures. After the mining of the working face is completed, the setup room and stopping line of the working face are bounded by the fracture angle formed by overburden failure on one side of the coal pillar; the mining impact is tensile deformation or no impact. At this time, there are only tensile or original fractures in the overburden, i.e., the area ranges from the coal pillar side to the overburden fracture;

2. Obvious overburden structure. When the overburden is broken to a certain height layer by layer under the mining influence, the broken block is hinged to form a masonry beam structure because the free space below does not meet the conditions of rock block sliding and instability. With the upward transmission of rock fracture, the sub-key layer within the fracture zone forms a hinged structure owing to the large fracture distance, and its return angle gradually decreases with the increase of the distance from the coal seam roof until it is transmitted to the top of the fracture zone, forming an obvious layer separation. Then, the mining fractures are the permanent through ones;

3. Closure of mining cracks in the overburden. As the working face advances, the mining cracks located in the fracture zone are developed periodicity in form of "formation-penetration-closure-compaction". When the overburden reaches critical mining, the mining cracks and separation layers gradually close under the periodic pressure of the main roof above the working face, reducing the water conductivity of the rock strata. Meanwhile, the equivalent subsidence coefficient reaches maximum. The caved zone and fracture zone are compacted within this range, therefore, the surface in the middle of the goaf is also the target area for effective utilization of the mining subsidence area due to the small surface residual deformation in this area.

Based on the above analysis, mining fractures are concentrated in the overburden structure at the boundary of the working face. When there are multiple sub-key layers in the fracture zone, the fracture angles of the rock strata differ slightly with the mechanical properties and burial depth. Therefore, it is necessary to analyze the damage and structure formation of the hard rock strata.

3. Hard Rock Failure and Structure Formation

Based on the key layer theory, the key layer controls the movement and deformation of the multi-layer rock above it. When the overburden failure is transmitted to the key layer, the failure will occur when the separation space length reaches the breaking distance of key layer. This process can be simplified as the shear failure of the key layer under the overburden load. When the shear stress reaches the peak, the rock sample will break, and its shear displacement can be used as the maximum value of rock bending and subsidence. Combined with the geological and mining conditions of the working face and based on the key strata theory, there are two sub-key layers in the fracture zone, and their lithology is sandstone. Therefore, the displacement of sandstone should be studied when the hard rock strata are broken.

3.1. Shear Deformation Test

As the shear test of the rock samples is related to the joint surface roughness and normal stress, this test only considers the influence of joint surface roughness and different normal stress on the shear test. By scanning the joint surface of the cylinder sample (50 mm × 100 mm) with a three-dimensional laser scanner, the slope root mean square Z_2 of 16 interface bisected section lines is calculated according to Formula (2) [39]:

$$Z_2 = \sqrt{\frac{1}{(l-1)(\Delta x)^2}\sum_{i=1}^{l-1}(Z_{i+1} - Z_i)^2} \tag{2}$$

where Z_i is the height coordinate of the joint surface profile; l is the number of data points; and Δx is the interval of data points.

The roughness of each section line (JRC_i) can be calculated by substituting each two-dimensional section line (Z_{2i}) into Formula (3) [40]. The joint roughness coefficient of the rock sample can be obtained by taking the weighted average value of the roughness of each section line:

$$JRC_i = 32.69 + 32.98\lg Z_{2i} \tag{3}$$

where Z_{2i} is the root mean square of the slope for the ith contour line; and JRC_i is the roughness coefficient of the ith contour line.

To analyze the stress–strain characteristics of rock samples at different mining depths, nine groups of rock samples were subjected to shear testing. The shear rate was set to 1 mm/min and terminated when the displacement reached 8 mm. The test parameters are shown in Table 2.

Table 2. Shear test parameters for each rock sample.

No.	S1	S2	S3	S4	S5	S6	S7	S8	S9
σ_{n}/MPa	3	4	6	9	12	15	18	21	24
JRC	6.64	8.54	7.35	12.37	7.59	8.13	10.18	7.87	8.70

Based on the normal stress, normal displacement, shear stress, and shear displacement obtained during the test, the shear stress displacement curve of sandstone joints was obtained, as shown in Figure 4.
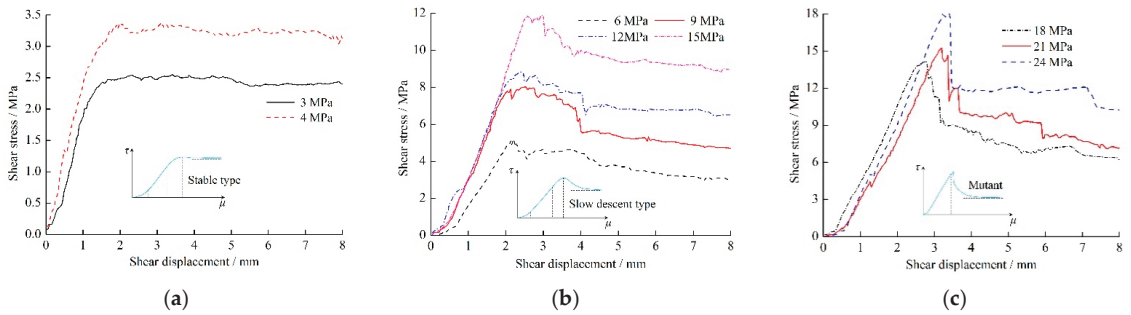
Figure 4. Shear stress displacement curves under different normal stresses. (**a**) Stable type; (**b**) Slow descent type; and (**c**) Mutant.

As seen in Figure 4, the shear stress displacement curve first increases and then decreases under different normal stresses. The process can be divided into compaction, linear, yield, and softening stages. In the post peak softening stage, the amplitude and rate of the decreasing shear stress increase with the increase of normal stress. The change characteristics of each stage are as follows:

1. Compaction stage. Owing to the incomplete contact between joint bulges (roughness) in the initial state, the contact area and pressure of joint bulges increase with the increase of shear displacement, and the shear stress increases nonlinearly;
2. Linear stage. When the displacement increases, the undamaged contact joint bulge increases the friction between joints, and the shear stress increases linearly;
3. Yield stage. The shearing of the joint bulge reduces the roughness coefficient and causes the shear stress to increase slowly until the shear bearing capacity of the joint reaches its peak;
4. Softening stage. With the increase of normal stress, the roughness of the joint surface smooths gradually, which shows that the reduction of shear stress increases with the increasing normal stress.

In conclusion, with the increase of shear stress, the damage degree of the sample also increases gradually, and obvious failure occurs when the normal stress is greater than 6 MPa. According to geological and mining conditions, the original rock load of overburden bending zone is approximately about 15 MPa. At this time, the displacement of the rock strata at peak stress is approximately about 5% of the sample along the shear direction. Combined with the shear test of joint samples with different lengths [41], the maximum subsidence deflection of the rock strata under the corresponding overburden load is 5% of the thickness of the broken rock strata.

3.2. Formation and Stability of Overburden Structure

Under the mining influence, when the rock stratum reaches the limit breaking distance, it breaks and forms a caved zone. There are voids between broken rocks in the caved zone, when reaching a certain height, therefore, the free space height under the rock layer directly affects the contact between rock blocks and is the key factor for forming the overburden structure.

When the buried depth of the coal seam is large, the rock layer before failure can be regarded as a beam model with a rectangular section, and the overburden load is evenly distributed above it. Combined with the key strata theory and fixed beam model, the maximum deflection of the fixed beam $\omega_{\max}$ can be obtained by Formula (4) [42]:

$$\omega_{\max} = \frac{qL_c{}^4}{384EI} = \frac{h\sigma_t^2}{8Eqb} \tag{4}$$

where h is the thickness of the structural rock stratum, m; σ_t is its tensile strength, MPa; q is the load borne by the rock, MPa; E is the elastic modulus, MPa; and b is the width of the rectangular section, m.

From the above formula, the maximum bending deformation before the initial fracture of rock stratum is shown to be primarily affected by its own mechanical parameters and ratio of thickness to width. To improve the feasibility of the maximum rock strata deflection in engineering, combined with the stress-strain characteristics of sandstone during the shear test, five percent of the strata thickness is set as its maximum subsidence deflection, and the following assumptions are made: (1) the hard rock stratum is regarded as a homogeneous continuum, and the masonry beam structure is formed when it is broken for the first time; (2) the key blocks in contact with the collapse zone are paved above that zone and are in a stable state due to the overburden load; and (3) the expansion coefficient of the caved zone is the final constant value, which has little effect on the overburden structure. Therefore, when the overlying strata form a masonry beam structure, the conditions meet the following formula:

$$\omega_{\max} + L\sin\theta + H_{\mathrm{m}}(k_0 - 1) \geq M \tag{5}$$

where $\omega_{\max}$ is 0.05 h, m; L is the initial limit breaking distance of the rock stratum, m; θ is the angle for the key blocks of the overburden structure, °; H_{m} is the height of the caved zone, m; k_0 is the expansion coefficient of the caved zone; and M is the mining thickness of the coal seam, m.

Combined with the sliding-rotation stability theory of surrounding rock structure [43], the conditions for no instability of the key blocks in the masonry beam are as follows:

$$\begin{cases} \text{not slip}: i \leq \tan\varphi + \frac{3}{4}\sin\theta \\ \text{not rotation}: \frac{P}{(i - 0.5\sin\theta)(h - l_z\sin\theta)} \leq 0.15\sigma_c \end{cases} \tag{6}$$

where $i = h/l_z$, l_z is the length of the periodic broken block, m; $\tan\varphi$ is the friction coefficient between broken blocks, 0.3; P is the load on the key block, MN; and σ_c is the compressive strength of the rock stratum, MPa.

Based on the physical simulation test and mining conditions of adjacent working faces, the initial breaking distance of the working face is 42.4 m; therefore, the length of the broken block is 21.2 m. According to Formula (5), the angle of the overburden structure, θ, is 5.12°; the periodic pressing step l_z near the working face is approximately 10 m, and the load on the key block is $P = \gamma(H_{li} - H_{\mathrm{m}})$, approximately 1.02 MPa. The overburden structure meets the required conditions for no instability.

4. Regional Division Method and Discussion of Mining Fracture

4.1. Division and Discrimination of Mining Fractures in Overburden

Mining fracture is the main basis for ensuring the safe mining under water and efficient gas drainage, evaluating the stability of overburden and revealing the mechanism of surface residual deformation in abandoned goaf. Combined with the physical simulation of the overburden migration under mining influence, through the layout of survey lines in the overburden fracture zone, the separation rate distribution of each layer is shown in Figure 5.

As shown in Figure 5a, (1) the shape of the separation rate curve for different layers in the overburden fracture zone is basically the same, a saddle shape with a high at both ends and a low in the middle; (2) the layer separation rate at the side of the setup room in the same layer is greater than that at the stopping line because the length and compaction time of the broken rock block at the side of the setup room are greater than that at the stopping line; (3) there are relatively few separated layers in the middle of the goaf due to the re-compaction of the broken rock block by overburden load, resulting in the closure of mining fractures; and (4) with the increase of the overburden failure height, the position of the maximum separation rate of the rock stratum shifts to the center of the goaf, indicating that the overburden structure in the fracture zone is trapezoidal upward conduction. Therefore, within the range of the overburden fracture zone, the representative positions of mining

fracture are the boundary and center of goaf and the overburden structure. Then, the fracture zone is divided into "four horizontal zones": original fracture, tensile fracture, structural void, and void compaction, as shown in Figure 5b.

(**a**)

(**b**)
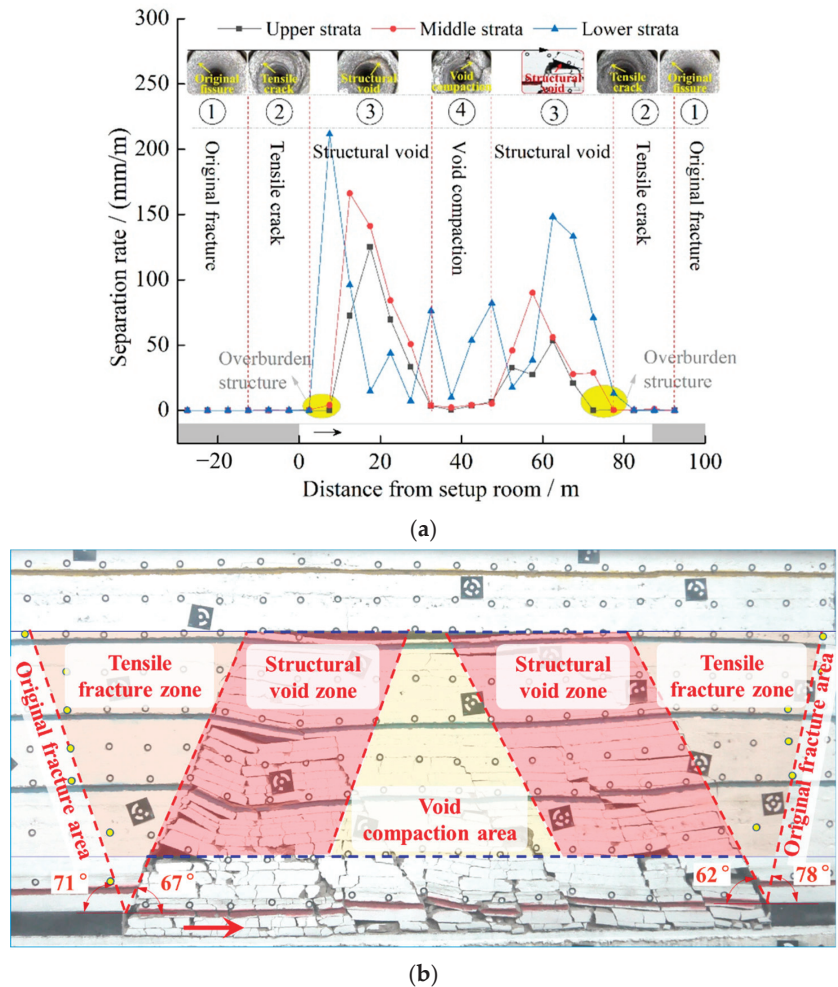
Figure 5. Distribution and division of mining fracture. (**a**) Distribution of separation rate in the fracture zone; (**b**) Division of overburden fracture under coal mining.

The height of the fracture zone is the range of each area in the vertical direction, and the boundaries in the horizontal direction are defined as follows:

1. Original fracture area. Combined with the mining subsidence theory and the maximum bending deflection of the rock stratum, the boundary with an inclination value of 3 mm/m (layer separation rate of 3‰) in the movement angle is the boundary between the original and tensile fractures, which is the position of the yellow point in the Figure 5b;

2. Tensile fracture zone. The connecting line between the measuring point with an inclination value of approximately 3 mm/m in the physical simulation and the mining boundary is taken as the boundary between the original and the tensile fracture zones. The interface angle at the setup room of the working face is 71°, while at

the stopping line, it is 78°. The rock block forms a masonry beam structure after the overburden is broken, therefore, the overburden shape and stress state change significantly. Therefore, the overburden fracture is taken as another boundary of the tensile fracture area. The length l_1 of this area at the top of the fracture zone is:

$$l_1 = H_{li}(\cot\theta_1 + \cot\theta_2) \qquad (7)$$

where H_{li} is the height of the water conduction fracture zone and can be calculated in the regulation, which is 36.4 m; and θ_1 and θ_2 are the movement and breaking angles of the overburden, respectively, at 71° and 67°. The length of this area is 27.98 m, and the length within the goaf is 15.45 m;

3. Structural void zone. The structural void zone begins when the masonry beam structure is formed. With the advance of the working face, as the fracture zone reaches the maximum, the separation gap between the fracture and bending zones reaches the maximum, and the overburden reaches the critical failure. Then, the midpoint of the ultimate breaking distance of the rock stratum at the bottom of the bending zone is taken as the base point, and the rock strata breaking boundaries are created parallel to the overburden structure. The area between the adjacent boundary lines is the structural fracture area. The relationship between overburden failure height and separation void meets the following conditions:

$$\begin{cases} H_{li}(k_0 - 1) \geq M + \omega \\ \omega \leq \omega_{\max} \end{cases} \qquad (8)$$

The bending deflection of the hard rock layer at the upper part of the fracture zone is the largest when it reaches the initial limit breaking distance. According to the above formula, when the overburden failure reaches the critical height and the adjacent layer reaches the initial limit breaking distance L, the advancing distance of working face with overburden critical mining is the largest, i.e., $L_s = H_{li}(\cot\theta'_1 + \cot\theta'_2) + L$. $L_s = 79.6$ m, and the error from the critical advancing distance (75 m) of the working face in Figure 5 is only 5.7%. Therefore, this formula can be used to determine the advancing distance of working face when the overburden failure reaches critical mining, and also to determine the range of the structural fracture area, providing a basis for overburden separation grouting and goaf stability evaluation;

4. Void compaction area. After overburden failure reaches supercritical mining, the separation gap of the rock stratum at the bottom of the bending zone reaches the maximum, which is equivalent to the bottom of the surface subsidence basin. This area is located in the middle of the structural fracture area. Combined with Figure 5 and the evolution of overburden fractures, it is consistent with the physical simulation.

4.2. Engineering Practice

Combined with the geological and mining conditions of the Liangbei coalmine, the surface movement and deformation enter into the decline stage (the surface subsidence rate is lower than 1.67 mm/d) after mining ceased five years (2019). A surface movement observation station is arranged above the coalfield, and the relationship between measuring points and working face is shown in Figure 6. It should be noted that in the physical simulation, the distribution of mining overburden voids is along the advancing direction of the working face, while the on-site monitoring is perpendicular to the advancing direction. This is mainly because the overburden damage and void distribution on the strike of the working face are basically consistent with the tendency. Therefore, the on-site monitoring data can verify the characteristics of overburden void distribution.
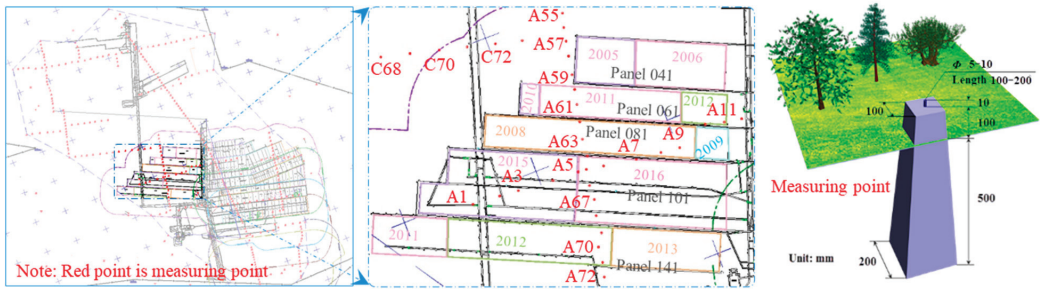
Figure 6. Location of old goaf and surface survey points.

Real-time kinematic have been used to monitor the surface residual deformation for 2 years, and the cumulative subsidence of the surface measurement points (A1–A12, A57–A72) is obtained, as shown in Figure 7.
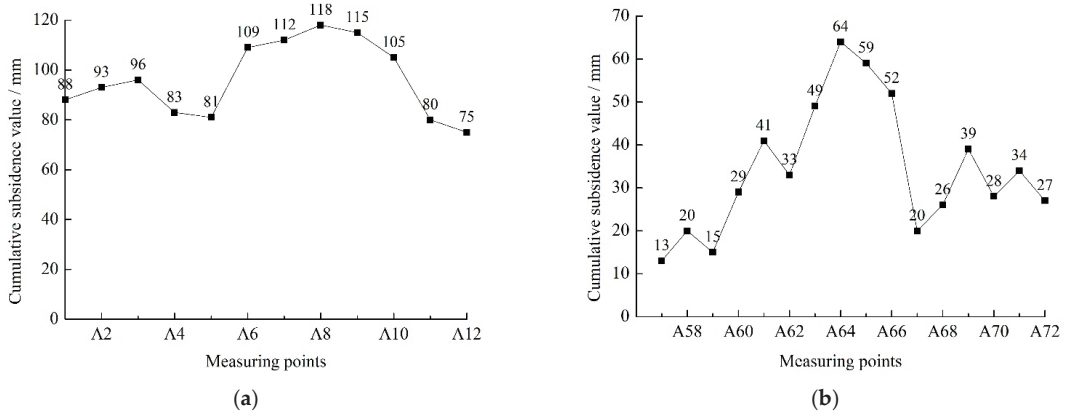
Figure 7. Cumulative surface subsidence in the goaf. (**a**) Measuring points A1–A12 (February 2019–October 2021). (**b**) Measuring points A57–A72 (February 2019–October 2021).

As shown in Figure 7a, in the near strike direction of the old goaf, the subsidence of the monitoring point at the boundary of the panel goaf is greater than that at the middle of the goaf. Primarily, overburden structure and voids are observed in the uncompact caved zone on both sides of the goaf. The cumulative maximum subsidence value of A8 at the boundary of the working face is 118 mm, which is mainly due to the latest mining time of the 101 panel, and the surface movement and deformation may not enter the decline stage.

To eliminate the influence of surface movement and deformation not fully entering the decline stage, the subsidence points of A54–A72 were measured from February 2019 to October 2021. As seen in Figure 7b, the cumulative subsidence curve of the measuring point shows first increasing and then decreasing variation characteristics. The subsidence value reaches the maximum at measuring point A64, which also verifies the accuracy of the above analysis. After passing point A68, the subsidence curve presents a wavy shape, owing to the fact that the measuring point at the rising point is located at the boundary of the working face and the one at the lowering point is located in the middle of the goaf, indicating that the void at the overburden structure gradually decreases under the long-term bearing action; the middle of the goaf will further compact the caved and fracture zones. However, the decline on both sides of the goaf is greater than that in the middle, which also verifies the rationality of overburden regional division.

5. Conclusions

(1) Based on the overburden critical failure, the characteristics of overburden fracture were analyzed. The fracture zone was divided horizontally into original rock fracture, tensile fracture, structural void, and void compaction areas, and the description of each area was proposed;

(2) The formation mechanism for the shape of the water conduction fracture zone was determined to be the same as the surface mining subsidence. The relationship between the maximum subsidence deflection of the hard rock layer and the thickness of the broken rock layer was clarified with the deduced theoretical formula, and the masonry beam structure was found to have long-term stability;

(3) Based on field monitoring of surface deformation, the subsidence characteristics of measurement points at different positions above the working face were analyzed. The overburden structure on both sides of the working face and the void in the uncompact caved zone was suggested to be the main factor causing different subsidence of the measuring points, and the rationality of overburden regional division was verified, which is vital for safe mining under water, accurate restoration of the eco-environment in mining subsidence areas, sustainable development of the mining industry, and economic growth.

Institutional Review Board Statement: Not applicable.

Informed Consent Statement: Not applicable.

Data Availability Statement: Relevant data are listed in the paper.

Conflicts of Interest: The authors declare no conflict of interest.

References

1. Bell, F.G.; Stacey, T.R.; Genske, D.D. Mining subsidence and its effect on the environment: Some differing examples. *Environ Geol.* **2020**, *40*, 135–152. [CrossRef]
2. Fan, L.M.; Ma, X.D. A review on investigation of water-preserved coal mining in western China. *Int. J. Coal Sci. Technol.* **2018**, *5*, 411–416. [CrossRef]
3. Karakus, M.; Tutmez, B. Fuzzy and Multiple Regression Modelling for Evaluation of Intact Rock Strength Based on Point Load, Schmidt Hammer and Sonic Velocity. *Rock Mech. Rock Eng.* **2006**, *39*, 45–57. [CrossRef]
4. Bai, E.H.; Guo, W.B.; Tan, Y. Negative externalities of high-intensity mining and disaster prevention technology in China. *Bull. Eng. Geol. Environ.* **2019**, *78*, 5219–5235. [CrossRef]
5. Sun, Q.; Zhang, J.X.; Li, M.; Zhou, N. Experimental evaluation of physical, mechanical, and permeability parameters of key aquiclude strata in a typical mining area of China. *J. Clean. Prod.* **2020**, *267*, 122109. [CrossRef]
6. Sasaoka, T.; Takamoto, H.; Shimada, H.; Oya, J.; Hamanaka, A.; Matsui, K. Surface subsidence due to underground mining operation under weak geological condition in Indonesia. *J. Rock Mech. Geotech. Eng.* **2015**, *7*, 337–344. [CrossRef]
7. Yu, S.C.; Xu, J.M.; Zhu, W.B.; Wang, S.H.; Liu, W.B. Development of a combined mining technique to protect the underground workspace above confined aquifer from water inrush disaster. *Bull. Eng. Geol. Environ.* **2020**, *79*, 3649–3666. [CrossRef]
8. Altun, A.O.; Yilmaz, I.; Yildirim, M. A short review on the surficial impacts of underground mining. *Sci. Res. Essay* **2010**, *21*, 3206–3212.

9. Yang, B.B.; Yuan, S.C.; Liang, Y.K.; Liu, J.W. Investigation of overburden failure characteristics due to combined mining: Case study, Henan Province, China. *Environ. Earth Sci.* **2021**, *80*, 143. [CrossRef]
10. Kim, J.M.; Parizek, R.R.; Elsworth, D. Evaluation of fully-coupled strata deformation and groundwater flow in response to longwall mining. *Int. J. Rock Mech. Min. Sci.* **1997**, *34*, 1187–1199. [CrossRef]
11. Wang, G.; Wu, M.M.; Wang, R.; Xu, H.; Song, X. Height of the mining-induced fractured zone above a coal face. *Eng. Geol.* **2017**, *216*, 140–152. [CrossRef]
12. Qian, M.G.; Miao, X.X.; Xu, J.L. Theoretical study of key stratum in ground control. *J. China Coal Soc.* **1996**, *21*, 225–230.
13. Xu, J.L.; Zhu, W.B.; Wang, X.Z. New method to predict the height of fractured water-conducting zone by location of key strata. *J. China Coal Soc.* **2012**, *37*, 762–769.
14. Rezaei, M.; Hossaini, M.F.; Majdi, A. A time-independent energy model to determine the height of destressed zone above the mined panel in longwall coal mining. *Tunn. Undergr. Space Technol.* **2015**, *47*, 81–92. [CrossRef]
15. Li, Z.; Xu, J.L.; Ju, J.F.; Zhu, W.B.; Xu, J.M. The effects of the rotational speed of voussoir beam structures formed by key strata on the ground pressure of stopes. *Int. J. Rock Mech. Min. Sci.* **2018**, *108*, 67–79. [CrossRef]
16. Castro, T.; Trueman, R.; Halim, A. A study of isolated draw zones in block caving mines by means of a large 3D physical model. *Int. J. Rock Mech. Min. Sci.* **2007**, *44*, 860–870. [CrossRef]
17. Hatherly, P. Overview on the application of geophysics in coal mining. *Int. J. Coal Geol.* **2013**, *114*, 74–84. [CrossRef]
18. Ghabraie, B.; Ren, G.; Zhang, X.; Smith, J. Physical modelling of subsidence from sequential extraction of partially overlapping longwall panels and study of substrata movement characteristics. *Int. J. Coal Geol.* **2015**, *140*, 71–83. [CrossRef]
19. Ju, M.H.; Li, X.H.; Yao, Q.L.; Liu, S.Y.; Liang, S.; Wang, X.L. Effect of sand grain size on simulated mining-induced overburden failure in physical model tests. *Eng. Geol.* **2017**, *226*, 93–106. [CrossRef]
20. Asaue, H.; Sasahara, M.; Yoshinaga, T.; Obara, Y.; Uchida, K.; Matsumoto, H. Clarifying geological structure for coal and marsh gas development using magnetotelluric method. *Acta Geodyn. Geomater.* **2013**, *10*, 155–162. [CrossRef]
21. Yu, B.; Zhao, J.; Kuang, T.J.; Meng, X.B. In situ investigations into overburden failures of a super-thick coal seam for longwall top coal caving. *Int. J. Rock Mech. Min. Sci.* **2015**, *78*, 155–162. [CrossRef]
22. Mills, K.W.; Garratt, O.; Blacka, B.G.; Daigle, L.C.; Rippon, A.C.; Walker, R.J. Measurement of shear movements in the overburden strata ahead of longwall mining. *Int. J. Min. Sci. Technol.* **2015**, *26*, 97–102. [CrossRef]
23. Han, P.H.; Zhang, C.; Ren, Z.P.; He, X.; Jia, S. The influence of advance speed on overburden movement characteristics in longwall coal mining: Insight from theoretical analysis and physical simulation. *J. Geophys. Eng.* **2021**, *18*, 163–176. [CrossRef]
24. Xu, D.J.; Peng, S.P.; Xiang, S.Y.; He, Y.L. A Novel Caving Model of Overburden Strata Movement Induced by Coal Mining. *Energies* **2017**, *10*, 476. [CrossRef]
25. Cao, Z.G.; Ju, J.F.; Xu, J.L. Distribution model of water-conducted fracture main channel and its flow characteristics. *J. China Coal Soc.* **2019**, *44*, 3719–3728.
26. Karacan, C.O.; Goodman, G. Hydraulic conductivity changes and influencing factors in longwall overburden determined by slug tests in gob gas ventholes. *Int. J. Rock Mech. Min. Sci.* **2009**, *46*, 1162–1174. [CrossRef]
27. Li, S.; Fan, C.J.; Luo, M.K.; Yang, Z.H.; Lan, T.W.; Zhang, H.F. Structure and deformation measurements of shallow overburden during top coal caving longwall mining. *Int. J. Min. Sci. Technol.* **2017**, *27*, 1081–1085. [CrossRef]
28. Hu, C.S.; Apel, D.; Sudak, L.J.; Liu, W.V.; Chu, Z.Y. Physical investigation on the behaviours of voussoir beams. *J. Rock Mech. Geotech.* **2020**, *12*, 516–527. [CrossRef]
29. Shi, X.C.; Zhang, J.X. Characteristics of overburden failure and fracture evolution in shallow buried working face with large mining height. *Sustainability* **2021**, *13*, 13775. [CrossRef]
30. Majdi, A.; Hassani, F.P.; Nasiri, M.Y. Prediction of the height of destressed zone above the mined panel roof in longwall coal mining. *Int. J. Coal Geol.* **2012**, *98*, 62–72. [CrossRef]
31. He, C.C.; Lu, W.Y.; Zha, W.H.; Wang, F. A geomechanical method for predicting the height of a water-flowing fractured zone in a layered overburden of longwall coal mining. *Int. J. Rock Mech. Min. Sci.* **2021**, *143*, 104798. [CrossRef]
32. Guo, W.B.; Zhao, G.B.; Lou, G.Z.; Wang, S.R. A New Method of Predicting the Height of the Fractured Water-Conducting Zone Due to High-Intensity Longwall Coal Mining in China. *Rock Mech. Rock Eng.* **2018**, *52*, 2789–2802. [CrossRef]
33. Palchik, V. Formation of fractured zones in overburden due to longwall mining. *Environ. Geol.* **2003**, *44*, 28–38. [CrossRef]
34. Zhou, D.W.; Wu, K.; Miao, X.X. Combined prediction model for mining subsidence in coal mining areas covered with thick alluvial soil layer. *Bull. Eng. Geol. Environ.* **2018**, *77*, 283–304. [CrossRef]
35. Bai, E.H.; Guo, W.B.; Zhang, D.S.; Tan, Y.; Guo, M.J.; Zhao, G.B. Using the Magnetotelluric Method for Detecting Aquifer Failure Characteristics under High-Intensity Mining of Thick Coal Seams. *Energies* **2019**, *12*, 4397. [CrossRef]
36. Guo, W.B.; Lou, G.Z. Definition and distinguishing method of critical mining degree of overburden failure. *J. China Coal Soc.* **2019**, *44*, 755–766.
37. Guo, W.B.; Zhao, G.B.; Bai, E.H. Critical failure of overlying rock strata and its criteria induced by high-intensity longwall mining. *J. China Coal Soc.* **2020**, *45*, 3657–3666.
38. Yu, Q.G.; Zhang, H.X.; Deng, W.N.; Zou, Y.P. Analysis of influencing factors of surface skewed subsidence based on key strata theory. *J. China Coal Soc.* **2018**, *43*, 1322–1327.
39. Tian, Y.C.; Liu, Q.S.; Liu, D.F.; Kang, Y.S.; Deng, P.H.; He, F. Updates to Grasselli's Peak Shear Strength Model. *Rock Mech. Rock Eng.* **2018**, *51*, 2115–2133. [CrossRef]

40. Li, Y.R.; Zhang, Y.B. Quantitative estimation of joint roughness coefficient using statistical parameters. *Int. J. Rock Mech. Min. Sci.* **2015**, *77*, 27–35. [CrossRef]
41. Barton, N.; Choubey, V. The shear strength of rock joints in theory and practice. *Rock Mech.* **1977**, *10*, 1–54. [CrossRef]
42. Chen, L.; Wu, B.; Xu, X.K.; Shang, Y.R. Determination of overburden failure height in alternate strata of mudstone and sandstone with fully mechanized caving method. *J. Min. Saf. Eng.* **2017**, *34*, 431–436.
43. Qian, M.G.; Zhang, D.L.; Li, L.J.; Kang, L.X.; Xu, J.L. "S-R" stability for the voussoir beam and its application. *Coal Technol. Northeast China* **1994**, *3*, 6–10.

Continuous Extraction and Continuous Backfill Mining Method Using Carbon Dioxide Mineralized Filling Body to Preserve Shallow Water in Northwest China

Yujun Xu [1], Liqiang Ma [1,2,*], Ichhuy NGO [1] and Jiangtao Zhai [1]

[1] Key Laboratory of Deep Coal Resources Mining, China University of Mining and Technology, Ministry of Education, Xuzhou 221116, China; xyj@cumt.edu.cn (Y.X.); ngoichhuy@cumt.edu.cn (I.N.); tb21020005b3ld@cumt.edu.cn (J.Z.)

[2] School of Energy, Xi'an University of Science and Technology, Xi'an 710054, China

* Correspondence: tb20020008b1@cumt.edu.cn; Tel.: +86-198-1625-2755

Abstract: The exploitation and utilization of coal resources are not only prone to causing water table lowering, but also produce a large amount of CO_2 and coal-based solid waste. A scientific concept that employs the CO_2 and solid wastes to develop filling bodies and inject them into the mined-out area, to sequestrate CO_2 and mitigate the overburden migration and thus preserve the overlying aquifer, is proposed. Continuous extraction and continuous backfill (CECB) mining was selected as the mining method to meet the aforementioned objectives. Additionally, carbon dioxide mineralized filling body (CMFB) under ambient temperature and pressure was developed, with fly ash as aggregate, and CO_2 gas, silicate additives and cement as accessories. The uniaxial compressive strength (UCS) and tensile strength of CMFB with various curing times and fly ash contents were tested indoors. A physical analogue simulation and FLAC^{3D} numerical calculation were then successively implemented on the premise of determining a similar material ratio of CMFB in analogue simulation and calibrating the parameters of the CMFB in numerical simulation. The deformation of aquifuge and water level lowering while using CECB and CMFB with various proportion of fly ash were obtained. When using the CMFB with 75% fly ash content and 28 d curing time, the maximum values of vertical displacement, horizontal displacement, inclination, horizontal deformation and curvature of aquiclude were 26 mm, 6.5 mm, 0.12 mm/m, 0.08 mm/m and 0.0015 mm/m^2, respectively, and the water table decreased 0.47 m. The results show that the CMFB with 75% fly ash is the most appropriate ratio to realize water preservation mining, CO_2 sequestration and harmless treatment of solid wastes, contributing to the green and sustainable development of coal areas.

Keywords: continuous extraction and continuous backfill (CECB); water preservation coal mining; carbon dioxide mineralized filling body (CMFB); aquifuge deformation; shallow water level lowering

1. Introduction

China's coal reserves are mainly distributed in northwest regions, among which those in Shanxi, Shaanxi, Inner Mongolia and Xinjiang are the most abundant and account for nearly 70% of China's total coal resources [1]. With the depletion of coal resources in east China, the focus of coal mining has gradually shifted to northwest China with an arid and semi-arid climate. Northwest areas are already the main coal producing areas in China, where the proved reserves make up more than two-thirds of the country's total [2–4].

However, the main coal producing areas in northwest China feature a dry climate, sparse vegetation, land desertification and water shortage. The water resources account for only 3.9% of the total water resources [5]. The Quaternary Salawusu formation aquifer is the only shallow aquifer with the significance of being a residential and ecological water supply [6–8]. Large-scale and high-intensity coal mining has resulted in the movement and destruction of the overburden, and the fractures in the overlying layers are prone to

occur. If the fissures act as a hydraulic exchange zone between the shallow aquifer and the goaf, a large amount of water in the aquifer will flow into the mined-out area, breaking the original supplement, runoff and discharge balance state of the aquifer, and thus lead to sharp water table lowering and large-range water resource loss [9,10]. Taking the water level statistics of the Yu-Shen coal area in Shaanxi Province as an example, an area where the water level drop is greater than 8 m and has exceeded 650 km^2, more than 70% is directly induced by high-intensity mining, which directly exacerbates the deterioration of the regional ecological environment [11]. In-depth research on water resource preservation and conservation in the mining areas has been conducted locally and abroad. Foreign experts analyzed the relationship between the mining-induced groundwater flow and the overlying strata migration and fracture development [12–14]. They studied the impact law of longwall mining on the water level of the overlying aquifer and the surrounding water environment, and evaluated the potential impact of mining on the surface and groundwater [15–18]. Additionally, the mining method was optimized according to the measured data of mining-induced groundwater level fluctuation obtained by the groundwater monitoring network [19–22]. The surface water and shallow aquifer were therefore protected from interference or damage, contributing to the realization of the sustainable and coordinative development of coal resources and shallow water resources [23–25]. Aiming at the problem of shallow surface water leakage during the process of coal mining in the Yu-Shen mining area, domestic scholars put forward the concept of water-preserving mining, and expounded its scientific connotation systematically [26]. They studied the stability of a water-resisting layer beneath the shallow water, and analyzed the relationship between the water table lowering and mining magnitude [27–29]. Water conservation mining methods, such as backfill mining, harmonic mining, partial mining, curtain grouting, overburden bed separation grouting and coal mine underground reservoir construction, have been proposed and put into implementation [30], the first of which is currently the most effective one for water preservation during coal extraction. Backfill mining includes longwall and shortwall backfill, and the former is confronted with the problems of insufficient filling time and filling space, and mutual impact and restriction between extraction and filling [31–35]. In view of the aforementioned problems, a CECB water preservation mining method which can realize the parallel and coordinated operation of mining and filling was proposed, contributing to mitigating the overburden migration and thus achieving extracting coal body beneath the shallow water [36–42].

On the other hand, the annual output of fly ash in 2018 in China exceeded 550 million tons, and the total storage volume was more than 3 billion tons [43]. Large quantities of fly ash produced by the combustion of coal in power plants have been causing air and soil pollution [44,45]. Harmless and large-scale treatment of fly ash is therefore necessary and urgent. Meanwhile, CO_2 emissions from coal consumption account for 72% and 28% of Chinese and global CO_2 emissions, respectively. The combustion of 1 ton of coal produces 2.4 tons of CO_2 [46]. In 2018, China's coal combustion emitted around 7.2 billion tons of CO_2 and it strives to achieve a carbon peak by 2030 and be carbon neutral by 2060 [47–50]. In this context, carbon sequestration has attracted the attention of the Chinese government and emphasis has been put on it. However, the total amount of carbon sequestration is only about 300,000 t/a, which is not enough to provide effective support for this goal [51]. In order to effectively cope with the continuous increase in CO_2 emissions and fly ash, sequestrating CO_2 to fly ash and developing CO_2 mineralized filling body (CMFB) is one of the most ideal and appropriate options [52]. CMFB is employed and injected into the mined-out area of mining roadways (MRs) of the CECB mining method to realize CO_2 sequestration. In the meantime, solid CMFB replaces coal body to support the roof and mitigate the migration of the overburden and water-resisting layer, which can help to preserve the valuable shallow water resources and achieve green and sustainable development of coal areas. However, the mechanical properties of CMFB with various material ratios, and the influence of CMFBs on mining-induced aquifuge stability, which is of great importance for shallow water preservation, are not clear. The control mechanism of

CMFBs on the shallow water level while using the CECB mining method requires further study. Further study to develop CMFB with different material ratios to not only sequestrate CO_2 but preserve and conserve the shallow water level, and thus protect and maintain the surface ecological environment, is necessary.

In view of the aforementioned problems, we carry out a prospective study on the development and application of CMFB at ambient pressure and temperature, with fly ash as aggregate and silicate additives, cement and CO_2 gas as accessories. The indoor mechanical parameter test of the CMFB with different curing times and material ratios is carried out. Based on the stress–strain curve of the testing results, the proportion of analogue materials of CMFB is optimized and determined, and the physical similarity simulation of overburden movement while using the CECB mining method and CMFB is implemented. Additionally, the CMFB strain-softening parameters in the numerical simulation are calibrated systematically, and the $FLAC^{3D}$ numerical calculation model is then constructed to simulate the aquiclude movement corresponding to CMFB with different fly ash contents while using the CECB mining method. Subsequently, the fluid–solid coupling module is employed to reveal the influence mechanism of different material ratios of CMFB on the variation law of the shallow aquifer water level. This paper proposes a concept that employs the CECB water preservation coal mining method to sequestrate CO_2 and replace the coal body to support the roof, contributing not only to the harmless treatment of fly ash, but also the achievement of shallow water preservation mining. The research results can provide a theoretical reference and guidance for the realization of CO_2 mineralized filling in mines in the future, which is conducive to green and sustainable mining.

2. CECB Mining Method to Sequestrate CO_2 and Preserve Shallow Water

The confined room is necessary for the CO_2 mineralization process and CECB mining is an ideal mining method to provide a closed space for CMFB since the MRs features good airtightness and flexible and adjustable dimensions. The CO_2 can be mineralized with the solid waste in the long run and water preservation can be realized by optimizing the material ratio of the CMFB and the dimensions of MRs.

Prior to CECB mining, the mining panel is divided into many MRs along two sides of the headgate, and the MRs are then allocated to different mining phases (generally 3–5). The three-dimensional sketch map of the MR arrangement of the CECB method is shown in Figure 1. The schematic map of the mining processes of the CECB method is shown in Figure 2.
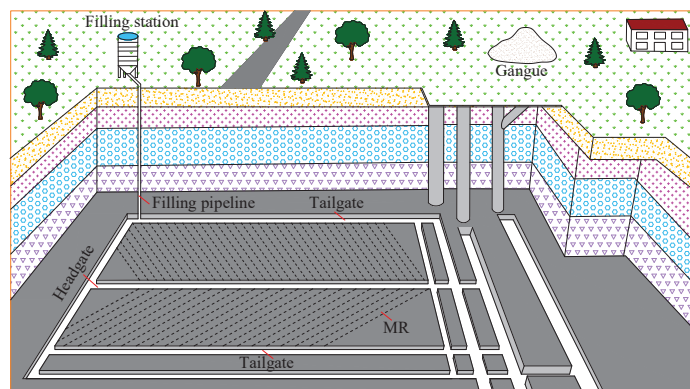
Figure 1. Three-dimensional sketch map of the MR arrangement of the CECB mining method.
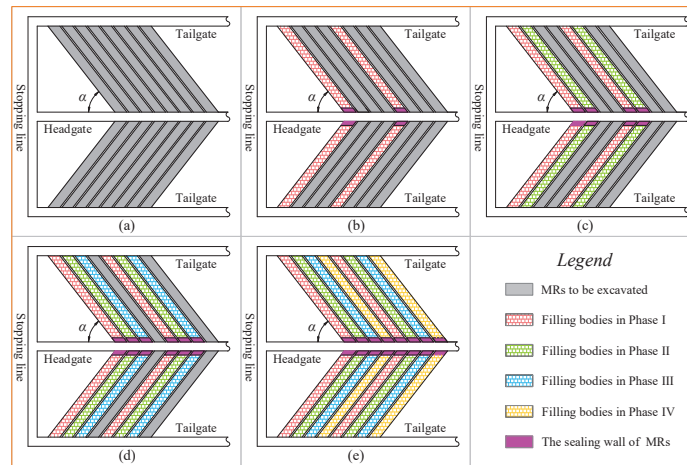
Figure 2. Schematic map of the processes of CECB. (**a**) The arrangement of MRs; (**b**) MRs of phase I have been excavated and filled; (**c**) MRs of phase II have been excavated and filled; (**d**) MRs of phase III have been excavated and filled; (**e**) MRs of phase IV have been excavated and filled. Reprinted with permission from ref. [32]. Copyright 2019 MDPI.

In order to mitigate the mining disturbance and thus to make the CMFB conducive to being injected, the length of the MR is generally less than 150 m while the width varies from 4.0 m to 7.0 m. The angle α between the MR and the headgate usually ranges from 40 to 60°. Skip extraction enables the roof of each mined-out MR to be supported by the coal body or the CMFB which has reached the designed strength. Hence, the drastic overburden deformation caused by insufficient longwall filling time can be averted. This method avoids the problem of uncoordinated operations between mining and filling during the longwall filling process. In addition, skip mining and filling make it feasible for the CMFB to stay in the three-dimensional stress state, which can increase the support strength of the filling body before it reaches the final strength. Both sides of the MRs, having been extracted, are always coal body or filling body that have reached the designed strength, which is conducive to controlling the migration and deformation of the overlying strata. For the purpose of effectively mitigating the movement of the overlying layers and avoiding the instability of the aquifuge, each MR will be sealed by a sealing wall and backfilled immediately after it is extracted. The MRs in the second phase will be extracted and backfilled after all MRs in the first phase are mined and backfilled. Finally, coal body in the mining panel is completely substituted by the CMFB to support the roof and preserve the shallow water. The CO_2 sequestration and coal extraction under shallow water bodies can be realized.

3. Development of the Carbon Dioxide Mineralized Filling Body

3.1. Specimen Preparation

The filling material is composed of aggregate and auxiliary materials, in which the aggregate plays the main bearing role as the main structure, and the auxiliary materials assume the roles of bonding, reinforcement and rapid setting. Low-calcium fly ash was selected as the aggregate, and CO_2 gas, silicate additives and cement were used as accessories to develop the CMFB with high content fly ash at ambient temperature and pressure. The grade F fly ash used in this study is from a power plant in Yuncheng City, Shanxi Province. OPC cement is from the local cement plant of Datun Town. Silicate additives were purchased online from Ningbo City, Zhejiang Province. The gas tank containing compressed CO_2 gas was bought from the local city.

The strength properties of the CMFB samples are highly dependent on the water–solid ratio. This research mainly studies the influence of the various ratios of the low-calcium fly ash to the cement on the uniaxial compressive strength (UCS) and tensile strength of CMFB, with the silicate additives and the concentration and flux of CO_2 being invariant. Therefore, a variable-controlling method was adopted to fix the water concentration at 30% of the total material, i.e., the water–solid ratio was set to 3:7. The test scheme is divided into 4 groups, namely FA55, FA65, FA75 and FA85, which denote the ratios of the fly ash to the total of the fly ash and the cement which are 55%, 65%, 75% and 85%, respectively. Each material ratio (the content of fly ash) includes two groups for the purpose of compressive and tensile tests. The curing times of each group are 3 d, 7 d, 14 d and 28 d, respectively. There are three specimens prepared for each setting time and each material ratio and each testing purpose, and the required number of compressive specimens and tensile specimens is $4 \times 4 \times 3 \times 2 = 96$ specimens. The detailed scheme is listed in Table 1.

Table 1. The schemes of material ratios of CMFB.

Scheme	Solid Mass Percentage (70 wt%)		FA *:CM * Ratio	Liquid Mass Percentage (30 wt%)		CO_2	Curing Time
	Fly Ash	Cement		Silicate Additives	Water		
FA55	55	45	11:9	10%	90 wt%	20 min	3/7/14/28
FA65	65	35	13:7	10%	90 wt%	20 min	3/7/14/28
FA75	75	25	15:5	10%	90 wt%	20 min	3/7/14/28
FA85	85	15	17:3	10%	90 wt%	20 min	3/7/14/28

* FA refers to the fly ash and CM denotes the cement.

The mortar samples were prepared according to the standard regulated by the state (GBT17671-1999), and the main process of the sample preparation is shown in Figure 3.

Figure 3. The process of CMFB specimen preparation and the mechanical tests.

① Weighing the fly ash and cement and mixing them evenly (Figure 3a). ② Weighing the particles of the silicate additives and putting them into a container to stir and melt (Figure 3b). ③ Mixing the dissolved silicate additive solution with evenly stirred fly ash and cement, and stirring until a uniform paste was obtained (Figure 3c). ④ Pouring the paste into the reactor with an automatic mixer, and stirring while introducing CO_2 gas for 20 min (Figure 3d,e). ⑤ Pouring the filling slurry into the standard molds made of a Jacqueline tube with dimensions of φ50 mm × 100 mm and φ50 mm × 50 mm, and shaking slightly to remove the incompletely reacted CO_2 bubbles. The noteworthy detail is that the bottoms of the molds were sealed with tape, and the bottoms and the tube wall of the molds were coated with waste oil to prevent the slurry from sticking to the mold (Figure 3f). ⑥ Taking out the samples from the molds after 12 h to 15 h after they were

poured, and putting them in the SHBY-40B standard curing box with constant temperature and humidity. The humidity is controlled at around 98%, with the curing temperature being 20 ± 2 °C, and the samples were cured for 3, 7, 14 and 28 days, respectively (Figure 3g). ⑦ The dimensions of the CMFB samples after the curing expiration was calibrated to make it a standard cylindrical filling body test piece that meets the dimension requirements of the mechanical test. Meanwhile, the upper and lower surfaces of the samples were polished smooth, and then the uniaxial compression tests and Brazilian splitting tests were implemented in the laboratory (Figure 3h–j).

The schematic diagram of CO_2 gas mixing with fresh slurry is shown in Figure 4.
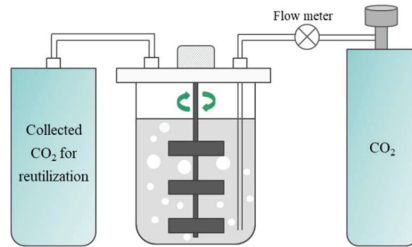
Figure 4. The chemical reaction between CMFB slurry and CO_2 is carried out under stirring.

3.2. Testing Results

3.2.1. Uniaxial Compressive Strength (UCS)

The UCS is particularly significant to improving the surrounding rock stress environment and evaluating the mechanical stability of the overlying strata. The WAW-1000D electro-hydraulic servo motor test system, with maximum load of 50 kN, was employed as the loading equipment in the experiment to test the UCS of the CMFB with various curing times and fly ash proportions. The displacement-controlled loading mode was adopted during the tests. Firstly, the fixed CMFB specimen was preloaded at a constant loading speed of 3 mm/min, and the target value was 0.05 kN, so that the filling body was in contact with the loading equipment. Then the force and displacement monitored on the computer was cleared, and the constant loading speed was adjusted to 0.3 mm/min and the target value was reset to 10 mm to conduct the UCS test. All tests were repeated 3 times to eliminate errors and the average value of UCS of each curing time and fly ash content was obtained.

The UCS variation laws of CMFBs with various curing times and fly ash contents are shown in Figure 5a,b, respectively. Some of the failure specimens after UCS test are illustrated in Figure 5c. According to the previous experience of filling body development without CO_2 [8], the UCS will decrease with increasing fly ash content, due to the fact that a drop in the latter means a decrease in hydration products. To the contrary, the UCS of CMFB samples increases first and then decreases with the rising proportion of the fly ash, reaching the maximum at 75%, and then decreases, showing almost the opposite trend to that of the filling body without CO_2. It is worth noting that when the fly ash content is 95%, the UCS of CMFB is too small to withstand preloading. The UCS of CMFB with 85% fly ash is 1.982, 2.356, 3.832 and 4.162 MPa, respectively, corresponding to curing times of 3, 7, 14 and 28 days. The UCS of CMFB with 85% fly ash is not only lower than those with 75% fly ash but also less than those with 65% in each curing time. Therefore, the addition of CO_2 and silicate additives exerts a significant impact on the UCS of CMFB. By analyzing the chemical reaction of different materials, we hold the view that the CO_2 accelerates the initial hydration of CMFB slurry and makes it able to form silica gel. In other words, the accelerated hydration and silica gel replaced the cementation identity of cement, and thus increased the UCS of CMFB.
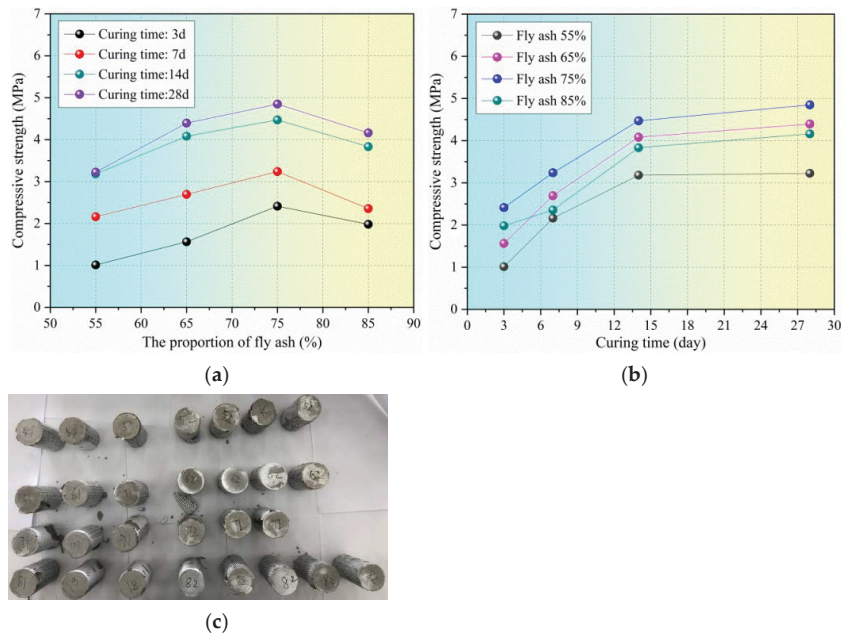
Figure 5. The UCS of CMFB with various fly ash contents and curing times. (**a**) Various fly ash contents; (**b**) various curing times; (**c**) some damaged specimens after the UCS test.

As Figure 5b shows, the UCS of CMFB rises with the growing setting time. The ascending curing time means more hydration, which implies more hydrates bind the particles together, and the occlusal friction between the particles leads to the increase in UCS. Taking the UCS of CMFB with 55% fly ash, for instance, the UCS is 1.012, 2.162, 3.181 and 3.224 MPa, corresponding to curing times of 3, 7, 14 and 28 d, respectively. The UCS grows sharply from 3 to 14 d curing time while it increases slightly from 14 to 28 d, which means the hydration after 14 d starts declining drastically.

3.2.2. Tensile Strength

During the field investigation of backfill mining face, it is found that many filling bodies suffer from instability due to the insufficient tensile strength and the incapability of resisting tensile deformation. Both the compression and bending failure of filling bodies are caused by tensile strain or shear strain exceeding the ultimate bearing capacity. It is therefore necessary to study the tensile strength of the filling body. By analyzing the mechanical properties from the indoor tensile test, the support quality of the filling body to the roof can be improved, and thus the stability of the overlying aquifuge and shallow water level can be maintained.

The Brazilian splitting method, a popular indirect measurement method, was employed for the indoor tensile strength test of the CMFB. The CMFB specimen was damaged along the radial direction under the load, rather than the splitting of the whole specimen. In addition, the surface roughness of most specimens means the linear loading cannot be guaranteed to be uniform, resulting in large dispersion of the measured data. Therefore, extra specimens were added to eliminate the problem of large dispersion of tensile strength data. The relationship between the tensile strength and the curing time and the content of fly ash, as well as the failure conditions of the specimens after the Brazilian splitting test, are shown in Figure 6.
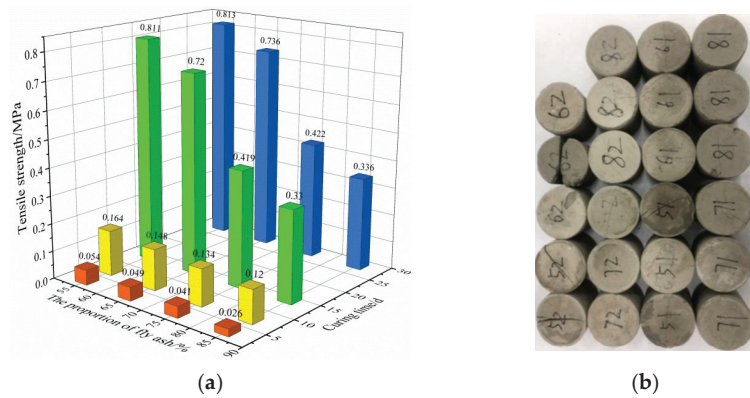
Figure 6. The tensile strength of CMFB and the physical map of specimens. (**a**) The tensile strength of CMFB with various curing times and fly ash contents; (**b**) the physical map of some specimens after the Brazilian splitting test.

4. Deformation of the Overlying Strata and Aquifuge

4.1. Main Parameters of Analogue Simulation

Based on the engineering and geological conditions of a coal mine in northwest China, a physical analogue model with dimensions of 2.5 × 0.2 × 1.24 m (length × width × height) was built in the laboratory in accordance with the principles of similarity theory. The geometric similarity ratio is 1:200. The model is divided into four mining phases, with 10 MRs in each mining phase. After all MRs in a mining phase are mined and backfilled, the MRs in the next phase start being extracted and filled until all MRs in the four mining phases are mined and filled. The dimensions of each MR are 6.0 × 2.6 m (width × height), and the filling rate is around 90% since the roof subsides before backfill.

Sand, calcium carbonate, gypsum, etc. were selected as raw materials to develop physical similarity materials of CMFB. The UCS stress–strain characteristics of similar materials with different material ratios were tested, and the stress–strain curves were compared with that of CMFB with 14 d curing time and 75% fly ash, so as to select the optimal material ratio of similar materials of CMFB for the physical similarity simulation. The test results of the stress–strain curves of the selected ideal similar material and the CMFB are shown in Figure 7, with the error being less than 4%. The material mixture ratio of strata and the CMFB in the analogue model is shown in Table 2.
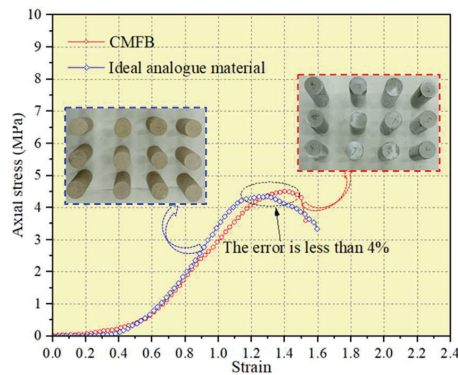
Figure 7. The stress–strain curves of the CMFB and its similar materials in analogue simulation.

Table 2. The material ratios of strata and CMFB in the physical analogue model.

No.	Lithology	Thickness (cm)	Water (kg)	Sand (kg)	Calcium Carbonate (kg)	Gypsum (kg)	Total (kg)	Remarks
1	Loess	4.0	1.67	13.64	0.68	0.68	16.67	Aquifer
2	Red clay	25.0	6.24	49.23	3.51	3.51	62.49	Aquifuge
3	Sandstone	16.6	8.96	69.11	5.76	80.63	164.46	
4	Sandy mudstone	31.5	18.95	149.32	10.66	10.66	189.59	
5	Medium sandstone	4.5	4.82	25.31	5.91	2.53	38.57	
6	Mudstone	21.0	15.41	121.41	8.67	8.67	154.16	Bedrock
7	Sandstone	3.0	2.5	18.76	1.88	1.88	25.02	
8	Fine sandstone	7.8	6.46	42.19	4.22	4.22	57.09	
9	Limestone	4.6	1.9	12.19	1.78	1.03	16.90	Roof
10	Coal seam	1.3	1.04	8.20	0.82	0.35	10.41	Coal
11	Bauxitic mudstone	4.7	1.04	8.33	0.52	0.52	10.41	Floor
12	CMFB	1.3	1.12	8.31	0.75	0.28	10.46	CMFB

After the analogue model was laid and dried for ten days, six survey lines were set in the front of the model to measure the deformation of the overlying layers and especially the aquifuge. Each survey line consists of 13 measuring points, and the distance between each measuring point is 0.2 m. The purpose of survey Line 1 is to monitor the deformation of the main roof, while Line 2 to Line 4 aim to measure the migration of the bedrock. Line 5 and Line 6 are arranged to monitor the deformation of the aquifuge and ground surface, respectively. The analogue model after all MRs are extracted and backfilled, as well as the arrangement of the measuring points, are shown in Figure 8.
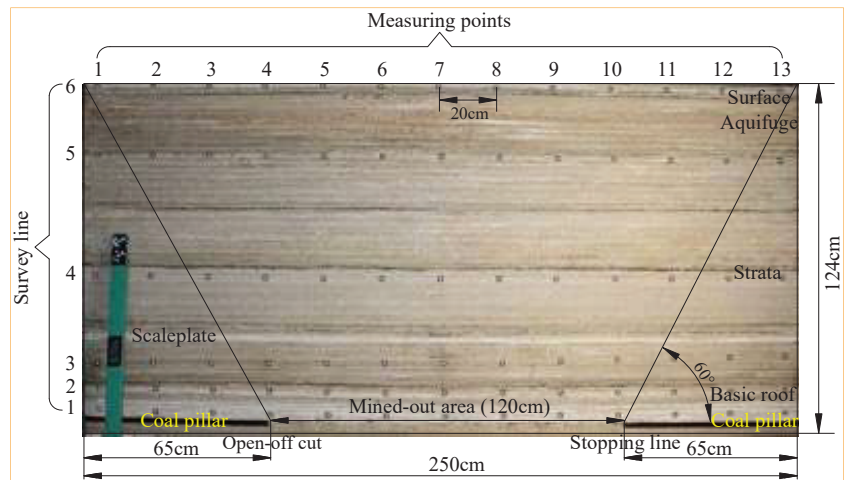
Figure 8. Physical analogue model of CECB mining after all MRs are extracted and backfilled.

4.2. Results of Analogue Simulation

The results indicate that there are no obvious fractures or cracks in the overlying strata and each stratum is still intact and undamaged after all MRs in the four mining phases are mined and backfilled, suggesting that the CECB method can effectively control the overlying strata migration and fracture development. During the experiment, the displacement of each measuring point was recorded by the Tianyuan 3D Photogrammetry System. The measured data were converted according to the geometric similarity ratio of 1:200. When all MRs were extracted and backfilled, the vertical displacement of 6 survey lines was monitored, as illustrated in Figure 9a. The dynamical deformation characteristics of the overlying aquiclude during four mining phases are shown in Figure 9b.
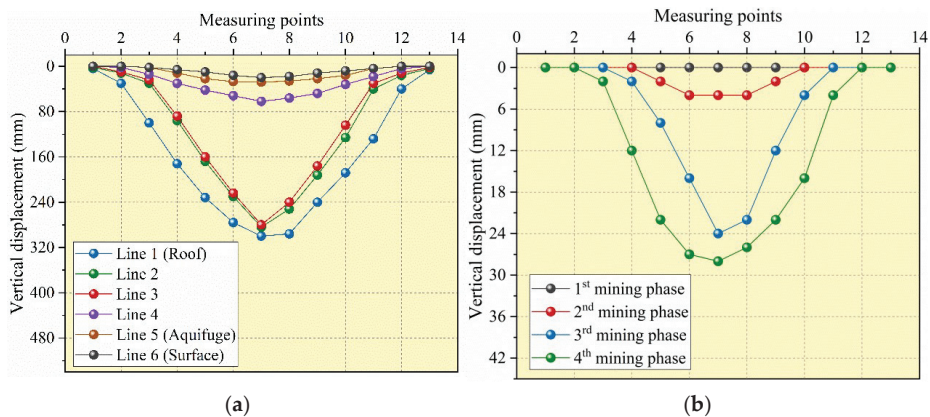
Figure 9. The deformation of the overburden and the aquifuge. (**a**) The vertical displacement of 6 survey lines after all MRs are extracted and backfilled; (**b**) the vertical deformation of the aquifuge during 4 mining phases.

The migration and displacement of the overlying strata in the last mining phase is of great significance for evaluating the roof-controlling effectiveness of the CECB mining. Therefore, the vertical displacement of the overlying strata in various positions was measured. As Figure 9a shows, after the MRs in the fourth mining phase were extracted and backfilled, the vertical displacement of the main roof and the lowest two strata of the bedrock, monitored by Line 1 to Line 3, is far more than that of the top stratum of the bedrock, the aquifuge and surface. The maximum vertical displacements of the six measuring lines are 300 mm, 284 mm, 280 mm, 62 mm, 28 mm and 20 mm, respectively. Moreover, the water-resisting layer measured by Line 5 was selected for separate analysis since its deformation is vital to prevent water flowing from its overlying aquifer, and thus realize shallow water preservation coal mining. It can be seen from Figure 9b that the vertical deformation of the aquifuge in the first stage remains stable and always equals 0, due to the long distance from the mining panel to the aquifuge and thus the low mining disturbance. During the first two mining stages, the vertical subsidence of the aquifuge rises slowly. By contrast, the vertical displacement of the water-resisting layer rises drastically from the 3rd to the 4th mining phase. After all MRs in the mining panel are extracted and filled, the maximum value of vertical displacement is 28 mm. Note that the value of horizontal displacement and horizontal deformation is too small to be detected by the Tianyuan 3D Photogrammetry System. The five indexes of aquifuge deformation will be further studied in Section 5.

5. Numerical Simulation of Aquiclude Deformation Using CECB and CMFB

5.1. Construction of the Numerical Simulation Model

Fast Lagrangian Analysis of Continua (FLAC^{3D}), a three-dimensional finite difference program developed by ITASCA in the United States, is one of the most widely used pieces of numerical analogue software in underground mining and geological engineering. The physical similar simulation model only detects vertical displacement of the aquifuge while the horizontal displacement is too small to detect. In addition, only CMFB with 14 d curing time and 75% fly ash content was taken into consideration in the physical simulation, which cannot study the influence of CMFB with different material ratios on the migration and stability of the aquifuge. In order to supplement the undetected horizontal displacement and horizontal deformation of the water-resisting layer and verify the results of the physical analogue simulation, a FLAC^{3D} numerical calculation model was established to simulate the deformation and water table lowering of the aquiclude using CECB mining and CMFB with 14 d curing time and various fly ash proportions, as shown in Figure 10. Based on

the engineering and geological conditions of a colliery which are the same as the physical analogue simulation, the adjacent strata with similar lithology are properly simplified and merged, and 12 strata were identified from bottom to top. With due consideration of the boundary effect and full mining, the dimensions of the model are determined to be 612 m × 558 m × 248 m (X × Y × Z). The deformation and velocity of the four boundaries of the numerical model located at the starting and ending point of the *X* and *Y* axis remain immobile. Meanwhile, the boundary at the starting point of the *Z* axis was fixed while the top surface was free without any restrictions.
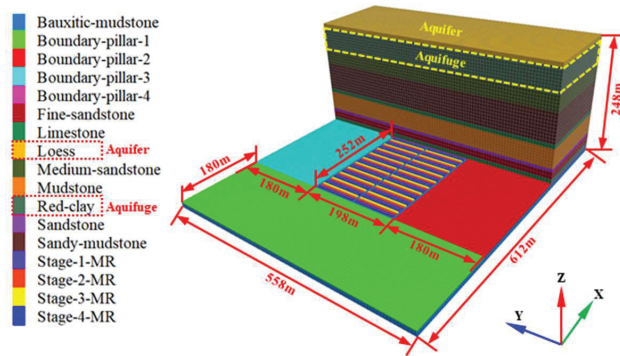
Figure 10. Numerical calculation model for simulating the aquifuge deformation under CECB.

The length of the four boundary coal pillars is 180 m. The mining panel whose dimensions are 240 m × 180 m (strike × dip) is surrounded by a haulage roadway with width of 6 m. The height and width of the MR are 2.6 m and 6 m, respectively. The CECB mining area is divided into four phases, and a total of 80 MRs are distributed on both sides of the main transportation roadway. There are 20 MRs in each phase, and skip and interval mining are adopted on the same side along the main haulage roadway. After one MR is mined, the next one on the other side of the main haulage roadway is extracted immediately and the mined-out MR is backfilled simultaneously. The third MR, which is 24 m (four times of the MR width) away from the first MR in the *X* direction, is extracted in the same way as the first MR. When the MRs in the first phase is mined and backfilled, the MRs in the second phase start being extracted and filled until all MRs in the four phases are extracted.

A Mohr–Coulomb constitutive model was chosen for the coal seam and its overlying and underlying strata. Therefore, it was employed to conduct uniaxial compression simulation tests of rock from various strata, so as to determine the mechanical parameters of different strata. The mechanical parameters of each stratum in the model are adjusted continuously, until the simulation results show good consistency with the stress–strain curve obtained from the laboratory test. The mechanical property parameters of various strata are listed in Table 3.

5.2. Determination of the Simulation Parameters of CMFB

According to the research in Section 3, the UCS of the CMFB increases rapidly when the setting time varies from 3 d to 14 d, while it slows down from 14 d to 28 d curing time, indicating that its strength and mechanical properties tend to be stable. Similarly, it takes 3 days to extract the coal body of each MR and 1 day to backfill it. The distance between the MR being extracted and the MR that was backfilled 14 days ago is generally greater than 70 m, so the filling body in the MR before day 14 is essentially immune to the current mining. It only bears the static load generated by ground pressure, and its mechanical environment is inclined to remain unchanged. Therefore, CMFB with 14 d curing time was selected for further analysis.

Table 3. The mechanical parameters of strata and coal seam of the numerical model.

Strata	Bulk Modulus (GPa)	Shear Modulus (GPa)	Cohesion (MPa)	Friction Angle (°)	Tensile Strength (MPa)	Bulk Density (kN·m³)	Thickness (m)
Loess	-	-	-	-	-	14.7	8
Red clay	0.08	0.05	0.33	27	0.12	19.7	50
Medium sandstone	3.2	2.0	1.6	31	1.4	20.6	33.2
Sandy mudstone	2.8	1.7	1	22	1	19.7	63
Limestone	7.2	5.5	2	40	4.0	24.0	9
Mudstone	2.9	2.1	1.4	19	1.1	28.6	42
Sandstone	6.81	5.91	10.7	40.6	2.2	2540	6
Fine sandstone	3.8	2.6	1.6	31	1.4	20.6	15.6
Limestone	7.2	5.5	2	40	4.0	24.0	9.2
Coal	2.2	0.76	1	20	1	18.7	2.6
Bauxitic mudstone	4.2	2.8	1.4	34	1.4	28.6	9.4

Moreover, the Young's modulus of the backfill is a significant index reflecting its supporting capacity to the overburden and water-resisting layer. The filling body with large elastic modulus has better mechanical properties, which can effectively alleviate the deformation and fracture development of the overburden, so as to reduce the mining-induced impact on the shallow aquifer. Conversely, the backfill with small elastic modulus has greater deformation under the same load than that of the larger one, leading to the increasing subsidence of overlying layers. The water-flowing fractures will therefore be well developed, which may form a water-conducting channel between the mined-out area and the overlying aquifer and trigger a mine water inrush disaster. According to the UCS test results of CMFB from the laboratory, the proportion of fly ash has a great influence on the elastic modulus of the backfill, while the Poisson's ratio is nearly unchanged and remains at 0.18 on average. The elastic modulus can be obtained by analyzing the slope of the stress–strain curve in the elastic deformation stage:

$$E_f = \frac{\sigma_b - \sigma_a}{\varepsilon_b - \varepsilon_a}, \tag{1}$$

where E_f is the elastic modulus of CMFB; σ_a and σ_b represent the stress of the starting and terminal point of the elastic deformation stage, respectively; ε_a and ε_b denote the strain of the origin and the end of the elastic deformation stage, respectively.

The bulk modulus and shear modulus can be calculated by:

$$K_f = \frac{E_f}{3(1 - 2\mu)}, G_f = \frac{E_f}{2(1 + \mu)}, \tag{2}$$

where K_f is the bulk modulus, G_f is the shear modulus and μ is the Poisson's ratio.

Table 4 lists the mechanical property parameters such as elastic modulus, bulk modulus and shear modulus of CMFB with different fly ash contents after being cured for 14 days.

Table 4. The physical and mechanical parameters of CMFB with 14 d curing time and various fly ash contents.

Proportion of Fly Ash (%)	Young's Modulus (GPa)	Bulk Modulus (GPa)	Shear Modulus (GPa)
FA55	0.4	0.21	0.17
FA 65	0.6	0.31	0.25
FA 75	1.0	0.52	0.42
FA 85	0.5	0.26	0.21

The strain-softening constitutive model was employed for CMFB. The cohesion, friction, dilation and tensile strength may soften after the beginning of plastic yield, while these properties are assumed to remain unchanged in the Mohr–Coulomb model. The strain-softening behavior of cohesion, friction angle and dilation based on plastic shear strain and plastic tensile strain were given in the form of specified table values, assuming that the two parameters in the table code are consecutive. The table values of these parameters were defined by the authors and they were obtained by back-analysis of the postfailure behavior of the CMFB.

Taking the CMFB with 14 d curing time and 75% fly ash content as an example, the stress–strain curves of the UCS test from the laboratory test and the numerical simulation, as well as the failure form of the CMFB specimen and the maximum shear strain of the numerical simulation model, were compared and analyzed to systematically calibrate the aforementioned parameters of the strain-softening constitutive model. The calibration results are shown in Figure 11.
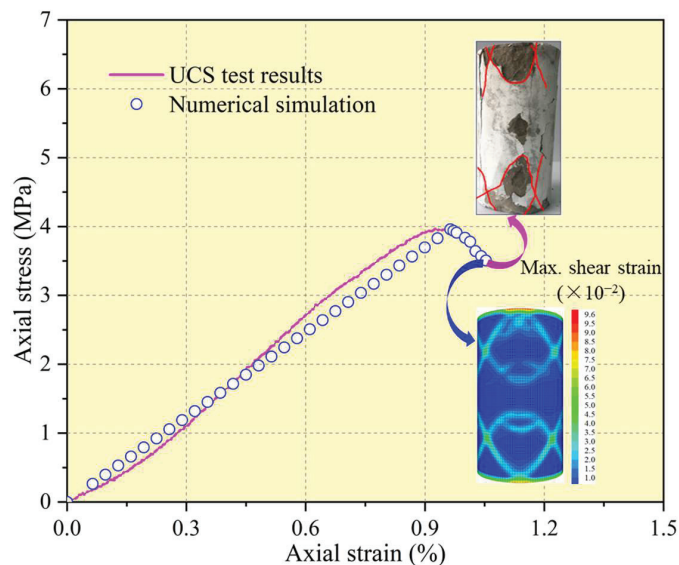
Figure 11. The stress–strain curves and failure model of CMFB from the laboratory UCS test and the numerical simulation.

This simulation considers that the cohesion and friction of CMFB decrease with the growing plastic shear strain, for the purpose of optimizing the numerical calculation steps. Their values are the residual value when the plastic shear strain is 0.01. The numerical results of the stress–strain curve and failure mode of the specimen were in good agreement with that of the indoor test results. In the numerical model, the maximum shear strain of the specimen shows an inclined and cross failure mode, which is consistent with that from the laboratory test. The parameters of the strain-softening model of the CMFB with various fly ash contents were calibrated and determined by the same means for the next study.

5.3. Mining-Induced Deformation of the Water-Resisting Layer

According to the calibrated strain-softening mechanical parameters of the CMFB, the numerical calculation of the movement of the water-resisting layer while using CECB mining and CMFB was carried out. After all MRs in the mining panel were extracted and backfilled and the maximum unbalance force was less than 10^{-5} kN, the numerical calculation process ended. The bottom of the aquiclude was sliced, with the normal vector parallel to the Z axis. Subsequently, the postprocessing software Tecplot was employed to extract the vertical and horizontal displacement values of the aquifuge in the section, and

the extracted data were imported to another postprocessor Surfer. The Kriging interpolation method was adopted to draw the contour of the vertical displacement and the horizontal displacement of the aquiclude while using the CECB water-preserving mining. Then, the differential function built into the Surfer software was utilized and the contour map of the inclination, curvature and horizontal deformation of the aquifuge were derived, by executing the first-order and second-order differential functions embedded in the software. Figure 12 shows the contour map of the five deformation indicators of the overlying aquifuge while injecting the CMFB with a 75% fly ash proportion into the mined-out MRs.

Both the positive and negative deformation values can reflect the migration and damage degree of the rock stratum, so only the absolute value was analyzed. As Figure 12 shows, under the conditions of injecting the CMFB, with the proportion of fly ash being 75%, into the mined-out MRs in the CECB mining panel, the maximum values of vertical displacement, horizontal displacement, inclination, horizontal deformation and curvature of the overlying aquifuge are 26 mm, 6.5 mm, 0.12 mm/m, the 0.08 mm/m and 0.0015 mm/m^2, respectively.

The maximum vertical judder of 26 mm is located in the middle of the aquifuge above the CECB mining panel and decreases up to its surrounding boundary, forming a typical subsidence basin. By contrast, the distribution of the tilt value is symmetrical with the perpendicular bisector of the X axis as the symmetrical point and the maximum values of 0.12 mm/m occur in the place of aquiclude over the two boundaries of the working face in the X direction, which is known as the open-off line and the stopping line. In addition, the maximum curvature of 0.0015 mm/m^2 arises in the water-resisting layer above the center of the mining panel, which is similar to the vertical displacement. The lowest value is situated in the vicinity of the working face. Hence, the curvature decreases to the minimum value of 0.0001 mm/m^2 first and then rises to 0.0009 mm/m^2 in the boundary of the model. Furthermore, the contour map of the horizontal displacement is similar to that of the tilt, with the maximum size of 6.5 mm at the overlying aquifuge over both sides of the CECB face along the X direction. The maximum horizontal deformation of 0.08 mm/m is in the center of the aquifuge, indicating the high probability of the development of vertical tensile fractures.

By using a similar method to the one above, the maximum values of the five deformation indexes of the water-resisting layer while using the CMFB with 55%, 65% and 85% fly ash were obtained, as shown in Figure 13.

The maximum values of five deformation indexes of the water-resisting layer decline first and then increase with the growing fly ash contents. When the fly ash proportion is 75%, the maximum value of all deformation indexes of the aquifuge is the smallest. The CMFB with 55% fly ash contributes to the five largest deformation indicators, which is completely opposite to the traditional cemented filling material using fly ash as aggregate and suggests that CO_2 and silicate additives exert a significant impact on the strength of the CMFB.

In a previous study on water preservation coal mining in the Yu-Shen mining area, the authors found that the index of horizontal deformation has a vital influence on the stability and integrity of the water-resisting layer. If the maximum horizontal deformation value of the aquifuge (red clay) exceeds 0.20 mm/m, which is greater than its allowable ultimate tensile strain, a vertical tensile micro-fracture in the aquiclude may occur. The micro-fractures are prone to developing into macro-cracks with wide aperture and high penetration rate under the condition of larger horizontal deformation. If the fractures go through the entire aquifuge and trigger a failure to resist water flow, the shallow water will percolate and flow into the mined-out area along the water-conducting fractures and water inrush will happen in the coal mine.
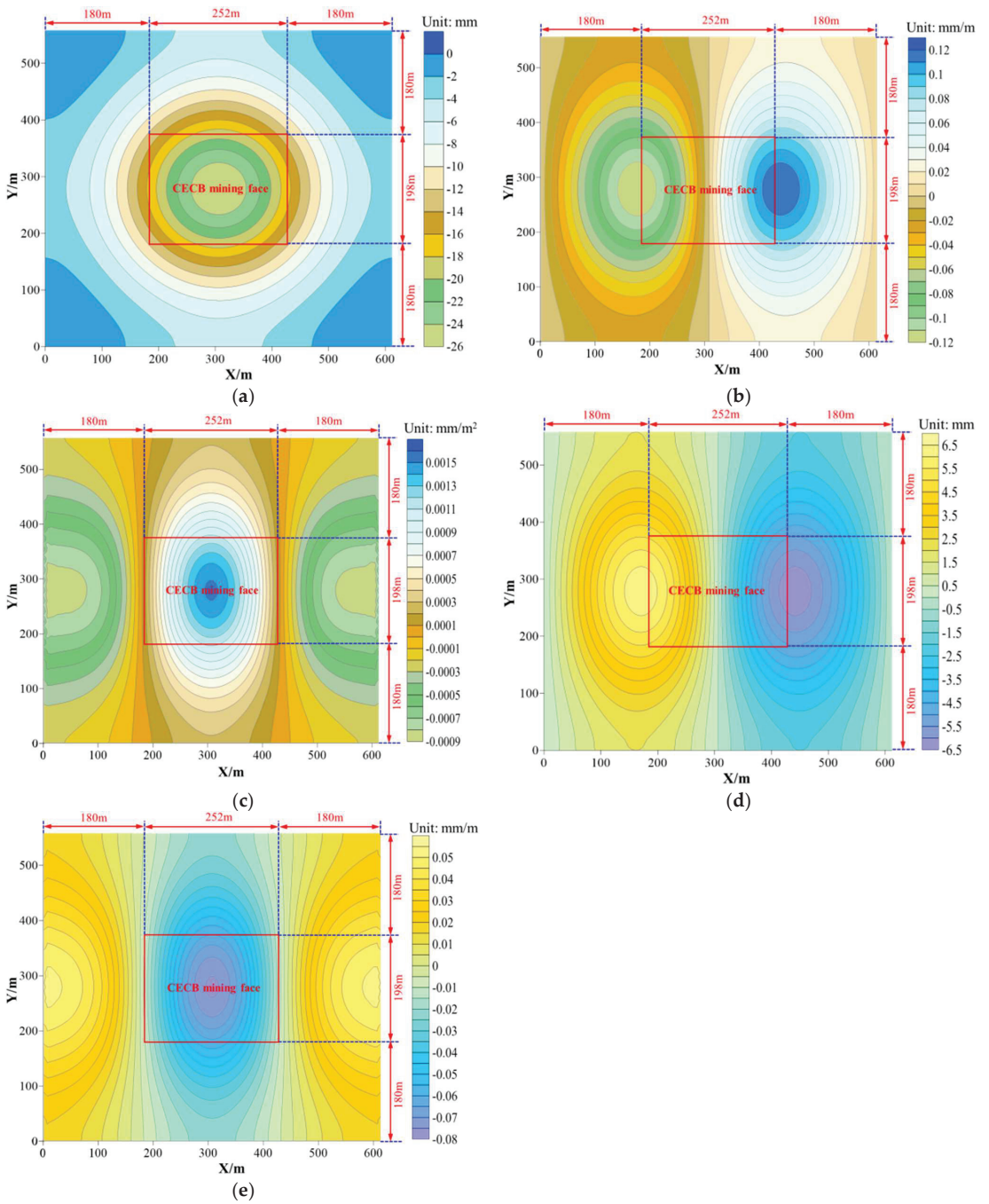
Figure 12. Numerical simulation results of the movement of aquifuge while using CECB and CMFB with 75% fly ash. (**a**) Vertical displacement; (**b**) tilt; (**c**) curvature; (**d**) horizontal displacement; (**e**) horizontal deformation.
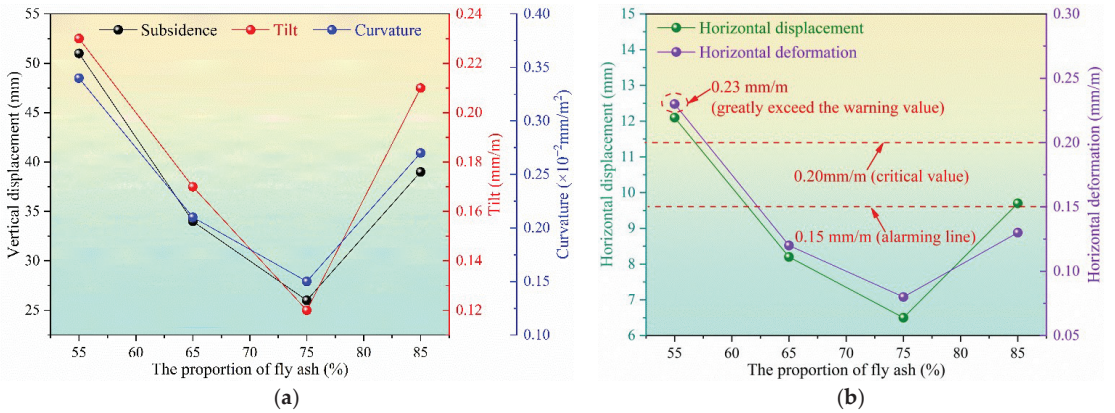
Figure 13. Numerical simulation results of the maximum values of five deformation indexes of the aquifuge with various proportions of fly ash. (**a**) The vertical displacement, tilt and curvature; (**b**) the horizontal displacement and horizontal displacement.

It can be seen from Figure 12b that the maximum horizontal deformation of the water-resisting layer is 0.23 mm/m while using CMFB with 55% fly ash content, which exceeds the critical value for realizing water-conserving coal mining. Moreover, the maximum horizontal deformation value corresponding to CMFB with 65% and 85% fly ash is 0.12 and 0.13 mm/m, both of which are approaching the warning value of 0.15 mm/m, and due consideration should thus be taken during the process of field implementation of CMFB.

5.4. Water Table Lowering of the Shallow Water
5.4.1. Establishment of Fluid–Solid Coupling Numerical Model

The fluid–solid coupling module was set to simulate the water level fluctuation of the shallow water while using CECB mining and CMFB with different fly ash contents. The "CONGIG fluid" code was employed to enter the seepage mode, and the "Initial PP" code was utilized to set the pore pressure and pore water pressure gradient. Moreover, the fluid–solid coupling numerical calculation mode was isotropic. The permeability coefficient of red clay (aquifuge) is less than 10^{-7} cm/s. The permeability coefficients of hard rocks, i.e., mudstone, bauxitic mudstone, sandy mudstone, sandstone, fine sandstone, medium sandstone and limestone, are greater than that of red clay, and are listed in Table 5. The tensile strength of the fluid is set to 10^{15} Pa and its porosity is set to 0.5, both of which are default values in the FLAC^{3D} software. The saturation is set to 1 and the Biot coefficient is also set to 1. The "Fix pp" code was used to set the top surface loess (shallow water) as a free surface where the water can flow in or out, while the surrounding and bottom boundaries of the numerical simulation model were set as impermeable boundaries without penetrating fluids.

Table 5. The permeability coefficient of the overlying strata.

Number	Lithology	Permeability Coefficient (cm/s)
1	Red clay	10^{-7}
2	Mudstone	10^{-6}
3	Bauxitic mudstone	10^{-5}
4	Sandy mudstone	10^{-5}
5	Sandstone	10^{-4}
6	Fine sandstone	10^{-4}
7	Medium sandstone	10^{-4}
8	Limestone	10^{-3}

5.4.2. Characteristics of Underground Aquifer in the Yu-Shen Coal Area

From bottom to top, there are total four types of aquifer in the Yu-Shen mining area, namely, the porous bedrock confined aquifer, burnt rock phreatic aquifer, Salawusu phreatic aquifer and unconsolidated porous phreatic aquifer, as shown in Figure 14.
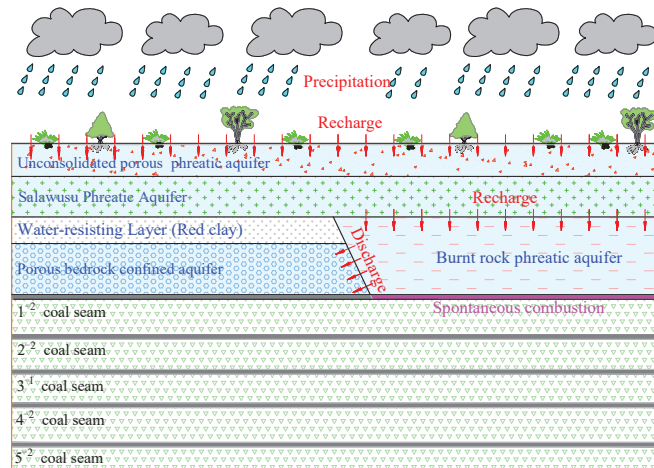
Figure 14. The major types of aquifers in Yu-Shen mining area.

The porous bedrock confined aquifer features minor porosity, high permeability, extremely low water yield property and restricted distribution range. Additionally, the burnt rock phreatic aquifer is primarily recharged from the overlying Salawusu phreatic aquifer and itself cannot form an independent water-storing formation. By contrast, the Salawusu Formation aquifer is widely distributed in the mining area, with thickness ranging from 0 m to 67.3 m and the water table being generally less than 10 m. The unconsolidated porous phreatic aquifer in the study area is weak and mainly recharged by precipitation, usually forming a united aquifer with the underlying Salawusu formation aquifer. The united buried shallow aquifer is what we called shallow water. It is the major aquifer in this area for domestic and ecological water supply, which needs to be considered during water conservation coal mining.

5.4.3. Numerical Simulation Results of Water Table Lowering of Shallow Water

The water level fluctuation can be investigated according to the change in pore water pressure since the shallow water is not a confined aquifer. The groundwater depression cone and the contour map of water table lowering employing the CECB water-conserving coal mining method and CMFB with 75% fly ash are shown in Figure 15. The groundwater level has decreased by 0.47 m, indicating a narrow variation in groundwater level. In addition, the water level drop of the shallow aquifer using CMFB with different fly ash contents is shown in Figure 16.

The main types of vegetation in the study area are Salix psammophila, Artemisia annua, Populus euphratica and Saliz matsudana. The buried depth of shallow water ranges from 0.5 m to 1.8 m, and the surface vegetation is flourishing and exuberant. According to the field investigation of academician Wang Shuangming [30], the relationships between the growth conditions of the aforementioned vegetation and the shallow water level are listed in Table 6. It can be seen that when the buried depth of groundwater exceeds 3.0 m, the growth of surface vegetation will be restrained and thus degraded. Therefore, the water table drop should not be greater than the range varying from 1.2 m to 2.5 m. In order to ensure the flourishing growth of surface vegetation above the CECB mining face, the mining-induced water table lowering should be strictly less than 1.2 m.

(**a**)   (**b**)
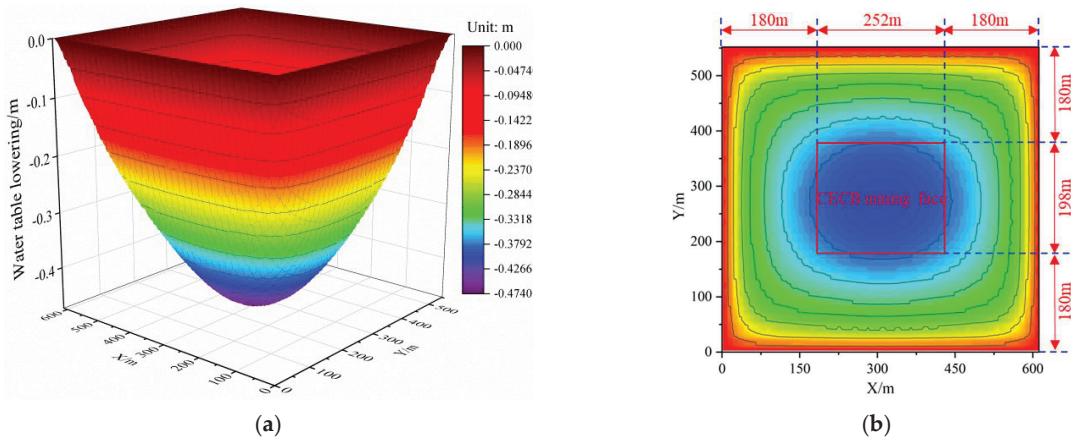
Figure 15. The numerical simulation results of shallow water level drop of the colliery when injecting the CMFB with 75% fly ash into the mined-out area. (**a**) The groundwater depression cone; (**b**) the contour map of water table lowering.
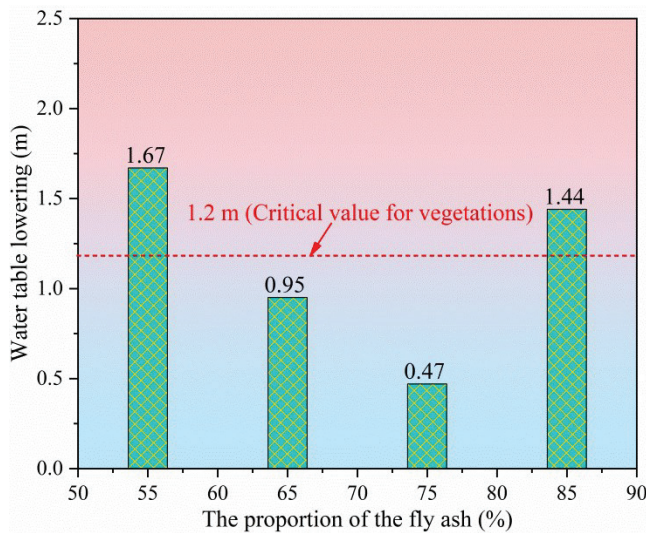
Figure 16. Fluid–mechanism coupling simulation of shallow water level lowering while injecting CMFB with different proportions of fly ash.

Table 6. The statistical results of the relationship between the growth of surface vegetation and the groundwater level [30].

Vegetation Type	Depth of the Shallow Buried Aquifer and the Growth of Vegetation			
Salix psammophila	<1.5 m (Luxuriant)	1.5 m–3.0 m (Good)	3.0 m–5.0 m (Normal)	>5.0 m (Poor)
Artemisia annua	<1.5 m (Luxuriant)	1.5 m–3.0 m (Good)	3.0 m–5.0 m (Normal)	>5.0 m (Poor)
Populus euphratica	<1.5 m (Luxuriant)	1.5 m–3.0 m (Good)	3.0 m–5.0 m (Normal)	>5.0 m (Poor)
Saliz matsudana	<3.0 m (Luxuriant)	3.0 m–7.0 m (Good)	7.0 m–12.0 m (Normal)	>12.0 m (Poor)

According to Figure 16, the decline in water level using CMFB with 55% and 85% fly ash is 1.67 and 1.44 m, respectively, neither of which meet the requirements for water conservation coal mining. By contrast, the CECB mining method using CMFB with 65%

fly ash has caused a 0.95 m water table drop, 80% of the critical groundwater level drop for surface vegetation, and is therefore an alternative since it is under the threshold. It is apparent that the CMFB with 75% fly ash was the most suitable one to protect precious shallow water and surface vegetation, contributing to water and ecology preservation coal mining.

6. Discussion

This paper describes a prospective investigation on developing carbon dioxide mineralized filling body (CMFB) at ambient temperature and pressure and sequestrating it in the MRs of the CECB mining method, offering a novel way to realize CO_2 sequestration. Additionally, CMFB development by using fly ash, etc. can contribute to the harmless treatment of solid wastes and prevent their pollution of air, soil and shallow water. Moreover, fly ash is cheap and can be widely obtained. Hence, selecting fly ash as aggregate in CMFB can greatly reduce the amount of cement and reduce the total filling costs. The research results are conducive to the coordinated development of coal extraction and water resource preservation, contributing to shifting the single situation of "water conservation mining" to "low-carbon collaborating solid waste treatment water conservation mining". The paper provides a theoretical basis and reference for the field implementation of CMFB in the future and thus facilitates the construction of green and sustainable mining areas.

Traditional CO_2 mineralized coal-based solid waste technology needs catalytic nucleation at high temperature and pressure to improve the reaction rate of CO_2 and mineralized nodule rate, which is difficult to realize in large-scale industrialization. Therefore, it is of great scientific and engineering significance to explore and develop CO_2 coal-based solid waste filling materials at ambient temperature and pressure. On the other hand, it is necessary for the CO_2 mineralization process to be carried out continuously in a relatively confined space, which is coincident with the characteristics of the CECB mining method. The MR of CECB has good leak tightness during and after mining and filling, and the dimensions of the MR can be adjusted flexibly. By optimizing the layout and the dimensions of the MR, it can not only ensure the long-term mineralization of coal-based solid waste with CO_2, but can also realize water preservation coal mining. However, the field application of CMFB needs to solve a series of problems, including large-scale CO_2 capture, filling material transportation and the weakening of the stability of CMFB after reacting with water.

At present, water preservation mining methods are primarily harmonic mining, partial mining, curtain grouting, overburden bed separation grouting and backfill mining. Harmonic mining optimizes the working face layout, the mining sequence and the advancing direction uniformly to counteract the movement of overlying strata. However, its popularity and applicability are limited due to the various distributions of protected objects (overlying aquifers, buildings and structures). In addition, the partial mining left coal pillar unmined permanently or abandon a portion of coal resources to support the roof and thus realize the mitigation of overburden deformation and thus shallow water loss. Hence, large amounts of resources are wasted and there is a low recovery rate of generally less than 50%. Additionally, curtain grouting injects the slurry into the cracks, pores or mining-induced fractures between the overlying shallow water and the mined-out area. The purpose of the method is to form a continuous curtain that can block the water percolation channel from the overlying aquifer to the gob. However, it suffers from limited adaptability and curtain instability after grouting in the long term. The overburden separation grouting fills the stratum separation space by drilling grouting, so as to mitigate the overburden subsidence and thus preserve the shallow aquifer. It can only be applied in the bed separation space where the lithology of the upper stratum is harder than that of the lower and the effects of reducing overburden subsidence are restricted. Backfill mining is currently the most effective method to control overlying layer migration and thus conserve the shallow water since it substitutes the coal body with the filling body to support the roof of the mined-out area, which can significantly lighten the overlying layer migration and shallow water loss [6].

Backfill mining is primarily longwall backfill mining and shortwall backfill mining. The former has the problems of insufficient filling time and filling space. The roof of the mined-out area subsides and collapses immediately after the coal seam is extracted. However, it takes a long time for the backfill to reach its designed strength, and the goaf roof cannot be supported in time. Therefore, the movement of the overlying strata is inevitable, giving rise to difficulty in safe and high-efficient coal extraction under shallow water. Moreover, since the mining and filling exist in the same space and are not separated completely in longwall backfill mining, the filling speed affects extraction progress, while equipment maintenance delays the filling process, contributing to the mutual influence and restriction between extraction and backfill. It is arduous for them to operate in parallel. By contrast, the CECB mining method sets the coal extraction roadway and the backfill roadway in two different positions, with a large distance between them. Skip and interval mining offer a separated space for extraction and backfill which ensures isolated filling and mining processes and can realize mining and filling simultaneously without mutual restrictions and effects. Additionally, the width of the roadway is narrow compared with that of longwall backfill mining which can reduce the immediate roof subsistence effectively [7].

The CECB method has the advantages of integrating extraction and excavation, parallel mining and filling operation, convenient moving of the working face, low investment and high recovery rate over other mining methods. Compared with traditional longwall backfill mining, the CECB method arranges the coal extraction system and backfill system in different positions, avoiding the interaction between mining and filling operation, and thus the working efficiency can be ensured. The exposed area of each MR is small and results in limited subsidence of the roof before backfill, which is beneficial to the primary stability of CMFB before reaching the designed strength. Therefore, CMFB is an ideal backfill material for CECB. However, the feasibility of other backfill mining methods, such as longwall backfill mining, needs further study, due to the fact that their mining processes are essentially different from that of CECB mining. For example, the mining space of longwall backfill mining is not completely separated from the filling space. It seems that injecting the CMFB into the flexible bags set ahead in the filling space is the only option, which may lead to CMFB instability since it cannot be sealed due to the rupture of the flexible materials.

The authors developed high water swelling filling material with fly ash as aggregate and lime, anhydrite, cement and additives as ingredients [8]. The viscosity, bleeding rate, expansion rate, uniaxial compressive strength, slump, initial setting and final setting time of specimens with different water–solid ratios were studied. With due consideration given to the specific engineering and geological conditions of the colliery, the reasonable water–solid ratio and the material ratio of filling materials were determined. In the XV2309 working face of Wangtaipu Coal Mine in Shanxi Province, an industrial test was carried out with the developed filling material [39]. The strength of the filling body is 5 MPa with 60 days' setting time, the average expansion rate is 7.63% and the average bleeding rate is only 0.1%. The deformation of the water-resisting layer is mitigated and water table lowering of the overlying aquifer is effectively controlled and reduced. The filling cost per ton of coal when all MRs are backfilled is CNY 120, which is slightly higher than CNY 100 for longwall backfill mining. In addition, the maximum daily and annual output of CECB exceeds 3000 t and 600,000 t, respectively, almost the same as that of longwall backfill mining. The previous research on the CECB mining method and the development and field application of high water expansion filling materials laid a solid foundation for further study on the field implementation of CMFB in future.

In general, the CECB water preservation mining method meets the strategic requirements of the coordinated development of coal resources and the ecological environment. It has been popularized and applied to Yuxing Colliery, Wangtaipu Colliery, Suncun Colliery, etc. in northwest China, since it can make full harmless use of solid wastes accumulated around the mining areas on the premise of safe and highly efficient coal extraction with a

high recovery rate. The practice results show that good economic, social and environmental benefits have been achieved in the aforementioned collieries. According to statistics, as of the end of 2020, a total of 2.60 million tons of coal resources have been recovered by CECB in dozens of coal mines and a total new profit of more than 40 million dollars has been achieved [11]. However, all the previous field implementations of CECB used cement paste filling materials, crushed gangue or high water content filling materials. At present, the field application of CO_2 gas adhering to the filling materials to realize CO_2 sequestration has not been reported. In following research, a scanning electron microscope, X-ray diffraction, Vicat instrument, etc. will be employed to analyze the mesostructure, setting time and the rheological properties of the CMFB, and further exploration of the mechanism of the reaction among CO_2 gas, solid wastes and additives will be carried out, so as to provide a valuable theoretical research basis for the field implementations of CMFB in the future.

In view of the hydrogeological conditions where the distance between the overlying aquifer and the coal seam is large and the aquiclude between them is thick, the material ratios of filling materials can be adjusted to cut down the filling cost on the premise of mitigating the overburden migration and thus preserving water resources. For example, in the industrial test of Wangtaipu Coal Mine, we adjusted the water–solid ratio of the filling body in the last mining phase from 0.8:1 to 0.9:1 since the water level is controlled successfully in the early mining phase. In addition, further study on the deformation of the aquiclude and the fluctuation of the water level under the conditions of partial backfill of MRs in CECB will be conducted. If the shallow water preservation coal mining can be realized without filling in the last one or two mining phases, a further reduction in filling cost will become reality.

7. Conclusions

The conclusions drawn from the research are as follows:

(1) The scientific concept of developing CMFB by making CO_2 react with coal-based solid waste such as fly ash at a normal temperature and pressure and injecting it into the confined MR of the CECB mining method, was proposed. It can contribute to constructing the "trinity" of green and low-carbon mining areas, with permanent CO_2 storage, harmless treatment of coal-based solid wastes and shallow water preservation.

(2) The CMFB was developed at ambient temperature and pressure by using fly ash as aggregate, and CO_2 gas, silicate additives and cement as accessories. The UCS and tensile strength of CMFB with various curing times (3 d, 7 d, 14 d, 28 d) and different fly ash contents (55%, 65%, 75%, 85%) were tested indoors. The test results show that the compressive and tensile strength of CMFB increases with longer setting time. With the rising fly ash proportion, the compressive strength of CMFB increases first and then decreases, reaching the maximum when the fly ash content is 75%, while the tensile strength diminishes continuously.

(3) The commonly and extensively utilized filling materials are primarily cemented filling materials, crushed gangue and high water content filling materials. When the backfill mining method was previously employed to extract coal bodies beneath the overlying aquifer on the premise of water preservation and conservation, measures were usually adjusted to local conditions and the filling bodies were developed by taking materials from a wide range of sources as the raw materials. For instance, in view of the typical geological feature of aeolian sand, widely distributed in the Yu-Shen mining area, Shaanxi province, northwest China, Liu Pengliang et al. developed a new aeolian sand paste-like material with aeolian sand being used as aggregate and alkali-activated fly ash being utilized as a cementing agent. It was then applied to the Yuyang Colliery and the problem of damage to Salawusu Formation Aquifer caused by longwall caving mining was tackled [53]. Additionally, in view of the collieries without sufficient and abundant gangue accumulation, Zhou Nan et al. developed a sand-based cemented paste filling material with widely distributed and low-cost Yellow River sand as filling aggregate and cement and fly ash as binder for Zhaoguan Colliery in Shandong Province of China, which is only 5 km away from

the Yellow River [48]. Zhou Huaqiang et al. used the developed paste filling materials to extract a large number of coal resources under the village [54]. Feng Guangming developed ultra-high water filling material and put forward the corresponding mining technology [55]. However, the above mining methods and filling materials only take the harmless treatment of solid wastes and the overlying aquifer preservation into account, without regarding CO_2 sequestration as one of the purposes of backfill mining. This paper brings the large-scale treatment of CO_2 into the scientific framework of colliery green mining, and puts forward the trinity concept of green mining for CO_2 sequestration, harmless treatment of solid wastes and shallow water table preservation, which is innovative compared with the previous research on water conservation coal mining. The research results can provide theoretical guidance for the development and field application of CMFB, and promote construction of green, low-carbon and sustainable coal areas.

(4) According to the stress–strain curve of the CMFB from the indoor UCS test, the material ratio of the similar material of CMFB was optimized and determined. The physical analogue model was then constructed to simulate the mining-induced deformation of the overburden and aquifuge while using the CECB mining. The subsidence of the aquiclude from physical analogue simulation shows good agreement with that from the numerical simulation. The maximum vertical displacement of the water-resisting layer is 28 m, only 7.7% higher than that of the numerical simulation.

(5) The FLAC^{3D} finite element software was employed to simulate the aquifuge deformation and water table lowering. The CMFB with 14 d curing time and various fly ash contents were taken for analysis. Based on the indoor test results and the numerical simulation results, the strain-softening parameters of CMFB in the numerical simulation model were calibrated systematically. The deformation of the water-resisting layer and the decline in the water level of the shallow water while injecting CMFB with different fly ash contents into the MRs of CECB were obtained. The CMFB with 75% fly ash can effectively protect the integrity and water-blocking stability of the overlying aquiclude and mitigate the water level drop of the underground aquifer, thus preserving the shallow water and surface vegetation and contribute to the construction of green and sustainable ecological mines.

Author Contributions: Y.X. conceived the research and wrote the original draft. L.M. revised and reviewed the manuscript. I.N. contributed to formal analysis. J.Z. was responsible for data curation. All authors have read and agreed to the published version of the manuscript.

Institutional Review Board Statement: Not applicable.

Informed Consent Statement: Not applicable.

Data Availability Statement: Not applicable.

Conflicts of Interest: The authors declare that they have no competing financial interest in connection with the work submitted.

Abbreviations

CECB	continuous extraction and continuous backfill
CMFB	carbon dioxide mineralized filling body
UCS	uniaxial compressive strength
MRs	mining roadways
FA	fly ash
CM	cement

FA55	the ratios of the fly ash to the total of the fly ash and the cement are 55%
FA65	the ratios of the fly ash to the total of the fly ash and the cement are 65%
FA75	the ratios of the fly ash to the total of the fly ash and the cement are 75%
FA85	the ratios of the fly ash to the total of the fly ash and the cement are 85%

References

1. Xu, Y.; Ma, L.; Khan, N.M. Prediction and maintenance of water resources carrying capacity in mining area-a case study in the yu-shen mining area. *Sustainability* **2020**, *12*, 7782. [CrossRef]
2. Zhang, D.; Fan, G.; Ma, L.; Wang, X. Aquifer protection during longwall mining of shallow coal seams: A case study in the Shendong Coalfield of China. *Int. J. Coal. Geol.* **2011**, *86*, 190–196. [CrossRef]
3. Li, L.; Li, F.; Zhang, Y.; Yang, D.; Liu, X. Formation mechanism and height calculation of the caved zone and water-conducting fracture zone in solid backfill mining. *Int. J. Coal Sci. Technol.* **2020**, *7*, 208–215. [CrossRef]
4. Ma, L.; Jin, Z.; Liang, J.; Sun, H.; Zhang, D.; Li, P. Simulation of water resource loss in short-distance coal seams disturbed by repeated mining. *Environ. Earth Sci.* **2015**, *74*, 5653–5662. [CrossRef]
5. Ma, L.; Zhang, D.; Jin, Z.; Wang, S.; Yu, Y. Theories and methods of efficiency water conservation mining in short-distance coal seams. *J. Chin. Coal Soc.* **2019**, *44*, 727–738.
6. Xu, Y. Study on "Five Maps, Three Zones and Two Zoning Plans" Water Conservation Mining Method in Yu-Shen Mining Area. Master's Thesis, China University of Mining Science & Technology, Xuzhou, China, 2019.
7. Xu, Y.; Ma, L.; Yu, Y. Water preservation and conservation above coal mines using an innovative approach: A case study. *Energies* **2020**, *13*, 2818. [CrossRef]
8. Wang, A.; Ma, L.; Wang, Z.; Zhang, D.; Li, K.; Zhang, Y.; Yi, X. Soil and water conservation in mining area based on ground surface subsidence control: Development of a high-water swelling material and its application in backfilling mining. *Environ. Earth Sci.* **2016**, *75*, 779. [CrossRef]
9. Sun, K.; Fan, L.; Xia, Y.; Li, C.; Chen, J.; Gao, S.; Wu, B.; Peng, J.; Ji, Y. Impact of coal mining on groundwater of Luohe Formation in Binchang mining area. *Int. J. Coal Sci. Technol.* **2021**, *8*, 88–102. [CrossRef]
10. Fan, L.; Ma, L.; Yu, Y.; Wang, S.; Xu, Y. Water-conserving mining influencing factors identification and weight determination in northwest China. *Int. J. Coal Sci. Technol.* **2019**, *6*, 95–101. [CrossRef]
11. Fan, L.; Ma, X. A review on investigation of water-preserved coal mining in western China. *Int. J. Coal Sci. Technol.* **2018**, *5*, 411–416. [CrossRef]
12. Newman, C.; Agioutantis, Z.; Leon, G.B.J. Assessment of potential impacts to surface and subsurface water bodies due to longwall mining. *Int. J. Min. Sci. Technol.* **2017**, *27*, 57–64. [CrossRef]
13. Stoner, J.D. Probable hydrologic effects of subsurface mining. *Ground Water Monit. R.* **1983**, *3*, 128–137. [CrossRef]
14. Karaman, A.; Akhiev, S.S.; Carpenter, P.J. A new method of analysis of water-level response to a moving boundary of a longwall mine. *Water Resour. Res.* **1999**, *35*, 1001–1010. [CrossRef]
15. Shultz, R.A. *Ground-Water Hydrology of Marshall County, West Virginia, with Emphasis on the Effects of Longwall Coal Mining*, 3rd ed.; New York Press: New York, NY, USA, 1988; pp. 68–106.
16. Booth, C.J.; Spande, E.D.; Pattee, C.T.; Miller, J.D.; Bertsch, L.P. Positive and negative impacts of longwall mine subsidence on a sandstone aquifer. *Environ. Earth Sci.* **1998**, *34*, 223–233. [CrossRef]
17. Booth, C. Groundwater as an environmental constraint of longwall coal mining. *Environ. Earth Sci.* **2006**, *49*, 796–803. [CrossRef]
18. Hill, J.G.; Price, D.R. The impact of deep mining on an overlying aquifer in western pennsylvania. *Ground Water Monit. R.* **1983**, *3*, 138–143. [CrossRef]
19. Howladar, M.F.; Karim, M.M. The selection of backfill materials for Barapukuria underground coal mine, Dinajpur, Bangladesh: Insight from the assessments of engineering properties of some selective materials. *Environ. Earth Sci.* **2015**, *73*, 6153–6165. [CrossRef]
20. Howladar, M.F. Coal mining impacts on water environs around the Barapukuria coal mining area, Dinajpur, Bangladesh. *Environ. Earth Sci.* **2012**, *70*, 215–226. [CrossRef]
21. Gandhe, A.; Venkateswarlu, V.; Gupta, R.N. Extraction of coal under a surface water body—A strata control investigation. *Rock Mech. Rock Eng.* **2005**, *38*, 399–410. [CrossRef]
22. Kim, J.M.; Parizek, R.R.; Elsworth, D. Evaluation of fully-coupled strata destrata and groundwater flow in response to longwall mining. *Int. J. Rock Mech. Min. Sci.* **1997**, *34*, 1187–1199. [CrossRef]
23. Raghavendra, N.S.; Deka, P.C. Sustainable development and management of ground water resources in mining affected area: A review. *Procedia Earth Planet. Sci.* **2015**, *11*, 598–604. [CrossRef]
24. Tiwary, R.K. Environmental impact of coal mining on water regime and its management. *Water Air Soil Pollut.* **2001**, *132*, 185–199. [CrossRef]
25. Robertson, J. Challenges in sustainably managing groundwater in the Australian Great Artesian Basin: Lessons from current and historic legislative regimes. *Hydrogeol. J.* **2020**, *28*, 343–360. [CrossRef]
26. Fan, L. Scientific connotation of water-preserved mining. *J. Chin. Coal Soc.* **2017**, *42*, 27–35.
27. Huang, Q. Impermeability of overburden rock shallow buried coal seam and classification of water conservation mining. *Chin. J. Rock Mech. Eng.* **2010**, *29*, 3622–3627.

28. Huang, Q. Simulation of clay aquiclude stability of water conservation mining in shallow-buried coal seam. *Chin. J. Rock Mech. Eng.* **2009**, *28*, 987–992.

29. Wang, S.; Huang, Q.; Fan, L.; Yang, Z.; Shen, T. Study on overburden aquclude and water protection mining regionazation in the ecological fragile mining area. *J. Chin. Coal Soc.* **2010**, *35*, 7–14.

30. Wang, S.; Huang, Q. *Coal Mining and Ecological Water Level Protection in Ecologically Fragile Areas*, 3rd ed.; Science Press: Beijing, China, 2010; pp. 92–106.

31. Wang, X.; Qin, D.; Zhang, D.; Sun, C.; Zhang, C.; Xu, M.; Li, B. Mechanical characteristics of superhigh-water content material concretion and its application in longwall backfilling. *Energies* **2017**, *10*, 1592. [CrossRef]

32. Wang, S.; Ma, L. Characteristics and control of mining induced fractures above longwall mines using backfilling. *Energies* **2019**, *12*, 4604. [CrossRef]

33. Huang, Y.; Zhang, J.; Yin, W.; Sun, Q. Analysis of overlying strata movement and behaviors in caving and solid backfilling mixed coal mining. *Energies* **2017**, *10*, 1057. [CrossRef]

34. Zhang, J.; Zhang, Q.; Sun, Q.; Gao, R.; Germain, D.; Abro, S. Surface subsidence control theory and application to backfill coal mining technology. *Environ. Earth Sci.* **2015**, *72*, 1439–1448. [CrossRef]

35. Ma, L.; Zhang, D.; Wang, S.; Xie, Y.; Yu, Y. Water-preserved mining with the method named "backfilling while mining". *J. Chin. Coal Soc.* **2018**, *43*, 62–69.

36. Zhang, J.X.; Sun, Q.; Zhou, N.; Jiang, H.Q. Research and application of roadway backfill coal mining technology in western coal mining area. *Arab. J. Geosci.* **2016**, *9*, 558. [CrossRef]

37. Cao, Z.Z. Joint bearing mechanism of coal pillar and backfilling body in roadway backfilling mining technology. *CMC-Comput. Mater. Con.* **2018**, *54*, 137–159.

38. Ma, L.; Xu, Y.; Zhang, D.S.; Lai, X.; Huang, K.; Du, H. Characteristics of aquiclude and surface deformation in continuous mining and filling with wall system for water conservation. *J. Min. Saf. Eng.* **2019**, *36*, 30–36.

39. Ma, L.; Jin, Z.; Liu, W.; Zhang, D.; Zhang, Y. Wongawilli roadway backfilling coal mining method—A case study in Wangtaipu coal mine. *Int. J. Oil Gas Coal Technol.* **2019**, *20*, 342–359. [CrossRef]

40. Yu, Y.; Ma, L. Application of roadway backfill mining in water-conservation coal mining: A case study in Northern Shaanxi, China. *Sustainability* **2019**, *11*, 3719. [CrossRef]

41. Yu, Y.; Ma, L.; Zhang, D. Characteristics of roof ground subsidence while applying a continuous excavation continuous backfill method in longwall mining. *Energies* **2020**, *13*, 95. [CrossRef]

42. Brent, G.F.; Allen, D.J.; Eichler, B.R.; Petrie, J.G.; Mann, J.P.; Haynes, B.S. Mineral carbonation as the core of an industrial symbiosis for energy-intensive minerals conversion. *J. Ind. Ecol.* **2012**, *16*, 94–104. [CrossRef]

43. Uliasz, B.A.; Mokrzycki, E. The potential of FBC fly ashes to reduce CO_2 emissions. *Sci. Rep.* **2020**, *10*, 1–9.

44. Olajire, A.A. A review of mineral carbonation technology in sequestration of CO_2. *J. Petrol. Sci. Eng.* **2013**, *109*, 364–392. [CrossRef]

45. Lippiatt, N.; Ling, T.C.; Pan, S.Y. Towards carbon-neutral construction materials: Carbonation of cement-based materials and the future perspective. *J. Build. Eng.* **2020**, *28*, 101062. [CrossRef]

46. Morandeau, A.; Thiéry, M.; Dangla, P. Impact of accelerated carbonation on OPC cement paste blended with fly ash. *Cem. Concr. Res.* **2015**, *67*, 226–236. [CrossRef]

47. Moon, E.J.; Choi, Y.C. Carbon dioxide fixation via accelerated carbonation of cement-based materials: Potential for construction materials applications. *Constr. Build. Mater.* **2019**, *199*, 676–687. [CrossRef]

48. Zhou, N.; Zhang, J.; Ouyang, S.; Deng, X.; Dong, C.; Du, E. Feasibility study and performance optimization of sand-based cemented paste backfill materials. *J. Clean. Prod.* **2020**, *259*, 120798. [CrossRef]

49. Wang, G.; Xu, Y.; Ren, H. Intelligent and ecological coal mining as well as clean utilization technology in China: Review and prospects. *Int. J. Min. Sci. Technol.* **2019**, *29*, 161–169. [CrossRef]

50. Qi, C.; Fourie, A. Cemented paste backfill for mineral tailings management: Review and future perspectives. *Miner. Eng.* **2019**, *144*, 106025. [CrossRef]

51. Belem, T.; Benzaazoua, M. Design and application of underground mine paste backfill technology. *Geotech. Geol. Eng.* **2008**, *26*, 147–174. [CrossRef]

52. Luo, Y.; Wu, Y.; Ma, S.; Zheng, S.; Zhang, Y.; Chu, P.K. Utilization of coal fly ash in China: A mini-review on challenges and future directions. *Environ. Sci. Pollut. Res.* **2021**, *28*, 18727–18740. [CrossRef]

53. Liu, P.; Zhang, H.; Cui, F.; Sun, K.; Sun, W. Technology and practice of mechanized backfill mining for water protection with aeolian sand paste-like. *J. Chin. Coal Soc.* **2017**, *42*, 118–126.

54. Chang, Q.; Yuan, C.; Wang, Y.; Zhang, B.; Zhou, H.Q. Semi-convex mechanical analysis on stability of step coal wall in fully mechanized mining with paste filling. *J. Chin. Univ. Min. Technol.* **2022**, *51*, 46–55.

55. Feng, G.; Wang, C.; Li, F.; Jia, K. Research on bag-type filling mining with super-high-water material. *J. Min. Saf. Eng.* **2011**, *28*, 602–607.

Review

Iron Recovery Technology of Red Mud—A review

Hao Kong, Tuo Zhou, Xinhua Yang, Yingli Gong, Man Zhang and Hairui Yang *

State Key Laboratory of Power Systems, Key Laboratory for Thermal Science and Power Engineering of Ministry of Education, Department of Energy and Power Engineering, Tsinghua University, Beijing 100084, China; kh19@mails.tsinghua.edu.cn (H.K.); zhoutuo@tsinghua.edu.cn (T.Z.); yangxh2021@mail.tsinghua.edu.cn (X.Y.); ylgong@mail.tsinghua.edu.cn (Y.G.); zhangman@mail.tsinghua.edu.cn (M.Z.)
* Correspondence: yhr@mail.tsinghua.edu.cn

Abstract: RM (red mud), which comes from the Bayer process, has a huge annual output and is harmful to the environment. Because of the high iron content in RM, the process of iron recovery from RM can reduce the amount of RM well and create economic benefits, so it is a promising process. The paper focuses on the review on the research of the iron recovery method from RM, which includes the physical recovery method, chemical recovery method and emerging recovery method. By comparing the advantages and disadvantages of these processes, it is concluded that the fluidized bed reduction is a promising process that can be rapidly applied to the industry, but it still needs more investigation to overcome the current technical difficulties in the near future.

Keywords: red mud; iron recovery; pyrometallurgical method; fluidized bed reduction

1. Introduction

As global aluminum production continues to increase, as the main by-product, the output of RM has also risen. On average, 1 to 1.5 tons of RM are produced for every ton of aluminum produced [1], and about 67–100 million tons of RM are produced annually in whole world [2]. So far, RM reserves have exceeded 2.7 billion tons [3]. How to utilize the RM has become an urgent problem to be solved.

Many scholars reviewed the utilization methods of RM, including utilization in road base and subgrade material [4], environmental remediation material [5], catalyst [6] and element recovery [7], etc. In these processes, due to the high iron content in RM, the iron recovery process can not only realize the decrement, innocuity and resource recovery but also create good economic benefits. Therefore, the iron recovery process from RM is becoming a hot topic [8]. The paper reviews the iron recovery process and gives the conclusions and prospects of the iron recovery process by comparing the advantages and disadvantages of each process.

2. Research Methodology

The purpose of this article is to review the progress of research on recovered iron processes and to show as many different processes as possible. By searching from Web of Science, ScienceDirect and CNKI based on the term "red mud", several published articles about iron recovery from RM have been selected in the article. The authors hope that this review article inspire scholars studying related fields.

3. The Production, Properties and Harm of Red Mud

There are three main processes for producing aluminum hydroxide, including the sintering method, the Bayer method, and the combined method. Among them, the aluminum hydroxide produced by the Bayer method accounts for about 95% of the total due to its simple process and low energy consumption [9]. In the article, the utilization of Bayer RM is discussed.

The most important ore used in the Bayer method is bauxite. The bauxite mainly consists of alumina trihydrate ($Al(OH)_3$), bomite (γ-AlO(OH)) and alumina (α-AlO(OH)), and it also contains kaolinite ($Al_4[Si_4O_{10}](OH)_8$), goethite (FeO(OH)), hematite (Fe_2O_3), anatase (TiO_2) and ilmenite ($FeTiO_3$ or $FeO.TiO_2$) [9,10]. The steps of the Bayer process are as follows [11]: the bauxite is pulverized and mixed with lime and sodium hydroxide, and the aluminum hydroxide slurry and solid residue are obtained after sedimentation and separation. The solid residue is red due to a large amount of iron oxide, so it is called red mud. Some scholars comprehensively summarized the chemical compound of RM [3,9,12], which varies widely with raw materials and processes. The chemical compound and mineral composition of RM used in a previous experiment [13] are shown in Table 1 and Figure 1, respectively. The main elements in RM include iron, silicon, titanium from bauxite, residual aluminum, sodium from sodium hydroxide and calcium from lime. Trace elements include rare earth elements, U, Th and other radioactive elements. The iron content of RM reaches more than 20% and even more than 40% in high iron RM.

Table 1. Chemical compound of RM used in previous experiment [13].

Compound	Wt %
Fe_2O_3	37.68
Al_2O_3	22.69
SiO_2	18.22
Na_2O	12.37
TiO_2	6.2
CaO	0.947
ZrO_2	0.543
NiO	0.238
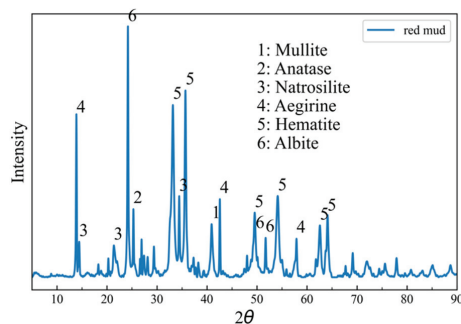
Figure 1. Mineral composition of RM used in previous experiment [13].

RM has the characteristics of fine particles, porosity, strong alkalinity and radiation [14]. As shown in Figures 2 and 3, RM have many pores inside, and most of the RM has a particle size of less than 10 μm. At present, most of the RM is disposed by stacking, which will not only increase the cost but also cause serious pollution to the environment. Due to the fine particle size of RM, it will be entrained by wind and pollute the air when it is stacked in the open air. It will leak into the ground when it rains and will cause water pollution and corrosion of buildings. The radioactivity of RM will also cause damage to the environment. On 4 October 2010, the dam wall of the Ajka oil refinery collapsed and the surrounding area was flooded with RM, causing serious pollution to the Danube River [15–18].
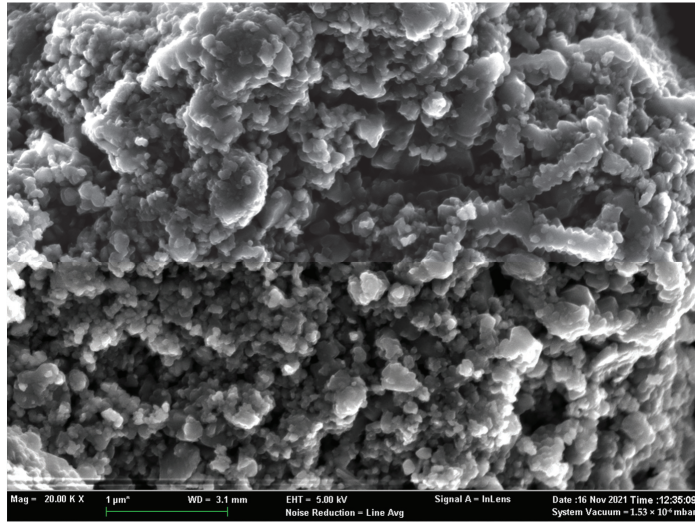
Figure 2. SEM image of RM used in previous experiment [13].
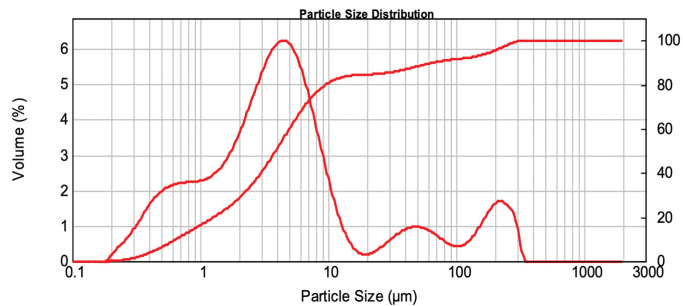
Figure 3. The particle size distribution of RM used in previous experiment [13].

4. Iron Recovery Process from Red Mud

Since both RM and iron ore contain a variety of metal elements, most of the iron recovery processes from RM reference the experience of mature processes in the metallurgical industry, such as the physical, hydro and pyrometallurgy method. There are also emerging processes such as the biological method, electrochemical method, etc. The research progress of these processes is introduced in the following sections.

4.1. Physical Recovery Method

The physical recovery method is to directly separate iron-bearing minerals based on the different physical properties and includes gravity separation, magnetic separation and flotation.

Gravity separation refers to the process of separating the mineral particles by the difference in relative density, particle size, shape and movement speed and direction in the medium. Liu et al. [19] adopted a combination of a two-stage cyclone and suspension cone concentrator for separation, and they obtained concentrate with the TFe of 48.83%. Jiang et al. [20] replaced the traditional straight cones with the cubic parabolic cones in the hydrocyclone, as shown in Figure 4, which effectively reduces the fine particle content in the underflow. However, the iron in the RM is concentrated in the fine particles, which account for a large proportion of RM and have a low iron grade, resulting in low TFe of the concentrate obtained by gravity separation.
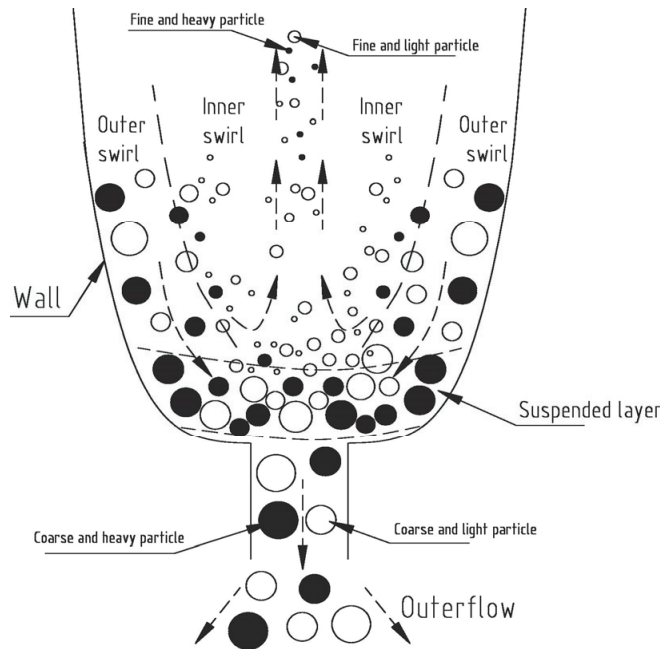
Figure 4. Particles in the parabolic cone [20].

Some scholars also use the magnetic separation process to separate the iron-containing part according to the magnetic difference. Jamieson et al. [21] combined low-intensity magnetic separation and wet high-intensity magnetic separation and obtained the concentrate with a Fe_2O_3 mass fraction of 56%. In order to increase the TFe of the concentrate, Li et al. [22] adopted a two-stage magnetic separation process; each stage includes weak magnetic separation and vertical ring strong magnetic separation. The TFe and recovery rate of the concentrate were 24.63% and 43.29%, respectively. The reason for the lower TFe may lie in that the iron in RM mainly exists in the form of hematite and goethite, which are magnetic or weak magnetic materials, so a higher magnetic field is required. Li et al. [23] used high gradient superconducting magnetic separation to improve the TFe of the concentrate. The mass fraction of the Fe_2O_3 was about 67%. The separation effect is not good and the cost is high. This may be due to the intergrowth of various elements in RM, including Al, Si, Na, Ti and Fe, such as aluminum in the form of high-alumina goethite and high-alumina hematite [21]. Magnetic separation cannot separate aluminum and iron, resulting in lower TFe in the concentrate.

Some scholars have used the selective functional groups to enrich the iron oxide in RM by the flotation process. Song et al. [24] studied the dealing effect of different collectors. When the methylenebisacrylamide ($C_6H_{12}N_4$) and starch was mixed as the collector, the TFe and iron recovery of the concentrate were 49.81% and 74.64%, respectively. When the sodium oleate ($C_{18}H_{33}NaO_2$) was used as the reverse collector, the TFe and iron recovery of the concentrate were 51.54% and 78.84%, respectively. Huang et al. [25] found that the humic substances have acidic functional groups and are more selective in interacting with iron oxides, the TFe and iron recovery and of the obtained concentrate were 61.12% and 86.25%, respectively.

Multiple physical methods were combined by some scholars. Rai et al. [26] obtained iron oxide and titanium oxide from RM by using the hydrocyclone due to their high density, and then, the iron is recovered by the two-stage magnetic separation. The mass fraction of Fe_2O_3 in the concentrate was 70% and the iron recovery was 75%.

The physical recovery method has the advantages of simple process and low energy consumption, but the iron recovery and TFe of the concentrate are not high enough to meet the need of industrial production. Because of the similar physical properties of iron minerals and veinlets, it is difficult to separate them by the traditional physical methods. On the one hand, some scholars adopted more advanced techniques such as high-gradient superconducting magnetic separation to separate them, but the cost is high. In the future, a physical method will be used mainly in conjunction with chemical methods, and scholars should develop corresponding physical methods based on chemical methods with simple steps, low energy consumption and low cost.

4.2. Chemical Recovery Method

The chemical recovery method refers to the process of converting iron in RM to other forms through chemical reactions and then extracting iron, which is divided into the hydrometallurgy method and pyrometallurgy method according to the type of chemical reaction.

4.2.1. Hydrometallurgy Method

The hydrometallurgy method mainly refers to the process of dissolving iron by acid leaching and then enriching iron. Some scholars studied the influence of acid leaching conditions on the leaching rate. Xie et al. [27] leached iron with hydrochloric acid (HCl) and studied the effects of temperature, acid concentration, leaching time, liquid–solid ratio and particle size on the leaching rate. They found that temperature and acid concentration have the greatest effect, while leaching time and liquid–solid ratio have the second effect. Reducing particle size within a certain size range can increase the leaching rate, but when the particle size was less than 150 μm, there was no significant effect on the leaching rate by reducing the particle size. The optimum conditions for the acid leaching were: red mud size 150 μm, acid leaching temperature 80 °C, acid concentration 10 mol/L, liquid–solid ratio 8:1, and acid leaching time 150 min, and the leaching rates of Fe was 95.1%. In addition to HCl, Chen et al. [28] used concentrated sulfuric acid, glacial acetic acid and oxalic acid $(C_2H_2O_4)$ to leach RM and studied the effects of acid concentration, leaching time and temperature on iron leaching. They found that sulfuric acid leaching was more effective and that increasing the sulfuric acid concentration and temperature can increase the iron leaching rate. The leaching mechanism was consistent with the core shrinking model controlled by internal diffusion. The maximum Fe leaching rate of 67.93% was achieved at a temperature of 50 °C, a sulfuric acid concentration of 2.8 mol/L, and a leaching time of 45 min.

By exploring the complete hydrometallurgy process, Yu et al. [29] leached RM with 1 mol/L $C_2H_2O_4$ at 75 °C for 2 h and then irradiated the solution with UV light for 1 h to reduce Fe^{3+} to Fe^{2+} by oxalate and formed a precipitate (β-FeC_2O_4·$2H_2O$) by combining with the remaining oxalate. Although the oxalate in the filtrate can be reused, the oxalate reacting with Fe^{3+} cannot be reused, which greatly increases the process cost. In order to reduce the amount of oxalate used in the process, Yang et al. [30] used dilute HCl for washing, sulfuric acid for acidity adjustment and 3 times stoichiometry of iron scraps instead of oxalate for the reduction in Fe^{3+} to reduce the use of oxalate to reduce cost. In addition, in order to reduce cost, Yang et al. [31] proposed a process shown in Figure 5, in which they leached RM with $C_2H_2O_4$, adjusted the pH with calcium carbonate to form a co-precipitation of calcium oxalate and iron hydroxide, and then used a mixture of hydrochloric acid and calcium chloride to selectively dissolve the precipitate and recover the oxalate and iron.
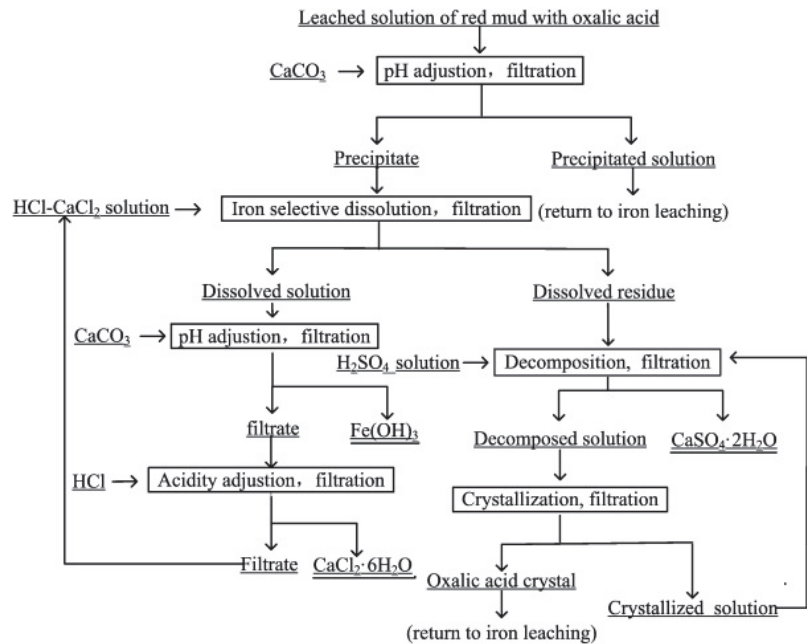
Figure 5. Hydrometallurgy process flow of Yang et al. [31].

In addition to $C_2H_2O_4$, Zhang et al. [32] leached the RM with hydrochloric acid for 4 h, added calcium chloride to form iron and scandium complexes and used D201 resin to adsorb iron complexes to achieve the separation of iron and scandium. The adsorption efficiency of iron exceeded 96%, while the adsorption of scandium was negligible. Calcium chloride could be recycled to reduce the cost. Zhang et al. [33] also used hydrochloric acid leaching and extracted iron with a mixture of 30% Aliquat 336, 15% 2-Octanol and 55% kerosene for 20 min. The iron leaching and extraction rates reached 95.9% and 95.7%, respectively. Sokolov et al. [34] also used a mixture of 1-octanol ($C_8H_{18}O$)and 1-decanol ($C_{10}H_{22}O$) (70%) with 2-undecanone ($C_{11}H_{22}O$) (30%) to extract iron from HCl solution. They obtained an $FeCl_3$ solution with the iron(III) content of 90.5 g/L and total impurities less than 50 mg/L.

Oxalate can form the precipitate by combining with Fe^{2+}, so $C_2H_2O_4$ becomes the main raw material for hydrometallurgy method. Because of the high cost of $C_2H_2O_4$, many scholars have optimized the process. The hydrometallurgy method can achieve both a high recovery rate and TFe in laboratory-scale experiments. The chemical reaction can be carried out at a lower temperature, so hydrometallurgy also has the advantage of low energy consumption. However, the hydrometallurgy method has complex steps. Due to the strong alkalinity of the RM, a large amount of acid is consumed during acid leaching, which makes the cost significantly high, making it difficult to promote in the industry. The method will also produces an acidic waste stream, which contains many metallic elements. Future research on the hydrometallurgy method could focus on how to reduce acid consumption during leaching such as treating RM with acidic solid waste or using the alkaline leaching process to extract iron, and how to recover other metallic elements as well as raw materials from the acidic waste stream after iron extraction. Industrial tests on the process should also be carried out.

4.2.2. Pyrometallurgical Method

The pyrometallurgy method is the process of changing the existing form of iron through a high-temperature chemical reaction and then separating. According to the form

of iron after reduction, the pyrometallurgy method can be classified into the reduction to Fe process and reduction to Fe_3O_4 process.

Many scholars have studied the pyrometallurgical process of reduction to Fe. Mishra et al. [35] used 200% excess petroleum coke to reduce iron at 1050 °C for 2 h. After reduction, most of the iron was recovered by magnetic separation, and the remaining iron was recovered by smelting. Raspopov et al. [36] have obtained cast iron by reacting with carbon in a resistance furnace at 1200–1500 °C. There are many factors affecting the reduction reaction including temperature, reaction time, etc. In order to improve the physical characteristics of obtained pig iron, Valeev et al. [37] roasted RM at 1750 °C and found the titanium carbide, and phosphide eutectic in pig iron as shown in Figure 6 gives it a high hardness, high strength and good fluidity. In order to effectively find the optimal working conditions, Guo et al. [38] used metallization rate as an indicator, which means the percentage of metallic iron to total iron, and they designed orthogonal experiments to find the best working condition. Under the best working condition, the metallization rate was 98.16% and the TFe of concentrate was 96.25%. Lazou et al. [39] conducted smelting reduction experiments at 1650 °C for 90 min in an induction furnace as shown in Figure 7, and they obtained pig iron with TFe of 92.74%. The backscattered electron (BSE) images of slag are shown as Figure 8, and the chemical composition of these phases is given in combination with the XRD results. They also used FactSage to predict elemental concentrations in the metal phase and found that the predicted Si and Cr concentrations were much higher than experimental values. Ning et al. [40] added CaO and Al_2O_3 to the reduced RM for composition adjustment, and they separated slag and iron at 1550 °C. The quality of pig iron obtained meets the requirements of steelmaking, and the slag-melting point is lower than 1400 °C with a strong desulfurization capacity.
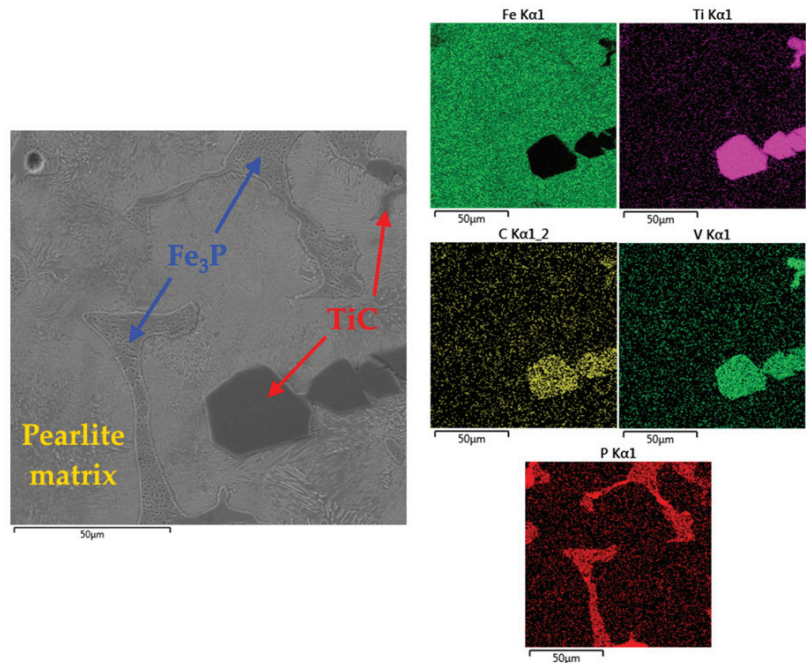
Figure 6. SEM images of the pig iron sample obtained at 1750 °C [37].
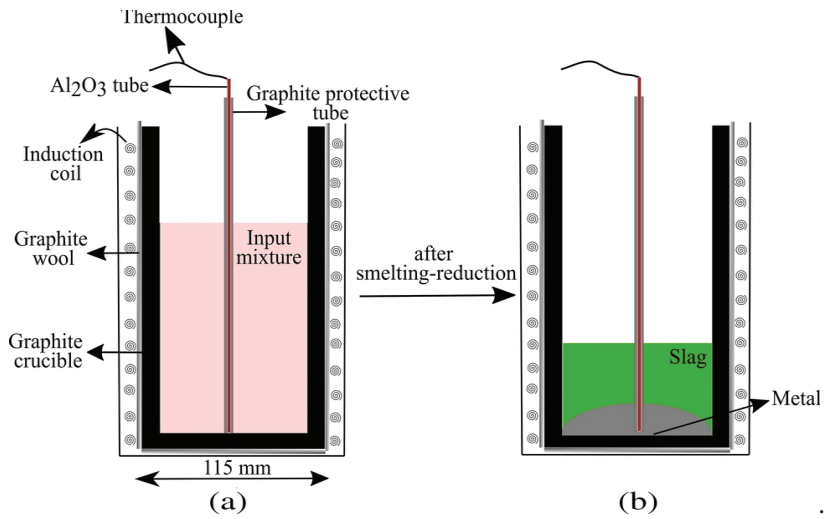
Figure 7. Schematic diagram of the smelting reduction process and input mixture (**a**) before and (**b**) after smelting [39].
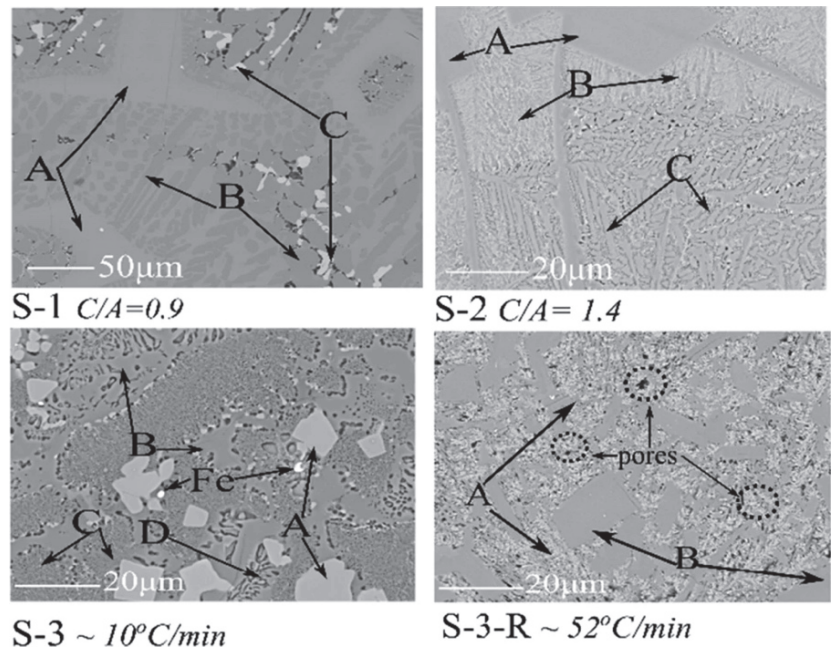
Figure 8. BSE images of slags obtained with different CaO/Al_2O_3 ratios (S-1 and S-2) and different cooling rates (S-3 and S-3-R) [39] A, B, C, and D represent four different phases.

Some scholars have found that better results are achieved by adding alkaline additives to the roasting. Zinoveev et al. [41] investigated the effect of the addition of Na_2CO_3 and K_2CO_3 on the reaction. The experimental results showed that iron can be almost completely reduced after roasting at 1000–1200 °C for 20 min. As shown in Figure 9, they found that iron grains in the sample with additive reduction were significantly larger. Under the best working condition, the recovery rate and TFe were 77.27% and 72.05% with the addition of

Na_2CO_3 and 92.39% and 70.77% with the addition of K_2CO_3. Liu et al. [42] used carbon powder as a reducing agent and $CaCO_3$ and $MgCO_3$ as additives, which can react with SiO_2 and Al_2O_3. The TFe, metallization rate and iron recovery of obtained concentrate were 88.77%, 96.98% and 81.40%, respectively. They added 13% slaked lime to the remaining silica–aluminate residue. The compressive strength of residue reached 24.10 MPa, which can be used as construction material. Huang et al. [43] investigated the mechanism of the reduction reaction with different additives. The experimental results indicated that Na_2CO_3 dissociates the basic oxide Na_2O, which can displace FeO from $2FeO·SiO_2$ and $FeO·Al_2O_3$. The generated $Na_2O·2SiO_2$ with a low melting point produces a liquid phase which can promote the diffusion of crystalline masses, accelerate the growth of Fe nuclei, as well as catalyze the carbon gasification reaction and increase the carbon activity and the rate of CO reduction of iron oxides. Adding CaF_2 can lower the melting point and viscosity of solid-phase products, optimize the heat and mass transfer conditions, and promote the mutual diffusion between ions and the growth and enrichment of iron grains. Finally, the metallization rate, TFe and recovery rate of obtained iron powder were 92.79%, 89.57% and 91.15%, respectively. Liu et al. [9] believed that an excessive liquid phase can also encapsulate the particles, leading to an incomplete reduction of iron oxides and partial dissolution of ferrous compounds in the RM, and some metallic iron particles encapsulated by the liquid phase cannot be recovered by magnetic separation, so the amount of the additive should be strictly controlled.
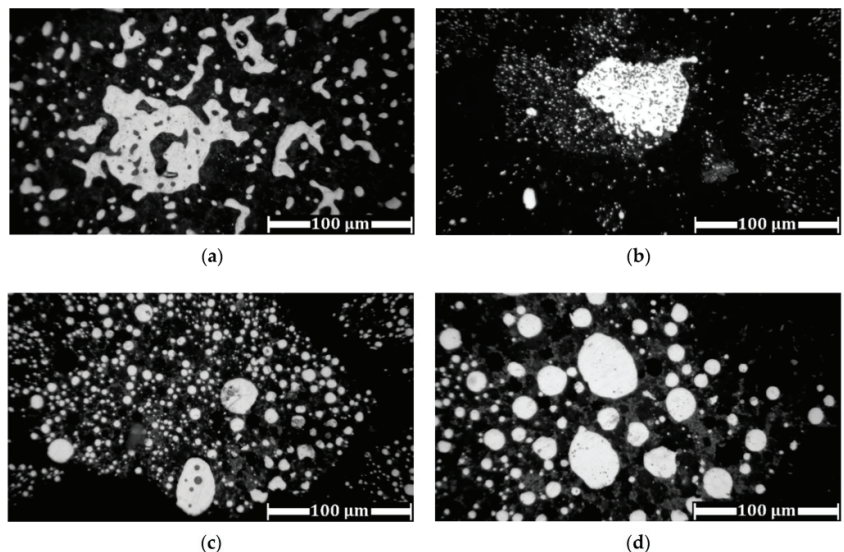
Figure 9. Microstructure of reduced samples after 3 h of roasting at 1200 °C with 17.1% Na_2CO_3 (**a**) and 22.01% K_2CO_3 (**b**), without additions at 1300 °C (**c**) and 1350 °C (**d**) [41].

Other heating methods of the process were also developed. Jayasankar et al. [44] applied thermal plasma technology in the process. The characteristics of high temperature, high energy fluxes, and plasma state of the plasma arc greatly reduce the reaction time. Agrawal et al. [45] demonstrated that microwave heating allows for rapid and uniform heating of the sample. They experimentally compared the carbothermal reduction reactions using muffle furnace and microwave heating, and they found that microwave heating significantly improves the TFe and recovery rate of iron at a lower time and with less reducing agent. They also observed ferrite spheres of appreciable size and purity in microwave-heated reduced samples, accounting for 8–10% of the total iron in the feed. In

addition, microwave heating provides faster reduction, cleaner process, and less energy and reductant consumption.

High-temperature reduction and melt separation make the process energy consumption too high; scholars found that the iron in the RM can be reduced to Fe_3O_4 at a lower temperature, and magnetic separation will greatly reduce the energy required for the process. Liu et al. [46] used coal coke as the reducing agent and soda lime as the additive, roasted RM at 1000 °C for 3 h, and followed that with water leaching to extract Al and Na and magnetic separation to extract Fe. The recovery rate and the TFe of the concentrate were 51.2% and 52.8%, respectively. Sadangi et al. [47] roasted RM at a temperature of 1150 °C for 60 min and obtained the concentrate with the TFe of 65.93% and the recovery rate of 61.85% by magnetic separation. They also demonstrated that the reduction reaction occurred from the outer surface of the particles to the inner core. Agrawal et al. [48] proposed the process of carbonation, pre-magnetic separation, reduction roasting and two-stage magnetic separation, and they chose charcoal as the reducing agent. The obtained concentrate had the TFe of 50.5% and the recovery rate of 70%.

When a solid reductant is used, the reaction temperature is still high, and the reaction needs to take a long time. If the gas reductant is used, the reaction temperature and time can be greatly reduced. Samouhos et al. [49] passed H_2 through the fixed bed reactor at 480 °C for 30 min and obtained the concentrate with the TFe of 54% after magnetic separation. They performed a Vibrating Sample Magnetometer (VSM) test on the concentrate and found that greater magnetism causes better enrichment. Tang et al. [50] pointed out that fluidized roasting in traditional pyrometallurgy has the advantages of fast reaction speed, rapid mass transfer, low energy consumption and uniform temperature. If the reaction is carried out in a fluidized bed with a gas reductant, the reaction temperature and reaction time can be further reduced. Some scholars applied fluidized roasting to the iron recovery process from RM; Liu et al. [51] chose CO as a reducing agent, reduced the RM in a fluidized bed at 540 °C for 15 min and obtained the iron concentrate with 56.41% TFe after magnetic separation. They also found that the magnetic force of the reduced RM was positively correlated with the dealing effect in the experiment. Yuan et al. [52] passed a mixture of H_2 and CO in the fluidized bed reactor to reduce RM at 520 °C, and this semi-industrial experiment was conducted continuously and steadily for 45 h. The recovery rate and TFe of the concentrate were 95.22% and 55.54%, respectively. Yu et al. [53] roasted the RM with a concentration of 30% CO in the fluidized bed at 560 °C for 15 min; after magnetic separation, the recovery rate and TFe of the obtained concentrate were 89.34% and 55.44%, respectively. According to the BSE image shown in Figure 10, they found that some fine silicon slag was embedded in the magnetite. In the magnetic separation process, the Fe-Al hercynite $(Fe(Al,Fe)_2O_4)$ transformed from alumogoethite would mix into the concentrate, leading to a decrease in the TFe of the concentrate. Li et al. [54] found that in the conventional pyrometallurgy process, the iron-bearing minerals in the fluidized roasted ore are closely embedded with the veinlets, reducing the TFe of the concentrate obtained by magnetic separation. This problem also occurs and is urgent to be solved in the fluidized reduction process of the RM.

In previous work, Kong et al. [13] conducted the experiment at the test rig shown in Figure 11, adjusted the gas velocity to enter the turbulent bed and observed a significant discoloration of the RM due to reduction within 5 min. The maximum moment in the VSM test of the reduced RM was used as a characterization of the dealing effect, and the effects of CO concentration, reaction temperature and reaction time were studied by using response surface analysis. The maximum moments of reduced RM under different working conditions are listed in Table 2. The variance distribution of RSM is listed in Table 3. The *p* value represents the strength of significance and the larger mean square value represents the greater the influence on the dealing effect. From Table 3, it can be found that the *p*-value of the model is 0.0032, and the underfitting phase is not significant, indicating that the model is reasonable. The order of influence of these three factors on the dealing effect is CO concentration, reaction time, and temperature. The response surface method (RSM) also

predicts the results accurately at the condition of longer reaction time as listed in Table 4. In the future, more attention will be paid on expanding the experimental condition design by evaluating the dealing effect by the TFe and recovery rate.
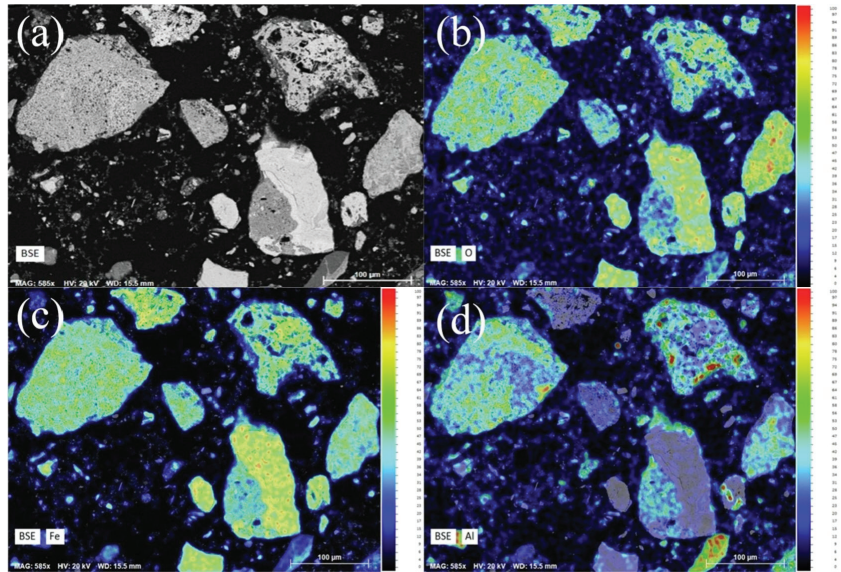
Figure 10. BSE image of roasted product and its map scanning: (**a**) BSE Image; (**b**) O; (**c**) Fe; (**d**) Al [53].
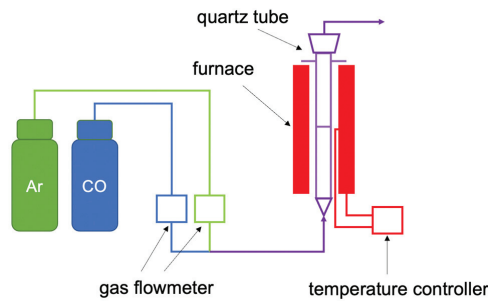
Figure 11. Schematic diagram of the experiment system [13].

Table 2. The maximum moments of reduced RM under different working conditions [13].

Temperature (°C)	CO Concentration (%)	Reaction Time (min)	Maximum Moment (A·m²/kg)
600	5	8	15.7401
550	8	2	15.4587
600	2	5	15.1976
500	5	2	13.9256
550	2	2	9.6766
600	8	5	15.2625
550	5	5	15.2115
550	5	5	15.2115
500	5	8	15.3054
500	2	5	10.2996
550	5	5	15.2115
600	5	2	14.1055
550	5	5	15.2115
550	2	8	14.6415
550	5	5	15.2115
500	8	5	14.7424
550	8	8	16.6117

Table 3. The variance distribution of RSM [13].

Source	Sum of Squares	df	Mean Square	F-Value	*p*-Value
Model	33.76	3	11.25	7.76	0.0032
Temperature	4.55	1	4.55	3.14	0.1
CO concentration	18.79	1	18.79	12.95	0.0032
Reaction time	10.42	1	10.42	7.19	0.0189
Lack of fit	18.86	9	2.1		
Pure error	0	4	0		

Table 4. Predicted moment and experimental moment [13].

Temperature (°C)	CO Concentration (%)	Reaction Time (min)	Experimental Moment (A·m^2/kg)	Predicted Moment (A·m^2/kg)
525	3.5	3.5	11.4235	12.8168
525	6.5	6.5	15.2387	15.4908
575	3.5	6.5	14.8505	14.7124
575	6.5	3.5	14.4225	15.1034

In the early studies, scholars mostly used the high-temperature roasting process to reduce Fe_2O_3 of RM to Fe and the smelting process to separate them. However, the high-temperature roasting process requires a temperature of more than 1200 °C and a time of more than 2 h, while the smelting process requires more than 1300 °C, which will result in a large amount of energy consumption. Some scholars improved the process based on the high-temperature roasting process, using a lower temperature of roasting to reduce Fe_2O_3 to Fe_3O_4 and using magnetic separation. The temperature required for roasting is 1000 °C, and magnetic separation can be carried out at room temperature, reducing the energy required for the process. Some scholars also found that the use of a fluidized reduction process can reduce the reaction temperature to 500 °C, and the reaction time is reduced to 30 min. It has also been found that the reaction time can be further reduced if the gas velocity is increased to reduce the RM in a turbulent bed.

The fluidization reduction process has a lower reaction temperature and shorter reaction time than other pyrometallurgical processes, which greatly reduces the energy consumption of the reaction, and simpler steps, which makes it easier to be promoted in the industrial applications. So, the fluidization reduction is a promising process. In future research, the iron grade and recovery rate of the concentrate should be improved. For the secondary solid waste generated after the recovery of iron, corresponding processes should also be developed to utilize or extract the elements.

4.3. Emerging Recovery Method

In addition to the above methods, the bioleaching method, which is considered as a green technology with low energy and cost, was also provided. Some scholars have studied the recovery of iron from kaolin [55], quartz sands [56], bauxite [57] and iron oxides ores [58]. Qu et al. [59] used Aspergillus niger to leach heavy metals from RM. When bioleaching was carried out at 1% pulp density, the leaching rate of iron reached a maximum 87.5%, which is significantly lower than hydrometallurgy method. Other metals will enter the leaching solution in large quantities. Eisele and Gabby [60] pointed out that anaerobic organisms are widely used in bioleaching iron processes, but anaerobic organisms require neutral or weakly acidic pH conditions, which leads to a large amount of acid neutralization during RM leaching, limiting the development of RM bioleaching. In the future, it is necessary to find microorganisms that can adapt to alkaline environments and selectively leach iron in the bioleaching process and implement larger scale experiments to verify the feasibility of the process.

In addition to bioleaching, Maihatchi Ahamed et al. [61] used the electrochemical method to recover iron, which can reduce energy consumption and CO_2 emissions compared to the pyrometallurgical method. The alkalinity of RM can reduce the amount of alkali added to the media. They found that the efficiency of the electrochemical method is low, which is probably due to the lower conductivity caused by the formation of triple-phase bubbles with the suspension. They also found that there was 3% Al and Na in the obtained concentrate and that the current yield of the RM was about a quarter of the current yield of the hematite at high current densities. Further research should be carried out to increase the current yield, improve the conductivity of the suspension and reduce impurities in the concentrate.

In the long term, the emerging method will become the mainstream method in the future due to its low energy consumption and environmental friendliness, but it will not be able to treat the urgent RM in a short time. The emerging method still needs a lot of work, such as improving the recovery rate and iron grade, larger scale experiments, reducing process costs, developing better processes, etc.

5. Conclusions

This paper reviewed three kinds of methods on recovering iron from RM, including physical, chemical and emerging methods. The following conclusions are obtained:

1. The physical method is to separate the iron-bearing part and the other parts based on different physical properties, including gravity separation, magnetic separation and flotation. These processes have the characteristics of simple process and low energy consumption, but the iron recovery rate and the TFe of the concentrate are low;

2. The hydrometallurgy method is the chemical method with acid leaching. The RM leached with acid can dissolve the metallic elements, and then the iron in the solution is extracted by precipitation formation, extraction or adsorption. The hydrometallurgy method has a high recovery rate and TFe of the concentrate, but the steps are complicated and require a large amount of acid to neutralize the alkalinity of the RM, resulting in high costs;

3. The pyrometallurgy method is the chemical method in which iron is reduced by thermochemical reaction and then separated by smelting or magnetic separation. The pyrometallurgy method can be divided into a reduction process into Fe and Fe_3O_4 according to the form of iron after reduction. The reduction process into Fe requires high temperature, high energy consumption and long reaction time, but the TFe of the concentrate is high. Comparingly, the reduction process into Fe_3O_4 in a fluidized bed will reduce the reaction temperature and reaction time, and the reduction in the turbulent bed will further reduce the reaction temperature and reaction time. However, the concentrate has a lower TFe, which should be the focus in future research. The fluidization reduction process is currently the most promising process and should be promoted on an industrial scale

4. The emerging method is a green and clean technology, but the current research is in the laboratory scale. In the future, process efficiency improvements, costing, and larger scale experiments are required. In the long term, the emerging method is a very promising process but requires a lot of research.

Author Contributions: Conceptualization, H.K. and H.Y.; methodology, H.K. and H.Y.; software, H.K. and X.Y.; validation, T.Z., M.Z. and H.Y.; formal analysis, H.K. and H.Y.; investigation, H.K. and H.Y.; resources, Y.G.; data curation, H.K.; writing—original draft preparation, H.K.; writing—review and editing, H.K. and H.Y.; visualization, H.K.; supervision, H.Y.; project administration, T.Z., M.Z and H.Y.; funding acquisition, M.Z. and H.Y. All authors have read and agreed to the published version of the manuscript.

Institutional Review Board Statement: Not applicable.

Informed Consent Statement: Not applicable.

Data Availability Statement: Not applicable.

Conflicts of Interest: The authors declare no conflict of interest.

References

1. Zhang, R.; Zheng, S.; Ma, S.; Zhang, Y. Recovery of Alumina and Alkali in Bayer Red Mud by the Formation of Andradite-Grossular Hydrogarnet in Hydrothermal Process. *J. Hazard. Mater.* **2011**, *189*, 827–835. [CrossRef] [PubMed]
2. International Aluminium Institute. Primary Aluminium Production—International Aluminium Institute. Available online: https://international-aluminium.org/statistics/primary-aluminium-production/ (accessed on 17 May 2022).
3. Khairul, M.A.; Zanganeh, J.; Moghtaderi, B. The Composition, Recycling and Utilisation of Bayer Red Mud. *Resour. Conserv. Recycl.* **2019**, *141*, 483–498. [CrossRef]
4. Mukiza, E.; Zhang, L.L.; Liu, X.; Zhang, N. Utilization of Red Mud in Road Base and Subgrade Materials: A Review. *Resour. Conserv. Recycl.* **2019**, *141*, 187–199. [CrossRef]
5. Wang, M.; Liu, X. Applications of Red Mud as an Environmental Remediation Material: A Review. *J. Hazard. Mater.* **2021**, *408*, 124420. [CrossRef]
6. Sushil, S.; Batra, V.S. Catalytic Applications of Red Mud, an Aluminium Industry Waste: A Review. *Appl. Catal. B Environ.* **2008**, *81*, 64–77. [CrossRef]
7. Liu, Z.; Li, H. Metallurgical Process for Valuable Elements Recovery from Red Mud—A Review. *Hydrometallurgy* **2015**, *155*, 29–43. [CrossRef]
8. Khanna, R.; Konyukhov, Y.; Zinoveev, D.; Jayasankar, K.; Burmistrov, I.; Kravchenko, M.; Mukherjee, P.S. Red Mud as a Secondary Resource of Low-Grade Iron: A Global Perspective. *Sustainability* **2022**, *14*, 1258. [CrossRef]
9. Liu, X.; Han, Y.; He, F.; Gao, P.; Yuan, S. Characteristic, Hazard and Iron Recovery Technology of Red Mud—A Critical Review. *J. Hazard. Mater.* **2021**, *420*, 126542. [CrossRef]
10. Liu, Y.; Naidu, R.; Ming, H. Red Mud as an Amendment for Pollutants in Solid and Liquid Phases. *Geoderma* **2011**, *163*, 1–12. [CrossRef]
11. Tabereaux, A.T.; Peterson, R.D. Chapter 2.5—Aluminum Production. In *Treatise on Process Metallurgy*; Seetharaman, S., Ed.; Elsevier: Boston, MA, USA, 2014; pp. 839–917. ISBN 978-0-08-096988-6.
12. Agrawal, S.; Dhawan, N. Evaluation of Red Mud as a Polymetallic Source—A Review. *Miner. Eng.* **2021**, *171*, 107084. [CrossRef]
13. Kong, H.; Zhang, S.; Yang, X.; Zhou, T.; Zhang, M.; Yang, H. Experimental Research on Pyrometallurgical Recovery of Iron from Red Mud. In Proceedings of the 24th Fluidized Bed Conversion Conference, Gothenburg, Sweden, 8–11 May 2022.
14. Reddy, P.S.; Reddy, N.G.; Serjun, V.Z.; Mohanty, B.; Das, S.K.; Reddy, K.R.; Rao, B.H. Properties and Assessment of Applications of Red Mud (Bauxite Residue): Current Status and Research Needs. *Waste Biomass Valorization* **2021**, *12*, 1185–1217. [CrossRef]
15. Boily, R. *Twenty Cases of Red Hazard, an Inventory of Ecological Problems Caused by Bauxite Residue from Alumina Production*; Inforex: Laval, QC, Canada, 2012.
16. Mayes, W.M.; Burke, I.T.; Gomes, H.I.; Anton, D.; Molnár, M.; Feigl, V.; Ujaczki, E. Advances in Understanding Environmental Risks of Red Mud After the Ajka Spill, Hungary. *J. Sustain. Metall.* **2016**, *2*, 332–343. [CrossRef]
17. Ruyters, S.; Mertens, J.; Vassilieva, E.; Dehandschutter, B.; Poffijn, A.; Smolders, E. The Red Mud Accident in Ajka (Hungary): Plant Toxicity and Trace Metal Bioavailability in Red Mud Contaminated Soil. *Environ. Sci. Technol.* **2011**, *45*, 1616–1622. [CrossRef] [PubMed]
18. Lockwood, C.L.; Stewart, D.I.; Mortimer, R.J.G.; Mayes, W.M.; Jarvis, A.P.; Gruiz, K.; Burke, I.T. Leaching of Copper and Nickel in Soil-Water Systems Contaminated by Bauxite Residue (Red Mud) from Ajka, Hungary: The Importance of Soil Organic Matter. *Environ. Sci. Pollut. Res.* **2015**, *22*, 10800–10810. [CrossRef] [PubMed]
19. Liu, P.; Jiang, L.; Yang, X.; Zhang, Y. Experimental Study on Iron Enrichment Performance of Red Mud by Total Gravity Separation. *Light Met.* **2017**, *6*, 6. [CrossRef]
20. Jiang, L.; Liu, P.; Yang, X.; Zhang, Y.; Li, F. Comparative Classification Studies of Red Mud by Using Hydrocyclones. *Miner. Eng.* **2019**, *131*, 124–130. [CrossRef]
21. Jamieson, E.; Jones, A.; Cooling, D.; Stockton, N. Magnetic Separation of Red Sand to Produce Value. *Miner. Eng.* **2006**, *19*, 1603–1605. [CrossRef]
22. Li, W.; Han, Y.; Liu, X.; Shan, Y.; Li, Y. Effect of Fluidized Magnetizing Roasting on Iron Recovery and Transformation of Weakly Magnetic Iron Mineral Phase in Iron Tailings. *Physicochem. Probl. Miner. Process.* **2019**, *55*, 906–916. [CrossRef]
23. Li, Y.; Wang, J.; Wang, X.; Wang, B.; Luan, Z. Feasibility Study of Iron Mineral Separation from Red Mud by High Gradient Superconducting Magnetic Separation. *Phys. C Supercond. Its Appl.* **2011**, *471*, 91–96. [CrossRef]
24. Song, S.; Kong, D.; Wei, Y. Flotation Study of High-Speed Iron Red Mud. *Yunnan Chem.* **2020**, *47*, 3.
25. Huang, Y.; Han, G.; Liu, J.; Wang, W. A Facile Disposal of Bayer Red Mud Based on Selective Flocculation Desliming with Organic Humics. *J. Hazard. Mater.* **2016**, *301*, 46–55. [CrossRef] [PubMed]
26. Rai, S.; Nimje, M.T.; Chaddha, M.J.; Modak, S.; Rao, K.R.; Agnihotri, A. Recovery of Iron from Bauxite Residue Using Advanced Separation Techniques. *Miner. Eng.* **2019**, *134*, 222–231. [CrossRef]

27. Xie, W.; Zhang, N.; Li, J.; Zhou, F.; Ma, X.; Gu, G.; Zhang, W. Optimization of Condition for Extraction of Aluminum and Iron from Red Mud by Hydrochloric Acid Leaching. *Chin. J. Environ. Eng.* **2017**, *11*, 5677–5682.

28. Chen, H.; Wang, T.; Ke, Y.; Wang, S. Discussion on Process Conditions and Mechanism of Sodium Ferric Acid Leaching from Red Mud. *Inorg. Salt Ind.* **2016**, *48*, 5.

29. Yu, Z.L.; Shi, Z.X.; Chen, Y.M.; Niu, Y.J.; Wang, Y.X.; Wan, P.Y. Red-Mud Treatment Using Oxalic Acid by UV Irradiation Assistance. *Trans. Nonferrous Met. Soc. China* **2012**, *22*, 456–460. [CrossRef]

30. Yang, Y.; Wang, X.; Wang, M.; Wang, H.; Xian, P. Recovery of Iron from Red Mud by Selective Leach with Oxalic Acid. *Hydrometallurgy* **2015**, *157*, 239–245. [CrossRef]

31. Yang, Y.; Wang, X.; Wang, M.; Wang, H.; Xian, P. Iron Recovery from the Leached Solution of Red Mud through the Application of Oxalic Acid. *Int. J. Miner. Process.* **2016**, *157*, 145–151. [CrossRef]

32. Zhang, X.; Zhou, K.; Wu, Y.; Lei, Q.; Peng, C.; Chen, W. Separation and Recovery of Iron and Scandium from Acid Leaching Solution of Red Mud Using D201 Resin. *J. Rare Earths* **2020**, *38*, 1322–1329. [CrossRef]

33. Zhang, X.-K.; Zhou, K.-G.; Chen, W.; Lei, Q.-Y.; Huang, Y.; Peng, C.-H. Recovery of Iron and Rare Earth Elements from Red Mud through an Acid Leaching-Stepwise Extraction Approach. *J. Cent. South Univ.* **2019**, *26*, 458–466. [CrossRef]

34. Sokolov, A.; Valeev, D.; Kasikov, A. Solvent Extraction of Iron(III) from Al Chloride Solution of Bauxite HCl Leaching by Mixture of Aliphatic Alcohol and Ketone. *Metals* **2021**, *11*, 321. [CrossRef]

35. Mishra, B.; Staley, A.; Kirkpatrick, D. Recovery of Value-Added Products from Red Mud. *Min. Metall. Explor.* **2002**, *19*, 87–94. [CrossRef]

36. Raspopov, N.A.; Korneev, V.P.; Averin, V.V.; Lainer, Y.A.; Zinoveev, D.V.; Dyubanov, V.G. Reduction of Iron Oxides during the Pyrometallurgical Processing of Red Mud. *Russ. Metall. Met.* **2013**, *2013*, 33–37. [CrossRef]

37. Valeev, D.; Zinoveev, D.; Kondratiev, A.; Lubyanoi, D.; Pankratov, D. Reductive Smelting of Neutralized Red Mud for Iron Recovery and Produced Pig Iron for Heat-Resistant Castings. *Metals* **2020**, *10*, 32. [CrossRef]

38. GUO, Y.; GAO, J.; XU, H.; ZHAO, K.; SHI, X. Nuggets Production by Direct Reduction of High Iron Red Mud. *J. Iron Steel Res. Int.* **2013**, *20*, 24–27. [CrossRef]

39. Lazou, A.; van der Eijk, C.; Tang, K.; Balomenos, E.; Kolbeinsen, L.; Safarian, J. The Utilization of Bauxite Residue with a Calcite-Rich Bauxite Ore in the Pedersen Process for Iron and Alumina Extraction. *Metall. Mater. Trans. B Process Metall. Mater. Process. Sci.* **2021**, *52*, 1255–1266. [CrossRef]

40. Ning, G.; Zhang, B.; Liu, C.; Li, S.; Ye, Y.; Jiang, M. Large-Scale Consumption and Zero-Waste Recycling Method of Red Mud in Steel Making Process. *Minerals* **2018**, *8*, 102. [CrossRef]

41. Zinoveev, D.; Grudinsky, P.; Zakunov, A.; Semenov, A.; Panova, M.; Valeev, D.; Kondratiev, A.; Dyubanov, V.; Petelin, A. Influence of Na_2CO_3 and K_2CO_3 Addition on Iron Grain Growth during Carbothermic Reduction of Red Mud. *Metals* **2019**, *9*, 1313. [CrossRef]

42. Liu, W.; Yang, J.; Xiao, B. Application of Bayer Red Mud for Iron Recovery and Building Material Production from Alumosilicate Residues. *J. Hazard. Mater.* **2009**, *161*, 474–478. [CrossRef]

43. Huang, Z.; Cai, L.; Zhang, Y.; Yang, Y.; Jiang, T. Na_2CO_3 and CaF_2-Enhanced Reduction of Iron Oxides in Red Mud. *J. Cent. South Univ. Nat. Sci. Ed.* **2010**, *41*, 7.

44. Jayasankar, K.; Ray, P.K.; Chaubey, A.K.; Padhi, A.; Satapathy, B.K.; Mukherjee, P.S. Production of Pig Iron from Red Mud Waste Fines Using Thermal Plasma Technology. *Int. J. Miner. Metall. Mater.* **2012**, *19*, 679–684. [CrossRef]

45. Agrawal, S.; Rayapudi, V.; Dhawan, N. Comparison of Microwave and Conventional Carbothermal Reduction of Red Mud for Recovery of Iron Values. *Miner. Eng.* **2019**, *132*, 202–210. [CrossRef]

46. Liu, W.; Sun, S.; Zhang, L.; Jahanshahi, S.; Yang, J. Experimental and Simulative Study on Phase Transformation in Bayer Red Mud Soda-Lime Roasting System and Recovery of Al, Na and Fe. *Miner. Eng.* **2012**, *39*, 213–218. [CrossRef]

47. Sadangi, J.K.; Das, S.P.; Tripathy, A.; Biswal, S.K. Investigation into Recovery of Iron Values from Red Mud Dumps. *Sep. Sci. Technol.* **2018**, *53*, 2186–2191. [CrossRef]

48. Agrawal, S.; Rayapudi, V.; Dhawan, N. Extraction of Iron Values from Red Mud. *Mater. Today Proc.* **2018**, *5*, 17064–17072. [CrossRef]

49. Samouhos, M.; Taxiarchou, M.; Pilatos, G.; Tsakiridis, P.E.; Devlin, E.; Pissas, M. Controlled Reduction of Red Mud by H_2 Followed by Magnetic Separation. *Miner. Eng.* **2017**, *105*, 36–43. [CrossRef]

50. Tang, Z.D.; Gao, P.; Han, Y.X.; Guo, W. Fluidized Bed Roasting Technology in Iron Ores Dressing in China—A Review on Equipment Development and Application Prospect. *J. Min. Metall. Sect. B Metall.* **2019**, *55*, 295–303. [CrossRef]

51. Liu, X.; Gao, P.; Yuan, S.; Lv, Y.; Han, Y. Clean Utilization of High-Iron Red Mud by Suspension Magnetization Roasting. *Miner. Eng.* **2020**, *157*, 106553. [CrossRef]

52. Yuan, S.; Liu, X.; Gao, P.; Han, Y. A Semi-Industrial Experiment of Suspension Magnetization Roasting Technology for Separation of Iron Minerals from Red Mud. *J. Hazard. Mater.* **2020**, *394*, 122579. [CrossRef]

53. Yu, J.; Li, Y.; Lv, Y.; Han, Y.; Gao, P. Recovery of Iron from High-Iron Red Mud Using Suspension Magnetization Roasting and Magnetic Separation. *Miner. Eng.* **2022**, *178*, 107394. [CrossRef]

54. Li, Y.-J.; Wang, R.; Han, Y.-X.; Wei, X.-C. Phase Transformation in Suspension Roasting of Oolitic Hematite Ore. *J. Cent. South Univ.* **2015**, *22*, 4560–4565. [CrossRef]

55. Aghaie, E.; Pazouki, M.; Hosseini, M.R.; Ranjbar, M. Kinetic Modeling of the Bioleaching Process of Iron Removal from Kaolin. *Appl. Clay Sci.* **2012**, *65–66*, 43–47. [CrossRef]

56. Štyriaková, I.; Mockovčiaková, A.; Štyriak, I.; Kraus, I.; Uhlík, P.; Madejová, J.; Orolínová, Z. Bioleaching of Clays and Iron Oxide Coatings from Quartz Sands. *Appl. Clay Sci.* **2012**, *61*, 1–7. [CrossRef]

57. Papassiopi, N.; Vaxevanidou, K.; Paspaliaris, I. Effectiveness of Iron Reducing Bacteria for the Removal of Iron from Bauxite Ores. *Miner. Eng.* **2010**, *23*, 25–31. [CrossRef]

58. Laguna, C.; González, F.; García-Balboa, C.; Ballester, A.; Blázquez, M.L.; Muñoz, J.A. Bioreduction of Iron Compounds as a Possible Clean Environmental Alternative for Metal Recovery. *Miner. Eng.* **2011**, *24*, 10–18. [CrossRef]

59. Qu, Y.; Lian, B.; Mo, B.; Liu, C. Bioleaching of Heavy Metals from Red Mud Using Aspergillus Niger. *Hydrometallurgy* **2013**, *136*, 71–77. [CrossRef]

60. Eisele, T.C.; Gabby, K.L. Review of Reductive Leaching of Iron by Anaerobic Bacteria. *Miner. Process. Extr. Metall. Rev.* **2014**, *35*, 75–105. [CrossRef]

61. Maihatchi Ahamed, A.; Pons, M.N.; Ricoux, Q.; Goettmann, F.; Lapicque, F. Production of Electrolytic Iron from Red Mud in Alkaline Media. *J. Environ. Manag.* **2020**, *266*, 110547. [CrossRef]

energies

Article

Height Prediction and 3D Visualization of Mining-Induced Water-Conducting Fracture Zone in Western Ordos Basin Based on a Multi-Factor Regression Analysis

Huiyong Yin [1,2]**, Fangying Dong** [1,2]**, Yiwen Zhang** [3]**, Wenju Cheng** [1,2]**, Peihe Zhai** [1,2,*]**, Xuyan Ren** [1,2]**, Ziang Liu** [1,2]**, Yutao Zhai** [4] **and Xin Li** [5]

[1] College of Earth Science and Engineering, Shandong University of Science and Technology, Qingdao 266590, China; huiyongy@sdust.edu.cn (H.Y.); 202082030047@sdust.edu.cn (F.D.); 202082030045@sdust.edu.cn (W.C.); 201901030313@sdust.edu.cn (X.R.); 202001030613@sdust.edu.cn (Z.L.)
[2] Shandong Provincial Key Laboratory of Depositional Mineralization & Sedimentary Mineral, Shandong University of Science and Technology, Qingdao 266590, China
[3] Shuifa Planning and Designing Co., Ltd., Jinan 250100, China
[4] Hebei Coal Research Institute Corporation Co., Ltd., Xingtai 054000, China; zhaiyt53090149@163.com
[5] Ningxia Coal Science and Technology Research Institute Co., Ltd., Ningxia 750004, China
* Correspondence: zph@sdust.edu.cn

Abstract: The mining-induced water-conducting fracture zone (WCFZ) plays a critical role in roof water damage prevention and ecological protection. The measured heights of the WCFZ were collected from 52 working faces or boreholes in the Ordos Basin mining area. Four factors influencing the mining-induced height of the WCFZ, i.e., mining thickness, proportion coefficient of hard rock, working width, and mining depth, were analyzed. The optimal unitary function model of each factor and the height of the WCFZ were obtained through single-factor analysis. The grey correlation method and fuzzy ordered binary comparison method were used to determine the comprehensive weight, and the weighted improved multiple regression model was obtained by combination and iteration. The relative error of the model was basically controlled within 10%. Finally, taking the Qingshuiying Coalfield as an application case, we predicted the mining-induced height of the WCFZ by using the new prediction model. The spatial distribution characteristics of the WCFZ were analyzed by the geographic information system. In addition, Groundwater Modeling System (GMS) software was used to build a 3D structure model of WCFZ height to visualize the spatial distribution rules of the WCFZ. The results showed that the height of the WCFZ can be predicted quantitatively by this new method, and the visualization of the WCFZ can be realized. The proposed method effectively analyzes and predicts the mining-induced height of the WCFZ so that water gushing risks from overlying aquifers can be prevented or mitigated in mines.

Keywords: western Ordos Basin; height of water-conducting fracture zone; grey correlation method; fuzzy ordered binary comparison method; multivariate nonlinear regression model; 3D visualization

1. Introduction

With the exhaustion of coal resources in eastern China, large coal production bases have gradually been moved to the western regions [1]. The ecological environment in western China is fragile, and the exploitation of coal resources can easily lead to the geological problems of the ecological environment [2–4]. Coal measure strata belong to weakly cemented rock with poor mechanical properties. The WCFZ in the roof of coal seam mining has a large mining-induced height, which poses a water inrush risk [5–7]. Therefore, accurate prediction of the mining-induced height of the WCFZ and accurate exploration of the hydraulic connection between the WCFZ and the overlying aquifer are among the most urgent problems in the western mining area.

The WCFZ is the failure zone of the overlying strata in coal mining and is one of the critical index factors to judge the water inrush in the roof. A large amount of observational data show that the overburden failure and displacement zoning of coal seam mining are apparent. According to the theory of "three top zones," the overlying formation can be divided into the fracture zone, caving zone, and curved belt. Because both the caving zone and fracture zone can direct water vertically, they are usually referred to as the WCFZ together. The combination of the two zones is the height of the mining-induced WCFZ [8]. The water inrush condition of the coal roof is determined by the development height of the WCFZ and the water-rich condition of the overlying strata. Only when the WCFZ connects the overlying water-rich aquifer can the conditions of roof water inrush occur [9–11].

Field measurement is the most direct and reliable method to obtain the height of the WCFZ. Because of its high cost and long time consumption, field measurements are often used to verify predicted results [12]. The prediction methods include the empirical formula, similar material simulation, numerical simulation, analogy analysis, and critical layer theory [13–16]. Among them, the empirical formula method based on measured data fitting is the most commonly used method to predict the height of the WCFZ. Xiang et al. (2020) obtained the height prediction formula of the WCFZ in the western mining area of China by multiple linear regression fitting and applied it to the 12511 working faces of Bulianta Coal Mine [17]. Xiaoshen et al. (2021) took 112201 working faces of Xiaobaodang Coal Mine as an example. In situ measurements, including fluid leakage, borehole TV, and similar simulations, were used to analyze the development regularity of the regional WCFZ [18]. Based on the analysis of mine exploration data, Gusev et al. (2018) presented a prediction scheme for determining the height of the WCFZ in salt formations with clay layers [19]. Based on the data processing system (DPS), Xiaobin et al. (2021) analyzed the factors influencing the height development of the WCFZ, introduced the sensitivity coefficient to establish a mathematical model, and proposed a formula for predicting the height of the WCFZ [20]. Yu et al. (2019) proposed the prediction equation of the WCFZ of soil-rock composite overburden [21]. They adopted the running water quantity of boreholes monitoring and distributed optical fiber sensing (DOFS) technology to conduct in situ measurements of the WCFZ height. Based on elastic foundation beam theory, Yun et al. (2018) studied the development mechanism of an overburden WCFZ in short-wall block filling mining in northwest China and established a height prediction model for an overburden WCFZ [22]. Tingen et al. (2020) studied the calculation method of the WCFZ height of Jurassic coal seam mining in northern Shaanxi based on the plate and shell theory and carried out experiments in the Jinjitan Coal Mine [23]. However, in the past, most attention has been paid to the prediction of the development height of the WCFZ, while the spatial distribution of the WCFZ and its spatial position relationship with the overlying water-rich strata have been ignored.

In this paper, we collected the measured heights of the WCFZ from 52 working faces or boreholes in the Ordos Basin mining area. Based on the comprehensive analysis of the coal mining method, mining thickness, proportion coefficient of hard rock, working width, and mining depth, the Statistics Package for Social Science (SPSS) software was used for single factor optimal regression analysis. The grey correlation method and fuzzy ordered binary comparison method were combined to obtain the combined weight values of each main control factor. Finally, the improved multivariate nonlinear regression model of the height of the WCFZ was obtained by using the numerical iteration method. The model was verified with five mining working faces in the study area, and the error analysis was compared with the calculation results of the empirical formula. Finally, the model was applied to Qingshuiying Coalfield. The safety partition of a roof crack in the study area was obtained from borehole data, and the 3D visual structure model of the WCFZ was constructed by GMS software. The aim was to provide a more accurate and reliable method for predicting and evaluating the height of the WCFZ in coal seam mining under similar conditions. It is of great significance to environmental protection, water conservation, and coal mining in an ecological fragile mining area.

2. Height Measurement of WCFZ in Western Ordos Basin

Due to the complexity and uncertainty of the geological structure and in situ stress changes in the rock mass in coal mining, the prediction of the height of the WCFZ is beyond the traditional investigation of hydrogeological conditions and geological structure. The height of the WCFZ in the roof of the coal seam is not influenced by a single factor but many factors. Researchers concluded that the factors affecting the height of the WCFZ are mainly as follows: mining method, mining thickness, coal seam angle, roof strata strength, roof strata combination structure, mining depth, and working width [17,19,24,25].

This paper studies the height prediction of the WCFZ in the western mining area of Ordos Basin. The location of the study area is shown in Figure 1. The measured height of the WCFZ is summarized in Table 1. In the Jurassic coal seam mining of Ordos Basin, most of them are thick and extra-thick coal seams with near-horizontal and gently inclined beddings. "Fully mechanized caving mining" is the main coal mining method in this area, and the influence of coal seam angle on the height of the WCFZ can be ignored in this study.
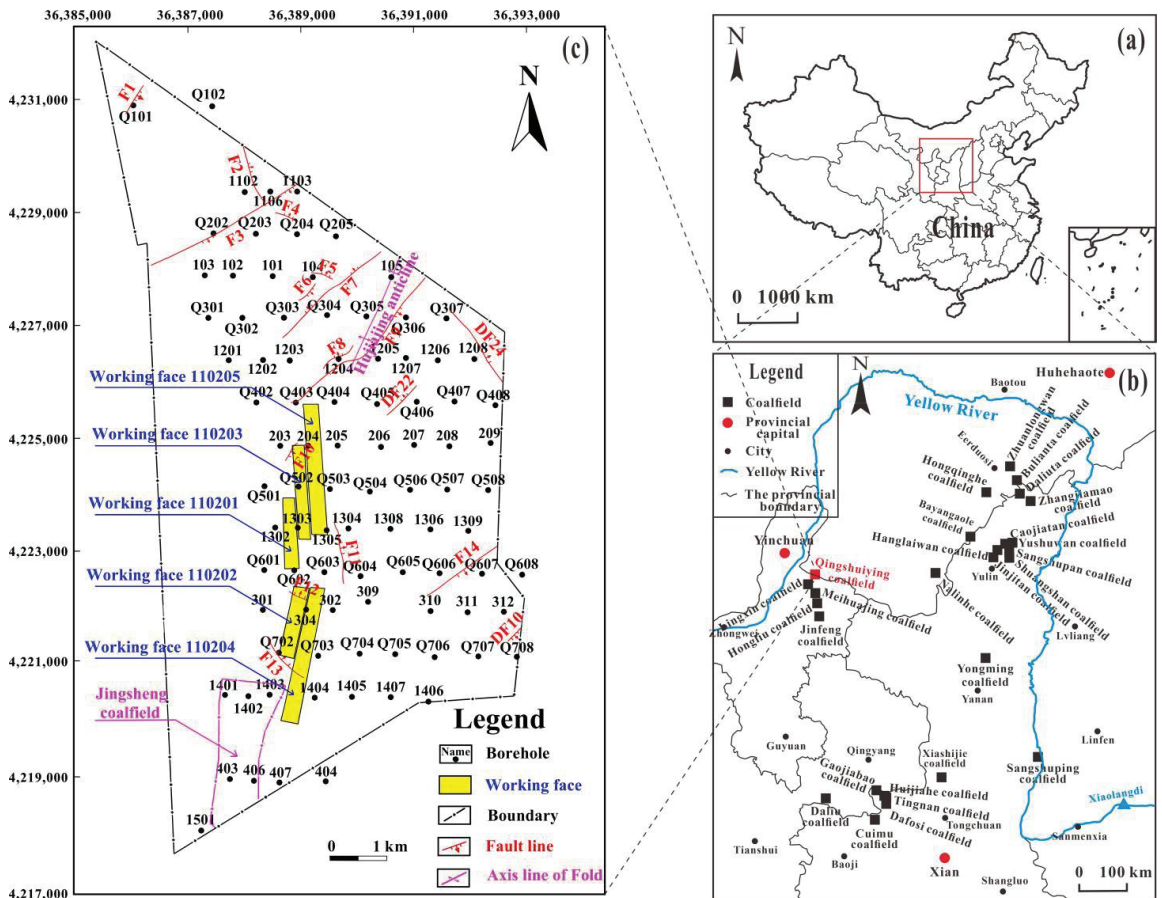
Figure 1. Location of study area: (**a**) Map of China, (**b**) Schematic diagram of location of each Coalfield, (**c**) Qingshuiying Coalfield.

Table 1. Measured height of WCFZ.

Coalfield	Working Face/Borehole	Mining Method	Mining Depth (S)/m	Working Width (L)/m	Mining Thickness (M)/m	Proportion Coefficient of Hard Rock (b)/m	Measured Height of WCFZ (Hf)/m
Bayangaole	311,101	ZF	620.00	260.00	5.27	0.78	126.00
Bulianta	12,406	ZF	200.00	310.00	4.50	0.69	89.50
Caojiatan	122,106	ZF	279.99	350.00	6.00	0.91	136.10
Cuimu	210,303	ZF	552.19	200.00	6.50		190.51
Dafosi	41,104	ZF	400.00	180.00	3.90		110.00
Daliu	1203	ZF	49.00	135.00	4.00	0.52	45.00
Daliuta	52,306	ZF	180.00	301.00	7.00	0.90	137.32
Gaojiabao	41,101	ZF	400.00	120.00	4.36		88.03
	30,101	ZF	300.00	248.00	7.50	0.67	112.60
Hanglaiwan	H3	ZF	241.30	300.00	4.50	0.69	108.32
	H4	ZF	244.00	300.00	4.50	0.74	114.38
Hongliulin	25,202	ZF	135.00	350.00	5.80		60.70
Hongqinghe	3−1101	ZF	669.00	240.00	6.10		107.00
	3−1401	ZF	740.00	241.00	6.00		106.10
Hujiahe	401,101	ZF	525.00	180.00	6.00	0.62	100.00
	401,102	ZF	650.00	180.00	10.00	0.62	133.00
	401,103	ZF	650.00	180.00	8.00	0.62	106.40
Jinjitan	101	ZF	260.00	300.00	5.50		108.59
	102	ZF	264.98	300.00	5.50	0.54	111.32
	12−2101	ZF	260.00	300.00	5.50	0.90	109.72
	JT6	ZF	270.20	300.00	5.00	0.912	120.25
	JKY2	ZF	260.00	300.00	5.50	0.70	122.64
	JSD2	ZF	247.60	300.00	5.50	0.44	115.00
	JSD4	ZF	232.38	300.00	5.50	0.79	146.18
Longde	205	ZF	195.90	182.00	3.96		75.78
	206	ZF	199.90	182.00	3.96		71.66
Namuhe		ZF	544.00	240.00	6.00		103.23
Sangshuping	3303	ZF	370.00	153.00	5.70	0.16	70.00
Shenshupan	No. 3	ZF	673.00	200.00	10.00	0.95	120.00
Shuangshan	No. 3	ZF	713.00	200.00	8.00	0.93	103.09
Tingnan	106	ZF	463.07	116.05	7.65	0.63	96.45
	107	ZF	453.00	116.00	7.60	0.62	86.40
	104	ZF	550.02	200.00	6.00	0.60	136.20
	105	ZF	575.00	200.00	6.00		135.23
	Y3	ZF	702.00	200.00	9.00	0.39	148.30
	Y1-1	ZF	533.20	200.00	7.50	0.35	140.20
	303	ZF	500.00	180.00	3.50		100.00
Xibu		ZF	568.40	180.40	2.94	0.85	57.00
		ZF	550.00	180.00	2.40	0.81	55.32
		ZF	489.00	160.00	4.50	0.47	54.79
		ZF	516.00	206.10	2.95	0.74	54.50
		ZF	420.50	209.00	3.90	0.52	52.01
		ZF	679.00	180.00	2.10	0.46	44.54
		ZF	412.00	157.00	2.20	0.09	35.40
Xiashijie	223	ZF	620.00	240.00	7.00		187.40
Yongming	5103	ZF	275.00	148.00	1.40		29.58
Yushuwan	20,104	ZF	280.00	255.00	5.00	0.75	135.40
	Y3	ZF	276.00	255.00	5.00	0.54	130.50
	Y4	ZF	279.30	255.00	5.00	0.62	137.30
	Y6	ZF	275.80	255.00	5.00	0.57	117.80
Zhangjiamao	3201	ZF	500.00	104.00	11.10	0.83	152.34
Zhuanlongwan	23,103	ZF	210.00	260.00	4.50		92.10

Note: "ZF" represents fully mechanized caving mining.

The stratum in the study area belongs to weakly consolidated rock, the coarse, medium, and fine clastic particles play the role of skeleton, and the clastic particles are mainly quartz,

feldspar, and debris. The particles are filled with clay minerals, and the cementation modes are contact cementation and mosaic cementation, with weak cementation. The hardness of sandstones mainly depends on clastic grains in the study area. Because it is difficult to quantify the roof strata strength and strata combination structure, we refer to the proportion coefficient of hard rock (*b*) as an approximate substitute for roof strata. The proportion coefficient of hard rock (*b*) refers to the ratio of the accumulated thickness of hard rock in the mining influence range above the roof to the mining influence range. The hard rock refers to fine sandstone, medium sandstone, and coarse sandstone. It is generally considered that 15 to 20 times the coal thickness is the most significant influence range of coal mining. Therefore, we selected 15 to 20 times the coal thickness as the mining influence range [26,27]. The equation is as follows:

$$b = \frac{\sum h}{(15 \sim 20)M} \tag{1}$$

where *M* is the mining thickness; $\sum h$ is the accumulated thickness of hard rock strata within the mining influence range.

Based on this, the influencing factors of the height of the WCFZ in this paper are mining thickness, proportion coefficient of hard rock, mining depth, and working width.

3. Univariate Regression Analysis

Based on the collected data of the WCFZ height and index factors (Table 1), SPSS software was first used for single factor regression analysis.

3.1. Mining Thickness (M)

The relationship between the height of the mining-induced WCFZ and the mining thickness is shown in Figure 2a. The correlation coefficients of the optimal unitary function model are compared in Table 2. The linear equation ($R^2 = 0.863$) was taken as the optimal unitary function model.
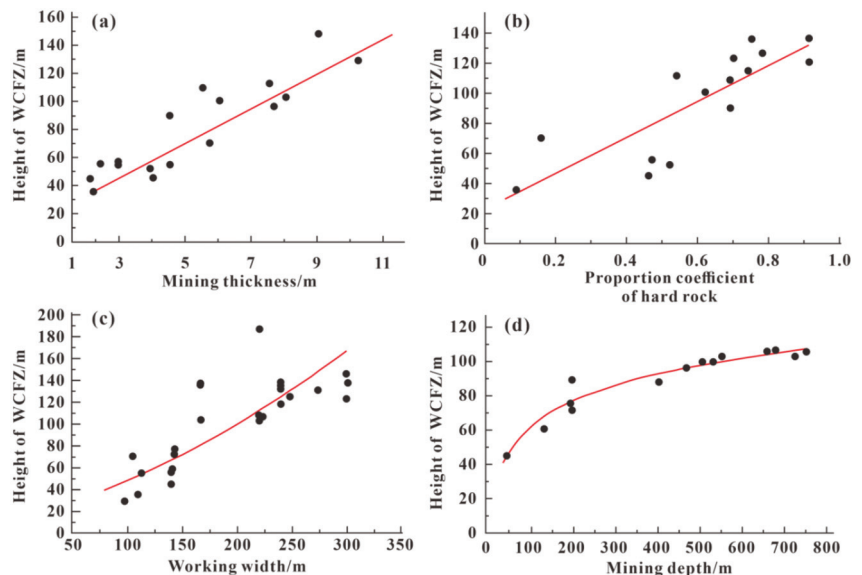
Figure 2. The relationship between the height of WCFZ and main controlling factors: (**a**) Mining thickness, (**b**) proportion coefficient of hard rock, (**c**) working width, (**d**) mining depth.

Table 2. Comparison of correlation coefficients of optimal function model with one variable.

	Linear Equation	Conic	Cubic Curve	Logistic Curve	S-Shape Curve	Exponential Curve	Power Function Curve
Mining thickness	**0.863**	0.852	\	\	\	0.825	0.829
Proportion coefficient of hard rock	**0.674**	\	\	0.539	0.549	\	0.587
Working width	0.620	\	0.712	0.660	**0.725**	0.636	\
Mining depth	0.834	0.923	\	**0.939**	0.859	0.764	0.934

3.2. Proportion Coefficient of Hard Rock (b)

The western mining area generally has no migmatite and igneous rock strata, so the proportion coefficient of hard rock mainly depends on the cumulative thickness of sandstone. Thicker sandstone indicates a greater proportion coefficient of hard rock. The relationship between the height of the WCFZ and proportion coefficient of hard rock is shown in Figure 2b. The correlation coefficients of the optimal unitary function model are compared in Table 2. The linear equation ($R^2 = 0.674$) was taken as the optimal unitary function model.

3.3. Working Width (L)

The working face with similar mining thickness, the proportion coefficient of hard rock, and the mining depth were selected to study the relationship between the height of the WCFZ and working width, as shown in Figure 2c. The correlation coefficients of the optimal unitary function model are compared in Table 2. The S-shaped curve ($R^2 = 0.725$) was taken as the optimal unitary function model.

3.4. Mining Depth (S)

The working face with similar mining thickness, the proportion coefficient of hard rock, and the working width were selected to study the relationship between the height of the WCFZ and mining depth, as shown in Figure 2d. The correlation coefficients of the optimal unitary function model are compared in Table 2. The logarithmic curve ($R^2 = 0.939$) was taken as the optimal unitary function model.

4. Multiple Regression Analysis to Predict the Height of WCFZ

4.1. Grey Correlation Method

4.1.1. Construction of Comparative Sequence

The comparative sequence of factors affecting the system behavior is constructed [28–31]:

$$X_i = (X_1, X_2, \cdots X_n) = \begin{pmatrix} X_1(1) & X_2(1) & \cdots & X_n(1) \\ X_1(2) & X_2(2) & \cdots & X_n(2) \\ \vdots & \vdots & \vdots & \vdots \\ X_1(m) & X_2(m) & \cdots & X_n(m) \end{pmatrix} \tag{2}$$

where *m* is the number of indicators; $X_i = (x_i(1), x_i(2), \ldots, x_i(m))^T, i = 1, 2, \ldots, n$.

4.1.2. Determination of Optimal Reference Sequence

An ideal optimal reference sequence can be selected from the matrix constructed in Equation (3):

$$X_0 = (x_0(1), x_0(2), \ldots, x_0(m)) \tag{3}$$

In order to eliminate the differences caused by different units of factors, Equation (4) is adopted for the dimensionless processing of variables:

$$\xi_i(k) \;=\; \frac{\min\limits_{i}|x_0(k)-x_i(k)| + \rho \cdot \max\limits_{i}|x_0(k)-x_i(k)|}{|x_0(k)-x_i(k)| + \rho \cdot \max\limits_{i}|x_0(k)-x_i(k)|} \tag{4}$$

where $k = 1, 2 \ldots m$ and ρ is the resolution coefficient, which is 0.5.

4.1.3. Calculation of Correlation Degree

The correlation degree is calculated by reference sequence and comparison sequence:

$$r_i \;=\; \frac{1}{m}\sum_{k=1}^{m}\xi_i(k) \tag{5}$$

4.1.4. Calculation of Weight of Each Factor

The weight of each factor is calculated according to formula:

$$\omega_i \;=\; \frac{r_i}{\sum_{i=1}^{n} r_i} \tag{6}$$

The final weight of each factor (w_i) is obtained by combining the collected measured data of the height of the WCFZ and index factors, and it is presented in Table 3.

Table 3. The comprehensive weight of each main control factor.

	Mining Thickness	Proportion Coefficient of Hard Rock	Working Width	Mining Depth
Weight determined by grey correlation analysis (w_i)	0.2995	0.2956	0.2398	0.1651
Weight determined by fuzzy ordered binary comparison (w_j)	0.449	0.316	0.164	0.071
Comprehensive weight (w_z)	0.39	0.31	0.2	0.1

4.2. Fuzzy Ordered Binary Comparison Method

4.2.1. Consistency Sequencing

First, the factors are compared by the following method, such as b_i and b_k [32–34]:

If b_i is more important than b_k, then $b_{ik} = 0$, $b_{ki} = 1.0$;

If b_i is as important as b_k, then $b_{ik} = 0.5$, $b_{ki} = 0.5$;

If b_i is less important than b_k, then $b_{ik} = 0$, $b_{ki} = 1.0$; where $k = 1, 2, \ldots, m$; $i = 1, 2, \ldots, m$.

Thus, the m × m order qualitative sorting decision sequence of the importance of the index set is obtained:

$$B \;=\; \begin{bmatrix} b_{11} & b_{12} & \ldots & b_{1m} \\ b_{21} & b_{22} & \ldots & b_{2m} \\ \ldots & \ldots & \ldots & \ldots \\ b_{m1} & b_{m2} & \ldots & b_{mm} \end{bmatrix} \text{ meet } \begin{cases} b_{ki} \text{ is either } 0, \ 0.5 \text{ or } 1.0 \\ b_{ki} + b_{ik} = 1.0 \\ b_{kk} + b_{ii} = 0.5 \end{cases} \tag{7}$$

According to Equation (8):

$$t_i \;=\; \sum_{j=1}^{m} b_{ij}, \; t_i(i = 1, 2, \ldots, m) \tag{8}$$

The consistency qualitative order of each index is obtained, and the new index set is constructed from large to small:

$$\hat{A} = \left(\overset{\wedge}{a_1}, \overset{\wedge}{a_2}, \ldots, \overset{\wedge}{a_m} \right), \ t1 \ > \ t2 \ > \ldots t_m \tag{9}$$

A consistent qualitative decision table is established for each factor in this study (Table 4) in the order of ordinal importance: $U = (U_1, U_2, U_3, U_4)$ = (mining thickness, proportion coefficient of hard rock, working width, mining depth).

Table 4. Qualitative judgment table of index ranking consistency of fixed weight factor set U.

	Mining Thickness	Mining Depth	Working Width	Proportion Coefficient of Hard Rock	t_i
Mining thickness	0.5	1	1	1	3.5
Mining depth	0	0.5	0	0	0.5
Working width	0	1	0.5	0	1.5
Proportion coefficient of hard rock	0	1	1	0.5	2.5

4.2.2. Mood Operators and Relative Weights

The index that is ranked first is taken as the standard, and the comparison results with other indexes are described by modal adverbs of different degrees, namely fuzzy modal operators. Fully considering people's discrimination ability and habits of thinking to distinguish similar things and the need for discrimination accuracy, we consider 11 mood operators, represented by a digital scale from I to XI. All scales and their corresponding weights are as follows: I (1.0), II (0.818), III (0.667), IV (0.538), V (0.429), VI (0.333), VII (0.250), VIII (0.176), IX (0.111), X (0.053), XI (0.0).

4.2.3. Ordered Binary Comparison and Quantization

For the index set A sorted by consistency, the binary comparison of adjacent indexes is made in turn. First, the fuzzy tone operator and relative weight value φ_{12} of index $\overset{\wedge}{a_2}$ are obtained by comparing index $\overset{\wedge}{a_1}$ and $\overset{\wedge}{a_2}$. Then, taking $\overset{\wedge}{a_2}$ as the criterion of ranking first, the fuzzy tone operator and relative weight value φ_{23} of $\overset{\wedge}{a_3}$ can be obtained by comparing index $\overset{\wedge}{a_2}$ and $\overset{\wedge}{a_3}$. According to $\varphi_{ij} = \varphi_{i,t-1} \cdot \varphi_{t-1,j}$, the weight of $\overset{\wedge}{a_3}$ relative to $\overset{\wedge}{a_1}$ is $\varphi_{13} = \varphi_{12} \cdot \varphi_{23}$. In this way, the relative weight of each factor is gradually obtained. The relative weight value of the index obtained by binary comparison is normalized, and finally, the index centralization vector is obtained:

$$w_j = (w_1, w_1, \ldots, w_m) \sum_{i=1}^{m} = 1 \tag{10}$$

Table 3 presents the final weight of each factor (w_j) that is obtained by combining the measured data of WCFZ height and index factors.

4.3. Comprehensive Weight Calculation

The weight of each factor w_i obtained by the grey correlation method and the weight of each factor w_j obtained by the fuzzy ordered binary comparison method are combined and improved to obtain the comprehensive weight w_z (Table 3). Using w_i and w_j to represent w_z linearly, the equation as follows:

$$w_z = (1 - \alpha)w_i + \alpha w_j \tag{11}$$

where α is the proportion of the weight of the fuzzy ordered binary comparison method in the comprehensive weight [35]:

$$\alpha = \frac{n}{n-1} \left[\frac{2}{n}(w_1 + 2w_2 + \cdots + nw_n) - \frac{n+1}{n} \right] \tag{12}$$

4.4. Model Determination

In this paper, the optimal unitary function model between the height of the WCFZ and the four main control factors obtained from the Section 2 analysis is as follows:

Mining thickness model:

$$H_f = a_1 M + a_2 \tag{13}$$

Proportion coefficient of hard rock model:

$$H_f = k_1 b + k_2 \tag{14}$$

Working width model:

$$H_f = \exp\left(c_1 + \frac{c_2}{L}\right) \tag{15}$$

Mining depth model:

$$H_f = t_1 \ln S + t_2 \tag{16}$$

where a_i, k_i, c_i, and t_i denote the hypothetical unknown number.

By substituting the comprehensive weight of each main control factor, the multivariate nonlinear regression equation is established as follows:

$$H_f = 0.39(a_1 M + a_2) + 0.31(k_1 b + k_2) + 0.2 \exp\left(c_1 + \frac{c_2}{L}\right) + 0.1(t_1 \ln S + t_2) \tag{17}$$

The multivariate nonlinear regression analysis is conducted and the coefficients of each main control factor are recalculated in Equation (17). Through combination and iteration, the multivariate nonlinear regression correction model for the height of the WCFZ is finally determined as follows:

$$H_f = 4.0M + 23.6b + 0.2e^{5.2 - \frac{470.7}{L}} + 1.2 \ln S + 7.8 \tag{18}$$

The fitting degree of the model is $R^2 = 0.903$.

5. Error Contrast Analysis

This paper selected Qingshuiying Coalfield, Meihuajing Coalfield, Jinfeng Coalfield, Lingxin Coalfield, and Hongliu Coalfield to verify the prediction accuracy of the model. For the purpose of the comparative error analysis, the "three under" rules [36] empirical formula was used to calculate the height of the WCFZ. The strata in the study area are weakly cemented rock, and the mechanical properties belong to the medium-hard rock strata. The height of the WCFZ was calculated by Equations (19) and (20):

$$H = \frac{100\sum M}{1.6\sum M + 3.6} \pm 5.6 \tag{19}$$

$$H = 20\sqrt{\sum M} + 10 \tag{20}$$

The calculated results of the prediction model and empirical formula were compared with the measured values for comparative error analysis in Table 5. Obviously, the height of the WCFZ predicted by the model in this paper was closer to the measured value. The relative error was mostly controlled within 10%. It showed that the height of the WCFZ predicted by this model is more consistent with the actual situation and can be applied to the research area.

Table 5. Error analysis of each formula.

Number	Working Face Name	Mining Thickness (*M*)/m	Proportion Coefficient of Hard Rock (*b*)/m	Mining Depth (*S*)/m	Working Width (*L*)/m	Measured Height of WCFZ/m	Empirical Formula (19)		Empirical Formula (20)		Prediction Model of This Paper	
							Predictive Value/m	Relative Error %	Predictive Value/m	Relative Error %	Predictive Value/m	Relative Error %
1	Qingshuiying Coalfield 11201	5.43	0.75	210	280	62.84	49.79	20.77	56.60	9.92	60.39	3.90
2	Meihuajing Coalfield 11201	2.7	0.65	220	256	46.45	39.69	14.55	42.86	7.72	46.18	0.59
3	Jinfeng Coalfield 011802	4.6	0.72	500	280	63.12	47.57	24.63	52.90	16.20	57.40	9.06
4	Lingxin Coalfield 051503	3.5	0.72	250	280	59.24	43.64	26.33	47.42	19.96	52.17	11.94
5	Hongliu Coalfield 1221	5.3	0.7	330	302	62.59	49.47	20.96	56.04	10.46	60.11	3.97
6	Hongliu Coalfield 1010206	5.28	0.68	280	300	56.02	49.42	11.77	55.96	0.11	59.28	−5.82

6. Study Case

6.1. Overview of the Study Area

The study area is a Coalfield of Qingshuiying, located in the western Ordos Basin (Figure 1c). The study area has mined five working faces: 110201, 110202, 110203, 110204, and 110205. The coal is part of the Jurassic Yan'an Formation, and the main minable coal seam is #2 coal at the present stage. Figure 3 shows the typical hydrogeological profile of Qingshuiying Coalfield. The research objective is to determine the mining-induced height of the WCFZ in the overlying rock.
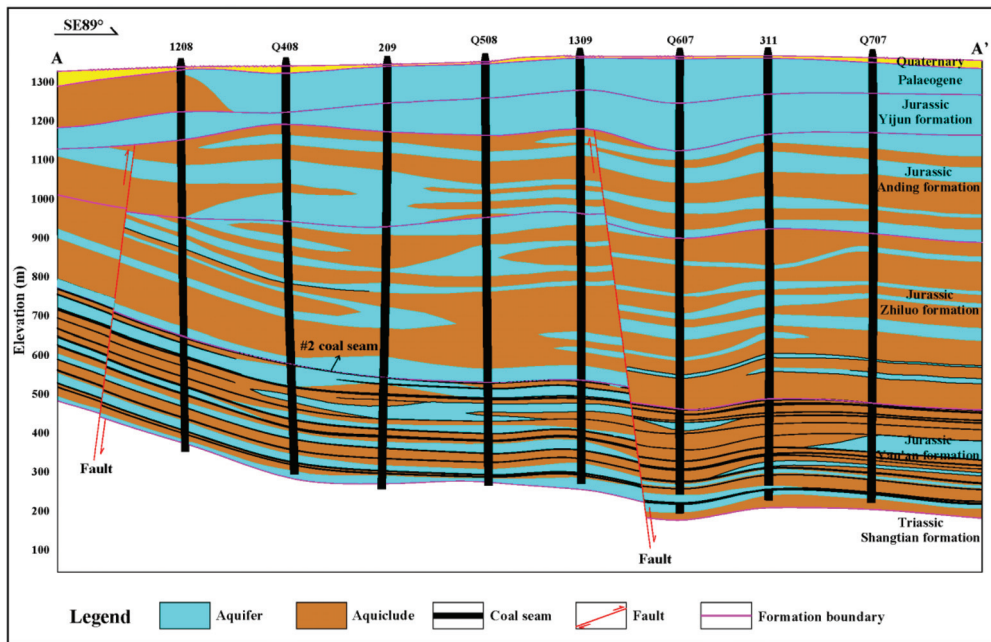
Figure 3. Hydrogeological profile of Qingshuiying Coalfield.

6.2. Calculation of the Height of WCFZ Based on Borehole

(1) Index factor acquisition

Mining thickness (*M*): The coal seam thickness was obtained based on the coal seam thickness identified in boreholes of the research area.

Proportion coefficient of hard rock (*b*): According to Equation (1), 15 times the coal seam thickness was taken as the statistical height. The total thickness of fine sandstone, medium sandstone, and coarse sandstone was used as the accumulated thickness of hard rock strata within the statistical height range. The ratio coefficient of hard rock at each borehole was calculated.

Working width (*L*): At present, Qingshuiying Coalfield has mined five working faces with a width of approximately 280 m. According to the Coalfield production continuity plan in the next years, the design width of the working face will basically remain unchanged, so the 280 m was taken as the working width.

Mining depth (*S*): According to the borehole revealing data of the research area, the buried depth of the coal seam floor at each borehole point was obtained as the mining depth at this point.

(2)   Calculation of the height of WCFZ

According to the prediction formula (16) of WCFZ height, the index factors obtained in the study area were substituted to calculate the WCFZ height of each borehole. The Kriging linear interpolation method was used to draw the height contour map of the WCFZ in the whole study area, as shown in Figure 4. In general, the height of the WCFZ in the study area was larger in the west (>60 m), especially in the northwest, while being smaller in the east.
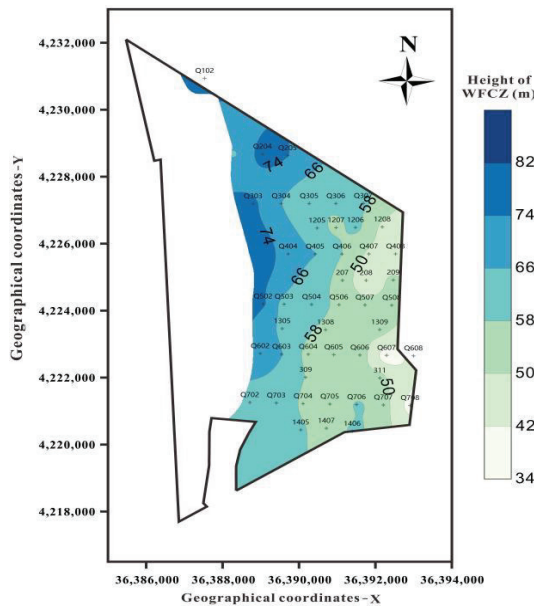
Figure 4. Contour map of height prediction of WFCZ.

6.3. Safety Zoning of Risk Cracking

The occurrence of roof water inrush depends on the height of the WCFZ and the water-rich condition of the strata. Generally, an aquifer has good water content and has the condition of filling water, whereas an aquiclude is generally poor in water and has water resistance. Connection of the WCFZ to the overlying aquifer is the key to judging the mine water inrushing. According to this judgment method, the whole study area can be divided into a cracking safe zone and cracking unsafe zone. If the WCFZ can connect to the overlying aquifer, it is an unsafe zone; otherwise, it is a safe zone. The partition results are

shown in Figure 5. The safety zone is mainly distributed in the northeast of the study area. Surprisingly, the region with a small height of the WCFZ in the southeastern part of the study area is an unsafe zone. This is because the height value of the WCFZ in this region is small, but it is developed into the overlying aquifer. If the aquifer is rich in water, the water will flow into the mining face along the WCFZ, which may cause water inrushing into the working face.
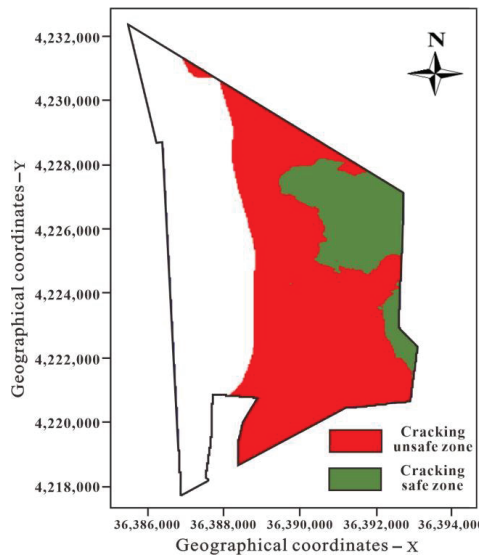
Figure 5. Partition diagram of cracking safety prediction.

6.4. 3D Structure Model of WCFZ

The Groundwater Modeling System (GMS) is a comprehensive, conceptual model-based Groundwater environment simulation software, with a good interface, and powerful pre-treatment and post-treatment functions. The GMS software can realize the conversion from borehole data to a 3D space model, which is quite prominent in constructing a 3D visualization hydrogeological structure model.

The spatial relationship between the WCFZ and overlying aquifer (aquiclude) is graphically displayed to show the distribution characteristics of the WCFZ in the study area. GMS software was used to construct a 3D hydrogeological structure model of the WCFZ based on the borehole formation data and the height of WCFZ data in the study area. By cutting and rotating models, the spatial distribution and connection with the overlying aquifer (aquiclude) of the WCFZ can be more intuitively understood [37–39].

In consideration of the possible influence range of the height of the WCFZ, the #2 coal seam floor was taken as the bottom boundary of the model, and 100 m upward of the maximum height of the WCFZ was taken as the top boundary of the model. From bottom to top, the strata in the study area consisted of #2 coal seam, WCFZ range, Aquiclude I, Aquifer I, Aquiclude II, Aquifer II, and Aquiclude III. The lithology revealed by each borehole was different, and the distribution of the aquifer or aquiclude was also different. Therefore, not every borehole completely contains the above strata. When the strata are pinched or missing, the thickness of the strata is treated as 0 m, which is represented as missing in the model. The Borehole Module of GMS was used to call the imported borehole hierarchical data file to build a 3D space model. Then, TINS interpolation was carried out to build triangular grids. The Solids Module was called to establish a 3D hydrogeological structure model. In order to make the thickness comparison between different strata more obvious, the model was enlarged 3 times along the Z-axis (Figure 6). The 3D solid model

was cut and rotated along different directions to obtain the 3D hydrogeological structure section of WFCZ (Figure 7), including four cross sections: A-A′, B-B′, I-I′, II-II′.
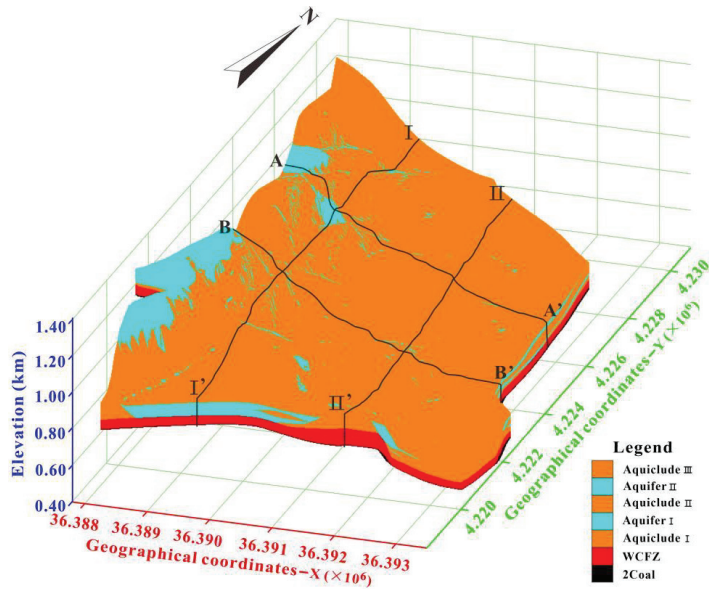
Figure 6. 3D hydrogeological structure model of WFCZ.
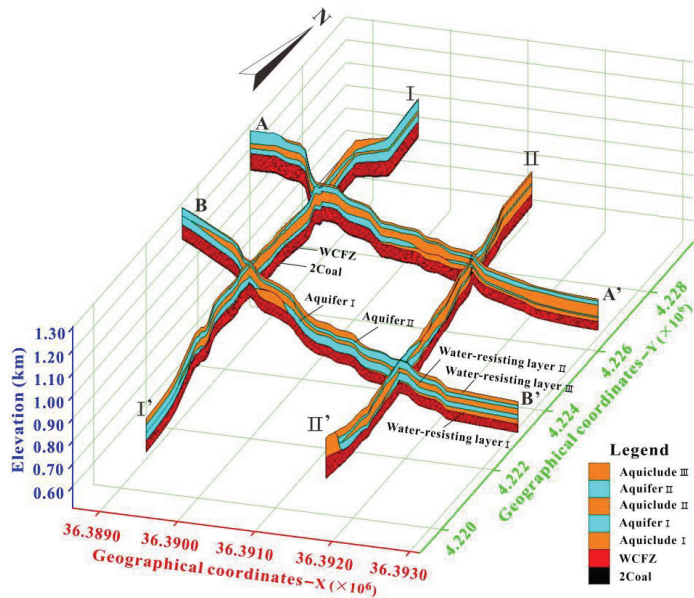
Figure 7. 3D hydrogeological structure section of WFCZ.

Figure 6 shows that the strata burial depth in the western part of the study area is smaller than that in the eastern part. The thickness of each aquifer varies significantly in different positions. Figure 7 shows that the height of the WCFZ decreases from west to east. The height of the WCFZ in the western part of the study area is larger, and the WCFZ directly connects the overlying aquifer I and connects aquifer II at a few positions.

The thickness of the aquiclude in the western part of the study area is relatively thin and discontinuous. Therefore, during the mining process of the #2 coal seam in the western part of the study area, the WCFZ easily connects the overlying aquifer and causes the roof water-inrush or sand collapse accident. The height of the WCFZ in the eastern part of the study area is relatively small, and the direct top of the WCFZ is a continuous aquiclude. Especially, the WCFZ in the northeast does not develop upward until aquiclude I. The thickness of aquifer I and aquifer II is very thin and discontinuous. Therefore, the risk of water inrush of #2 coal mining in the northeast of the study area is smaller. The height of the WCFZ in the southeast of the study area is also smaller, but the upper boundary of the WCFZ in most positions are developed into aquifer I, resulting in a higher risk of roof water inrush. In conclusion, the analysis results of the 3D hydrogeological structure model of the WCFZ are consistent with the prediction results of the cracking safety zone obtained above. The model can well show the height of the WCFZ and its relationship with the overlying aquifer (aquiclude), which can provide a theoretical basis for the prevention and control of Coal Mine roof water damage.

7. Conclusions

This study established a new multiple regression prediction model for the height of the WCFZ proposed based on analyzing the measured data and influencing factors of the height of the WFCZ in the western Ordos Basin. It was used to predict the height of the WFCZ in Qingshuiying Coalfield, and the 3D hydrogeological structure model of the WFCZ was carried out. The main conclusions were as follows:

1. The optimal unitary function models of mining thickness and proportion coefficient of hard rock were unitary linear equations, with R^2 of 0.863 and 0.674, respectively. The optimal unitary function models of the working width were S-shaped curves with R^2 of 0.725. The optimal unitary function models of mining depth were logarithmic curves with R^2 of 0.939. The sensitivity of each factor to the height of the WCFZ was in this order: mining thickness > proportion coefficient of hard rock > working width > mining depth.
2. Based on the comprehensive consideration of five influencing factors: mining method, mining thickness, proportion coefficient of hard rock, working width, and mining depth, a multiple regression prediction model for the height of the WCFZ under fully mechanized caving in the western Ordos Basin area was established. The error of this model was basically controlled within 10%, which is much smaller than the traditional empirical equations.
3. The prediction model was applied to Qingshuiying Coalfield, and the height of the WCFZ was predicted based on borehole data. The distribution characteristics of the WCFZ height showed an increased trend from southeast to northwest in the study area, and the prediction zone of cracking safety was obtained by reference to the water-rich condition of the strata.
4. A 3D visualization model of the WCFZ was established in the study area to clearly show the spatial distribution law of the WCFZ and the spatial relationship between the WCFZ and the overlying aquifer (aquiclude). The visualization model has achieved the desired application effect and provided an advanced technology for the prevention and control of Coal Mine water.

Informed Consent Statement: Not applicable.

Data Availability Statement: Not applicable.

Conflicts of Interest: The authors declare no conflict of interest.

References

1. Wang, T.; Shao, L.Y.; Xia, Y.C.; Fu, X.H.; Sun, Y.Z.; Sun, Y.J.; Ju, Y.W.; Bi, Y.L.; Yu, J.C.; Xie, Z.Q.; et al. Major achievements and future research directions of the coal geology in China. *Geol. China* **2017**, *44*, 242–262. [CrossRef]
2. Guo, X.; Hu, Z.; Fu, S.; Dong, Y.; Jiang, G.; Li, Y. Experimental study of the remediation of acid mine drainage by Maifan stones combined with SRB. *PLoS ONE* **2022**, *7*, e0261823. [CrossRef] [PubMed]
3. Jiao, Y.Q.; Wang, S.M.; Fan, L.M.; Wu, L.Q.; Rong, H.; Zhang, F. Key elements and framework model of groundwater system in Jurassic coal measures of Ordos Basin. *J. China Coal Soc.* **2020**, *45*, 2411–2422. [CrossRef]
4. Gu, J.Y.; Zhang, X.Y. Sedimentary characteristics and sequence framework of intracontinental foreland Basin in the western China. *Acta Sedimentol. Sin.* **2005**, *23*, 187–193.
5. Li, P.Y. Mine water problems and solutions in China. *Mine Water Environ.* **2018**, *37*, 217–221. [CrossRef]
6. Liu, S.L.; Li, W.P.; Wang, Q.Q. Height of the Water-flowing fractured zone of the Jurassic coal seam in northwestern China. *Mine Water Environ.* **2018**, *37*, 312–321. [CrossRef]
7. Zhang, T.; Zhao, Y.X.; Gan, Q.; Nie, X.D.; Zhu, G.P.; Hu, Y. Investigations into mining-induced stress-fracture- seepage field coupling in a complex hydrogeology environment: A case study in the bulianta colliery. *Mine Water Environ.* **2019**, *38*, 632–642. [CrossRef]
8. Light, D.D.M.; Donovan, J.J. Mine-water flow between contigu-ous flooded underground coal mines with hydraulically compro- mised barriers. *Environ. Eng. Geosci.* **2015**, *21*, 147–164. [CrossRef]
9. Adams, R.; Younger, P.L. A strategy for modeling groundwater rebound in abandoned deep mine systems. *Groundwater* **2001**, *39*, 249–261. [CrossRef]
10. Booth, C.J. Strata-movement concepts and the hydrogeological impact of underground coal mining. *Groundwater* **1986**, *24*, 507–515. [CrossRef]
11. Miao, X.X.; Cui, X.M.; Wang, J.A.; Xu, J.L. The height of fractured water-conducting zone in undermined rock strata. *Eng. Geol.* **2011**, *120*, 32–39. [CrossRef]
12. Wang, H.L.; Jia, C.Y.; Yao, Z.K.; Zhang, G.B. Height measurement of the water-conducting fracture zone based on stress monitoring. *Arab. J. Geosci.* **2021**, *14*, 1392. [CrossRef]
13. Zhai, W.; Li, W.; Huang, Y.L.; Ouyang, S.Y.; Ma, K.; Li, J.M.; Gao, H.D.; Zhang, P. A Case Study of the Water Abundance Evaluation of Roof Aquifer Based on the Development Height of Water-Conducting Fracture Zone. *Energies* **2020**, *13*, 4095. [CrossRef]
14. Chen, Y.; Zhu, S.Y. Determination of caved and water-conducting fractured zones of "two soft and one hard" unstable coal seam. *Acta Geod. Geophys.* **2020**, *55*, 451–475. [CrossRef]
15. Guo, C.F.; Yang, Z.; Li, S.; Lou, J.F. Predicting the water-conducting fracture zone (WCFZ) height using an MPGA-SVR approach. *Sustainability* **2020**, *12*, 1809. [CrossRef]
16. Zhao, D.K.; Wu, Q. An approach to predict the height of fractured water-conducting zone of coal roof strata using random forest regression. *Sci. Rep.* **2018**, *8*, 10986. [CrossRef]
17. He, X.; Zhao, Y.X.; Zhang, C.; Han, P.H. A model to estimate the height of the water-conducting fracture zone for longwall panels in western China. *Mine Water Environ.* **2020**, *39*, 823–838. [CrossRef]
18. Xie, X.S.; Hou, E.K.; Wang, S.M.; Sun, X.Y.; Hou, P.F.; Wang, S.B.; Xie, Y.L.; Huang, Y.A. Formation mechanism and the height of the water-conducting fractured zone induced by middle deep coal seam mining in a sandy region: A case study from the Xiaobaodang coal mine. *Adv. Civ. Eng.* **2021**, *2021*, 6684202. [CrossRef]
19. Gusev, V.N.; Ilyukhin, D.A. Determination of water conducting fracture zone for mining and geological conditions of the Verkhnekamsk salt deposit. In Innovation-Based Development of the Mineral Resources Sector: Challenges and Prospects: Proceedings of the 11th Russian-German Raw Materials Conference, Potsdam, Germany, 7–8 November 2018; CRC Press: Boca Raton, FL, USA, 2018; pp. 195–204.
20. Li, X.B.; Li, Q.S.; Xu, X.H.; Zhao, Y.Q.; Li, P. Multiple influence factor sensitivity analysis and height prediction of water-conducting fracture zone. *Geofluids* **2021**, *2021*, 8825906. [CrossRef]
21. Liu, Y.; Liu, Q.M.; Li, W.P.; Li, T.; He, J.H. Height of water-conducting fractured zone in coal mining in the soil-rock composite structure overburdens. *Environ. Earth Sci.* **2019**, *78*, 242. [CrossRef]
22. Zhang, Y.; Cao, S.G.; Guo, S.; Wan, T.; Wang, J. Mechanisms of the development of water-conducting fracture zone in overlying strata during shortwall block backfill mining: A case study in Northwestern China. *Environ. Earth Sci.* **2018**, *77*, 543. [CrossRef]
23. Zhu, T.E.; Li, W.P.; Wang, Q.Q.; Hu, Y.B.; Fan, K.F.; Du, J.F. Study on the height of the mining-induced water-conducting fracture zone under the Q(2l) loess cover of the Jurassic coal seam in Northern Shaanxi, China. *Mine Water Environ.* **2020**, *39*, 57–67. [CrossRef]
24. Du, F.; Gao, R. Development patterns of fractured water-conducting zones in Longwall mining of thick coal seams-a case study on safe mining under the Zhuozhang River. *Energies* **2017**, *10*, 1856. [CrossRef]

25. Fan, H.; Wang, L.G.; Lu, Y.L.; Li, Z.L.; Li, W.S.; Wang, K. Height of water-conducting fractured zone in a coal seam overlain by thin bedrock and thick clay layer: A case study from the Sanyuan Coal Mine in North China. *Environ. Earth Sci.* **2020**, *79*, 125. [CrossRef]

26. Shi, L.Q.; Wu, H.B.; Li, Y.L.; Lv, W.K. Optimization model of PCA-GA-Elman for development height prediction of water-conducting fissure zone. *J. Henan Polytech. Univ.* **2021**, *40*, 10–18. [CrossRef]

27. Hu, X.J.; Li, W.P.; Cao, D.T.; Liu, M.C. Index of multiple factors and expected height of fully mechanized water flowing fractured zone. *J. China Coal Soc.* **2012**, *37*, 613–620. [CrossRef]

28. Aydin, H.; Bayram, A.; Esme, U.; Kazancoglu, Y.; Guven, O. Application of grey relation analysis (GRA) and taguchi method for the parametric optimization of friction stir welding (FSW) process. *Mater. Tehnol.* **2010**, *44*, 205–211.

29. Kim, G.Y.; Jong, Y.; Liu, S.F. Generalized hybrid grey relation method for multiple attribute mixed type decision making. *J. Grey Syst.* **2014**, *26*, 142–153.

30. Wakchaure, K.N.; Thakur, A.G.; Gadakh, V.; Kumar, A. Multi-Objective optimization of friction stir welding of aluminium alloy 6082-T6 using hybrid taguchi-grey relation analysis-ANN method. *Mater. Today Proc.* **2018**, *5*, 7150–7159. [CrossRef]

31. Xia, X.T.; Meng, F.N.A.; Lv, T.M. Grey relation method for calculation of embedding dimension and delay time in phase space reconstruction. *J. Grey Syst.* **2010**, *22*, 105–116.

32. Cui, Z.C.; Yang, Y.Z.; Gao, X.L.; Xiao, H.; Liu, H.C. Research and application of ecological river courses restoration technology. In Proceedings of the International Conference on Water Resource and Environment, Shanghai, China, 23–26 July 2016. [CrossRef]

33. Scannapieco, D.; Naddeo, V.; Zarra, T.; Belgiorno, V. River water quality assessment: A comparison of binary and fuzzy logic-based approaches. *Ecol. Eng.* **2012**, *47*, 132–140. [CrossRef]

34. Wang, W.C.; Xu, D.M.; Chau, K.W.; Lei, G.J. Assessment of river water quality based on theory of variable fuzzy sets and fuzzy binary comparison method. *Water Resour. Manag.* **2014**, *28*, 4183–4200. [CrossRef]

35. Liu, H. Research on Determination method of Index Weight in Comprehensive Evaluation. *J. Hebei Univ. Technol.* **1996**, *4*, 75–80.

36. State Bureau of Coal Industry. *Rules for Coal Pillar Reservation and Coal Pressure Mining in Buildings, Water Bodies, Railways and Main Shafts*; Coal Industry Press: Beijing, China, 2017.

37. Alessandro, S.; Paola, M.; Giuseppe, P.; Paolo, C.; Francesco, P.; Valentina, C.; Michele, S. The Integration of 3D Modeling and Simulation to Determine the Energy Potential of Low-Temperature Geothermal Systems in the Pisa (Italy) Sedimentary Plain. *Energies* **2018**, *11*, 1591. [CrossRef]

38. Zhang, L.Q.; Dong, D.L.; Zhang, F.; Xu, Z.C. A novel three-dimensional mine area hydrogeological model based on groundwater modeling systems. *J. Coast. Res.* **2020**, *105*, 141–146. [CrossRef]

39. Du, B. Model investigation for groundwater aquifer structure in a mining area based on groundwater modeling system (GMS). *Coal Geol. China* **2020**, *32*, 27–32. [CrossRef]

Article

Prediction of the Height of Water-Conductive Fractured Zone under Continuous Extraction and Partial Backfill Mining Method—A Case Study

Yujun Xu [1], Liqiang Ma [1,2,*], Ichhuy NGO [1] and Jiangtao Zhai [1]

[1] Key Laboratory of Deep Coal Resources Mining, China University of Mining and Technology, Ministry of Education, Xuzhou 221116, China; xyj@cumt.edu.cn (Y.X.); ngoichhuy@cumt.edu.cn (I.N.); tb21020005b3ld@cumt.edu.cn (J.Z.)

[2] School of Energy, Xi'an University of Science and Technology, Xi'an 710054, China

* Correspondence: tb20020008b1@cumt.edu.cn; Tel.: +86-1981-6252-755

Abstract: Longwall backfill mining effectively mitigates the height of water-conductive fractured zone (HWCFZ), preventing it from reaching the overlying aquifer and thus preserving the groundwater. However, it has the disadvantages of insufficient filling time and space as well as the mutual constraints between filling and mining. A novel continuous extraction and partial backfill (CEPB) water-preserving mining method was therefore proposed. The analytic hierarchy process (AHP) method was employed to identify the factors affecting the HWCFZ of CEPB, and five main factors, namely, the hard-rock lithology ratio, mining height and depth, and the width of the Wongawilli and protective block, were determined based on the weight distribution. UDEC software was used to establish a numerical model to simulate the HWCFZ under five factors. By using a multiple linear regression analysis of the numerical simulation results, a model for predicting the HWCFZ was established. It was applied in a colliery of the Yu-Shen mining area, and the HWCFZ was 57.7 m, 9% higher than that of borehole television logging of 53.1 m from the field measurement, indicating its rationality. Subsequently, the model was generalized and applied to the whole mining area, and the thematic map of the HWCFZ and the protective zone thickness of CEPB and longwall caving mining were obtained. The criterion for water-preserving mining based on the equivalent permeability coefficient of the protective zone is then proposed, which can provide guidance for the mining parameters optimization of the CEPB.

Keywords: continuous extraction and partial backfill (CEPB); analytic hierarchy process (AHP); height of water-conductive fractured zone (HWCFZ); thickness of protective zone; criterion for water-preserving coal mining

1. Introduction

Because the coal resources in eastern regions are on the verge of depletion, the focus of coal extraction has gradually shifted to the ecologically fragile mining areas in Northwest China [1–3]. The coal reserves in northwest regions make up nearly 70% of the country's total, while the water resources are scarce, accounting for only 3.9% of the country's total. Large-scale and high-intensity mining activities have resulted in severe migration and breakage of overburden and the development and propagation of water-conductive fractures. When it reaches the overlying aquifer, a series of ecological environment degradation problems such as water-table lowering, vegetation withering, and land desertification will occur [4–7]. Discerning how to predict the HWCFZ accurately and realize the coordinated development of coal resources exploitation and water resources preservation presents an urgent problem to be solved [8,9].

Several water-preserving mining methods have been put into implementation to lower the HWCF and block water-diversion channels, such as longwall backfill mining,

strip mining, room and pillar mining, curtain grouting, and overburden bed-separation grouting [10–14]. The first one is currently the most effective mining method to control overburden movement and fractures development [15]. However, it is confronted with insufficient filling time and filling space as well as the mutual restrictions between extraction and backfill. The roof of the mined-out area subsides and collapses quickly with the coal body being extracted, while it takes a long time for the backfill to reach the designed strength. Hence, the roof cannot be supported in time, and the overburden migration and the fractures development are inevitable, bring difficulty to safe and high-efficiency coal extraction beneath the underground aquifer. In addition, there are mutual constraints between mining and filling processes. In other words, the filling speed affects the process of coal extraction, while the mining equipment maintenance delays the filling process [16–18]. It is arduous for them to operate in parallel. Therefore, some authors have put forward a novel continuous extraction and continuous backfill mining method [19,20]. It features a multi-roadway layout as well as parallel operation between extraction and backfill. The method uses roadway skip mining and filling to ensure that there are always coal bodies or filling bodies to support the roof at any moment, contributing to the mitigation of the migration and breakage of the overlying layers and thereby the HWCFZ, and is therefore an effective way to realize coal extraction under water bodies [21,22].

However, during the process of generalizing and applying the mining method in Northwest China, we found that if the distance between the coal seam and the overlying aquifer is great enough, with a relatively thick water-resisting layer between them, the CEPB may also maintain the stability of the hard and thick layer (key stratum) beneath the aquiclude despite the bed separation between the key stratum and its underlying layer occurring. Under this circumstance, the fractures stop developing upward at the key stratum, and the overlying aquifuge can maintain integrity and water-resisting capability [23]. In other words, under certain geological conditions, the CEPB can not only effectively constrain the HWCFZ and realize water-preserving coal mining but also ameliorate the problems of scarce filling materials and high filling cost to a certain extent [24]. However, the mining-induced disturbance and overburden migration intensifies with the decreasing filling rate, and the probability of overburden failure and instability increases, which will also promote the development of the water-diversion fractures. If the water-flowing fractures develop to the overlying aquifer, it will not only lead to water resources loss, but also may trigger mine water inrush disaster. Hence, it is crucial to accurately predict the HWCFZ under various engineering and hydrogeological conditions as well as different mining parameters of CEPB, so as to realize water-preserving coal mining in the dual sense of ecology and economy.

In-depth research on the WCFZ and water-preserving coal mining has been conducted at home and abroad. Although foreign experts have not defined the concept of water-preserving mining systematically, they have done large amounts of work on coal extraction under water bodies and argued that the surface and groundwater should be regarded as environmental constraints of longwall coal mining [25–27]. Water environments and the hydrologic effects induced by coal extraction have been investigated and assessed in various foreign collieries [28–33]. Research on sustainable development and management of groundwater resources for water-preserving mining is also popular among coal mines abroad [34,35]. In addition, they have divided the overburden into the caved zone, the interconnected fractured zone, the unconnected fractured zone, the micro-fracture zone, and the fracture-free zone. The combined range of the caved zone and the interconnected fractured zone is named WCFZ, where water can percolate and flow through from the overlying aquifer to the gob [36,37]. They have also illustrated the characteristics of WCFZ from the perspectives of permeability, water flow, and the height of destressed zone [38,39].

Domestic experts have studied the developing mechanism of water-flowing fractures and water-preserving coal mining by means of analogue simulation, mechanical modeling, and mathematical method. Fan Limin put forward the concept of water-conservation coal mining and believed that the groundwater level can be preserved by mitigating the mining

disturbance of overburden and lowering the HWCFZ. If the sufficient thickness of the protective zone between the overlying water bodies and WCFZ can be guaranteed, the groundwater can be blocked and prevented from penetrating into the gob [40,41]. Liu Shiliang et al. studied the HWCFZ in shallow and deep coal seams by means of multiple regression analysis, GIS, and borehole television logging [42–49]. Huang Qingxiang put forward the concepts of upward and downward fracture and studied the formation, distribution, and evolution of fractures [50,51]. Miao Xiexing et al. investigated the HWCFZ in extremely thick coal seams from the perspectives of key stratum, arch structure, overburden lithology, and soil–rock composite structure [52–57]. Zhang Jixiong et al. studied the relationships among the HWCFZ, the filling rate, and the mining height under longwall solid backfill mining and proposed a formula for estimating the HWCFZ [58–60]. Guo Wenbing analyzed the failure transmission process of overburden in high-intensity mining and established a mechanical model of unsupported rock and cantilever rock for predicting the HWCFZ [61]. Wu Qiang et al. obtained the prediction formula of the HWCFZ with due regard to different mining parameters, including the inclination, mining height, the buried depth of coal seam, the length and advancing length of working face, as well as the overburden lithology [62,63]. Wang Fangtian and Xu Zhimin studied the development law of mining-induced water-conductive fractures under gullies and reservoirs, respectively [64,65]. Zhang Yun and Deng Xuejie studied the development mechanism of WCFZ under the conditions of shortwall block mining and upward slicing longwall-roadway cemented backfill mining by using UDEC software and mechanical analysis, respectively [66–68]. Hou enke proposed a predicting formula for WCFZ based on genetic-algorithm support-vector-machine method [69]. Lian analyzed the main geological and mining factors affecting the development of ground cracks [70].

The above research has laid a solid foundation and enriched the framework for the investigation of HWCFZ. However, the research object is the HWCFZ in longwall working face, and the prediction of the HWCFZ of CEPB mining method has not been reported. There are many factors affecting the HWCFZ of CEPB. To establish an estimation model for the HWCFZ under the influence of multiple factors, the main controlling factors must be determined, and the minor factors should be laid aside. The comprehensive evaluation methods, including the AHP, Delphi method, weighted averages, fuzzy comprehensive evaluation, principal component analysis, and BP neural network method, are the most commonly employed methods to tackle complex problems affected by various indicators [15,71].

The AHP is widely employed to conduct multi-criteria decision analyses and thus evaluate the groundwater potentiality in low desert lands and semi-arid regions [72,73]. The AHP is usually used by combining other methods such as GIS, frequency ratio, and certainty factor models to plot the zoning map of groundwater probability index [74–77]. It is also of great significance to identify the potential groundwater recharge sites [78]. AHP combined with geospatial techniques can be employed to delineate the potential zones of groundwater [79]. Moreover, it can be utilized to assess the impact of hydro-geological environment on availability of groundwater [80]. On top of being used to evaluate the hydrochemical characteristics and water quality of groundwater [81], AHP can also be employed to assess the development of macro- and micro-cracks and fractures under different conditions by combining it with other research methods [82]. For instance, it can be used to predict the ground fracturing and compound-mode crack propagation law of the roadway under impact loading [83–85]. Furthermore, water-conductive fractures of overlying strata are induced by the fact that the deformation and stress of the stratum exceed its critical values. AHP can also be utilized to assess the mining-induced stress field and the movement of overburden, so as to better study the water-conducting fracture [86–89].

In this paper, AHP will be employed to construct a triple-level model to identify the factors affecting the HWCFZ of CEPB and obtain the main controlling factors. The influencing mechanisms of hard-rock lithology ratio, mining height and buried depth of coal seam, and the width of Wongawilli block and protective block on the HWCFZ will be illustrated

by utilizing UDEC numerical simulation software. A prediction model of the HWCFZ of CEPB will be then established by using multiple regression analysis of the numerical results. Subsequently, the model will be generalized and applied in the whole Yu-Shen mining area after its rationality and validity is verified by field measurement. The thematic map of the HWCFZ and the thickness of protective zone will be obtained. Moreover, based on the equivalent permeability coefficient of the protective zone, a criterion for water-preserving mining will be proposed. The research results can provide theoretical basis and guidance for the layout of working face and the optimization of mining parameters of CEPB, which is conducive to realizing water-preserving coal mining on the premise of economic maximization.

2. CEPB Water-Preserving Coal Mining Method

The CEPB water-conservation mining method is proposed by combining the advantages of Wongawilli fast mining and roadway skip mining. The three-dimensional conceptual diagram is shown in Figure 1. Taking the protective block with three mining phases as an example, the specific mining process of CEPB is illustrated in Figure 2.
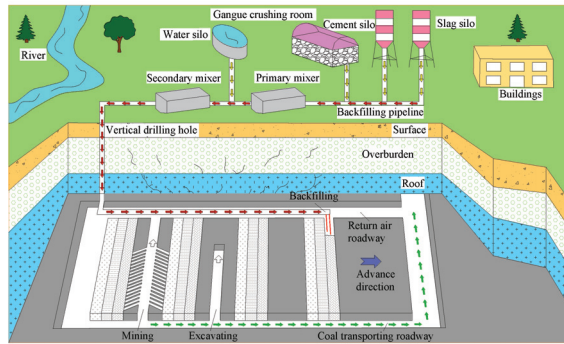
Figure 1. The three-dimensional overview of CEPB water-conservation coal mining method.
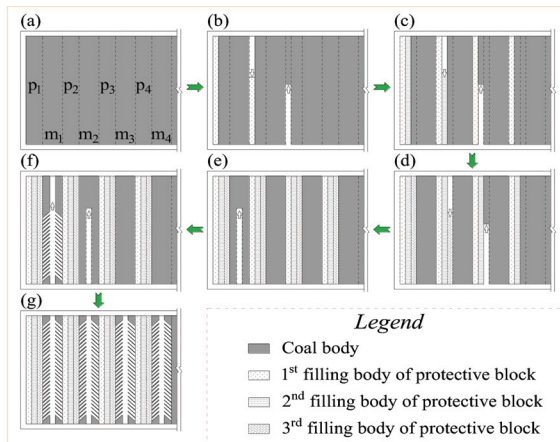
Figure 2. The sketch map of the extracting and filling process of CEPB mining. (**a**) Layout of the mining and protective block. (**b**) The MR in the first mining phase of protective block is being excavated. (**c**) The MR in the second mining phase of protective block is being excavated. (**d**) The MR in the third mining phase of protective block is being excavated. (**e**) The MR of Wongawilli block is being excavated. (**f**) The chamber of the Wongawilli block is being extracted. (**g**) All Wongawilli block is extracted.

Prior to coal extraction and filling, the entire mining panel is firstly divided into several mutually spaced protective blocks (P_1, P_2, P_3, ... , P_n) and Wongawilli mining blocks (m_1, m_2, m_3, ... , m_n) along the strike direction. As shown in Figure 2b,d, in order to overcome the problems of mutual restrictions and achieve parallel operations between extraction and backfill, the mining roadways (MRs) in the protective block are extracted and backfilled at intervals. The MR is filled immediately once it is extracted, and the MR in the next protective block is mined at the same time, forming a parallel operation mode of mining and filling. After all coal bodies in the MRs of the first stage are replaced with filling bodies, the MRs in the second phase will be extracted and backfilled. Coal extraction of the Wongawilli mining block is then carried out after all coal bodies in the protective block are replaced with filling bodies, as shown in Figure 2e,g. It is worth noting that the Wongawilli block is only extracted without being backfilled. At the moment, the filling body of the protective block that has reached the design strength acts as the isolation coal pillar to support the roof and constrain the migration of the overlying layers. Bolt support, which is indispensable for the MRs of the protective block, is unnecessary for the chambers of the Wongawilli block. Therefore, the width of the protective block is usually narrower than that of Wongawilli block, since the support process will delay the mining progress and lower the mining efficiency.

The coal-extracting technology and the equipment for CEPB are illustrated in Figure 3. As Figure 3a shows, coal mining and loading of the Wongawilli and protective block are completed by the continuous mining machine, and then the coal is transported to the continuous conveyor using shuttle car by intermittent transportation. After that, the coal body is shifted to the shaft station by scraper conveyor. Additionally, the bolt installation of roof of the MR in the Wongawilli and protective block is completed by hydraulic drill. The sealing of MRs in the protection block, the layout of filling pipeline, and the filling effect of MR are shown in Figure 3b. The equipment employed for the coal extraction of Wongawilli mining block is the same as that for the protection block, as illustrated in Figure 3c.

(a)

(b)

(c)
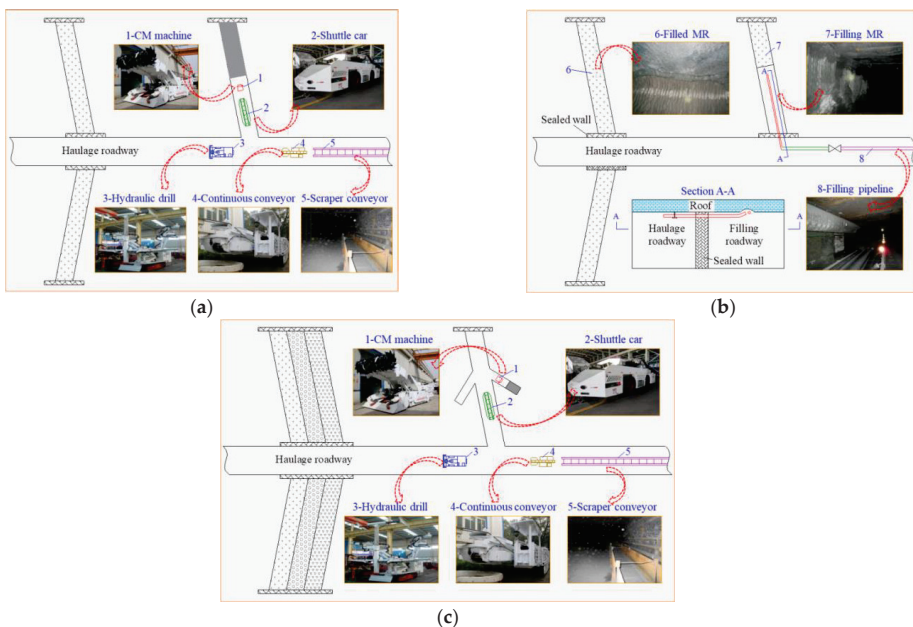
Figure 3. The schematic diagram of the extracting and backfilling process and the corresponding equipment for CEPB mining method. (**a**) The mining process of the protective block. (**b**) The filling process of the protective block. (**c**) The mining process of the Wongawilli block.

3. Factors Identification and Weights Determination of the HWCFZ of CEPB

3.1. Identification of the Influencing Indicators

The AHP method establishes the judgment matrix by comparing the relative importance of two indexes and then obtains the weights distribution by calculating the maximum eigenvalue and corresponding eigenvector of the judgment matrix. It combines qualitative and quantitative analysis methods and can identify the main controlling factors from many complicated indicators on the basis of the weights distribution [4]. The influential factors of HWCFZ of CEPB are complex and hierarchical, reaching a good agreement with the features of AHP capable of resolving many multi-leveled problems. Therefore, they were employed to construct a triple-leveled model so as to identify the indicators affecting the HWCFZ and discern their degrees of importance. In the AHP model, 3 factors were selected as secondary indicators, i.e., overburden system, mining system, and backfill system. Meanwhile, 10 indexes, namely, hard-rock lithology ratio, the thickness and the buried depth of coal seam, the width of the Wongawilli and protective block, and the compression amount of the backfill, were chosen as tertiary factors, as illustrated in Figure 4 [90,91].
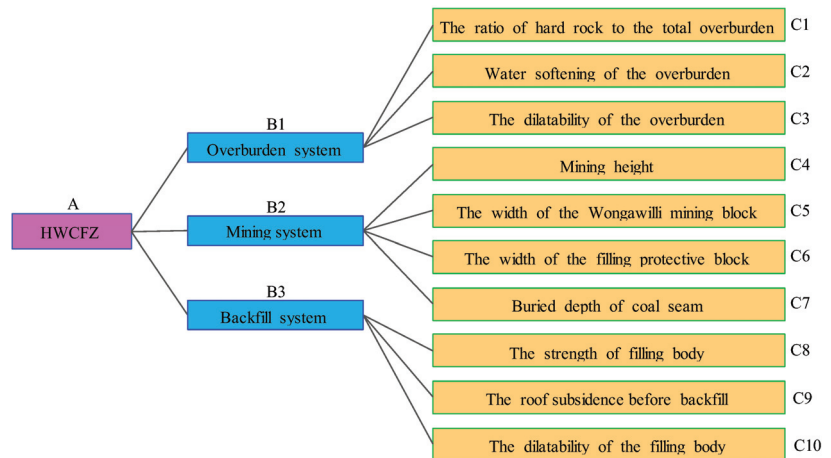
Figure 4. The triple-leveled model of HWCFZ of CEPB mining method.

(1) Overlying strata system

The overburden lithology exerts significant impact on the development of water-diversion fractures. For the overlying stratum with hard-rock lithology, the sudden overburden migration is prone to causing the development and propagation of cracks in a wide range, since it is brittle and tends to be broken easily. By contrast, the soft rock formation is liable to sink as a whole with the advance of mining, which is conducive to the compaction and closure of the fractures and thereby lowering the HWCFZ.

The estimation of HWCFZ using empirical formulas from the current norms needs to classify the overburden rocks into hard, medium-hard, weak, and extremely weak ahead of time based on uniaxial compressive strength, which is complex and cannot reflect the stratigraphic structure. Hence, the hard-rock lithology ratio R_h proposed by Hu Xiaojuan was modified to represent them [63]. In this paper, the R_h is defined as the ratio of the thickness of the hard-rock strata to the overburden's total. Hard rock refers to fine sandstone, medium sandstone, coarse sandstone, migmatite, igneous rock, etc.

$$R_h = \sum_{i=0}^{i=m} h_i / H \tag{1}$$

In this equation, H is the total thickness of the overburden, m; h_i is the thickness of the ith overlying layer, m; m is the number of the hard rock.

Note that R_h ranges from 0 to 1. $R_h = 0$ suggests that the overburden lithology is extremely soft, while $R_h = 1$ indicates extremely stiff overlying strata. The index R_h can be calculated and determined by borehole histogram.

Additionally, when water-softened rocks are soaked by water, their strength becomes lower and the plastic strain property is enhanced and tends to argillization, giving rise to fracture closure and the improvement of capability of resisting water seepage. Furthermore, the argillized and fragmented particles of soft rocks are inclined to migrate with the water flow, which is advantageous to blocking the water-conducted channel generated by the underlying strata and prevent the water-flowing fractures from developing upward. On the other hand, the soft rock formation with good dilatability expands significantly when encountering water, and it is beneficial to the re-closing of the fractures. Hence, although mining-induced water-diversion fractures go through the entire stratum, it may become unconnected and non-penetrating due to dilatability.

(2) Coal mining system

Mining height is one of the most crucial factors affecting the development of HWCFZ of CEPB. A higher mining height denotes a greater degree of mining-induced disturbance of the overlying layers and thereby a higher HWCFZ. Moreover, the breakage of basic roof and the degree to which water-conducted fractures develop depends directly on the width of the Wongawilli block, and it is therefore an indispensable indicator for estimating the HWCFZ. The large span of the Wongawilli block is prone to causing the maximum stress or deformation of a basic roof by exceeding its ultimate values, contributing to overburden breakage and the growth of HWCFZ. Furthermore, the protective block is divided into several MRs, and the mining-induced disturbance of overlying layers from each MR is small due to its limit span. The greater the number of MRs is, the smaller the overburden loading shared by the filling body in the protective block, which is more conducive to mitigating the overburden movement and the propagation of water-diversion fractures. As a result, the span of the protective block is also a vital indicator that should be taken into consideration during the investigation of HWCFZ. In addition, the MRs in the protective block need anchoring support, while it is unnecessary for the chambers in the Wongawilli block to be bolted. Therefore, in order to improve the mining efficiency and lower the mining costs, the span of the protection block is generally much smaller than that of the Wongawilli block. Moreover, it is universally acknowledged that the root cause of the fractures' emergence may be the maximum stress on the rock stratum being greater than its ultimate stress due to stress concentration of the in situ stress. The original rock stress increases with the increasing buried depth, giving rise to the increasing stress grade of the overlying strata. Therefore, the mining depth also makes a significant difference to the development of the HWCFZ.

(3) Backfill system

The final height of protective block is of great significance for ameliorating roof movement and thereby fractures' development. The filling body of MRs in different mining phases of the protection block gradually bears the loading and deforming. The ultimate height refers to the mining height minus the final compaction of the filling body and plus the swelling rate of the backfill. As a result, it is primarily affected by the strength of the filling body, the roof subsidence after extraction and before backfill, and the expansion rate of the backfill.

3.2. Weights Distribution

Experts and scholars engaged in water-preserving coal mining method and HWCFZ prediction were invited to assign the weight of each factor based on a scale of 1–9 and the reciprocal scaling method proposed by Thomas. L. Saaty [4]. The following judgment matrixes were constructed according to the feedback given by the experts:

$$W_{A\sim B} = \begin{bmatrix} 1 & 1/4 & 2 \\ 4 & 1 & 8 \\ 1/2 & 1/8 & 1 \end{bmatrix} W_{B_1\sim C} = \begin{bmatrix} 1 & 2 & 4 \\ 1/2 & 1 & 2 \\ 1/4 & 1/2 & 1 \end{bmatrix} W_{B_2\sim C} = \begin{bmatrix} 1 & 2 & 4 \\ 1/2 & 1 & 2 \\ 1/4 & 1/2 & 1 \end{bmatrix} W_{B_3\sim C} = \begin{bmatrix} 1 & 2 & 3 \\ 1/2 & 1 & 3/2 \\ 1/3 & 2/3 & 1 \end{bmatrix}$$

Taking an overlying strata system whose matrix is $W_{B_1\sim C}$ as an example, its maximum eigenvalue was calculated to be 3.0000, and the corresponding eigenvector was W = [0.5714, 0.2857, 0.1429]. Then, the consistency test was conducted by using Equations (2) and (3):

$$C.I. = (\lambda_{max} - n)/(n - 1) \tag{2}$$

where *C.I.* refers to the consistency index; λ_{max} refers to the largest eigenvalue; *n* refers to the number of elements in the matrix $W_{B_1\sim C}$.

$$C.R. = (C.I.)/(R.I.) \tag{3}$$

In this equation, *C.R.* is the consistency ratio; *R.I.* is the average consistency index.

The relative weights of elements in the matrix should be redistributed under the condition of $C.R. \geq 0.1$. Otherwise, the weights distribution was acceptable. The *C.R.* of the matrix $W_{B_1\sim C}$ was 0, which is much less than 0.1, indicating the relative weights assigned by the experts were reasonable and scientific.

The weight of the overlying strata is 0.1818. Therefore, the weights of the three third-level indicators included in the overlying strata system are 0.1039, 0.0519, and 0.0259, respectively. The consistency tests of the other matrixes were conducted in the same way, and the final calculation results are listed in Table 1. After finishing the consistency test, the weights distribution of all the influencing factors was obtained, as shown in Table 2.

Table 1. Results of consistency test of the experts' scores.

Matrix	Sort Vector	λ_{max}	C.I.	R.I.	C.R.
A~B	[0.1818, 0.7273, 0.0909]	3.0000	0	0.52	0
B_1~C	[0.5714, 0.2857, 0.1429]	3.0000	0	0.52	0
B_2~C	[0.4285, 0.2142, 0.2142, 0.1432]	4.0025	0.0025	0.89	0.0028
B_3~C	[0.5455, 0.2727, 0.1818]	3.0000	0	0.52	0

Table 2. Weights distribution of various factors affecting the HWCFZ while using CEPB.

Weights of Layer B	Weights of Layer C
Overlying strata B1 0.1818	The ratio of the hard rock to the total overburden C1 0.1039
	Water softening of the overburden C2 0.0519
	The dilatability of the overburden C3 0.0259
Mining parameters B2 0.7273	Mining height C4 0.3112
	The width of the mining block C5 0.1558
	The width of the protective block C6 0.1041
	Mining depth C7 0.1562

Table 2. *Cont.*

Weights of Layer B	Weights of Layer C
	The strength of filling body C8 0.0496
Filling body B3 0.0909	The compression of C9 0.0248
	The dilation of the filling body C10 0.0165
Total weights of layer B 1.0000	Total weights of layer C 1.0000

4. Prediction Model of the HWCFZ While Using CEPB Mining

4.1. Construction of Numerical Calculation Model of the HWCFZ

Universal Discrete Element Program (UDEC), a software program for discrete element modeling, is widely utilized to simulate the behavior of discontinuous media such as fractures or jointed rock masses. Therefore, it was employed to establish a numerical calculation model to simulate the evolution law and distribution characteristics of WCFZ of CEPB under different mining and filling schemes, as shown in Figure 5.

Lithology	Thickness
Sandstone	12m
Clay	6m
Stony loess	10m
Mudstone	18m
Sandy mudstone	6m
Sandstone	10m
Fine sandstone	8m
Mudstone	6m
Coarse sandstone	8m
Siltstone	4m
Sandy mudstone	5m
Coal seam	4m
Fine sandstone	10m

Figure 5. Numerical model to simulate the HWCFZ of the CEPB mining method.

Based on the drilling data of a colliery in Yu-Shen mining area, the overlying layers with similar lithology were merged, and 13 strata were determined from bottom to top. With due consideration of the boundary effect and full mining, the dimensions of the numerical simulation model were designed to be 300 m × 107 m (X × Y). The length of the CEPB mining panel was 120 m, with 90 m coal pillars left unmined on each side of the working face. The left and right sides of the model were fixed in the X direction, and the bottom boundary was fixed in the Y direction. The Mohr-Coulomb model was selected for the coal seam and its underlying and overlying strata, while the double-yield model was employed for the gangue backfill. The mechanical parameters of each stratum were calibrated in 3 steps. Firstly, preliminary assignment was conducted according to the existing mechanical parameters of strata. Subsequently, the stress–strain curves obtained from the laboratory tests of uniaxial compressive strength and numerical simulations of rock specimens of various strata, as well as the failure modes of the specimens in the laboratory tests and the plastic zone distribution of the numerical simulation, were compared. Thirdly, the parameters of the specimen of each stratum were reassigned and optimized repeatedly until the results from indoor test and numerical calculation reached good agreement. The mechanical parameters of the strata are shown in Tables 3 and 4.

Table 3. The physical and mechanical parameters of stratum (block).

No.	Stratum	Density (kg/m³)	Bulk Modulus (GPa)	Shear Modulus (GPa)	Friction Angle (°)	Cohesion (MPa)	Tensile Strength (MPa)
1	Clay	1900	0.28	0.09	25	2.0	0.9
2	Mudstone	2200	13.5	11.7	23	1.3	1.0
3	Sandy mudstone	2260	12.3	10.5	22	1.5	1.3
4	Sandstone	2520	12.2	10.8	42	2.5	3.6
5	Fine sandstone	2540	21.1	13.5	42	3.2	1.3
6	Coarse sandstone	2600	15.3	8.3	31	2.4	1.6
7	Siltstone	2510	10.8	8.1	38	2.8	1.8
8	Coal seam	1400	2.5	1.7	28	1.7	1.5

Table 4. The physical and mechanical parameters of stratum (contact).

No.	Stratum	Normal Stiffness (GPa)	Shear Stiffness (GPa)	Cohesion (MPa)	Friction Angle (°)	Tensile Strength (MPa)
1	Clay	3	2	2	18	1.0
2	Mudstone	9	7	2	10	1.8
3	Sandy mudstone	6	4	4	10	3.2
4	Sandstone	7	5	8	14	5.7
5	Fine sandstone	8	6	6	13	6.3
6	Coarse sandstone	6	5	5	25	5.4
7	Siltstone	10	8	7	20	4.3
8	Coal seam	4	2	3	15	1.2

During the simulation process, the height of overburden remains unchanged. For different mining heights, the mining height ascends by appropriately reducing the thickness of floor. The increase in coal seam buried depth is obtained by compensating for the initial stress at the top of the numerical model. According to the in situ stress gradient, the in situ stress grows by 0.25 MPa for every 100 m lower.

The hard-rock lithology ratio is obtained by changing the mechanical parameters of blocks and joints of the overlying layers. The "crack" code was used to set virtual vertical joints every 5 m in the coal seam, and then the "zone model null" code was utilized to extract the coal body in the MR of the protective block. The "zone model dy" code was immediately employed to simulate the strain-hardening property of the gangue backfill of the MR after extraction. The cap pressure and other parameters of the double-yield model are calibrated by the universally acknowledged Terzaghi's model [71].

$$\sigma = \frac{E_0}{\alpha}(e^{\alpha\varepsilon} - 1) \qquad (4)$$

In this equation, E_0 is the initial elastic modulus of the solid backfill, and σ and ε are the stress and strain of the gangue backfill, respectively; α is a dimensionless constant.

Note that coal extraction and the previously mined-out area's backfill are carried out simultaneously during the simulation process. The extracting and filling time and the roof subsidence after excavation and before backfill are not taken into account.

4.2. Distribution Characteristics of the Water-Diversion Fractures

Based on the five main controlling indicators affecting the HWCFZ of CEPB, the HWCFZ was simulated under various mining heights, mining depths, hard-rock lithology ratios, and the width of the Wongawilli and protective block. The orthogonal simulation schemes were listed in Table 5.

Table 5. The orthogonal schemes for simulating the HWCFZ of CEPB mining.

No.	Mining Height	Buried Depth	The Hard-Rock Lithology Ratio	The Width of the Wongawilli Block	The Width of the Protective Block
1	2.0/3.0/4.0/5.0/5.5	300	0.4	45	15
2	3.0	100/200/300/400/500	0.4	45	15
3	3.0	300	0.2/0.4/0.6/0.8/1.0	45	15
4	3.0	300	0.4	15/30/45/60/75	15
5	3.0	300	0.4	45	5/10/15/20/25

The developing mechanism of the water-flowing fractures of CEPB mining is essentially different from that of longwall mining, since their working face layout and mining process are totally distinct. Furthermore, since the filling bodies in various mining phases of the protective block bear the load gradually and are compressed asynchronously, the support role that the protective block plays also differs from that of the protective pillars in strip mining and room and pillar mining [11,12]. A scheme from Table 5 provides an example to illustrate the development and distribution characteristics of water-diversion fractures under CEPB mining. The concrete mining and filling parameters are as follows: the width of the Wongawilli block and protective block are 25 and 15 m, respectively; the hard-rock lithology ratio is 0.4; the mining height and depth is 4.0 and 100 m, respectively. The numerical simulation results for the WCFZ of CEPB are shown in Figure 6.
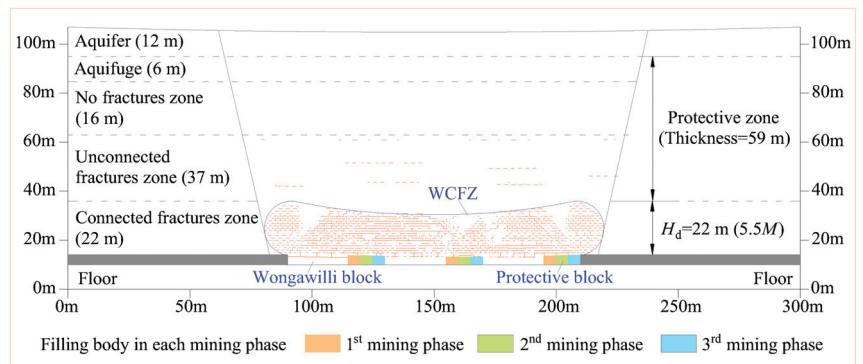
Figure 6. Numerical simulation results of WCFZ distribution while using CEPB mining.

Based on the analysis illustrated in Figure 6, from bottom to top, the whole overlying strata system can be divided into several zones according to the degree of fractures development, i.e., the connected fractures zone (22 m), the unconnected fractures zone (37 m), and the no-fracture zone (16 m). During the process of numerical simulation, two codes were used, "plot open red" and "plot slip red". The first code aims to plot the two types of open fractures. The first kind consists of open fractures that occur in the interface between two adjacent overlying layers, owing to the vertical displacement of the lower stratum exceeding the upper one. These sorts of fracture are what are called bed-separation fractures. The second sort consists of open fractures that emerge inside each stratum, due primarily to the tensile stress of interior joints being greater than their ultimate stress. Furthermore, as the word "slip" indicates, the aim of the second code is to plot the internal slip fractures or joints in each rock formation, owing mainly to the shear stress being greater than its shear strength. Moreover, it is interesting that the open fractures are usually in horizontal direction, while the slip fractures are prone to developing in the perpendicular direction. The connected fractures zone refers to the section where the transverse and vertical fractures intersect or, even if there is no intersection and merging, are extremely close to each other. Therefore, the interconnected fractures zone makes it

feasible for overlying water bodies to flow through, which is similar to the function of the WCFZ. Under this circumstance, the HWCFZ of CEPB can be defined as the thickness of the connected fractures zone. Hence, the HWCFZ of CEPB is 22 m, 5.5 times the mining height. Moreover, the distance between the overlying aquifer and the top boundary of WCFZ, which is known as a protective zone, makes a crucial difference to water-preserving coal mining. It can be seen that the protective zone, with thickness being 59 m (15 *M*), includes the aquifuge, the integral strata, and the strata with unconnected fractures.

4.3. Regression Analysis of Single Factors Affecting the HWCFZ

(1)   The HWCFZ corresponding to various mining heights (*M*)

Figure 7 shows the variation of the HWCFZ with various mining heights. The HWCFZ increases linearly with the growing mining height. The HWCFZ corresponding to the 2.0 m mining height is 30 m, while it ascends to 50 m at 5.5 m mining height, indicating that the rising mining height will further contribute to the development of water-diversion fractures.
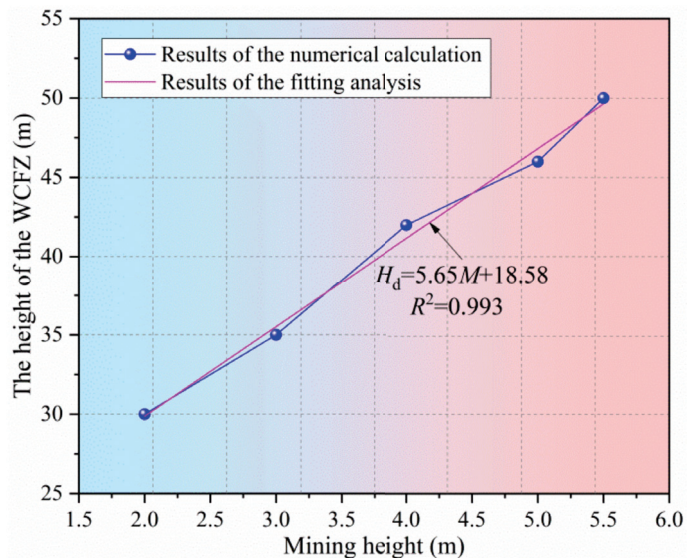
Figure 7. The relationship between the HWCFZ and various mining heights.

(2)   The HWCFZ corresponding to different mining depths (*H*)

The relationship between the HWCFZ and the burial depth of the coal seam is illustrated in Figure 8. The HWCFZ rises approximately linearly with the increasing mining depth, but the growth rate is limited and restricted. When the mining depth is 100 m, the HWCFZ is 33 m, and it only develops to 38 m with the mining depth rising to 500 m. This suggests that the increase in buried depth will promote the development of WCFZ, while the influence exerted on the HWCFZ is minor. The main reason for this is that the deep buried depth with high in situ stress is liable to result in horizontal unloading of the stratum, contributing to the propagation of fractures. In contrast, the horizontal unloading occurs in a small range, and its influence on the cracks propagation is thus restrained.
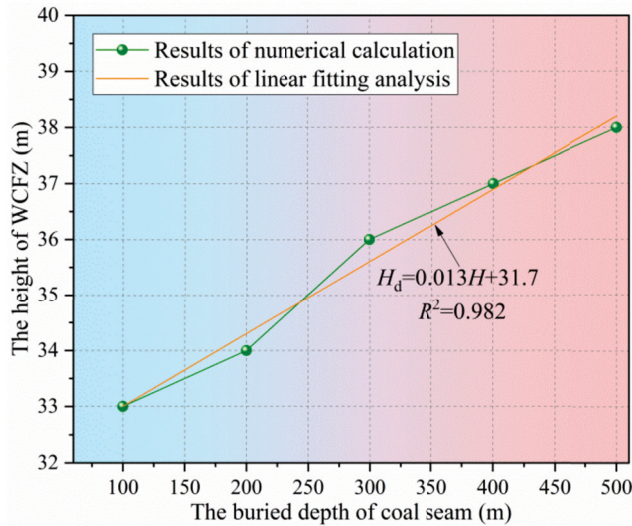
Figure 8. The relationship between the HWCFZ and different buried depths.

(3)   The HWCFZ corresponding to various hard-rock lithology ratios (R_h)

The variation in the HWCFZ with the hard-rock lithology ratio R_h is shown in Figure 9. The HWCFZ grows linearly with the increasing R_h. The HWCFZ rises from 32 m to 46 m, with the R_h varying from 0.2 to 1.0. This indicates that with the R_h rising, vertical and horizontal fractures are inclined to be generated under the joint actions of tensile and shear, contributing to the development of cracks.
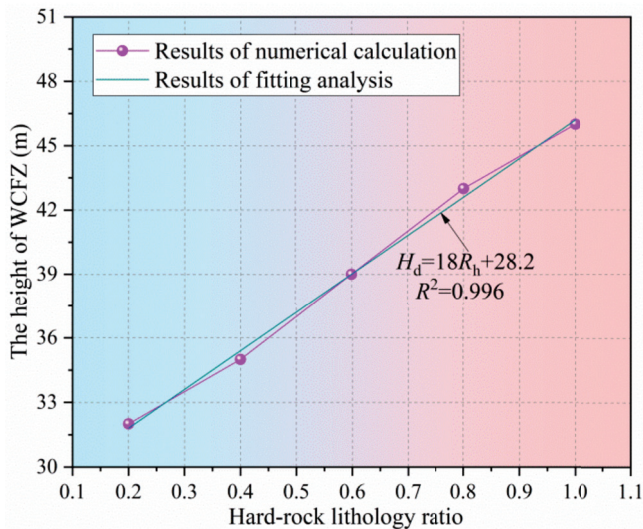
Figure 9. The relationship between the HWCFZ and various hard-rock lithology ratios.

(4)   The HWCFZ corresponding to different widths of Wongawilli block (w_m)

The relationship between the HWCFZ and the width of the Wongawilli block is shown in Figure 10. The HWCFZ rises with the increase in the span of the Wongawilli block w_m, but the growth rate tapers off until reaching a constant. It is obvious that the relation curve between the HWCFZ and w_m is nearly a logarithmic function. The HWCFZ ascends sharply

when the w_m ranges from 15 to 30 m, and subsequently, the rising rate slows down when it varies from 30 to 75 m. Therefore, the adjustment of w_m can directly affect the movement of the overlying strata and the development law of the water-conductive fractures when it is small, while it makes nearly no difference to the HWCFZ, since the span is wide enough and similar to the longwall caving mining.
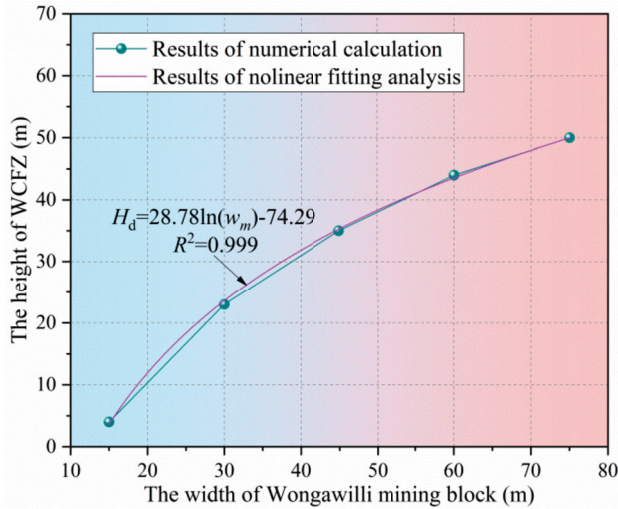
Figure 10. The relationship between the HWCFZ and various widths of Wongawilli mining block.

(5)　The HWCFZ corresponding to various widths of the protective block (w_p)

As illustrated in Figure 11, the HWCFZ decreases from 62 to 7 m, with the w_p rising from 5 to 25 m. There is a negative correlation between the HWCFZ and the width of protective block, suggesting that the width of the filling bodies in the protective block is significant enough to mitigate the overburden movement and lower the HWCFZ.
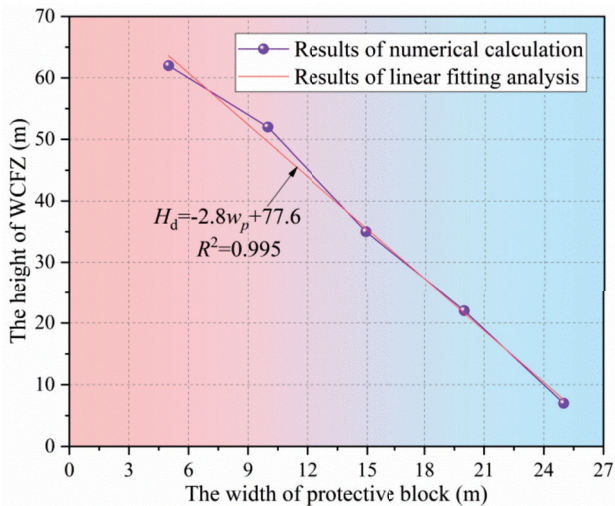
Figure 11. The relationship between the HWCFZ and various widths of the protective block.

4.4. Prediction Model of the HWCFZ of CEPB Mining Method

According to the numerical simulation results of the HWCFZ, the relationships between 5 main controlling factors and the HWCFZ were separately fitted, and the 5 functions were obtained. Therefore, a multiple nonlinear regression model was established [63,66]:

$$H_d = \varphi_0 + \varphi_1 M + \varphi_2 H + \varphi_3 R_h + \varphi_4 \ln w_m + \varphi_5 w_p, \tag{5}$$

where H_d is the HWCFZ of CEPB; M is the mining height, m; H refers to the buried depth of coal seam, m; R_h denotes the hard-rock lithology ratio; w_m and w_p represent the width of Wongawilli and protective block, m; $\varphi_0, \varphi_1, \varphi_2, \varphi_3, \varphi_4, \varphi_5$ are constants.

Here, let $M = x_1, H = x_2, R_h = x_3, \ln(w_m) = x_4, w_p = x_5$. Then, the multiple nonlinear regression model in Equation (5) was be converted into a multiple linear regression model:

$$H_d = \varphi_0 + \varphi_1 x_1 + \varphi_2 x_2 + \varphi_3 x_3 + \varphi_4 x_4 + \varphi_5 x_5, \tag{6}$$

The regression coefficient $\varphi_0, \varphi_1, \varphi_2, \varphi_3, \varphi_4, \varphi_5$ was calculated by the least square method, and the process was as follows:

$$f(x_i) = \sum (H_i - \hat{H}_i)^2 = \sum (H_i - \varphi_0 - \varphi_1 x_{1i} - \varphi_2 x_{2i} - \varphi_3 x_{3i} - \varphi_4 x_4 - \varphi_5 x_{5i})^2 = \min, \tag{7}$$

where the independent variables $x_{1i}, x_{2i}, \cdots, x_{ni}$ and the dependent variables y_i are all specific known observed values. In order to obtain the regression coefficient, the derivative of $\varphi_0, \varphi_1, \varphi_2, \varphi_3, \varphi_4, \varphi_5$ was taken, and its first derivative was set to 0, allowing us to obtain the following:

$$\begin{cases} G_{11}\varphi_1 + G_{12}\varphi_2 + G_{13}\varphi_3 + G_{14}\varphi_4 + G_{15}\varphi_5 = G_{1y} \\ G_{21}\varphi_1 + G_{22}\varphi_2 + G_{23}\varphi_3 + G_{24}\varphi_4 + G_{25}\varphi_5 = G_{2y} \\ G_{31}\varphi_1 + G_{32}\varphi_2 + G_{33}\varphi_3 + G_{34}\varphi_4 + G_{35}\varphi_5 = G_{3y} \\ G_{41}\varphi_1 + G_{42}\varphi_2 + G_{43}\varphi_3 + G_{44}\varphi_4 + G_{45}\varphi_5 = G_{4y} \\ G_{51}\varphi_1 + G_{52}\varphi_2 + G_{53}\varphi_3 + G_{54}\varphi_4 + G_{55}\varphi_5 = G_{5y}, \end{cases} \tag{8}$$

where, $G_{ij} = G_{ji} = \sum (x_{ij} - \hat{x}_i)(x_{ij} - \hat{x}_j), G_{iy} = \sum (x_{ij} - \hat{x}_i)(y_i - \hat{y}_i)$.

Because $G_{i1}, G_{i2}, G_{i3}, G_{i4}, G_{i5}, G_{iy} (i = 1, 2, 3, 4, 5)$ were obtained according to the numerical calculation results, $x_{ij}, y_i, \overline{x}_j, \overline{x}_i, \overline{y}_i$ $(i = 1, 2, 3, 4, 5)$ are known, and $\varphi_0, \varphi_1, \varphi_2, \varphi_3, \varphi_4, \varphi_5$ are 5 unknowns with 5 equations. $\varphi_1, \varphi_2, \varphi_3, \varphi_4, \varphi_5$ were solved by the determinant or elimination method, and then φ_0 was obtained.

Moreover, when judging the closeness of the linear relationship between variables in the regression equation, we needed a quantitative index, namely the correlation coefficient:

$$R\left[R^2(y, 1, 2, 3, 4, 5) = \left(\sum (\hat{y}_i - \overline{y})^2\right) / \left(\sum (y_i - \overline{y})^2\right)\right], \tag{9}$$

The closer R is to 1, the more accurate the regression equation is.

Based on the simulation results and the aforementioned procedure, SPSS software was employed to conduct multiple linear regression analysis of the HWCFZ under 5 main controlling factors, namely, the mining height and depth, hard-rock lithology ratio, and the width of the Wongawilli and protective block. The prediction model for HWFZ of CEPB is:

$$H_d = 5.60M + 0.013H + 17.86R_h + 29.02 \ln w_m - 2.68 w_p - 61.6 \quad R^2 = 0.92, \tag{10}$$

5. Verification and Field Implementation of the Prediction Model

5.1. Verification of the Prediction Model of HWCFZ

A colliery employing the CEPB mining method in the Yu-Shen mining area was selected to estimate the HWCFZ using the model, so as to verify its reliability and rationality. The mining height and the buried depth of the coal seam are 4 and 240 m, respectively.

Additionally, the hard-rock lithology ratio is 0.6, and the widths of the Wongawilli and protective block are 70 and 15 m, respectively. By employing the predicting formula, the HWCFZ was calculated to be 57.7. Subsequently, CXK7.2 (A) mine borehole imager was chosen to implement the borehole television logging, as shown in Figure 12. The detection results of HWCFZ are shown in Figure 13.

Figure 12. Field measurement of borehole television logging for determining the HWCFZ. (**a**) The operating platform for borehole television logging. (**b**) The panoramic camera. (**c**) The support bar to transport the camera to the detection position. (**d**) The depth counter to measure the distance from the starting point of the drillhole to the detection position. (**e**) The camera guide to make it easy for the camera to pass through.
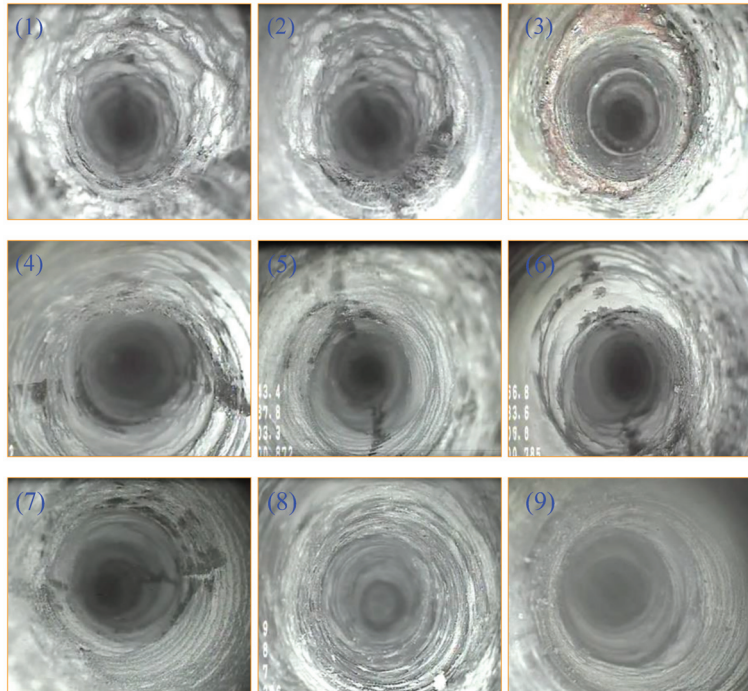
Figure 13. The image of borehole television logging. Images (1) to (9) show the picture when the distance from the starting point of the borehole to the detection position is approximately 15, 22, 30, 41, 52.6, 53, 55, 62, and 68.7 m, respectively.

Based on the results of borehole peeping illustrated in Figure 13, that the following can be observed: (1) A large number of longitudinal and oblique fractures are developed with

vertical height varying from 5.6 to 15.1 m, resulting in the fragmentation of surrounding rock. (2) Peeling occurs on the borehole wall in the range of 21.6–24.4 m, which lowers the aperture and makes it difficult for the probe to pass through. (3) Transverse cracks appear with height ranging from 27.3 to 38.5 m, indicating a bed separation occurring here. (4) There is a longitudinal fissure of around 1.9 m from 40.4 to 42.3 m. (5) The surrounding rock at 52.6 m breaks to a large extent, and it is dislocated on the right side of the borehole wall. (6) There are multiple longitudinal fissures whose lengths are approximately 0.5 m between 52.6 and 53.1 m. (7) The lateral and vertical micro-cracks emerge with the height varying from 53.6 to 55.9 m, and the surrounding rock of the wall is slightly peeled off. (8) The wall in the range of 57.7–68.7 m is relatively rough, but there is no obvious vertical or lateral fissure. (9) The surrounding rock of the borehole wall above 68.7 m is relatively smooth and integral without any fractures.

To sum up, the fractures are relatively developed in the range of 5.6–53.1 m, and the cracks gradually change from macroscopic fissures to micro-fissures with the vertical height ranging from 53.1 to 57.7 m. Therefore, when the height exceeds 53.1, the overlying strata belong to the non-penetrating fracture zone, so the HWCFZ can be determined to be 53.1 m. The error between the results of HWCFZ from the prediction model and the borehole television logging is 9%, verifying the rationality and validity of the model.

5.2. Generalization and Application of the Model

The model was generalized and applied to the whole Yu-Shen mining area on the basis of verifying its rationality and validity. Based on the data on the thickness and burial depth of the first-mined coal seam and the stratigraphic structure from 400 hydrogeological boreholes, the HWCFZ of 400 boreholes under various widths of Wongawilli and protective block were obtained. Subsequently, the thickness of the protective zone of each borehole was calculated by subtracting the HWCFZ from the distance between the aquifer and the first-mined coal seam. The thematic map of the HWCFZ and the thickness of protective zone were plotted by using Kriging interpolation method, so as to provide guidance for the field application of the CEPB in the Yu-Shen mining area.

5.2.1. Thickness and Burial Depth of the First-Mined Coal Seam

The coal-bearing strata in the Yu-Shen coal area are the Jurassic Yan'an Formation strata. There are five main mineable coal seams, i.e., 1^{-2}, 2^{-2}, 3^{-1}, 4^{-2}, 5^{-2} coal seams from top to bottom, with the overall dip angle varying from 1 to 3°. The contour map of the thickness of the first-mined coal seam is illustrated in Figure 14a. Moreover, the lithology of the overlying layers whose thickness ranges between 0 and 650 m from the east to the west is dominated by mudstone, sandy mudstone, and sandstone. The contour map of the buried depth of the first-mined coal seam was drawn and shown in Figure 14b.

5.2.2. Zoning Map of Hard-Rock Lithology Ratio

Based on the characteristics of the spatial combination relationship of the overlying strata, the stratigraphic structure in the Yu-Shen coal area can be classified into five types, including sand–soil–bedrock, sand-bedrock, bedrock, soil–bedrock and burnt rock. Firstly, sand–soil–bedrock consists of sand strata, aquifuge, and bedrock, covering an area of more than 80% of its territory. According to the drilling data, the hard-rock lithology R_h of this structure can be set to 0.6. The sand-bedrock is composed of sand layers and bedrock, and the R_h of this structure is 0.8. The Salawusu aquifer lies on the structure directly, without a continuous water-resisting layer separating them. Thirdly, the bedrock overburden is exposed to the earth's surface directly, and the R_h is 1.0. It is unnecessary to take this structure into account during the process of water-preserving mining due to its extremely low water-richness property. In addition, the soil-bedrock overburden is composed of aquifuge and bedrock, and the R_h is determined to 0.4 based on the overburden lithology. Burnt rock, with thickness ranging from 30 to 50 m, is the product of rock alteration resulting from the spontaneous combustion of coal seams. Since the strata are fragmented

and broken and the rock is brittle with low ultimate stress, the water-diversion fractures develop directly to the shallow aquifer, contributing to water resources loss and water table lowering. Hence, the R_h of this structure is determined to be 1.0. The distribution of R_h based on the five stratigraphic structures is shown in Figure 15.

(a)

(b)
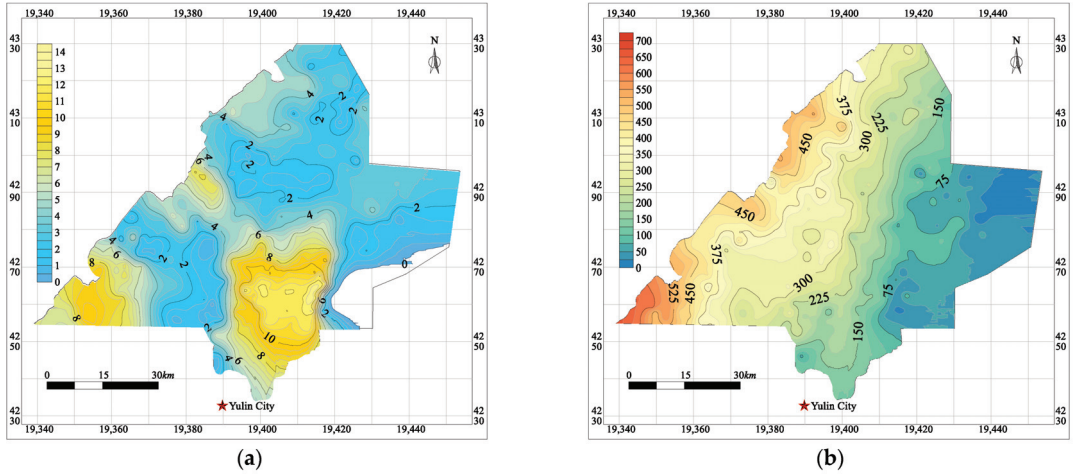
Figure 14. Thematic map of the occurrence conditions of the first-mined coal seam in the Yu-Shen mining area. (**a**) Contour map of the first-mined coal seam thickness; (**b**) Contour map of the buried depth of the first-mined coal seam.

I	II	III	IV	V
Sand-soil-bedrock (R_h=0.6)	Sand-bedrock (R_h=0.8)	Bedrock (R_h=1.0)	Soil-bedrock (R_h=0.4)	Burnt rock (R_h=1.0)
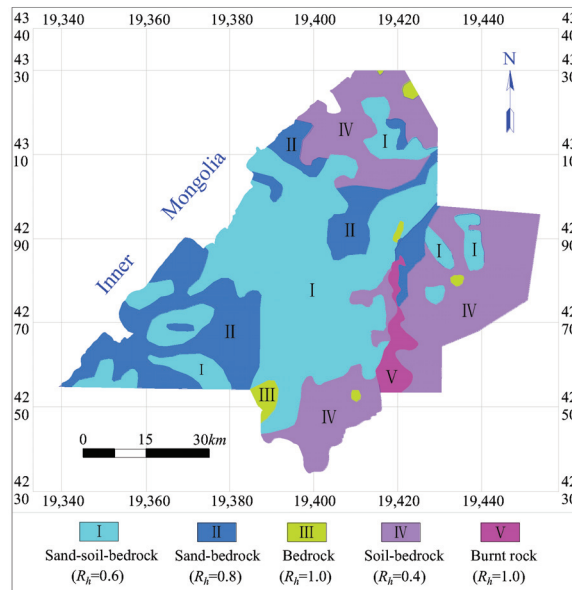
Figure 15. Zoning map of the hard-rock lithology ratio (R_h) in the Yu-Shen mining area.

5.2.3. Characteristics of Underground Aquifer

From first-mined coal seam to the surface, the underground aquifer in the Yu-Shen mining area is composed of the confined aquifer of porous bedrock, burnt-rock phreatic aquifer, Salawusu formation aquifer, and the unconsolidated porous phreatic aquifer.

The unconsolidated porous phreatic aquifer with extremely thin thickness is primarily recharged from precipitation, and it tends to form a complete and uniform aquifer with its underlying Salawusu Formation aquifer. The porous-bedrock-confined aquifer with little porosity and weak water yield property is distributed in restricted range. The burnt-rock phreatic aquifer is mainly recharged by its overlying Salawusu aquifer and it is not an aquifer in essence, since it itself cannot form a water-storing structure. The Salawusu Formation aquifer is widely distributed in the mining area, with thickness varying from 0 to 67.3 m. The maximum water table depth of Salawusu aquifer is 15 m, while it is generally less than 10 m in most regions in the Yu-Shen coal area. It provides the major supply source for domestic and ecological water demand. Hence, it is the primary source that needs to be taken into consideration while investigating water-preserving coal mining. Furthermore, the thickness of the protective zone can quantitatively characterize the spatial relationship between the HWCFZ and the water level of the Salawusu aquifer to a certain extent. The emphasis should be put on it, since it is indispensable for realizing water-preserving mining in the coal area.

5.2.4. HWCFZ and Protective Zone Thickness under CEPB and Longwall Caving Mining

(1)   HWCFZ of the CEPB mining method

According to the occurrence of the first-mined coal seam and the zoning map of the hard-rock lithology ratio obtained by 400 geological drilling holes in the study area, the HWCFZ of each borehole was calculated under CEPB mining using Equation (10). Adjusting the ratio of the width of the Wongawilli block to that of the protective block with due regard to the actual situation on site, three schemes listed in Table 6 were designed to illustrate the controlling effects of extracting and filling parameters on the HWCFZ and the thickness of the protective zone.

Table 6. The various extracting and filling schemes of CEPB mining method.

Number	Width of Wongawilli Block	Width of Protective Block
Scheme I	25	15
Scheme II	45	15
Scheme III	75	10

By employing the Kriging interpolation method, the thematic map of the HWCFZ and the thickness of the protective zone under various schemes were plotted, as shown in Figures 16–18.

(**a**)   (**b**)
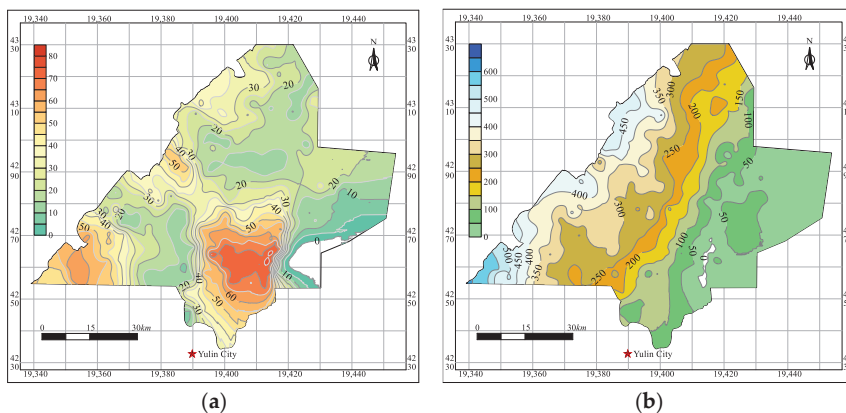
Figure 16. Thematic map of scheme I while using CEPB mining method in the Yu-Shen coal area. (**a**) Contour map of the HWCFZ; (**b**) Contour map of the thickness of protective zone.
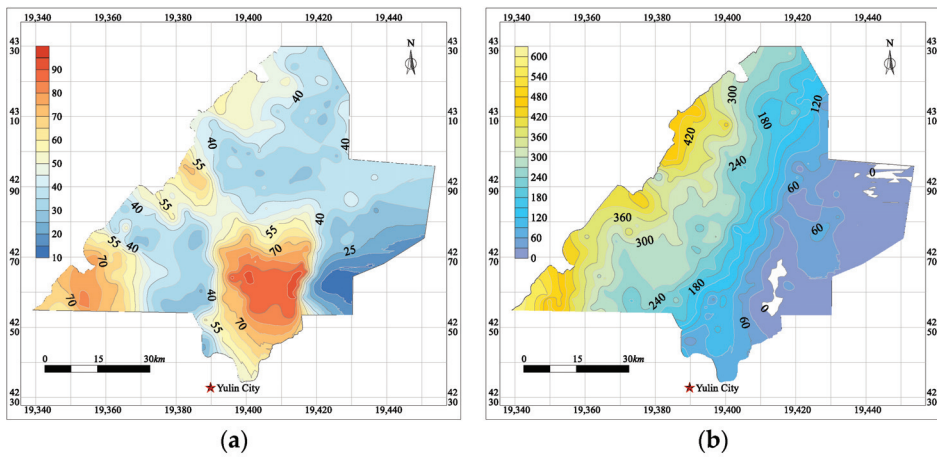
Figure 17. Thematic map of scheme II while using CEPB mining method in the Yu-Shen coal area. (**a**) Contour map of the HWCFZ; (**b**) Contour map of the thickness of protective zone.
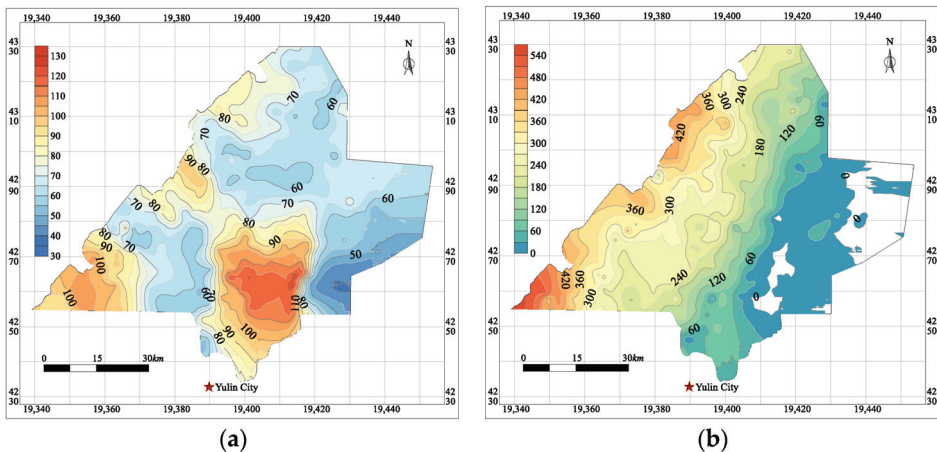
Figure 18. Thematic map of scheme III while using CEPB mining method in the Yu-Shen coal area. (**a**) Contour map of the HWCFZ; (**b**) Contour map of the thickness of the protective zone.

(2)　HWCFZ of the longwall caving mining

The majority of the main mineable coal seams in the eastern mining area of China belong to the Permian system, which is different from that of Jurassic coal seams in the Yu-Shen coal area. Furthermore, the hydrogeological and engineering conditions in this area differ from those in the eastern mining area significantly [4]. Hence, the traditional formulae for predicting HWCFZ of longwall caving mining are inapplicable to the Yu-Shen mining area. With due regard to various stratigraphic structures, i.e., the sand soil bedrock, sand bedrock, bedrock, soil-bedrock, the author once established a HWCFZ prediction model under longwall caving mining in the study area [30]. It was employed in this paper to compare the HWCFZ between the CEPB and the longwall caving mining [4,30]. Based on the drilling data and Equation (11), the thematic map of HWCFZ and the thickness of

the protective zone under longwall caving mining were drawn using Kriging method, as illustrated in Figure 19.

$$\begin{cases} H_f = 21.75M + 28.28 \text{ R}^2 = 0.99 \text{ (Sand-soil-bedrock)} \\ H_f = 22.20M + 37.13 \text{ R}^2 = 0.97 \text{ (Sand-bedrock)} \\ H_f = 16.70M + 30.80 \text{ R}^2 = 0.97 \text{ (Bedrock)} \\ H_f = 21.97M + 28.42 \text{ R}^2 = 0.98 \text{ (Soil-bedrock)}, \end{cases} \quad (11)$$

where H_f is the HWCFZ under longwall caving mining; M is the mining height.
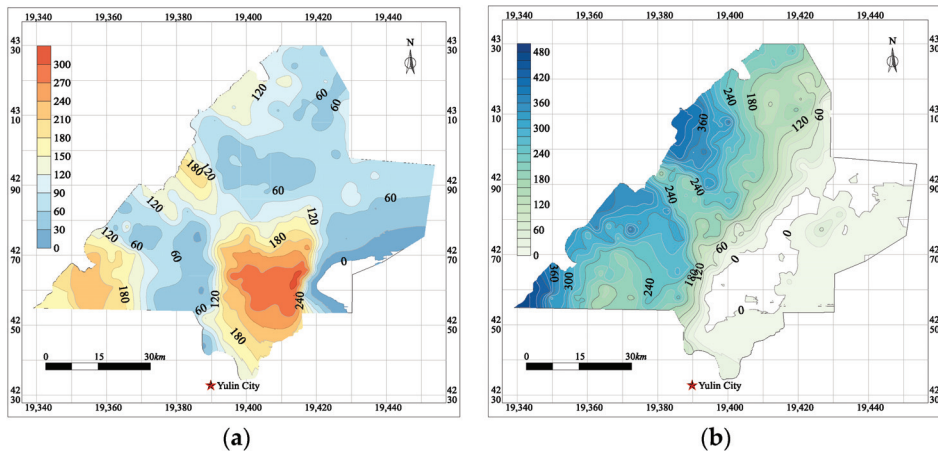
Figure 19. Thematic map of longwall caving mining in the Yu-Shen coal area. (**a**) Contour map of the HWCFZ; (**b**) Contour map of the thickness of protective zone.

(3)   The HWCFZ and protective zone thickness of CEPB and longwall caving mining

It can be seen from Figures 16–19 that the HWCFZ of CEPB in the Yu-Shen mining area increases from northwest to southeast. The maximum values of the three schemes are 85 m, 100 m, and 135 m, respectively, located in the southeastern boundary. Our analysis is that the stratigraphic structure here is burnt rock. The overlying stratum develops fissures and cavities due to the roof collapse and later weathering induced by the spontaneous combustion of coal seam, and the rock mass is relatively fragmented. Hence, in this area, the water-conducted fractures go up rapidly and connect the Salawusu aquifer with the underground mined-out area, triggering water level drop and mine water inrush. Therefore, CEPB mining method is also unsuitable for the burned-rock area, and mining activities should be strictly prohibited in this area. The HWCFZ gradually decreases around the burned-rock region, and the minimum is in the soil-bedrock area in the eastern border of the Yu-Shen coal area. However, there is no Salawusu aquifer in this area, so the investigation on the HWCFZ is insignificant.

Additionally, the HWCFZ is not the only influencing factor for water-preserving mining. The thickness of the protective zone is also of great significance for conserving the overlying aquifer. In contrast to the HWCFZ, as a whole, the thickness of the protective zone of boreholes in the east area is generally lower than for those in the west, with the maximum values of the three schemes being 700 m, 630 m, and 570 m, respectively. As the ratio of the width of the Wongawilli block to that of the protective block increases, the HWCFZ grows while the thickness of the protective zone decreases. The maximum value of the HWCFZ of the scheme III of CEPB is 135 m, which is far less than that of 330 m of the longwall caving mining. Furthermore, the maximum thickness of the protective zone is 570 and 500 m, respectively, in scheme III of CEPB and longwall mining. Both the maximum of HWCFZ and the thickness of the protective zone indicate that even narrow protective

block can effectively mitigate the overburden migration and thereby the development of water-flowing fractures, implying that the CEPB is more effective in water-preserving mining than longwall caving mining.

5.3. Criterion for Realizing Water-Preserving Coal Mining

5.3.1. Equivalent Permeability of the Protective Zone

The thickness of the protective zone is an indispensable index to evaluate its water-blocking ability. Generally, the thicker the protective zone is, the lower the risk that groundwater percolates through it. However, the water-resisting property of the overlying strata varies with varying lithology in the Yu-Shen coal area. The water-seepage-resisting capabilities of different strata of the protective zone are characterized by the permeability coefficient, as listed in Table 7.

Table 7. Permeability coefficient of various lithology in the Yu-Shen coal area [4].

Lithology	Permeability Coefficient (cm/s)
Clay	1×10^{-11}–5×10^{-9}
Mudstone	1×10^{-11}–1×10^{-8}
Sandy mudstone	3×10^{-9}–6×10^{-5}
Siltstone	1×10^{-9}–2×10^{-5}
Fine sandstone	2×10^{-7}–2×10^{-4}
Medium sandstone	9×10^{-7}–5×10^{-4}
Coarse sandstone	9×10^{-7}–6×10^{-3}

During the previous research on water-preserving coal mining in the Yu-Shen mining area, the authors found that a protective zone composed of 12 m clay can effectively ameliorate water infiltration from the overlying Salawusu aquifer to the mined-out area, while an overlying layer with 30 m clay can completely eradicate water seepage. The water-resisting ability of the overlying layer with lithology of sandstone, sandy mudstone, shale, and mudstone is lower than that of clay stratum. In order to quantitatively characterize the water-blocking capability of the protective zone, the equivalent permeability coefficient of the protective zone was calculated:

$$k_e = \left(\sum_{i=p}^{q} H_i \right) / \left[\sum_{i=p}^{q} \left(\frac{H_i}{k_i} \right) \right], \tag{12}$$

where k_e denotes the equivalent permeability of the protective zone, m/d; H_i is the ith overlying stratum thickness, m; k_i is the permeability coefficient of the ith overlying stratum, m/d; p and q are the number of the lowest and highest rock stratum in the protective zone, respectively.

Broadly speaking, for the stratigraphic structure with soil aquiclude existing, such as sand–soil–bedrock and soil–bedrock structure, the lithological compositions of the protective zone can be classified into three types: (1) If the distance between the Salawusu aquifer and the first-mined coal seam is large enough, the protective zone consists of the aquiclude and its underlying integral bedrock as well as the bedrock without connected fractures. (2) As the distance become short, the water-conductive fractures may develop into the Salawusu aquifer, and the protective zone is composed of a part or the entire of the aquifuge. (3) When the coal–water spacing is further reduced, the WCFZ may directly penetrate the aquiclude and reach the Salawusu aquifer. At the moment, the thickness of the protection zone is negative, indicating that it does not exist. In addition, as far as the sand–bedrock and bedrock overburden is concerned, there are two types of components of the protective zone: (1) If the coal–water spacing is large, the protection zone is composed of the lower intact bedrock or the bedrock with non-penetrating fractures. (2) When the distance is short, the fissure develops through the bedrock to the Salawusu aquifer, and the protective zone does not exist at this time.

The main aquiclude in the Yu-Shen coal area includes the loess in the Lishi Formation and the adjacent red soil in the Pliocene Baode Formation. The Lishi Formation is composed of grayish-yellow sandy loam and silty clay, with thickness varying from 0 to 110 m and 23 m on average. The Baode Formation consists of brown-red clay and silty clay, with an average thickness of 30 m. Furthermore, the lithology of bedrock is primarily sandy mudstone, siltstone, fine sandstone, etc., with an average permeability of 10^{-4} cm/s after coal extraction. Hence, Formula (12) was employed to calculate the equivalent permeability of the protective zone and the thematic maps under various mining methods, and mining parameters are illustrated in Figure 20.
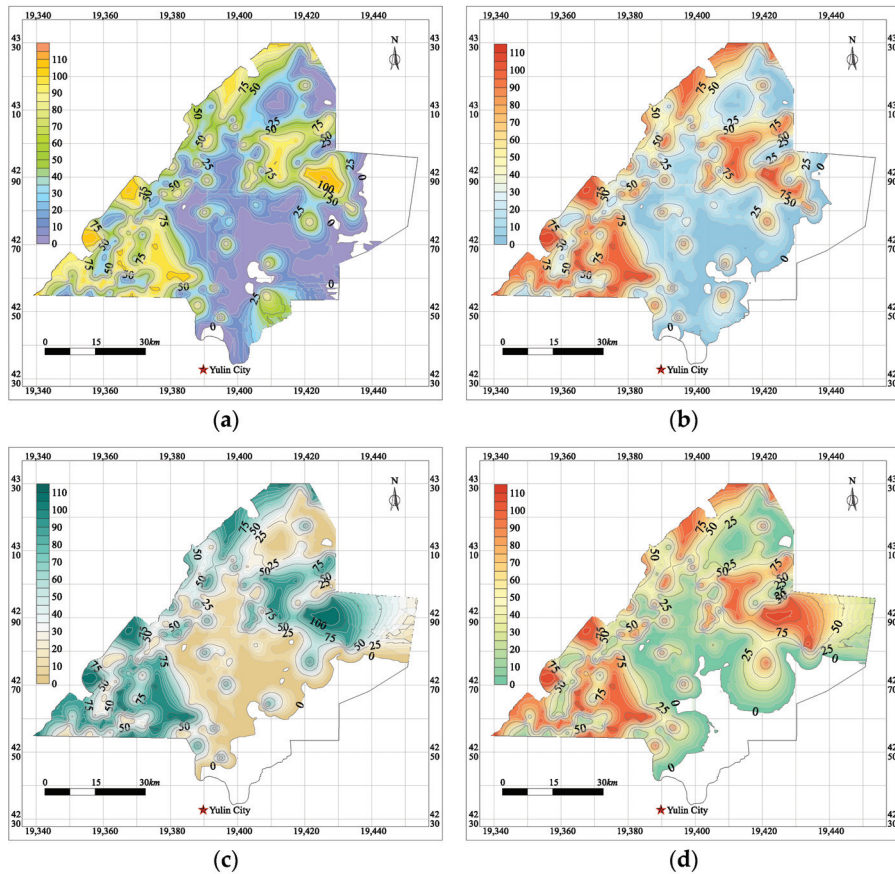
Figure 20. Thematic maps of the equivalent permeability ($\times 10^6$) of the protective zone under different mining schemes. (**a**) Scheme I; (**b**) Scheme II; (**c**) Scheme III; (**d**) Longwall caving mining.

It can be seen from Figure 20 that the equivalent permeability of the protective zone of the boreholes in the southwest and north is greater than that in other places. This indicates that there is no aquifuge beneath the Salawusu aquifer, or the thickness of the aquiclude in these two regions is far thinner than that in the south and east. Meanwhile, the permeability of bedrock is far greater than that of clay, leading to the large equivalent permeability of the protective zone. In addition, the water-conducting fissures in the vicinity of the eastern and southern boundary are highly developed, and the HWCFZ is higher than the level of the aquiclude (if it exists) and reaches the overlying aquifer, contributing to the absence of the protective zone, as shown in the blank and unfilled area in Figure 20. Therefore,

the equivalent permeability of the protective zone here is absent instead of equal to 0, and water-preserving mining is difficult in these two areas.

As illustrated in Figure 20a–c, as the ratio of the span of the Wongawilli block to that of protective block increases, the blank and unfilled area also increases. Compared with scheme III of CEPB mining, the blank area extends to the mideast part while using longwall caving mining. It is worth noting that the northeastern border of the mining area belongs to the soil–bedrock structure, without Salawusu aquifer occurring over the aquifuge. There are extremely few drilling data in this area, since it makes no difference to water-preserving mining. Due to the limitations of Kriging interpolation method, as the blank and unfilled area shifts to the west, the northeastern border of scheme III of CEPB and the longwall caving mining is also interpolated, as shown in Figure 20c,d.

5.3.2. Criterion for Realizing Water-Preserving Mining

Assuming that the vertical water flow in the protective zone of each borehole follows the Darcy's law, the criterion of whether water-preserving coal mining can be realized is proposed on the basis of comparing the equivalent permeability (equivalent water seepage rate) of the protective zone to the recharge rate of the Salawusu Formation aquifer:

$$k_e \Delta H \leq V_s \sum_{i=p}^{q} H_i, \tag{13}$$

where ΔH is the hydraulic head pressure difference between the upper and lower boundary of the protective zone; k_e is the equivalent permeability coefficient of the protective zone; H_i is the thickness of the ith overlying layer of the protective zone; p and q are the number of the lowest and highest stratum of the protective zone, respectively; V_s is the recharge rate of the Salawusu formation aquifer.

According to the field measurement results of the recharge rate of the Salawusu aquifer, in the vicinity of the central regions of Yu-Shen mining area, the vertical seepage velocity of the water in the protective zone is much lower than the recharge velocity of the aquifer, contributing to the full realization of water-preserving coal mining under CEPB mining. In addition, in a small part of the midwest area, the longwall fully mechanized mining can also realize water-preserving coal mining. Hence, the CEPB mining in this area is not optimal compared with longwall mining, which has high mining efficiency and recovery rate. Note that in the vicinity of the burnt-rock area on the eastern boundary where the overlying strata are fragmented and broken, water-preserving coal mining cannot be achieved despite employing CEPB mining method.

6. Discussion

(1) AHP is a subjective weighting method. Since the identification of indexes and the determination of the relative weight in the paper was mainly provided by scholars engaged in HWCFZ prediction and water-preserving mining in Northwest China, we will further our study to confirm whether the indicators and the weights distribution are applicable to other mining areas.

(2) The prediction result of HWCFZ is consistent with the field test results, indicating it is scientific, reasonable, and reliable. Moreover, the model can not only accurately predict the HWCFZ in the Yu-Shen coal area but also be generalized and employed in other mining areas situated in Northwest China, as long as they share the occurrence of coal seam, overlying aquifer, and the stratigraphic structure in common. However, the prediction model with due consideration of five main controlling factors is only applicable to ordinary mining areas in Northwest China. For mining areas with coal seam thickness up to 100 m in Xinjiang province, it is obviously inapplicable.

(3) When the overlying aquifer is extremely close to the coal seam, the Wongawilli block should be backfilled in the same way as the protective block, since the water-flowing fractures always reach the water body, regardless of how to optimize the mining

parameters. In this context, the CEPB has shifted to the continuous extraction and continuous backfill mining method. Moreover, the Wongawilli and the protective block share equipment requirements such as filling pipeline in common, and additional improvement is unnecessary for filling Wongawilli block, contributing to a simple and convenient transformation of mining methods.

(4) The field industrial test shows that the filling cost per ton of coal when both the Wongawilli and protective block are backfilled is less than 120 yuan, which is slightly higher than that of the longwall backfill mining of 100 yuan. In addition, the maximum annual output of CEPB can reach 600,000 tons, being similar to that of longwall backfill mining. If the mining method only backfills the protective block, while leaving the Wongawilli block unbackfilled, the filling cost per ton of coal of CEPB will be further reduced. It can also lower the requirements for large-scale raw filling material sources and cut down the filling cost in order to realize water-preserving coal mining. On the other hand, in order to separate the chamber and support the roof for a short term and prevent stress concentration at the edge of the Wongawilli block, a small amount of narrow coal pillars have been discarded and left unmined. The recovery rate of CEPB mining is approximately 85%. However, compared with the recovery rate of 40% of partial mining methods, such as room and pillar mining, strip mining, and height-limiting mining, CEPB can still be regarded as an ideal water-preserving mining method with high recovery rate. This method has been currently applied to Yuyang, Suncun, and Wangtaipu collieries, and dual benefits of economy and ecology have been achieved, indicating its good prospects for generalization and application.

(5) When using UDEC to simulate the HWCFZ of CEPB, the selection of the constitutive model is the crucial procedure, since different types of filling materials correspond to various constitutive models. The double-yield constitutive model is ideal for simulating the strain-hardening mechanical behavior of the compressed gangue after it is conveyed to the MRs of the protective block. Considering that there is no cohesion between gangue particles, the tensile and shear effects in the double-yield model are therefore ignored, and only the volumetric yield effect is considered. In order to make the simulation results closer to the actual situation, Terzaghi's model, an ideal model to simulate the relationship between stress and strain of the gangue, was employed to correct the cap pressure of filling bodies in the MRs. On the other side, if the MR is injected with paste filling materials, the strain-softening constitutive model is the most suitable one to be chosen. The cohesion, friction, expansion and tensile strength of the model may soften after the beginning of plastic yield, while these properties are assumed to remain unchanged in the Mohr–Coulomb model. The softening behavior of cohesion, friction, and dilatation based on plastic shear strain is given in the form of specified table value, and it is assumed that the two consecutive parameters in the table command are linear. As a function of plastic tensile strain, the tensile strength is also given by the specified table value.

7. Conclusions

The following conclusions are drawn from the above research:

(1) The CEPB mining method was proposed for water-preserving coal mining by combining the advantages of Wongawilli rapid mining method with the roadway skip mining. This method overcomes the problems of high filling cost and insufficient source of raw filling materials caused by high filling rate of the continuous extraction and continuous backfill mining. Based on the characteristics of overburden as well as the distance between coal seam and the overlying aquifer, the mining and filling parameters, such as the width of the Wongawilli and the protective block, can be flexibly adjusted, so as to control the HWCFZ and realize water-conservation mining in order to maximize the economic benefits.

(2) A triple-leveled structure model, with 3 sub-factors and 10 third-tier indicators, was established by employing the analytic hierarchy process (AHP) method to identify

the influencing factors of the HWCFZ of CEPB mining. According to the weight distribution, among the second-level influencing factors, the coal mining system is the most significant one, with a weight of 0.7273. The mining height, whose weight is 0.3112, is the most important indicator among the third-tier factors. Based on the weight distribution, five main controlling factors affecting the HWCFZ were determined, i.e., the hard-rock lithology ratio, the mining height and depth and the width of Wongawilli and protective block.

(3) UDEC software was employed to construct the numerical calculation models, and the orthogonal numerical simulation scheme including five main controlling factors was designed. The HWCFZ of CEPB under the conditions of different mining parameters was simulated by adopting control variable method, and the linear and nonlinear fitting of single factor were carried out. Then, by using the multiple linear regression function embedded in SPSS software, the prediction model of HWCFZ of CEPB was obtained: $H_d = 5.60M + 0.013H + 17.86R_h + 29.02\ln w_m - 2.68w_p - 61.6$ $R^2 = 0.92$.

(4) The estimation model was employed with a colliery in Yu-Shen mining area, and the HWCFZ was calculated to be 57.7 m, 9% higher than that of 53.1 m from the borehole television logging, verifying its rationality and reliability. It was then generalized and applied to the whole Yu-Shen coal area. According to the hydrogeological characteristics of 400 boreholes in the mining area, the thematic map of the HWCFZ and the thickness and equivalent permeability of the protective zone under CEPB and longwall caving mining were drawn, respectively. A criterion for achieving water-preserving coal mining was proposed on the basis of the equivalent permeability coefficient of the protective zone and the recharge rate of its upper Salawusu aquifer. The research results can provide theoretical guidance to optimize the mining parameters of CEPB for water-preserving and water-conservation mining in Northwest China.

(5) Further in-depth study on mining-induced permeability deterioration under CEPB will be conducted. In this paper, the average permeability coefficient after coal extraction is used when calculating the equivalent permeability coefficient of the protective zone above the WCFZ. In the future research process, it is necessary to obtain the mining-induced permeability coefficient of each specific stratum, so as to more accurately predict whether water-conservation and water-preserving coal mining can be realized under different mining and filling parameters while using CEPB mining method.

Author Contributions: Conceptualization, Y.X.; methodology, Y.X.; software, Y.X. and J.Z.; validation, I.N. and J.Z.; formal analysis, Y.X.; investigation, Y.X.; data curation, I.N.; writing—original draft preparation, Y.X.; writing—review and editing, L.M.; supervision, L.M.; project administration, L.M.; funding acquisition, L.M. All authors have read and agreed to the published version of the manuscript.

Institutional Review Board Statement: Not applicable.

Informed Consent Statement: Not applicable.

Data Availability Statement: Not applicable.

Conflicts of Interest: The authors declare that they have no competing financial interests in connection with the work submitted.

References

1. Zhang, D.S.; Fan, G.W.; Ma, L.Q.; Wang, X.F. Aquifer protection during longwall mining of shallow coal seam: A case study in the Shendong Coalfield of China. *Int. J. Coal Geol.* **2011**, *86*, 190–196. [CrossRef]
2. Wang, S.M.; Huang, Q.X.; Fan, L.M.; Yang, Z.Y.; Shen, T. Study on overburden aquclude and water protection mining regionazation in the ecological fragile mining area. *J. China Coal Soc.* **2010**, *35*, 7–14.

3. Ma, L.Q.; Zhang, D.S.; Jin, Z.Y.; Wang, S.K.; Yu, Y.H. Theories and methods of efficiency water conservation mining in short-distance coal seams. *J. China Coal Soc.* **2019**, *44*, 727–738.
4. Xu, Y.J. Study on "Five Maps, Three Zones and Two Zoning Plans" Water Conservation Mining Method in Yushen Mining Area. Master's Thesis, China University of Mining Science & Technology, Xuzhou, Jiangsu, China, 2019; p. 6.
5. Sun, K.; Fan, L.M.; Xia, Y.C.; Li, C.; Chen, J.P.; Gao, S.; Wu, B.Y.; Peng, J.; Ji, Y.W. Impact of coal mining on groundwater of Luohe Formation in Binchang mining area. *Int. J. Coal Sci. Technol.* **2021**, *8*, 88–102. [CrossRef]
6. Li, W.P.; Wang, Q.Q.; Liu, S.L.; Pei, Y.B. Study on the creep permeability of mining-cracked N2 laterite as the key aquifuge for preserving water resources in Northwestern China. *Int. J. Coal Sci. Technol.* **2018**, *5*, 315–327. [CrossRef]
7. Guo, J.S.; Ma, L.Q.; Zhang, D.S. Management and utilization of high-pressure floor-confined water in deep coal mines. *Mine Water Environ.* **2019**, *38*, 780–797. [CrossRef]
8. Ma, L.Q.; Guo, J.S.; Liu, W.P.; Zhang, D.S.; Yu, Y.H. Water conservation when mining multiple, thick, closely-spaced coal seams: A case study of mining under weishan lake. *Mine Water Environ.* **2019**, *38*, 643–657. [CrossRef]
9. Ma, L.Q.; Jin, Z.Y.; Liang, J.M.; Sun, H.; Zhang, D.S.; Li, P. Simulation of water resource loss in short-distance coal seams disturbed by repeated mining. *Environ. Earth Sci.* **2015**, *74*, 5653–5662. [CrossRef]
10. Wang, S.K.; Ma, L.Q. Characteristics and control of mining induced fractures above longwall mines using backfilling. *Energies* **2019**, *12*, 4604. [CrossRef]
11. Gao, W.; Ge, M. Stability of a coal pillar for strip mining based on an elastic-plastic analysis. *Int. J. Rock Mech. Min. Sci.* **2016**, *87*, 23–28. [CrossRef]
12. Gian, F.N.C.; Tais, R.C.; Vidal, F.N.T. Optimization of room-and-pillar dimensions using automated numerical models. *Int. J. Min. Sci. Tech.* **2019**, *29*, 797–801.
13. Yuan, S.C.; Han, G.L. Combined drilling methods to install grout curtains in a deep underground mine: A case study in Southwest China. *Mine Water Environ.* **2020**, *39*, 902–909. [CrossRef]
14. Wang, X.Y.; Wu, W.D.; Wu, B.W. Grouting of bed separation spaces to control sliding of the high-located main key stratum during longwall mining. *Q. J. Eng. Geol. Hydrogeol.* **2020**, *53*, 569–578. [CrossRef]
15. Xu, Y.J.; Ma, L.Q.; Khan, N.M. Prediction and maintenance of water resources carrying capacity in mining area-a case study in the Yu-Shen mining area. *Sustainability* **2020**, *12*, 7782. [CrossRef]
16. Huang, P.; Spearing, A.J.S.; Feng, J.; Jessu, K.V.; Guo, S. Effects of solid backfilling on overburden strata movement in shallow depth longwall coal mines in West China. *J. Geophys. Eng.* **2018**, *15*, 2194–2208. [CrossRef]
17. Zhang, Y.; Cao, S.; Zhang, N.; Zhao, C. The application of short-wall block backfill mining to preserve surface water resources in northwest China. *J. Clean. Prod.* **2020**, *261*, 121232. [CrossRef]
18. Zhang, J.X.; Sun, Q.; Zhou, N.; Jiang, H.Q.; Deon, G.; Sami, A. Research and application of roadway backfill coal mining technology in western coal mining area. *Arab. J. Geosci.* **2016**, *9*, 1–10. [CrossRef]
19. Ma, L.; Xu, Y.; Zhang, D.S.; Lai, X.; Huang, K.; Du, H. Characteristics of aquiclude and surface deformation in continuous mining and filling with wall system for water conservation. *J. Min. Saf. Eng.* **2019**, *36*, 30–36.
20. Ma, L.Q.; Jin, Z.Y.; Liu, W.; Zhang, D.S.; Zhang, Y. Wongawilli roadway backfilling coal mining method-a case study in Wangtaipu coal mine. *Int. J. Oil Gas Coal Technol.* **2019**, *20*, 342–359. [CrossRef]
21. Ma, L.Q.; Zhang, D.S.; Wang, S.K.; Xie, Y.S.; Yu, Y.H. Water-preserved mining with the method named "backfilling while mining". *J. Chin. Coal Soc.* **2018**, *43*, 62–69.
22. Yu, Y.H.; Ma, L.Q.; Zhang, D.S. Characteristics of roof ground subsidence while applying a continuous excavation continuous backfill method in longwall mining. *Energies* **2020**, *13*, 95. [CrossRef]
23. Yu, Y.H.; Ma, L.Q. Application of roadway backfill mining in water-conservation coal mining: A case study in northern Shaanxi, China. *Sustainabiltity* **2019**, *11*, 3719. [CrossRef]
24. Wang, A.L.; Ma, L.Q.; Wang, Z.W.; Zhang, D.S.; Li, K.; Zhang, Y.; Yi, X.J. Soil and water conservation in mining area based on ground surface subsidence control: Development of a high-water swelling material and its application in backfilling mining. *Environ. Earth Sci.* **2016**, *75*, 779. [CrossRef]
25. Gandhe, A.; Venkateswarlu, V.; Gupta, R.N. Extraction of coal under a surface water body-a strata control investigation. *Rock Mech. Rock Eng.* **2005**, *38*, 399–410. [CrossRef]
26. Booth, C.J. Groundwater as an environmental constraint of longwall coal mining. *Environ. Earth Sci.* **2006**, *49*, 796–803. [CrossRef]
27. Winters, W.R.; Capo, R.C. Ground water flow parameterization of an Appalachian coal mine complex. *Ground Water* **2004**, *42*, 700–710. [CrossRef]
28. Howladar, M.F. Coal mining impacts on water environs around the Barapukuria coal mining area, Dinajpur, Bangladesh. *Environ. Earth Sci.* **2012**, *70*, 215–226. [CrossRef]
29. Hill, J.G.; Price, D.R. The impact of deep mining on an overlying aquifer in western pennsylvania. *Ground Water Monit. R* **1983**, *3*, 138–143. [CrossRef]
30. Stoner, J.D. Probable hydrologic effects of subsurface mining. *Ground Water Monit. R* **1983**, *3*, 128–137. [CrossRef]
31. Arkoc, O.; Ucar, S.; Ozcan, C. Assessment of impact of coal mining on ground and surface waters in Tozakli coal field, Kırklareli, northeast of Thrace, Turkey. *Environ. Earth Sci.* **2016**, *75*, 514. [CrossRef]
32. Newman, C.; Agioutantis, Z.; Leon, G.B.J. Assessment of potential impacts to surface and subsurface water bodies due to longwall mining. *Int. J. Min. Sci. Tech.* **2017**, *27*, 57–64. [CrossRef]

33. Booth, C.J. The effects of longwall coal mining on overlying aquifers. *Geol. Soc.* **2002**, *198*, 17–45. [CrossRef]
34. Raghavendra, N.S.; Deka, P.C. Sustainable development and management of ground water resources in mining affected area: A review. *Procedia Earth Planet. Sci.* **2015**, *11*, 598–604. [CrossRef]
35. Robertson, J. Challenges in sustainably managing groundwater in the Australian Great Artesian Basin: Lessons from current and historic legislative regimes. *Hydrogeol. J.* **2020**, *28*, 343–360. [CrossRef]
36. Palchik, V. Formation of fractured zones in overburden due to longwall mining. *Environ. Geol.* **2003**, *44*, 28–38. [CrossRef]
37. Majdi, A.; Hassani, F.P.; Nasiri, M.Y. Prediction of the height of destressed zone above the mined panel roof in longwall coal mining. *Int. J. Coal Geol.* **2012**, *98*, 62–72. [CrossRef]
38. Adhikary, D.P.; Guo, H. Measurement of longwall mining induced strata permeability. *Geotech. Geol. Eng.* **2014**, *32*, 617–626. [CrossRef]
39. Adhikary, D.P.; Guo, H. Modelling of longwall mining-induced strata permeability change. *Rock Mech. Rock Eng.* **2015**, *48*, 345–359. [CrossRef]
40. Fan, L.M.; Ma, X.D. A review on investigation of water-preserved coal mining in western China. *Int. J. Coal Sci. Technol.* **2018**, *5*, 411–416. [CrossRef]
41. Fan, L.M.; Ma, L.Q.; Yu, Y.H.; Wang, S.K.; Xu, Y.J. Water-conserving mining influencing factors identification and weight determination in northwest China. *Int. J. Coal Sci. Technol.* **2019**, *6*, 95–101. [CrossRef]
42. Wang, G.; Wu, M.M.; Wang, R.; Xu, H.; Song, X. Height of the mining-induced fractured zone above a coal face. *Eng. Geol.* **2017**, *216*, 140–152. [CrossRef]
43. Liu, S.L.; Li, W.P.; Wang, Q.Q. Height of the water-flowing fractured zone of the jurassic coal seam in Northwestern China. *Mine Water Environ.* **2018**, *37*, 312–321. [CrossRef]
44. Guo, W.; Zou, Y.; Hou, Q. Fractured zone height of longwall mining and its effects on the overburden aquifers. *Int. J. Min. Sci. Technol.* **2012**, *22*, 603–606. [CrossRef]
45. Shi, L.Q.; Xin, H.Q.; Zhai, P.H.; Li, S.C.; Liu, T.B.; Yan, Y.; Wei, W.X. Calculating the height of water flowing fracture zone in deep mining. *J. Chin. Univ. Min. Technol.* **2012**, *41*, 37–41.
46. Liu, X.S.; Tan, Y.L.; Ning, J.G.; Tian, C.L.; Wang, J. The height of water-conducting fractured zones in longwall mining of shallow coal seams. *Geotech. Geol. Eng.* **2015**, *33*, 693–700. [CrossRef]
47. Liu, Y.; Yuan, S.C.; Yang, B.B.; Liu, J.W.; Ye, Z.Y. Predicting the height of the water-conducting fractured zone using multiple regression analysis and GIS. *Environ. Earth Sci.* **2019**, *78*, 422. [CrossRef]
48. Wang, H.Z.; Zhang, D.S.; Wang, X.F.; Zhang, W. Visual exploration of the spatiotemporal evolution law of overburden failure and mining-induced fractures: A case study of the Wangjialing coal mine in China. *Miner. Basel* **2017**, *7*, 35. [CrossRef]
49. Wu, W.D.; Bai, J.B.; Wang, X.Y.; Zhu, Z.J.; Yan, S. Field investigation of fractures evolution in overlying strata caused by extraction of the jurassic and carboniferous coal seams and its application: Case study. *Int. J. Coal Geol.* **2019**, *208*, 12–23. [CrossRef]
50. Huang, Q.; Han, J.B. Study on fracture evolution mechanism of shallow-buried close coal seam mining. *J. Min. Safe. Eng.* **2019**, *36*, 706–711.
51. Huang, Q.; Du, J.W.; Hou, E.K.; Yang, F. Research on overburden and ground surface cracks distribution and formation mechanism in shallow coal seams group mining. *J. Min. Safe Eng.* **2019**, *36*, 7–15.
52. Miao, X.X.; Cui, X.M.; Wang, J.N.; Xu, J.L. The height of fractured water-conducting zone in undermined rock strata. *Eng. Geol.* **2011**, *120*, 32–39. [CrossRef]
53. Zhang, Y.X.; Tu, S.H.; Bai, Q.S.; Li, J.J. Overburden fracture evolution laws and water-controlling technologies in mining very thick coal seam under water-rich roof. *Int. J. Min. Sci. Technol.* **2013**, *23*, 693–700. [CrossRef]
54. Wang, F.; Xu, J.L.; Chen, S.J.; Ren, M.Z. Method to predict the height of the water conducting fractured zone based on bearing structures in the overlying strata. *Mine Water Environ.* **2019**, *38*, 767–779. [CrossRef]
55. Wang, F.; Xu, J.L.; Xie, J.L. Effects of arch structure in unconsolidated layers on fracture and failure of overlying strata. *Int. J. Rock Mech. Min. Sci.* **2019**, *114*, 141–152. [CrossRef]
56. Bai, H.Y.; Li, W.P.; Chen, X.J.; Huang, X. Development rules of water flowing and fracture zone at deep buried soil-rock interface during mining. *J. Eng. Geol.* **2017**, *25*, 1322–1327.
57. Liu, Y.; Liu, Q.M.; Li, W.P.; Li, T.; He, J.H. Height of water-conducting fractured zone in coal mining in the soil-rock composite structure overburdens. *Environ. Earth Sci.* **2019**, *78*, 242. [CrossRef]
58. Zhang, J.X.; Jiang, H.Q.; Deng, X.J.; Ju, F. Prediction of the height of the water-conducting zone above the mined panel in solid backfill mining. *Mine Water Environ.* **2014**, *33*, 317–326. [CrossRef]
59. Li, L.; Li, F.M.; Zhang, Y.; Yang, D.M.; Liu, X. Formation mechanism and height calculation of the caved zone and water-conducting fracture zone in solid backfill mining. *Int. J. Coal Sci. Technol.* **2020**, *7*, 208–215. [CrossRef]
60. Zhao, B.C.; Liu, Z.R.; Tong, C.; Wang, C.L. Relation between height of water flowing fractured zone and mining parameters. *J. Min. Safe Eng.* **2015**, *32*, 634–638.
61. Guo, W.B.; Zhao, G.B.; Lou, G.; Wang, S. A new method of predicting the height of the fractured water-conducting zone due to high-intensity longwall coal mining in China. *Rock Mech. Rock Eng.* **2019**, *52*, 2789–2802. [CrossRef]
62. Wu, Q.; Shen, J.J.; Liu, W.T.; Wang, Y. A RBFNN-based method for the prediction of the developed height of a water-conductive fractured zone for fully mechanized mining with sublevel caving. *Arab. J. Geosci.* **2017**, *10*, 172. [CrossRef]

63. Hu, X.J.; Li, W.P.; Cao, D.T.; Liu, M.C. Index of multiple factors and expected height of fully mechanized water flowing fractured zone. *J. China Coal Soc.* **2012**, 37, 613–620.
64. Wang, F.T.; Tu, S.H.; Zhang, C.; Zhang, Y.W.; Bai, Q.S. Evolution mechanism of water-flowing zones and control technology for longwall mining in shallow coal seams beneath gully topography. *Environ. Earth Sci.* **2016**, 75, 1309. [CrossRef]
65. Xu, Z.M.; Sun, Y.J.; Dong, Q.H.; Zhang, G.W.; Li, S. Predicting the height of water-flow fractured zone during coal mining under the Xiaolangdi reservoir. *Int. J. Min. Sci. Technol.* **2010**, 20, 434–438. [CrossRef]
66. Zhang, Y.; Cao, S.G.; Guo, S.; Wan, T.; Wang, J.J. Mechanisms of the development of water-conducting fracture zone in overlying strata during shortwall block backfill mining: A case study in Northwestern China. *Environ. Earth Sci.* **2018**, 77, 543. [CrossRef]
67. Deng, X.J.; Zhang, J.X.; Zhou, N.; de Wit, B.; Wang, C.T. Upward slicing longwall-roadway cemented backfilling technology for mining an extra-thick coal seam located under aquifers: A case study. *Environ. Earth Sci.* **2017**, 76, 789. [CrossRef]
68. Deng, X.J.; Yuan, Z.X.; Lan, L.X.; de Wit, B.; Zhang, J.W. Roof Movement and Failure Behavior When Mining Extra-Thick Coal Seams Using Upward Slicing Longwall-Roadway Cemented Backfill Technology. *Adv. Mater. Sci. Eng.* **2020**, 2020, 5828514. [CrossRef]
69. Hou, E.K.; Wen, Q.; Ye, Z.N.; Chen, W.; Wei, J.B. Height prediction of water-flowing fracture zone with a genetic-algorithm support-vector-machine method. *Int. J. Coal Sci. Technol.* **2020**, 7, 740–751. [CrossRef]
70. Lian, X.G.; Hu, H.F.; Li, T.; Hu, D.S. Main geological and mining factors affecting ground cracks induced by underground coal mining in Shanxi Province, China. *Int. J. Coal Sci. Technol.* **2020**, 7, 362–370. [CrossRef]
71. Sun, Q.; Zhang, J.X.; Zhou, N.; Qi, W.Y. Roadway backfill coal mining to preserve surface water in western China. *Mine Water Environ.* **2018**, 37, 366–375. [CrossRef]
72. El-Magd, S.A.A.; Eldosouky, A.M. An improved approach for predicting the groundwater potentiality in the low desert lands; El-Marashda area, Northwest Qena City, Egypt. *J. Afr. Earth Sci.* **2021**, 179, 104200. [CrossRef]
73. Masoud, A.M.; Pham, Q.B.; Alezabawy, A.K.; El-Magd, S.A.A. Efficiency of geospatial technology and multi-criteria decision analysis for groundwater potential mapping in a Semi-Arid region. *Water* **2022**, 14, 882. [CrossRef]
74. Saranya, T.; Saravanan, S. Groundwater potential zone mapping using analytical hierarchy process (AHP) and GIS for Kancheep-uram District, Tamilnadu, India. *Model. Earth Syst. Env.* **2020**, 6, 1105–1122. [CrossRef]
75. Razandi, Y.; Pourghasemi, H.R.; Neisani, N.S.; Rahmati, O. Application of analytical hierarchy process, frequency ratio, and certainty factor models for groundwater potential mapping using GIS. *Earth Sci. Inform.* **2015**, 8, 867–883. [CrossRef]
76. Rahmati, O.; Nazari, S.A.; Mahdavi, M.; Pourghasemi, H.R.; Zeinivand, H. Groundwater potential mapping at Kurdistan region of Iran using analytic hierarchy process and GIS. *Arab. J. Geosci.* **2015**, 8, 7059–7071. [CrossRef]
77. Jothibasu, A.; Anbazhagan, S. Modeling groundwater probability index in Ponnaiyar River basin of South India using analytic hierarchy process. *Model. Earth Syst. Environ.* **2016**, 2, 1–14. [CrossRef]
78. Sandoval, J.A.; Tiburan, J.C.L. Identification of potential artificial groundwater recharge sites in Mount Makiling Forest Reserve, Philippines using GIS and Analytical Hierarchy Process. *Appl. Geogr.* **2019**, 105, 73–85. [CrossRef]
79. Murmu, P.; Kumar, M.; Lal, D.; Sonkerb, I.; Singhc, S.K. Delineation of groundwater potential zones using geospatial techniques and analytical hierarchy process in Dumka district, Jharkhand, India. *Groundw. Sustain. Dev.* **2019**, 9, 100239. [CrossRef]
80. Ghosh, D.; Mandal, M.; Banerjee, M.; Karmakar, M. Impact of hydro-geological environment on availability of groundwater using analytical hierarchy process (AHP) and geospatial techniques: A study from the upper Kangsabati river basin. *Groundw. Sustain. Dev.* **2020**, 11, 100419. [CrossRef]
81. Hao, Y.; Herong, G.; Honghai, Z.; Meichen, W.; Jun, L.; Hongxia, F.; Yaqi, J.; Yaru, Z. Hydrochemical characteristics and water quality evaluation of shallow groundwater in Suxian mining area, Huaibei coalfield, China. *Int. J. Coal Sci. Technol.* **2020**, 7, 825–835.
82. Hui, Y.; Housheng, J.; Shaowei, L.; Zhihe, L.; Baoyu, L. Macro and micro grouting process and the influence mechanism of cracks in soft coal seam. *Int. J. Coal Sci. Technol.* **2021**, 8, 969–982.
83. Jun, W.; Jingxuan, Y.; Fengfeng, W.; Tengfei, H.; al Shams, F. Analysis of fracture mechanism for surrounding rock hole based on water-filled blasting. *Int. J. Coal Sci. Technol.* **2020**, 7, 704–713.
84. Rui, G.; Tiejun, K.; Yanqun, Z.; Wenyang, Z.; Chunyang, Q. Controlling mine pressure by subjecting high-level hard rock strata to ground fracturing. *Int. J. Coal Sci. Technol.* **2021**, 8, 1336–1350.
85. Chengxiao, L.; Dongming, G.; Yuantong, Z.; Chen, A. Compound-mode crack propagation law of PMMA semicircular-arch roadway specimens under impact loading. *Int. J. Coal Sci. Technol.* **2021**, 8, 1302–1315.
86. Rui, W.; Penghui, Z.; Kulatilake, P.H.S.W.; Hao, L.; Qingyuan, H. Stress and deformation analysis of gob-side pre-backfill driving procedure of longwall mining: A case study. *Int. J. Coal Sci. Technol.* **2021**, 8, 1351–1370.
87. Jinfu, L.; Fuqiang, G.; Jinghe, Y.; Yanfang, R.; Jianzhong, L.; Xiaoqing, W.; Lei, Y. Characteristics of evolution of mining-induced stress field in the longwall panel: Insights from physical modeling. *Int. J. Coal Sci. Technol.* **2021**, 8, 938–955.
88. André, V. Various phases in surface movements linked to deep coal longwall mining: From start-up till the period after closure. *Int. J. Coal Sci. Technol.* **2021**, 8, 412–426.
89. Xiaolou, C.; Ke, Y.; Zhen, W. Breaking and mining-induced stress evolution of overlying strata in the working face of a steeply dipping coal seam. *Int. J. Coal Sci. Technol.* **2021**, 8, 614–625.

90. Xu, Y.J.; Ma, L.Q.; Yu, Y.H. Water preservation and conservation above coal mines using an innovative approach: A case study. *Energies* **2020**, *13*, 2818. [CrossRef]
91. Xu, Y.J.; Ma, L.Q.; Ngo, I.H.; Zhai, J.T. Continuous extraction and continuous backfill mining method using carbon dioxide mineralized filling body to preserve shallow water in Northwest China. *Energies* **2022**, *15*, 3614. [CrossRef]

Multicomponent Transient Electromagnetic Exploration Technology and Its Application

Xingchun Wang [1,2,*], **Qingquan Zhi** [1,2,*], **Junjie Wu** [1,2], **Xiaohong Deng** [1,2], **Yue Huang** [1,2], **Qi'an Yang** [3] **and Jinhai Wang** [4]

[1] Institute of Geophysical and Geochemical Exploration, Chinese Academy of Geological Sciences, Langfang 065000, China; wjj498211@126.com (J.W.); dengxiaohong@mail.cgs.gov.cn (X.D.); huangyue@mail.cgs.gov.cn (Y.H.)

[2] Laboratory of Geophysical EM Probing Technologies, Ministry of Natural Resources, Langfang 065000, China

[3] Qinghai No. 5 Geological and Mineral Exploration Institute, Xining 810013, China; wkyyqa@163.com

[4] Qinghai No. 3 Geological and Mineral Exploration Institute, Xining 810008, China; huzi115@163.com

* Correspondence: wxingchun@mail.cgs.gov.cn (X.W.); zhiqingquan@gmail.com (Q.Z.)

Abstract: To take full advantage of the multicomponent transient electromagnetic method, we summarize the advantages of multicomponent exploration based on simulation calculation. We have carried out experiments on the effectiveness of the method in the known copper-nickel mining area. The results show that the characteristic curve of the horizontal component can effectively point to the central direction of the low-resistivity ore body and reflect the occurrence of the ore body. The degree of coupling between the vertical component and the ore body is high, which is beneficial for quantitative inversion. The results for the horizontal component and vertical component interpretations are consistent, which reduces the limitation of conventional single vertical component interpretation and effectively improves the work efficiency in field work.

Keywords: transient electromagnetic method; multicomponent; zero contour; directivity; occurrence; copper-nickel deposit

1. Introduction

In recent decades, the vertical component of the transient electromagnetic method (TDEM) has been a research focus because of its easy measurement, high signal-to-noise ratio, easy inversion, and easy interpretation [1–7]. However, the horizontal-component (HC) signal is weak, and the signal-to-noise ratio is low, which makes its interpretation relatively slow. With the emergence of a three-component (3C) TDEM system, research on 3C interpretation technology has become popular, including ground and borehole TDEM [8–15]. Some scholars have simulated the multicomponent aspects of the fixed loop, analyzed HC characteristics with various occurrences of plate, and made interpretations in combination with the geological section. These studies have shown that the HC information is helpful for interpreting anomalies; however, the researchers only made single-profile analyses [16,17]. Jintao Liu has analyzed the advantages of multicomponent interpretation and has obtained good results from the field data measured in a hydrogeological survey [18]. Zihao Han has calculated the different components of TDEM. The results show that the HC is more sensitive to the low-resistivity body than the verticals; however, the author provided only predictive suggestions without further analysis [19]. Shaocong Tan has illustrated the superiority of the multicomponent interpretation by defining the characteristic function of the ratio vertically and horizontally [20]. By changing the relative position between the transmitter loop and the plate, Wang has carried out a 3C simulation of the fixed loop. The results show that the combination of HC information is helpful in determining the ground projection center and the attitude of the plate [21]. Zonge and Carlson have discussed the role of multiple components in pipeline detection, and their research results have shown

that HC can identify the cables underground that vertical components cannot [22,23]. Chen has made a multicomponent simulation, and the results show that multicomponent data is superior to a single component in the judgment of conductor direction and position, especially in the detection of unknown explosives [24].

By changing the size and orientation of the plate in the homogeneous half-space, we carried out 3C forward simulation of fixed loop and found that the variation characteristics of the HC zero contour were closely related to the orientation and center of the plate. For fixed-loop devices, we know that a rectangular loop has two symmetric axes, and we generally define the direction of the X component parallel to the field line, so thatthe zero contour of the X component is approximately perpendicular to the field line.

The HC profile of a fixed loop always has a zero point, when the medium subsurface is a homogeneous half-space or layered medium. The zero-value point is on the axis of symmetry; otherwise, the zero-value point of the X component will deviate from the axis of symmetry of the transmitting loop. As shown in Figure 1, the size of the transmitting loop is 500 m × 900 m, and 5 lines are arranged symmetrically in the loop with a distance of 100 m; the length of line is 800 m. The line is L0, L100, L200, L300, and L400 from south to north. L200 coincides with the east-west symmetry axis of the transmitting loop.
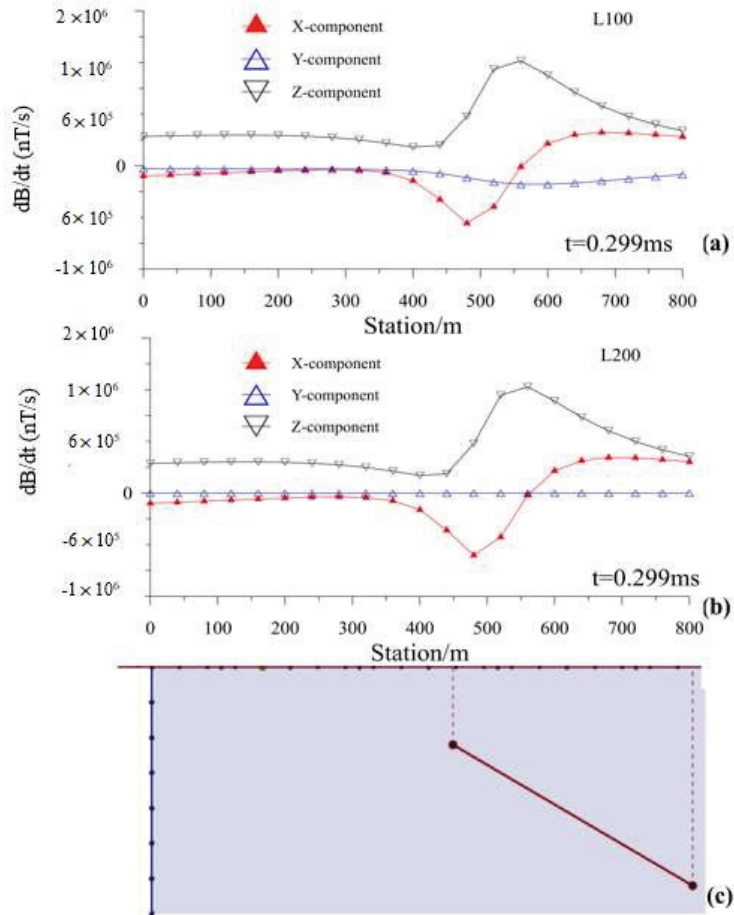
Figure 1. Characteristic curves of 3C TDEM simulation on profile L100 (**a**) and profile L200 (**b**) at sampling time 0.299 ms with the forward resistivity model (**c**).

Figure 1a,b exhibit the 3C profiles for L100 and L200, respectively. Figure 1c shows the forward resistivity model. It is a homogeneous half-space with resistivity of 800 Ω·m. The size of the plate inside the model is 400 m × 400 m, with conductivity of 20 S. The coordinates of the top center of the plate are (480, 200, −65), and the plate inclines 30 degrees toward the east. As shown in Figure 1a,b, the Z-components show apparently positive features, while the X-components cross the zeros. The Y-components show negative anomalies for profile L100 but show near zeros for L200 because of the symmetry.

When there are many lines in the loop, the zero-value points of all the lines form a curve, which is called the zero-contour line, and it coincides with the axis of symmetry when subsurface medium is a homogeneous half-space or layered medium [25].

In this paper, we performed multicomponent-3D-forward modeling of the fixed loop for plates with different sizes (relative to the transmitting loop) and summarize its rules. We then made an analysis of the multicomponent TDEM data collected from a copper-nickel ore deposit. The results show that multicomponent data analysis is superior to single-component data in determining the central location and occurrence of ore bodies. In addition, the qualitative interpretation of the HC is consistent with the quantitative inversion of the vertical component.

2. Forward Modelling

2.1. Multicomponent Response Characteristics of a Small, Inclined plate

When the medium underground does not satisfy the one-dimensional assumption, the HC is no longer equal to zero, and the central and occurrence of the low-resistivity body subsurface can be inferred. Figure 2a shows a 3D forward model of an eastward-inclined plate in a homogeneous half-space. The parameters were as follows: line spacing 100 m in the east-west direction, field line length 900 m, station spacing 50 m, Crone 50 ms standard sampling channel selected, ramp 1 ms, transmitter loop size 1000 m × 1000 m, transmitter current 20 A, homogeneous half-space resistivity was 600 Ω·m, plate size 400 m × 200 m, plate conductivity 100 S, buried plate depth 175 m, and plate incline to the east 35 degrees. We received the data in a loop, and the stations started from point 50 and ended at 950 (Figure 2b). The large red loop was the transmitter loop, and the inner light green loop was the projection of the inclined plate on the ground.
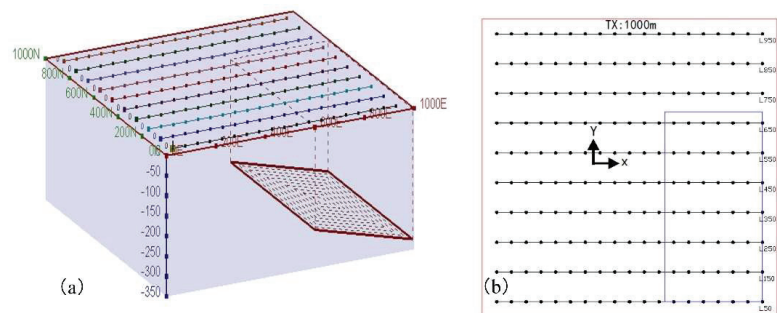
Figure 2. 3D forward model of the fixed loop: (**a**) 3D forward model, (**b**) plan for 3D model.

Figure 3 shows the relationship between the Z-component contour and the HC zero contour with different delays. In Figure 3, the black dotted line is the X component's zero contour, the blue line is the Y component's zero contour, the background is the Z-component's contour map, and the red, dotted rectangle is the projection of the plate. With sampling time increasing, the abnormal center of the Z component gradually approached the center of the surface projection until they coincided. We also found that in the early period, the position of the HC's zero contour was close to the axis of symmetry for the transmitting loop. With increasing sampling time, the HT's zero contour gradually deviated from the axis of symmetry due to the existence of the plate, and their intersection gradually

moved closer to the center of the surface projection. The variation trend of the characteristic curve of the HC and the anomaly center of the Z component pointed to the anomaly center. This indicated that the HC had directivity, but we could not judge whether the plate was inclined or not.
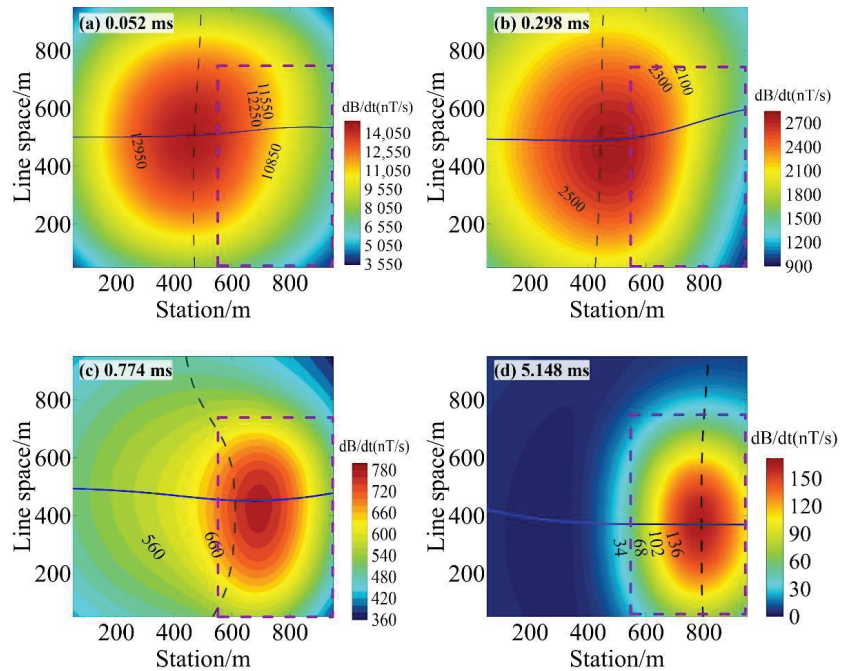
Figure 3. Three-component feature synthesis map with different sampling times (inclined plate): (**a**) 0.052 ms; (**b**) 0.298 ms; (**c**) 0.774 ms; (**d**) 5.148 ms.

2.2. Multicomponent Response Characteristics of a Big, Inclined Plate

In field work, we rarely know the distribution characteristics of the ore body; the transmitter loop and the ore body cannot be well coupled. Therefore, we designed the model shown in Figure 4 to illustrate the advantages of HC.

The model parameters are as follows: the size of transmitter loop is 800 m × 900 m, and eight east-west lines are arranged symmetrically in the loop; line space is 100 m; and its length is 800 m. It is a homogeneous half-space with resistivity of 1000 Ω·m. The size of the plate inside the model is 300 m × 800 m, with conductivity of 30 S. The coordinates of the top center of the plate are (−560, 355, −40). It inclines 25 degrees toward the east.

Figure 4a is a 3D diagram, and Figure 3b is a plane-relative position diagram of the plate and the zero contour of the X-component with different delays.

As shown in Figure 3b, the dashed quadrilateral is the projection of the plate on the ground; with increasing sampling time, the X-component zero contour gradually moves westward and points to the projection center of the plate. We have completed the simulation for X component, and this characteristic also applies to the Y component, and their intersection must point to the projection center of the plate. Figure 5 is the Z-component contour map with different sampling delays. With increasing sampling time, the anomaly center of the Z component gradually approached the projection center of the plate.
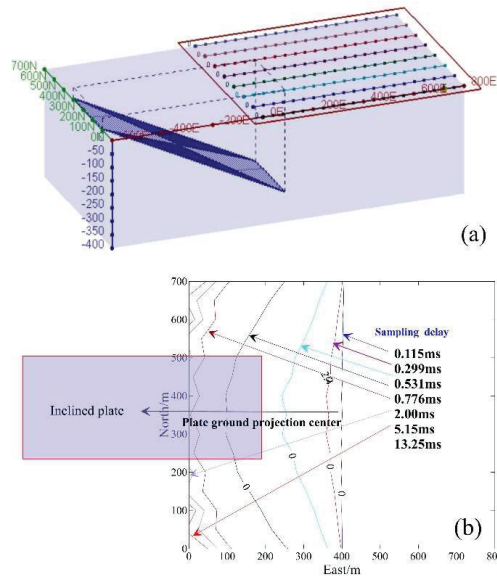
Figure 4. 3D forward models for fixed-loop and X-component characteristic curves: (**a**) 3D forward model; (**b**) relative position of the plate and the X-component zero contour.
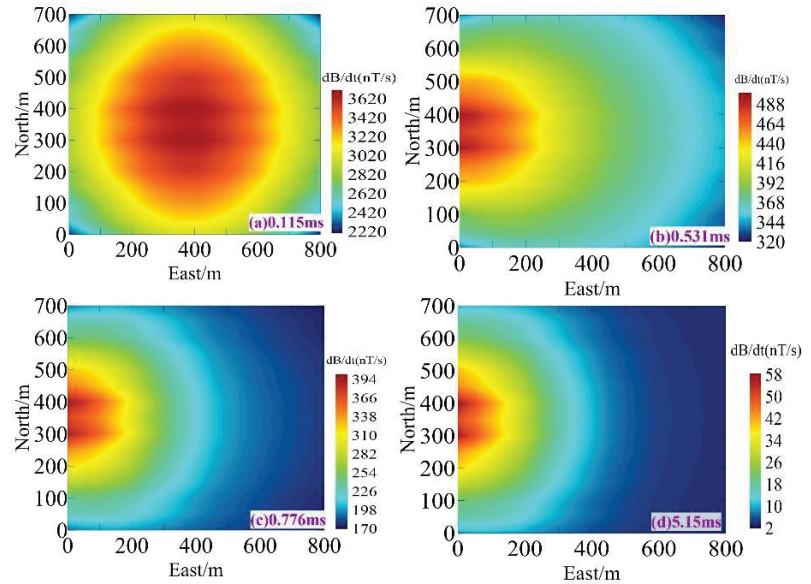
Figure 5. Three-component feature synthesis maps with different sampling times: (**a**) 0.115 ms; (**b**) 0.531 ms; (**c**) 0.776 ms; (**d**) 5.15 ms.

Combining the results of Figures 4b and 5, we find that the HC's zero contour helps determine the low-resistance ore body's center. The zero contour of the X component moved west, contrary to the eastward dip direction of the plate set in the previous. We can infer the plate's inclination according to the variations in the HC zero contour. It also shows that after the ore-body positioning is determined by 3C TDEM, the later work can

be carried out in a targeted manner, which is conducive to improving the efficiency of field work.

2.3. Analysis of Forward Modeling Results

The functions of the X component and the Y component are equivalent. That the direction of the survey line is the same as that of the X component is a constructed factor. According to the relative size and inclination angle of the plate and the coupling degree between the transmitter loop and the plate, we have completed the corresponding forward calculation. It turned out that the changes in parameters, such as the relative size, inclination angle, and position of the subsurface plate relative to the transmitting loop led to changes in the position of the HC zero contour, and the corresponding vertical-component-plane-anomaly center also changed. Interpretation of multicomponent TDEM data can predict the dips and center positions of ore bodies underground.

3. Multicomponent Transient Electromagnetic Method Tests in Copper-Nickel Ore

This copper-nickel deposit is found in the hinterland of east Kunlun with a higher degree of exploration. TDEM was listed as one of the main methods according to the requirements and objectives of the validity test of geophysical methods. According to the orebody distribution characteristics, we completed forward modeling and finally selected the fixed-source 3C measurement method.

3.1. Geological Setting

The survey area is on the northern slope of the western section of east Kunlun and the southern margin of the Qaidam Basin. The tectonic units belong to the east Kunlun arc basin system of the Qin-Qi-Kun orogenic system (Figure 6). The tectonic pattern of the arc basin system is relatively clear, and the main orogenic period is Caledonian [26].
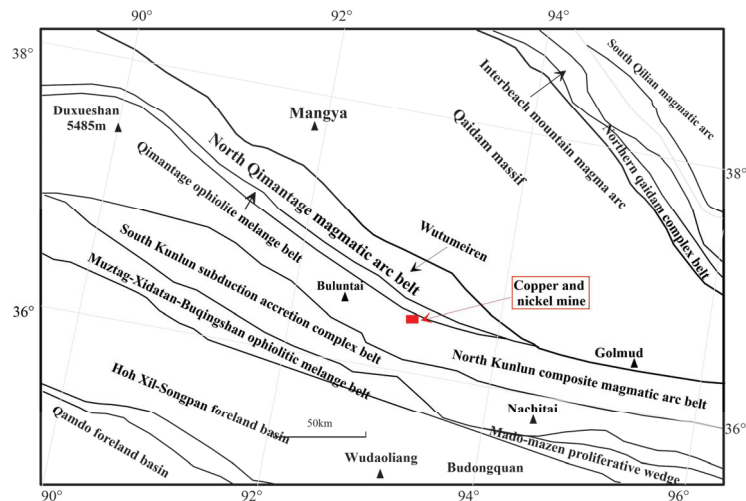
Figure 6. Regional structure map of the Cu-Ni mining study area.

The deposit is a magmatic molten copper-nickel sulfide deposit. The nickel ore occurs in peridotite and pyroxenite. It is hidden under the Jinshuikou group in the section. The rock comprises pyroxenite, peridotite, oligoclase, and gabbro. The ore-bearing lithology is mainly dihedral peridotite and pyroxenite. The ore minerals are mainly chalcopyrite, nickel pyrite, magnetite, and pyrrhotite [27,28].

Most ore bodies occur in layered form, and the upper part is mainly disseminated and massive ore, while the middle and lower part are mainly densely disseminated and dense

massive ore. A few ore bodies are lenticular and funnel-shaped in the upper part of the rock mass, forming overhanging ore bodies, or are banded in the rock mass.

The measurement results of the physical properties of rocks show that the ore rock in the area has the characteristics of "low resistivity, high polarization, high magnetism, and high density." In this area, gravity, magnetic, electromagnetic, and other geophysical work have been carried out, effectively delineating the boundaries of ore-bearing rock mass. On the geophysical characteristic parameters of the surrounding rock and ore bearing in the Cu-Ni mining area, we found that the profiles' distribution characteristics of resistivity, polarization, and magnetic susceptibility objectively reflected the occurrence characteristics of ore bodies [29,30].

3.2. Method and Technique

Due to the steep terrain, we selected a fixed loop for data acquisition and the Pulse-EM system produced by the Crone Company of Canada for receiving and transmitting. The system is equipped with a rod core probe that can realize HC data acquisition when adjusted to horizontal state; the sensor is 58 mm in length and 63 mm in diameter, and its effective area is 3850 square meters.

The geologic profile was in a north-south direction with a drilling distance of 80 m. The direction of the three components followed the right-hand rule, in which the positive direction of the X component is consistent with the northwest direction of the survey line; the positive direction of the Y component is the southwest direction, perpendicular to the survey line; and the Z component is vertically upward. According to terrain conditions and other factors, we arranged a 600 m × 600 m transmitting loop on the ground, as shown in Figure 7. The green rectangle is the transmitting loop. According to the field test results and the geological profile position, the main parameters were as follows: the transmitting current was 15 A, the time base was 50 ms, the line distance was 80 m, the station distance was 50 m, and the 3C survey lines from east to west were Lines 9, 11, 13, 15, and 17. Due to the steep terrain, we abandoned some points during collection.

All the red exploration points in Figure 7 are ore-seeing boreholes. According to the differences in ore body occurrence, we chose to lay the transmitting loop on the north side of exploration Lines 9–17. We collected the data of 3C inside and outside the transmitting loop. Due to the limitations of interpretation technology, we only studied the data inside the transmitting loop.

Figure 7. Geological map and TDEM test area.

3.3. Processing and Explanation

Figure 8 shows the Z-component contour and the corresponding HC zero contour with different delays. The black dotted and blue lines are the zero-contour curves of the X and Y components, respectively. According to the previous results, this corresponds to the second model, where the low resistance body underground is significantly larger than the transmitting loop.

Figure 8. Three-component feature synthesis maps with different sampling times: (**a**) 0.052 ms; (**b**) 0.114 ms; (**c**) 0.298 ms; (**d**) 0.774 ms; (**e**) 2 ms; (**f**) 5.148 ms.

When we increased the sampling time, the Z-component anomaly center gradually shifted from the early scattered anomalies to the southeast direction. This outcome shows that the anomalous bodies underground are scattered in shallow areas, while in the deep areas, they are mainly concentrated in the southeast of the transmitter loop, and the position of the HC zero contour gradually moves to the southwest until it becomes stable. Compared with the transmitter loop's symmetry axis, the X component's zero contour obviously moves southward, and the Y component's zero contour obviously shifts to the east. This phenomenon indicates that the low-resistivity body underground has the characteristic of sloping northward and westward. According to the geological data, we found that the ore body inclines obviously to the west, and the north side is suddenly pinched out.

The intersection of the HC zero contour and the abnormal center of the vertical component point to the southeast of the transmitting loop, which indicates this is the center of a low-resistivity body underground.

3.4. Z-Component Quantitative Inversion

Professional TDEM software (Maxwell) was used to invert and interpret the Z-component data. Before inversion, we preprocessed the data, such as late-sampling channel interception according to noise level and appropriate filtering. According to the petrophysical measurements and borehole core logging results, the initial model of transient electromagnetic inversion is set to a layered model. One-dimensional inversion was carried out using the Beowulf module of Maxwell. Two-dimensional and three-dimensional interpolation were carried out for one-dimensional inversion data, which were displayed in two-dimensional (2D) section and three-dimensional (3D) volume, respectively, and the 2D section was compared with the existing geological section to verify the effectiveness of the method.

3.4.1. Section Inversion Interpretation and Comparison

Figure 9 shows the comparison of the TDEM-inverted resistivity sections and the geological profiles of Lines 11 and 17. The geological section shows that the thickness of ore-bearing rock mass in Line 11 is larger than that of Line 17, and both are inclined in the northwest direction. The buried depth of the ore body in Line 17 is larger, and the maximum buried depth is approximately 420 m. Compared with that of Line 11, the top interface of the ore body of Line 17 is approximately 100 m lower than that of Line 11, indicating that the ore body gradually decreases from east to west. The resistivity-inversion section shows that the two survey lines have obvious northwest inclination. The thickness and buried depth of the low-resistivity area on the inversion section can objectively reflect the occurrence characteristics of the ore bodies.
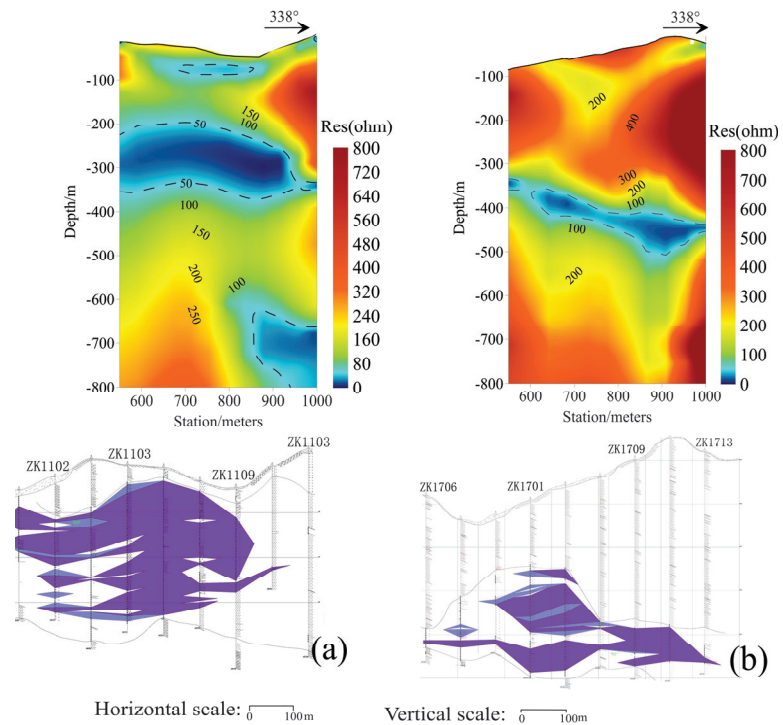
Figure 9. Resistivity-inversion section and geology sections for L11 and L17: (**a**) L11; (**b**) L17.

3.4.2. Three-Dimensional Geoelectric Model Analysis

Combined with the continuity of ore-bearing rock mass in the geological section and the TDEM-inversion results, we constructed a 3D geoelectric model in the transmitting loop. The 3D isosurface with resistivity of about 50 Ω•m can reflect the 3D spatial distribution characteristics of ore bodies, as shown in Figure 10. The lower part is a 3D geoelectric model, and the upper part is a 3C characteristic diagram when the sampling delay is 0.774 ms. The 3D geoelectric model has an obvious southwest tendency, and the thickest and shallowest area coincides with the high anomaly center of the vertical component and the position of the HC-zero-contour intersection. This is consistent with the forward modeling results of the second model. The qualitative interpretation results of the HC and the quantitative interpretation results of the vertical component confirm each other. The quantitative inversion results are consistent with the spatial distribution pattern of the ore-bearing rock mass, showing that the multicomponent joint interpretation is more reliable than the traditional single-component interpretation.
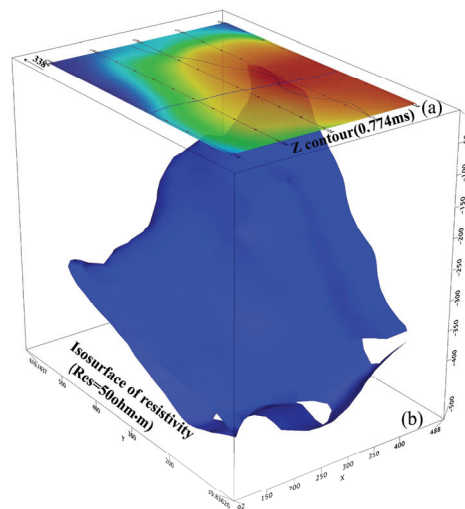
Figure 10. A 3D geoelectric model and multicomponent response characteristic diagram. (**a**) multicomponent response characteristic diagram at 0.774 ms; (**b**) 3D geoelectric model.

4. Conclusions

The terrain in the area for this study is very undulating, and the inversion work is carried out based on co-surface receiving and transmitting; there is a certain error in the inversion depth, but it does not affect the explanation of the problem. Through the inversion and interpretation of the simulated and field data, the multicomponent TDEM interpretation technique has the following advantages:

(1) Similar to the vertical component, the change trend of the zero-contour intersection of HC is directional, and its movement direction always points to the center of the ore body projected on the ground. This inspired us to quickly determine the anomaly center orientation through a 3C line in field work, which substantially reduced the cost of field data acquisition.

(2) Under certain conditions, the tendency of the ore body can be judged according to the variation characteristics of the HC 's zero contour.

(3) Multicomponent combined analysis overcomes the limitation of traditional vertical component interpretation and improves the reliability of interpretation results.

References

1. El-Kaliouby, H. Groundwater prospecting in a hard-rock coastal area using off-set TDEM method: Case study. In *SEG Technical Program Expanded Abstracts*; Society of Exploration Geophysicists: San Antonio, TX, USA, 2019; pp. 2755–2758.
2. Srigutomo, W.; Warsa, W.; Sule, R.T.; Widarto, D.S. Time-Domain Electromagnetic (TDEM) Baseline Survey for CCS in Gundih Area. In Proceedings of the 12th SEGJ International Symposium, Tokyo, Japan, 18–20 November 2015; pp. 1–6.
3. Wang, X.C.; Deng, X.H.; Chen, X.D.; Zhang, J.; Wu, J.J.; Zhi, Q.Q.; Yang, Y. Application Effect of TEM Based on High Temperature Superconducting Sensor in Qingchengzi Ore-Concentrated Area. *Earth Sci.* **2021**, *46*, 1871–1880. [CrossRef]
4. Singh, N.P.; Mogi, T. Electromagnetic response of a large circular loop source on a layered earth: A new computation method. *Pure Appl. Geophys* **2005**, *162*, 181–200. [CrossRef]
5. Al-Salmi, H.A.; El-Kaliouby, H. Application of Time-Domain Electromagnetic method in Mapping Sea water intrusion in Al-Batinah Coastal plain, Al Batinah, Sultant of Oman. In Proceedings of the International Conference on Engineering Geophysics, Al Ain, United Arab Emirates, 15–18 November 2015. pp. 1–6. [CrossRef]
6. Juillard, J.; Barmon, B.D.; Berthiau, G. A simple analytical 3D eddy current model. *IEEE Trans. Magn.* **2000**, *36*, 258–266. [CrossRef]
7. An, D. Research of Three-Component Transient Electromagnetic Response. Ph.D. Thesis, Jilin University, Changchun, China, 2009.
8. Jiang, B.Y. *Practical Near-Field Magnetic Transient Electromagnetic Survey*; Geological Press: Beijing, China, 1998; pp. 199–236.
9. Niu, Z.L. *The Principle of Time Domain Electromagnetic Method*; Central South University Press: Changsha, China, 2007; pp. 249–266.
10. Xue, G.Q.; Li, X.; Di, Q.Y. Progress in research on forward and inverse problems of transient electromagnetic method. *Prog. Geophys.* **2008**, *23*, 1165–1172. [CrossRef]
11. Qi, Z.P. Research on Multi-Component Interpretation Technology of Transient Electromagnetic. Ph.D. Thesis, Chang'an University, Xi'an, China, 2009.
12. Qi, Z.P.; Zhi, Q.Q.; Li, X.; Zeng, Y.Q.; Zhang, Y.Y. Three-component global apparent resistivity definition and three-component joint inversion of large-scale source transient electromagnetic. *Geophys. Geochem. Explor.* **2014**, *38*, 742–749. [CrossRef]
13. Yang, H.J.; Pan, H.P.; Luo, M.; Meng, Q. Numerical Modeling for Transient Anomalous Secondary Electromagnetic of Tabular Orebody in Borehole. *Earth Sci.* **2015**, *24*, 1689–1700. [CrossRef]
14. Lv, G.Y. Current Situation and Development Trend of Transient Electromagnetic Method. *Comput. Tech. Geophys. Geochem. Explor.* **2007**, *29*, 111–115.
15. Zhou, N.N.; Xue, G.Q.; Li, H. Distinguishing ability to thin layer of loop-source TEM horizontal components. *Prog. Geophys.* **2014**, *29*, 2347–2355. [CrossRef]
16. Xi, Z.Z.; Liu, J.; Long, X.; Hou, H.T. Study on three-component measurement method based on transient electromagnetic method. *J. Cent. South Univ.* **2010**, *41*, 272–276. [CrossRef]
17. Liu, J. Research on Three-Component Measurement Using Transient Electromagnetic Method. Ph.D. Thesis, Central South University, Changsha, China, 2009.
18. Liu, J.T.; Gu, H.M.; Hu, X.Y. Analysis of Three-component Interpretation of Transient Electromagnetic Method. *Yangtze River* **2008**, *39*, 114–116. [CrossRef]
19. Han, Z.H. Horizontal Components Response and its Application of Magnetic Sources Transient Electromagnetic Method. Ph.D. Thesis, China University of Geosciences (Beijing), Beijing, China, 2009.
20. Tan, S.C.; Wang, H.; Xia, Z.H.; Zhou, S. The three-component joint processing and interpretation of transient electromagnetic method. *Chin. J. Nonferrous Met.* **2012**, *22*, 909–914. [CrossRef]
21. Wang, X.C.; Zheng, X.P.; Deng, X.H.; Zhang, J.; Wu, J.J.; Zhi, Q.Q.; Yang, Q.A. The characteristics of horizontal components in fixed source loops and its application. *Geophys. Geochem. Explor.* **2016**, *40*, 1166–1172.
22. Carlson, N.R.; Zonge, K.L. The utility of horizontal component measurements in random-walk TEM surveys. In *Environment and Engineering Geophysical Society*; Environmental & Engineering Geophysical Society: Denver, CO, USA, 2003; pp. 523–532. [CrossRef]
23. Carlson, N.R.; Zonge, K.L. Early-time, multi-Component mobile TEM for Deep metal detection. In Proceedings of the 15th EEGS Symposium on the Application of Geophysics to Engineering and Environmental Problems, Las Vegas, NV, USA, 10–14 February, 2002. pp. 1–11. [CrossRef]

24. Chen, C.S.; Chiu, W.H.; Lin, C. Three component time-domain electromagnetic surveying: Modeling and data analysis. *Piers. Online* **2008**, *4*, 475–480. [CrossRef]
25. Wang, X.C.; Yang, Y.; Deng, X.H.; Zhang, J.; Wu, J.J. Effective test for three-component data of fixed TEM in Xiarihamu Cu-Ni ore mine. *Comput. Tech. Geophys. Geochem. Explor.* **2016**, *38*, 327–333. [CrossRef]
26. Zhang, Z.W.; Wang, C.Y.; Liu, C.; Wang, Y.L.; Qian, B.; Li, W.Y.; You, M.X.; Zhang, J.W. Mineralization Characteristics and Formation Mechanism of the Intrusions in Xiarihamu Magmatic Ni-Cu Sulfide Deposit, East Kunlun Orogenic Belt, Northwest China. *NW Geol.* **2019**, *3*, 35–45. [CrossRef]
27. Fan, Y.; Meng, F.C.; Duan, X.P. The Protoliths of the Xiarihamu Eclogites from the Western Part of East Kunlun and Continent/Arc-Continent. *Acta Geol. Sin.* **2018**, *3*, 482–502. [CrossRef]
28. Du, W.; Ling, J.L.; Zhou, W.; Wang, Z.X.; Xia, Z.D.; Xia, M.Z.; Fan, Y.Z.; Jiang, C.Y. Geological characteristics and genesis of Xiarihamu nickel deposit in East Kunlun. *Miner. Depos.* **2014**, *4*, 713–726. [CrossRef]
29. Guo, Y.Z.; Guo, X.; Wang, X.C.; Li, L. A study of exploration direction of Xiarihamu HS26 anomaly area based on polarization rate of rocks in East Kunlun, Qinghai Province. *Geophys. Geochem. Explor.* **2016**, *2*, 353–359. [CrossRef]
30. Lv, Q.Y.; Jing, R.Z. On the chargeability characteristics of rock and ore from Xiarihamu Cu-Ni sulfidedeposit and its prospecting significance in east Kunlun, Qinghai province. *Comput. Tech. Geophys. Geochem. Explor.* **2015**, *2*, 177–181. [CrossRef]

Article

An Integrated Gray DEMATEL and ANP Method for Evaluating the Green Mining Performance of Underground Gold Mines

Yang Li, Guoyan Zhao *, Pan Wu and Ju Qiu

School of Resources and Safety Engineering, Central South University, Changsha 410083, China; leonly@csu.edu.cn (Y.L.); panwuly@csu.edu.cn (P.W.); daisy_qiu@csu.edu.cn (J.Q.)
* Correspondence: gyzhao@csu.edu.cn; Tel.: +86-135-0731-1842

Abstract: Green mining (GM) can achieve the harmonious development of mineral resource exploitation and environmental protection. Performance evaluation is the key to promoting GM. This research explores favorable methods to evaluate the green mining performance (GMP) of underground gold mines. First, according to the specific characteristics of underground gold mines, an evaluation criteria system for GM is formulated. Meanwhile, the weights are calculated using an integrated gray DEMATEL and ANP technique, which considers the correlation between indicators. Subsequently, the solution methodology for performance evaluation is proposed based on normalization of indicators. Finally, six underground gold mines are utilized as case studies to verify the methodological feasibility. The results of the empirical study show that there is a significant gap between ordinary mines and pilot green mines, and this study, via comparison analysis and cause–effect analysis, gives direction for mines improvement. Not only will the work provide technical and theoretical support for the evaluation and construction of similar green mines, it will also serve as a reference for government policy implementation.

Keywords: green mining; green mining performance; integrated Gray DEMATEL and ANP; evaluation system; sustainable development; underground gold mines

1. Introduction

The mining industry provides raw materials for socio-economic development, while unregulated mining operations may also cause serious ecological problems [1]. China, as a major mining country, faces an even tougher situation [2]. To solve the environmental problems and achieve sustainable development, China has proposed a green mining (GM) policy [2–4], with financial and tax incentives. Furthermore, many mines have joined the ranks of GM construction. Now comes the question of which mine is performing better. The government has to implement policy according to green mining performance (GMP), and mine enterprises have to improve by comparison. GMP evaluation of mines using appropriate and scientific approaches becomes particularly important [5,6], playing a critical role in promoting GM [6,7].

Considering the diversity of GM evaluation criteria, this would be a complicated matter of multicriteria decision-making (MCDM). Scholars have conducted studies on specific mines using different methods. Zhou et al. [1] adopted a fuzzy comprehensive evaluation method to assess the green surface mine in China. Chen et al. [5] put forward a Driver–Pressure–State–Impact–Response framework to formulate the GM evaluation indicator, and the PCA method was used to evaluate the interactions between human and environmental systems. Jiskani et al. [8] analyzed the Green and climate-smart mining of open-pit mines, fuzzy AHP was applied to determine weights, and the Grey clustering method was used to classify the result into concrete levels. Liang et al. respectively assessed the GMP through the Hesitant Fuzzy ORESTE–QUALIFLEX method [6] and MCDM combined with a picture fuzzy information approach [9]. Qi et al. [10] proposed an

evaluation system of GM construction, and determined the critical factor of GM by the two-step fuzzy DEMATEL model. Based on uncertainty measurement theory, Wang et al. [11] evaluated GM grades with six coupled methods, and finally selected the optimal method by credible degree recognition.

Although the above research addressed similar GMP evaluation tasks, the criteria system and MCDM methods are quite different. This is because the mineral species and mining method have to be considered while developing the evaluation criteria, and MCDM methods are selected based on the collected indicator data. Thus, it would be significant to develop specific appropriate and efficient evaluation methods [9,12]. For this purpose, in order to formulate an applicable GMP evaluation system to underground gold mines, the characteristics of mines have to be fully considered [13], and the principles of GM [14–17] are required for referencing.

The study area is located in Jiaodong Peninsula, one of the most important gold origins for China [18]. Firstly, the geological conditions in the region are exceedingly complicated, with fault structures and fractured zones [19] dispersed across the mining sites, posing safety risks, and the risk for accidents to occur is greater due to underground space limitations. Accordingly, safety production (SP) holds great meaning for GM, with this criterion being the basic condition for evaluating GMP [1,11]. Secondly, waste rock stockpiles and unregulated discharge of tailings [20] can cause environmental damage. However, the utilization rates of solid waste are quite low in local underground gold mines. To some extent, these solid wastes can be used in alternative ways. For example, tailings can be used for underground filling, and the waste rock crushed into stone as building materials. Thus, the comprehensive utilization (CU) of mining solid wastes should be considered as the evaluation criterion for GMP [7,21]. Thirdly, gold ore mined by drilling and blasting, emits dust and blasting fumes [22]. In addition, hydrogenated tailings can contaminate water bodies and soil without proper disposal [23–25]. Green emphasizes environmental protection (EP), which is also an essential criterion for GMP. Finally, the original intention of GM is to obtainn resources in an eco-friendly and efficient manner, with mining efficiency (ME) [26] representing the key component. In summary, SF-CU-EP-ME should be considered comprehensively to formulate a GMP evaluation criteria system for underground gold mines.

For the sake of relative fairness, indicators should be accurately calculable to eliminate subjective judgments. In terms of weight, the determination is a multilevel, complex, and comprehensive procedure, thus correlation and constraints between the indicators [1] should be considered. However, previous GMP evaluation research works have not employed indicator correlations to calculate weights. Therefore, it is necessary to devise a method for determining weights based on the relationship between indicators. For this goal, integrated DEMATEL-ANP [27,28] is extremely capable of solving this issue; DEMATEL is used to determine the factors influencing interaction, with ANP used to obtain the relative weight. However, crisp values occur in this method, which is inappropriate and imprecise for describing the information [9,29,30]. To conquer this limitation, the gray theory was exploited to transform crisp values into interval gray numbers, which improves the reality of decision-making data. Consequently, gray DEMATEL is adopted to examine the causal relationship in an uncertain environment, and then the ANP method to calculate the relative weight based on the influential relationship acquired from gray DEMATEL [31,32]. Finally, metrics need to be converted into scores. However, traditional grading methods, will yield no distinction between the same levels. A linear transformation approach would be a reasonable option.

In summary, an evaluation system is established to evaluate GMP for underground gold mines. In this respect, an evaluation criteria system is formulated in consideration of the characteristics and principles of GM, while an integrated gray DEMATEL and ANP method are devised to determine the relative weights, and a linear transformation strategy is used to convert index values to corresponding scores. Compared to other methods, the criteria system constructed in this work is more target-oriented. In addition, the

indicators can be calculated accurately to avoid human error, and the weighting and converting procedures of indicators are relatively fair. With regard to the above advantages, this study is rendered both feasible and reasonable.

The structure of this paper is designed as follows. Section 2 introduces the methodology in detail, including the technical route, indicators, and method. Section 3 provides a case study using the collected decision-making data from experts and indicator values from underground gold mines, with the results computed. Section 4 makes cause–effect and comparative analysis based on the results, and some managerial implications are also involved. Section 5 summarizes the paper and presents suggestions.

2. Methodology

In this section, the clear GMP evaluation system for underground gold mines is established, as well as the calculation method of each indicator. Procedures of the adopted integrated methods are described in detail. The entire flowchart is indicated in Figure 1.
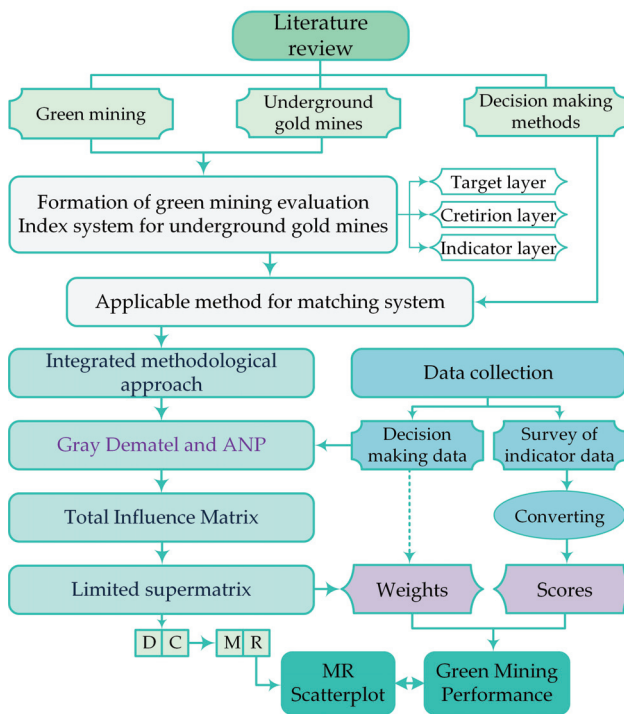
Figure 1. Flowchart for evaluating GMP of underground gold mines.

2.1. Evaluation Criteria

The GMP evaluation criteria for underground gold mines are first identified. Selecting suitable indicators is essential for the performance evaluation of green mines [6]. To find suitable indicators for the criteria layer, some principles must be followed. Data with easy accessibility principle is a prerequisite. The calculable principle ensures data accuracy and relative fairness, and the independence principle guarantees sensible structure. Within the SF-CU-EP-ME framework defined earlier, indicator layers also need to be determined, considering the specific characteristics of underground gold mines and referencing literature [1,5,6,9,11] related to GMP, the indicators under each criterion level were determined gradually. The evaluation system includes four criteria and twenty indicators. For clarity, the framework is shown in Figure 2. The calculation method of each indicator is shown in Table A1, and the following are thorough explanations of these criteria.
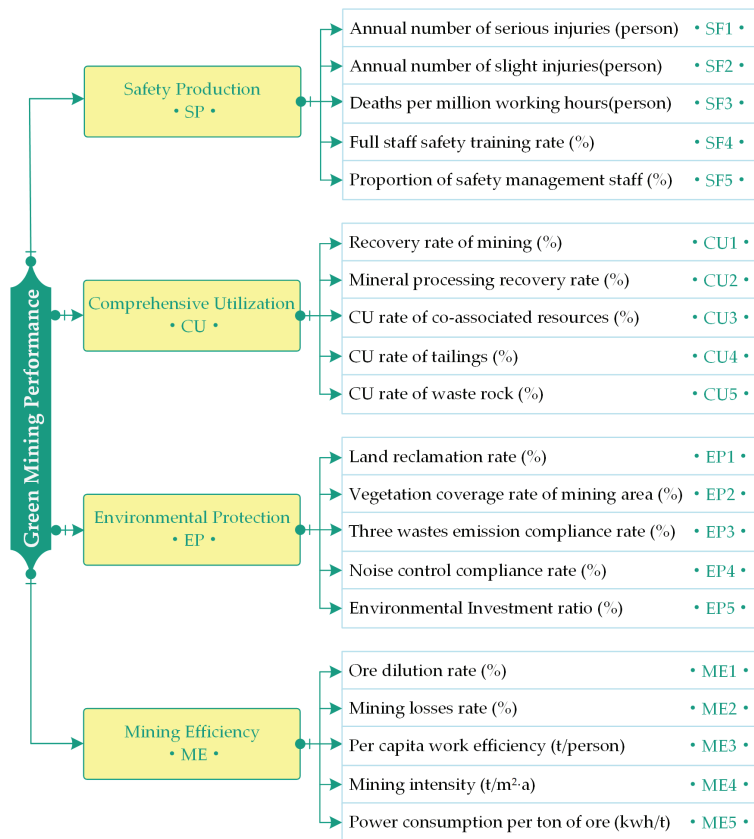
Figure 2. GMP evaluation criteria system for underground gold mines.

2.1.1. Safety Production

Safety production is a policy that must be followed by mining enterprises, requiring the minimization of work-related injuries among workers. Consequently, three indications of work-related injuries [1,11] are identified, containing the annual number of serious injuries SF1, annual number of slight injuries SF2 and deaths per million working hours SF3, these indicators meet smaller-is-better. Safety training [33,34] and management are critical for improving the safety situation in underground mining. Workers' emergency reaction capabilities may be improved by safety training, which can successfully prevent and reduce the occurrence of safety accidents. Safety management [1,34] is primarily concerned with the organization and implementation of enterprise safety management planning, guidance, inspection, and decision making. It is also the critical link in ensuring that production is conducted in the best possible safety conditions. As a result, the full staff safety training rate SF4 and the proportion of safety management staff SF5 were determined, with higher is better.

2.1.2. Comprehensive Utilization

Comprehensive utilization of resources includes two aspects. One is to improve the utilization rate of the resources themselves, and the other is to realize the comprehensive utilization of solid waste. In the case of underground gold mines, the resources are mainly gold metal or other associated resources. From this aspect, improving the mining recovery rate (CU1) [7], mineral processing recovery rate (CU2) [5] and the utilization rate of associated resources (CU3) [6,14] are conducive to the CU of resources. The solid waste

includes waste rock from mining and tailings from processing, which will occupy industrial land and pollute the environment without depositing. Actually, the waste produced in gold mines is also a valuable resource, which is worth developing and utilizing [13,14]. Through comprehensive utilization, the waste can be turned into treasure, which not only can solve the problem of solid waste pollution, but can also create economic benefits. Therefore, comprehensive utilization rate of tailings (CU4) [7,8] and waste rock (CU5) [8] are determined.

2.1.3. Environmental Protection

On the one hand, the mining landscape is very important. However, waste rock piles and tailing ponds occupy land, which destroys the natural landscape, and causes environmental pollution. Land reclamation is the activity of restoring damaged land to a usable state, the strength can be demonstrated by land reclamation rate EP1 [1,5,11,14]. The main focus of mine greening is to restore vegetation by greening and planting barren areas to increase the vegetation coverage rate of mining area (EP2) [5,6,11,14] and fulfill the goal of optimizing the landscape. On the other hand, pollution emission [3,7] control is extremely important for environmental protection, including three wastes [6] and noise [8]. Pollution emissions need to meet national standards, thus two indicators (EP3, EP4) related to compliance rate are used to describe the process. Finally, the environmental investment ratio (EP5) [5,26], is one of the main indicators to measure the harmonious relationship between environmental protection and economic development, which can improve the quality of the environment and prevent ecological degradation. All these indicators present with higher being better.

2.1.4. Mining Efficiency

Ore dilution refers to the reduction of ore grade due to the mixing of waste rock during the mining process. Ore losses describe the phenomenon of ore being discarded or not fully extracted during mine production due to various reasons (such as complex geological conditions, improper mining methods and transportation problems, etc.). Ore dilution and losses severely affect mining efficiency [26], with the ore dilution rate (ME1) [14] and mining losses rate (ME2) [14] being used to quantify this process. Per capita work efficiency (ME3) [11] is used for measuring the labor efficiency of mining enterprises, with higher values for the mechanization degree and mining efficiency being better. Mining intensity in underground mines refers to the annual amount of ore produced per square meter of mining area. Mining intensity [35] is high if there is good continuity and a high rate of progress of mining preparation, and more blocks are being retrieved at the same time; conversely, mining intensity is poor when continuity, mining area, and rate of block retrieval are low. Mining intensity is a comprehensive indicator reflecting the mining efficiency, denoted by ME4. During the mining process, it is highly efficient to achieve the same production goal with less energy. Hence, ME5 is exploited to reflect the energy consumption [5,7,14] level of mining.

2.2. Integrated Gray DEMATEL and ANP

DEMATEL is a system science technique proposed by American scholars A.Gabus and E.Fontela [36] in 1972. It is applicable for analyzing the interdependent relationships among factors in a complex system and ranking them for long-term strategic decision making [37]. The Gray DEMATEL technique is upgraded from the typical DEMATEL approach, the general steps are gray number normalization and clarification, and the remaining steps are consistent with the typical DEMATEL technique.

To obtain the initial decision data, decision-makers are asked to specify the influence degree of one indicator on another indicator, utilizing five different integer scales [36], as shown in Table 1. Next, according to Table 1, crisp values are converted into interval gray numbers, which contain the upper and lower bounds. The Gray DEMATEL method consists of the following steps.

Table 1. Relative influence index.

Crisp Values	Linguistic Variables	Interval Gray Number
0	No influence	[0, 0]
1	Low influence	[0, 0.25]
2	Medium influence	[0.25, 0.5]
3	High influence	[0.5, 0.75]
4	Very high influence	[0.75, 1]

Step 1: Normalization of the upper and lower bounds.

$$
\begin{cases}
\underline{\otimes}\tilde{x}_{ij}^k = \left(\underline{\otimes}x_{ij}^k - \min \underline{\otimes}x_{ij}^k\right)/\triangle_{\min}^{\max} \\
\overline{\otimes}\tilde{x}_{ij}^k = \left(\overline{\otimes}x_{ij}^k - \min \overline{\otimes}x_{ij}^k\right)/\triangle_{\min}^{\max} \\
\triangle_{\min}^{\max} = \max \overline{\otimes}x_{ij}^k - \min \underline{\otimes}x_{ij}^k
\end{cases}
\tag{1}
$$

where $\underline{\otimes}\tilde{x}_{ij}^k$ is the lower bound of the expert's raw score after transforming it into the interval gray number. Correspondingly, $\overline{\otimes}\tilde{x}_{ij}^k$ is the normalized upper bound.

Step 2: Converting fuzzy data into crisp Scores.

$$
\begin{cases}
Y_{ij}^k = \dfrac{\left(\underline{\otimes}\tilde{x}_{ij}^k \left(1-\underline{\otimes}\tilde{x}_{ij}^k\right)+\left(\overline{\otimes}\tilde{x}_{ij}^k \times \underline{\otimes}\tilde{x}_{ij}^k\right)\right)}{\left(1-\underline{\otimes}\tilde{x}_{ij}^k+\overline{\otimes}\tilde{x}_{ij}^k\right)} \\
Z_{ij}^k = \underline{\otimes}\tilde{x}_{ij}^k + Y_{ij}^k \triangle_{\min}^{\max}
\end{cases}
\tag{2}
$$

Y_{ij}^k is the calculated preliminary crisp value, and Z_{ij}^k is ultimate crisp value.

Step 3: Generating the direct influence matrix combining experts' weights.

$$
Z_{ij} = w_1 Z_{ij}^1 + w_2 Z_{ij}^2 + \cdots + w_k Z_{ij}^k
\tag{3}
$$

where w_i is the attribute weight of expert i, and the sum of $w_1, w_2, \cdots, w_k$ is one.

As a result, make the diagonal elements as zero, the group direct influence matrix is Z.

$$
Z = \begin{bmatrix}
0 & z_{12} & \cdots & z_{1n} \\
z_{21} & 0 & \cdots & z_{2n} \\
\vdots & \vdots & 0 & \vdots \\
z_{n1} & z_{n2} & \cdots & z_{nn}
\end{bmatrix} = \left(z_{ij}\right)_{n \times n}
\tag{4}
$$

Step 4: Normalizing the initial influence matrix.

$$
X = \frac{Z}{\max\left(\sum_{j=1}^n x_{ij}\right)}, 1 \le i \le n
\tag{5}
$$

Step 5: Constructing the total influence matrix T.

$$
T = \left(X + X^2 + X^3 + \cdots + X^{h \to \infty}\right) = X(1-X)^{-1}
\tag{6}
$$

Step 6: Producing the influential relation map.

$$M_i = D_i + C_i = \sum_{j=1}^{n} t_{ij} + \sum_{i=1}^{n} t_{ij}$$

$$R_i = D_i - C_i = \sum_{j=1}^{n} t_{ij} - \sum_{i=1}^{n} t_{ij}$$

(7)

Let D_i denote the sum of rows, which indicates the degree of influence, while C_i represents the sum of columns, which shows the degree of being influenced. M_i denotes centrality and prominence in the system, whereas R_i denotes the causality of indicators, and reflects the relationship in the system.

At last, the total influence matrix is regarded as the unweighted supermatrix of ANP [38]. After normalization, we can obtain the weighted supermatrix, while it self-multiplies, has converged and become a stable supermatrix [39]. This new matrix is called a limited supermatrix, and the relative weights of each criterion can be obtained from this matrix.

2.3. Performance Evaluation

There are large gaps in the collected evaluation data, and normalization of the data is necessary, which facilitates scientific calculations and accuracy.

For "smaller-is-better" indicators, the normalized value $x_i(k)$ can be calculated as:

$$x_i(k) = \frac{\min(x_i)}{x_i(k)}, \ for \ 1 \leq i \leq n, \ 1 \leq k \leq m.$$

(8)

For "larger-is-better" indicators, the normalized value $x_i(k)$ can be calculated as:

$$x_i(k) = \frac{x_i(k)}{\max(x_i)}, \ for \ 1 \leq i \leq n, \ 1 \leq k \leq m.$$

(9)

where $\max(x_i)$ and $\min(x_i)$ represent the maximum and minimum values.

$$Scores = \sum_{i=1}^{n} w_i x_i(k), \ i = 1, \cdots, n; \ k = 1, \cdots, m.$$

(10)

Finally, a simple additive weighting method [40] is used to rank the performance, which reflects the advantages of indicators while maintaining simplicity of calculation [41]. The weight of each indicator can be calculated by the GDANP method, the normalized evaluation data multiplied by weights obtain the score of each indicator, and summing up the scores gives the evaluation results, as shown in Equation (10).

3. Case Study

3.1. Case Description

Shandong Gold Mining Co., Ltd is the largest gold producer in China, and it is devoted to GM for environmental protection and sustainable development. This corporation has so far established a series of national pilot green mines, with the remainder of the numerous mines still under construction. Discovering the gaps between the pilot sites and the rest of the mines becomes crucial, facilitating reference and experience learning. For this purpose, six underground gold mines were selected. Three of them are pilot green mines (denoted as M1, M2, M3), the rest are under construction (denoted as M4, M5, M6).

M1 has taken the initiative to collaborate with nationally renowned scientific research institutes, picking appropriate mining methods based on rock classification, and optimizing mining parameters. To accomplish safe and effective mining, the upward approach filling mining technique, wide approach filling mining method, and automated pan area mining method are employed thoroughly. Mining loss and depletion rates have been significantly

lowered. M2 focuses on the comprehensive utilization of resources, which applies the medium-deep hole pre-controlled top section filling mining method to improve the ore recovery rate. At the same time, the beneficiation process has been modified to improve the recovery rate of gold. M3 is dedicated to the reuse of solid waste. Parts of the tailings and waste rocks are used to solidify and fill the quarry area, while the remainder is utilized to manufacture concrete bricks, resulting in greater economic advantages and the transformation of trash into treasure. Each mine bears its own unique characteristics, and by adjusting to local conditions, each mine has achieved significant achievements in the GM process. Therefore, it is essential to pick these three pilot mines as a study reference.

3.2. Data Collection

Data collection is divided into two parts: expert decision data and evaluation data of underground mines. Expert decision data were acquired from the questionnaires. Three conditions must be met for the selection of experts: first, the experts must be independent of the mines involved in the evaluation; second, they must have extensive work experience in underground gold mining; and third, they must be familiar with or have participated in the evaluation of green mining. After screening, six experts were confirmed, and the statistic information and gray weights of the selected experts are illustrated in Table 2.

Table 2. Statistics of experts in GM.

Experts	Education	Working Years	Position	Gray Weights
E1	Bachelor	17	Engineer	[0.3, 0.4]
E2	Doctor	28	Professor	[0.7, 1.0]
E3	Master	23	Deputy mine manager	[0.5, 0.6]
E4	Bachelor	19	Senior Engineer	[0.3, 0.5]
E5	Master	30	Mine manager	[0.6, 0.8]
E6	Doctor	25	Supervisors	[0.7, 0.9]

The questionnaire was completed by all six of the selected experts, who carefully answered pertinent topics. The initial decision matrix can be derived from the surveys, and all of the data are valid. The expert decision matrix was calculated by using the GDANP method, the total influence matrix Table A2, the weighted supermatrix in Table A3 and the limited supermatrix Table A4 can be obtained, respectively.

The evaluation data of underground gold mines are obtained through onsite investigation, assisted by the relevant mine production manager. The collected original evaluation data are shown in Table A5. For these "smaller-is-better" indicators (SP1, SP2, SP3, ME1, ME2, ME5), which can be normalized through Equation (8), indicators with a minimum value of zero need to be handled by the overall moving method, and the rest are "larger-is-better" indicators, which can be normalized by Equation (9). The normalized evaluation data are shown in Table A6.

3.3. Results

In this study, the formulated evaluation index comprises three hierarchical layers: the target layer, the criterion layer, and the indicator layer. Based on corresponding principles, the evaluation system for underground mines including four criteria and twenty indicators are determined.

Considering the correlation of indicators, an integrated evaluation method based on GDANP is used to calculate the weight of indicators, from the limited supermatrix, the weight of each indicator can be calculated, as shown in Table 3. Finally, the ranking order of the criteria is CU≻ME≻EP≻SP, CU becomes the most important criterion for GM.

The score of each underground gold mine can be calculated according to Equation (10), and the results are shown in Table A7. For clarity, Figure 3 depicts the results. There is a clear gap between the mines under construction and the pilot green mines, and this also demonstrates the validity of the method proposed in this study, which can efficiently

discriminate between two types of mines. Finally, the rankings for these mines are as follows: M3≻M1≻M2≻M5≻M4≻M6.

Table 3. Weights of indicators computed by using GDANP.

Criteria	Weight	Rank	Indicator	Local Weight	Global Weight	Rank
SP	0.1881	4	SP1	0.2103	0.0396	14
			SP2	0.1480	0.0278	16
			SP3	0.2335	0.0439	11
			SP4	0.1816	0.0342	15
			SP5	0.2263	0.0426	12
CU	0.3130	1	CU1	0.3035	0.0950	2
			CU2	0.0443	0.0139	17
			CU3	0.0321	0.0101	20
			CU4	0.3402	0.1065	1
			CU5	0.2799	0.0876	3
EP	0.2384	3	EP1	0.2370	0.0565	7
			EP2	0.1676	0.0399	13
			EP3	0.2085	0.0497	9
			EP4	0.0577	0.0138	18
			EP5	0.3291	0.0785	5
ME	0.2606	2	ME1	0.1736	0.0452	10
			ME2	0.2139	0.0558	8
			ME3	0.2563	0.0668	6
			ME4	0.3070	0.0800	4
			ME5	0.0489	0.0127	19
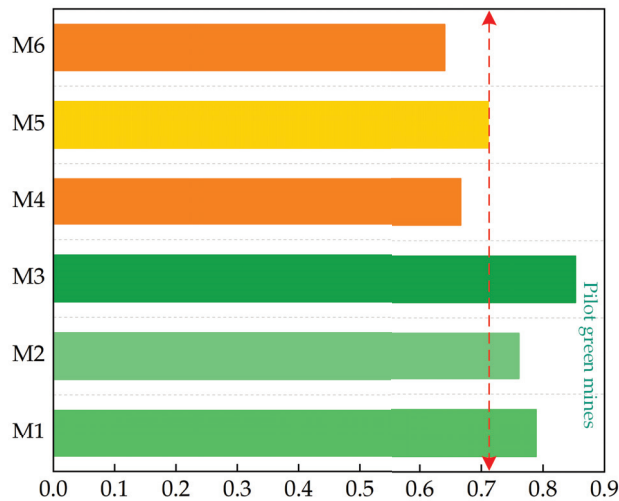
Figure 3. The GMP evaluation results for underground gold mines.

4. Discussions

4.1. Cause–Effect Analysis

The influence index and relationship index are the core factors of DEMATEL analysis [10]. The former indicates the factor's ability to influence the system. The larger the value, the higher the degree of influence. The latter has positive and negative values, belonging to the cause group and effect group, respectively. This is because the relationship index is calculated by $(D_i - C_i)$, positive values indicate the influence degree exceeds the influenced degree, and negative values are dominated by the influenced degree. Theoretically,

the cause group affects the factors in the effect group, thus they are the system-identified issues that demand priority improvement. The results are shown in Table 4.

Table 4. Prominence and relation of each indicator.

	Row Sum (D_i)	Column Sum (C_i)	Influence Index	Relationship Index
SP1	0.8226	1.0446	1.8672	−0.2220
SP2	0.5563	0.9534	1.5098	−0.3971
SP3	0.9574	0.8633	1.8207	0.0941
SP4	0.8058	1.1066	1.9123	−0.3008
SP5	1.0360	0.5023	1.5383	0.5337
CU1	1.0911	0.4550	1.5461	0.6362
CU2	0.2505	0.2636	0.5142	−0.0131
CU3	0.1804	0.1330	0.3135	0.0474
CU4	1.5329	1.2658	2.7986	0.2671
CU5	1.3308	0.8463	2.1770	0.4845
EP1	1.0006	1.6760	2.6766	−0.6754
EP2	0.6908	1.3902	2.0810	−0.6993
EP3	0.9933	1.0061	1.9993	−0.0128
EP4	0.2978	0.4253	0.7231	−0.1274
EP5	1.5072	1.8853	3.3925	−0.3781
ME1	0.6488	0.1690	0.8178	0.4799
ME2	0.7502	0.4161	1.1663	0.3341
ME3	0.6951	0.7732	1.4683	−0.0780
ME4	0.9986	0.5897	1.5883	0.4089
ME5	0.1326	0.5142	0.6468	−0.3817

A cause–effect diagram is a tool to logically organize and graphically display the causes associated with specific effects [29]. The influence and relationship values were used to plot the cause–effect diagram, as shown in Figure 4. Typically, this diagram is divided into four categories, core causal, inferior causal, core effect and inferior effect.
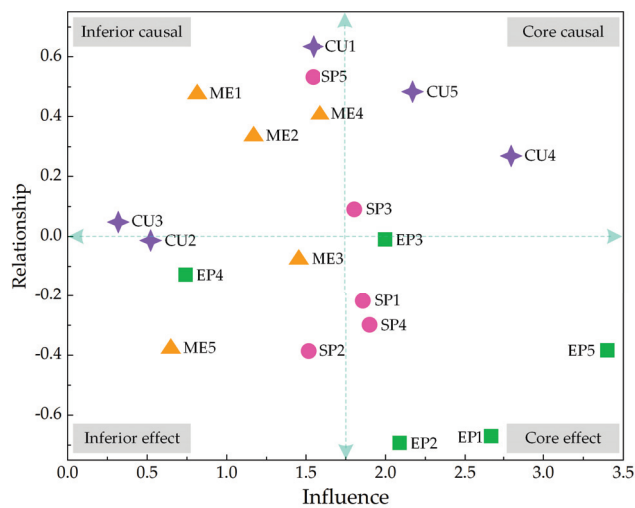
Figure 4. Casual–effect diagram of indicators.

The core causal group with large prominence and positive relation, CU5, CU4, and SP3 are concluded in this cluster, elements in this group have the topmost priority for improvement. The inferior causal group with small prominence and positive relation, SP5, CU1, CU3, ME1, ME2, ME4 are classified in this region, they require immediate improvement

but with high priority. SP2, CU2, EP4, ME3, ME5 with small prominence and negative relation, affiliated to the inferior effect group, are improved indirectly with medium priority. The rest with large prominence and negative relation belong to the core effect group, which are affected by elements in other groups. In this way, the elements in the causal groups are improved, and the corresponding effect groups will be upgraded as well. Therefore, the order of improvements can be determined based on the priority of indicators, as shown in Table A8, red for topmost priority, purple for high priority, and cyan for medium priority.

4.2. Comparative Analysis

A comparative analysis is required to understand the strengths and weaknesses of specific mines. Figure 5 indicates the performance of the underground gold mine in different fields. From each dimension, M1 and M2 underperform in terms of SP, M4, M5, and M6 has a poor degree of CU, M6 has the lowest EP score, and M4 and M6 have significant weaknesses in terms of ME. Each mine includes aspects that need to be improved when broken down into distinct indicators. Table A8 demonstrates the prospective improvement elements for each mine.
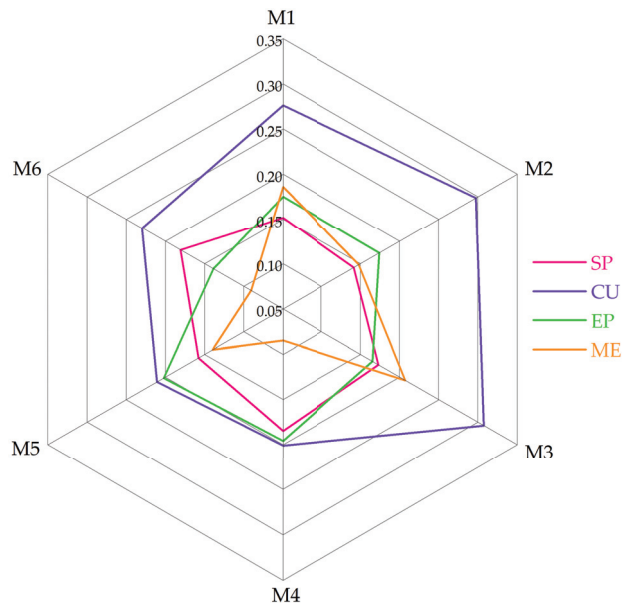
Figure 5. The GMP distributions of underground gold mines.

From a holistic view, the pilot green mines are developed in a more balanced way, and they have great advantages in terms of CU. This is because CU has a high degree of association with other indicators, especially CU4 and CU5 which are used for underground filling. These not only control ground pressure and prevent surface collapse (benefits for SP), but also solve the EP pressure, and the filling mining method improves ME. Correspondingly, these are the driving factors for green mines to enhance CU.

In terms of scores, M3 performs the best, M1 and M2 still show space for improvement, M4 and M6 perform poorly and have a large gap between the pilot green mine. M5 has the most potential to develop into a green mine.

More importantly, to validate the feasibility of this research, a comparative analysis with other related studies is crucial.

(1) Comparison of evaluation criteria

This paper proposed an evaluation criteria framework, applicable to underground metal mines. Compared with the most similar GMP evaluation study, the criteria system in the literature [9] is very abstract, which is not conducive to the accuracy of evaluation. Meanwhile, the selection of indicators was kept simple based on the essential requirements of green mining [7]. Thus, the easy accessibility of evaluation information is determined as a prerequisite to choosing indicators. The proposed evaluation system is flexible, and the criterion can be more specific in future studies.

(2) Comparison of weight determination methods

The analytic network process method is widely used for MCDM [42,43], but the calculation process is complicated. To compensate for the shortcomings of this single method, hybrid evaluation methods with ANP [44,45] were proposed. The weights in this research were determined using an integrated Gray DEMATEL and ANP approach, which was employed for the first time in the GMP evaluation sector. In comparison to other methods, this approach fully utilizes the correlation between indicators and simplifies the calculation process [39]. Therefore, the calculated weights are more reasonable.

(3) Comparison of the results

The GMP evaluation studies usually assess the same type of mines [6,9], and this paper selected three pilot green mines as control group. The proposed method is capable of distinguishing between two types of mines, which verifies the feasibility of this research. The results show that CU is the most important criterion in GM, and this can be corroborated by the related research [7]. Moreover, the cause–effect analysis provided a reasonable order for mine improvements, which has not been found in GMP evaluation studies. Thus, the proposed suggestions are more informative than similar studies.

To sum up, the advantages of proposed approaches summarized as follows:

- Evaluation indicators are specific and data easy to obtain, the calculability of evaluation information guarantees the relative fairness of evaluation.
- Weights are calculated by correlation between indicators, and with the cause–effect analysis guide for mine improvements, the suggestions are more informative.
- Data of six underground gold mines were collected, the proposed method can distinguish between two types of mines, which verify the feasibility of proposed method.

4.3. Managerial Implications

Management of mining processes and monitoring of their performance is a basic prerequisite for continual improvement [46], and the performance evaluation of mines is the key to promoting green mine construction [7]. Figure 6 reveals the role of evaluation in GM. The evaluation has profound implications and broad application value, pushing mines to practice green mining, and serving as a strong tool for the government to encourage policy implementation.

Figure 6. The role of evaluation in green mining.

Mines are compared in the evaluation process, and the results point out the advantages and weaknesses of mines, which indicate the way forward for improvement and upgrading. For sustainable development, mines have to identify and solve gaps; this purpose becomes the driving force for GM. When the mines have performed excellently in green mining and reached the industry-leading level, they will be recognized as green mines. The designation is certificated by the government, and evaluation plays an important role in this procedure, guiding the decision-making of the government. The mines create social environmental benefits, and the government supports financial and tax incentives to mines depending on the GMP, highlighting a mutually beneficial situation. Mines provide social and environmental benefits, while the government provides financial and tax incentives to mines based on GMP, creating a win–win scenario.

5. Conclusions

The integral elements of the GM for underground gold mines include safety production, comprehensive utilization of resources, environmental protection, and mining efficiency. In order to measure the GMP of different mines, an evaluation system is proposed in this study, which consists of four criteria and twenty indicators. Considering the correlation of indicators, an integrated GDANP method has been exploited to evaluate the GMP for six underground gold mines. The results demonstrate the rank order as well as the gap between the mines. Furthermore, the weaknesses of each mine are analyzed in a broad dimension, and the advantages of pilot green mines are explained in a reasonable manner. Subsequently, the cause–effect analysis categorizes indicators into four groups, with the priority defined by the prominence and relation of each indicator. To solve the gaps, mines have to implement improvements sensibly. Finally, this research explored the effect of evaluation on mining management and the government.

Indeed, there are some limitations to this study, e.g., the lack of evidence to prove which proposed method was the best. Perhaps the presented evaluation framework can be extended with other MCDM approaches. Indicators can be added to make the system more comprehensive, and the evaluation criteria can be improved in future studies.

In summary, this paper mainly evaluated the GMP for underground gold mines and provided ideas for improvements. The evaluation framework applies to underground metal mines, and some indicators in the formulated system are likely to work for similar environments. The proposed methodology can also be exploited in other evaluation studies where the indicators are correlated. The results of this research may be used as a reference for GM in other mines, as well as to assist government policy implementation.

Abbreviations

The following abbreviations are used in this manuscript:

CU	Comprehensive utilization
EP	Environmental protection
GDANP	Gray DEMATEL and ANP
GM	Green mining
GMP	Green mining performance
MCDM	Multi-Criteria Decision-Making
ME	Mining efficiency
SP	Safety production

Appendix A

Table A1. Calculation method for indicators.

Indicator	Calculation Method	Unit
SP1	Number of serious injuries per year	person
SP2	Number of light injuries per year	person
SP3	Number of deaths/Million working hours $\times 10^6$	person
SP4	Number of people receiving systematic security training/All staff $\times$ 100%	%
SP5	Number of people engaged in full-time safety production management/All staff $\times$ 100%	%
CU1	Mined ore/Reserves of ore owned by the mining area $\times$ 100%	%
CU2	Mass of useful fraction in concentrate/Mass of useful fraction in the ore inducted $\times$ 100%	%
CU3	Mass of co-associated minerals that have been utilized/Mass of contained co-associated minerals $\times$ 100%	%
CU4	Annual tailings utilization/Total annual tailings production $\times$ 100%	%
CU5	Annual amount of waste rocks utilized/Total amount of waste rocks produced annually $\times$ 100%	%
EP1	Reclaimed land area/Damaged land area $\times$ 100%	%
EP2	Greening area/Actual greenable area $\times$ 100%	%
EP3	Actual emission of three wastes/Permitted emission of three wastes $\times$ 100%	%
EP4	The area where the noise control meets the national standard/The noise area of the mine $\times$ 100%	%
EP5	Annual environmental protection investment/Annual revenue of the mine $\times$ 100%	%
ME1	(Geological grade of original ore - grade of extracted ore)/Geological grade of original ore $\times$ 100%	%
ME2	(Industrial reserves - actual ore mined)/Industrial reserves $\times$ 100%	%
ME3	Total monthly ore production/Number of all employees	t/person
ME4	The annual amount of ore mined from the mining face/Gross area of the back-mining area	t/m$^2 \cdot$a
ME5	Annual power consumption/Annual gold ore production	kWh/t

Table A2. The total influence matrix.

	SP1	SP2	SP3	SP4	SP5	CU1	CU2	CU3	CU4	CU5	EP1	EP2	EP3	EP4	EP5	ME1	ME2	ME3	ME4	ME5
SP1	0.0767	0.1590	0.1465	0.2019	0.1079	0.0014	0.0003	0.0001	0.0073	0.0049	0.0108	0.0089	0.0095	0.0050	0.0367	0.0016	0.0018	0.0222	0.0169	0.0030
SP2	0.1418	0.0485	0.1039	0.1304	0.0576	0.0007	0.0004	0.0001	0.0038	0.0019	0.0036	0.0027	0.0034	0.0011	0.0074	0.0018	0.0019	0.0240	0.0194	0.0022
SP3	0.1887	0.1619	0.0903	0.2988	0.1873	0.0003	0.0001	0.0000	0.0017	0.0010	0.0022	0.0018	0.0019	0.0009	0.0068	0.0005	0.0005	0.0066	0.0052	0.0008
SP4	0.2191	0.2303	0.1737	0.0920	0.0532	0.0004	0.0001	0.0001	0.0020	0.0012	0.0026	0.0021	0.0023	0.0011	0.0080	0.0006	0.0007	0.0086	0.0067	0.0010
SP5	0.2373	0.1695	0.2225	0.3125	0.0578	0.0004	0.0001	0.0000	0.0020	0.0013	0.0027	0.0022	0.0024	0.0012	0.0084	0.0006	0.0006	0.0076	0.0060	0.0009
CU1	0.0148	0.0063	0.0054	0.0039	0.0021	0.0181	0.0341	0.0258	0.0836	0.0846	0.0742	0.0635	0.0462	0.0196	0.1394	0.0330	0.1848	0.1129	0.0949	0.0439
CU2	0.0025	0.0027	0.0017	0.0010	0.0005	0.0049	0.0002	0.0184	0.0300	0.0106	0.0261	0.0194	0.0476	0.0088	0.0653	0.0002	0.0010	0.0012	0.0018	0.0067
CU3	0.0023	0.0025	0.0016	0.0009	0.0005	0.0043	0.0002	0.0001	0.0273	0.0075	0.0194	0.0129	0.0484	0.0046	0.0330	0.0002	0.0009	0.0014	0.0019	0.0108
CU4	0.0565	0.0432	0.0452	0.0223	0.0125	0.1618	0.0055	0.0041	0.0891	0.1671	0.2583	0.2548	0.1104	0.0233	0.1446	0.0056	0.0298	0.0229	0.0203	0.0554
CU5	0.0153	0.0116	0.0113	0.0058	0.0032	0.1145	0.0039	0.0029	0.2226	0.0646	0.2721	0.2105	0.0801	0.0270	0.1723	0.0040	0.0211	0.0164	0.0144	0.0570
EP1	0.0188	0.0110	0.0141	0.0069	0.0039	0.0289	0.0010	0.0007	0.1598	0.0898	0.0987	0.2144	0.0581	0.0476	0.2158	0.0011	0.0054	0.0048	0.0048	0.0152
EP2	0.0070	0.0060	0.0053	0.0028	0.0015	0.0198	0.0007	0.0005	0.1032	0.0724	0.1279	0.0688	0.0464	0.0254	0.1807	0.0007	0.0037	0.0032	0.0034	0.0113
EP3	0.0236	0.0327	0.0129	0.0091	0.0047	0.0152	0.0008	0.0005	0.0838	0.0473	0.2223	0.0801	0.0522	0.0308	0.2082	0.0020	0.0042	0.0134	0.0300	0.1193
EP4	0.0056	0.0324	0.0041	0.0044	0.0020	0.0031	0.0001	0.0001	0.0155	0.0125	0.0295	0.0251	0.0252	0.0153	0.1153	0.0002	0.0007	0.0014	0.0016	0.0038
EP5	0.0148	0.0174	0.0103	0.0060	0.0032	0.0306	0.0011	0.0008	0.1532	0.1232	0.2921	0.2486	0.2497	0.1513	0.1433	0.0014	0.0060	0.0070	0.0101	0.0371
ME1	0.0025	0.0024	0.0018	0.0010	0.0005	0.0070	0.1842	0.0699	0.0355	0.0270	0.0282	0.0231	0.0273	0.0095	0.0693	0.0049	0.0353	0.0900	0.0180	0.0117
ME2	0.0035	0.0036	0.0025	0.0014	0.0008	0.0091	0.0108	0.0011	0.0438	0.0399	0.0553	0.0452	0.0462	0.0228	0.1665	0.0107	0.0122	0.1597	0.0959	0.0191
ME3	0.0028	0.0028	0.0020	0.0011	0.0006	0.0068	0.0105	0.0039	0.0378	0.0207	0.0378	0.0292	0.0352	0.0127	0.0875	0.0539	0.0562	0.0428	0.1719	0.0789
ME4	0.0105	0.0093	0.0078	0.0041	0.0023	0.0268	0.0088	0.0036	0.1583	0.0661	0.1079	0.0739	0.1093	0.0162	0.0708	0.0422	0.0456	0.1689	0.0348	0.0313
ME5	0.0004	0.0003	0.0003	0.0001	0.0001	0.0009	0.0007	0.0003	0.0055	0.0025	0.0043	0.0031	0.0042	0.0010	0.0061	0.0037	0.0039	0.0583	0.0317	0.0048

Table A3. The weighted supermatrix for indicators.

	SP1	SP2	SP3	SP4	SP5	CU1	CU2	CU3	CU4	CU5	EP1	EP2	EP3	EP4	EP5	ME1	ME2	ME3	ME4	ME5
SP1	0.0735	0.1668	0.1697	0.1824	0.2148	0.0031	0.0013	0.0011	0.0058	0.0058	0.0065	0.0064	0.0095	0.0117	0.0195	0.0095	0.0044	0.0286	0.0286	0.0058
SP2	0.1358	0.0509	0.1203	0.1179	0.1146	0.0015	0.0013	0.0010	0.0030	0.0023	0.0021	0.0019	0.0034	0.0026	0.0039	0.0104	0.0045	0.0310	0.0329	0.0044
SP3	0.1806	0.1698	0.1046	0.2701	0.3729	0.0007	0.0004	0.0003	0.0013	0.0012	0.0013	0.0013	0.0019	0.0022	0.0036	0.0029	0.0013	0.0086	0.0088	0.0015
SP4	0.2097	0.2415	0.2012	0.0832	0.1060	0.0008	0.0005	0.0004	0.0016	0.0015	0.0016	0.0015	0.0023	0.0026	0.0042	0.0037	0.0016	0.0111	0.0114	0.0019
SP5	0.2272	0.1778	0.2578	0.2824	0.1151	0.0008	0.0004	0.0004	0.0016	0.0015	0.0016	0.0016	0.0024	0.0027	0.0045	0.0033	0.0015	0.0099	0.0101	0.0018
CU1	0.0141	0.0067	0.0063	0.0035	0.0042	0.0398	0.1292	0.1936	0.0661	0.1000	0.0443	0.0457	0.0459	0.0462	0.0740	0.1953	0.4441	0.1461	0.1609	0.0853
CU2	0.0024	0.0028	0.0020	0.0009	0.0011	0.0108	0.0007	0.1383	0.0237	0.0125	0.0156	0.0139	0.0473	0.0207	0.0346	0.0014	0.0023	0.0015	0.0031	0.0130
CU3	0.0022	0.0026	0.0018	0.0008	0.0010	0.0095	0.0006	0.0009	0.0216	0.0088	0.0116	0.0093	0.0481	0.0108	0.0175	0.0014	0.0021	0.0018	0.0032	0.0209
CU4	0.0541	0.0453	0.0524	0.0202	0.0249	0.3555	0.0208	0.0310	0.0704	0.1975	0.1541	0.1833	0.1097	0.0548	0.0767	0.0334	0.0715	0.0296	0.0345	0.1076
CU5	0.0147	0.0122	0.0131	0.0053	0.0064	0.2517	0.0147	0.0219	0.1759	0.0764	0.1623	0.1514	0.0796	0.0636	0.0914	0.0237	0.0507	0.0213	0.0244	0.1108
EP1	0.0180	0.0115	0.0163	0.0063	0.0078	0.0635	0.0038	0.0056	0.1262	0.1061	0.0589	0.1542	0.0577	0.1120	0.1144	0.0064	0.0129	0.0061	0.0082	0.0295
EP2	0.0067	0.0063	0.0062	0.0025	0.0030	0.0435	0.0026	0.0038	0.0815	0.0856	0.0763	0.0495	0.0461	0.0598	0.0958	0.0044	0.0089	0.0041	0.0058	0.0220
EP3	0.0226	0.0343	0.0150	0.0082	0.0094	0.0334	0.0030	0.0037	0.0662	0.0559	0.1327	0.0576	0.0519	0.0724	0.1104	0.0116	0.0101	0.0174	0.0509	0.2320
EP4	0.0054	0.0340	0.0047	0.0040	0.0040	0.0068	0.0005	0.0006	0.0123	0.0147	0.0176	0.0181	0.0251	0.0359	0.0612	0.0011	0.0016	0.0018	0.0027	0.0074
EP5	0.0142	0.0183	0.0119	0.0054	0.0064	0.0673	0.0042	0.0060	0.1210	0.1456	0.1743	0.1788	0.2482	0.3559	0.0760	0.0083	0.0143	0.0090	0.0172	0.0722
ME1	0.0024	0.0025	0.0021	0.0009	0.0011	0.0153	0.6988	0.5250	0.0280	0.0319	0.0168	0.0166	0.0271	0.0222	0.0368	0.0290	0.0848	0.1164	0.0305	0.0228
ME2	0.0033	0.0038	0.0029	0.0013	0.0015	0.0201	0.0411	0.0084	0.0346	0.0472	0.0330	0.0325	0.0460	0.0535	0.0883	0.0634	0.0294	0.2065	0.1626	0.0372
ME3	0.0027	0.0029	0.0024	0.0010	0.0012	0.0149	0.0399	0.0293	0.0299	0.0245	0.0226	0.0210	0.0350	0.0299	0.0464	0.3190	0.1350	0.0553	0.2915	0.1535
ME4	0.0100	0.0098	0.0090	0.0037	0.0045	0.0589	0.0334	0.0267	0.1251	0.0781	0.0644	0.0532	0.1086	0.0382	0.0376	0.2497	0.1096	0.2185	0.0590	0.0609
ME5	0.0004	0.0004	0.0003	0.0001	0.0002	0.0021	0.0028	0.0021	0.0043	0.0030	0.0026	0.0023	0.0042	0.0024	0.0033	0.0222	0.0095	0.0754	0.0537	0.0094

Table A4. The limited supermatrix for indicators.

	SP1	SP2	SP3	SP4	SP5	CU1	CU2	CU3	CU4	CU5	EP1	EP2	EP3	EP4	EP5	ME1	ME2	ME3	ME4	ME5
SP1	0.0396	0.0396	0.0396	0.0396	0.0396	0.0396	0.0396	0.0396	0.0396	0.0396	0.0396	0.0396	0.0396	0.0396	0.0396	0.0396	0.0396	0.0396	0.0396	0.0396
SP2	0.0278	0.0278	0.0278	0.0278	0.0278	0.0278	0.0278	0.0278	0.0278	0.0278	0.0278	0.0278	0.0278	0.0278	0.0278	0.0278	0.0278	0.0278	0.0278	0.0278
SP3	0.0439	0.0439	0.0439	0.0439	0.0439	0.0439	0.0439	0.0439	0.0439	0.0439	0.0439	0.0439	0.0439	0.0439	0.0439	0.0439	0.0439	0.0439	0.0439	0.0439
SP4	0.0342	0.0342	0.0342	0.0342	0.0342	0.0342	0.0342	0.0342	0.0342	0.0342	0.0342	0.0342	0.0342	0.0342	0.0342	0.0342	0.0342	0.0342	0.0342	0.0342
SP5	0.0426	0.0426	0.0426	0.0426	0.0426	0.0426	0.0426	0.0426	0.0426	0.0426	0.0426	0.0426	0.0426	0.0426	0.0426	0.0426	0.0426	0.0426	0.0426	0.0426
CU1	0.0950	0.0950	0.0950	0.0950	0.0950	0.0950	0.0950	0.0950	0.0950	0.0950	0.0950	0.0950	0.0950	0.0950	0.0950	0.0950	0.0950	0.0950	0.0950	0.0950
CU2	0.0139	0.0139	0.0139	0.0139	0.0139	0.0139	0.0139	0.0139	0.0139	0.0139	0.0139	0.0139	0.0139	0.0139	0.0139	0.0139	0.0139	0.0139	0.0139	0.0139
CU3	0.0101	0.0101	0.0101	0.0101	0.0101	0.0101	0.0101	0.0101	0.0101	0.0101	0.0101	0.0101	0.0101	0.0101	0.0101	0.0101	0.0101	0.0101	0.0101	0.0101
CU4	0.1065	0.1065	0.1065	0.1065	0.1065	0.1065	0.1065	0.1065	0.1065	0.1065	0.1065	0.1065	0.1065	0.1065	0.1065	0.1065	0.1065	0.1065	0.1065	0.1065
CU5	0.0876	0.0876	0.0876	0.0876	0.0876	0.0876	0.0876	0.0876	0.0876	0.0876	0.0876	0.0876	0.0876	0.0876	0.0876	0.0876	0.0876	0.0876	0.0876	0.0876
EP1	0.0565	0.0565	0.0565	0.0565	0.0565	0.0565	0.0565	0.0565	0.0565	0.0565	0.0565	0.0565	0.0565	0.0565	0.0565	0.0565	0.0565	0.0565	0.0565	0.0565
EP2	0.0399	0.0399	0.0399	0.0399	0.0399	0.0399	0.0399	0.0399	0.0399	0.0399	0.0399	0.0399	0.0399	0.0399	0.0399	0.0399	0.0399	0.0399	0.0399	0.0399
EP3	0.0497	0.0497	0.0497	0.0497	0.0497	0.0497	0.0497	0.0497	0.0497	0.0497	0.0497	0.0497	0.0497	0.0497	0.0497	0.0497	0.0497	0.0497	0.0497	0.0497
EP4	0.0138	0.0138	0.0138	0.0138	0.0138	0.0138	0.0138	0.0138	0.0138	0.0138	0.0138	0.0138	0.0138	0.0138	0.0138	0.0138	0.0138	0.0138	0.0138	0.0138
EP5	0.0785	0.0785	0.0785	0.0785	0.0785	0.0785	0.0785	0.0785	0.0785	0.0785	0.0785	0.0785	0.0785	0.0785	0.0785	0.0785	0.0785	0.0785	0.0785	0.0785
ME1	0.0452	0.0452	0.0452	0.0452	0.0452	0.0452	0.0452	0.0452	0.0452	0.0452	0.0452	0.0452	0.0452	0.0452	0.0452	0.0452	0.0452	0.0452	0.0452	0.0452
ME2	0.0558	0.0558	0.0558	0.0558	0.0558	0.0558	0.0558	0.0558	0.0558	0.0558	0.0558	0.0558	0.0558	0.0558	0.0558	0.0558	0.0558	0.0558	0.0558	0.0558
ME3	0.0668	0.0668	0.0668	0.0668	0.0668	0.0668	0.0668	0.0668	0.0668	0.0668	0.0668	0.0668	0.0668	0.0668	0.0668	0.0668	0.0668	0.0668	0.0668	0.0668
ME4	0.0800	0.0800	0.0800	0.0800	0.0800	0.0800	0.0800	0.0800	0.0800	0.0800	0.0800	0.0800	0.0800	0.0800	0.0800	0.0800	0.0800	0.0800	0.0800	0.0800
ME5	0.0127	0.0127	0.0127	0.0127	0.0127	0.0127	0.0127	0.0127	0.0127	0.0127	0.0127	0.0127	0.0127	0.0127	0.0127	0.0127	0.0127	0.0127	0.0127	0.0127

Table A5. Collected data from underground gold mines.

	SP1	SP2	SP3	SP4	SP5	CU1	CU2	CU3	CU4	CU5	EP1	EP2	EP3	EP4	EP5	ME1	ME2	ME3	ME4	ME5
M1	0.00	6.00	0.00	100.00	2.20	93.10	94.96	100.00	65.14	100.00	100.00	100.00	100.00	100.00	0.60	3.47	6.90	118.85	8.34	22.11
M2	7.00	7.00	0.00	100.00	1.15	95.79	95.13	71.46	84.30	100.00	67.90	100.00	100.00	100.00	1.28	4.25	4.21	19.76	9.80	47.03
M3	0.00	0.00	0.00	100.00	3.20	95.52	92.52	60.00	94.93	100.00	20.00	100.00	100.00	100.00	2.00	4.00	4.00	141.58	9.45	28.50
M4	0.00	1.00	0.00	100.00	4.95	93.62	96.50	72.63	0.00	100.00	100.00	100.00	100.00	100.00	1.42	12.00	6.38	22.38	5.38	24.58
M5	0.00	0.00	0.00	100.00	1.45	96.44	95.95	83.32	5.33	100.00	38.53	97.00	100.00	100.00	3.10	13.95	1.44	56.30	4.13	8.83
M6	0.00	0.00	0.00	100.00	4.10	89.55	85.00	81.71	30.00	100.00	20.00	99.00	99.00	98.00	1.00	10.08	10.45	41.42	5.75	108.81

Table A6. The normalized evaluation matrix.

	SP1	SP2	SP3	SP4	SP5	CU1	CU2	CU3	CU4	CU5	EP1	EP2	EP3	EP4	EP5	ME1	ME2	ME3	ME4	ME5
M1	1.0000	0.5385	1.0000	1.0000	0.4444	0.9654	0.9840	1.0000	0.6862	1.0000	1.0000	1.0000	1.0000	1.0000	0.1935	1.0000	0.2087	0.8395	0.8510	0.3994
M2	1.0000	0.5000	1.0000	1.0000	0.2319	0.9933	0.9858	0.7146	0.8880	1.0000	0.6790	1.0000	1.0000	1.0000	0.4134	0.8165	0.3420	0.1395	1.0000	0.1878
M3	1.0000	1.0000	1.0000	1.0000	0.6465	0.9905	0.9588	0.6000	1.0000	1.0000	0.2000	1.0000	1.0000	1.0000	0.6452	0.8675	0.3600	1.0000	0.9643	0.3098
M4	1.0000	0.8750	1.0000	1.0000	1.0000	0.9708	1.0000	0.7263	0.0000	1.0000	1.0000	1.0000	1.0000	1.0000	0.4581	0.2892	0.2257	0.1581	0.5490	0.3592
M5	1.0000	1.0000	1.0000	1.0000	0.2929	1.0000	0.9943	0.8332	0.0561	1.0000	0.3853	0.9700	1.0000	1.0000	1.0000	0.2487	1.0000	0.3977	0.4214	1.0000
M6	1.0000	1.0000	1.0000	1.0000	0.8283	0.9286	0.8808	0.8171	0.3160	1.0000	0.2000	0.9900	0.9900	0.9800	0.3226	0.3442	0.1378	0.2926	0.5867	0.0812

Table A7. The weighted normalized evaluation matrix.

	SP1	SP2	SP3	SP4	SP5	CU1	CU2	CU3	CU4	CU5	EP1	EP2	EP3	EP4	EP5	ME1	ME2	ME3	ME4	ME5	Scores
M1	0.0396	0.0150	0.0439	0.0342	0.0189	0.0917	0.0137	0.0101	0.0731	0.0876	0.0565	0.0399	0.0497	0.0138	0.0152	0.0452	0.0116	0.0561	0.0681	0.0051	0.7889
M2	0.0396	0.0139	0.0439	0.0342	0.0099	0.0944	0.0137	0.0072	0.0946	0.0876	0.0384	0.0399	0.0497	0.0138	0.0324	0.0369	0.0191	0.0093	0.0800	0.0024	0.7608
M3	0.0396	0.0278	0.0439	0.0342	0.0275	0.0941	0.0133	0.0060	0.1065	0.0876	0.0113	0.0399	0.0497	0.0138	0.0506	0.0392	0.0201	0.0668	0.0772	0.0039	0.8531
M4	0.0396	0.0244	0.0439	0.0342	0.0426	0.0922	0.0139	0.0073	0.0000	0.0876	0.0565	0.0399	0.0497	0.0138	0.0359	0.0131	0.0126	0.0106	0.0439	0.0046	0.6662
M5	0.0396	0.0278	0.0439	0.0342	0.0125	0.0950	0.0138	0.0084	0.0060	0.0876	0.0218	0.0387	0.0497	0.0138	0.0785	0.0113	0.0558	0.0266	0.0337	0.0127	0.7112
M6	0.0396	0.0278	0.0439	0.0342	0.0353	0.0882	0.0122	0.0082	0.0337	0.0876	0.0113	0.0395	0.0492	0.0135	0.0253	0.0156	0.0077	0.0195	0.0469	0.0010	0.6403

Table A8. Potential improvements for underground gold mines.

	SP1	SP2	SP3	SP4	SP5	CU1	CU2	CU3	CU4	CU5	EP1	EP2	EP3	EP4	EP5	ME1	ME2	ME3	ME4	ME5
M1		✓			✓										✓	✓				
M2		✓			✓			✓								✓		✓		
M3								✓			✓					✓				
M4								✓	✓									✓	✓	
M5					✓				✓		✓	✓					✓		✓	✓
M6						✓	✓		✓		✓		✓	✓	✓				✓	

References

1. Zhou, Y.; Zhou, W.; Lu, X.; Jiskani, I.M.; Cai, Q.; Liu, P.; Lin, L. Evaluation Index System of Green Surface Mining in China. *Min. Metall. Explor.* **2020**, *37*, 1093–1103. [CrossRef]
2. Qi, R.; Liu, T.; Jia, Q.; Sun, L.; Liu, J. Simulating the Sustainable Effect of Green Mining Construction Policies on Coal Mining Industry of China. *J. Clean Prod.* **2019**, *226*, 392–406. [CrossRef]
3. Zhao, Y.; Zhao, G.; Zhou, J.; Pei, D.; Liang, W.; Qiu, J. What Hinders the Promotion of the Green Mining Mode in China? A Game-Theoretical Analysis of Local Government and Metal Mining Companies. *Sustainability* **2020**, *12*, 2991. [CrossRef]
4. Liu, Y.; Zhang, C.; Huang, Y.; Xiao, Z.; Han, Y.; Ren, G. Climate Impact of China's Promotion of the Filling Mining Method: Bottom-Up Estimation of Greenhouse Gas Emissions in Underground Metal Mines. *Energies* **2021**, *14*, 3273. [CrossRef]
5. Chen, J.; Jiskani, I.M.; Jinliang, C.; Yan, H. Evaluation and Future Framework of Green Mine Construction in China Based on the DPSIR Model. *Sustain. Environ. Res.* **2020**, *30*, 13. [CrossRef]
6. Liang, W.; Dai, B.;Zhao, G.; Wu, H.Assessing the Performance of Green Mines via a Hesitant Fuzzy ORESTE–QUALIFLEX Method. *Mathematics* **2019**, *7*, 788. [CrossRef]
7. Chen, J.; Jiskani, I.M.; Lin,A.; Zhao, C.; Jing, P.; Liu,F.; Lu,M. A Hybrid Decision Model and Case Study for Comprehensive Evaluation of Green Mine Construction Level. *Environ. Dev. Sustain.* **2022**. [CrossRef]
8. Jiskani, I.M.; Cai, Q.; Zhou, W.; Ali Shah, S.A. Green and Climate-Smart Mining: A Framework to Analyze Open-Pit Mines for Cleaner Mineral Production. *Resour. Policy* **2021**, *71*, 102007. [CrossRef]
9. Liang, W.; Dai, B.; Zhao, G.; Wu, H. Performance Evaluation of Green Mine Using a Combined Multi-Criteria Decision Making Method with Picture Fuzzy Information. *IEEE Access* **2019**, *7*, 174139–174154. [CrossRef]
10. Qi, R.; Li, S.; Qu, L.; Sun, L.; Gong, C. Critical Factors to Green Mining Construction in China: A Two-Step Fuzzy DEMATEL Analysis of State-Owned Coal Mining Enterprises. *J. Clean Prod.* **2020**, *273*, 122852. [CrossRef]
11. Wang, J.; Hu, B.; Chang, J.; Li, H. Case Studies and Evaluation of Green Mining Considering Uncertainty Factors and Multiple Indicator Weights. *Geofluids* **2020**, *2020*, 1–15. [CrossRef]
12. Zhang, P.; Duan, N.; Dan, Z.; Shi, F.; Wang, H. An Understandable and Practicable Cleaner Production Assessment Model. *J. Clean Prod.* **2018**, *187*, 1094–1102. [CrossRef]
13. Ashraf, S.; Abdullah, S.; Mahmood, T.; Aslam, M. Cleaner Production Evaluation in Gold Mines Using Novel Distance Measure Method with Cubic Picture Fuzzy Numbers. *Int. J. Fuzzy Syst.* **2019**, *21*, 2448–2461. [CrossRef]
14. Liang, W.; Luo, S.;Zhao, G. Evaluation of Cleaner Production for Gold Mines Employing a Hybrid Multi-Criteria Decision Making Approach. *Sustainability* **2019**, *11*, 146. [CrossRef]
15. Huang, J.; L, Y.; Yue, P. Review on the Evaluation of Green Development of Mining Industry. *IOP Conf. Ser. Earth Environ. Sci.* **2021**, *859*, 012094. [CrossRef]
16. Yu, G.; Huang, Q.; Zhao, X.; Wang, W. Efficiency Evaluation and Optimization of Green Mining for Coal Enterprises Based on DEA. *Appl. Mech. Mater.* **2013**, *295–298*, 2864. [CrossRef]
17. Li, X.; Yang, J.; Yan, H.; Cao, H. Study on Evaluation Index System of Green Mine Construction. *IOP Conf. Ser. Earth Environ. Sci.* **2017**, *94*, 012182. [CrossRef]
18. Zhu, S.; Chu, Z.; Li, L.; Miao, S.; Xu, J. Deep Geological Characteristics and Ore Predition of Vein 175 in Linglong Gold Field in Jiaodong Area, Shandong Province. *Earth Sci.* **2021**, *10*, 128.
19. Na, Y.; Yang, Y. Study on Genesis of Gold Deposit and Mineralization Enrichment Regularity Based on Mapping Analysis. In Proceedings of the 2017 9th International Conference on Measuring Technology and Mechatronics Automation (ICMTMA), Changsha, China, 14–15 January 2017; pp. 236–239. Available online: https://www.webofscience.com/wos/alldb/full-record/WOS:000401696400055 (accessed on 30 April 2022).
20. Chen, C. Hazards Identification and Characterisation of the Tailings Storage Facility Dam Failure and Engineering Applications. *Int. J. Min. Reclam. Environ.* **2022**, 1–20. [CrossRef]
21. Li, L.; Xu, L.J.; Chen, D.M. Connotation and Technology System of Green Mining of Manganese Resources. *Adv. Mater. Res.* **2013**, *734–737*, 540–545. [CrossRef]
22. Mensah, M.K.;Drebenstedt, C.; Annam, B.V.; Armah, E.K. Occupational Respirable Mine Dust and Diesel Particulate Matter Hazard Assessment in an Underground Gold Mine in Ghana. *J. Health Pollut.* **2020**, *10*, 200305. [CrossRef] [PubMed]

23. Amoakwah, E.; Ahsan, S.; Rahman, M.A.; Asamoah, E.; Essumang, D.K.; Ali, M.; Islam, K.R. Assessment of Heavy Metal Pollution of Soil-Water-Vegetative Ecosystems Associated with Artisanal Gold Mining. *Soil Sediment Contam.* **2020**, *29*, 788–803. [CrossRef]

24. Zhang, C.; Wang, X.; Jiang, S.; Zhou, M.; Li, F.; Bi, X.; Xie, S.; Liu, J. Heavy Metal Pollution Caused by Cyanide Gold Leaching: A Case Study of Gold Tailings in Central China. *Environ. Sci. Pollut. Res.* **2021**, *28*, 29231–29240. [CrossRef] [PubMed]

25. Zhao, G.; Li, X.; Zhu, J.; Zhao, X.; Zhang, J.; Zhai, J. Pollution Assessment of Potentially Toxic Elements (PTEs) in Soils around the Yanzhuang Gold Mine Tailings Pond, Pinggu County, Beijing, China. *Int. J. Environ. Res. Public Health* **2021**, *18*, 7240. [CrossRef] [PubMed]

26. Wang, Y.; Lei, Y.; Wang, S. Green Mining Efficiency and Improvement Countermeasures for China's Coal Mining Industry. *Front. Energy Res.* **2020**, *8*, 18. [CrossRef]

27. Nazir, M.; Cavus, N. Quality Evaluation of Learning Management Systems Using Dematel-Anp. In Proceedings of the International Technology, Education and Development Conference, Valencia, Spain, 6–8 March 2017; pp. 5754–5760. Available online: https://www.webofscience.com/wos/alldb/full-record/WOS:000427401300097 (accessed on 30 April 2022).

28. Rostamzadeh, S.; Abouhossein, A.; Chalak, M.H.; Vosoughi, S.; Norouzi, R. An Integrated DEMATEL-ANP Approach for Identification and Prioritization of Factors Affecting Falls from Height Accidents in Construction Industry. *Int. J. Occup. Saf. Ergon.* **2022**, 1–31. [CrossRef]

29. Jiskani, I.M.; Cai, Q.; Zhou, W.; Lu, X.; Shah, S. An Integrated Fuzzy Decision Support System for Analyzing Challenges and Pathways to Promote Green and Climate Smart Mining. *Expert Syst. Appl.* **2022**, *188*, 116062. [CrossRef]

30. Liang, W.; Zhao, G.; Wu, H.; Dai, B. Risk Assessment of Rockburst via an Extended MABAC Method under Fuzzy Environment. *Tunn. Undergr. Space Technol.* **2019**, *83*, 533–544. [CrossRef]

31. Mubarik, M.S.; Kazmi, S.H.A.; Zaman, S.I. Application of Gray DEMATEL-ANP in Green-Strategic Sourcing. *Technol. Soc.* **2021**, *64*, 101524. [CrossRef]

32. Liu, X.; Deng, Q.; Gong, G.; Zhao, X.; Li, K. Evaluating the Interactions of Multi-Dimensional Value for Sustainable Product-Service System with Grey DEMATEL-ANP Approach. *J. Manuf. Syst.* **2021**, *60*, 449–458. [CrossRef]

33. Jiskani, I.M.; Han, S.; Rehman, A.U.; Shahani, N.M.; Tariq, M.; Brohi, M.A. An Integrated Entropy Weight and Grey Clustering Method–Based Evaluation to Improve Safety in Mines. *Min. Metall. Explor.* **2021**, *38*, 1773–1787. [CrossRef]

34. Han, S.; Chen, H.; Long, R.; Qi, H.; Cui, X. Evaluation of the Derivative Environment in Coal Mine Safety Production Systems: Case Study in China. *J. Clean Prod.* **2017**, *143*, 377–387. [CrossRef]

35. Xiao, W.; Chen, W.; Deng, X. Coupling and Coordination of Coal Mining Intensity and Social-Ecological Resilience in China. *Ecol. Indic.* **2021**, *131*, 108167. [CrossRef]

36. Yazdi, M.; Khan, F.; Abbassi, R.; Rusli, R. Improved DEMATEL Methodology for Effective Safety Management Decision-Making. *Saf. Sci.* **2020**, *127*, 104705. [CrossRef]

37. Si, S.; You, X.; Liu, H.; Zhang, P. DEMATEL Technique: A Systematic Review of the State-of-the-Art Literature on Methodologies and Applications. *Math. Probl. Eng.* **2018**, *2018*, 3696457. [CrossRef]

38. Liu, C.; Li, K.; Jiang, P.; Li, D.; Su, L.; Lu, S.; Li, A. A Hybrid Multiple Criteria Decision-Making Technique to Evaluate Regional Intellectual Capital: Evidence from China. *Mathematics* **2021**, *9*, 1676. [CrossRef]

39. Rao, S. A Hybrid MCDM Model Based on DEMATEL and ANP for Improving the Measurement of Corporate Sustainability Indicators: A Study of Taiwan High Speed Rail. *Res. Transp. Bus. Manag.* **2021**, *41*, 100657. [CrossRef]

40. Hwang, C.; Yoon, K. *Multiple Attribute Decision Making: Methods and Applications*; Springer: Berlin/Heidelberg, Germany, 1981.

41. Wudhikarn, R. The Hybrid Intellectual Capital Valuation Method. *Ekon. Istraz.* **2021**, *34*, 2115–2134. [CrossRef]

42. Wudhikarn, R.; Chakpitak, N.; Neubert, G. An Analytic Network Process Approach for the Election of Green Marketable Products. *Benchmarking* **2015**, *22*, 994–1018. [CrossRef]

43. Wudhikarn, R.; Chakpitak, N.; Neubert, G. Use of an Analytic Network Process and Monte Carlo Analysis in New Product Formula Selection Decisions. *Asia Pac. J. Oper. Res.* **2015**, *32*, 1550007. [CrossRef]

44. Wudhikarn, R. Improving the Intellectual Capital Management Approach Using the Hybrid Decision Method. *J. Intellect. Cap.* **2018**, *19*, 670–691. [CrossRef]

45. Wu, W. Choosing Knowledge Management Strategies by Using a Combined ANP and DEMATEL Approach. *Expert Syst. Appl.* **2008**, *35*, 828–835. [CrossRef]

46. Teplická, K.; Khouri, S.; Beer, M.; Rybárová, J. Evaluation of the Performance of Mining Processes after the Strategic Innovation for Sustainable Development. *Processes* **2021**, *9*, 1374. [CrossRef]

Article

Green Mining Strategy Selection via an Integrated SWOT-PEST Analysis and Fuzzy AHP-MARCOS Approach

Pan Wu, Guoyan Zhao * and Yang Li

School of Resources & Safety Engineering, Central South University, Changsha 410083, China;
panwuly@csu.edu.cn (P.W.); leonly@csu.edu.cn (Y.L.)
* Correspondence: gyzhao@csu.edu.cn

Abstract: Deciding on an appropriate development strategy is one of the most crucial aspects of the mining industry's green transition. This research introduces a novel integrated decision support model that can be applied to analyze various environmental factors and determine development strategies. In this study, a strengths, weaknesses, opportunities, and threats (SWOT) analysis is employed from multiple perspectives, including political, economic, social, and technological (PEST), to assess the internal and external factors that influence green mining. The fuzzy analytic hierarchy process (AHP) is used to analyze the factor weights quantitatively, and the fuzzy Measurement of Alternatives and Ranking according to Compromise Solution (MARCOS) method is used to rank and select development strategies. According to the results, "grasp the trend of green development and improve the protection and exploitation level of mineral resources" is found to be the final optimal strategy. Comparative analysis and sensitivity analysis confirmed the accuracy of the model and the case study results.

Keywords: green mining; development strategy; SWOT-PEST analysis; fuzzy AHP; fuzzy MARCOS

1. Introduction

Global companies are driven to make a green transformation due to escalating ecological degradation and pollution [1]. Under the government's severe resource and environmental policies, as well as the fiercely competitive market, green development has become an unavoidable trend [2]. The green development model is an important path towards "intensive and economical utilization of resources, reduction of environmental damage, improvement of labor productivity, and enhancement of sustainable development capabilities" [3]. A healthy ecological environment has become the focus of the government and society more than ever [4]. Mining, as an industry that pollutes and destroys the environment, is much worse [5,6]. It has become a critical industry to address as part of the process of achieving green development. Mining not only provides employment and income, but it is also the pillar of the energy supply chain [7]. Mining companies used to focus on mining productivity and profit margins, with the environment being the least important issue. This development model resulted in the continuing deterioration of the mining area's ecological environment, significant waste of mineral resources [8,9], and negative social consequences. The situation is changing due to the background of the gradual depletion of resources and the growing popularity of green concepts. Resources and environmental protection have now been elevated to become the top priority in mining, based on the construction of a long-term sustainable profit model [10].

As mining activities involve the whole life cycle from exploration to production, closure, and restoration, it makes the green transformation of mines a multi-dimensional, long-term process [11]. Traditional technologies and conceptions have given way to a new, more sustainable production model in this process [12]. Developed mining countries such as in Europe and the United States put forward the concept with the same connotation

as green mining as early as the 19th century, but, initially, it was limited to the greening of the mining environment [13]. In China, the specific concept of green mining was first proposed by Qian in 2003 for coal mines [14]. Subsequently, the government proposed a series of policy requirements for green practices in mines. The overall goal of establishing a fundamental pattern of green mines was put forward in 2009 in China [15]. Later, in 2016, it was proposed to form a new pattern of green mines and the establishment of 661 green mine pilot units was approved [16]. In 2018, the green mine construction standards of nine major industries were proposed, and the green mine construction began to be standardized [17]. Nowadays, the fundamental pattern of green mine construction has a general outline, but it is confronting complicated political, economic, social, and technological considerations at home and abroad in its new stage of growth and promotion. In recent years, with the dual background of building an innovative country and a green development strategy, some new concepts, such as developing smart mines and tailless mines [18], have been proposed. Some challenges, such as deep mining, the comprehensive utilization of resources, and ecological restoration, have made partial breakthroughs and innovations [19], and the release and implementation of a series of policy incentive documents have forced mining enterprises to re-examine their development model, promote the establishment of green mine transformation, and gain a competitive edge [20].

Due to differences in mine scale, category, area, and other factors, decision makers in mining companies have gaps in the transformation strategies they can choose as a part of the process of pursuing green transformation [21]. Therefore, it is not only technology that drives green transformation but also the planning and selection of development strategies [22]. However, because the mining industry is such a complicated system, strategic planning and decision making are challenging [23]. It is necessary for mining companies to analyze their internal and external influencing factors and implement the right strategy at the right time and place in order to maintain dynamic competitiveness [24], which can only be achieved through holistic strategic planning. There are few such studies in the context of China's mining development. Therefore, from this perspective, this study uses SWOT as the most basic tool for strategic analysis and selection. After the introduction, the second part of the article presents the literature review. The third part introduces the methodology and proposes an AHP-MARCOS strategic decision analysis model based on SWOT-PEST analysis, and the fourth part presents a case study. The next section compares three methods, namely MARCOS, FTOPSIS, and FMABAC, to verify the accuracy of the case analysis and conduct a sensitivity analysis. Finally, the conclusions and prospects of this study are presented.

2. Literature Review

SWOT analysis is a well-known analysis method in modern strategic management and planning. Using the SWOT analysis method to make strategic decisions based on the research objectives and current environment of the research object can make full use of strengths, eliminate weaknesses, seize opportunities, and deal with threats [25], resulting in a positive match between internal and external factors [26]. The SWOT analysis was developed in the 1960s [27] and is now extensively utilized in various industries, such as construction, energy, e-commerce, etc. Yuan [28] provided critical strategies for construction waste management in the construction industry based on SWOT analysis. Terrados et al. [29] conducted strategic planning for renewable energy development with the help of a SWOT analysis tool. Zhao et al. [30] introduced SWOT analysis to explore strategies for high-level development of China's e-commerce industry. Novikov [31] employed SWOT to analyze the high-tech strategic development of manufacturing enterprises. Kolbina [32] and Bohari et al. [33] conducted a SWOT analysis of the food business. SWOT analysis is applicable in the energy sector. Liu et al. [34] identified the influencing factors of the low-carbon economy development of mining companies through SWOT analysis, proposed a framework structure for developing a low-carbon economy, and constructed a new development model of mines. Nikolaou and Evangelino [35] used SWOT tools to

analyze the problems faced in the practice of environmental management in Greek mines. Jiskani et al. [36] used a multi-criteria-based SWOT analysis of sustainable planning for the mining and mineral industry in Pakistan. The environmental factors of traditional SWOT analysis are complex. To classify the complex factors clearly and provide a reference for subsequent strategy formulation, Dong et al. [37] integrated the variables of the selected environmental factors into politics, the economy, society, and technology by introducing the PEST tool, which provides a clear direction for the analysis of SWOT environmental factors [38].

A single SWOT analysis, on the other hand, can give a subjective qualitative assessment of development competitiveness [39], which is the foundation for strategy formulation. However, a single SWOT analysis cannot completely evaluate the strategic decision-making process [40] since it is impossible to determine the relative influence of various factors on strategic decision making by quantifying the importance of these factors. Therefore, many researchers have extensively combined SWOT analysis with other quantitative evaluation approaches. Multi-criteria decision making (MCDM) is the most used method, such as the analytic hierarchy process (AHP), the analytical network (ANP), etc., which determines the relative significance of the various factors in the proposed strategy [41] and overcomes the shortcomings of traditional SWOT analysis. Considering that real-life decision-making processes are frequently ambiguous, fuzzy logic may be used in MCDM. The AHP technique has become the most prominent MCDM method in mining research due to its ease of use, high repeatability, support for group decision making, and ability to apply to fuzzy sets [42]. In addition, the AHP technique allows the SWOT model to be incorporated into the hierarchy to quantify the factors [43]. According to studies, combining the SWOT analysis approach with the fuzzy AHP method helps handle decision-making challenges in a variety of sectors. For example, Erdogan and Kara [44] integrated SWOT and Fuzzy AHP models to analyze Turkey's maritime transport strategy options, Buyukozkan et al. [45] studied healthy tourism strategy options, and Solangi et al. [46] explored Pakistan's sustainable energy strategic planning. Most of the above studies are based on case studies, showing that SWOT combined with the AHP methods can be successfully applied to case studies. It is reasonable to use SWOT analysis combined with Fuzzy AHP method for quantitative research in this study.

For strategic decision making, this study employs a new ranking method, Measurement of Alternatives and Ranking According to Compromise (MARCOS), which was proposed by Stevic et al. [47] in 2020 and was subsequently improved by Stankovic et al. [48]. Despite the fact that the MARCOS method is a relatively new method, due to its advantages of stability and applicability in different MCDM methods, scientific articles using the MARCOS method have been published frequently in recent years and it has been applied in a variety of fields [49,50], but its application in the mining field is very limited. The use of the MARCOS approach in the mining area, as well as embedding PEST into a SWOT tool for a full internal and external factor analysis to create the Fuzzy AHP hierarchy, are the contributions and originality of this research.

3. Methodology

This section presents the implemented analytical model, the proposed decision-making method, and other preparations to deepen the connection between the theoretical frameworks. First, the SWOT-PEST analysis method is described, then the Fuzzy set theory is introduced, further introducing the complete steps of Fuzzy AHP, and finally the Fuzzy MARCOS method and its steps are described. In the proposed method, AHP is used to obtain criterion weights, and MARCOS is employed to evaluate and rank the alternatives. AHP is easy to use, repeatable, and supports group decision making in a hierarchical structure, while MARCOS is characterized by flexibility when considering compromise solutions based on relative importance. The combination of two methods makes the model less complex even when there are a large number of criteria or alternatives. Figure 1 depicts the phases of the proposed integrated decision model.
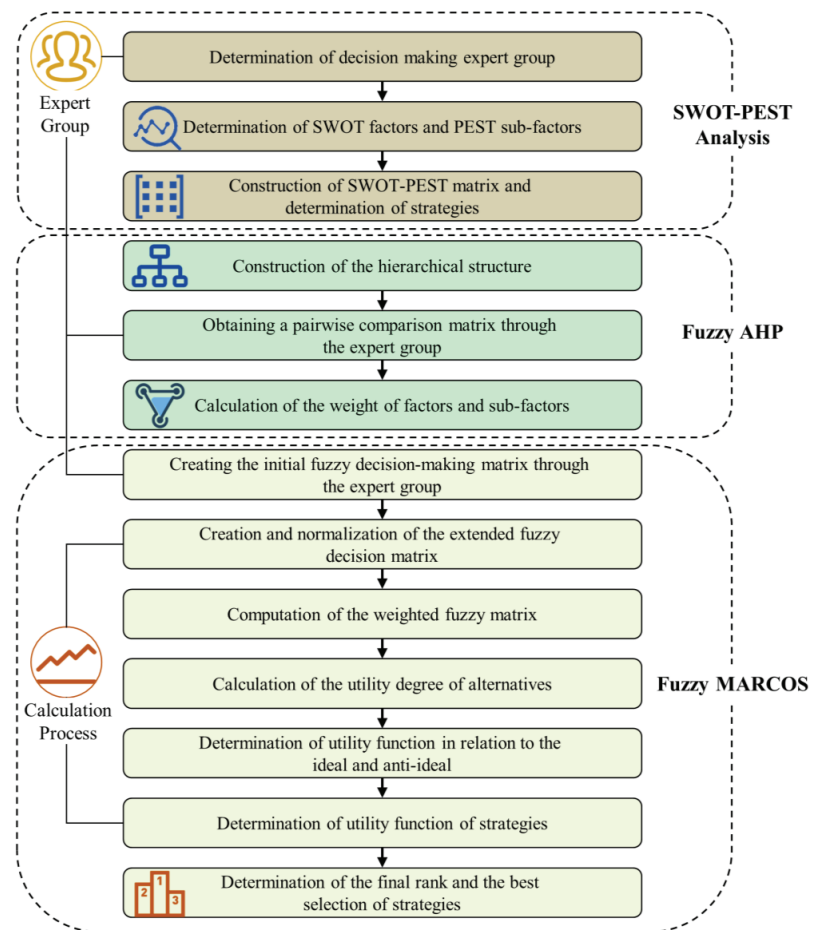
Figure 1. The proposed methodology of the research.

3.1. SWOT-PEST Analysis

SWOT analysis is a useful technique for environmental analysis. It can summarize the internal and external situations of the research object, as well as examine its strengths, weaknesses, opportunities, and threats. It can lead to several more scientific and comprehensive observations. This approach can be used as a guide for developing strategic plans.

PEST analysis is a method for macro-environmental analysis that utilizes environmental scanning to investigate four factors in the total environment: political, economy, society, and technology. It is one of the most significant models for macro-environmental analysis. It assesses the impact of these factors on strategic objectives and strategy formulation by using factor analysis in four aspects to comprehend the macro environment as a whole.

It is not appropriate to analyze an object's development just based on external or internal aspects when there are several contributing factors. As shown in Table 1 and Figure 2, this work develops a SWOT-PEST matrix analysis model from the perspective of a comprehensive paradigm to obtain numerous environmental factors. The SWOT-PEST analysis approach combines SWOT and PEST analysis, in which internal factors (strengths and weaknesses) and external macro-environmental factors (opportunities and threats) are included for systematic investigation and analysis. Policy, economy, society, and technology are put into the SWOT analysis framework to consider and systematically

analyze the strengths, weaknesses, opportunities, and threats to obtain a comprehensive and clear overview of the environmental factors at hand, and to serve as a foundation for strategy formulation.

Table 1. PEST-embedded SWOT analysis.

PEST	SWOT			
	Strengths	**Weaknesses**	**Opportunities**	**Threats**
Politics	SP	WP	OP	TP
Economy	SE	WE	OE	TE
Society	SS	WS	OS	TS
Technology	ST	WT	OT	TT

Figure 2. SWOT-PEST matrix.

3.2. Utilized Fuzzy-Based Method

3.2.1. Preliminaries of Fuzzy Set Theory

To cope with the uncertainty or ambiguity of objects, L.A. Zadeh developed the fuzzy set theory in 1965 [51].

A fuzzy set $\widetilde{A} = \left\{ (x, \mu_{\widetilde{A}}(x)) \big| x \in X \right\}$ is a set of ordered pairs, X is a subset of real numbers R, where $\mu_{\widetilde{A}}(x)$ is called the membership function, which assigns each object x a membership level from zero to one [52].

Fuzzy set theory has been widely employed to handle practical situations in which decision makers must examine and deal with inaccurate data since its conception. Different fuzzy numbers can be chosen depending on multiple realities. TFN is a specific case of trapezoidal fuzzy numbers that occurs when the two most promising values of a trapezoidal fuzzy number are the same value. Due to its computational simplicity and ability to enable representation and information processing in fuzzy environments [53], triangular fuzzy numbers (TFNs) are employed in many applications. TFNs are typically employed to record the ambiguity of parameters relevant to the decision-making process. They are represented by boundaries rather than clear numbers to reflect the uncertainty decision makers encounter in pairwise comparison matrices. The membership function of a triangular fuzzy number, denoted as $\widetilde{A} = (l, m\, u)$, is as follows

$$\mu_{\widetilde{A}}(x) = \begin{cases} 0 & if\ x \leq l \\ \frac{x-l}{m-l} & if\ l \leq x \leq m \\ \frac{u-x}{u-m} & if\ m \leq x \leq u \\ 0 & if\ x \leq u \end{cases} \tag{1}$$

A triangular fuzzy number $\widetilde{A}$ is a possible range with upper and lower bounds, where m is the most likely value [54]. Consider two TFNS, $\widetilde{A} = (a_1, a_2, a_3)$ and $\widetilde{B} = (b_1, b_2, b_3)$, the main operational laws [55] for two triangular fuzzy numbers A and B are as follows

$$\widetilde{A} \oplus \widetilde{B} = (a_1, a_2, a_3) \oplus (b_1, b_2, b_3) = (a_1 + b_1, a_2 + b_2, a_3 + b_3) \tag{2}$$

$$\widetilde{A} \otimes \widetilde{B} = (a_1, a_2, a_3) \otimes (b_1, b_2, b_3) = (a_1 b_1, a_2 b_2, a_3 b_3) \tag{3}$$

$$\lambda \otimes \widetilde{A} = \lambda \otimes (a_1, a_2, a_3) = (\lambda a_1, \lambda a_2, \lambda a_3) \ \lambda > 0, \ \lambda \in R \tag{4}$$

$$\widetilde{A}^{-1} = (\frac{1}{a_3}, \frac{1}{a_2}, \frac{1}{a_1}) \tag{5}$$

3.2.2. Fuzzy AHP Approach

There are several improved models for fuzzy AHP. Reference [56] compares the advantages and disadvantages of different Fuzzy AHP methods. This study adopts the method proposed by Chang [57], which has been applied in various fields because of its low computational complexity and wide applicability. Let $\widetilde{A} = (\widetilde{a}_{ij})_{m \times n}$ be a fuzzy pairwise comparison matrix, where $\widetilde{a}_{ij} = (l_{ij}, m_{ij}, u_{ij})$. The steps of Chang's method can be described as follows:

Step 1: Calculate the value of the fuzzy synthetic extent with respect to the *i*-th object of the *k*-level index as follows

$$\widetilde{V}_i^k = \sum_{j=1}^n \widetilde{a}_{ij}^k \otimes \left[\sum_{i=1}^n \sum_{j=1}^n \widetilde{a}_{ij}^k\right]^{-1}, \ i = 1, 2, \ldots, n \tag{6}$$

Step 2: Calculate the degree of possibility between two fuzzy synthetic extent values. The degree of possibility is defined as follows

$$P(V_1 > V_2) = height(V_1 \cap V_2) = \begin{cases} 0 & if \ l_2 \geq u_1 \\ \frac{l_2 - u_1}{(m_1 - u_1) - (m_2 - l_2)} & otherwise \\ 1 & if \ m_1 \geq m_2 \end{cases} \tag{7}$$

Step 3: The degree of possibility for a fuzzy number to be greater than the other *k* fuzzy numbers can be defined as follows

$$P(V \geq V_1, V_2, \ldots, V_k) = P[(V \geq V_1) \ and \ (V \geq V_2) \ and \ \ldots \ and \ (V \geq V_k)] \\ = \min P(V \geq V_i) \ i = 1, 2, \ldots, k \tag{8}$$

Step 4: Assume that $d'(C_i) = \min P(V_i > V_k)$ for $k = 1, 2, \ldots, n \ (i \neq k)$. Then the weight vector can be given as follows

$$W'_C = [d'(C_1), d'(C_2), \ldots, d'(C_n)]^T \tag{9}$$

where $C_i \ (i = 1, 2, \ldots, n)$.

Step 5: The normalized weight vector needs to be obtained through normalization

$$W_C = [d(C_1), d(C_2), \ldots, d(C_n)]^T \tag{10}$$

Step 6: Repeat the procedures above to obtain the weight W_i of the next level indicator; then the total weight of the indicator is calculated as follows

$$TW_i = W_C \times W_i \tag{11}$$

3.2.3. Fuzzy MARCOS Approach

The Measurement of Alternatives and Ranking according to Compromise Solution (MARCOS) is a new multi-criteria analysis method. The MARCOS approach is based on a predetermined connection between alternatives and their reference values, which represent ideal and anti-ideal points. For decision making, the MARCOS method employs a utility function, which represents alternatives to ideal and anti-ideal solutions. The optimal alternative is the one that is closest to the ideal solution while being the farthest from the

anti-ideal solution. A fuzzy version of the MARCOS method was proposed by Torkayesh, AE et al. [58]. The steps of the method are as follows:

Step 1: The decision maker constructs an initial decision matrix based on the linguistic terms of the alternatives under multiple criteria.

Step 2. Construct an extended initial fuzzy matrix by defining ideal (AI) and anti-ideal (AAI) solutions.

The anti-ideal solution (AAI) and the ideal solution (AI) are obtained by applying Equations (12) and (13)

$$\widetilde{A}(AAI) = \begin{cases} \min\limits_{i} x_{ij} & if\ j \in B \\ \max\limits_{i} x_{ij} & if\ j \in C \end{cases} \tag{12}$$

$$\widetilde{A}(AI) = \begin{cases} \max\limits_{i} x_{ij} & if\ j \in B \\ \min\limits_{i} x_{ij} & if\ j \in C \end{cases} \tag{13}$$

where B represents the benefit criterion that needs to be maximized, and C represents the cost criterion that needs to be minimized.

Step 3: Normalize the initial fuzzy decision matrix. Depending on the criteria involved, normalize using Equation (14)

$$\widetilde{n} = (n_{ij}^{l},\ n_{ij}^{m},\ n_{ij}^{u}) = \begin{cases} (\frac{x_{id}^{l}}{x_{ij}^{u}},\ \frac{x_{id}^{l}}{x_{ij}^{m}},\ \frac{x_{id}^{l}}{x_{ij}^{l}})\ if\ j \in C \\ (\frac{x_{ij}^{l}}{x_{id}^{u}},\ \frac{x_{ij}^{m}}{x_{id}^{u}},\ \frac{x_{ij}^{u}}{x_{id}^{u}})\ if\ j \in B \end{cases} \tag{14}$$

where l, m, u are the parameters in the triangular fuzzy number, respectively.

Step 4: Calculate the weighted fuzzy matrix $\widetilde{V}$ by multiplying the normalized matrix $\widetilde{n}$ by the weight coefficient $\widetilde{w}_j$ of the indicator according to Equation (15).

$$\widetilde{v}_{ij} = (v_{ij}^{l},\ v_{ij}^{m},\ v_{ij}^{u}) = \widetilde{n}_{ij} \otimes \widetilde{w}_{j} = (n_{ij}^{l} \times w_{j}^{l},\ n_{ij}^{m} \times w_{j}^{m},\ n_{ij}^{u} \times w_{j}^{u}) \tag{15}$$

Step 5: The calculation of the $\widetilde{S}_i$ matrix implies the sum of values by rows (alternatives), including the anti-ideal and ideal solution by applying Equation (16)

$$\widetilde{S}_i = \sum_{i=1}^{n} \widetilde{v}_{ij} \tag{16}$$

Step 6: Calculation of the utility degree of alternatives $\widetilde{K}_i$. The utility degrees of an alternative in relation to the anti-ideal and ideal solution are obtained by using Equations (17) and (18).

$$\widetilde{K}_i^- = (\frac{\widetilde{s}_i}{\widetilde{s}_{ai}}) = (\frac{s_i^l}{s_{ai}^u},\ \frac{s_i^m}{s_{ai}^u},\ \frac{s_i^u}{s_{ai}^u}) \tag{17}$$

$$\widetilde{K}_i^+ = (\frac{\widetilde{s}_i}{\widetilde{s}_{id}}) = (\frac{s_i^l}{s_{id}^u},\ \frac{s_i^m}{s_{id}^u},\ \frac{s_i^u}{s_{id}^u}) \tag{18}$$

Step 7: Calculate the fuzzy matrix $\widetilde{T}_i$ and $\widetilde{D}$ by using Equations (19) and (20)

$$\widetilde{T}_i = \widetilde{t}_i = (t_i^l,\ t_i^m,\ t_i^u) = \widetilde{K}_i^- + K_i^+ = (\widetilde{k}_i^{-l} + \widetilde{k}_i^{+l}, \widetilde{k}_i^{-m} + \widetilde{k}_i^{+m}, \widetilde{k}_i^{-u} + \widetilde{k}_i^{+u}) \tag{19}$$

$$\widetilde{D} = (d^l,\ d^m,\ d^u) = \max_{i} \widetilde{t}_{ij} \tag{20}$$

Step 8: Defuzzify the fuzzy number $\widetilde{D}$ by using Equation (21)

$$df_{def} = \frac{l + 4m + u}{6} \tag{21}$$

Step 9: Determine the utility functions for the ideal and anti-ideal solutions via Equations (22) and (23)

$$f(\widetilde{K}_i^+) = \frac{\widetilde{K}_i^-}{df_{def}} = (\frac{k_i^{-l}}{df_{def}}, \frac{k_i^{-m}}{df_{def}}, \frac{k_i^{-u}}{df_{def}}) \tag{22}$$

$$f(\widetilde{K}_i^-) = \frac{\widetilde{K}_i^+}{df_{def}} = (\frac{k_i^{+l}}{df_{def}}, \frac{k_i^{+m}}{df_{def}}, \frac{k_i^{+u}}{df_{def}}) \tag{23}$$

where $\widetilde{K}_i^-$, $\widetilde{K}_i^+$, $f(\widetilde{K}_i^+)$, $f(\widetilde{K}_i^-)$ should be defuzzified.

Step 10: Determine the utility functions of alternatives: utility functions $f(K_i)$ of alternatives are obtained through Equation (24)

$$f(K_i) = \frac{K_i^+ + K_i^-}{1 + \frac{1-f(K_i^+)}{f(K_i^+)} + \frac{1-f(K_i^-)}{f(K_i^-)}} \tag{24}$$

Step 11: Rank the alternatives according to their final utility value.

4. Case Study

In this section, the applicability of the proposed model is demonstrated through a case study. All countries throughout the world are developing sustainable development models that are tailored to their own needs, and the mining sector is experiencing a transformation towards sustainable green development and has achieved certain results in the past few years. Through the establishment of a long-term policy mechanism, mine resources and environmental problems have been improved to a certain extent. Today, China has innovatively developed and adopted modern mining technologies, implemented green concepts in mines, issued a series of green mine construction guidelines, and set up some green mine demonstration sites. It is necessary to determine an appropriate development strategy for the green transformation of mines under this trend.

4.1. SWOT-PEST Analysis of Green Mining in China

China's green mining development strategy is influenced by the combination of internal and external environments. This study adopts the PEST-embedded SWOT analysis method to identify the internal and external factors of the slow progress of green mine construction, and construct a specific SWOT analysis matrix. Through the analysis, various major strengths and opportunities for the development of green mining technology, as well as weaknesses and threats in the development process of green mining, are discovered.

To provide data for strategy analysis, we conducted extensive literature research on relevant themes and approaches. Based on the survey results, as shown in Figure 3, an analysis matrix with four strengths, four weaknesses, four opportunities, and four threats was identified by employing a SWOT-PEST analysis. Green mining strategies were given based on interviews with the expert group. DM1 has more than three decades of experience in the mining industry, specializing in mining development in China. DM2 has extensive experience in the Chinese mining sector. DM3 has extensive experience in researching the sustainable development of China's mining industry. Each of the three professionals has significant mining expertise and experience.

4.2. Determining the Weights of Criteria by Fuzzy AHP

The evaluation criteria for the alternatives must be defined initially in Fuzzy AHP. We constructed a hierarchical model (Figure 4) containing the objective layer, the criterion layer, the sub-criteria layer, and the strategy layer, as shown in Figure 3, with one objective, four criteria, sixteen sub-criteria, and eight methods, based on the influencing factors identified by the SWOT-PEST study.

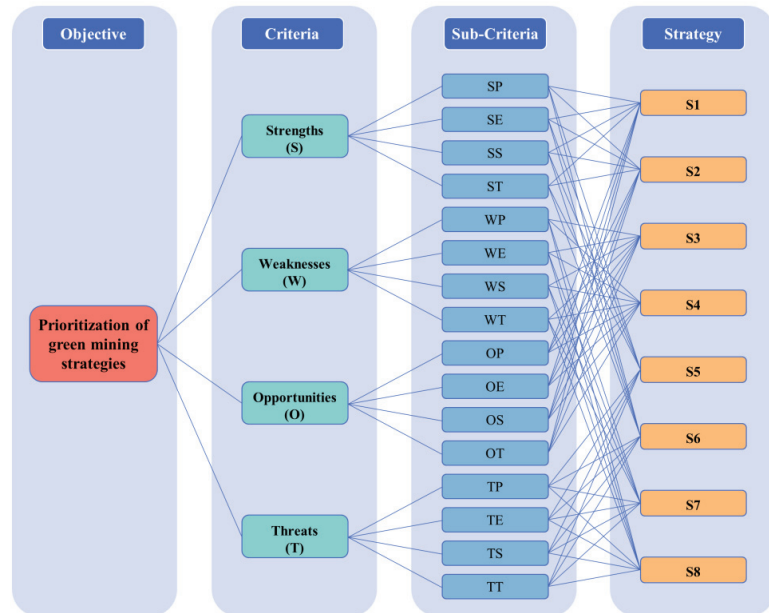**Figure 3.** SWOT-PEST analysis matrix of China's green mining industry.

Figure 4. Hierarchical structure model of SWOT-PEST matrix.

Followed by the identification of the criteria and sub-criteria, different priority weights for each criterion and sub-criteria are determined by linguistic comparison terms and their equivalent triangular fuzzy numbers (TFN), which are defined by Khazaeni [53] in Table 2.

Table 2. Fuzzy Fundamental Scale.

Linguistic Term	Fuzzy Number	Triangular Fuzzy Scale	Reciprocal Fuzzy Scale
Equally significant (ES)	$\tilde{1}$	(1, 1, 1)	(1, 1, 1)
Weakly more significant (WMS)	$\tilde{3}$	(1, 3, 5)	(1/5, 1/3, 1)
Strongly more significant (SMS)	$\tilde{5}$	(3, 5, 7)	(1/7, 1/5, 1/3)
Very strongly significant (VSS)	$\tilde{7}$	(5, 7, 9)	(1/9, 1/7, 1/5)
Absolutely significant (AS)	$\tilde{9}$	(7, 9, 9)	(1/9, 1/9, 1/7)

Tables 3–7 show the fuzzy comparison matrices for the criterion and sub-criteria and the calculated weights. The consistency check results show that all calculated C.R. values satisfy C.R. < 0.1. Therefore, all evaluations obtained from the panel are consistent. There is no need to repeat the evaluation process.

Table 3. The fuzzy comparison matrix of criteria with respect to the objective.

Criteria	S	W	O	T	Criteria Weight
S	ES		VSS	SMS	0.353
W	SMS	ES	WMS		0.164
O			ES	WMS	0.273
T		AS		ES	0.210

(C.R. = 0.001 < 0.1).

Table 4. The fuzzy comparison matrix of sub-criteria with respect to criteria S.

Sub-Criteria	SP	SE	SS	ST	Relative Weight
SP	ES	WMS			0.377
SE		ES	SMS		0.286
SS	VSS		ES	SMS	0.117
ST	SMS	WMS		ES	0.220

(C.R. = 0.043 < 0.1).

Table 5. The fuzzy comparison matrix of sub-criteria with respect to criteria W.

Sub-Criteria	WP	WE	WS	WT	Relative Weight
WP	ES	WMS	VSS		0.166
WE		ES		SMS	0.291
WS		SMS	ES	SMS	0.170
WT	WMS			ES	0.373

(C.R. = 0.045 < 0.1).

Table 6. The fuzzy comparison matrix of sub-criteria with respect to criteria O.

Sub-Criteria	OP	OE	OS	OT	Relative Weight
OP	ES	WMS	SMS		0.221
OE		ES	MS	SMS	0.217
OS			ES	WMS	0.338
OT	VSS			ES	0.224

(C.R. = 0.073 < 0.1).

Table 7. The fuzzy comparison matrix of sub-criteria with respect to criteria T.

Sub-Criteria	TP	TE	TS	TT	Relative Weight
TP	ES		VSS	SMS	0.131
TE	SMS	ES	WMS		0.257
TS			ES	WMS	0.430
TT		AS		ES	0.182

(C.R. = 0.039 < 0.1).

The standard weight results obtained by the fuzzy AHP method are shown in Table 8. Furthermore, Figure 5 shows the distribution of the SWOT indicator weights based on overall weights.

Table 8. Weights of criteria and sub-criteria.

Criteria	Criteria Weight	Sub-Criteria	Relative Weight	Overall Weight
S	0.353	SP	0.377	0.134
		SE	0.286	0.101
		SS	0.117	0.041
		ST	0.220	0.078
W	0.164	WP	0.166	0.027
		WE	0.291	0.048
		WS	0.170	0.028
		WT	0.373	0.061
O	0.273	WP	0.221	0.060
		OE	0.217	0.059
		OS	0.338	0.092
		OT	0.224	0.061
T	0.210	TP	0.131	0.028
		TE	0.257	0.054
		TS	0.430	0.090
		TT	0.182	0.038
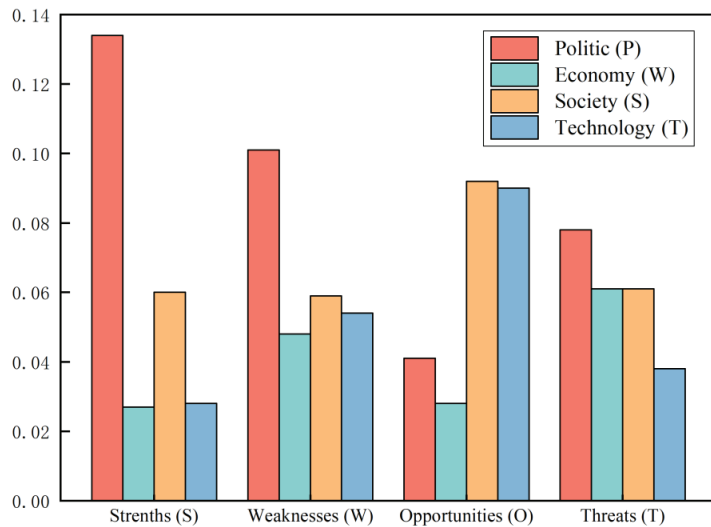
Figure 5. The overall weight distribution of SWOT-PEST factors.

4.3. Ranking the Strategies by Fuzzy MARCOS

The determined set of suitable strategies given in Table 5 is used in this section. The expert group evaluated alternative strategies based on the SWOT-PEST sub-criteria using the language terms listed in Table 9 [48]. A consensus process was applied during the evaluations. The evaluations of the expert group concerning the strategies are given in Table 10.

Table 9. Valuation scale for strategies.

Linguistic Term	TFN
Extremely poor (EP)	(1, 1, 1)
Very poor (VP)	(1, 1, 3)
Poor (P)	(1, 3, 3)
Medium poor (MP)	(3, 3, 5)
Medium (M)	(3, 5, 5)
Medium good (MG)	(5, 5, 7)
Good (G)	(5, 7, 7)
Very good (VG)	(7, 7, 9)
Extremely good (EG)	(7, 9, 9)

Table 10. Evaluation of green mining strategies by the group of experts.

GMS	SP	SE	SS	ST	WP	WE	WS	WT	OP	OE	OS	OT	TP	TE	TS	TT
S1	EG	EG	EG	EG	MG	G	G	MG	EG	EG	G	EG	MG	EG	G	MG
S2	M	MG	MG	G	MG	MG	G	VG	EG	EG	EG	VG	G	G	VG	MG
S3	EG	MG	MG	EG	G	G	EG	MG	EG	EG	EG	G	M	EG	MG	G
S4	EG	VG	EG	EG	G	EG	VG	G	EG	EG	EG	EG	P	EG	EG	M
S5	G	VG	G	G	G	VG	EG	G	VG	EG	VG	VG	VG	VG	G	M
S6	EG	G	G	EG	EG	G	EG	EG	EG	VG	EG	EG	EG	VG	G	G
S7	MG	VP	VG	P	EG	MG	EG	G	MG	VP	M	MP	EG	VG	EG	MG
S8	MG	MG	MG	G	M	G	G	VG	EG	EG	EG	G	EG	EG	G	M

For the SWOT-PEST model, the S and W factors are benefit-type, and the W and T factors are cost-type. Therefore, the fuzzy anti-ideal solution and the fuzzy ideal solution are obtained by using Equations (12) and (13); then the extended initial fuzzy matrix is constructed, and the extended initial fuzzy matrix is then normalized using Equation (14).

The weighted fuzzy matrix $\widetilde{V}$ is obtained through Equation (15), where the overall weights of the SWOT factors given in Table 8 are used, and $\widetilde{S}_i$, representing the sum of the elements of the weighted fuzzy matrix, is obtained using Equation (16), as shown in Table 11 below.

Table 11. The sum of the elements of the weighted fuzzy matrix.

$\widetilde{S}_i$	$(\tilde{s}_i^l, \tilde{s}_i^m, \tilde{s}_i^u)$	$\widetilde{S}_i$	$(\tilde{s}_i^l, \tilde{s}_i^m, \tilde{s}_i^u)$
$\widetilde{S}_{aai}$	(0.387, 0.443, 0.561)	$\widetilde{S}_5$	(0.590, 0.665, 0.795)
$\widetilde{S}_1$	(0.632, 0.786, 0.844)	$\widetilde{S}_6$	(0.603, 0.717, 0.791)
$\widetilde{S}_2$	(0.559, 0.686, 0.764)	$\widetilde{S}_7$	(0.446, 0.502, 0.633)
$\widetilde{S}_3$	(0.608, 0.733, 0.819)	$\widetilde{S}_8$	(0.590, 0.660, 0.825)
$\widetilde{S}_4$	(0.647, 0.761, 0.894)	$\widetilde{S}_{ai}$	(0.700, 0.841, 1.000)

The utility degree of $\widetilde{K}_i^-$, $\widetilde{K}_i^+$ in relation to the anti-ideal and ideal solution are calculated by Equations (17) and (18), and, in addition, the fuzzy matrix $\widetilde{T}_i$ value is obtained by Equation (19). It is necessary to use Equation (20) to find the maximum t_i and $\widetilde{D} = (1.800, 2.710, 3.588)$, and then use Equation (21) to defuzzify the number $\widetilde{D}$ to obtain the number $df_{def} = 2.705$.

According to the obtained utility degree $\widetilde{K}_i^+$ and df_{def}, the utility function $f(\widetilde{K}_i^+)$ about the ideal can be obtained by applying Equation (22), and similarly, according to the obtained utility degree $\widetilde{K}_i^-$ and df_{def}, the utility function $f(\widetilde{K}_i^-)$ about the anti-ideal can be obtained by applying Equation (23): it is shown in the following Table 12.

Table 12. Obtained $\widetilde{K}_i^+$, $\widetilde{K}_i^-$, and $\widetilde{T}_i$ values.

I	$\widetilde{K}_i^+$	$\widetilde{K}_i^-$	$\widetilde{T}_i$	$f(\widetilde{K}_i^+)$	$f(\widetilde{K}_i^-)$
1	(0.632, 0.935, 1.206)	(1.126, 1.775, 2.181)	(1.758, 2.710, 3.387)	(0.416, 0.656, 0.806)	(0.234, 0.346, 0.446)
2	(0.559, 0.816, 1.092)	(0.996, 1.549, 1.974)	(1.554, 2.364, 3.066)	(0.368, 0.572, 0.730)	(0.206, 0.302, 0.404)
3	(0.608, 0.871, 1.170)	(1.084, 1.654, 2.116)	(1.692, 2.525, 3.285)	(0.401, 0.611, 0.782)	(0.225, 0.322, 0.432)
4	(0.647, 0.905, 1.277)	(1.153, 1.719, 2.310)	(1.800, 2.624, 3.588)	(0.426, 0.635, 0.854)	(0.239, 0.335, 0.472)
5	(0.590, 0.791, 1.136)	(1.052, 1.502, 2.055)	(1.642, 2.293, 3.192)	(0.389, 0.555, 0.760)	(0.218, 0.292, 0.420)
6	(0.603, 0.853, 1.130)	(1.075, 1.619, 2.044)	(1.677, 2.472, 3.175)	(0.397, 0.599, 0.756)	(0.223, 0.315, 0.418)
7	(0.446, 0.597, 0.905)	(0.795, 1.134, 1.637)	(1.241, 1.732, 2.542)	(0.294, 0.419, 0.605)	(0.165, 0.221, 0.335)
8	(0.590, 0.785, 1.179)	(1.051, 1.490, 2.132)	(1.641, 2.275, 3.310)	(0.389, 0.551, 0.788)	(0.218, 0.290, 0.436)

Defuzzify $\widetilde{K}_i^-$, $\widetilde{K}_i^+$, $f(\widetilde{K}_i^+)$, and $f(\widetilde{K}_i^-)$ by Equation (21) to obtain sharp values K_i^-, K_i^+, $f(K_i^+)$, and $f(K_i^-)$. Finally, the utility function $f(K_i)$ of the alternatives is obtained by Equation (24), and the alternatives are sorted according to the value of the utility function. The final results are shown in Table 13, and the strategies are ranked as S1 > S4 > S3 > S6 > S2 > S8 > S5 > S7. A comparative and sensitivity analysis was performed to confirm these results and is shown in the next section.

Table 13. Final results of fuzzy MARCOS method and ranking of the GMS.

GMS	K_i^+	K_i^-	$f(K_i^+)$	$f(K_i^-)$	$f(K_i)$	Order
S1	0.930	1.735	0.641	0.344	0.768	1
S2	0.819	1.527	0.565	0.303	0.576	5
S3	0.877	1.636	0.605	0.324	0.672	3
S4	0.924	1.723	0.637	0.342	0.757	2
S5	0.815	1.519	0.562	0.301	0.569	7
S6	0.857	1.599	0.591	0.317	0.639	4
S7	0.623	1.161	0.429	0.230	0.315	8
S8	0.818	1.524	0.563	0.302	0.574	6

The results indicate that the most important dimensions that mines should focus on are the strengths and opportunities associated with GM. The criteria weights obtained through the fuzzy AHP method are shown in Table 3, with a total percentage of 52% for strengths and weaknesses and 48% for opportunities and threats. It shows that internal (strengths and weaknesses) factors and external (opportunities and threats) factors have almost equal importance. Table 10 and Figure 5 show that SP, SE, OS, TS, and ST are the five factors with the highest global weights, indicating that with increased government policy support (SP), positive economic conditions (SE), and a surging demand for resources (OS), Chinese mining companies should take its innovative national strategy as a starting point and make improving its R&D capacity for green technology innovation in mines a development priority (ST) in order to avoid being caught in a global mining environmental pollution problem in the long term (TS). The GMS ranking order indicates that the three most important digital conversion strategies are S1, S4, and S3. These are "Grasp the trend of green development and improve the protection and development level of mineral resources", "Strengthen technological research and development, improve technological innovation capabilities, and focus on the development of green technologies", and "Absorb the advanced organization and management experience of developed countries in the mining industry, and standardize and improve the mine green guarantee mechanism".

## 5. Validation of Results and Sensitivity Analysis

Result validation and sensitivity analysis are carried out in two processes in this section.

5.1. Comparison with Other Approaches

It is necessary to compare the results obtained by Fuzzy MARCOS with those acquired by using other fuzzy methods in order to validate the results of this study [47]. Therefore,

two methods, fuzzy MABAC (Multiple Attribute Boundary Approximate Area Comparison) and TOPSIS (Technique for Order Performance Through Similarity to Ideal Solutions), are used to test the accuracy of the results obtained by the fuzzy MARCOS method.

The results of the comparative analysis are shown in Figure 6; the y-axis represents the ranking, with shorter histograms indicating higher rankings. Comparing the ranking of the fuzzy MARCOS method and the fuzzy TOPSIS method, the change in the ranking results of the eight strategies is the exchange of two groups of adjacent strategies. Comparing the fuzzy MARCOS method and the fuzzy MABAC method, the change in the ranking results of the eight strategies is the order of the last three strategies, and the other orders are the same.
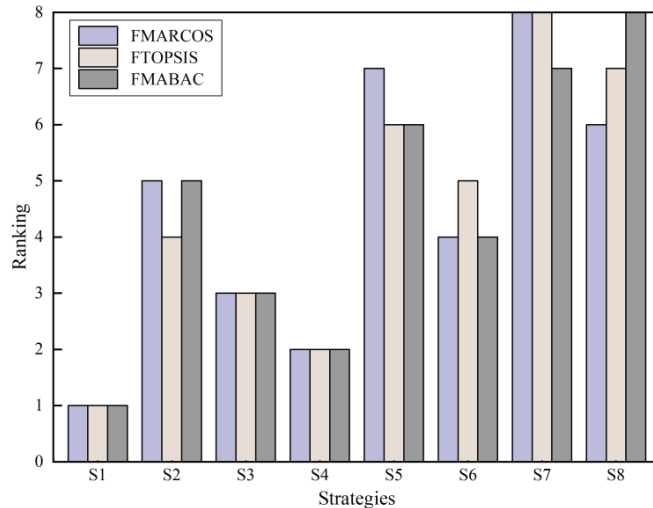
Figure 6. Rank of alternatives with different fuzzy methods.

The overall results show that there is little difference between the ranking results of these strategies. The results of the fuzzy MARCOS method are basically the same as those of FMABAC and FTOPSISs. It can be seen that the results obtained by the fuzzy MARCOS method are accurate.

5.2. Sensitivity Analysis

The sensitivity analysis is conducted by changing the weights of criteria to evaluate the impact of individual criteria on prioritization [59]. Therefore, this study changed the weights of the SWOT criteria to investigate the impact of changing the criteria weights on GMS's prioritization. For this purpose, five cases are determined by changing the weight of the SWOT criteria. In one case, the weights of the four SWOT criteria are set to be equal (0.250), and in the other four cases, only one criterion was set to be relatively important (0.400) [60], while the others remained the same (0.200). Different cases of SWOT criteria weights are given in Table 14.

Table 14. Different weights of the SWOT criteria in different cases.

Criteria	Initial Value	C1	C2	C3	C4	C5
S	0.353	0.250	0.400	0.200	0.200	0.200
W	0.164	0.250	0.200	0.400	0.200	0.200
O	0.273	0.250	0.200	0.200	0.400	0.200
T	0.210	0.250	0.200	0.200	0.200	0.400

Then, the fuzzy MARCOS method is applied to the weights determined for each case, and, furthermore, the utility function $f(K)$ value is updated according to the weights. Table 15 presents the GMS utility function values obtained. Based on the updated utility function value, a ranking of the GMS is obtained. Table 16 shows the new ranking order of GMS under different cases. Here, to compare with the initial study, C0 is added to indicate the preliminary results of the study.

Table 15. The weights of the SWOT factors in different cases.

Factors	Relative Weight	C0	C1	C2	C3	C4	C5
SP	0.377	0.134	0.094	0.151	0.075	0.075	0.075
SE	0.286	0.101	0.072	0.114	0.057	0.057	0.057
SS	0.117	0.041	0.029	0.047	0.023	0.023	0.023
ST	0.220	0.078	0.055	0.088	0.044	0.044	0.044
WP	0.166	0.027	0.042	0.033	0.066	0.033	0.033
WE	0.291	0.048	0.073	0.058	0.116	0.058	0.058
WS	0.170	0.028	0.043	0.034	0.068	0.034	0.034
WT	0.373	0.061	0.093	0.075	0.149	0.075	0.075
OP	0.221	0.060	0.055	0.044	0.044	0.088	0.044
OE	0.217	0.059	0.054	0.043	0.043	0.087	0.043
OS	0.338	0.092	0.085	0.068	0.068	0.135	0.068
OT	0.224	0.061	0.056	0.045	0.045	0.090	0.045
TP	0.131	0.028	0.033	0.026	0.026	0.026	0.052
TE	0.257	0.054	0.064	0.051	0.051	0.051	0.103
TS	0.430	0.090	0.108	0.086	0.086	0.086	0.172
TT	0.182	0.038	0.046	0.036	0.036	0.036	0.073

Table 16. The obtained $f(K)$ and strategy ordering in different cases.

GMS	C0		C1		C2		C3		C4		C5	
	$f(K_i)$	Order	$f(K_i)$	Order	$f(K_i)$	Order	$f(K_i)$	Order	$f(K_i)$	Order	$f(K_i)$	Order
S1	0.768	1	0.803	1	0.827	1	0.793	1	0.802	1	0.779	1
S2	0.576	5	0.618	6	0.543	7	0.626	4	0.671	5	0.629	6
S3	0.672	3	0.743	2	0.718	3	0.725	2	0.767	3	0.760	2
S4	0.757	2	0.722	3	0.745	2	0.665	3	0.771	2	0.701	3
S5	0.569	7	0.623	5	0.606	5	0.593	7	0.644	7	0.645	5
S6	0.639	4	0.666	4	0.682	4	0.603	5	0.712	4	0.665	4
S7	0.315	8	0.308	8	0.272	8	0.355	8	0.272	8	0.339	8
S8	0.574	6	0.605	7	0.544	6	0.601	6	0.654	6	0.617	7

Figure 7 presents the distribution of the GMS rankings from an overall perspective. The results obtained show that there is little variation in the prioritization among these cases, and these small differences do not affect the validity of the study. The initial results of this study using the fuzzy MARCOS method can be confirmed. Furthermore, "Grasp the trend of green development and improve the protection and exploitation level of mineral resources" is the most appropriate GMS in all cases.
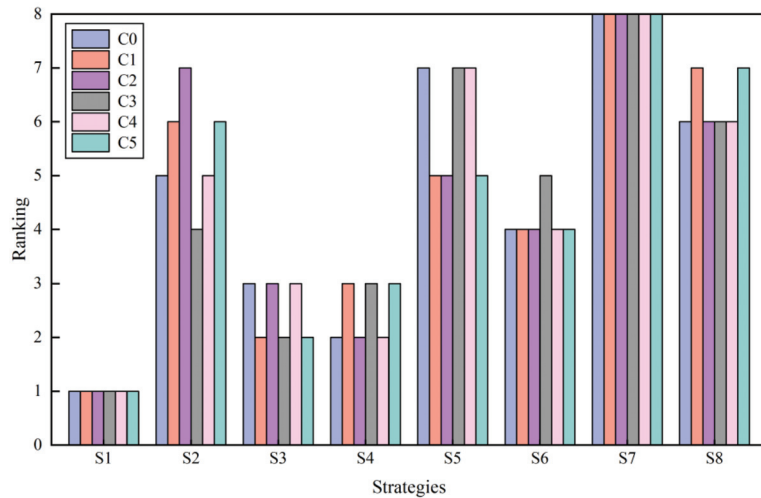
Figure 7. The comparison of the ranked orders of the GMSs in different cases.

6. Conclusions

In view of the importance of the mining industry's green transformation and the driving force of strategic planning for the green transformation, it is essential to take measures to conduct research on the strategic decision making of green mine construction. Accordingly, this study supports this decision making by constructing a new SWOT-PEST matrix and a decision support model. The proposed decision support model and the SWOT-PEST matrix are validated using China's green mining construction case. The SWOT-PEST tool was used to conduct a comprehensive analysis of internal and external driving and hindering factors, resulting in the identification of four main criteria and 16 sub-criteria. Then the interaction of these factors was studied, and eight macro strategies were formulated. The group expert decision making based on fuzzy terms is introduced to make the decision-making process more scientific and rational. A comprehensive selection of strategies is carried out using two steps: the fuzzy AHP and fuzzy MARCOS method based on SWOT-PEST analysis. Firstly, the importance and weight of SWOT-PEST factors are determined by fuzzy AHP. Then, the recently proposed Fuzzy MARCOS method is adopted for strategy ranking. Finally, the fuzzy TOPSIS and the fuzzy MABAC methods are used to verify the results of the fuzzy MARCOS method. The impact of the SWOT factor weights on the results is evaluated by sensitivity analysis, which verifies the robustness of the proposed method. This paper's major contributions can be summarized as follows:

- To the best of the authors' knowledge, this paper is the first combined method of study using quantitative SWOT-PEST analysis based on the combined fuzzy AHP and fuzzy MARCOS methods.
- The SWOT-PEST, a combined analysis tool, is used for the first time to create a hierarchical index system for selecting green mining development strategies, which provides a systematic quantitative framework for selecting green mining development strategies and fills a research gap in this area.
- A case study was carried out concerning the mining industry in China. For green mining, policy support is the prerequisite, technological innovation is the key link, and organization and management are the basic guarantees.

This study provides a systematic quantitative framework for selecting green mining strategies. The model can be applied not only in the mining sector, but also in other industries by analyzing distinct factors and strategies. In the future, it is possible to investigate whether and how to formulate an extended version of the fuzzy analysis.

References

1. Cheba, K.; Bak, I.; Szopik-Depczynska, K.; Ioppolo, G. Directions of green transformation of the European Union countries. *Ecol. Indic.* **2022**, *136*, 15. [CrossRef]
2. Chen, J.H.; Jiskani, I.M.; Lin, A.G.; Zhao, C.C.; Jing, P.X.; Liu, F.J.; Lu, M.Y. A hybrid decision model and case study for comprehensive evaluation of green mine construction level. *Dev. Sustain.* **2022**. [CrossRef]
3. Xu, R.; Chen, X.D.; Zhang, F.F. Green Technology Innovation and Sustainable Development Based on Data Fusion Mining. *Ekoloji* **2019**, *28*, 1825–1833.
4. Wang, Z.M.; Zhou, W.; Jiskani, I.M.; Luo, H.T.; Ao, Z.C.; Mvula, E.M. Annual dust pollution characteristics and its prevention and control for environmental protection in surface mines. *Sci. Total Environ.* **2022**, *825*, 153949. [CrossRef]
5. Wang, Y.; Wu, X.L.; He, S.Y.; Niu, R.Q. Eco-environmental assessment model of the mining area in Gongyi, China. *Sci. Rep.* **2021**, *11*, 18. [CrossRef]
6. Jang, H.; Topal, E. Transformation of the Australian mining industry and future prospects. *Min. Technol.* **2020**, *129*, 120–134. [CrossRef]
7. Zhu, R.Q.; Lin, B.Q. Energy and carbon performance improvement in China's mining Industry: Evidence from the 11th and 12th five-year plan. *Energy Policy* **2021**, *154*, 8. [CrossRef]
8. Chen, J.H.; Jiskani, I.M.; Chen, J.L.; Hui, Y. Evaluation and future framework of green mine construction in China based on the DPSIR model. *Sustain. Environ. Res.* **2020**, *30*, 10. [CrossRef]
9. Guo, W.B.; Guo, M.J.; Tan, Y.; Bai, E.H.; Zhao, G.B. Sustainable Development of Resources and the Environment: Mining-Induced Eco-Geological Environmental Damage and Mitigation Measures-A Case Study in the Henan Coal Mining Area, China. *Sustainability* **2019**, *11*, 4366. [CrossRef]
10. Jiskani, I.M.; Cai, Q.X.; Zhou, W.; Lu, X.; Shah, S.A.A. An integrated fuzzy decision support system for analyzing challenges and pathways to promote green and climate smart mining. *Expert Syst. Appl.* **2022**, *188*, 116062. [CrossRef]
11. Zhou, Y.L.; Zhou, W.; Lu, X.; Jiskani, I.M.; Cai, Q.X.; Liu, P.; Li, L. Evaluation Index System of Green Surface Mining in China. *Min. Metall. Explor.* **2020**, *37*, 1093–1103. [CrossRef]
12. Markard, J.; Raven, R.; Truffer, B. Sustainability transitions: An emerging field of research and its prospects. *Res. Policy* **2012**, *41*, 955–967. [CrossRef]
13. Shang, D.L.; Yin, G.Z.; Li, X.S.; Li, Y.J.; Jiang, C.B.; Kang, X.T.; Liu, C.; Zhang, C. Analysis for Green Mine (phosphate) performance of China: An evaluation index system. *Res. Policy* **2015**, *46*, 71–84. [CrossRef]
14. Qian, M.G. Technological system and green mining concept. *Coal Sci. Technol. Mag.* **2003**, *4*, 1–3.
15. Ministry of Natural Resources of China (MNR). National Mineral Resources Planning (2008–2015). Available online: http://www.gov.cn/zwgk/2010-08/23/content_1686388.htm (accessed on 18 April 2022).
16. Ministry of Natural Resources of China (MNR). Notice of the Ministry of Land and Resources on the List of the Fourth Batch of National Pilot Units for Green Mines. Available online: http://www.mnr.gov.cn/gk/tzgg/201408/t20140801_1991297.html (accessed on 18 April 2022).
17. Ministry of Natural Resources of China (MNR). Announcement of the Ministry of Natural Resources on Issuing 9 Industry Standards including the "Code for Green Mine Construction in the Non-metallic Mining Industry". Available online: http://gi.mnr.gov.cn/201804/t20180418_1768058.html (accessed on 18 April 2022).
18. Wang, G.F.; Xu, Y.X.; Ren, H.W. Intelligent and ecological coal mining as well as clean utilization technology in China: Review and prospects. *Int. J. Min. Sci. Technol.* **2019**, *29*, 161–169. [CrossRef]

19. Qi, R.; Liu, T.Y.; Jia, Q.X.; Sun, L.; Liu, J.Y. Simulating the sustainable effect of green mining construction policies on coal mining industry of China. *J. Clean. Prod.* **2019**, *226*, 392–406. [CrossRef]
20. Wang, S.F.; Sun, L.C.; Huang, L.Q.; Li, X.B.; Shi, Y.; Yao, J.R. Non-explosive mining and waste utilization for achieving green mining in underground hard rock mine in China. *Trans. Nonferr. Met. Soc. China* **2019**, *29*, 1914–1928. [CrossRef]
21. Jiskani, I.M.; Moreno-Cabezali, B.M.; Rehman, A.U.; Fernandez-Crehuet, J.M.; Uddin, S. Implications to secure mineral supply for clean energy technologies for developing countries: A fuzzy based risk analysis for mining projects. *J. Clean. Prod.* **2022**, *358*, 132055. [CrossRef]
22. Jiskani, I.M.; Cai, Q.X.; Zhou, W.; Lu, X. Assessment of risks impeding sustainable mining in Pakistan using fuzzy synthetic evaluation. *Res. Policy* **2020**, *69*, 101820. [CrossRef]
23. Prosser, C.D. Geoconservation, Quarrying and Mining: Opportunities and Challenges Illustrated Through Working in Partnership with the Mineral Extraction Industry in England. *Geoheritage* **2018**, *10*, 259–270. [CrossRef]
24. Khaba, S.; Bhar, C. Quantifying SWOT analysis for the Indian coal mining industry using Fuzzy DEMATEL. *Benchmarking* **2017**, *24*, 882–902. [CrossRef]
25. Abdel-Basset, M.; Mohamed, M.; Smarandache, F. An Extension of Neutrosophic AHP-SWOT Analysis for Strategic Planning and Decision-Making. *Symmetry-Basel* **2018**, *10*, 116. [CrossRef]
26. Khan, M.I. Evaluating the strategies of compressed natural gas industry using an integrated SWOT and MCDM approach. *J. Clean. Prod.* **2018**, *172*, 1035–1052. [CrossRef]
27. Andrews, K.R. *The Concept of Corporate Strategy*; Dow Jones-Irwin: Homewood, IL, USA, 1965.
28. Yuan, H.P. A SWOT analysis of successful construction waste management. *J. Clean. Prod.* **2013**, *39*, 1–8. [CrossRef]
29. Terrados, J.; Almonacid, G.; Hontoria, L. Regional energy planning through SWOT analysis and strategic planning tools. Impact on renewables development. *Renew. Sustain. Energy Rev.* **2007**, *11*, 1275–1287. [CrossRef]
30. Zhao, J.K.; Liu, H.L.; Xue, W.X. PEST Embedded SWOT Analysis on China's E-Commerce Industry Development Strategy. *J. Electron. Commer. Organ.* **2019**, *17*, 55–68. [CrossRef]
31. Novikov, S.V. Strategic analysis of the development of high-technology manufacturing facilities. *Russ. Eng. Res.* **2018**, *38*, 198–200. [CrossRef]
32. Kolbina, O. SWOT analysis as a strategic planning tool for companies in the food industry. *Probl. Econ. Transit.* **2015**, *57*, 74–83. [CrossRef]
33. Bohari, A.M.; Hin, C.W.; Fuad, N. The competitiveness of halal food industry in Malaysia: A SWOT-ICT analysis. *Geogr.-Malays. J. Soc. Space* **2013**, *9*, 1–9.
34. Liu, Z.W.; Zhao, J.H.; Gao, P.Z. Exploration for the Low-carbon Economic Development Model of Large-scale Coal Enterprises Based on the SWOT Model. In Proceedings of the 1st International Conference on Energy and Environmental Protection (ICEEP 2012), Hohhot, China, 23–24 June 2012.
35. Nikolaou, I.E.; Evangelinos, K.I. A SWOT analysis of environmental management practices in Greek Mining and Mineral Industry. *Res. Policy* **2010**, *35*, 226–234. [CrossRef]
36. Jiskani, I.M.; Shah, S.A.A.; Cai, Q.X.; Zhou, W.; Lu, X. A multi-criteria based SWOT analysis of sustainable planning for mining and mineral industry in Pakistan. *Arab. J. Geosci.* **2020**, *13*, 1108. [CrossRef]
37. Dong, H.; Liu, Z.G.; Kong, K.; Li, T.; Ma, Q.L. Evaluation of Input-Output Efficiency of Sports Industry Based on SWOT-PEST Model. *J. Math.* **2021**, *2021*, 11. [CrossRef]
38. Pan, Y.J.; Peng, K.; Peng, H.X.; Zhang, J.; Zeng, M.; Huang, C.S. Evaluation Model and Empirical Study on the Competitiveness of the County Silicon Crystal Industry. *Sustainability* **2019**, *11*, 360. [CrossRef]
39. Antony, J. A SWOT analysis on Six Sigma: Some perspectives from leading academics and practitioners. *Int. J. Product. Perform. Manag.* **2012**, *61*, 691–698. [CrossRef]
40. Arslan, O.; Er, I.D. SWOT analysis for safer carriage of bulk liquid chemicals in tankers. *J. Hazard. Mater.* **2008**, *154*, 901–913. [CrossRef]
41. Shahin, A.; Mahbod, M.A. Prioritization of key performance indicators: An integration of analytical hierarchy process and goal setting. *Int. J. Product. Perform. Manag.* **2007**, *56*, 226–240. [CrossRef]
42. Jiskani, I.M.; Cai, Q.X.; Zhou, W.; Shah, S.A.A. Green and climate-smart mining: A framework to analyze open-pit mines for cleaner mineral production. *Res. Policy* **2021**, *71*, 102007. [CrossRef]
43. Oreski, D. Strategy development by using SWOT-AHP. *TEM J.* **2012**, *1*, 283–291.
44. Erdogan, A.; Kara, G. Determining the maritime transportation policy of Turkey. *Int. J. Marit. Eng.* **2019**, *161*, 437–448. [CrossRef]
45. Buyukozkan, G.; Mukul, E.; Kongar, E. Health tourism strategy selection via SWOT analysis and integrated hesitant fuzzy linguistic AHP-MABAC approach. *Socio-Econ. Plan. Sci.* **2021**, *74*, 14. [CrossRef]
46. Solangi, Y.A.; Tan, Q.M.; Mirjat, N.H.; Ali, S. Evaluating the strategies for sustainable energy planning in Pakistan: An integrated SWOT-AHP and Fuzzy-TOPSIS approach. *J. Clean. Prod.* **2019**, *236*, 14. [CrossRef]
47. Stevic, Z.; Pamucar, D.; Puska, A.; Chatterjee, P. Sustainable supplier selection in healthcare industries using a new MCDM method: Measurement of alternatives and ranking according to COmpromise solution (MARCOS). *Comput. Ind. Eng.* **2020**, *140*, 15. [CrossRef]
48. Stankovic, M.; Stevic, Z.; Das, D.K.; Subotic, M.; Pamucar, D. A New Fuzzy MARCOS Method for Road Traffic Risk Analysis. *Mathematics* **2020**, *8*, 457. [CrossRef]

49. Brkovic, N. A Novel Integrated FUCOM-MARCOS Model for Evaluation of Human Resources in a Transport Company. *Logistics* **2020**, *4*, 14.

50. Ulutas, A.; Karabasevic, D.; Popovic, G.; Stanujkic, D.; Nguyen, P.T.; Karakoy, C. Development of a Novel Integrated CCSD-ITARA-MARCOS Decision-Making Approach for Stackers Selection in a Logistics System. *Mathematics* **2020**, *8*, 1672. [CrossRef]

51. Zadeh, L.A. Fuzzy set. *Inf. Control* **1965**, *8*, 338–353. [CrossRef]

52. Kim, Y.; Chung, E.S. Fuzzy VIKOR approach for assessing the vulnerability of the water supply to climate change and variability in South Korea. *Appl. Math. Model.* **2013**, *37*, 9419–9430. [CrossRef]

53. Khazaeni, G.; Khanzadi, M.; Afshar, A. Fuzzy adaptive decision making model for selection balanced risk allocation. *Int. J. Proj. Manag.* **2012**, *30*, 511–522. [CrossRef]

54. Chen, J.F.; Hsieh, H.N.; Do, Q.H. Evaluating teaching performance based on fuzzy AHP and comprehensive evaluation approach. *Appl. Soft Comput.* **2015**, *28*, 100–108. [CrossRef]

55. Lee, S. Determination of Priority Weights under Multiattribute Decision-Making Situations: AHP versus Fuzzy AHP. *J. Constr. Eng. Manag.* **2015**, *141*, 9. [CrossRef]

56. Buyukozkan, G.; Kahraman, C.; Ruan, D. A fuzzy multi-criteria decision approach for software development strategy selection. *Int. J. Gen. Syst.* **2004**, *33*, 259–280. [CrossRef]

57. Chang, D.Y. Applications of the extent analysis method on fuzzy AHP. *Eur. J. Oper. Res.* **1996**, *95*, 649–655. [CrossRef]

58. Torkayesh, A.E.; Zolfani, S.H.; Kahvand, M.; Khazaelpour, P. Landfill location selection for healthcare waste of urban areas using hybrid BWM-grey MARCOS model based on GIS. *Sustain. Cities Soc.* **2021**, *67*, 16. [CrossRef]

59. Božanić, D.; Tešić, D.; Kočić, J. Multi-criteria FUCOM—Fuzzy MABAC model for the selection of location for construction of single-span bailey bridge. *Appl. Manag. Eng.* **2019**, *2*, 132–146. [CrossRef]

60. Wang, Y.; Xu, L.; Solangi, Y.A. Strategic renewable energy resources selection for Pakistan: Based on SWOT-Fuzzy AHP approach. *Sustain. Cities Soc.* **2020**, *52*, 14. [CrossRef]

Green Mining Takes Place at the Power Plant

Zhiyi Zhang [1,2,3,*], Hao Liu [2,*], Hui Su [2] and Qiang Zeng [1]

[1] School of Ecology and Environment, Xinjiang University, Urumchi 830046, China; zengqiang@xju.edu.cn
[2] School of Geology and Mining Engineering, Xinjiang University, Urumchi 830046, China; suhui054710@163.com
[3] Collaborative Innovation Center of Green Mining and Ecological Restoration for Xinjiang Mineral Resources, Urumchi 830046, China
*   Correspondence: xjuzhiyi@163.com (Z.Z.); liu_xj2017@163.com (H.L.); Tel.: +86-0991-211-1408 (H.L.)

Abstract: The number of large coal power plants, characterized by pithead plants, is increasing rapidly in major coal mining countries around the world. Overburden movement caused by coal mining and greenhouse gas emissions caused by coal thermal power generation are intertwined, and have become important challenges for mine ecological environment protection at present and in the future. In order to provide more options for green mining in large coal power plants, a large coal power base in northwest China was taken as the researching background in this paper, and a green mining model considering the above two aspects of ecological environment damages was proposed; that is, the carbon dioxide greenhouse gas produced by coal-fired power plants can be geologically trapped in goaf, whose overburden stability is controlled by backfill strips made of solid mine waste. In order to explore the feasibility of this model, the bearing strength of the filled gray brick consisting mainly of aeolian sand and fly ash under different curing methods was firstly studied, and it was discovered that the strength of the gray brick significantly improved after carbonization curing. After that, X-ray diffraction (XRD) and scanning electron microscopy (SEM) were employed to compare the mineral composition and its spatial morphology in gray brick before and after carbonization, and it is believed that the formation of dense acicular calcium carbonate after carbonization curing was the fundamental reason for the improvement of its bearing strength. Finally, a series of stope numerical models were established with UDEC software to analyze the surface settlement, crack propagation height and air tightness of the overlying strata, respectively, when goaf was supported by the backfilling strips with carbonized gray brick. The research results of this paper showed that the stability of overlying strata in goaf can be effectively controlled by adjusting the curing methods, width and spacing of the filled gray brick, so as to facilitate the following geological sequestration of carbon dioxide greenhouse gas in goaf. Consequently, the ecological environment damages caused by coal mining and utilization in a large coal power base can be resolved as a whole, and the purpose of green mining can be achieved as desired.

Keywords: green mining; low-carbon utilization; backfill mining; carbon dioxide storage; gray brick

1. Introduction

For several decades, coal has significantly contributed to global energy needs, accounting for 25% of global energy production in 2000, 30% in 2010 and 27% in 2020 [1]. However, in the process of coal mining, it often brings about serious overburden movement, which causes the loss of groundwater resources and surface collapse, changes the soil structure and seriously damages the ecological environment [2,3]. For example, in China, the area of land destroyed by mining has reached 2 million hm^2 [4], in which the area of settlement land has reached 1 million hm^2 [5]. These mining impacts pose significant environmental, socio-economic and mining layout challenges. For this reason, these adverse impacts and mitigation measures have been extensively studied in several countries, including Russia [6], Australia [7,8], the United Kingdom [9], South Africa [10,11], India [12,13] and

Germany [14]. Meanwhile, the number of large coal power plants, characterized by pithead plants, is increasing rapidly in major coal mining countries around the world. Overburden movement caused by coal mining and greenhouse gas emission caused by coal thermal power generation are intertwined, and have become an important challenges for mine ecological environment protection at present and in the future, as shown in Figure 1.
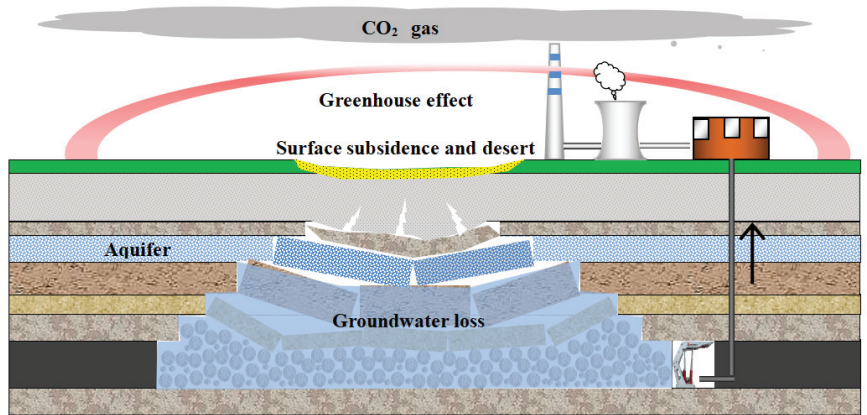
Figure 1. Ecological and environmental effects of the traditional coal exploitation and utilization mode in large coal power bases.

To resolve the problems of the environmental damage caused by the mining and utilization of coal as a fossil fuel in large coal power bases, an innovative mode of green mining and low-carbon utilization of the coal resources is proposed, as shown in Figure 2. Firstly, the aeolian sand abundant on the surface of mining area and fly ash produced by thermal power plant are used as the main raw materials to make the embryo body of filling gray brick. Then, the gray brick is curved with carbon dioxide gas from the thermal power plant and backfilled in the underground gob to support overlying strata. Finally, the carbon dioxide gas can be injected and stored in the gob.
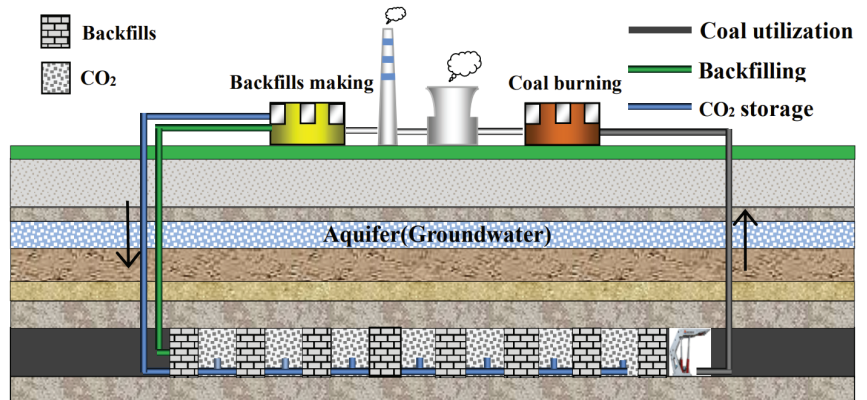
Figure 2. Innovative mode of green mining and low-carbon utilization for coal resources in large coal power bases.

In the past few decades, backfilling has been extensively applied in underground coal mining to resolve safety and environmental problems. The backfill bodies were employed to reduce ground subsidence [15,16], underground water-loss [17,18] and so forth. Meanwhile, backfill mining employs coal gangue (CG), fly ash (FA) and tailings as primary materials

to provides a feasible approach for treatment and utilization of solid wastes from mining industries [19,20]. On this basis, many valuable studies have been carried out recently. For the first time, a mixture of classified tailings with cement began to be tested in 1969 at the Mount Isa mine in Australia. This technology has been successfully applied in many mines in Canada and Sweden. In Russia (USSR), tailings were first used to prepare a monolithic backfill in 1969 at the Riddersky mine. In 1970, one chamber was laid at the Gaisky mine (USSR). Currently, man-made wastes are widely used in the production of backfill composite around the word. Technogenic waste replaces not only the inert filler, but also the binder. Ercikdi et al. used waste glass and silica fumes as artificial pozzolanas to prepare tailings cementing filling materials and investigated the effect of the type of waste materials on the early strength and later strength of the filled object [21,22]. Feng et al. studied the mechanical properties of cemented filling materials in which gangue was partially replaced by waste concrete [23,24]. Peyronnard and Benzaazoua studied the effect of CAlSiFrit and deinking sludge fly ash as partial binder replacement in cemented paste backfill (CPB) [25]. Cihangir et al. used alkali-activated neutral and acidic blast furnace slags (AASs) with aqueous sodium silicate (LSS), and sodium hydroxide (SH) were tested as alternative binders to OPC for CPB of high-sulfide mill tailings [26]. Deng et al. developed a new type of cemented filling material, using waste rock as a coarse aggregate, FA as a fine powder, slag as an activator and ordinary Portland cement as a binder [24,27]. Xu et al. studied the strength development and microstructure evolution of cemented tailings backfill containing different binder types and contents [28]. Zhou et al. explored the feasibility of replacing cementitious filling materials with air-accumulated sand as aggregate, and investigated the effects of fly ash (FA) content, cement content, lime slag (LS) content and concentration on the mechanical properties of air-accumulated sand-based cementitious filling materials [24]. Wang et al. used hydrogen peroxide (H_2O_2) as a chemical blowing agent to improve the foaming performance of the cemented foam and the reinforcing effect of the foam based on the cemented foam with gangue and fly ash as the main raw materials [29]. Ermolovich et al. studied the possibility of creating and using nanomodified backfill material based on the waste from enrichment of water-soluble ores [30].

Analyzing the above, it can be noted that reducing or ablating the damage to the ecological environment caused by mining activities green mining is a very topical issue. With the centralized mining and utilization of coal resources, related environmental problems will appear at the same time, which provides a possibility for the comprehensive solution of various problems. Therefore, the purpose of this study is exploring a green mining model that simultaneously controls the strata stability over goaf and geologic sequestration of carbon dioxide greenhouse gas in goaf. To achieve this goal, the following tasks need to be addressed: (1) how to prepare the backfilling material in goaf with certain mine solid waste, and provide it with the bearing strength to meet the requirements through appropriate curing method; (2) how to evaluate the stability of the overlying strata after goaf is backfilled by the above-designed materials.

2. Materials and Methods

2.1. Experimental Materials

The cementing agents used in the experiments were quicklime and gypsum. The quicklime was produced by the Tianshan Cement Factory in Xinjiang, China. The main composition of quicklime is CaO, but it also contains a small amount of SiO_2 and MgO; its CaO content reaches up to 89%, as shown in Figure 3a,d. The gypsum was purchased from the factory as β-type hemihydrate gypsum ($2CaSO_4 \cdot H_2O$). The main chemical composition of gypsum includes CaO and SO_3, and it also contains a small amount of SiO_2, Al_2O_3 and Fe_2O_3, as shown in Figure 3b,e. The fly ash used in the experiments was class II fly ash produced by the Hongyanchi Power Plant in Urumqi, Xinjiang, China. The average particle size of the fly ash is 0.035 mm. The fly ash is primarily composed of mullite and quartz; the SiO_2 content is 55% and Al_2O_3 content is 25%, as shown in Figure 3c,f. The aggregate

used in the experiments was aeolian sand from the Shanshan Desert, Xinjiang, China, with a particle size primarily between 0.1–0.25 mm and a non-uniformity coefficient of 1.82.
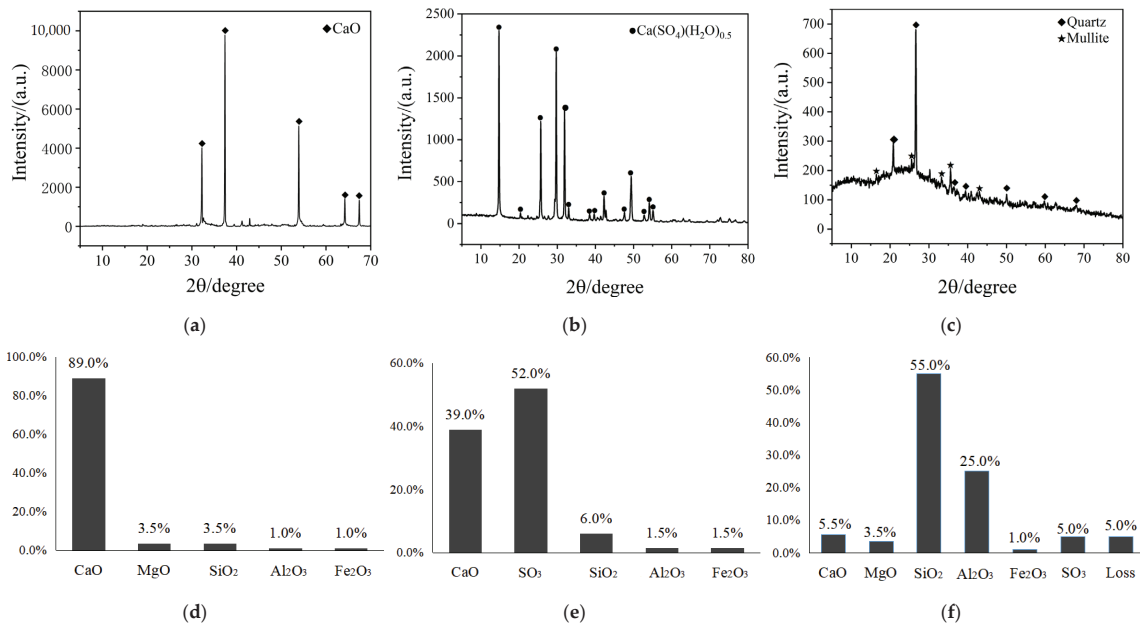
Figure 3. Experimental materials. (**a**) XRD pattern of quicklime; (**b**) XRD pattern of gypsum; (**c**) XRD pattern of fly ash; (**d**) chemical element content of quicklime; (**e**) chemical element content of gypsum; (**f**) chemical element content of fly ash. Here, XRD indicates X-ray diffraction analysis.

2.2. Specimen Preparation and the Experimental Study

In this study, the ratio of water: cement was 2:3, and the ratio of gypsum: fly ash: quicklime: aeolian sand was 1:2:3:12. The dry ingredients were mixed and thoroughly homogenized using a blender (HJW-60 series) for 3 min before water was added into the mixture, and then stirred for another 2 min. After mixing, the mixed slurry was cast into an iron mold with dimensions of 5 cm × 5 cm × 5 cm and three specimens were made for each curing age using different curing methods to reduce the test error. The specimens were then subjected to natural, autoclave, carbon dioxide and autoclave–carbon dioxide curing for 4 days, 8 days, 12 days and 16 days [31], as shown in Table 1. Finally, uniaxial compressive strength (UCS) tests, carbonization tests, X-ray diffraction analysis (XRD) tests and scanning electron microscope (SEM) tests were carried out on the specimens, as shown in Figure 4.

The UCS tests on gray brick were carried out using the SANS brand hydraulic single shaft compressor in the Mechanics Laboratory, School of Mechanical Engineering, Xinjiang University, China, as per the Chinese standard (JGJ/T 70-2009). The maximum test force of a uniaxial compressor is 300KN, and the accuracy of the force value is below ±0.3%. According to the standard, a displacement loading model was used to avoid specimens rapidly breaking [32]. In this way, the whole stress–strain curve was obtained. In this study, the pre-peak loading speed was 0.1 mm/s and the loading speed after the peak was 0.2 mm/s. The XRD tests were carried out using a D8 Advance X-ray powder diffractometer (Bruker AXS GmbH), and the radiation source of this instrument is Cu target. The scanning range 2θ is 5°~80° and the scanning speed is 10°/min. The SEM tests were carried out using a LEO-1430VP scanning electron microscope (Zeiss, Oberkochen, Germany) with the magnification of 50~20,000 times. Carbonation depth of gray brick under different curing methods was detected using the phenolphthalein alcohol method (phenolphthalein alcohol

solution with mass fraction of 1% as chromogenic agent) [33], and carbonation depth was measured by digital carbonation depth scale (China Zhuolin Science and Technology, Beijing, China), with measuring accuracy of 0.01 mm and measuring range of 0–25 mm.

Table 1. Specimens' curing method.

| Specimen Number	Curing Age	Curing Methods
I-A-1, I-A-2, I-A-3 I-B-1, I-B-2, I-B-3 I-C-1, I-C-2, I-C-3 I-D-1, I-D-2, I-D-3	4 days 8 days 12 days 16 days	After 12 h resting, the specimens were demolded and cured in a humid and ventilated natural environment.
II-A-1, II-A-2, II-A-3 II-B-1, II-B-2, II-B-3 II-C-1, II-C-2, II-C-3 II-D-1, II-D-2, II-D-3	4 days 8 days 12 days 16 days	After 12 h resting, the specimens were placed directly on the inner surface of the autoclave equipment without demolding. After 5 h of autoclave curing in an environment of 0.165 Mpa and 130 °C, the specimens were taken out and then demolded in a humid and ventilated natural environment for curing.
III-A-1, III-A-2, III-A-3 III-B-1, III-B-2, III-B-3 III-C-1, III-C-2, III-C-3 III-D-1, III-D-2, III-D-3	4 days 8 days 12 days 16 days	After 12 h resting, the specimens were demolded and cured in drying dishes with CO_2 concentration of 0.25 mol/L and pressure of 718.98 Pa.
IV-A-1, IV-A-2, IV-A-3 IV-B-1, IV-B-2, IV-B-3 IV-C-1, IV-C-2, IV-C-3 IV-D-1, IV-D-2, IV-D-3	4 days 8 days 12 days 16 days	After resting for 12 h, the specimens were placed cured in the autoclave equipment for 5 h, and then the specimens were taken out and demolded in drying dishes with CO_2 concentration of 0.25 mol/L and pressure of 718.98 Pa for curing.
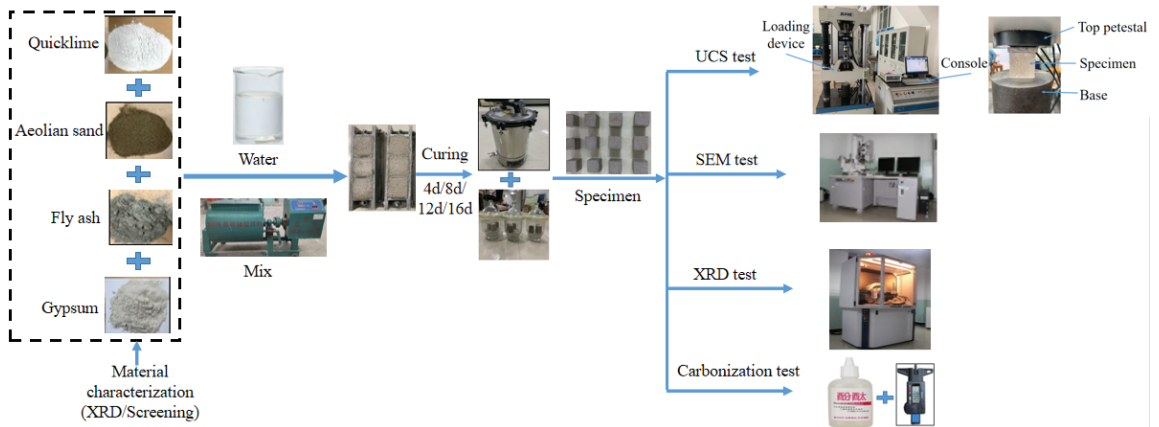
Figure 4. Experimental process. Here, SEM indicates scanning electron microscope.

2.3. Study on the Overburden Control Effect of Gray Brick in Backfill Mining

2.3.1. Establishing a Numerical Model

UDEC is a two-dimensional numerical calculation program based on a continuum simulation discrete element, which mainly simulates the mechanical behavior of discontinuous medium (such as joint block) under static or dynamic load conditions. UDEC discontinuous media is reflected by the combination of separated blocks, and the joints are treated as boundary conditions between blocks, allowing blocks to move and turn along the joint surface [34]. UDEC can clearly simulate the development of cracks in overlying strata during gray brick backfill mining, so as to achieve the desired simulation effect. Because large amounts of coal resources are distributed in western China with shallow buried depths, large thicknesses and thin overlying rock strata, the stratum conditions in the mining area in western China were simplified into three components: a bedrock layer, a weak cementation layer and loose overburden (Figure 5a) [35,36]. Based on this, a typical

numerical model was established. The block division of the different coal strata in the model is shown in Figure 5b. The established model was 500 m in length and 340 m in height, and the heights of the floor, coal seam, roof, bedrock layer, weak cemented layer and loose overburden were 22 m, 8 m, 6 m, 94 m, 100 m and 100 m, respectively. The bottom boundary of the model was fixed, the surrounding boundary was displacement constrained and the upper boundary was free. The Mohr–Coulomb yield criterion was used to calculate the constitutive relationship of the block. The strata joints were simplified into horizontal and vertical joints, and the surface contact Coulomb slip model was adopted. Boundary coal pillars of 100 m were reserved on the left and right sides of the model to eliminate the boundary effect, and the actual advance length was 300 m. The mechanical parameters of each rock layer are shown in Table 2.
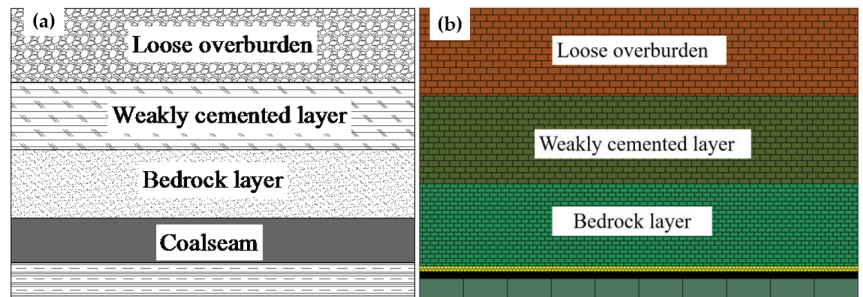
Figure 5. UDEC numerical model. (**a**) Typical stratum conditions in the Xinjiang mining area; (**b**) numerical model.

Table 2. Mechanics parameters of the rock strata used in simulation.

Stratum	Density Kg/m^3	Bulk Modulus /GPa	Shear Modulus /GPa	Friction Angle /Degree	Cohesion /MPa	Tensile Strength /MPa
Loose overburden	2200	0.05	0.03	25	0.7	0
Weakly cemented layer	2580	1.03	7.5	44	3.5	2
Bedrock layer	2700	2.52	1.6	48	6.97	5.4
Roof	2700	2.52	1.6	48	6.97	5.4
Coal seam	1470	7.9	5.5	37	3.02	3
Floor	1700	5.15	4	36	2.21	2.26

2.3.2. Simulation Scheme

The full-height mining method was adopted, and the advance step of the working face was 10 m in this simulation. In addition, the mechanical parameters of the gray brick after 16 days of autoclave–carbon dioxide curing were used as the simulation parameters. The calculated time step for each step from the retrieval was determined to be 2000 steps based on the time effect of the site. Considering the filling equipment and the actual situation at mining sites, the top connection rate was set to 95% for the simulation. The specific simulation scheme is shown in Table 3.

Table 3. Simulation scheme.

| Simulation Variables		Expected Simulation Results
Different filling spacing	Different filling strip width	Surface subsidence and height of crack propagation
10 m, 15 m, 20 m, 25 m, 30 m, 35 m	11 m, 12 m, 13 m, 14 m, 15 m, 16 m	

3. Results and Discussion

3.1. Analysis of the Bearing Strength of the Gray Brick

Typical uniaxial compression total stress–strain data of gray brick under different curing methods were selected for the analysis and are plotted in Figure 6a–d. It can be seen that, under different curing methods, the shapes of the total stress–strain curves of the gray brick are basically the same and the plastic characteristics of the gray brick do not change. The compressive deformation curves of the gray brick are similar to that of typical rock and experience four stages throughout the entire stress and strain process, namely the pore compaction stage (the concave curve), the elastic deformation stage (the oblique line), the plastic ring breaking stage (the concave curve) and the post-peak failure stage (the post-peak curve).
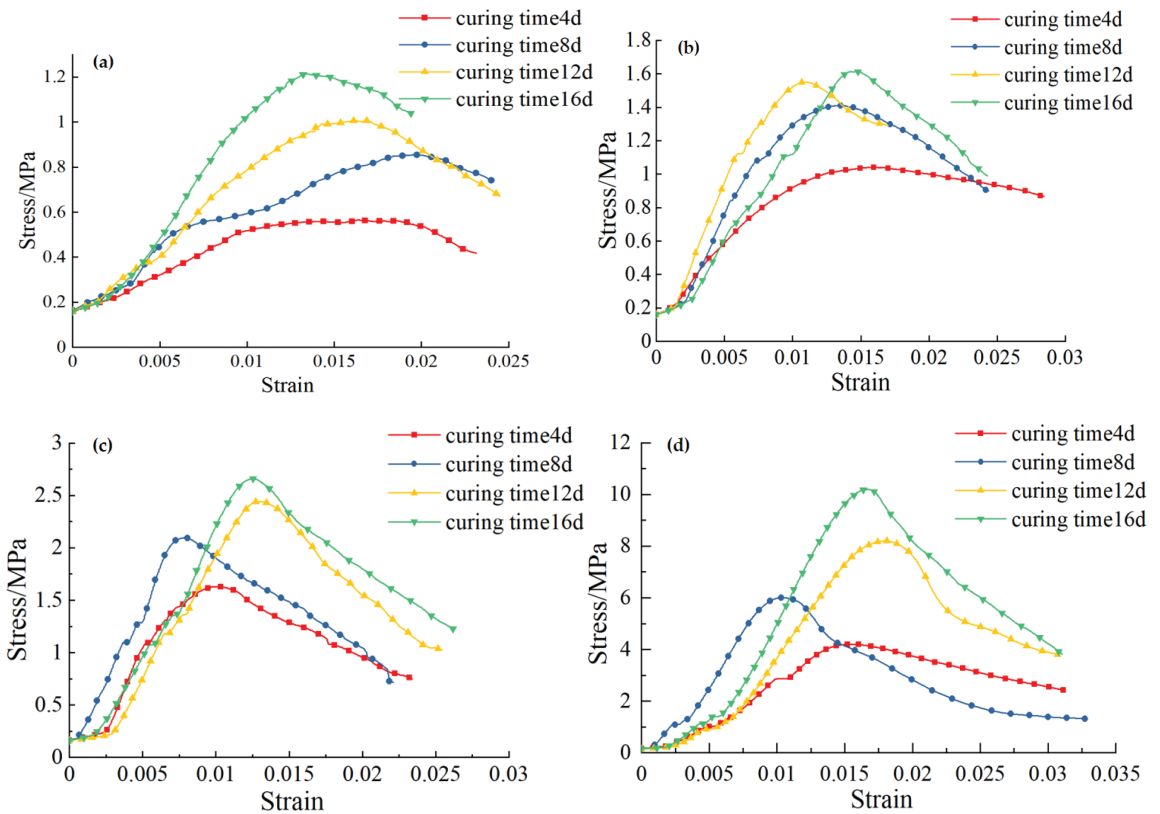

Figure 6. Complete stress–strain curves of gray brick under different curing methods. (**a**) Natural curing; (**b**) autoclave curing; (**c**) carbon dioxide curing; (**d**) autoclave–carbon dioxide curing.

The uniaxial compressive strengths of the gray brick under different curing methods and curing ages are shown in Figure 7. The results indicate that, under autoclave curing, carbon dioxide curing and autoclave–carbon dioxide curing, the bearing strength of the gray brick increased to different degrees compared with that of natural curing. The uniaxial compressive strength of the gray brick under 16 days of natural curing was 1.25 MPa, while the uniaxial compressive strengths of gray brick under 16 days of autoclave curing, carbon dioxide curing and autoclave–carbon dioxide curing were 1.58 MPa, 2.58 MPa and 9.65 MPa, respectively, increasing by 26%, 98% and 668%, respectively, compared with natural curing.
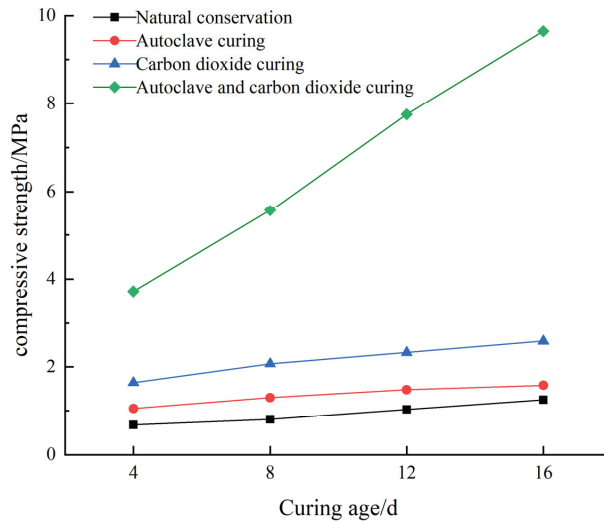
Figure 7. Bearing strengths of gray brick under different curing methods.

To study the failure modes of gray brick under different curing methods, typical failure surfaces under the different curing methods were selected to draw crack maps, as shown in Figure 8a–d. The results indicate that, under the different curing methods, there were two main cracks running through the samples, accompanied by several microcracks on the surfaces of the gray brick; these cracks had the same characteristics for all methods. Therefore, changing the curing method did not change the failure mode of the gray brick; all brick showed typical X-shaped conjugate shear failure.
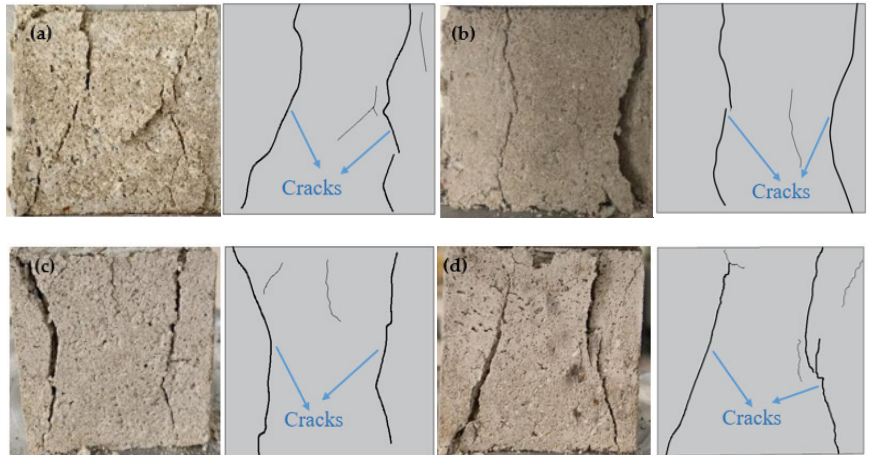
Figure 8. Failure modes of the gray brick under different curing methods. (**a**) Natural curing; (**b**) autoclave curing; (**c**) carbon dioxide curing; (**d**) autoclave–carbon dioxide curing.

3.2. Carbonation Curing Mechanism Analysis of the Gray Brick

The carbonization degrees of the gray brick under different curing methods were measured and the test results were analyzed, as shown in Figure 9a,b. It can be seen in Figure 9b that, under natural and autoclaved curing conditions, carbonization of the gray brick basically did not occur. The carbonization depths of the gray brick under 16 days of carbon dioxide curing and autoclave–carbon dioxide curing were 4.1 mm and

8.9 mm, respectively. Obviously, the carbonization degree of the gray brick was promoted by autoclave curing and, with increasing curing age, the carbonization rate of the gray brick slowed.
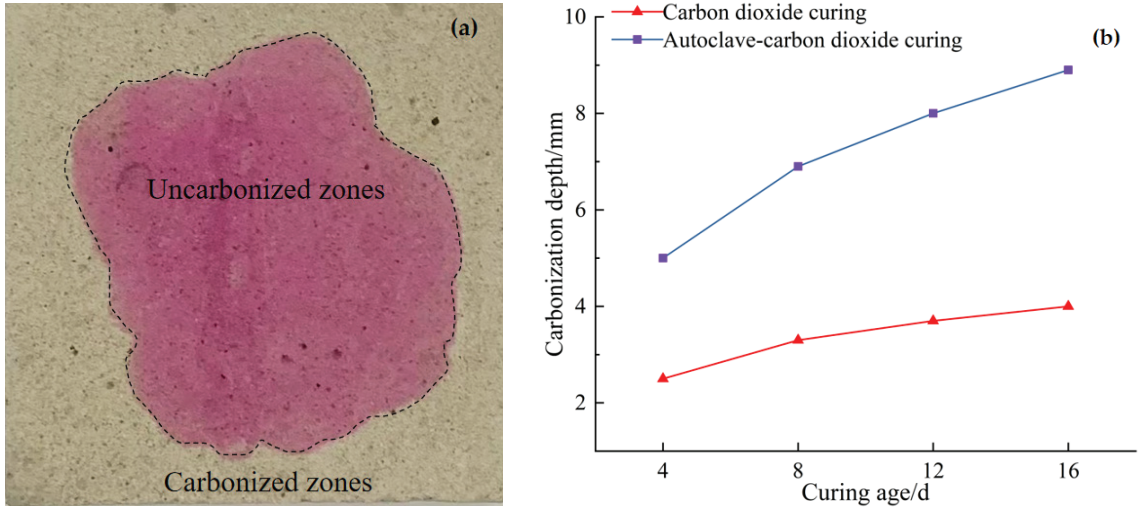

Figure 9. Carbonization depths of gray brick under different curing methods. (**a**) Carbonation diagram of specimen III-A-2; (**b**) carbonation depths of gray brick.

To study the mechanism of the increasing bearing strength of gray brick following carbonization, the internal hydration products and internal structure of the uncarbonized and carbonized parts of specimen III-A-2 were analyzed via XRD and SEM, as shown in Figure 10a–d. It can be seen that the internal compactness of the uncarbonized gray brick was small and that they contained a lot of gaps and pores; therefore, the bearing strength was primarily provided by the friction between the small internal particles. The main hydration products of the carbonized gray brick were $CaCO_3$ and $CaSO_4(H_2O)_2$, rather than $Ca(OH)_2$. In addition, the internal gaps and pores of the uncarbonized gray brick were filled by interlaced and needle shaped $CaCO_3$, resulting in higher compactness and integrity.

3.3. Stability Analysis of the Overlying Strata Filled with Gray Brick Strips

The simulation results showed that the maximum surface subsidence always occurred directly above the goaf, and this subsidence under mining with different filling spacings and filling strip widths is shown in Figure 11. It can be seen that the maximum surface subsidence reached a maximum of 0.675 m when the filling spacing was 35 m and the width of the filling strip was 11 m and that it reached a minimum of 0.403 m when the filling spacing was 10 m and the width of the filling strip was 16 m. The maximum surface subsidence could be reduced obviously when the filling spacing decreased from 35 m to 20 m and the filling strip width increased from 11 m to 13 m. In order to describe the quantitative relationship between the maximum surface subsidence (S) and the filling strip spacing (x) and the filling strip width (y) more accurately, the Gauss2D function of the Origin software was used to obtain the fitting relationship between above parameters, as shown in Equation (1). According to the results of fitting calculation, the fitting correlation coefficient (R^2) was 0.9926, the mean square error (MSE) was 3.86×10^{-5} and the root mean square error (RMSE) was 0.0062, and the goodness of this fit was acceptable.

$$S = 59.3 - 58.9e^{-\frac{(x+4.7)^2}{421362} - \frac{(y-17.9)^2}{34322}} \quad (x:\ 10\text{–}35\text{ m};\ y:\ 11\text{–}16\text{ m}) \tag{1}$$
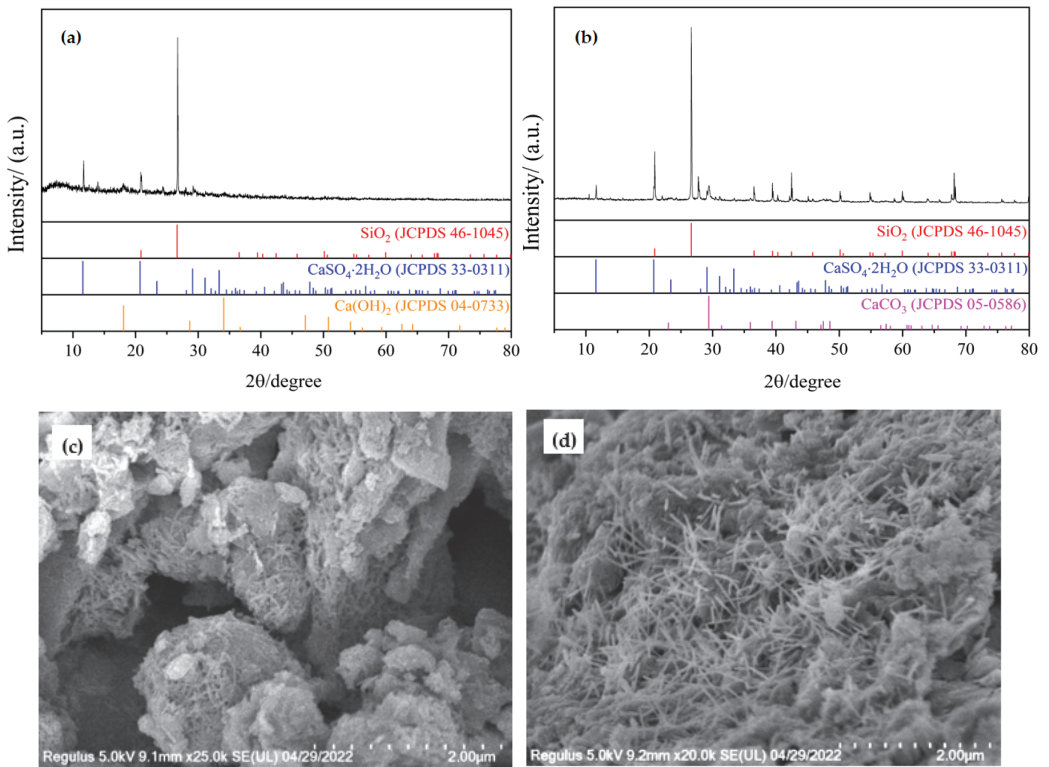
Figure 10. Comparison of the products and structures in the uncarbonized and carbonized parts of specimen III-A-2. (**a**) XRD of the uncarbonized part; (**b**) XRD of the carbonized part; (**c**) SEM of the uncarbonized part; (**d**) SEM of the carbonized part.
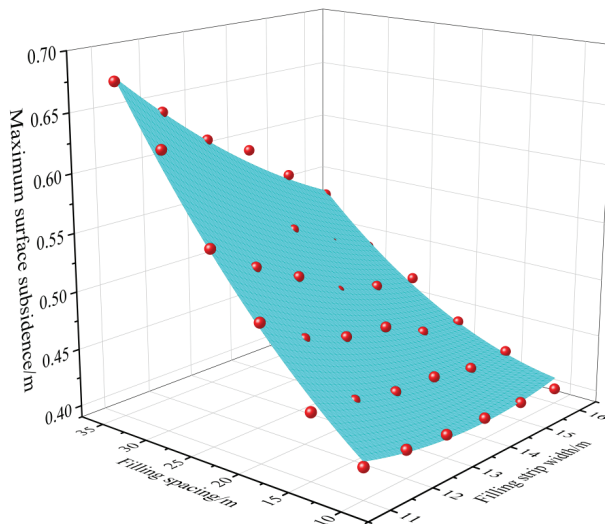
Figure 11. Fitting surface of the maximum surface subsidence with different filling spacings and filling strip widths.

According to Equation (1), the maximum surface subsidence (*S*) has an exponential relationship with filling strip spacing (*x*) and filling strip width (*y*). Further, the maximum surface subsidence (*S*) decreases continuously with decreasing filling spacing (*x*) and increasing filling strip width (*y*), which provides a valuable reference for controlling the maximum surface subsidence (*S*) through adjusting the backfill settings. The primary consideration for the filling strips spacing (*x*) is to avoid the caving of the immediate roof strata over the gob due to fact that the gob must be kept integrated for the purpose of following storage of carbon dioxide gas. The filling strip width (*y*) is commonly limited by the construction speed of filling strips because the backfilling speed and mining speed need to be consistent to ensure the continuity of backfill mining operations. In practice, the filling strips spacing (*x*) can be adjusted in a larger range compared with the filling strip width (*y*) because of the fact that the time for backfilling in a backfill mining cycle is always limited. Consequently, it is more feasible to control the maximum surface subsidence (*S*) by adjusting the filling strip spacing (*x*). It also should be noted that the parameters except for filling strip spacing (*x*) and filling strip width (*y*) in Equation (1) are only applicable to the engineering geological conditions in this study, and should be adjusted according to the mining depth, rock strata mechanics and backfilling materials' strength in different cases. It can be determined that the relationship between the maximum surface subsidence (*S*) and filling strip spacing (*x*) and width (*y*) described in Equation (1) could represent the general surface subsidence of underground mines in northwest China with the overburden composed of loose layer, weakly cemented layer and bedrock layer from top to bottom.

In the simulation process, if the joint contact appears to slip and have tensile failure, this indicates that the contact has fractured; that is, that cracks appear in the overburden [37]. The overburden fracture height under different filling spacings and filling strip widths is shown in Table 4. Based on the overburden fracture heights under different filling settings obtained from Table 4, the fracture propagation height (*H*) variation diagram of the overburden with different filling spacing (*x*) and filling strip widths (*y*) are drawn, as shown in Figure 12. In order to describe the quantitative relationship between the fracture propagation height (*H*) and the filling strip spacing (*x*) and the filling strip width (*y*) more accurately, the Gauss2D function of the Origin software was used to obtain the fitting relationship between above parameters, as shown in Equation (2). According to the results of fitting calculation, the fitting correlation coefficient (R^2) was 0.99938, the mean square error (MSE) was 15.2, and the root mean square error (RMSE) was 3.897 and the goodness of this fit was acceptable.

$$H = 30.9 + 719294\mathrm{e}^{-\frac{(x-109.1)^2}{1352} - \frac{(y+28.2)^2}{327.7}} \quad (x:\ 10\text{–}35\ \mathrm{m};\ y:\ 11\text{–}16\ \mathrm{m}) \tag{2}$$

According to Equation (2), the fracture propagation height (*H*) has an exponential relationship with filling strip spacing (*x*) and filling strip width (*y*). Further, the fracture propagation height (*H*) decreases continuously with decreasing filling spacing (*x*) and increasing filling strip width (*y*), which provides a valuable reference for controlling the fracture propagation height (*H*) through adjusting the backfill settings. It also should be noted that the parameters except for filling strip spacing (*x*) and filling strip width (*y*) in Equation (2) are only applicable to the engineering geological conditions in this study, and should be adjusted according to the mining depth, rock strata mechanics and backfilling materials' strengths in different cases. It can be determined that the relationship between the fracture propagation height (*H*) and filling strip spacing (*x*) and width (*y*) described in Equation (2) could represent the general fracture distribution of underground mines in northwest China with the overburden composed of loose layer, weakly cemented layer and bedrock layer from top to bottom.

Table 4. Fracture propagation height of different filling spacings and filling strip widths.
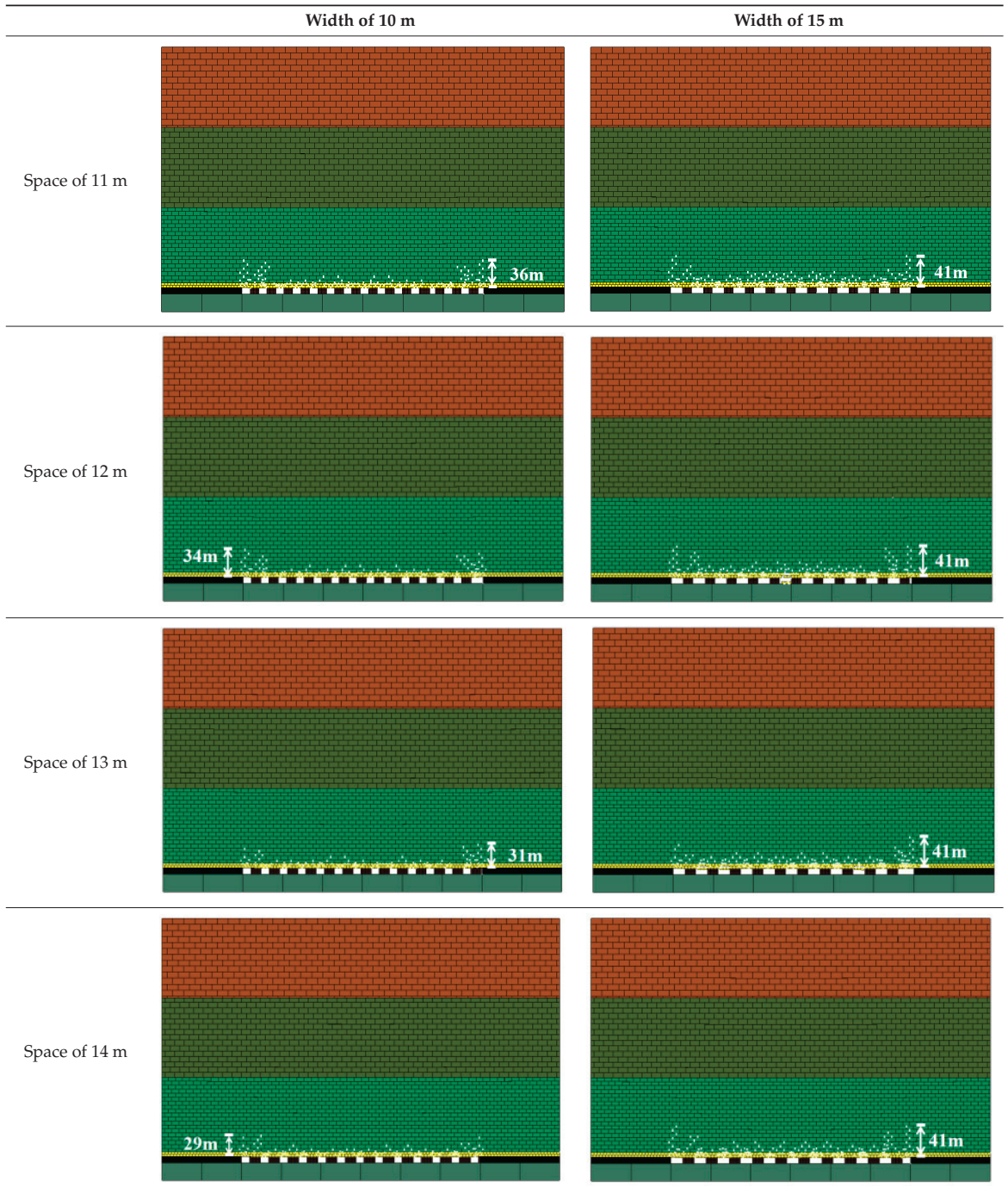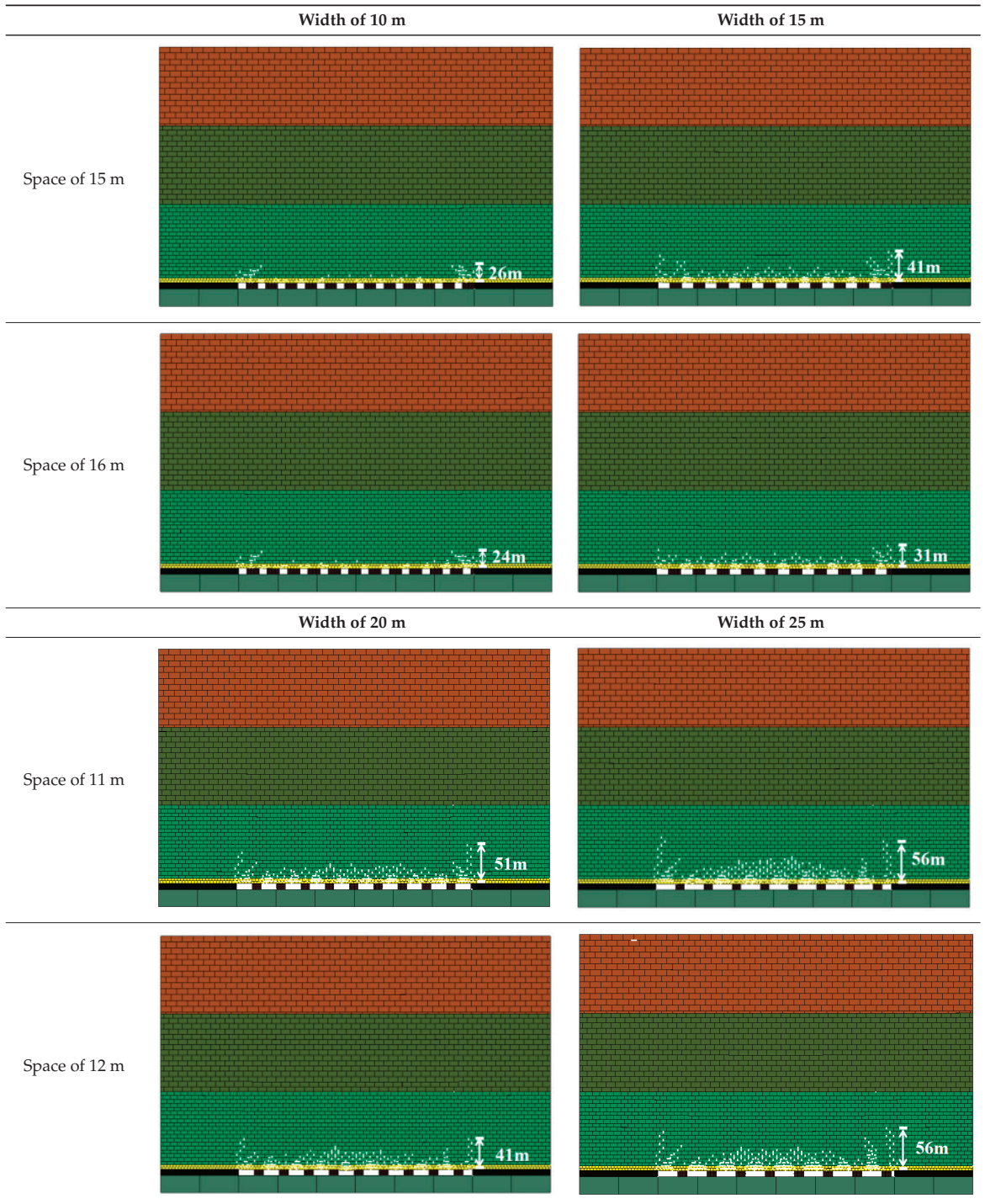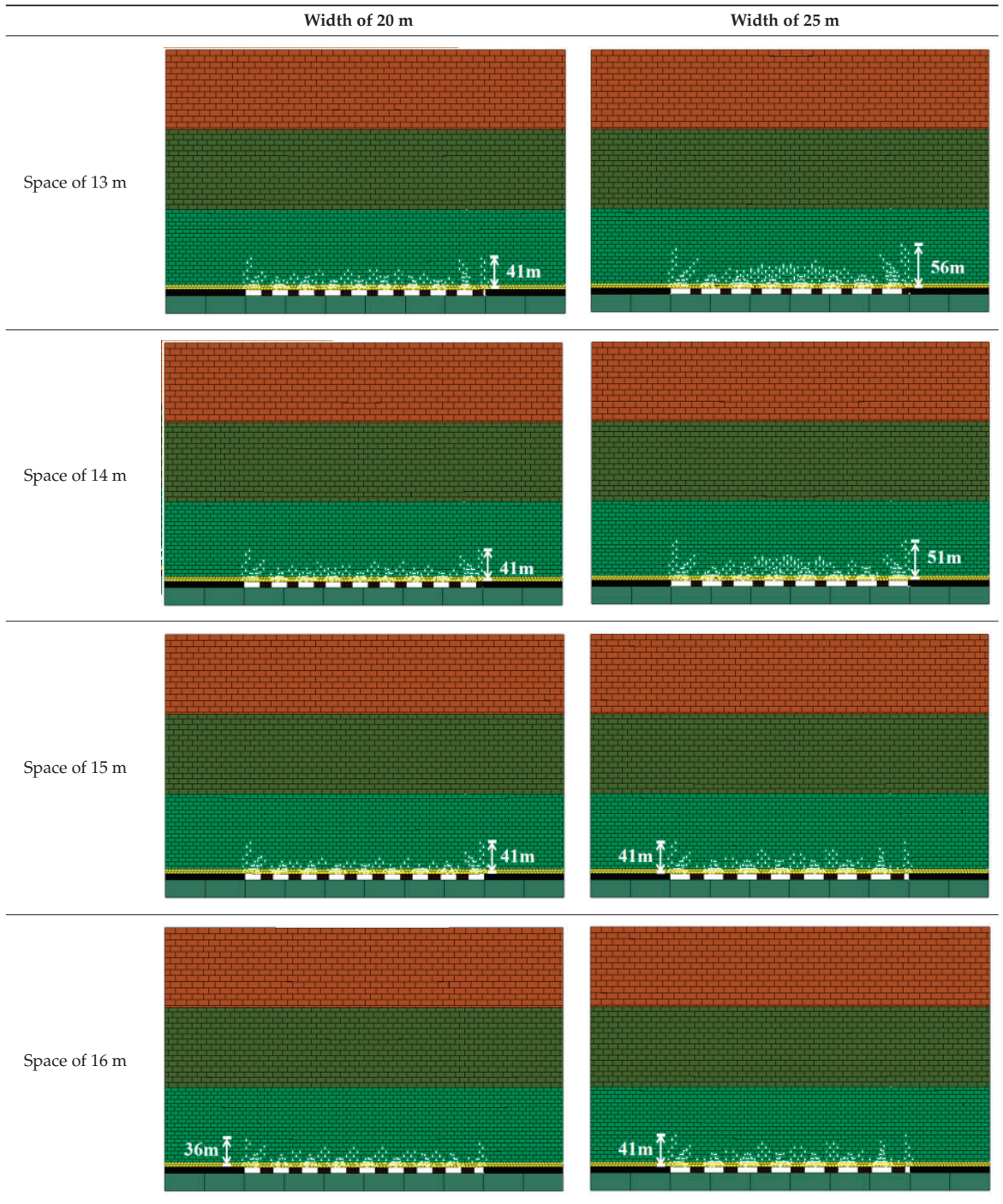
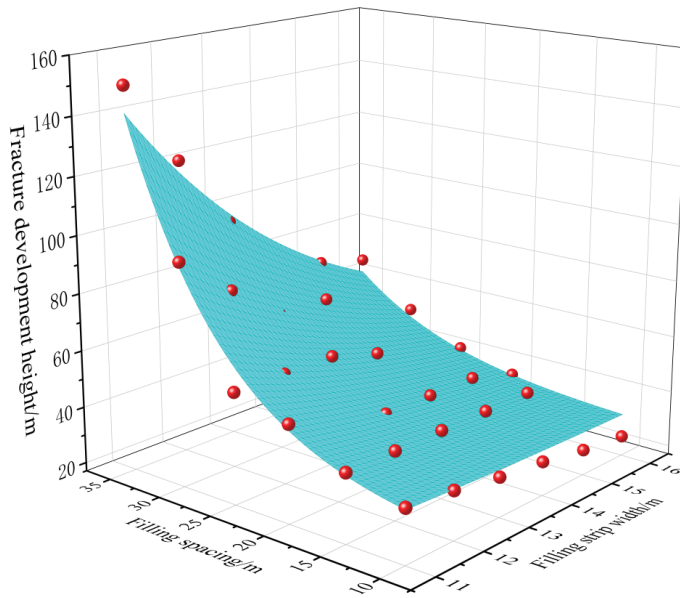|	Width of 10 m	Width of 15 m
Space of 11 m	36m	41m
Space of 12 m	34m	41m
Space of 13 m	31m	41m
Space of 14 m	29m	41m

Table 4. *Cont.*

Width of 10 m	Width of 15 m
Space of 15 m	26m	41m
Space of 16 m	24m	31m

Width of 20 m	Width of 25 m
Space of 11 m	51m	56m
Space of 12 m	41m	56m

Table 4. *Cont.*

	Width of 20 m	Width of 25 m
Space of 13 m		
Space of 14 m		
Space of 15 m		
Space of 16 m		

Figure 12. Fitting surface of different filling spacings, filling strip widths and overburden fracture propagation heights.

3.4. Evaluation of the Gas Tightness of Overlying Rock Filled with Gray Brick Strips

There are two main aspects that need to be considered with respect to the escape of CO_2 from goaf. The first aspect is that, when the capping pressure is less than the CO_2 sealing pressure, the formation stress is redistributed; this is primarily reflected in an increase in the capping cracks and permeability, resulting in the escape of the sequestered CO_2 [38,39]. Because of the depth of the coal buried in mining areas in western China, the CO_2 storage pressure in the goaf is small; therefore, it is difficult to reach the cap rock breakthrough pressure. Accordingly, this was not studied in this paper. The second aspect is that of the permeability of CO_2 through the micropores of the cap as a result of the difference in the pressure gradient, which is primarily related to the permeability coefficient of the cap. In general, the permeability of the bedrock layers is in the range of 10^{-1}–10^{-3} μm^2 because of the high internal microporosity; the permeability of the weakly cemented layer is generally relatively low at 10^{-11}–10^{-5} μm^2. Moreover, gas seepage is a slow and long-term process that can be calculated using Darcy's law:

$$Q = KA(P_1^2 - P_2^2)/2P_0\mu L \tag{3}$$

where Q is the gas flow through rock, cm^3/s; A is the cross-sectional area of gas passing through the rock, cm^2; μ is the Viscosity of gas, MPa·s; P_1 and P_2 are the rock inlet and outlet gas pressure, MPa; L is the Length of the rock, cm; K is the Permeability coefficient of gas to rock, μm^2; and P_0 is Atmospheric pressure, MPa.

Using Darcy's law, the CO_2 escape amount under different filling spacings and filling strip widths in this numerical model was calculated, where the strike length of the model working face was set to 200 m, the CO_2 sequestration pressure was set to 1 MPa, the permeability of the bedrock layer was set to 10^{-3} μm^2 and the permeability of the weakly cemented layer was set to 10^{-5} μm^2 combined with the actual situation of the goaf. The calculated results are shown in Figure 13. In order to describe the quantitative relationship between the gas escape quantity (Q) and the filling strip spacing (x) and the filling strip width (y) more accurately, the Gauss2D function of the Origin software was used to obtain the fitting relationship between above parameters, as shown in Equation (4). According

to the results of fitting calculation, the fitting correlation coefficient (R^2) was 0.99679, the mean square error (MSE) was 3.4, and the root mean square error (RMSE) was 1.84, and the goodness of this fit was acceptable.

$$Q = 6.58 + 786.5e^{-\frac{(x-109.1)^2}{703.9} - \frac{(y+21.9)^2}{282.3}} \quad (x: \ 10\text{–}35 \text{ m}; \ y: \ 11\text{–}16 \text{ m}) \tag{4}$$
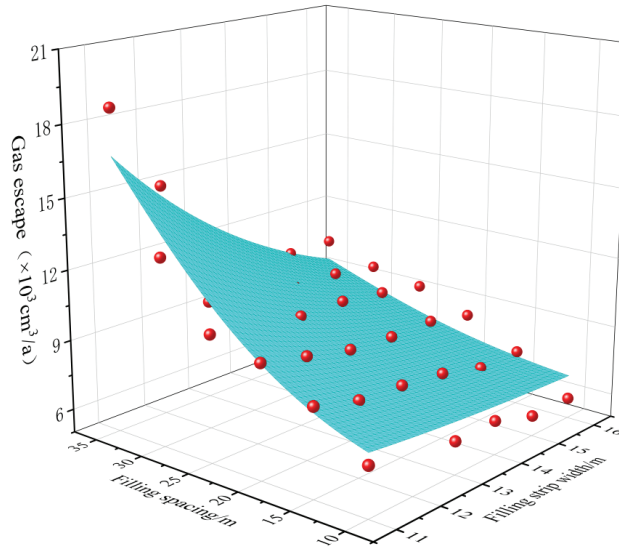
Figure 13. Fitting surfaces of different filling spacings and strip filling widths with the gas escape amount.

According to Equation (4), the gas escape quantity (Q) has an exponential relationship with filling strip spacing (x) and filling strip width (y). Further, the fracture gas escape quantity (Q) decreases continuously with decreasing filling spacing (x) and increasing filling strip width (y), which provides a valuable reference for controlling the gas escape quantity (Q) through adjusting the backfill settings. It also should be noted that the parameters except for filling strip spacing (x) and filling strip width (y) in Equation (4) are only applicable to the engineering geological conditions in this study, and should be adjusted according to the mining depth, rock strata mechanics and backfilling materials' strengths in different cases. It can be determined that the relationship between the gas escape quantity (Q) and filling strip spacing (x) and width (y) described in Equation (4) could represent the general gas escape quantity of underground mines in northwest China with the overburden composed of loose layer, weakly cemented layer and bedrock layer from top to bottom.

4. Conclusions

In this paper, geological and environmental challenges encountered during coal mining and power generation in large coal power bases were considered as a whole, the bearing strength of gray brick after carbonation curing for backfill mining and the stability of the overlying strata after strip backfilling for the geological storage of carbon dioxide were investigated, and the main conclusions were as follows:

(1) After carbonization curing, the strength of gray brick is significantly improved. The uniaxial compressive strengths of the backfill gray brick after 16 days of autoclave curing, carbon dioxide curing and autoclave–carbon dioxide curing are 1.58 MPa, 2.58 MPa, and 9.65 MPa, respectively, reflecting increases of 26%, 98% and 668%, respectively, compared with natural curing. All bricks show X-shape conjugate shear failure. The main hydration

product of the backfill gray brick under carbonization curing conditions is $CaCO_3$, as opposed to $Ca(OH)_2$, which is found under non-carbonization curing conditions. In addition, the internal gaps and pores of the backfill gray brick following carbonization curing are filled by interlaced and needle shaped $CaCO_3$, resulting in higher compactness and integrity.

(2) The stability of overburden is obviously improved by gray brick strip filling. UDEC numerical simulation results show that the maximum surface subsidence reached a maximum of 0.675 m when the filling spacing was 35 m and the width of the filling strip was 11 m, and that it reached a minimum of 0.403 m when the filling spacing was 10 m and the width of the filling strip was 16 m. When the filling spacing was 35 m and the filling strip width was 11 m, the overburden fracture height reached a maximum of 149 m. When the filling spacing was 10 m and the filling strip width was 16 m, the overburden fracture height reached a minimum of 24 m. The surface subsidence, fracture extension and gas tightness of the overlying strata could be improved gradually by increasing the width and reducing the spacing of the brick filling strips.

The results of this paper could provide effective references for green mining and low-carbon utilization of the coal resources in large coal power bases in other countries around the world.

References

1. Theocharis, A.I.; Zevgolis, I.E.; Roumpos, C.; Koukouzas, N.C. 3D Numerical Analysis for the Valorization Potential of Spoil Heaps by Shallow Foundations. *Sustainability* **2022**, *14*, 7363. [CrossRef]
2. Yang, X.; Yao, W.; Li, P.; Hu, J.; Latifi, H.; Kang, L.; Wang, N.; Zhang, D. Changes of SOC Content in China's Shendong Coal Mining Area during 1990–2020 Investigated Using Remote Sensing Techniques. *Sustainability* **2022**, *14*, 7374. [CrossRef]
3. Motyka, J.; d'Obyrn, K.; Sracek, O.; Postawa, A.; Źróbek, M. Pit Lakes Affected by a River Contaminated with Brines Originated from the Coal Mining Industry: Evolution of Water Chemistry in the Zakrzówek Horst Area (Krakow, Southern Poland). *Energies* **2022**, *15*, 4382. [CrossRef]
4. Chen, F.; Liu, J.; Zhang, X.; Wang, J.; Jiao, H.; Yu, J. Review on the Art of Roof Contacting in Cemented Waste Backfill Technology in a Metal Mine. *Minerals* **2022**, *12*, 721. [CrossRef]
5. Ajayi, S.A.; Ma, L.; Spearing, A.J.S. Ground Stress Analysis and Automation of Workface in Continuous Mining Continuous Backfill Operation. *Minerals* **2022**, *12*, 754. [CrossRef]
6. Rybak, J.; Khayrutdinov, M.M.; Kuziev, D.A.; Kongar-Syuryun, P.B.; Babyr, N.V. Prediction of the geomechanical state of the rock mass when mining salt deposits with stowing. *J. Min. Inst.* **2022**, *253*, 61–70. [CrossRef]
7. Lim, B.; Alorro, R.D. Technospheric Mining of Mine Wastes: A Review of Applications and Challenges. *Sustain. Chem.* **2021**, *2*, 38. [CrossRef]
8. Jankowski, J.; Spies, B. Impact of longwall mining on surface water–groundwater interaction and changes in chemical composition of creek water. In Proceedings of the XXXV IAH Congress, Lisbon, Portugal, 17–21 September 2007.
9. Edmonds, C. Five decades of settlement and subsidence. *Q. J. Eng. Geol. Hydrogeol.* **2018**, *51*, 403–416. [CrossRef]
10. Van Der Merwe, J.N. Effects of coal mining on surface topography in South Africa-updates and extensions. *J. S. Afr. Inst. Min.* **2018**, *118*, 777–786. [CrossRef]
11. Isiaka, A.I.; Durrheim, R.J.; Manzi, M.S. High-resolution seismic reflection investigation of subsidence and sinkholes at an abandoned coal mine site in South Africa. *Pure Appl. Geophys.* **2019**, *176*, 1531–1548. [CrossRef]

12. Tiwari, A.; Narayan, A.B.; Dwivedi, R.; Swadeshi, A.; Pasari, S.; Dikshit, O. Geodetic investigation of landslides and land subsidence: Case study of the Bhurkunda coal mines and the Sirobagarh landslide. *Surv. Rev.* **2018**, *52*, 134–149. [CrossRef]

13. Konicek, P.; Soucek, K.; Stas, L.; Singh, R.; Sinha, A. Practices to Control Rock Burst in Deep Coal Mines of Upper Silesian Coal Basin and Their Applicability for Disergarh Seam of Raniganj Coalfield. In Proceedings of the ISRM International Symposium—6th Asian Rock Mechanics Symposium, New Delhi, India, 23–27 October 2010; OnePetro: Richardson, TX, USA, 2010.

14. Greiving, S.; Gruehn, D.; Reicher, C. The Rhenish Coal-Mining Area—Assessing the Transformational Talents and Challenges of a Region in Fundamental Structural Change. *Land* **2022**, *11*, 826. [CrossRef]

15. Chang, Q.; Chen, J.; Zhou, H.; Bai, J. Implementation of Paste Backfill Mining Technology in Chinese Coal Mines. *Sci. World J.* **2014**, *2014*, 821025. [CrossRef] [PubMed]

16. Yao, Q.; Feng, T.; Liao, Z. Damage characteristics and movement of inclined strata with sublevel filling along the strike in the steep seam. *J. China Coal Soc.* **2017**, *42*, 3096–3105.

17. Ma, D.; Zhang, J.; Duan, H.; Huang, Y.; Li, M.; Sun, Q.; Zhou, N. Reutilization of gangue wastes in underground backfilling mining: Overburden aquifer protection. *Chemosphere* **2021**, *264*, 128400. [CrossRef]

18. Zhang, J.; Li, M.; Taheri, A.; Zhang, W.; Wu, Z.; Song, W. Properties and Application of Backfill Materials in Coal Mines in China. *Minerals* **2019**, *9*, 53. [CrossRef]

19. Qi, C.; Fourie, A. Cemented paste backfill for mineral tailings management: Review and future perspectives. *Miner. Eng.* **2019**, *144*, 106025. [CrossRef]

20. Behera, S.K.; Mishra, D.P.; Singh, P.; Mishra, K.; Mandal, S.K.; Ghosh, C.N.; Kumar, R.; Mandal, P.K. Utilization of mill tailings, fly ash and slag as mine paste backfill material: Review and future perspective. *Constr. Build. Mater.* **2021**, *309*, 125120. [CrossRef]

21. Zhao, Y.; Taheri, A.; Karakus, M.; Chen, Z.; Deng, A. Effects of water content, water type and temperature on the rheological behaviour of slag-cement and fly ash-cement paste backfill. *Int. J. Min. Sci. Technol.* **2020**, *30*, 271–278. [CrossRef]

22. Ercikdi, B.; Cihangir, F.; Kesimal, A.; Deveci, H.; Alp, İ. Utilization of industrial waste products as pozzolanic material in cemented paste backfill of high sulphide mill tailings. *J. Hazard. Mater.* **2009**, *168*, 848–856. [CrossRef]

23. Feng, G.R.; Ren, Y.F.; Zhang, X.Y.; Guo, Y.X.; Kang, L.X. The activating experimental research of fly ash for mining filling material in Tashan Mine. *J. China Coal Soc.* **2011**, *36*, 732–737.

24. Zhou, N.; Ma, H.; Ouyang, S.; Germain, D.; Hou, T. Influential Factors in Transportation and Mechanical Properties of Aeolian Sand-Based Cemented Filling Material. *Minerals* **2019**, *9*, 116. [CrossRef]

25. Peyronnard, O.; Benzaazoua, M. Estimation of the cementitious properties of various industrial by-products for applications requiring low mechanical strength. *Resour. Conserv. Recycl.* **2011**, *56*, 22–33. [CrossRef]

26. Cihangir, F.; Ercikdi, B.; Kesimal, A.; Turan, A.; Deveci, H. Utilisation of alkali-activated blast furnace slag in paste backfill of high-sulphide mill tailings Effect of binder type and dosage. *Miner. Eng.* **2012**, *30*, 33–43. [CrossRef]

27. Deng, X.; Klein, B.; Tong, L.; de Wit, B. Experimental study on the rheological behavior of ultra-fine cemented backfill. *Constr. Build. Mater.* **2018**, *158*, 985–994. [CrossRef]

28. Xu, W.; Cao, P.; Tian, M. Strength Development and Microstructure Evolution of Cemented Tailings Backfill Containing Different Binder Types and Contents. *Minerals* **2018**, *8*, 167. [CrossRef]

29. Wang, X.; Zhang, J.; Li, M.; Gao, F.; Taheri, A.; Huo, B.; Jin, L. Expansion Properties of Cemented Foam Backfill Utilizing Coal Gangue and Fly Ash. *Minerals* **2022**, *12*, 763. [CrossRef]

30. Ermolovich, E.A.; Ivannikov, A.L.; Khayrutdinov, M.M.; Kongar-Syuryun, C.B.; Tyulyaeva, Y.S. Creation of a Nanomodified Backfill Based on the Waste from Enrichment of Water-Soluble Ores. *Materials* **2022**, *15*, 3689. [CrossRef] [PubMed]

31. Bai, X.C.; Duan, Z.H. Development of the Light Quality and High Strength Fly Ash Brick. *J. Henan Univ. Nat. Sci.* **2009**, *39*, 5.

32. Zhang, X.; Lin, J.; Liu, J.; Li, F.; Pang, Z. Investigation of Hydraulic-Mechanical Properties of Paste Backfill Containing Coal Gangue-Fly Ash and Its Application in an Underground Coal Mine. *Energies* **2017**, *10*, 1309. [CrossRef]

33. Zhang, C.; Wang, L.; Yao, Y.; Shi, X.Y. Determination of Concrete Carbonation Depth by Testing the pH Value of Layer-by-layer Grinding Concrete Samples. *Mater. Rep.* **2022**, *36*, 7.

34. Zhang, G.C.; Tao, G.Z.; Meng, X.J.; Li, Y.; Qu, Z.; Xu, R.H.; Yu, S.C.; Chen, M.; Zhou, G.L.; Luan, H.J. Failure law of weak overburden stratum underlying extra-thick alluvium. *J. China Coal Soc.* **2022**.

35. Li, Y.; Zhao, B.; Yang, J.; Sun, J.; Huang, W.; Li, Z.; Wang, B. Experimental Study on the Influence of Confining Pressure and Bedding Angles on Mechanical Properties in Coal. *Minerals* **2022**, *12*, 345. [CrossRef]

36. Wang, X.; Zhu, W.; Xie, J.; Han, H.; Xu, J.; Tang, Z.; Xu, J. Borehole-Based Monitoring of Mining-Induced Movement in Ultrathick-and-Hard Sandstone Strata of the Luohe Formation. *Minerals* **2021**, *11*, 1157. [CrossRef]

37. Hoek, E.; Brown, E.T. Practical estimates of rock mass strength. *Int. J. Rock Mech. Min. Sci.* **1997**, *34*, 1165–1186. [CrossRef]

38. Wang, S.M.; Shen, Y.J.; Sun, Q.; Liu, L.; Shi, Q.M.; Zhu, M.B.; Zhang, B.; Cui, S.D. Underground CO_2 storage and technical problems in coal mining area under the "dual carbon" target. *J. China Coal Soc.* **2022**, *47*, 45–60.

39. Liu, L.; Wang, S.M.; Zhu, M.B.; Zhang, H.; Hou, D.Z.; Xun, C.; Zhang, X.Y.; Wang, X.L.; Wang, M. CO_2 storage-cavern construction and storage method based on functional backfill. *J. China Coal Soc.* **2022**, *47*, 1072–1086.

Research on the Mechanical Properties of Flexible Material Backfilling Wall in Gob-Side Entry Retaining

Dongdong Pang [1,2,3], **Yong Zhou** [3,*], **Xingang Niu** [4,5], **Kai He** [6], **Chuanming Li** [1,2,3] and **Zhongqi Chen** [1,2,3]

1   School of Mining Engineering, Anhui University of Science and Technology, Huainan 232001, China
2   Coal Mine Safety Mining Equipment Innovation Center of Anhui Province, Huainan 232001, China
3   State Key Laboratory of Mining Response and Disaster Prevention and Control in Deep Coal Mine, Anhui University of Science & Technology, Huainan 232001, China
4   Gas Research Branch, China Coal Technology and Engineering Group Chongqing Research Institute, Chongqing 400037, China
5   State Key Laboratory of the Gas Disaster Detecting Preventing and Emergency Controlling, China Coal Technology and Engineering Group Chongqing Research Institute, Chongqing 400037, China
6   School of Civil Engineering and Transportation, South China University of Technology, Guangzhou 510640, China
*   Correspondence: zhouyong0068@163.com

Abstract: In order to solve the problems of the uneven deformation of Gangue Filled Wall and the difficulty of large-scale promotion of roadway side support, and to achieve the purposes of direct disposal of coal mine waste, reducing costs, and protecting the environment, the failure mechanics model of the bagged gangue was established, and the mechanical action relationship between longitudinal external load and transverse external load of gangue woven bag was deduced. Through the uniaxial compression test of large-scale flexible backfill (coal gangue of different particle sizes), it was obtained that when the strain is 0.2, the bearing capacity of particles with particle sizes between 0 and 10 mm is greater than 5 MPa, and when the strain is 1.27, the bearing capacity of particles with particle thicknesses between 10 and 20 mm is greater than 0 mpa, which meets the requirements of resistance value and resistance growth rate of gob side entry. In the "load deflection" test of backfill (gangue) samples, it was found that the maximum failure load of wet shotcrete is greater than that of dry shotcrete, and the wet shotcrete can withstand greater deformation under the same load conditions. Through the analysis of the experimental results of "flexural strength thickness" and "maximum failure load thickness", it was finally determined that the thickness of the spray layer with good flexibility and sufficient support force is controlled at about 80 mm.

Keywords: flexibility; backfilling wall with coal gangue; gob-side entry retaining; crushing-grading; packed coal gangue; flexural strength; mechanical property; concrete

1. Introduction

Using coal gangue as a material for backfilling walls in gob-side entry retaining can solve waste disposal problems, and greatly reduce the cost [1,2]. However, the strong compressibility and the non-uniform stress–strain relationship of coal gangue can lead to a large amount of roof subsidence and a poor seal between the roof and the backfilling wall. Using coal gangue as a dynamic backfilling material based on the core technologies of "crushed gangue grading" and "crushed gangue packing" can increase the modulus of elasticity of coal gangue for backfilling walls. To study the stress–strain characteristics of coal gangue as a "flexible" material for backfilling walls is a prerequisite to improve its performance in gob-side entry retaining.

Gob-side entry retaining is to retain the roadway of the last working section and use it as a return airway for the next adjacent working section. It increases the coal mining rate, saves resources, and reduces land subsidence [3,4]. Russian, Eastern European, and

North American scientists have conducted a lot of research in this area [5,6], including Kongar-Syuryun, Ch.; Ivannikov, A.; Khayrutdinov, A. et al. [7], who consider mining waste as a product and propose its use in a closed cycle of mineral extraction. Kowalik, T.; Kim, J.and Ubysz, A. [8,9] evaluated the effects of three different sizes of recycled concrete materials (recycled coarse aggregate (RCA) with a size of 4.75–25 mm, recycled fine aggregate (RFA) with a size of 0.15–4.75 mm, and recycled powder (RP) with a size of less than 0.15 mm on the fresh and hardened mechanical properties of concrete. Ermolovich, E.A. [10] studied the strength properties of the fill mass, and the comparative analytical method was used. The strength properties of the backfill were measured in standard test periods, taking into account the intensity of hardening of the backfill material (after 7, 14, 28, 60, and 90 days). Grabinsky, M. [11] conducted a more in-depth study on the material properties and mechanical properties of cement paste backfill (CPB) materials. Rybak, J., Gorbatyuk, S.M., and Bujanovna-Syuryun, K.C. et al. [12] assessed the impact of the mining project on the ecosystem of the region. The important concept of industrial waste in the closed cycle of mining engineering was considered. It was proven that it is possible to adopt systematic methods to comprehensively develop mineral resources without waste production. Canadian scholars Nujaim, M. et al. [13] studied the geomechanical behavior of the interaction between waste rock characteristics and mine backfill. It was shown that the backfill stability of gangue backfill is affected by particle gradation and compactness. Rybak, J., Ermolovich, E.A., et al. [14], based on the water-soluble ore industrial waste activated by nano-modified materials, created a filler with improved strength characteristics, and the characteristics (chemical and particle size composition) of backfill aggregate based on the water-soluble ore enriched waste were obtained. Yue, X., Tu, M., and Du K. et al. [15–17] conducted a lot of work in the improvement of gob side entry retaining technology and the quantitative design of filling walls.

In practice, roadside packing support went through wood cribs [18,19], close-standing props [20,21], reutilization of coal gangue and fly ash as underground backfill materials for surface subsidence control [22], stability control of gob-side entry retaining in the fully mechanized caving face based on a compatible deformation model [23], the mechanism of coordinated deformation of backfill [24], concrete block [25,26] and composite filling [27], and complex system pump backfilling [28], but the development of all these technologies cannot fully satisfy the actual needs. In particular, with the rapid development of new materials, people become increasingly aware that the nature of gob-side entry retaining is a proper selection of materials for roadside packing based on their properties. The packing materials have gone through gypsum, lime plus Portland cement [29], coal gangue, binding materials [30], high-water quick-setting materials, and anhydrite, etc. [31]. Some of these materials commonly known as "hard" materials can immediately provide strong support resistance, but cannot adapt to roof subsidence, leading to wall leakage, etc., while some others commonly known as "flexible" materials can well adapt to roof subsidence, but the cost is too high, and the system constructed is too complex and hard for wide promotion.

In recent years, scholars at home and abroad have conducted a lot of research on the filling and utilization of waste ore, and the aggregate structure composition and material characteristics of backfill materials, combined with the characteristics of water-soluble ore industrial waste, created a filling volume with higher strength, and measured the strength characteristics of backfill rock and soil with different composition structures within the standard test cycle [32,33]. Analyzing the above, it can be noted that efficient utilization of waste coal gangue resources in mines is a very topical issue. Therefore, the purpose of this study was to give full play to the resource utilization rate of waste coal gangue and improve the mechanical properties of coal gangue backfill materials to meet the urgent needs of efficient and safe mining in deep coal mines and, to achieve this, it is necessary to solve the following tasks: (1) in terms of gangue crushing and strict particle size classification, study the stress–strain characteristics of coal gangue particles with different particle sizes, optimize the particle grading of coal gangue, and improve the elastic modulus and uniformity bearing performance of coal gangue backfill material after compaction;

(2) regarding the characteristics and process effect of concrete cementitious material, explore the spray layer thickness of coal gangue concrete cementitious material, improve the support resistance of the filling wall, and optimize the resistance-increasing characteristics.

In this paper, the stress and strain characteristics of coal gangue particles with different diameters and the packed crushed gangue were studied. Through crushing and strict particle size classification, the discreteness of the stress–strain relationship resulting from the individual randomness and difference of underground gangue tailings was avoided. Packing the crushed coal gangue can increase regional lateral pressure and the support resistance of the entire backfilling wall, and improve the uniformity of the internal support. According to the "load-deflection" test, the maximum destructive load of wet-spray concrete is greater than that of dry-spray concrete, and under the same load conditions, wet-spray concrete can withstand greater deformation. Through the relationship analysis between "flexural strength–thickness" and "maximum destructive load–thickness", the thickness of the spray layer with good flexibility and sufficient support force was finally controlled at about 80 mm. Improved flexural strength, performance, and good toughness and deformation ability, improved stability of concrete strength, and a quantitative design of the backfilling wall with coal gangue can ultimately be achieved to ensure the safety of the gob-side entry retaining.

2. Materials and Methods

2.1. Mechanical Model

Woven bags filled with coal gangue (hereafter referred to as gangue bags) were placed under a vertical external load σ_1 and horizontal external load σ_3; their shape changes are shown in Figure 1. The coal gangue inside the woven bag can produce 4 component forces under σ_1 and σ_3: the vertical external load, the horizontal external load σ_1, the vertical additional stress σ_2, and the horizontal additional stress σ_4. The latter two are caused by internal tension within the gangue bag. The mechanical model of a gangue bag is shown in Figure 2 [34].
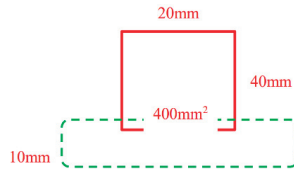
Figure 1. Schematic diagram of force deformation of gangue woven bags.
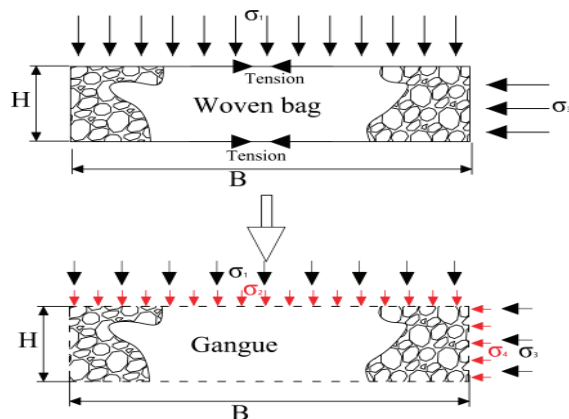
Figure 2. The mechanical model of a gangue bag failure.

where:

$$\sigma_2 = \frac{2T}{B}, \ \sigma_4 = \frac{2T}{H} \tag{1}$$

T is the tensile strength of the gangue bag, kN/m; *H* is the thickness of the gangue bag, m; *B* is the length of the gangue bag, m; $T = \varepsilon E = E\Delta l / l$, where *E* is the modulus of elasticity, Δl is the increment of circumference, and *l* is the circumference.

When the gangue bag reaches the breaking limit, the maximum and minimum principal stresses satisfy the following conditions:

$$\sigma_1 + \sigma_2 = K_p(\sigma_3 + \sigma_4) \tag{2}$$

After transformation, we have

$$\sigma_1 = \sigma_3 K_p + \frac{2T}{B}\left(mK_p - 1\right) = \sigma_3 K_p + 2c\sqrt{K_p} \tag{3}$$

where K_p is the passive earth pressure coefficient; *m* is the length–height ratio of the gangue bag. The above formula shows that the cohesion increases with *H*.

2.2. Test Principles and Methods

To study the stress–strain characteristics of "flexible" material backfilling walls, we first need to examine the stress–strain characteristics of the entire backfilling wall and the packed coal gangue composing it. In this paper, some coal gangue was selected from the mines, and was crushed and classified into three types in terms of particle diameters: 20–40 mm, 10–20 mm, and 0–10 mm. Coal gangue was crushed on site by mining jaw crusher (C6x). In this study, magnesia cement was used as a binder, which contained 75%–85% magnesium oxide (MgO). Magnesia cement (TR5745-001-92534212-2014) is produced by mixing magnesium oxide pre-calcined to 800 °C with a 30% aqueous solution of $MgCl_2$ (two weight parts of MgO per one weight part of anhydrous $MgCl_2$). Coal gangue (gangue extracted from roof, floor, and interlayer during mining and gangue picked out during coal washing) was used as aggregate. Coal gangue (the gangue extracted from the roof, floor, and interlayer during mining and the gangue picked out during coal washing) was used as aggregate. Its main components are Al_2O_3 and SiO_2. In addition, it also contains varying amounts of Fe_2O_3, Cao, MgO, Na_2O, K_2O, P_2O_5, SO_3, and trace rare elements (gallium, vanadium, titanium, cobalt). The material ratio of wet shotcrete is cement (P·o 42.5 ordinary portland cement). The mass ratio of sand (medium and coarse sand, fineness modulus greater than 2.5) and crushed gangue (above particle size) was 1:1.5:2.25, the water cement ratio was 0.4~0.5, and the processing size of the backfill material was 750 mm × 500 mm × 35 mm. We reprocessed woven bags of different sizes such as 750 mm × 500 mm × 30 mm, 700 mm × 500 mm × 35 mm, and 700 mm × 500 mm × 35 mm, filled in the woven bags separately with crushed coal gangues whose particles were in the above three size fractions, and then used the compactor to compact the filling. By studying the stress and strain relationship of these gangue bags, the optimum size of the gangue bags was determined.

Since the lateral displacement needs to be constrained for the coal gangue packing body in gob-side entry retaining, and at a macro scale, the axial stress–strain relationship is not affected by the presence or absence of woven bags, and a macro-scale pressure cell with fixed lateral constraints was designed. According to the actual mining situation, particles of coal gangue constituting the flexible material packing body in three different size fractions (0–10 mm, 10–20 mm, and 20–40 mm) were selected to perform the experiment. By examining the mechanical properties of particles in different size fractions, reasonable decisions in terms of size fractions for coal gangue backfilling in gob-side entry retaining were made.

2.3. Test of the Uniaxial Compression

We added 110 g of water, 2.4 g of superplasticizer (cement), and 300 g of cement into the mixing tank, and fully mixed until a completely uniform slurry appeared; then, 18 g accelerator (cement) was added and mixed for 5 s. Next, we tested the setting time with the Vicat instrument, and recorded the initial setting time and final setting time before repeating the measurement of the setting time; the error of the two measurements should not exceed 5″, and the average value of the two measurements was taken as the setting time. The above steps were repeated to measure the setting time of different water–cement ratios. It was found that the greater the water cement ratio is, the longer the initial and final setting time is. The initial and final setting time of the 0.45 water–cement ratio was about 1/2 of that of the 0.50 water–cement ratio; When the water–cement ratio was less than 0.4, the setting time was too fast, and was prone to pipe plugging and other problems, affecting the construction; when the water cement ratio was greater than 0.5, the setting time slowed down significantly, which makes it difficult for the thickness of the spray layer to exceed 5 cm, and the wet shotcrete was difficult to bond to the surrounding rock. The spray layer is easy to crack and peel off, which cannot meet the support requirements. The best range of water–cement ratio is 0.4~0.5. The best water cement ratio can ensure that the wet shotcrete can quickly set to the surface of the surrounding rock, and the early and long-term strength of the concrete can be significantly improved. By testing and adding alkali free liquid accelerator in wet shotcrete, the initial setting time and final setting time were significantly shortened. The initial setting time was 3′10″, which can effectively prevent slag from falling from the shotcrete layer. The final setting time was 8′40″, which can quickly improve the support strength. Wet shotcrete was prepared according to the water–cement ratio of 0.45, cement: sand: stone 1:1.5:2.25, 6% accelerator and 1% water reducer; dry shotcrete was prepared according to the water cement ratio of 0.5, cement: sand: stone 1:2:2, 3.5% accelerator, and was injected into the 300 mm × 300 mm × 300 mm cube mold, and was stirred evenly with a vibrating table to prevent bubbles. It was cured according to GB/T50081-2002 [35], and immediately put into a standard curing room with a temperature of 20 ± 2 °C and a relative humidity of more than 95%. The surface of the test piece should be kept wet and cured to the required age.

An overall digital closed-loop control, equal-rate displacement control, and constant test force control in the test process were realized by adopting the DOLI EDC controller and the MOOG direct-acting proportional servo valve and combining them with a computer for a control measurement system. The bagged gangue compression adopts a trolley-type plate structure; the plate size was 750 mm × 500 mm, and the thickness was 35 mm. During the experiment, the bagged gangue was placed in the center of the pressure plate, and the load was applied slowly and evenly; when the pressure head is compressed under the uniaxial press, the load and the corresponding strain value were recorded. The experiment ended when the load reached 5.5 MPa, and the test piece was replaced, as shown in Figure 3.

The uniaxial compression test for macro scale flexible material (coal gangue) packing body was performed using a conventional single-axis press. The dimensions of the macro-scale pressure cell were 300 mm × 300 mm × 300 mm, the maximum pressure was 5.5 MPa, the loading rate was 2 mm/min, and the measurement range of the load transducer was 500 kN. Though there was a load transducer in the laboratory whose measurement range is 2500 kN, for a test piece with cross section of 300 mm × 300 mm, the load transducer with a measurement range 500 kN was the most appropriate and ensured high-precision results. The specific experimental site is shown in Figure 4.
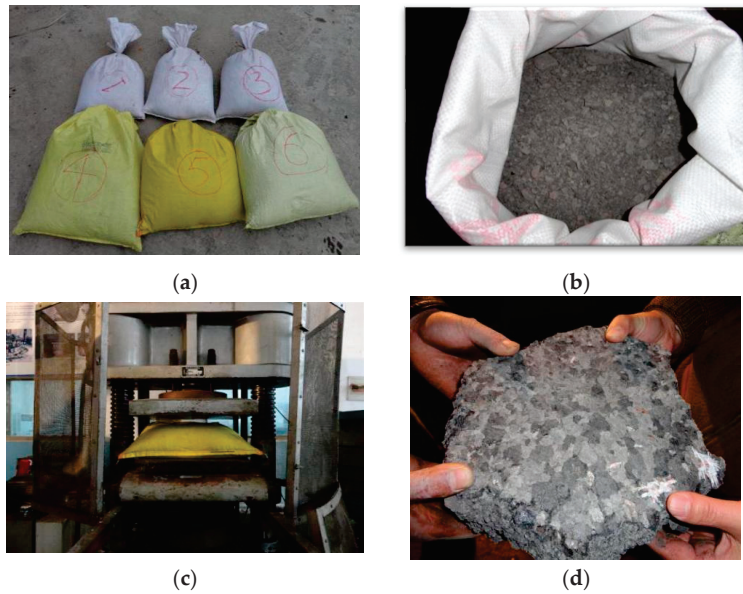
Figure 3. Field diagram of the stress-and-strain experiment of packed gangue; (**a**) coal gangue woven bags of different size; (**b**) particles of crushed coal gangue for experiment; (**c**) CSS-YAW3000 electronic universal testing machine; (**d**) compacted coal gangue block.

Figure 4. Large-scale flexible filling body field experiment diagram.

2.4. Flexural Strength and Load-Deflection Test

Bending strength: the ultimate breaking stress of the material per unit area when it bears the bending moment (or the ultimate stress when the material is damaged by the action of bending load). Load: external forces and other factors that cause internal forces and deformations of structures. Deflection: the linear displacement of the centroid of a cross section perpendicular to the axis during bending deformation.

(1)　Purpose of the test

The flexural strength of large-scale concrete specimens after curing for 1 day, 7 days, and 28 days was tested. The relationships between "load-deflection", "flexural strength–thickness", and "maximum failure load–thickness" were determined.

(2)   Test raw materials

The raw materials of cement, stone, sand, and admixture were provided by Tongxin Coal Mine and transported back to the school for specimen production, as shown in Figure 5.

Figure 5. TZS-type digital flexural testing machine.

(3)   Specimen preparation

According to the requirements of the test content, dry and wet concrete beams were made, as shown in Figure 6. The sizes of the flexural strength test specimens (unit mm) were $200 \times 40 \times 20$, $400 \times 80 \times 40$, $600 \times 100 \times 60$, $800 \times 120 \times 80$, $1000 \times 140 \times 100$, and $1200 \times 160 \times 120$.

Figure 6. The flexural strength specimens.

Matters needing attention:

a. Before making specimens, the test mold should be cleaned and coated with a layer of oil on the inner wall.

b. when loading the mold, layered loading, the thickness of the first layer of loading should be 20~40 mm, the thickness of the second loading should be 40~80 mm, and when loading the vibrating bar, the concrete ramming should be smoothed with a spatula.

c. Finally, the standard maintenance is adopted: after a day of mold removal, the mold is immediately put into a curing room with a temperature of $20 \pm 2\ °C$ and relative humidity above $95\ °C$ for maintenance.

(4)   Test device and test process

A TZS digital display flexural testing machine (as shown in Figure 6) was used to test the flexural strength of dry and wet shotcrete. A three-point loading device was used to test load-deflection. The resistance strain gauge was bonded to the center position at the bottom of the specimen to test the relationship between mid-span deflection and load. The testing process was as follows:

a. After the large-scale specimen is taken out from the curing room, its surface was wiped clean, and then the test was carried out;

b. We placed the specimen on the test device for loading. The installation size deviation of the device specimen shall not be greater than 1 mm. The bearing surface of the specimen shall be the side of the specimen when it is formed. The contact surface between bearing and bearing surface and cylinder should be smooth and uniform, otherwise it should be flat.

c. The applied load should be kept uniform and continuous, 0.08–0.10 Mpa per second; when the specimen was close to failure and began to undergo sharp deformation, the loading was immediately stopped until the specimen was completely destroyed. Then the failure load and deflection were recorded.
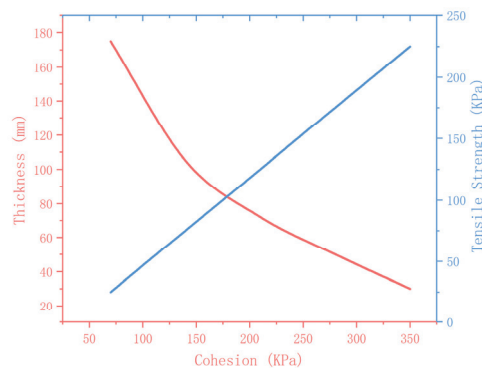
3. Results and Discussion

3.1. Analysis of Influence of Cohesion of Coal Gangue Woven Bags

The average cohesion of the gangue bags can be obtained by converting Formula (4):

$$c = \frac{T}{\sqrt{K_p}} \left(\frac{K_p}{H} - \frac{1}{B} \right) \tag{4}$$

The relationship between the thickness of the gangue bag and the tensile strength and cohesion is shown in Figure 7.


Figure 7. Analysis of the influence of cohesive force on vermiculite woven bags.

The experimental results showed that the tensile strength and the cohesion of packed coal gangue had a linear relationship; the thickness and the cohesion were in hyperbolic distribution in the first interval. Less thickness of the packed coal gangue meant a greater cohesion. Considering the actual production schedule of coal mine, the coal gangue woven bags should not be too small or too thin, and meanwhile the workers' labor intensity also required that the coal gangue woven bags not be too large. Coal gangue woven bags of 450 mm, 450 mm, and 150 mm in length, width, and height, respectively, were the most appropriate.

*3.2. Analysis for the Stress-and-Strain Relationship of Flexible Material (Coal Gangue)
Packing Body*

Due to the limitations of laboratory equipment and test conditions and some idealized factors in theoretical study, it is impossible to conduct a holistic study based on actual mining height, nor to conduct quantitative and qualitative analysis of the support resistance provided by the backfilling wall of flexible material (coal gangue). However, coal gangues in the flexible material packing body are under fixed lateral constraints whether they are packaged or not. Coal gangues packing could ensure a better uniformity and effectiveness of the lateral constraint within the flexible material packing body. The resulting axial stress–strain relationship for particles in 0–10 mm, 10–20 mmm and 20–40 mm size fractions is shown in Figure 8.
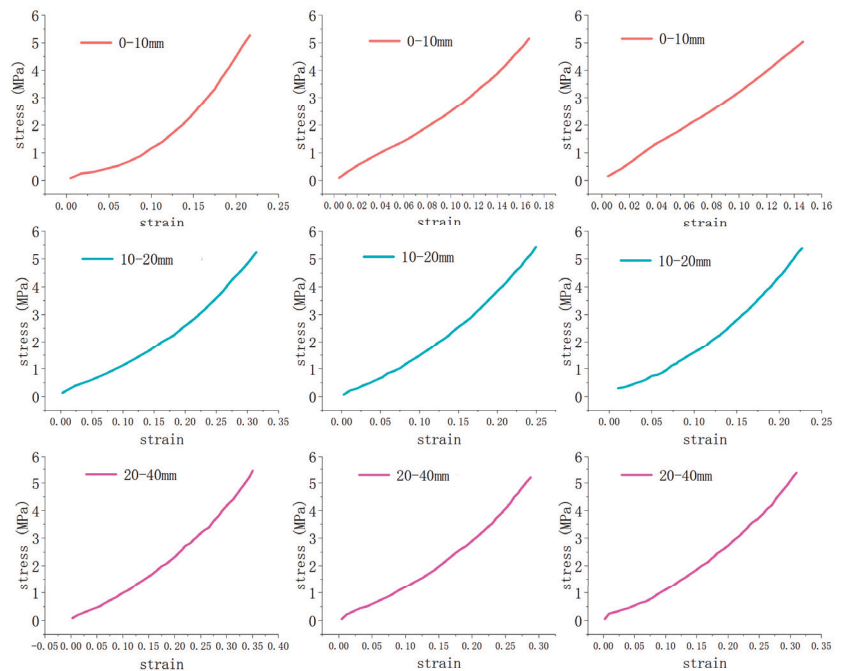

Figure 8. Stress-strain curves of flexible material backfilling body.

Figure 8 shows that within the range of 0–10 mm, when the stress reached 5 MPa, the strain was 0.22, 0.17, and 0.15, respectively, and the stress–strain ratio was 22.73, 29.41, and 33.33; within the range of 10–20 mm, the stress reached 5 MPa. When the strain was 0.31, 0.25 and 0.23, respectively, the stress–strain ratio was 16.13, 20, and 21.74; in the 20–30 mm grain size range, when the stress reached 5 MPa, the strain was 0.35, 0.28 and 0.32, respectively, and the stress–strain ratio was 14.29, 17.86, and 15.63. The difference in stress–strain ratios in each particle size range was small, indicating the reliability of the experimental data. At the same time, the average stress–strain ratios of 0–10 mm, 10–20 mm, and 20–40 mm grain grades were 28.49, 19.29, and 15.92, respectively, which shows that the load-bearing effect in the three particle size ranges showed a decreasing law. The smaller the coal gangue particle diameter is, the smaller the bulking factor is. The bearing capacity of coal gangue particles both in 0–10 mm size fractions when the strain was 0.2 and in 10–20 mm size fractions when the strain was 0.27 were all over 5 Mpa, which can meet the supporting force requirement for backfilling walls in gob-side entry retaining. Based on the considerations of those factors such as the crusher equipment conditions and the labor intensity, etc., and field experience, the particle diameter of the packed gangue

should be less than 20 mm to meet the requirements of backfilling wall deformation and support resistance.

3.3. The Strain Characteristics Analysis of Macro-Scale Pressure Cell

Strain gauges were installed on the front and back of the pressure cell to analyze the lateral strain and axial strain of the pressure cell under pressure. The specific results are shown in Figures 9 and 10.
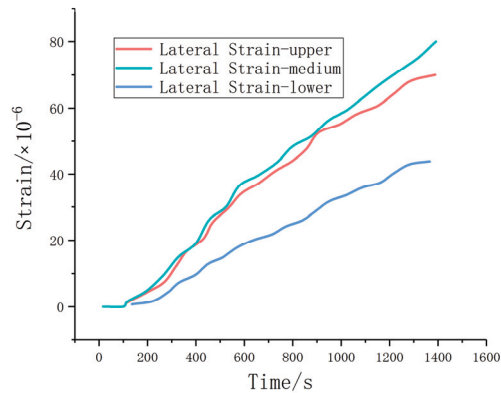
Figure 9. Lateral strain–time curve of press cell under stress.
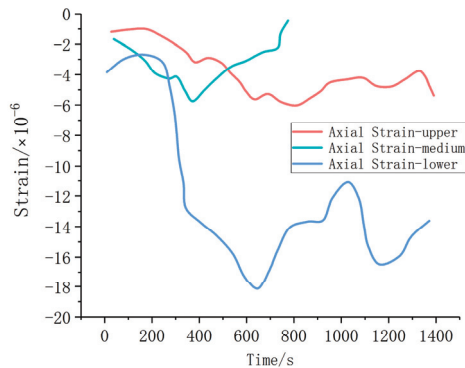
Figure 10. Axial strain–time curve of press cell under stress.

Results analysis showed that the lateral deformation of the pressure cell was relatively uniform. The lateral strain showed an almost linear increase over time. The lateral strain in the upper-middle part was higher than in the lower part, which was mainly caused by the top-to-bottom pressurization. The lateral strain in the middle part was higher than in the upper part, which was mainly due to the larger amount of compression of the coal gangue when the pressure plate was pressed near the middle of the pressure cell, leaving a hollowed upper part. The effect of the axial deformation curve was not ideal, and there was no regular deformation, which indicated that the frictional force between the axial flexible material (coal gangue) packing body and the press cell was uneven, resulting from the irregular particle sizes; the lateral strain was less than a ten thousandth, indicating that the stiffness of pressure cell could meet the requirements.

3.4. "Flexibility–Thickness" Relationship

Reasonable spray thickness should give full play to the characteristics of its flexible support, that is, the surrounding rock is required to have a certain plastic displacement

to reduce the surrounding rock pressure. Improve the folding resistance of spray layer; ensure that the spray layer ADAPTS to the change of surrounding rock; ensure that the spray layer itself is not damaged; and maximize material savings. According to the flexural strength test, the relationship between flexural strength–thickness and maximum failure load–thickness is analyzed by the relationship between flexural strength–thickness and maximum failure load–thickness.

According to the flexural strength tests of concrete at different scales, we drew the "flexural strength–thickness" relationship curve as shown in Figure 11.
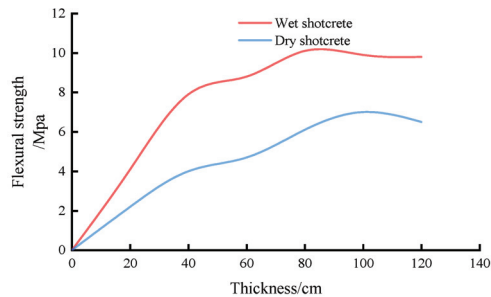
Figure 11. Relationship curve of flexural strength and thickness.

It can be seen from the figure above that the flexural strength of both dry and wet shotcrete increased with the increase of thickness. When the thickness of dry shotcrete reached 100 mm, its flexural strength hardly increased. Wet shotcrete thickness reached 60 mm, and its flexural strength increase was very slow, and the thickness of the wet shotcrete reached 60 mm flexural strength and dry shotcrete thickness was 100 mm when the flexural strength was almost equal, so when the roadway support is against the folding strength requirement phase at the same time, adopting the wet shotcrete support can reduce the spray layer thickness, maintaining the flexibility of the spraying layer and also saving materials.

3.5. "Maximum Failure Load–Thickness" Relationship

According to the flexural strength tests of concrete at different scales, the "maximum failure load–thickness" relationship curve was drawn as shown in Figure 12.
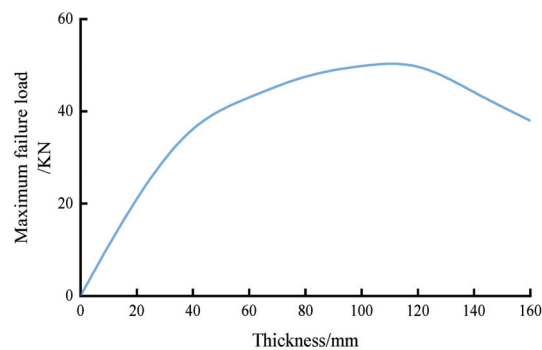
Figure 12. Relationship curve of maximum failure load and thickness.

According to the figure above, when the thickness was less than 80 mm, the maximum failure load increased with the increase of thickness. When the thickness was between 80 mm and 100 mm, the maximum failure load almost never increased and reached the maximum. When the thickness was greater than 120 mm, the maximum failure load

decreased with the thickness increasing. As the thickness changed, the support capacity of spray layer also changed, which can be divided into three stages.

(1) Flexible stage

When the wet shotcrete thickness was less than 80 mm, the shotcrete thickness was relatively small and in a flexible stage. Before the initial hardening of spray layer, it was a flexible support, which can adapt to the deformation of surrounding rock. After hardening, the strength increased, and the rigid support ability could effectively limit the deformation of the surrounding rock.

When the spray layer was very thin, the support capacity was low, causing shear damage, and the spray layer was easy to crack and peel off. Spray layer thickness was calculated according to "shear type" failure, as shown in Figures 13 and 14.
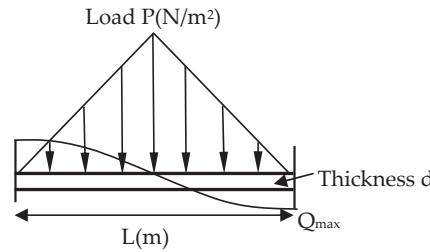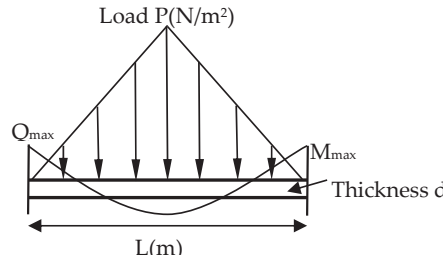

Figure 13. Reple shear failure.

Figure 14. Bending failure resistance.

In order to prevent damage to the spray layer, the spray layer thickness can meet the following conditions:

$$d \geq \frac{3pl^2}{8b[\tau]} \tag{5}$$

where, d is the spray layer thickness; p is load; l is the size of dangerous rock; b is the size of dangerous rock along the longitudinal direction of roadway; $[\tau]$ is the allowable shear strength; $[\tau] = \tau/K$, $\tau = 0.2f_c$, τ is the shear strength of shotcrete; f_c is the uniaxial compressive strength of shotcrete; K is the safety factor.

(2) Maximum supporting capacity stage

When the thickness of wet shotcrete was 80–120 mm, the support capacity reached the maximum and transitioned from the flexible state to the rigid state, and the failure form gradually changed from shear failure to bending failure. At this stage, although the support capacity was the largest, and the flexibility was not enough for the easily deformed surrounding rock, which is not conducive to roadway support.

(3) Rigid stage

When the wet shotcrete thickness was greater than 120 mm, the shotcrete thickness was relatively large and in a rigid state. The greater the stiffness of spray layer, the more

difficult to adapt to the deformation of surrounding rock, and the load would increase, resulting in bending failure. As shown in Figure 14, it can be concluded that no bending failure occurred in the spray layer, and its thickness met the following conditions:

$$d \geq \sqrt{\frac{5pl^3}{16b[\sigma]}} \qquad (6)$$

where, $[\sigma]$ is the allowable flexural tensile strength, $[\sigma] = \sigma_1/K$, $\sigma_1 = 0.15f_c$, σ_1 is the flexural tensile strength of shotcrete.

This indicates that the thickness of spray layer must be controlled when flexible support is adopted for large section broken coal roadway. The thickness of the spray layer with good flexibility and sufficient support force should be controlled at about 80 mm.

4. Conclusions

In this paper, through the stress–strain experimental study of coal gangue particles with different particle sizes, the crushing and strict particle size classification of gangue were optimized, and the problem of uneven deformation caused by gangue as a filling wall was solved.

(1) The experimental results showed that the particle size of 0–20 mm had large support resistance and resistance-increasing speed, which can meet the technical requirements of retaining roadways along the goaf; the experimental results showed that the bagged gangue improved the support resistance of the whole filling wall and the uniformity of internal support force

(2) According to the "load deflection" test analysis, wet shotcrete can withstand greater deformation under the same load conditions; even when the concrete cracked and the deflection was very large, it was still very gentle and showed good toughness.

(3) Through the analysis of the relationship between "flexural strength thickness" and "maximum failure load thickness", the optimal spray layer thickness was finally determined to be controlled at about 80 mm.

Author Contributions: Formulation or evolution of overarching research goals, D.P.; Preparation, creation and presentation of the published work, Y.Z.; Conducting a research and investigation process, X.N.; Development or design of methodology; creation of models, K.H.; Acquisition of the financial support for the project, C.L.; Provision of study materials, reagents, laboratory samples, Z.C. All authors have read and agreed to the published version of the manuscript.

Data Availability Statement: The data used for conducting classifications are available from the corresponding author authors upon request.

References

1. Gong, P.; Ma, Z.; Ni, X.; Zhang, R.R. An experimental investigation on the mechanical properties of gangue concrete as a roadside support body material for backfilling gob-side entry retaining. *Adv. Mater. Sci. Eng.* **2018**, *2018*, 1326053. [CrossRef]
2. Gong, P.; Ma, Z.; Zhang, R.R.; Ni, X.; Liu, F.; Huang, Z. Surrounding rock deformation mechanism and control technology for gob-side entry retaining with fully mechanized gangue backfilling mining: A case study. *Shock. Vib.* **2017**, *2017*, 6085941. [CrossRef]
3. Zhu, Z.; He, M.C.; Wang, X.C.; Yuan, H.P. Mechanical Model and Control Technology of Roadside Gangues in Gob-Side Entry Retaining by Roof Cutting. *Geotech. Geol. Eng. Int. J.* **2020**, *38*, 849–860. [CrossRef]
4. Zhang, Y.Q.; Tang, J.X.; Xiao, D.Q.; Sun, L.L.; Zhang, W.Z. Spontaneous caving and gob-side entry retaining of thin seam with large inclined angle. *Int. J. Min. Sci. Technol.* **2014**, *24*, 441–445. [CrossRef]

5. Đurđevac Ignjatović, L.; Krstić, V.; Radonjanin, V.; Jovanović, V.; Malešev, M.; Ignjatović, D.; Đurđevac, V. Application of Cement Paste in Mining Works, Environmental Protection, and the Sustainable Development Goals in the Mining Industry. *Sustainability* **2022**, *14*, 7902. [CrossRef]

6. Khairutdinov, A.; Ubysz, A.; Adigamov, A. The concept of geotechnology with a backfill is the path of integrated development of the subsoil. *IOP Conf. Ser. Earth Environ. Sci.* **2021**, *684*, 012007. [CrossRef]

7. Kongar-Syuryun, C.H.; Ivannikov, A.; Khayrutdinov, A.; Tyulyaeva, Y. Geotechnology using composite materials from man-made waste is a paradigm of sustainable development. *Mater. Today Proc.* **2021**, *38*, 2078–2082. [CrossRef]

8. Kowalik, T.; Ubysz, A. Waste basalt fibers as an alternative component of fiberconcrete. *Mater. Today Proc.* **2021**, *38*, 2055–2058. [CrossRef]

9. Kim, J.; Grabiec, A.M.; Ubysz, A. An Experimental Study on Structural Concrete Containing Recycled Aggregates and Powder from Construction and Demolition Waste. *Materials* **2022**, *15*, 2458. [CrossRef]

10. Ermolovich, E.A.; Ivannikov, A.L.; Khayrutdinov, M.M.; Kongar-Syuryun, C.B.; Tyulyaeva, Y.S. Creation of a Nanomodified Backfill Based on the Waste from Enrichment of Water-Soluble Ores. *Materials* **2022**, *15*, 3689. [CrossRef] [PubMed]

11. Grabinsky, M.; Jafari, M.; Pan, A. Cemented Paste Backfill (CPB) Material Properties for Undercut Analysis. *Mining* **2022**, *2*, 103–122. [CrossRef]

12. Rybak, J.; Gorbatyuk, S.M.; Bujanovna-Syuryun, K.C.; Khairutdinov, A.M.; Tyulyaeva, Y.S.; Makarov, P.S. Utilization of Mineral Waste: A Method for Expanding the Mineral Resource Base of a Mining and Smelting Company. *Metallurgist* **2021**, *64*, 851–861. [CrossRef]

13. Nujaim, M.; Belem, T.; Giraud, A. Experimental Tests on a Small-Scale Model of a Mine Stope to Study the Behavior of Waste Rock Barricades during Backfilling. *Minerals* **2020**, *10*, 941. [CrossRef]

14. Rybak, J.; Adigamov, A.; Kongar-Syuryun, C.; Khayrutdinov, M.; Tyulyaeva, Y. Renewable-Resource Technologies in Mining and Metallurgical Enterprises Providing Environmental Safety. *Minerals* **2021**, *11*, 1145. [CrossRef]

15. Yue, X.; Tu, M.; Li, Y.; Chang, G.; Li, C. Stability and Cementation of the Surrounding Rock in Roof-Cutting and Pressure-Relief Entry under Mining Influence. *Energies* **2022**, *15*, 951. [CrossRef]

16. Du, K.; Yang, C.Z.; Su, R.; Tao, M.; Wang, S.F. Failure properties of cubic granite, marble, and sandstone specimens under true triaxial stress. *Int. J. Rock Mech. Min. Sci.* **2020**, *130*, 104309. [CrossRef]

17. Du, K.; Li, X.F.; Tao, M.; Wang, S.F. Experimental study on acoustic emission (AE) characteristics and crack classification during rock fracture in several basic lab tests. *Int. J. Rock Mech. Min. Sci.* **2020**, *133*, 104411. [CrossRef]

18. Sheng, L.I.; Jun-Wen, L.I.; Fan, C.J.; Luo, M.K.; Han, Y.L. Roof subsidence laws and control technology for gob-side entry retaining in fully-mechanized top-coal caving face. *J. China Coal Soc.* **2015**, *40*, 1989–1994.

19. Zhang, X.F. Research on stability of gateway retained along goaf in thin seam with hard roof and hard coal. *Coal Sci. Technol.* **2014**, *42*, 22–25.

20. He, K.; Chang, J.; Pang, D.; Sun, B.; Yin, Z.; Li, D. Iterative algorithm for the conformal mapping function from the exterior of a roadway to the interior of a unit circle. *Arch. Appl. Mech.* **2022**, *92*, 971–991. [CrossRef]

21. Li, M.; Zhang, J.; Li, A.; Zhou, N. Reutilisation of coal gangue and fly ash as underground backfill materials for surface subsidence control. *J. Clean. Prod.* **2020**, *254*, 120113. [CrossRef]

22. Shi, X.; Jing, H.; Ning, J.; Zhao, Z.; Zhu, J. Stability Control of Gob-Side Entry Retaining in Fully Mechanized Caving Face Based on a Compatible Deformation Model. *CMES-Comput. Modeling Eng. Sci.* **2020**, *124*, 315–343. [CrossRef]

23. Liu, X.S.; Ning, J.G.; Tan, Y.L.; Xu, Q.; Fan, D.Y. Coordinated supporting method of gob-side entry retaining in coal mines and a case study with hard roof. *Geomech. Eng.* **2018**, *15*, 1173–1182. [CrossRef]

24. Du, K.; Li, X.F.; Yang, C.Z.; Zhou, J.; Chen, S.J.; Manoj, K. Experimental investigations on mechanical performance of rocks under fatigue loads and biaxial confinements. *J. Cent. South Univ.* **2020**, *27*, 2985–2998. [CrossRef]

25. Du, K.; Li, X.F.; Su, R.; Tao, M.; Lv, S.Z.; Luo, J.; Zhou, J. Shape ratio effects on the mechanical characteristics of rectangular prism rocks and isolated pillars under uniaxial compression. *Int. J. Min. Sci. Technol.* **2022**, *32*, 347–362. [CrossRef]

26. Kong, D.; Li, Q.; Wu, G.; Song, G. Characteristics and control technology of face-end roof leaks subjected to repeated mining in close-distance coal seams. *Bull. Eng. Geol. Environ.* **2021**, *80*, 8363–8383. [CrossRef]

27. Panchal, S.; Deb, D.; Sreenivas, T. Mill tailings based composites as paste backfill in mines of U-bearing dolomitic limestone ore. *J. Rock Mech. Geotech. Eng.* **2018**, *10*, 310–322. [CrossRef]

28. Zheng, J.; Zhu, Y.; Zhao, Z. Utilization of limestone powder and water-reducing admixture in cemented paste backfill of coarse copper mine tailings. *Constr. Build. Mater.* **2016**, *124*, 31–36. [CrossRef]

29. Cao, W.; Yi, W.; Peng, J.; Li, J.; Yin, S. Recycling of phosphogypsum to prepare gypsum plaster: Effect of calcination temperature. *J. Build. Eng.* **2022**, *45*, 103511. [CrossRef]

30. Moghadam, M.J.; Ajalloeian, R.; Hajiannia, A. Preparation and application of alkali-activated materials based on waste glass and coal gangue: A review. *Constr. Build. Mater.* **2019**, *221*, 84–98. [CrossRef]

31. Jarzyna, A.; Bąbel, M.; Ługowski, D.; Vladi, F. Petrographic Record and Conditions of Expansive Hydration of Anhydrite in the Recent Weathering Zone at the Abandoned Dingwall Gypsum Quarry, Nova Scotia, Canada. *Minerals* **2022**, *12*, 58. [CrossRef]

32. Rybak, J.; Kongar-Syuryun, C.; Tyulyaeva, Y.; Khayrutdinov, A.M. Creation of Backfill Materials Based on Industrial Waste. *Minerals* **2021**, *11*, 739. [CrossRef]

33. Golik, V.I.; Razorenov, Y.; Puzin, V.S.; Stas', G.V. Differentiated Assessment of Stability of Exposed Rock Surfaces in Sublevel Stoping with Backfill. *J. Min. Sci.* **2021**, *57*, 787–794. [CrossRef]

34. Liu, L. Technology of Gob—Side Entry Retaining Based on Flexible Filling Wall with Bagged Gangue. *Coal Eng.* **2015**, *47*, 47–49. [CrossRef]

35. *GB/T50081-2002*; Standard for Test Methods of Mechanical Properties of Ordinary Concrete [S]. 2003. Available online: https://www.codeofchina.com/standard/GBT50081-2002.html (accessed on 10 January 2003).

Utilization Methods and Practice of Abandoned Mines and Related Rock Mechanics under the Ecological and Double Carbon Strategy in China—A Comprehensive Review

Kun Du [1], Junjie Xie [1], Manoj Khandelwal [2] and Jian Zhou [1,*]

[1] School of Resource and Safety Engineering, Central South University, Changsha 410083, China
[2] Institute of Innovation, Science and Sustainability, Federation University Australia, Ballarat, VIC 3350, Australia
* Correspondence: j.zhou@csu.edu.cn

Abstract: Governance of abandoned mines has become a pressing issue for China. The utilization of abandoned mines is a technology that can solve the problem of governance and recreate the value of mines, which is in line with the current strategic goals of ecological protection and double carbon in China. In this paper, the various utilization models and the advances in rock mechanics of abandoned mines across the globe are summarized and reviewed. The utilization models of abandoned mines can be categorized into four aspects: Energy storage, Waste treatment, Ecological restoration, and carbon dioxide (CO_2) sequestration. There are a number of applications and uses of abandoned mines, such as pumped storage, compressed air storage, salt cavern gas/oil storage construction, carbon dioxide storage and utilization, radioactive waste disposal and treatment, and tourism development. Various progress practices of abandoned mines are discussed in detail with emphasis on the national conditions of China. The basic rock mechanics problems and advances involved in the construction of the facilities related to the utilization of abandoned mines are discussed and evaluated. The establishment of relevant research and experimental platforms will contribute to the sustainable development of China's mining industry and the improvement of clean technologies.

Keywords: double carbon; abandoned mines; resource development and utilization; rock mechanics

1. Introduction

Environmental problems, such as melting glaciers, sea-level rise, and increased climate extremes caused by the greenhouse effect and animal extinction due to ecological destructions are becoming increasingly serious day by day. Many countries have pledged to do their part to combat climate change. It would be an impressive display of global solidarity if global greenhouse gas emissions fall sharply over the next decade. As one of the signatories of the 2016 Paris Agreement, China has put forward the double carbon goal strategy, i.e., reaching the carbon peak in 2030 and carbon neutrality in 2060. In addition, China has formulated its strictest ecological policy in history and fulfilled "the green mountains and waters being the golden and silver mountains" strategy. The construction, development, and progression of greener mines have become an important component of ecological and environmental protection in China. As one of the developing countries and a major consumer of energy, China's demand for energy has been continuously growing, and the country has surpassed the United States in terms of total annual greenhouse gas emissions and currently ranks first in the world. Figure 1 shows cumulative GHG emissions and per capita GHG emissions of the top 10 countries (data from [1,2]).

To reduce carbon emissions, China's "14th Five-Year Plan" and "Vision 2035" propose to vigorously develop renewable energy and resource-saving technologies. In recent years, China has seen rapid development of renewable energy, led by wind power and photovoltaic, with a growing share of power generation. It is planned to reach a total

installed capacity of over 1.2 billion kilowatts of wind and solar power in 2030, with the proportion of non-fossil energy consumption reaching around 25% [3]. However, there are many constraints in the development of renewable energy, for example, the difficulty and costs of hydropower construction are increasing, wind power and photovoltaics cannot supply electricity constantly, and nuclear power produces a large amount of radioactive waste every year [4–7].
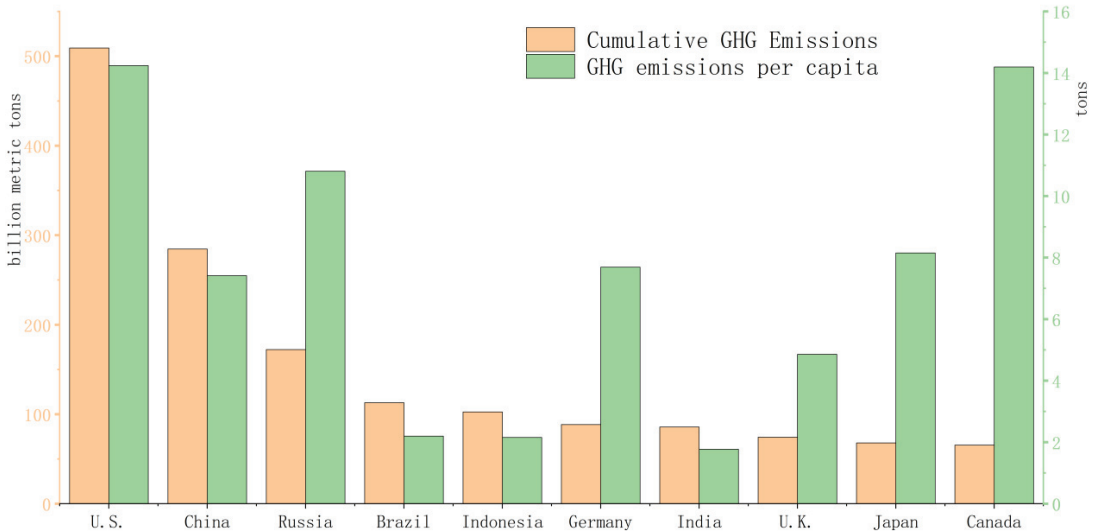
Figure 1. Top 10 countries with cumulative GHG emissions from fossil fuels, land use, and forestry from 1850 to 2021 and GHG emissions (CO_2 emissions from the burning of fossil fuels for energy and cement production) per capita in these countries in 2020.

In the mining industry, mining companies around the world are aiming to minimize carbon emissions over the next 10 to 15 years, with the goal of reaching net-zero emissions by 2050. At the same time, China has continuously increased mine supervision and eliminated outdated production capacity. The number of mines has decreased by 80% in the past 20 years, and there are at least 20,000 abandoned mines [8]. However, abandoned mines do not indicate that they are really 'abandoned'. On the contrary, the resources they contain, such as space, tourism, mine water, and coal bed methane, have a significant value-in-use. The research into the use of abandoned mines around the world today focuses on four main areas: Energy storage, ecological development, permanent sequestration, and CO_2 utilization (Figure 2). In addition, abandoned mines can be used to build special places, such as deep ground laboratories, confidential centers, medical clinics, and arsenals, etc. A 1500-m deep abandoned gold mine in the United States was developed to establish a deep ground laboratory for the study of particle physics. Ukraine used an abandoned rock salt mine to open a hospital specializing in the treatment of asthma patients [9].
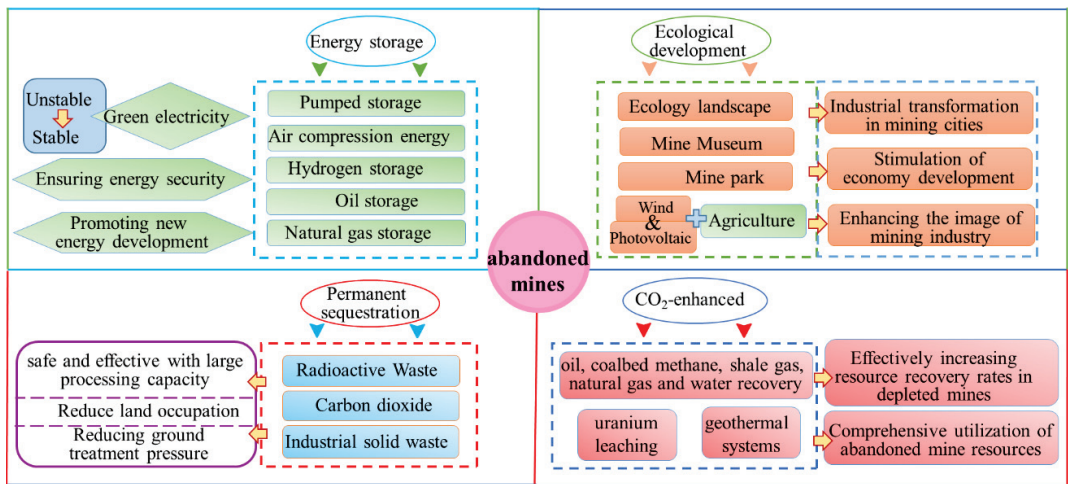
Figure 2. Abandoned mine utilization mode.

China's ecological civilization cannot be separated from the remediation of abandoned mines. The rational use of abandoned mines from the perspective of resource reuse can create economic values, improve the energy structure, and help in achieving the "double carbon" goal. Therefore, in this paper, utilization of abandoned mines in China and abroad has been discussed incorporating the basic rock mechanics challenges and issues.

This paper summarizes and reviews the various utilization models of abandoned mines and the progress of rock engineering around the world. Section 2 describes specific abandoned mine utilization methods and the strengths and weaknesses of China in terms of resource potential, current development status, and the extent of development in other countries. Section 3 describes the basic rock mechanics involved in abandoned mine utilization and emphasizes the importance of coupling studies for the long-term stability of rock masses. Section 4 provides a conclusion and prospect of abandoned mine utilization technology and development in China. Notably, the review not only includes mines that have been abandoned due to safety, backward technology, poor management, etc., but also includes resource-exhausted mines and hard-to-use resource storage areas, such as unmineable coal seams.

## 2. Utilization Model of Abandoned Mines

This section discusses the underground energy storage, radioactive waste storage, CO_2 sequestration, and ecological development of abandoned mines in the context of China.

2.1. Using Abandoned Mines to Build Underground Energy Storage

Large-scale energy storage is a solution to cope with the unstable power supply of renewable energy sources, such as photovoltaic and wind power and to guarantee the strategic needs of the country. The huge space contained in the abandoned mines can provide a guarantee for large-scale underground energy storage. Underground energy storage can be categorized into underground water storage, gas storage, and oil storage according to the energy medium.

Abandoned underground mines with huge space are the best places to build energy storage reservoirs. China is fortunate to have a large number of underground mines. The total amount of underground space available in China's coal mines is about 4×10^8 m^3, and the existing salt cavern space is 1.3×10^8 m^3. The available underground space has a good growth momentum and great potential for utilization with the elimination of backward mines and the continuous exploitation of rock salt mines [10,11]. Figure 3

shows the characteristics of subsurface space and rock salt distribution in China (the data of underground space from [10] and rock salt data comes from the official websites of Chinese county and city governments).
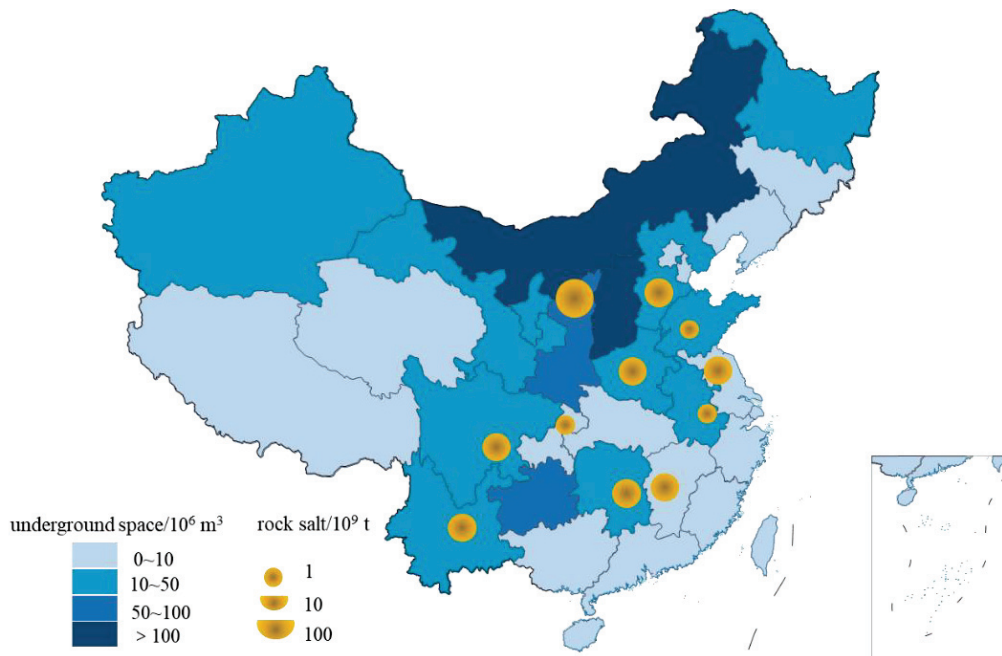

Figure 3. Estimates of underground space as of 2020 and distribution of proven rock salt reserves.

2.1.1. Underground Water Reservoir

The construction of underground water reservoirs in abandoned mines can be summarized in three models, such as storage and filtration of mine water, geothermal utilization model, and pumped hydroelectric storage (PHS) plants system. It has been found that high-intensity mining of coal causes serious damage to water reservoirs and resources. A study performed by Gu Dazhao et al. [12], showed that currently, China produces about 6.88×10^9 m^3 of coal mine water per year, with an average utilization rate of about 35% with a huge potential for upgrading this in the near future. Considering the climatic conditions in northwestern China, the mine water storage filters are capable of providing water for industrial and mining use and agricultural irrigation in the vicinity. By the end of 2020, China had more than 17 underground coal mine filter storage reservoirs built or under construction in Shaanxi, Shanxi and Inner Mongolia provinces alone, with a total storage capacity of 26,486,000 m^3 [13].

Low- and medium-temperature geothermal energy is widely distributed in China. The geothermal resources shallower than 200 m are equivalent to 9.5 billion tons of standard coal, and the geothermal energy from 200 to 3000 m is 12.5 billion tons of standard coal [14]. The geothermal utilization model of abandoned mines is usually a closed-loop or open-loop structure formed by injection wells (cold water injection), upper reservoirs (cold water), lower reservoirs (hot water), production wells (hot water extraction), and energy conversion plants. Figure 4 shows the geothermal energy utilization model of abandoned mines. Underground reservoirs act as water and energy storage in this model. As mining gradually moves deeper, geothermal resources will be more abundant in abandoned mines in the future, and the use of geothermal power generation will be better than the other renewable energy sources in terms of utilization factor, power generation cost,

and stability [15]. At present, the construction of underground water reservoirs in the geothermal mode of abandoned mines in China is still in the planning stage. In addition, it is proposed to use Functional Backfill to store heat/energy, while filling the goaf according to the characteristics of high-temperature in deep mining of metal mines. Moreover, as reported by Liu et al. [16,17], it is suggested to establish a unique mine backfill coupled heat exchange system that can realize geothermal energy recovery.
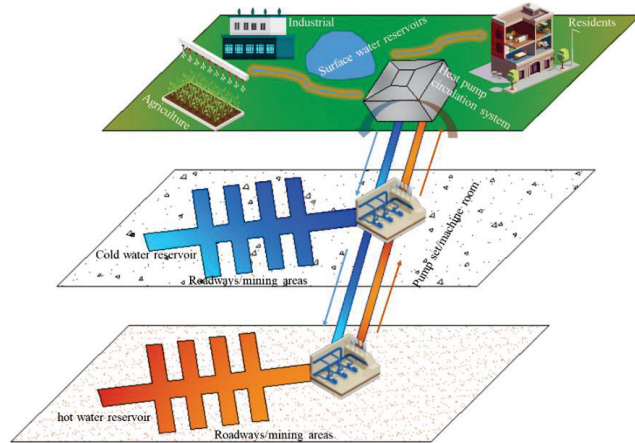
Figure 4. Geothermal energy utilization model of abandoned mines.

The development of PHS plants has a history of more than 100 years. It is the power storage system with the most mature technology and the highest actual energy conversion rate (about 80%) among all large-scale energy storage methods [18]. China's north and northwest plains lack natural high drop terrain conditions suitable for the establishment of surface pumped storage power plants, thus the use of abandoned mines is an ideal choice for construction [19]. Figure 5 shows the PHS plants system using an abandoned mine.
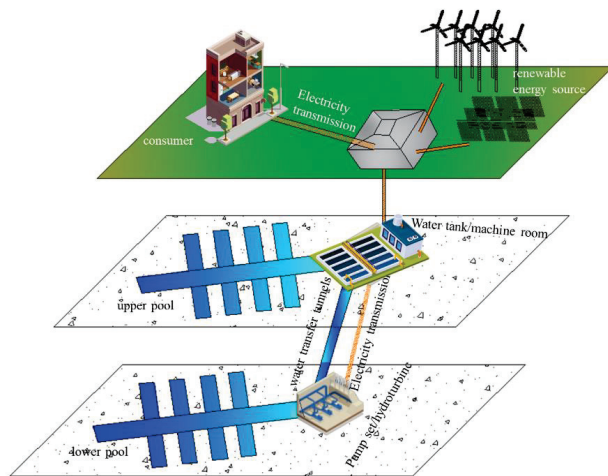
Figure 5. PHS plants system using abandoned mines.

In 1992, the State of New Jersey agreed to use abandoned iron ore mines to build the Mt. Hope PHS plant project, with a total capacity of 2000 MW, second only to the Bath County PHS plant (2100 MW) in the United States. The Mt. Hope PHS plant adopts a

closed-circulation water system power generation mode, relying only on lake water, mine water, and natural precipitation to meet all water needs [20–22]. Most of the coal mines in Spain were phased out in 2018, and the transformation of the tunnel system in the northern Asturias coal mining area into the lower reservoir of the underground pumped storage project was planned, with a storage capacity of about 200,000 m^3 at a depth of 300–600 m [23]. In 2015, the Czech Republic launched a research project on the operation of a pumped-storage power plant at the closed Jeremenko hard coal mine (near the Ostrava River), using the existing mine drainage system after nearly 4.5 years of preparation, which was expected to reach a power of 732 kW, actually about 680 kW (400 V), with a storage capacity of 3000 m^3 [24]. Germany is carrying out the project "Using Abandoned Mines to Store Wind Power". A team of scientists from the Technical University of Clausthal and industry representatives have designated 104 abandoned underground mines suitable for the construction of pumped storage power plants and gradually worked on these mines between 2015 and 2018 [25,26]. At the same time, the project team selected the abandoned metal mine Wiemannsbucht in the Harz area for a pilot simulation study for the construction of an underground pumped-storage power plant [27]. Abandoned metal mines have a deeper mining depth compared to coal mines, which can provide greater hydraulic fall and better lithology and more stable underground space. In 2016, Germany carried out a feasibility study on the construction of an underground PHS plant in the Prosper-Haniel coal mine and provided a conceptual model of the plant. The plant is a closed system with a maximum output of 200 MW and a storage cycle of about 4 h (800 MWh), with the lower storage reservoir being the original shaft at a depth of 600–1000 m with a capacity of 600,000 m^3 [28,29]. After completion, it will be the world's first abandoned coal mine to be used as an energy storage facility.

The use of abandoned mines to construct PHS plants in China is in the research stage as a whole, and there are no examples yet. Table 1 shows the projects of using mines to construct a PHS plant in China.

Table 1. The projects of using mines to construct pumped storage in China.

Location	Project Name	Status	Mine Type	Capacity
Jurong, Jiangsu Province	Shi Dangshan PHS plant Project [30]	Feasibility Study	Upper reservoir: Open-pit quarry Lower reservoir: Underground copper mine	1 billion kWh/year
Fuxin, Liaoning Province	Fuxin Haizhou Mine PHS plant Project [31,32]	Feasibility Study	350 m deep open-pit coal mine	3.6 million kW
Zibo Shandong Province	Huadian Zichuan Kunlun Town Multi-energy Complementary Energy Complex Project [33]	Under construction	Underground coal mines	22 million kW

2.1.2. Salt Cavern Gas Storage (SCGS)

Salt rocks are commonly used to build oil and gas storage reservoirs due to their excellent physicochemical properties. The United States completed the geological survey of known salt mines in the country as early as the last century (before 1978) [34]. It also has built hundreds of salt cavern oil and gas storages and attaches great importance to the development of hydrogen storage. SCGSs in operation in the world is mainly distributed in North America and Europe, with Germany and the United States in the majority [35].

Latest development of salt cavern storage in China is summarized as follows. In 2007, the first SCGS—Jintan gas storage was officially put into operation for gas injection [36]. The number of existing oil storage facilities in China are not able to meet the strategic needs, but the proportion is significantly increasing every year. Moreover, there is no hydrogen storage examples in China at present [35]. The first batch of compressed air energy storage (CAES) projects had been connected to the grid in 2021. There is a huge gap in China in terms of salt cavern energy storage compared to Germany, the United States, and other developed countries. However, China is pushing salt cavern storage technology, with a number of CAES and natural gas storage projects coming on stream [37,38].

1. CAES is considered to be the second most suitable technology for GW-scale large-scale power storage after pumped hydro storage. The types of gas storage caves for CAES can be mostly divided into salt caverns, hard rock caves, abandoned mines, and aquifers. Figure 6 shows the use of underground caves to build a CAES plant. To date, there are only two large-scale compressed air energy storage plants in commercial operation in the world, namely the Huntorf power plant in Germany built in 1978 and the McIntosh power plant in the United States built in 1991 [39]. Both were built in salt caverns and are functioning well today.
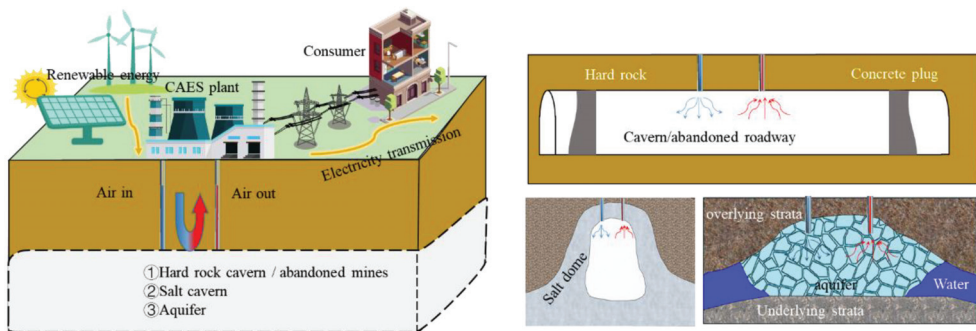
Figure 6. Construction of CAES plant using underground caves.

When discussing the feasibility of developing CAES, low-cost, large-scale available storage is critical. With the fact that it takes several years to dissolve a usable salt cavern, the use of existing salt caverns is an economically viable option. From China's Jintan salt cavern CAES construction experience, salt cavern gas storage has a number of advantages, such as low construction cost, small footprints, good sealing, safety, and stability [11].

2. Underground hydrogen storage has many advantages over surface storage, including safer storage, smaller footprints, larger storage capacity, and lower cost. Taylor et al. [40] pointed out that large-scale underground storage is only one-tenth or even less than the cost of surface storage facility. Zivar [41] and Tarkowski [42] discussed that among the three types (depleted reservoirs, aquifers, and salt caverns) of subsurface hydrogen storage, salt cavern hydrogen storage is the best option from various perspectives, including gas tightness of the reservoir, gas volume, extraction efficiency, biochemical reactions, and practical experience. According to CEDIGAZ (International Gas Information Association) 2019 data, salt cavern storage of natural gas now accounts for 26% of global deliverables [43].

The United Kingdom, the United States, Germany, and other countries have already built salt cavern hydrogen storage pilots [44–46]; however, to date, China has no underground hydrogen storage practice. It has been found that there is no essential difference between hydrogen storage in salt caverns and natural gas storage [41,42]. China has more than 10 years of experience in natural gas storage in salt caverns, and there is great potential for developing hydrogen storage in salt caverns. The results of a study performed by

Yang Chunhe (Year, Ref), showed that the hollowed salt caverns of abandoned salt mines in Jintan have long-term storability values [47]. In September 2021, the Institute of Rock and Soil Mechanics, Chinese Academy of Sciences established a joint research center for hydrogen and helium storage technology in salt caverns with China National Salt Industry Group Company Limited. In combination with the trends of hydrogen development in China, a "production-storage-use" integrated hydrogen chain was proposed. Fang et al. [48] proposed an integrated hydrogen energy "production-storage-use" chain for three development scenarios from salt cavern hydrogen storage reservoirs in the context of China.

2.2. CO_2 and Radioactive Waste Sequestration

Deep sequestration of CO_2 and radioactive waste is a key technology that countries all over the world have reached a consensus on. Using abandoned mine shafts for storage can save costs and increase throughput.

2.2.1. CO_2 Geological Storage and Utilization

CO_2 storage technology is a key method to achieve the double carbon goal, which mainly includes separate storage in depleted oil and gas reservoirs, coal seams, and saltwater layers, and CO_2-enhanced uranium leaching/enhanced coal bed methane recovery/enhanced oil recovery/enhanced natural gas recovery/enhanced shale gas recovery/enhanced water recovery/enhanced geothermal systems (CO_2-EUL/ECBM/EOR/EGR/ESGR/EWR/EGS) [49]. Figure 7 shows CO_2 geological storage and utilization technology. Considering the storage volume and technical level, this section discusses the application of CO_2 in depleted oil and gas reservoirs and coal mines. When filling abandoned mines, it can imitate the natural CO_2 mineral absorption process, and use solid waste containing alkaline or alkaline earth metal oxides to form CO_2-solid waste composite materials through carbonation reaction, thereby filling the mines and stabilizing CO_2 for a long period of time.
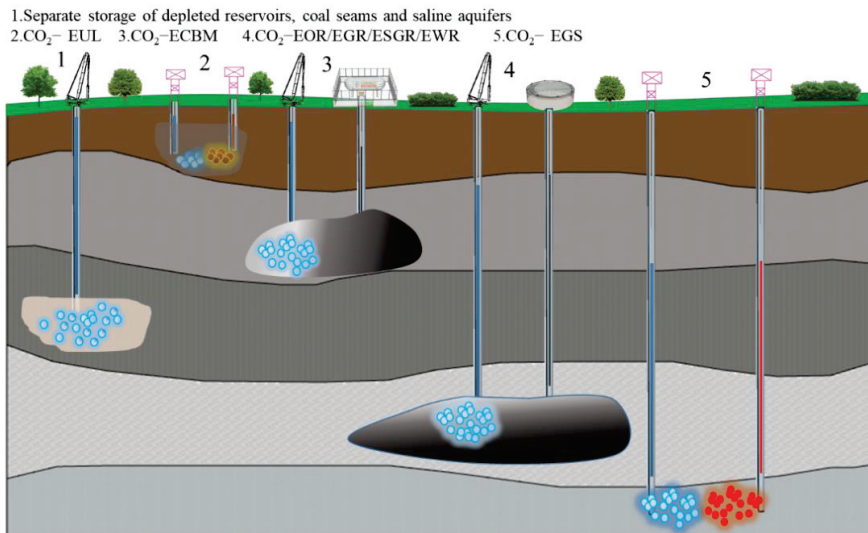
Figure 7. CO_2 geological storage and utilization technology.

1. Approximately 84 million tons of CO_2 are piped to depleted oil fields each year in the US to sequester and effectively increase oil production, and the US government is strongly encouraging this method [50]. In 2002, Australia used the Otway Basin

depleted gas field for carbon sequestration, which is the largest demonstration project of CO_2 geological storage in Australia [51]. Chinese gas reservoirs are mainly located in the Ordos, Sichuan, Bohai Bay and Tarim Basins. About 15.3 billion tons of CO_2 can be sequestered using depleted gas reservoirs, and about 9 billion tons of CO_2 can be sequestered by CO_2-EGR technology [52]. However, China's natural gas industry started late and will not see large-scale depleted gas fields for a long period of time [53]. Therefore, China's carbon sequestration demonstration projects are primarily depleted fields. China's oil fields are mainly concentrated in the Songliao, Bohai Bay, Ordos and Junggar Basins, and about 5.1 billion tons of CO_2 can be sequestered through CO_2-EOR [52]. CO_2-EOR in China started in the early years. In 1963, CO_2-EOR experiments were carried out in Daqing Oilfield, and it was proved that it could increase the production by 10% [54]. In 2010, Shenhua Group (now CHN ENERGY) launched the first demonstration project of the whole process of CO_2 capture and geological storage in China [55]. By 2020, more than 15 CO_2-EOR demonstration projects have already been conducted in China in several provinces, including Jilin, Heilongjiang, Shaanxi, Shandong, Henan, and Jiangsu [50].

Compared with the United States and other countries, the disadvantageous conditions are that China's oilfields have complex strata structure, strong heterogeneity, low or ultra-low permeability, low porosity, and poor oiliness. CO_2-EOR technology will be challenged by high miscible phase pressures, severe gas fouling, heavy solid phase deposition, and complex reservoir development [56]. Moreover, the CO_2 infused in China is mainly gaseous and liquid and is transported by road, while the US has a mature pipeline transportation system, and all the CO_2 used for infusion is supercritical CO_2.

2. Geological caprocks that are not affected by mining disturbances and coal seams with good air tightness can achieve CO_2 storage. Coal seams are one of the most ideal sites for geological storage in China due to their huge open space and highly stable adsorption of CO_2, especially the ability to displace coalbed methane [57–59]. According to the estimation performed by Yu et al. [60], the CO_2 storage capacity of Chinese coal seams is nearly 142.67×10^9 t. In addition, Liu et al. [59] estimated the storage capacity of coal seams with a depth of 300–1500 m in China to be 12.078×10^9 t. Coal mine goafs and non-minable coal seams contain a large amount of coalbed methane resources, and the permeability of coal reservoirs in China is generally low. CO_2-ECBM is one of the potential methods to increase the production in low permeable coal seams. The main component of coalbed methane is methane, similar to natural gas. Using coalbed methane can prevent it from escaping into the air and increase the greenhouse effect. China is rich in coal-bed methane resources. Among the 30 major onshore coal-bearing basins in China, the amount of coal-bed methane resources are 29.82×10^{12} m^3 at a burial depth of 2000 m or less, and the recoverable resources are 12.51×10^{12} m^3. Among them, the gas content of the Qinshui Basin in Shanxi reaches 21.85 m^3/t, with a high recoverability factor [61]. According to statistics, the residual coalbed methane with a development value in Shanxi Province alone reached 72.6×10^9 m^3 [62].

The CO_2-ECBM field trial was first conducted by the United States in 2001 with a 95% coalbed methane recovery rate. Field trials of different scales have been conducted accordingly in Japan, the EU, and Canada [63]. Since the 1990s, China has been studying the feasibility of this technology [64], which is still in the pilot test phase. In 2004, China United Coal Bed Methane Co. Ltd. conducted a series of pilot injection and monitoring studies in Liulin and Shizhuang in the Qinshui-Linfen Basin.

2.2.2. Radioactive Waste Sequestration

The disposal of radioactive waste is considered to be one of the greatest problems in the world. Improper disposal may bring serious consequences. For example, in 2021, Japan discharged the Fukushima nuclear wastewater into the sea, which caused serious

environmental pollution and aroused strong condemnation from all over the world. Using the unique underground space created by abandoned mines to dispose of radioactive waste is one of the most effective methods. Table 2 shows underground disposal facilities of low-and-intermediate-level radioactive wastes constructed using abandoned mines in Germany and the Czech Republic.

Table 2. Abandoned mine shafts as disposal facilities of low-and-intermediate-level radioactive wastes.

Country	Name	Mine Type	Introduction [65]
Germany	Asse	Rock Salt	Up to 765 m deep, 125,000 barrels of low-level radioactive waste and 1300 barrels of intermediate-level radioactive waste were stored during 1967–1968, and were later suspended due to salt water infiltration.
	Morsleben	Rock Salt	The mining depth is 300–500 m. In 1971, the goaf was directly used as a disposal area. By 2014, before the disposal site was closed, a total of 36,752 m^3 of waste had been disposed of.
	Konrad	Iron	Storage of low-calorie radioactive waste, which accounts for about 90% of all radioactive waste in Germany, with a disposal scheme similar to that of the Asse disposal facility.
Czech Republic	Richard	Limestone	Operating in 1964, it is scheduled to close in 2070. In the existing roadway of the reinforcement part, the waste is disposed of in the roadway of 70~90 m underground.
	Bratrství	Uranium	One roadway and five chambers have been transformed and reinforced for the disposal of radioactive waste. It started in 1974 and is still in operation.

Research on the permanent disposal of high-level radioactive waste began in the United States in 1955 [66], and after extensive research, deep rock-salt reservoirs were set as the preferred target. The Waste Isolation Pilot Plant (WIPP) has been using the Salado salt mine to receive radioactive waste left over from nuclear weapons research and production since 1999 [34]. The Chinese scholars Ding and Xie [67] both also proposed the use of underground salt caverns for nuclear waste disposal.

In China, granite with high strength and excellent mechanical properties [68,69] is selected as the carrier of the disposal. At present, the geological disposal of high-level radioactive waste in China has entered the preparation stage of the underground laboratory. The main structure scheme of spiral slope + three shafts + two-story level road is adopted, and test platforms are constructed at 280 and 560 m under the Beishan Mountains of Gansu [70]. Figure 8 shows China's underground radioactive waste disposal repository.
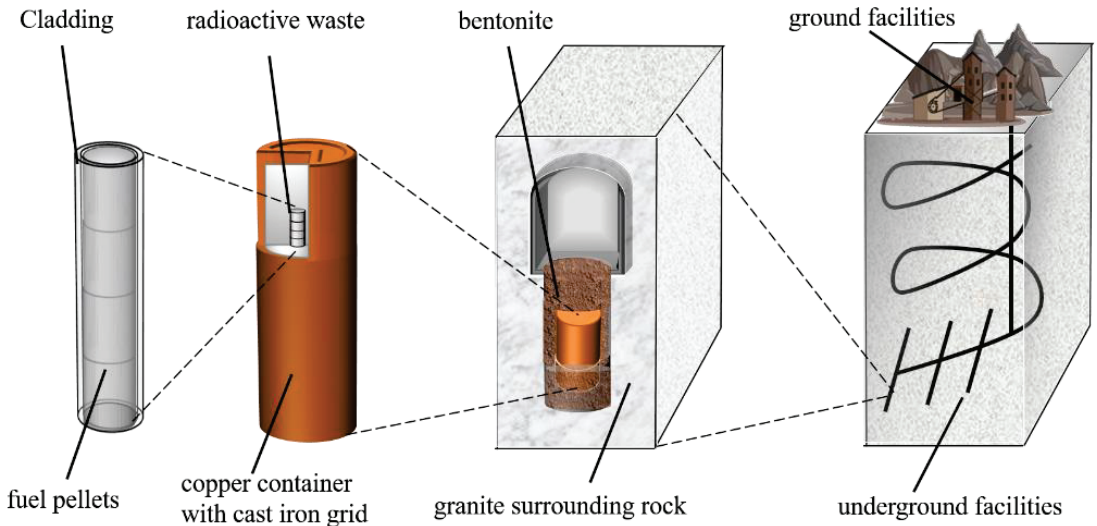
Figure 8. Model of underground radioactive waste disposal repository in China.

2.3. Abandoned Mine Ecological Resource Development

The ecological development of abandoned mines is mainly expressed in the form of tourism. As shown in Figure 9, the more common forms of tourism in abandoned mines can be roughly divided into the close-to-nature model of building parks and gardens with the abundant light and water storage capacity characteristics of open-pit mines; and the humanistic exploration model of building underground exploration tours and experiences with the interactive long-walled spaces of underground mines and the chambers along the tunnel.
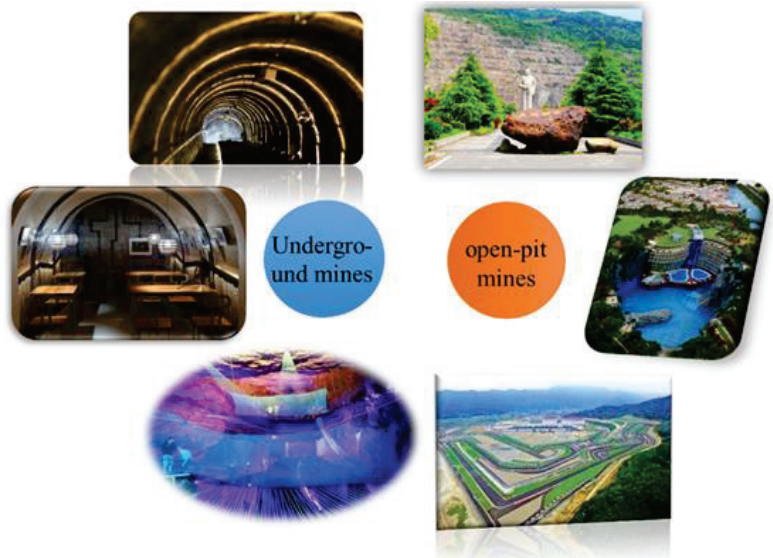
Figure 9. Ecological development model of abandoned mines.

In China, there is a rich experience in tourism development of abandoned open-pit mines. The more famous ones are Inter Continental Shanghai Wonderland Hotel and Hubei Huangshi National Mine Park. In addition, China is actively exploring the use of flat land formed by abandoned open-pit mines to develop a new agro-tourism model of "renewable energy generation + agriculture + tourism".

China is still in the exploration stage of tourism development of abandoned underground mines. Figure 10 shows the form of tourism development for the underground space (figure elements from [71]).
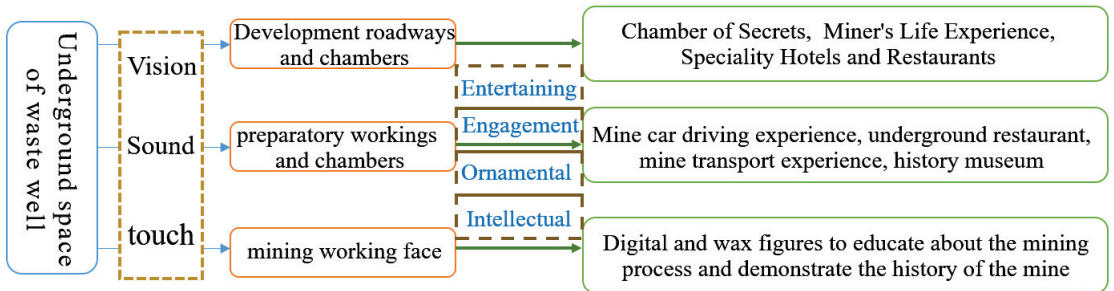

**Figure 10.** Abandoned underground mine tourism project development.

The development of mine tourism resources is constrained by many aspects, such as minerals, government, economy, and natural conditions. Taking the construction of China's national mine parks as an example, there are four batches of 88 national mine parks, most of which are concentrated in the eastern and central provinces, and less in the western provinces. The spatial distribution is clearly coupled with China's four major economic zones, and the richer the history and heritage of mining development, the more likely it will be a National Mine Park [72]. It can be inferred that the tourism resources of abandoned mines are concentrated in the surrounding areas with good economic development and mining history.

3. Basic Rock Mechanics of Using Abandoned Mines

The rock mechanics challenges of using abandoned mines to construct underground projects can be summarized in two aspects: 1. The geological characteristics of abandoned mines, such as rock mass lithology, hydrology and earthquake, as well as the mining characteristics of internal rock mass spatial structure. For example, cylindrical columns are more reliable than prismatic isolated pillars [73] and height to width ratios and width to thickness ratios have a great influence on the bearing ability of rocks [74]. 2. Requirements of underground engineering operation on the surrounding rock. For example, the surrounding rock of abandoned mine used for underground water reservoir construction must be impacted by water flow in different degrees for a long period of time, which requires high mechanical properties of surrounding rock.

3.1. PHS Plants/Underground Water Reservoir

Figure 11 shows construction requirements and rock mechanics of abandoned mine PHS plants. The engineering and stress environment of the underground water reservoir of the abandoned mine PHS plant is as follows:
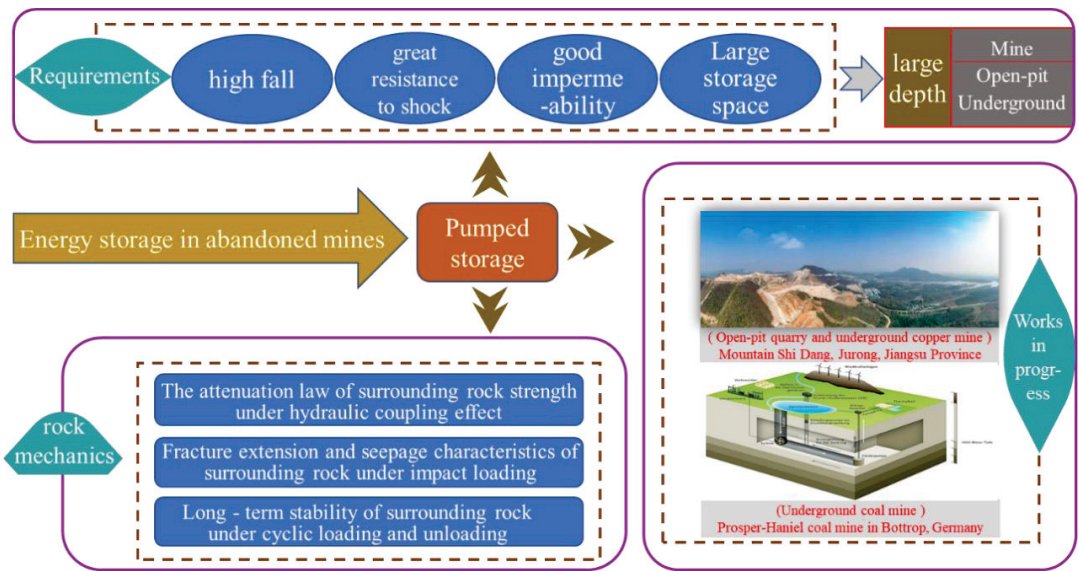
Figure 11. Construction requirements and rock mechanics of abandoned mine PHS plants.

The surrounding rock of the underground water reservoir and the artificial dam are in a high crustal stress environment;

The collapsed rock mass and the overlying rock in the goaf are in a state of movement for a long period of time, which produce lateral pressure on the surrounding rock of the reservoirs;

Long-term frequent pumping and filling of water in the reservoir produce strong cyclic fatigue load on the surrounding rock;

Effect of strong dynamic impact on surrounding rock of reservoir, such as high drop and large flow impact, wave and its reflection in tunnel and mine quake.

3.2. Underground Energy Storage

In China, large-scale oil reserves are carried out by sealing caverns with underground water, and most of the existing operating and large-scale underground gas storage are salt caverns. Therefore, only the rock mechanics of the construction of salt cavern gas storage are introduced here.

Depending on the frequency of gas used in the gas storage, stress cyclic loads of different time frequencies will be formed and an inhomogeneous thermal field will be generated near the inlet and outlet of the salt cavern. Li et al. [75] proposed a coupled thermodynamic model of wellbore-salt cavern that can be used for the thermal state analysis of salt caverns considering the cyclic conditions of natural gas storage reservoirs. Contrary to Europe and other western countries, where salt rocks are mostly salt domes, salt deposits in China generally have the characteristics of many layers and a thin single layer. Complex geological conditions increase the possibility of underground energy storage risks [47,76,77]. Therefore, many scholars have studied the influence of the interlayer on the shape and stability of gas storage reservoirs. [78–81]. In addition, salt is easily soluble in water, and gas storage in salt caverns is in the form of gas storage clusters. Therefore, extra attention should also be paid to the groundwater distribution and the influence of stress distribution in adjacent salt caverns when selecting the site for gas storage. Figure 12 illustrates the general framework of salt cave gas storage.
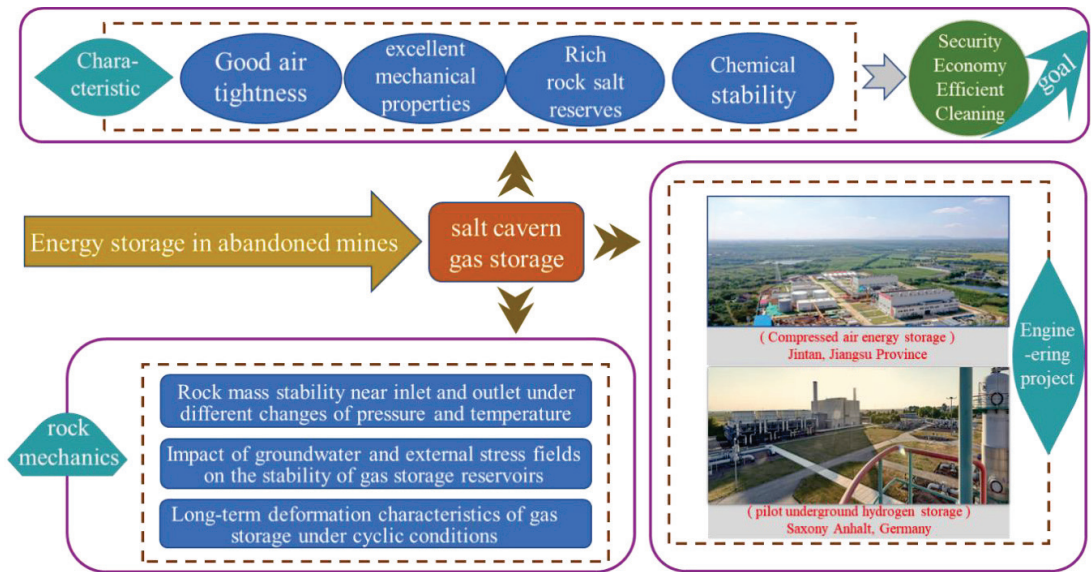
**Figure 12.** General framework of salt cave gas storage.

3.3. CO$_2$ and Radioactive Waste Sequestration

CO$_2$ geological sequestration mechanisms can be divided as physical and chemical sequestration mechanisms. Among them, physical sequestration mechanisms include tectonic stratigraphic sequestration, bounded sequestration, and hydrodynamic sequestration; whereas chemical sequestration mechanisms include dissolution sequestration and mineralization sequestration, etc. With current estimates, CO$_2$-EOR and CO$_2$-ECBM have the greatest potential for CO$_2$ storage in China, thus only the related rock mechanics issues with these two are presented here. The CO$_2$ sequestration depth is generally below 800 m, where the temperature and pressure conditions maintain the CO$_2$ in a liquid or supercritical state. Supercritical carbon dioxide can dissolve organic matter in sequestered rocks, such as coal matrix, forming voids, and reducing the strength of the surrounding rock. Carbon dioxide reacts chemically with water and acid roots and metal ions in the formation, corroding the rock, promoting crack expansion, and further reducing strength. In CO$_2$-ECBM, supercritical CO$_2$ is adsorbed in the formation of expansion stress and shear deformation, reducing the formation strength, seriously affecting the integrity and possibly leading to CO$_2$ leakage. In actual engineering, the injection of carbon dioxide is periodic, and the change of rock mass strength under the condition of cyclic injection of CO$_2$ is different [82].

For the disposal of radioactive waste, the difficulty for China and the world lies in the high-level waste (HLW). The HLW deep-buried point is in a state of high in situ stress. To safely bury it for a long period of time, three development stages of fatigue failure of rock mass under microseismic conditions should be considered [83]. Due to the continuous decay of nuclides, a large amount of heat is released, and the temperature at the deep burial point is high and subject to fluctuating changes. HLW has the nature of nuclide migration, and it is necessary to ensure the tightness of the repository, especially since there should be no water connected to the biosphere nearby. To achieve biosphere isolation in ten thousand years or even tens of thousands of years, the near-field and far-field thermal-hydraulic-mechanical coupling process and long-term behavior estimation was performed during the geological disposal (excavation, operation, and later closure) of high-level nuclear waste. In summary, HLW deep burial requires the following rock mechanics studies:

1. The evolution law of temperature and pressure of the surrounding rock.
2. The rock rupture process and fracture expansion law.
3. The long-term stability and shape change law of the facility.
4. The influence of possible earthquakes and water flows on the stability of the facility. Figure 13 illustrates the use of abandoned mines for permanent sequestration of carbon dioxide and radioactive waste.
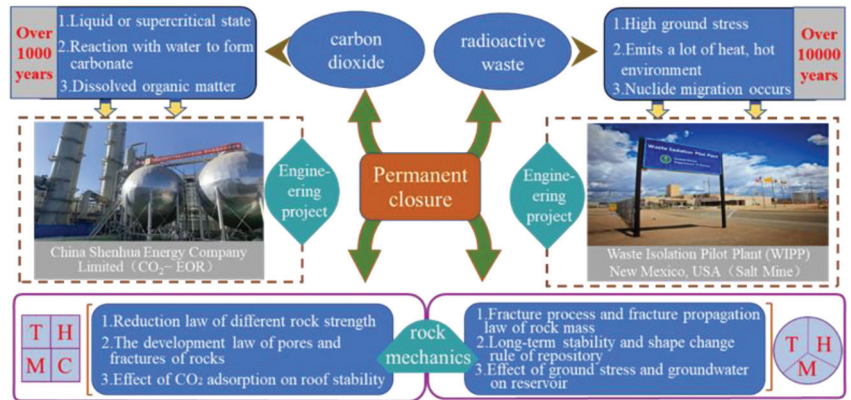
Figure 13. Use of abandoned mines for permanent CO_2 and radioactive waste sequestration.

4. Conclusions and Prospects

The reuse of abandoned mines is a low-carbon environmental technology that saves resources and brings a series of socio-economic benefits, which is important for China to realize the construction of ecological civilization and achieve the double carbon goal. To date, most of the utilization models of abandoned mines remain a world problem. Developed countries, such as the United States, Germany, and the United Kingdom were the first to start research on the use of abandoned mines and have established a series of industrial projects with a considerable degree of experience that can be used as a reference for China.

China has a large number of abandoned mines with high potential for utilization. However, most of the utilization technologies are still in the pioneering research stage and only a few have entered the industrial demonstration stage. Moreover, compared with European and American countries, abandoned mines in China have more complex geological conditions, and significant rock mechanics challenges, issues, and problems, which need to be solved. Existing engineering research should learn from foreign experience and combine it with China's own engineering geological conditions to explore the utilization mode of abandoned mines that conforms to China's national conditions. Investment in research on key utilization models, such as energy storage and CO_2 sequestration in abandoned mines should be increased. Furthermore, an increasing number of industrial demonstration projects should be established, and key rock mechanics issues should be tackled in a proper manner. Finally, exploring a mature business model from mining to the reuse of abandoned mines will achieve sustainable development of the mining industry.

Author Contributions: Conceptualization, K.D. and J.Z.; methodology, K.D. and J.Z.; writing—original draft preparation, J.X.; writing—review and editing, M.K., K.D. and J.Z. All authors have read and agreed to the published version of the manuscript.

Data Availability Statement: The data presented in this study are available on request from the corresponding author.

Conflicts of Interest: The authors declare that they have no conflict of interest.

References

1. Global Cumulative CO₂ Emissions by Country 1850–2021. Available online: https://www.statista.com/statistics/1267683/cumulative-CO2-emissions-fossil-fuel-land-use-forestry-worldwide-by-country/ (accessed on 10 July 2022).
2. Friedlingstein, P.; O'Sullivan, M.; Jones, M.W.; Andrew, R.M.; Hauck, J.; Olsen, A.; Peters, G.P.; Peters, W.; Pongratz, J.; Sitch, S.; et al. Global Carbon Budget 2020. *Earth Syst. Sci. Data* **2020**, *12*, 3269–3340. [CrossRef]
3. Circular of The State Council of The State Council on the Issuance of the Action Plan for Carbon Peak by 2030 (Guofa (2021) No. 23). Available online: http://www.gov.cn/zhengce/content/2021-10/26/content_5644984.htm (accessed on 9 March 2022). (In Chinese)
4. Li, X.; Chen, Z.; Fan, X.; Cheng, Z. Hydropower development situation and prospects in China. *Renew. Sustain. Energy Rev.* **2018**, *82*, 232–239. [CrossRef]
5. Li, T.; Zhou, X.; Wang, L.; Cui, D. Necessity of Spent Fuel Disposal and Environmental Chemical Behavior of Repository. *Nucl. Chem. Radiochem.* **2020**, *42*, 513–523. (In Chinese)
6. Li, J.; Chen, S.; Wu, Y.; Wang, Q.; Liu, X.; Qi, L.; Lu, X.; Gao, L. How to make better use of intermittent and variable energy? A review of wind and photovoltaic power consumption in China. *Renew. Sust. Energ. Rev.* **2021**, *137*, 110626. [CrossRef]
7. Zhou, X.; Fan, S.; Sun, H.; Tang, L.; Ma, F. Practices of environmental protection, technological innovation, economic promotion and social equity in hydropower development: A case study of cascade hydropower exploitation in China's Dadu River basin. *Clean Technol. Environ. Policy* **2021**, *23*, 2827–2841. [CrossRef]
8. Wang, J.; Jürgen, K.; Li, Y. Some Thoughts on Resource Utilization and Sustainable Development in Closing Coal Mining Areas. *J. Min. Sci.* **2021**, *6*, 633–641. (In Chinese) [CrossRef]
9. Chang, C.; Zou, Y. A review of domestic and foreign abandoned mine resource development model. *Resour. Dev. Mark.* **2014**, *30*, 425–429. (In Chinese)
10. Xie, H.; Gao, M.-Z.; Liu, S.; Zhou, H.-W.; Zhang, R.-X.; Liu, Z. Study on underground Space Capacity Estimation and Exploitation of Zhang Anlin Coal Mine. *J. Coal* **2018**, *43*, 1487–1503. (In Chinese) [CrossRef]
11. Mei, S.; The Alum Joan; Qin, G.-L.; Tian, F.; Xue, X.; Li, R. Advanced adiabatic compressed air energy storage technology and application prospect of salt cave gas storage. *Power Grid Technol.* **2017**, *41*, 3392–3399. (In Chinese) [CrossRef]
12. Gu, D.; Peak, W.L.; Cao, Z.; Wu, B.; Jiang, B.; Yang, Y. England Development strategy and engineering technology of mine water protection and utilization in China's coal mines. *J. Coal* **2021**, *46*, 3079–3089. (In Chinese) [CrossRef]
13. Zhang, C.; Wang, F.; Bai, Q. Underground space utilization of coalmines in China: A review of underground water reservoir construction. *Tunn. Undergr. Space Technol.* **2021**, *107*, 103657. [CrossRef]
14. Cai, M.; Duo, J.; Chen, X.; Mao, J.; Tang, C.; Liu, Z.; Ji, H.; Ren, F.; Guo, Q.; Li, P. Study on the strategy of deep mineral and geothermal resources co-extraction. *China Eng. Sci.* **2021**, *23*, 43–51. (In Chinese) [CrossRef]
15. Wang, J.; Kong, Y.; Cheng, Y. Distribution and exploitation of geothermal resources in China. *Int. Clean Energy Forum.* **2019**, 81–88+584. (In Chinese) [CrossRef]
16. Liu, L.; Xin, J.; Zhang, B.; Zhang, X.; Wang, M.; Qiu, H.; Chen, L. Exploration of basic theory and application of functional filling in mines. *J. Coal* **2018**, *43*, 1811–1820. (In Chinese) [CrossRef]
17. Zhang, S.Y.; Wen, D.; Zhao, Y.J.; Liu, L.; Zhang, B.; Ziyuan, C.; Wang, M.; Tu, B.B. Thermal-force performance and heat transfer process of mine thermal/energy storage fillers. *J. Coal* **2021**, *46*, 3158–3171. (In Chinese) [CrossRef]
18. Pickard, W.F. The History, Present State, and Future Prospects of Underground Pumped Hydro for Massive Energy Storage. *Proc. IEEE* **2012**, *100*, 473–483. [CrossRef]
19. Xie, H.; Hou, Z.F.; Peak; Zhou, L. New technology of underground pumped Storage power generation in Gao Yanan Coal Mine: Principle, present situation and prospect. *J. Coal* **2015**, *40*, 965–972. (In Chinese) [CrossRef]
20. Shiers, P.F.; Fisher, F.S.; Kosberg, J.A. *The Mt. Hope Waterpower Porject: A Pumped Storage Facility that Enhances the Environment While Supplying On-Demand Electrical Needs*; ASCE: Reston, VA, USA, 1995; pp. 521–532.
21. Pei, J. Characteristics of the Mount Hope Pumped Storage power Station in the United States. *Hydroelectr. Power* **1996**, *12*, 34. (In Chinese)
22. Rodzianko, P.; Fisher, F.S. Developing Mt. Hope: The megawatt line. *Hydro Rev.* **1992**, *11*, 7.
23. Menendez, J.; Oro, J.; Loredo, J.; Vega, M. Underground pumped-storage hydro power plants with mine water in abandoned coal mines. In Proceedings of the IMWA 13th International Congress, Lappeenranta, Finland, 25–30 June 2017.
24. Peczkis, G. Practical possibilities of pumped-storage power plants implementation in liquidated underground mines. *J. Power Technol.* **2021**, *101*, 213–225.
25. Alvarado Montero, R.; Niemann, A.; Schwanenberg, D. Concepts for pumped-storage hydro-electricity using underground coal mines. The wise find pleasure in water: Meandering through water science and engineering. In Proceedings of the 35th IAHR World Congress, Chengdu, China, 8–13 September 2013; pp. 6519–6526.

26. Luick, H.; Niemann, A.; Perau, E.; Schreiber, U. Coalmines as Underground Pumped Storage Power Plants (UPP)—A Contribution to a Sustainable Energy Supply? *Geophys. Res. Abstr.* **2012**, *14*, 4205.

27. Xi, F.; Zhang, J.; Wang, Y.; Yan, R. Technical Key Points and Feasibility Analysis of Underground Pumped Storage Power Stations in Abandoned Mines in China. *Sci. Technol. Rev.* **2020**, *38*, 41–50. (In Chinese)

28. Montero, R.; Wortberg, T.; Binias, J.; Niemann, A. Integrated assessment of underground pumped-storage facilities using existing coal mine infrastructure. In Proceedings of the 4th IAHR Europe Congress, Liege, Belgium, 29 July 2016; pp. 953–960.

29. Untertägige Pumpspeicherwerke. Available online: https://www.uni-due.de/wasserbau/upsw_phase2.php (accessed on 23 March 2022).

30. The Municipal Development and Reform Commission Serves to Promote the Construction of the Shidangshan Pumped-Storage Power Station Project | Jurong Municipal Development and Reform Commission. Available online: http://www.jurong.gov.cn/jrfgjxw/bmdt/202109/84cd0ea841e14ae0a37a4ef63df4ee04.shtml (accessed on 24 March 2022). (In Chinese)

31. Fuxin Haizhou Mine Pumped Storage Power Station Project Preliminary Work Cooperation Agreement Signed in Beijing. Available online: http://www.fuxin.gov.cn/newsinfo.jsp?id=68445 (accessed on 24 March 2022). (In Chinese)

32. China Three Gorges Corporation Electronic Procurement Platform. Available online: https://eps.ctg.com.cn/cms/channel/1ywgg1/2566.htm (accessed on 24 March 2022). (In Chinese).

33. Zuo, F.; Liu, T. Shandong Provincial Bureau of Geology and Mineral Resources Media Report [Dongzhong Daily Client] The First Domestic Abandoned Mine Pumped Storage Multi-Energy Complementary Industry Project Started. Available online: http://dkj.shandong.gov.cn/art/2022/3/3/art_110121_10297193.html (accessed on 24 March 2022). (In Chinese)

34. Johnson, K.S.; Gonzales, S. *Salt Deposits in the United States and Regional Geologic Characteristics Important for Storage of Radioactive Waste*; Y/OWI/SUB-7414/1; U.S. Department of Energy Office of Scientific and Technical Information: Washington, DC, USA, 1978.

35. Li, N.; Zhao, Y.; Wang, T.; Yang, C. Disciplinary Information Team of Wuhan Literature and Information Center, Chinese Academy of Sciences; Team of Underground Oil and Gas Storage and Development Research Center, Wuhan Institute of Geomechanics, Chinese Academy of Sciences; Trend Watch: International Salt Cave Energy Storage Strategy and Technology Development Situation Analysis. *Proc. Chin. Acad. Sci.* **2021**, *36*, 1248–1252. (In Chinese) [CrossRef]

36. Cheng, W.; Yang, C. Let Salt Cavern Storage Take Root in China—Chinese Academy of Sciences. Available online: https://www.cas.cn/xzfc/202004/t20200415_4741245.shtml (accessed on 21 March 2022). (In Chinese).

37. Construction of the Largest Salt Cavern Gas Storage in Asia in Qianjiang—Hubei Provincial People's Government Portal. Available online: https://www.hubei.gov.cn/hbfb/szsm/202102/t20210209_3343039.shtml (accessed on 23 March 2022). (In Chinese)

38. Zhu, Z.; Tao, G.; Zhao, X.; China Energy Construction Co., Ltd. Enterprise News China Energy Construction Organized the Country's First (Set) 600 MW Salt Cavern Compressed Air Energy Storage Project Feasibility Study Review Meeting. Available online: http://www.ceec.net.cn/art/2022/2/23/art_11016_2520085.html (accessed on 23 March 2022). (In Chinese).

39. Tang, X. Current Status of Compressed Air Energy Storage Technology. *Energy Res. Util.* **1995**, *3*, 25–27. (In Chinese)

40. Taylor, J.B.; Alderson, J.E.A.; Kalyanam, K.M.; Phillips, L.A.; Lyle, A.B. Technical and economic assessment of methods for the storage of large quantities of hydrogen. *Int. J. Hydrogen Energy* **1986**, *11*, 5–22. [CrossRef]

41. Zivar, D.; Kumar, S.; Foroozesh, J. Underground hydrogen storage: A comprehensive review. *Int. J. Hydrogen Energy* **2021**, *46*, 23436–23462. [CrossRef]

42. Tarkowski, R.; Czapowski, G. Salt domes in Poland—Potential sites for hydrogen storage in caverns. *Int. J. Hydrogen Energy* **2018**, *43*, 21414–21427. [CrossRef]

43. Natural Gas Infrastructure Databases—Cedigaz. Available online: https://www.cedigaz.org/databases/natural-gas-infrastructure-databases/#underground-gas-storage-database (accessed on 11 July 2022).

44. Liebscher, A.; Wackerl, J.; Streibel, M. Geologic Storage of Hydrogen—Fundamentals, Processing, and Projects. In *Hydrogen Science and Engineering: Materials, Processes, Systems and Technology*; John Wiley & Sons, Ltd.: Hoboken, NJ, USA, 2016; pp. 629–658. ISBN 978-3-527-67426-8.

45. Crotogino, F. *Assessment of the Potential, the Actors and Relevant Business Cases for Large Scale and Long Term Storage of Renewable Electricity by Hydrogen Underground Storage in Europe*; HyUnder: Huesca, Spain, 2013.

46. Panfilov, M.; Gravier, G.; Fillacier, S. Underground storage of H_2 and H_2-CO_2-CH_4 mixtures. In *ECMOR X-10th European Conference on the Mathematics of Oil Recovery*; European Association of Geoscientists & Engineers: Utrecht, The Netherlands, 2006. [CrossRef]

47. Yang, C.; Liang, W.; Wei, D.; Yang, H. Feasibility study on underground storage of salt rock energy in China. *J. Rock Mech. Eng.* **2005**, *24*, 4409–4417. (In Chinese)

48. Fang, Y.; Hou, Z.; Yue, Y.; Ren, L.; Chen, Q.; Liu, J. A new type of multifunctional salt cavern hydrogen storage for integration of hydrogen energy industry. *Eng. Sci. Technol.* **2022**, *54*, 128–135. (In Chinese) [CrossRef]

49. Li, Q.; Liu, G.; Li, X.; Chen, Z. Intergenerational evolution and presupposition of CO_2 capture, utilization and storage technology from a multi-dimensional perspective. *Eng. Sci. Technol.* **2022**, *54*, 157–166. (In Chinese) [CrossRef]

50. Hill, L.B.; Li, X.; Wei, N. CO_2-EOR in China: A comparative review. *Int. J. Greenh. Gas Control.* **2020**, *103*, 103173. [CrossRef]

51. Urosevic, M.; Pevzner, R.; Shulakova, V.; Kepic, A.; Caspari, E.; Sharma, S. Seismic monitoring of CO_2 injection into a depleted gas reservoir—Otway Basin Pilot Project, Australia. *Energy Procedia* **2011**, *4*, 3550–3557. [CrossRef]

52. Cai, B.; Li, Q.; Zhang, X.; Cao, C.; Cao, L.; Chen, W.; Chen, Z.; Dong, J.; Jiang, Y.; Jiang, F.; et al. *China Carbon Dioxide Capture Utilization and Storage (CCUS) Annual Report (2021) China CCUS Path Study*; Environmental Planning Institute, Ministry of Ecology and Environment, Wuhan Institute of Geomechanics, Chinese Academy of Sciences, China Agenda 21 Management Center: Wuhan, China, 2021. (In Chinese)

53. Tang, Y.; Yang, R.; Bian, X. A Review of CO_2 Sequestration Projects and Application in China. *Sci. World J.* **2014**, *2014*, 381854. [CrossRef]

54. Wu, Y.A.; Carroll, J.J.; Du, Z. (Eds.) *Carbon Dioxide Sequestration and Related Technologies: Wu/Carbon*; John Wiley & Sons, Inc.: Hoboken, NJ, USA, 2011; ISBN 978-1-118-17555-2.

55. Song, X.; Yang, S. Current status of CCS technology at home and abroad and China's active countermeasures. *Reserv. Eval. Dev.* **2011**, *1*, 25–30. (In Chinese) [CrossRef]

56. Yue, X.; Zhao, R.; Zhao, F. Technical Challenges of CO_2 Enhanced Oil Recovery in my country. *China Sci. Technol. Pap. Online* **2007**, *7*, 487–491. (In Chinese)

57. Baena-Moreno, F.M.; Rodriguez-Galan, M.; Vega, F.; Alonso-Farinas, B.; Vilches Arenas, L.F.; Navarrete, B. Carbon capture and utilization technologies: A literature review and recent advances. *Energy Sources Part A-Recovery Util. Environ. Eff.* **2019**, *41*, 1403–1433. [CrossRef]

58. Golding, S.D.; Uysal, I.T.; Boreham, C.J.; Kirste, D.; Baublys, K.A.; Esterle, J.S. Adsorption and mineral trapping dominate CO_2 storage in coal systems. *Energy Procedia* **2011**, *4*, 3131–3138. [CrossRef]

59. Liu, Y.; Li, X.; Bai, B. Preliminary evaluation of CO_2 coal seam storage capacity in China. *Chin. J. Rock Mech. Eng.* **2005**, *24*, 2947–2952. (In Chinese)

60. Yu, H.; Zhou, G.; Fan, W.; Ye, H. Predicted CO_2 enhanced coalbed methane recovery and CO_2 sequestration in China. *Int. J. Coal Geol.* **2007**, *71*, 345–357. [CrossRef]

61. Geng, M.; Chen, H.; Chen, Y.; Zeng, L.; Chen, S.; Jiang, X. Method and results of the fourth round of national coalbed methane resource evaluation. *Coal Sci. Technol.* **2018**, *46*, 64–68. (In Chinese) [CrossRef]

62. Yang, H.; Lian, B.; Shi, J.; He, L. Policy Research on Reuse of CBM Resources in Coal Mine Gobs (Abandoned Mine) under the "Double Carbon" Target. *China Min. Mag.* **2022**, *31*, 5. (In Chinese)

63. Fang, Z.; Li, X.; Li, H.; Chen, H. Feasibility study of mixed gas flooding technology for coalbed methane. *Geotech. Mech.* **2010**, *31*, 3223–3229. (In Chinese) [CrossRef]

64. Qin, Y. Mechanism of CO_2 enhanced CBM recovery in China: A review. *J. China Univ. Min. Technol.* **2008**, *18*, 406–412. [CrossRef]

65. Ilg, P.; Gabbert, S.; Weikard, H.-P. Nuclear Waste Management under Approaching Disaster: A Comparison of Decommissioning Strategies for the German Repository Asse II. *Risk Anal.* **2017**, *37*, 1213–1232. [CrossRef] [PubMed]

66. Leigh, C.D.; Hansen, F.D. *Salt Disposal of Heat-Generating Nuclear Waste*; Sandia National Laboratories: Albuquerque, NM, USA, 2011.

67. Ding, G.; Xie, P. Methods for disposing of nuclear waste in underground salt caverns. *Chin. J. Undergr. Space Eng.* **2006**, *2*, 1068–1071+1080. (In Chinese)

68. Du, K.; Yang, C.; Su, R.; Tao, M.; Wang, S. Failure properties of cubic granite, marble, and sandstone specimens under true triaxial stress. *Int. J. Rock Mech. Min. Sci.* **2020**, *130*, 104309. [CrossRef]

69. Du, K.; Li, X.; Tao, M.; Wang, S. Experimental study on acoustic emission (AE) characteristics and crack classification during rock fracture in several basic lab tests. *Int. J. Rock Mech. Min. Sci.* **2020**, *133*, 104411. [CrossRef]

70. Construction of Beishan Underground Laboratory in China. Available online: http://www.caea.gov.cn/n6758881/n6758890/c6812169/content.html (accessed on 10 April 2022). (In Chinese)

71. Han, Y.; Liu, Q.; Wu, B.; Yang, K.; Dong, Z. Research on the Development and Utilization Mode of Underground Space Tourism Resources in Abandoned Mine. *Coal Geol. Explor.* **2021**, *49*, 79–85. (In Chinese)

72. He, X.; Wang, X. Research on the Spatial Distribution of China's National Mining Parks. *Sci. Technol. Manag. Land Resour.* **2014**, *31*, 50–56. (In Chinese)

73. Du, K.; Su, R.; Tao, M.; Yang, C.; Momeni, A.; Wang, S. Specimen shape and cross-section effects on the mechanical properties of rocks under uniaxial compressive stress. *Bull. Eng. Geol. Environ.* **2019**, *78*, 6061–6074. [CrossRef]

74. Du, K.; Li, X.; Su, R.; Tao, M.; Lv, S.; Luo, J.; Zhou, J. Shape ratio effects on the mechanical characteristics of rectangular prism rocks and isolated pillars under uniaxial compression. *Int. J. Min. Sci. Technol.* **2022**, *32*, 347–362. [CrossRef]

75. Li, W.; Chen, G.; Ding, S.; Zhang, Y. A method for assessing the gas capacity based on thermodynamic state analysis for salt cavern during operation. *J. Energy Storage* **2022**, *50*, 104316. [CrossRef]

76. Zhang, N.; Ma, L.; Wang, M.; Zhang, Q.; Li, J.; Fan, P. Comprehensive risk evaluation of underground energy storage caverns in bedded rock salt. *J. Loss Prev. Process Ind.* **2017**, *45*, 264–276. [CrossRef]

77. Li, L.; Liang, W.; Lian, H.; Yang, J.; Dusseault, M. Compressed air energy storage: Characteristics, basic principles, and geological considerations. *Adv. Geo-Energy Res.* **2018**, *2*, 135–147. [CrossRef]

78. Zhang, G.; Liu, Y.; Wang, T.; Zhang, H.; Wang, Z.; Zhao, C.; Chen, X. Pillar stability of salt caverns used for gas storage considering sedimentary rhythm of the interlayers. *J. Energy Storage* **2021**, *43*, 103229. [CrossRef]

79. Zhang, N.; Shi, X.; Wang, T.; Yang, C.; Liu, W.; Ma, H.; Daemen, J.J.K. Stability and availability evaluation of underground strategic petroleum reserve (SPR) caverns in bedded rock salt of Jintan, China. *Energy* **2017**, *134*, 504–514. [CrossRef]

80. Li, J.; Tang, Y.; Shi, X.; Xu, W.; Yang, C. Modeling the construction of energy storage salt caverns in bedded salt. *Appl. Energy* **2019**, *255*, 113866. [CrossRef]

81. Zhang, G.; Wang, Z.S.; Liu, Y.X.; Luo, N.; Dong, J.W. Research on stability of the key roof above horizontal salt cavern for compressed air energy storage. *Rock Soil Mech.* **2021**, *42*, 800–812. [CrossRef]

82. Su, E.; Liang, Y.; Chang, X.; Zou, Q.; Xu, M.; Sasmito, A.P. Effects of cyclic saturation of supercritical CO_2 on the pore structures and mechanical properties of bituminous coal: An experimental study. *J. CO_2 Util.* **2020**, *40*, 101208. [CrossRef]

83. Du, K.; Sun, Y.; Zhou, J.; Wang, S.; Tao, M.; Yang, C.; Khandelwal, M. Low amplitude fatigue performance of sandstone, marble, and granite under high static stress. *Geomech. Geophys. Geo-Energy Geo-Resour.* **2021**, *7*, 68. [CrossRef]

Isolation and Characterization of A Novel Iron–Sulfur Oxidizing Bacterium *Acidithiobacillus Ferrooxidans* YQ-N3 and its Applicability in Coal Biodesulfurization

Wenbo Li [1,2], Qiyan Feng [1,2,*] and Ze Li [1,2]

[1] School of Environment Science and Spatial Informatics, China University of Mining and Technology, Xuzhou 221116, China

[2] Engineering Research Center of Ministry of Education for Mine Ecological Restoration, China University of Mining and Technology, Xuzhou 221116, China

*   Correspondence: fqycumt@126.com

Abstract: *Acidithiobacillus ferrooxidans* is a chemotrophic, aerobic, acidophilic, and Gram-negative bacterium that plays a key role in iron and sulfur cycling and has a wide range of applications in the industrial field. A novel *A. ferrooxidans* strain, hereinafter referred to as strain "YQ-N3", was isolated from sediments of a river polluted by acid mine drainage (AMD) of an abandoned mine in Shanxi, China. The whole genome sequencing results revealed that *A. ferrooxidans* YQ-N3 has a 3,217,720 bp genome, which is comprised of one circular chromosome and five circular plasmids (Plasmid A, Plasmid B, Plasmid C, Plasmid D, Plasmid E). Plasmid E, a new plasmid, had not been annotated in the reference database. *A. ferrooxidans* YQ-N3 had a close evolutionary relationship with *A. ferrooxidans* ATCC23270 and *A. ferridurans* JCM18981 and exhibited higher similarity in its genomic structure with *A. ferrooxidans* ATCC23270. Multiple genes related to environmental resistance and iron and sulfur metabolism were predicted from its genome. *A. ferrooxidans* YQ-N3 can remarkably increase the oxidation rate of Fe^{2+} and S^0 and enhance the hydrophilicity of S^0, which was supported by functional gene analysis and laboratory experiments. The biological desulfurization experiment demonstrated that *A. ferrooxidans* YQ-N3 can reduce the sulfur content in coal by removing pyrite sulfur and organic sulfur.

Keywords: *Acidithiobacillus ferrooxidans*; complete genome; comparative genomics; iron–sulfur oxidation; biodesulfurization

1. Introduction

Acidithiobacillus ferrooxidans (*A. ferrooxidans*) is an aerobic, acidophilic, Gram-negative, chemotrophic prokaryote [1]. This bacterium is widely present in acidic mine soils, puddles, and environments containing iron or sulfur deposits. Its major energy sources are iron, sulfur, and sulfide minerals, and its metabolites include sulfate and Fe^{3+} [2]. Therefore, this bacterium plays a key role in the natural biogeochemical cycles of Fe and S. *A. ferrooxidans* participates in the oxidation of metal sulfide minerals in mining areas via the oxidation of Fe^{2+} and reduced sulfur compounds, resulting in acid mine drainage (AMD) in mining areas. Due to its low pH, high sulfate, and heavy metal contents, AMD can severely impact the surrounding soil and groundwater [3]. In fact, the United States Environmental Protection Agency (EPA) has reported that the environmental risks posed by AMD are second only to global warming and ozone depletion [4]. However, despite considerable efforts to identify the generation mechanisms of AMD and potential removal strategies, little progress has been made toward the development of effective AMD mitigation methods.

Due to its capacity to oxidize Fe^{2+} and reduce sulfur compounds on an industrial scale, *A. ferrooxidans* has been widely applied in bioleaching, biological desulfurization, biosynthesis, and biochemical production [5]. For instance, Lorenzo-Tallafigo et al. developed a

new process for the recovery of lead, silver, and gold from polymetallic sulfide ores using *A. ferrooxidans* and demonstrated that the process was cleaner than using traditional hydrometallurgical methods (e.g., hot brine leaching) [6]. The process included a bio-oxidation stage, where sulfides were oxidized in the presence of extremophiles, followed by pickling and citric acid leaching, after which lead was successfully recovered. Nie et al. isolated *A. ferrooxidans* Z1 from printed circuit board waste and confirmed that *A. ferrooxidans* Z1 was able to extract 96% of copper from waste printed circuit boards at an initial Fe^{2+} concentration of 12 g L^{-1} after seven days [7]. *A. ferrooxidans* can also be used to produce a variety of biomaterials, including schwertmannite, jarosite, iron–sulfur clusters (ISC), and magnetosomes [8]. Additionally, the biological desulfurization of coal would greatly contribute to its clean utilization. Rout et al. reported that *A. ferrooxidans* cells catalyzed the removal of sulfur in both organic and inorganic forms in coal samples, and approximately 79% of the total sulfur was removed from coal samples during a microbiological desulfurization process in a 500 mL flask within 14 days [9]. Currently, most studies on *A. ferrooxidans* have focused on model strains (e.g., ATCC23270), whereas newly discovered *A. ferrooxidans* strains have not been studied in depth. Therefore, examining novel *A. ferrooxidans* strains may provide new insights into the involvement of *A. ferrooxidans* in biogeochemical cycles and its applicability in the biological desulfurization of coal.

In this study, a novel *A. ferrooxidans* strain was isolated from sediments of a river polluted by the AMD of an abandoned mine in Shanxi, China. The whole genome of the newly isolated strain was sequenced, the oxidation features of Fe^{2+}, S^0, and FeS_2 were studied, and the performance of coal desulfurization was also tested. Additionally, the genomic characteristics, the capacity to oxidize iron and sulfur, and the environmental adaptability of the newly discovered strain were analyzed from a comparative and functional genomics perspective. Therefore, this study provides a theoretical basis for studying the formation and processing of AMD, as well as for the development and optimization of industrial applications using *A. ferrooxidans* YQ-N3.

2. Materials and Methods

2.1. Isolation, Purification, and Identification

Due to the growth characteristics of *A. ferrooxidans*, Leathen or 9K media are often used during the isolation and purification of this bacterium [10]. In this study, 9K medium was selected for the isolation and purification of *A. ferrooxidans*. The 9K liquid medium is composed of solutions A and B. Solution A is composed of 3.00 g/L $(NH_4)_2 \cdot SO_4$, 0.10 g/L KCl, 0.655 g/L $K_2HPO_4 \cdot 3H_2O$, 0.50 g/L $MgSO_3 \cdot 7H_2O$, and 0.01 g/L $Ca(NO_3)_2 \cdot 4H_2O$. After the preparation of solution A, the pH of the solution was adjusted to 1.8 with 1:1 concentrated sulfuric acid and sterilized in an autoclave at 121 °C for 20 min. Solution B contains $FeSO_4 \cdot 7H_2O$ and was sterilized using a microporous membrane (d = 0.22 μm). After cooling down to room temperature, Solution A was evenly mixed with Solution B before use. Furthermore, the 9K solid medium contained Solution A, Solution B, and Solution C. Solutions A and B were prepared as described above, whereas solution C was a 7.5 g/L agarose solution. After solution C was heated and dissolved, it was sterilized in an autoclave at 121 °C for 20 min. Once solution A was cooled to approximately 60 °C, it was mixed with Solution B. When the pH was adjusted to 2.0, Solution C was quickly added to the mixture to make a solid medium [11].

The strains used in this study were isolated from sediments of a river polluted by AMD from an abandoned mine in Shanxi, China. Following aseptic procedures, the sediment samples were collected and stored at 4 °C and then transported to the laboratory. Next, 10 g of sediment sample was added to 100 mL of sterile water and the mixture was incubated at 30 °C and 180 r/min for three days. The samples were then filtered to obtain a bacterial solution, which was stored at 4 °C. The bacteria-containing solution was inoculated into an Erlenmeyer flask containing 9K liquid medium at a 10% inoculum volume. Next, the flask was covered with a perforated sealing film (polypropylene, Beckman) and transferred to a constant temperature incubator at 30 °C and 180 r/min for continuous enrichment

culture. Once the bacteria had multiplied until the medium turned reddish–brown, the culture was inoculated into a new 9K liquid medium at a 10% inoculum volume rate, and isolation and purification were performed after 5–6 consecutive enrichments. The enrichment experiments were conducted in triplicate. An alternate solid–liquid culture method was used for the isolation and purification of *A. ferrooxidans*. The gradient dilution method was adopted during the isolation. Sterile sulfuric acid solution (pH = 1.8) was used to dilute the enriched bacterial liquid samples, and each sample was sequentially diluted from the initial concentration 10, 10^2, 10^3, 10^4, 10^5, and 10^6 times. Next, 0.2 mL of bacterial solutions at different concentrations was inoculated into the solidified 9K solid medium and evenly coated using a sterile coating rod. After coating, the Petri dish was placed upright in a constant temperature incubator at 30 °C for 10 h, after which the Petri dish was incubated upside down to prevent contamination caused by the backflow of water to the 9K solid medium. Isolation and purification were performed when the liquid medium turned reddish–brown. This process was repeated until pure strains were obtained.

A small amount of bacterial solution was taken after isolation and purification, after which a 1–1.5 cm diameter bacterial smear was evenly spread on a glass slide with a sterile inoculation loop, and ammonium oxalate crystal violet staining solution was added in a dropwise fashion to the smeared area, which was then stained for 1 min and washed with water. After blotting with absorbent paper, anhydrous ethanol was also added in a dropwise fashion to cover the entire smear area and then washed with water for 30 s. After blotting with absorbent paper, safranin dye solution was added in a dropwise fashion and stained for 1 min. The samples were then washed with water, blot dried with absorbent paper, and placed under a light microscope to observe bacterial morphology and Gram staining. Afterward, 100 mL of bacterial liquid cultured to the logarithmic phase was centrifuged at high speed at 4 °C, fixed with 2.5% glutaraldehyde overnight, and centrifuged to store the bacteria. The bacteria were subjected to gradient dehydration with 30%, 50%, 75%, 90%, and 100% ethanol (10 min per step). The samples were then freeze-dried at −20, −40, −60, and −80 °C and kept at each temperature for 12 h. After sample loading and gold spraying, the samples were examined via scanning electron microscopy (Regulus 8100, Hitachi High-Tech, Tokyo, Japan). Next, 20 μL of resuspended samples were placed dropwise on 200-mesh grids and incubated at room temperature for 10 min. Then, the cell morphology was examined using a transmission electron microscope (HT7700, Hitachi High-Tech, Tokyo, Japan).

Bacterial cultures in the logarithmic phase were frozen and centrifuged to obtain the bacterial cells for DNA purification and taxonomic classification based on 16S rRNA gene sequences. The extracted sample DNA was amplified by 16S rRNA, and PCR amplification was performed using a PCR instrument (2720 PCR instrument) with the 27F (5'- AGA GTT TGA TCC TGG CTC AG-3') and 1492R (5'-GGT TAC CTT GTT ACG ACT G-3') primer pair. The PCR amplification reaction system (30 μL) included 2 X EasyTaq SuperMix (15.0 μL), 27F (1μL), 1492R (1μL), DNA (1–2 μL), and ddH$_2$O (up to 30 μL). The amplification consisted of a pre-denaturation step at 94 °C for 5 min, 25 cycles (denaturation at 94 °C for 30 s, annealing at 57 °C for 30 s, extension at 72 °C for 90 s), extension at 72 °C for 7 min, and storage at 4 °C. The amplicons were sequenced with a 3730 sequencer for the first generation of double-ended sequencing to obtain an ABI sequencing peak map file. After assembly, the sequence was compared with the 16s sub-library to identify closely related species. Upon comparing the 16S rRNA sequences in the NCBI database, the 19 strains that were closest to the species level were selected and the NJ (Neighbor-Joining) method was used to construct a phylogenetic tree using the MEGA 6.0 software to visualize the evolutionary relationship of the sample and the near-source species.

The bacteria obtained in the experiment were identified as pure *A. ferrooxidans*, after which their growth conditions were studied, including the optimum growth pH, temperature, and inoculum size. The cells were cultured in growth media at different pH conditions (pH 1.2, 1.8, 2.4, 3.0, 3.6, and 4.2) to explore the optimal pH conditions for bacterial growth. The cells were cultured at 15, 20, 25, 30, 35, and 40 °C to study the optimal

growth temperature. Finally, the cultures were inoculated with 5%, 10%, 15%, and 20% of the inoculum to explore the optimal inoculum amount. A blood cell counting plate was used to observe and calculate the bacterial concentration.

2.2. Whole genome Sequencing

The bacteria collected above were sent to Beijing BMK Biological Co., Ltd., and whole genome sequencing was carried out using PacBio sequencing technology. The experimental process was performed according to the standard protocol provided by PacBio [12], including sample quality detection, library construction, library quality detection, and library sequencing. Low-quality and short fragments with a length of less than 2000 bp were removed from the reads obtained after sequencing, and clean reads were obtained for genome assembly and functional annotation. To fully display the features of the genome, a genome circle diagram of a single sample was generated using the Circos software (Version 0.69-6, http://www.circos.ca (accessed on 4 January 2023)) and a variety of information was displayed in the diagram to provide a comprehensive and intuitive understanding of the characteristics of the bacterial genome. Chromosome genes were predicted using Glimmer and the plasma genome was predicted using GeneMarkS [13,14]. The predicted genome was compared with the COG and KEGG databases based on protein sequence, and functional annotation was performed to obtain the corresponding gene function information. Upon sequencing the whole genome of *A. ferrooxidans* YQ-N3, short-length circular consensus sequencing (ccs) reads were filtered out from the raw data as a quality control measure. The filtered ccs reads were assembled de novo, and the assembled genome was corrected for errors. Once the assembly was completed, genome analysis and functional annotation were performed. Mobile genetic elements (MGEs) can help bacteria overcome challenges or occupy dominant niches. Therefore, studying the MGEs in the *A. ferrooxidans* YQ-N3 genome could provide insights into their ability to adapt to environmental changes. In this study, we analyzed three types of MGEs: genome islands, prophages, and CRISPR (clustered regularly interspersed short palindromic repeats)-Cas. Gene island prediction of the *A. ferrooxidans* YQ-N3 genome was performed using Islander (Version 1.2, http://www. pathogenomics.sfu.ca/islandviewer/ (accessed on 4 January 2023)) [15]. Prophage prediction was performed using Phage_Finder (phage-finder.sourceforge.net) [16]. CRISPR-Cas prediction was performed using Minced [17].

2.3. Comparative Genomic Analysis

To further examine the genomic characteristics of *A. ferrooxidans* YQ-N3, the genomes of five strains closest to it at the species level based on 16S rRNA sequences were selected for comparative analysis. The genome sequences of the selected strains (*A. ferrooxidans* ATCC23270, *A. ferrooxidans* BY0502, *A. ferridurans* JCM18981, *A. thiooxidans* ATCC 19377, and *A. ferrivorans* SS3) were obtained from the GenBank database. Glimmer 3.0 (http://ccb. jhu.edu/software/glimmer/index.shtml (accessed on 4 January 2023)) and GeneMarkS (Predictive Plasmid Genome) software (Version 4.3, http://topaz.gatech.edu/GeneMark (accessed on 4 January 2023)) were used to predict the coding sequence (CDS) of genome. The core gene and pan-genome in the predicted sequence were analyzed using BPGA (Bacterial Pan-genome Analysis tool ver. 1.2, https://iicb.res.in/bpga/index.html (accessed on 4 January 2023)). The empirical power law equation and exponential equation were used to calculate the extrapolation of the pan-genome and core genome curves, respectively [18,19]. ANI analysis of the selected genome was conducted by using the pyani software following the ANIm method. AAI analysis of the selected genome was performed using the CompareM software (https://github.com/dparks1134/CompareM (accessed on 4 January 2023)). Genome alignments between *A. ferrooxidans* YQ-N3 and *A. ferrooxidans* ATCC23270, *A. ferrooxidans* BY0502, *A. ferridurans* JCM18981, *A. thiooxidans* ATCC 19377, and *A. ferrivorans* SS3 were conducted using the MUMmer software (ver. 3.23, https://sourceforge.net/projects/mummer/files/latest/download (accessed on 4 January 2023)) related to the ucmer comparison method. Based on protein sequence

alignments, the coding genes predicted on the *A. ferrooxidans* YQ-N3 and the genome of the other five studied strains were compared with the COG (clusters of orthologous groups of proteins) databases for functional annotation, and the corresponding functional annotations were obtained.

2.4. Oxidation Characteristics of Fe^{2+}, S^0, and FeS_2

As the dominant microbe in metallic sulfide mining areas, *A. ferrooxidans* plays a vital role in Fe and S biogeochemical cycling [20]. Therefore, studies on the Fe^{2+}, S^0, and FeS_2 oxidation capacities of novel *A. ferrooxidans* strains are essential, specifically due to their theoretical and practical values.

This study characterized the *A. ferrooxidans* strain YQ-N3 isolated in the previous stage, and its ability to oxidize $FeSO_4 \cdot 7H_2O$, S^0, and FeS_2 as energy sources was discussed. The preserved YQ-N3 strain was transferred to 9K medium containing $FeSO_4 \cdot 7H_2O$, S^0, and FeS_2 with 10% of the inoculum, and was then placed in a constant temperature culture shaker at 30 °C and 180 r/min for multiple activations. The bacterial density was determined using a hemocytometer, after which acclimated log-phase bacteria were collected. The domesticated strains were inoculated into 9K medium containing $FeSO_4 \cdot 7H_2O$, S^0, and FeS_2 at a 10% inoculum volume proportion, and the bacterial concentration and Fe^{2+}, Fe^{3+}, SO_4^{2-}, pH, and Eh in the culture system were monitored thereafter. The specific experimental design is shown in Table 1. Three parallel groups and one blank control were set for each group of experiments.

Table 1. Study design for the assessment of Fe^{2+}, S^0, and FeS_2 oxidation using *A. ferrooxidans* YQ-N3.

Group	Energy Source	Bacterial Inoculum
A.f Oxidation Fe^{2+}	$FeSO_4 \cdot 7H_2O$ (8.95 g)	10%
Control 1	$FeSO_4 \cdot 7H_2O$ (8.95 g)	0%
A.f Oxidation S^0	S^0 (0.5 g)	10%
Control 2	S^0 (0.5 g)	0%
A.f Oxidation FeS_2	FeS_2 (5 g)	10%
Control 3	FeS_2 (5 g)	0%

All experiments were conducted with 200 mL of 9K medium without Fe.

At the end of the experiment, mineral samples generated via the oxidation of Fe^{2+} and FeS_2 before and after the reaction were collected. The samples were then ground and screened for mineral composition analysis. The phases and components of the collected samples were determined via X-ray diffraction (XRD) using an X-ray diffractometer (Bruker D8 ADVANCE, Karlsruhe, Germany) with Cu Kα radiation operating at 40 kV and 30 mA. The samples were scanned at a 0.02 °/s rate to record the patterns within a 2θ range of 3–105°; the mineral composition of the sample was then analyzed.

2.5. Coal Biodesulfurization Experiment

To explore the applicability of *A. ferrooxidans* YQ-N3 in coal desulfurization, three coal samples with different sulfur content from different mining areas in China were selected to conduct biological desulfurization experiments. The sulfur contents of the coal samples are shown in Table 2. The coal desulfurization experiments were conducted using a sequential batch experiment approach. Each coal sample was set with six groups of experiments, which included three replicates and one blank. Coal samples were taken at 5, 10, 15, 20, 25, and 30 days, respectively, to detect the sulfur contents. The experiment was carried out in 250 mL conical flasks in a constant temperature culture shaker at 30 °C and 180 r/min. All conical flasks contained 90 mL 9K liquid medium (free Fe^{2+}), 5 g of coal sample powder (200 mesh), and 10 mL of *A. ferrooxidans* YQ-N3 bacterial solution (2.0×10^7 cells/mL). The initial pH of all growth media was adjusted to 2. The total sulfur and sulfur contents of coal samples were analyzed according to the national standards (GB/T214-1996 and GB/T215-1996) of China.

Table 2. Sulfur contents of coal samples.

Coal Samples	Total S	S_p, Ad	S_o, Ad	S_s, Ad
I	3.46%	1.02%	0.81%	1.63%
II	3.02%	1.27%	0.83%	0.92%
III	2.77%	0.83%	1.42%	0.52%

S_p, ad: sulfur in the form of pyrite; S_o, ad: sulfur in organic form; S_s, ad: sulfur in the form of sulfate.

3. Results and Discussion

3.1. Growth Characteristics of A. ferrooxidans YQ-N3

In this study, sediment was collected from a river polluted by AMD of an abandoned mine in Shanxi, China. The sediment samples were treated with sterile water and inoculated in 9K-Fe^{2+} liquid medium for enrichment culture. After cultivation, all three replicate cultures exhibited the same characteristics. The color of the medium gradually changed from light blue–green to turbid, after which it became clear red–brown after continued cultivation. After culturing on 9K-Fe^{2+} solid medium for 30 days via the dilution coating method, colonies appeared on the plate, as illustrated in Figure 1A. The colonies were round, with prominent centers, neat edges, and yellow surroundings. After repeated solid–liquid alternating culture, the bacteria were collected, and DNA was extracted for 16S rRNA gene amplification and sequencing. After gene amplification, there was a single clear target band, which has 99.93% similarity with *Acidithiobacillus ferrooxidans* (NR_074193.1) according to the comparison between the sequencing results and BLAST. Therefore, the bacterial strain was named *A. ferrooxidans* YQ-N3. The collected bacteria were diluted several times using normal saline and then observed via Gram staining, thus confirming that the bacteria were Gram-negative. Optical microscope observations showed that the bacteria were rod-shaped (both as single cells and aggregates) and were able to swim rapidly. SEM and TEM analyses indicated that the bacteria had a short rod shape with blunt rounded ends, as shown in Figure 1B,C, with a length of approximately 0.8–1.2 μm and a width of 0.2–0.5 μm.
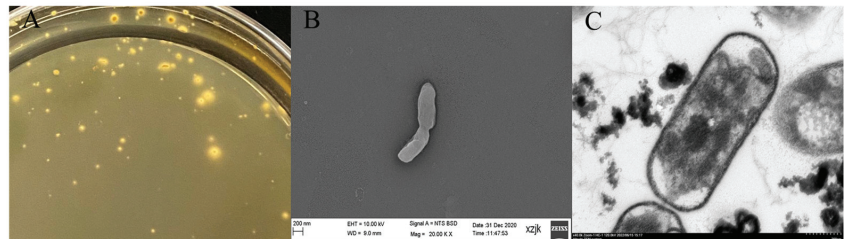
Figure 1. Phenotypic features of the new isolated *A. ferrooxidans* YQ-N3. ((**A**) is colonies on the plate; (**B**) is morphology of *A. ferrooxidans* YQ-N3 under SEM; (**C**) is morphology of *A. ferrooxidans* YQ-N3 under TEM.).

Upon comparing the 16S rRNA sequences in the GenBank database, the 18 strains that were closest at the species level were selected, and the NJ method was used to construct the phylogenetic tree of *A. ferrooxidans* YQ-N3 using the MEGA 6.0 software, as shown in Figure 2. The phylogenetic tree analyses demonstrated that *A. ferrooxidans* YQ-N3 was distinct from *Pseudomonas*, *Oceanicoccus*, *Luteimonas*, and *Xanthomonas*, but appeared to be related to *A. thiooxidans*, *A. ferridurans*, and *A. ferrivorans*. Particularly, the 16S rDNA sequence of *A. ferrooxidans* YQ-N3 was more than 99.93% similar to that of *A. ferrooxidans* ATCC23270, and it was therefore concluded that the isolated strains were *A. ferrooxidans*.

Figure 2. Phylogenetic tree of *A. ferrooxidans* YQ-N3 sequences and other sequences obtained from the GenBank database.

After screening and obtaining pure *A. ferrooxidans* YQ-N3 cultures, the optimum growth conditions were explored. Our findings demonstrated that *A. ferrooxidans* YQ-N3 could grow at a pH range of 1.6–2.4 and a temperature range of 20–35 °C, and were therefore consistent with previous studies. The strain achieved optimal growth at an initial pH of 1.8, a temperature of 30 °C, and an inoculum volume of 10%. Under these conditions, *A. ferrooxidans* YQ-N3 could reach a density of up to 2.3×10^8 cells/mL after 16 h.

3.2. Genome Overview of A. ferrooxidans YQ-N3

Whole genome analysis indicated that the genome size of *A. ferrooxidans* YQ-N3 was 3,217,720 bp, including one circular chromosome and five circular plasmids (Plasmid A, Plasmid B, Plasmid C, Plasmid D, and Plasmid E). The sequence length of the circular chromosome was 3,043,496 bp and the GC content was 58.64%. To fully demonstrate the genome features of *A. ferrooxidans* YQ-N3, a genome circle plot was drawn using the Circos software (Figure 3). A total of 3200 coding sequences (CDs), 6 rRNAs, 46 tRNAs, and 18 sRNAs were predicted. The annotation results of plasmids are shown in Table 3. The sequence length of the circular Plasmid A was 79,659 bp and the GC content was 61.64%. The length of Plasmid B was 34,460 bp and the GC content was 60.54%. The sequence length of Plasmid C was 29,178 bp and the GC content was 62.67%. The sequence length of Plasmid D was 23,017 bp and the GC content was 60.69%. The sequence length of Plasmid E was 7910 bp and the GC content was 52.40%. Among them, the Plasmid E sequence had not been annotated in the reference database. The complete genome sequences for the main chromosome and Plasmids A-E of *A. ferrooxidans* YQ-N3 were submitted to the GenBank database under accession numbers CP084172.1, CP084173.1, CP084174.1, CP084175.1, CP084176.1, and CP084177.1, respectively. *A. ferrooxidans* can grow in a variety of extreme environments and has great potential applications in industries such as bioleaching and biological desulfurization [21–23]. However, there are 26 published genomes of *A. ferrooxidans* strains, and therefore the whole genome sequencing and analysis of *A. ferrooxidans* YQ-N3 could provide key insights into its genetic properties and potential applicability. To understand the differences between the genomes of *A. ferrooxidans* YQ-N3 and other *A. ferrooxidans* strains, the genome information of *A. ferrooxidans* YQ-N3 and *A. ferrooxidans* that has been published in GenBank was selected for tabulation analysis, as shown in Supplementary Materials Table S1. The genome size distribution of *A. ferrooxidans* was 2.82631–4.18422 Mb, the GC content was 56.8%–58.9%, and the CDS (coding sequence) distribution was 2705–3998. The genome size, GC%, and number of CDSs of *A. ferrooxidans* YQ-N3 are similar to those of other *A. ferrooxidans* strains. However, with the exception

of *A. ferrooxidans* YQ-N3, the assembled *A. ferrooxidans* genome in the published database included no more than five plasmids.

Figure 3. Circular genome map of *A. ferrooxidans* YQ-N3. From outside to center: genes on the direct strand, genes on the complementary strand, tRNAs (orange), rRNA (purple), CRISPR (blue), and genomic island (green). GC-skew and sequencing depths are also displayed. (**A**) Chromosome, (**B**) Plasmid A, (**C**) Plasmid B, (**D**) Plasmid C, (**E**) Plasmid D, and (**F**) Plasmid E.

Table 3. Table of Plasmids' Annotation Details.

| Location	Sequence Length (Bp)	GC Content (%)	Accession Number	Accession Strain Name	Accession Plasmid Name	Identity (%)
Plasmid E	7910	52.4	-	-	-	-
Plasmid D	23,017	60.69	NC_015188.1	*Acidiphilium multivorum* AIU301	pACMV4	88.265
Plasmid C	29,178	62.67	NC_015178.1	*Acidiphilium multivorum* AIU301	pACMV1	88.293
Plasmid B	34,460	60.54	NC_009470.1	*Acidiphilium cryptum* JF-5	pACRY04	96.491
Plasmid A	79,659	61.64	NC_009469.1	*Acidiphilium cryptum* JF-5	pACRY03	99.949

"-" indicates no data.

3.3. Comparative Genomic Analysis

A summary of the features of six selected genomes is listed in Table 4. These strains were collected from different environments around the world but mainly from acid mine drainage. These genomes vary in size by approximately 0.44 Mb (ranging from 2.98 to 3.42 Mb) with coding sequence (CDS) numbers ranging from 2927 to 3498 and the G+C contents of the genomes ranging from 53% to 58.8%. Figure 4 shows the results of ANI and AAI analysis among strains. The squares with different colors show the similarity of nucleotides and amino acids among stains. It can be seen that *A. ferrooxidans* YQ-N3 is closely related to *A. ferrooxidans* ATCC23270 and *A. ferridurans* JCM18981. The ANI value and AAI value between *A. ferrooxidans* YQ-N3 and *A. ferrooxidans* ATCC23270 exceeded 95%, indicating that *A. ferrooxidans* YQ-N3 and *A. ferrooxidans* ATCC23270 are the same species. The results of the whole genome alignment between *A. ferrooxidans* YQ-N3 and the selected genomes are shown in Figure 5. Our findings indicated that the genomic arrangement of *A. ferrooxidans* YQ-N3 has the best co-linearity with *A. ferrooxidans* ATCC23270, and has better co-linearity with *A. ferridurans* JCM18981 than with *A. ferrooxidans* BY0502. This result demonstrates that *A. ferrooxidans* YQ-N3 and *A. ferrooxidans* ATCC23270 have closer evolutionary distances and highlights the abundant evolutionary progress of *A. ferrooxidans*.

Table 4. General features of bacterial genomes used in this study.

Strain	Geographic Origin	Genome Size (Mb)	GC%	Level	CDS	Genes
A. ferrooxidans YQ-N3	Shanxi, China	3.22	58.7	Complete	3195	3252
A. ferrooxidans ATCC23270	Bituminous coal mine effluent	2.98	58.8	Complete	2927	3087
A. ferrooxidans BY0502	Gansu, China	2.98	56.8	Contig	3026	3186
A. ferridurans JCM18981	Okayama, Japan	2.98	58.4	Complete	2802	3043
A. thiooxidans ATCC 19377	-	3.42	53	Contig	3498	3584
A. ferrivorans SS3	Norilsk, Russia	3.20	56.5	Complete	3089	3200

"-" indicates no data.
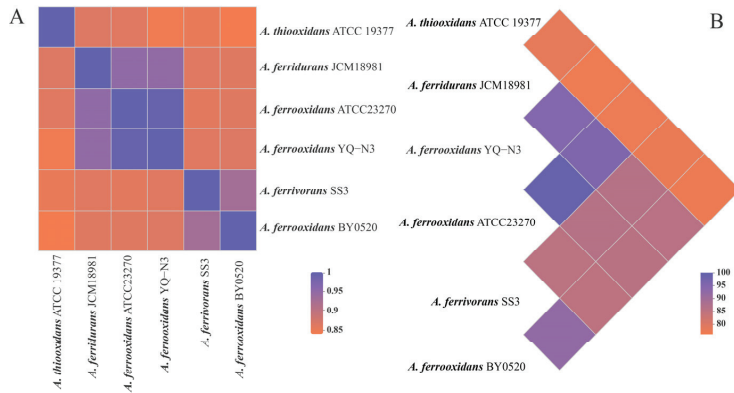
Figure 4. Strain ANI matrix thermogram (**A**) and strain AAI triangle thermogram (**B**).
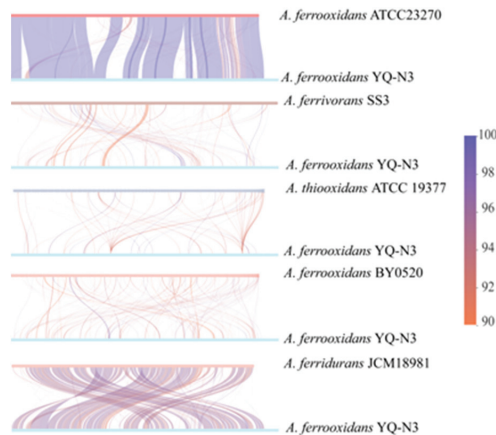
Figure 5. Whole genome alignment between *A. ferrooxidans* YQ-N3 and the selected genomes.

The bacterial pan-genome (BGPA) was used to identify orthologous groups among the studied genomes to reveal the unique genomic characteristics of the studied strains. The results are shown in Figure 6. The pan-genome contains 6062 genes, including 1400 core genomes and 2918 unique genomes. Figure 6B shows the curve of the relationship between the pan-genome size, core genome size, and genome number. According to the formula of the relationship curve between the pan-genome size and genome number ($f(n) = 2239.763n^{0.497} + 580.101$), we can conclude that the pan-genome in this study is open-type ($0 < 0.497 < 1$) [24], which means that as the number of sequenced genomes continues to increase, the pan-genome size will increase indefinitely. The core genome is composed of

genes that exist in all strains and is generally related to the basic biological functions and main phenotypic characteristics of bacteria. The unique genome is composed of genes only existing in some strains and genes unique to a strain, which reflects the diversity of strains and is generally related to some special biological metabolic pathways and environmental adaptation, such as antibiotic production, tolerance, and virulence. The rich specific genome content in this study indicates that the studied strains may undergo horizontal gene transfer (HGT) to improve their own survival competitiveness and increase microbial diversity [25].
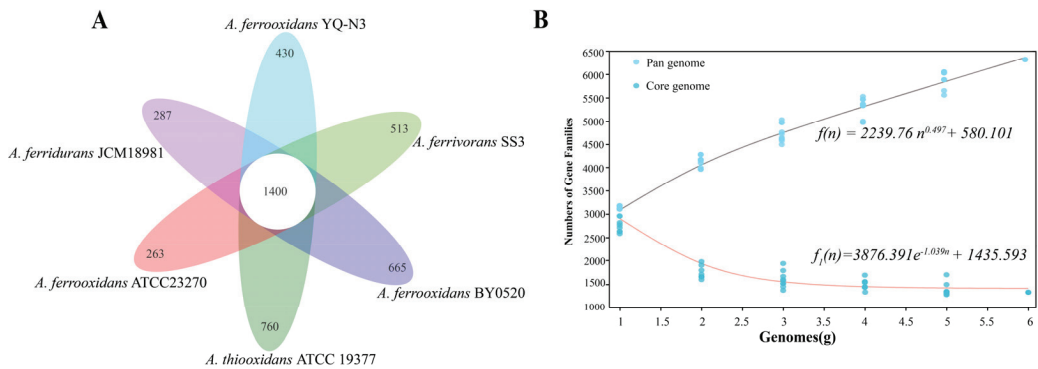
Figure 6. Pan-genome analysis of strains in this study. (**A**) Venn diagram of the pan-genome; (**B**) mathematical modeling of the pan-genome and core genome of strains in this study.

Figure 7 shows the COG annotation category and function statistics of the studied strains. These COGs were divided into four categories and 24 functional classes. The proportion of genes related to replication, recombination, and repair (L), cell wall/membrane/envelope biogenesis (M), energy production and conversion (C), and inorganic ion transport and metabolism (P) was slightly higher than that of genes with other functions, accounting for 5.55%–7.18%, 8.16%–9.71%, 6.66%–7.58%, and 5.55%–6.89% of all annotated genes, respectively. Additionally, defense mechanisms accounted for 4.92%–5.91% of all annotated genes, suggesting that these strains have a strong ability to self-repair and resist harsh environments [1]. *A. ferrooxidans* YQ-N3 has a total of 2571 genes annotated in COG, accounting for approximately 80.34% of the total number of genes. Compared to other strains, *A. ferrooxidans* YQ-N3 had the most genes associated with functions supporting P, L, and J (translation, ribosomal structure, and biogenesis). Moreover, the distribution of functional genes in the *A. ferrooxidans* YQ-N3, *A. ferrooxidans* ATCC23270, and *A. ferrooxidans* BY0502 genomes showed a similar pattern.

A. ferrooxidans is widely found in metal mines, high-sulfate coal mines, and other extreme environments due to its high environmental resistance, as well as its tolerance to metal ions and high acidity [26]. The characterization of genes associated with environmental resistance in *A. ferrooxidans* YQ-N3 would provide insights into the mechanisms that mediate its adaptability, which also lays the foundation for future research on its survival state and industrial application value in extreme environments. The results of COG annotation showed that the YQ-N3-gene-1491 and YQ-N3-gene-2286 located in the chromosome were annotated as ENOG410ZI6F and their COG description was "heavy metal transport detoxification protein", which further suggested that this strain was resistant to heavy metals. Some metal resistance genes have also been found, such as cusA, cusB, cusR, and cusS. Previous studies have demonstrated that the cus proton pump system is widely distributed in Gram-negative bacteria and is associated with copper and silver resistance in *A. ferrooxidans* [27]. In fact, cusA, cusB, and cusF possess metal-binding sites, and Cu^{2+} is directly transferred from protein to protein in the cus system during ion transport, thereby reducing the potential toxicity of free Cu^{2+} to cells [28,29]. Nan et al. linked the adaptability

of *A. ferrooxidans* to chemotactic movement and quorum sensing (QS), both of which allow this bacterium to grow, develop, and reproduce in extreme environments [30].
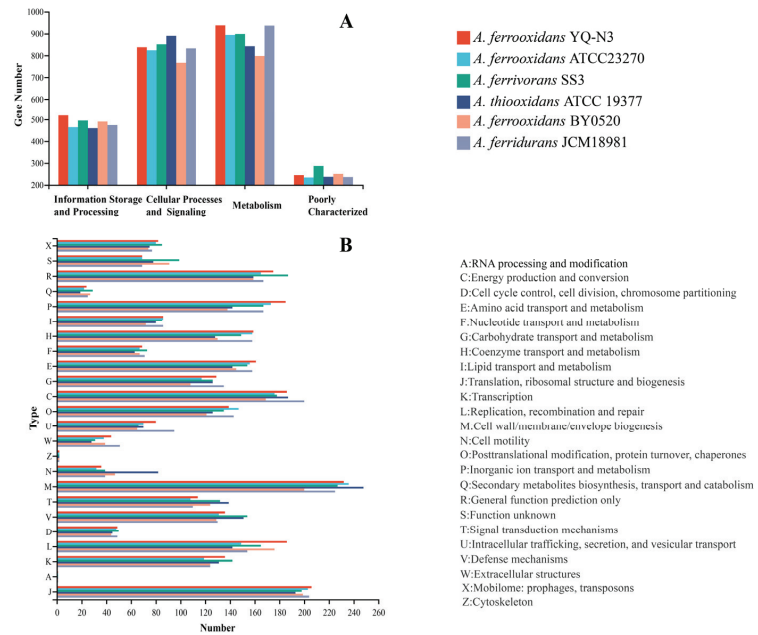

Figure 7. Comparison of COG categories (**A**) and COG functions (**B**) of strains in this study.

3.4. MEGs

More than 20% of genes in microbial genomes may be obtained through horizontal gene transfer (HGT), and these genes are usually referred to as mobile genetic elements (MGEs) [31,32]. MGEs refer to some exogenous gene fragments by way of the HGT that can be incorporated into bacterial genomes to adapt to environmental changes or improve the likelihood of survival. These fragments generally contain genes that encode the enzymes of other proteins with specific functions to help bacteria overcome adverse conditions or take advantage of resources that otherwise could not be exploited. The gene islands often carry functional genes, contain integrase and plasmid conjugation-related factors [33]. The prophage sequence often contained some functional genes, such as antibiotic resistance genes and virulence genes, among others, all of which enhanced the adaptability of this bacterium to its environment [34]. The CRISPR/Cas system is a prokaryotic immune system designed to resist the invasion of exogenous genetic material [35]. Integrators can enhance the adaptability of bacteria by capturing exogenous genes. Some studies have indicated that HGT is the main mechanism for acidophilic bacteria to adapt to heavy metal-rich environments [36–38]. The research on MGEs is helpful to further explore the whole genome characteristics of species. In this study, we analyzed the MGEs of *A. ferrooxidans* YQ-N3 from phages, genomic islands (GIs), and integrons. The predicted results indicated that the chromosome of *A. ferrooxidans* YQ-N3 contained 10 gene islands and Plasmid A contained one gene island. In turn, these gene islands contained a total of 181 CDs. The linear map of genome islands is shown in Figure 8. The description of genes 1255, 1259, 1624, 1270, and 1274 are "DEAD/DEAH box helicase", "hypothetical protein", "phage anti-repressor Ant", "M48 family metalloprotease", and "MULTISPECIES: restriction endonuclease", respectively. Interestingly, our analyses indicated that a prophage genome had integrated into the chromosome of *A. ferrooxidans* YQ-N3. The sequence length of the prophage was 17,089 bp and had 19 CDs, in addition to having a 58.64% GC content. The chromosome of *A. ferrooxidans* YQ-N3 was predicted to contain four CRISPRs with

average repeat lengths of 27, 28, 23, and 27 bp, respectively. The average lengths of the spacer sequences were 27, 32, 43, and 45 bp, respectively. An integron was also found on a chromosome of *A. ferrooxidans* YQ-N3. Its structure is shown in Figure 9; its length was 123 bp, including 9 CDs. Therefore, from the perspective of the whole genome, *A. ferrooxidans* YQ-N3 is likely resistant to heavy metals and is highly adaptable, making it a promising candidate for various industrial applications such as biological desulfurization, bioleaching, metal processing, and others.
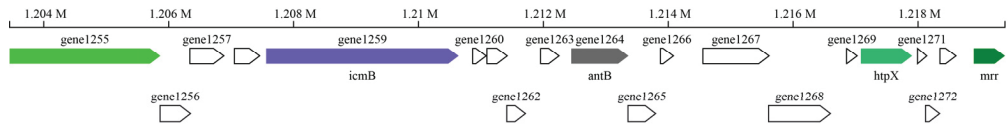
Figure 8. Linear map of genome islands. (The arrows represent genes, the length of the arrow represents the gene length, the direction indicates that the gene is encoded by a sense chain or antisense chain, and the color represents its COG function classification. The arrow without color represents that the corresponding COG function is not annotated. COG function classifications of gene 1252, gene 1259, gene 1264, htpX and mrr are type L, type S, type K, type O and type V).
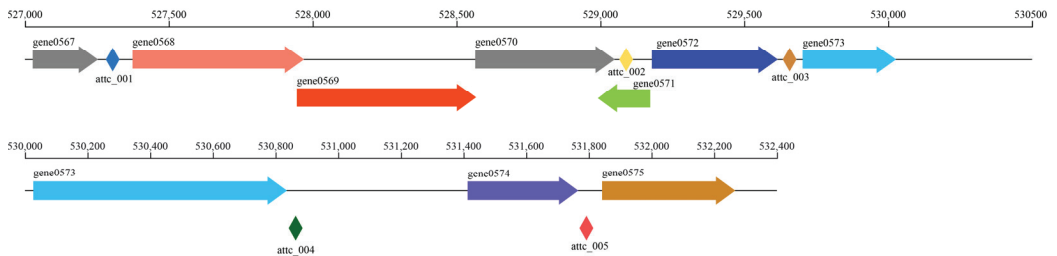
Figure 9. Integron structure diagram (attC is the recombination site necessary for integration).

3.5. Genes Associated with Iron and Sulfur Metabolism

To further understand the whole genome characteristics of *A. ferrooxidans* YQ-N3, its genes related to iron and sulfur metabolism were deeply explored from a functional gene perspective. According to the KEGG annotation results of *A. ferrooxidans* YQ-N3, the genes related to iron and sulfur metabolism are summarized in Table S2. Our findings demonstrated that this strain possesses multiple genes related to Fe^{2+} oxidation metabolism and sulfur metabolism. For example, cyc2, cyc1, coxB, coxA, and coxC, which encode the Rus operon components, were identified in *A. ferrooxidans* YQ-N3. Moreover, hdrB, hdrA, hdrC, tusA, and dsrE, which encode the HdrABC (isodisulfide reductase complex), were also detected. *A. ferrooxidans* is a chemoautotrophic bacterium with a complex energy metabolism pathway, which obtains energy through the oxidation of Fe^{2+} and reduction of sulfur compounds, and generates energy to sustain its growth by fixing carbon and nitrogen in the air [39,40]. The oxidative metabolism of ferrous and sulfur compounds by *A. ferrooxidans* makes this bacterium especially well suited to industrial applications [41]. Previous studies have demonstrated that Fe^{2+} oxidation by *A. ferrooxidans* in the electron transport chain has two patterns, including the downhill potential gradient and the uphill potential gradient [42]. Most electrons generated via Fe^{2+} oxidation pass along the downhill potential gradient. Specifically, electrons generated by Fe^{2+} oxidation enter the cytoplasm from the outer cell membrane, then pass to the cytochrome protein cyc2, after which they are received by rus, a ceruloplasmin, and passed to cyc2, a cytochrome protein. Afterward, they are received by cytochrome oxidase aa3 and then passed to O_2, where they finally combine with protons to generate H_2O [43]. In this process, the oxidation process of the rus operon plays a dominant role, and the rus operon is composed of multiple genes including cyc2, coxA, coxB, coxC, and rus [44]. Furthermore, studies on

the regulation of the expression of key rus operon genes in model microorganisms show that the expression of the rus operon is induced by Fe^{2+} [45,46]. The sqr gene, which encodes the sulfide quinone reductase enzyme, has been previously identified in various *A. ferrooxidans* strains [47]. doxDA encoding thiosulfate quinone reductase was also identified in ATCC23270 and CCM4253. When elemental sulfur was used as an energy source, the transcription level of the heterodisulfide reductase (HdrABC) complex encoded by ten genes including hdrB, hdrA, hdrC2, tusA, and hdrB2 was significantly upregulated, indicating that this complex was related to sulfur metabolism in *A. ferrooxidans* [48]. The query of functional genes confirmed that *A. ferrooxidans* YQ-N3 can oxidize Fe^{2+} and sulfur, but its metabolic pathways require being further explored.

3.6. Oxidation of Fe^{2+}, S^0, and Pyrite

During Fe^{2+} oxidation by *A. ferrooxidans* YQ-N3, the color of the medium gradually shifted from clear light green to yellow–green at first. After 16 h, the medium completely changed to reddish–brown. Then, a yellow precipitate gradually appeared in the reaction system. The blank control group did not exhibit any obvious color change. Figure 10 shows the trends of pH, ORP, Fe^{2+} content, and total iron content of the medium during Fe^{2+} oxidation. According to Figure 10A, the pH in the experiment involving *A. ferrooxidans* YQ-N3 increased from 1.8 to 2.16 after 48 h, and then rapidly decreased to 1.7. ORP also increased throughout the experiment but this trend decelerated slightly after 48 h. In the blank control group, pH and ORP showed a slight upward trend throughout the experiment. This can be attributed to H^+ consumption by the oxidation of Fe^{2+} into Fe^{3+} [49]. Fe^{3+}, SO_4^{2-}, and other cations (e.g., K^+, Na^+, NH_4^+) begin to react as the Fe^{3+} content increases, which results in the production of H^+ and the minerals jarosite ($KFe_3(SO_4)_2(OH)_6$) and ammoniojarosite (($NH_4)_2Fe_6(SO_4)_4(OH)_{12}$) (Figure 11), which is consistent with previous studies [50]. Therefore, the pH rapidly decreased and the ORP increase rate slowed down in the later stage of the experimental group [51]. Figure 10B shows that the Fe^{2+} content in the experiment involving *A. ferrooxidans* YQ-N3 continued to decrease rapidly and the Fe^{2+} content reached 0 mg/L when the reaction reached 60 h. The total iron concentration decreased by approximately 2700 mg/L during the whole reaction period, whereas only 14.5% Fe^{2+} was oxidized and the total iron concentration in the blank control group remained unchanged for 96 h. This can be attributed to the fact that *A. ferrooxidans* YQ-N3 accelerates the oxidation of Fe^{2+}, and the Fe^{3+} generated by the reaction leads to a decrease in the total iron content in the liquid phase. Fe^{2+} is naturally oxidized and generates free Fe^{3+} in the blank control group during the reaction, and therefore the total iron content remained unchanged in the system.
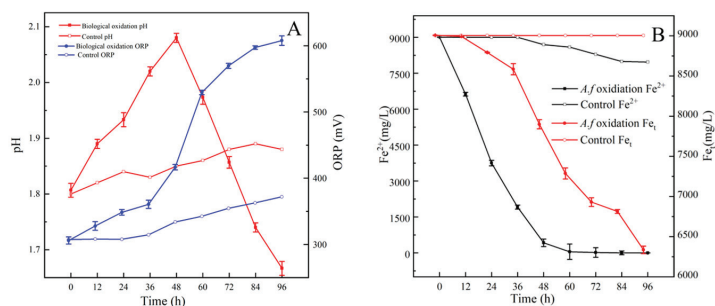
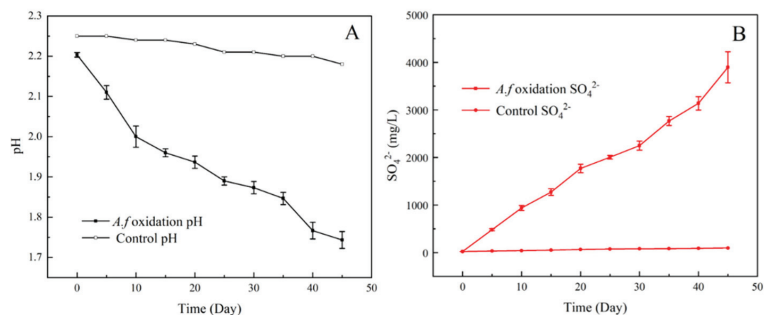**Figure 10.** Trends of physicochemical indexes during Fe^{2+} oxidation by *A. ferrooxidans* YQ-N3.((**A**) is the change of pH and ORP; (**B**) is the change of content Fe^{2+} and total Fe. The error bar represents the standard deviation of three parallel experiments).
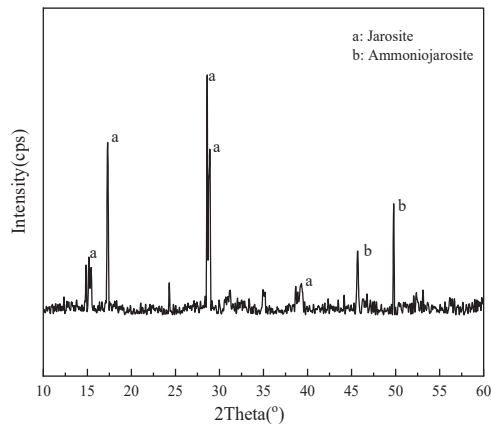
**Figure 11.** XRD pattern of minerals generated by Fe^{2+} oxidated by *A. ferrooxidans* YQ-N3.

During the oxidation of S^0 by *A. ferrooxidans* YQ-N3, the medium gradually changed from clear and colorless to light yellow, the particle size of sulfur powder gradually became smaller, and its hydrophobicity gradually weakened. However, no obvious change was observed during the reaction of the blank control group. This phenomenon was mainly because *A. ferrooxidans* adsorbed on the surface of S when oxidizing it and secreted hydrophilic organic substances that covered the surface of S to enhance its hydrophilicity [52,53]. During the oxidation of S^0 by *A. ferrooxidans* YQ-N3, the pH value of the medium decreased from 2.2 to 1.74, whereas the SO_4^{2-} concentration of the medium increased to 3896.66 mg/L after 45 d (Figure 12). This can be attributed to the release of H^+ through the oxidation of S^0 to SO_4^{2-}.


Figure 12. Trends of physicochemical indexes during S^0 oxidation by *A. ferrooxidans* YQ-N3. ((**A**) is the change of pH; (**B**) is the change of content SO_4^{2-}. The error bar represents the standard deviation of three parallel experiments).

Figure 13 illustrates the trends of pH, ORP, SO_4^{2-}, Fe^{2+}, and Fe_t during pyrite oxidation by *A. ferrooxidans* YQ-N3. In the experimental group, the pH value decreased from 1.9 to 1.2 after 45 d, the ORP increased from 353 to 632 mV after 45 d, the SO_4^{2-} concentration increased to 5433.8 mg/L after 45 d, the Fe^{2+} content decreased drastically from 43.6 mg/L to a negligible level after 23 d, and the Fe_t content increased to 3853 mg/L after 45 d. Characterization by XRD revealed that pyrite oxidized by *A. ferrooxidans* YQ-N3 contains jarosite and FeOOH, in addition to quartz impurities (Figure 14). In the blank control group, the pH value decreased slightly, the ORP decreased and then slightly increased, the SO_4^{2-} concentration increased to 563 mg/L after 45 d, the Fe^{2+} content increased to 178.2 mg/L after 45 d, and the Fe_t concentration increased to 197.7 mg/L after 45 d. This could be because the H^+ released by the oxidation of S^0 into SO_4^{2-} exceeded the levels

consumed by Fe^{2+} oxidation. *A. ferrooxidans* YQ-N3 can accelerate the oxidation of Fe^{2+} to Fe^{3+} and pyrite oxidation can be carried out continuously and rapidly. The dissolved Fe mainly exists in the form of Fe^{3+} in this system, and therefore ORP continues to increase.
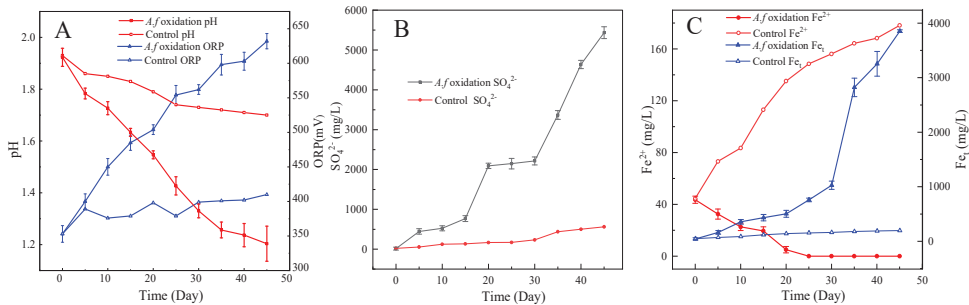
Figure 13. Trends of physicochemical indexes during FeS_2 oxidation by *A. ferrooxidans* YQ-N3. ((**A**) is the change of pH and ORP; (**B**) is the change of content SO_4^{2-}; (**C**) is the change of content Fe^{2+} and total Fe. The error bar represents the standard deviation of three parallel experiments).
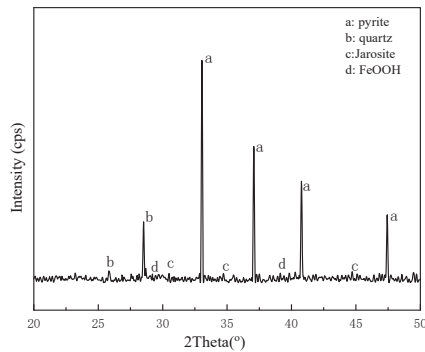

Figure 14. XRD pattern of residues after FeS_2 was oxidated by *A. ferrooxidans* YQ-N3.

The oxidation of different energy substances (Fe^{2+}, S^0, and pyrite) by *A. ferrooxidans* YQ-N3 was investigated via the shake bottle experiment. The results indicate that *A. ferrooxidans* YQ-N3 can accelerate the oxidation of Fe^{2+} and that it contributes to the formation of minerals such as jarosite and ammoniojarosite while also accelerating the oxidation of S^0 and enhancing its hydrophilicity. *A. ferrooxidans* YQ-N3 can also achieve rapid and continuous oxidation of pyrite by accelerating Fe^{2+} oxidation, thereby increasing the ORP. As a result, the pH value decreased, the SO_4^{2-} concentration increased, and minerals (e.g., jarosite and FeOOH) were generated, all of which are hallmarks of the AMD generation process [54]. These findings suggest that *A. ferrooxidans* YQ-N3 can accelerate the production of AMD.

3.7. Desulfurization of Coal

The direct combustion of coal can lead to a variety of environmental pollution problems. For example, the main reason for the formation of acid rain is the SO_2 gas released by the direct combustion of coal [55]. Therefore, it is particularly important to develop efficient desulfurization technology. The microbial desulfurization of coal not only promotes environmental protection but is also highly efficient and consumes few resources [56]. *A. ferrooxidans* is a commonly used coal desulfurization bacteria. Therefore, it is of great significance to study the coal desulfurization ability of *A. ferrooxidans* YQ-N3. The performance of *A. ferrooxidans* YQ-N3 during the coal desulfurization is illustrated in Figure 15.
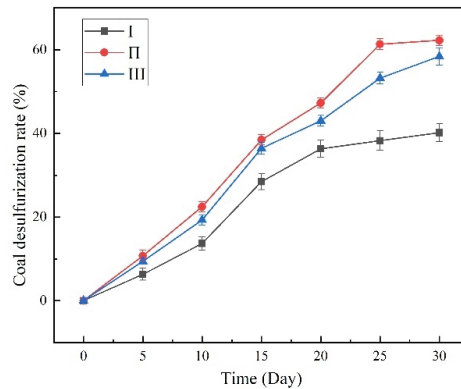
Figure 15. Sulfur removal efficiency during desulfurization.

During the desulfurization process, the sulfur removal rate of *A. ferrooxidans* YQ-N3 on the three coal samples continued to increase, and the sulfur removal rate of coal sample II was higher than that of coal samples III and I. After 30 days of reaction, the total sulfur removal rates of the I, II, and III coal samples were 40.17%, 62.25%, and 58.40%, respectively.

Table 5 shows the coal desulfurization characteristics of strain *A. ferrooxidans* YQ-N3 and other *A. ferrooxidans*. Our findings indicated that the coal desulfurization ability of *A. ferrooxidans* YQ-N3 was at a medium level. This may be due to the fact that the strain only grew in the ferrous environment and was not domesticated in any environment before the coal desulfurization experiments. Domesticated strains in specific environments (e.g., medium containing pyrite) and the optimization of desulfurization experimental parameters may improve the desulfurization capacity of *A. ferrooxidans* YQ-N3 [57].

Table 5. Main characteristics of different desulfurization strains.

Strain	Geographic Origin	Highest Desulfurization Rate for Coal	Desulfurization Reaction Time	References
A. ferrooxidans YY2	Guizhou, China	75%	30 days	[56]
A. ferrooxidans LY01	Guizhou, China	67.8%	13 days	[57]
A. ferrooxidans	Johannesburg, South Africa	79%	14 days	[58]
A. ferrooxidans LX5	China	31.6%	32 days	[59]
A. ferrooxidans DSM 583	-	30.84%	12 h	[60]
A. ferrooxidans YQ-N3	Shanxi, China	62.25%	30 days	This study

"-" indicates no data.

Additionally, coal chemical analysis of coal samples after the desulfurization reaction was carried out. The results showed that the total sulfur content of I after the reaction was 2.07%, including 0.43% pyrite sulfur, 0.36% organic sulfur, and 1.28% sulfate sulfur. The total sulfur content of II was 1.14%, including 0.32% pyrite sulfur, 0.29% organic sulfur, and 0.53% sulfate sulfur. Coal sample III contains 1.165 total sulfur, 0.26% pyrite sulfur, 0.42% organic sulfur, and 0.48% sulfate sulfur. It can be seen that the sulfur removal rate for coal samples with high pyrite content (II) is higher than that for coal samples with high organic sulfur content (III), and higher than that for coal samples with high sulfate sulfur content (I). Some studies showed that the desulfurization capacity of *A. ferrooxidans* is mainly due to the ability of this bacterium to oxidize pyrite in coal [8]. The mechanisms through which *A. ferrooxidans* oxidizes the pyrite in coal can be divided into two modes: direct action and indirect action. The direct action mechanism refers to that during the oxidation of pyrite. Particularly, the bacteria uses the adhesion of fixed organs, pili, or mineral surfaces to directly adsorb on the pyrite surface. Pyrite is directly decomposed

into ferrous ions and sulfur through protein secretion or other metabolites (ferrous oxidase, cytochrome C oxidase, cytochrome oxidoreductase, etc.), and sulfur is further oxidized to SO_4^{2-} by *A. ferrooxidans* [58,61]. Indirect action means that although *A. ferrooxidans* cells adsorb on the surface of minerals, they do not directly oxidize pyrite, but oxidize Fe^{2+} to Fe^{3+} in solution. Fe^{3+} has a strong oxidation ability to oxidize pyrite to release Fe^{2+} and generate H^+ and SO_4^{2-}. Fe^{2+} is further oxidized in solution to generate Fe^{3+}. This process is repeated to continuously remove pyrite from coal [62]. The organic sulfur compounds of coal exist in the form of thiols, mercaptans, sulfide, and disulfide linkages, as well as complex thiophene moieties. Organic sulfur is considered more recalcitrant compared to its inorganic counterparts. Rout et al. reported that the microbial desulfurization process assisted by *A. ferrooxidans* successfully resulted in the removal of 84.75% of organic sulfur from coal samples. The authors also reported that *A. ferrooxidans* performed oxidative desulfurization of the model sulfur-containing organic compound dibenzothiophene to 2-hydroxy biphenyl through the formation of dioxy-dibenzothiophene [9,63]. Therefore, the results of this study have demonstrated that *A. ferrooxidans* YQ-N3 cells are capable of biological desulfurization. Therefore, these cells can be used to oxidize pyrite sulfur and organic sulfur in coal.

4. Conclusions

A novel *A. ferrooxidans* strain was isolated from sediment from a river polluted by the AMD of an abandoned mine in Shanxi, China. Whole genome sequencing analyses revealed that the genome of *A. ferrooxidans* YQ-N3 includes one circular chromosome and five circular plasmids, among which one plasmid had not been annotated in public databases. *A. ferrooxidans* YQ-N3 is closely related to *A. ferrooxidans* ATCC23270 and *A. ferridurans* JCM18981, and its distribution of functional genes is similar to that of *A. ferrooxidans* ATCC23270 and *A. ferrooxidans* BY0502. This newly identified strain possesses multiple genes related to iron and sulfur metabolism. However, additional studies are required to characterize its energy metabolism pathways. The results of functional genome analysis and laboratory experiments jointly demonstrated that *A. ferrooxidans* YQ-N3 can accelerate the oxidation of Fe^{2+}, S^0, and FeS_2. Additionally, a 62.25% total sulfur removal rate was achieved in the biological coal desulfurization experiments conducted in this study. This study not only established a theoretical foundation for future research on the generation and treatment of AMD but also isolated a new bacterial strain that could be used for industrial desulfurization, biometallurgy, and the disposal of waste electronic products.

References

1. Zhan, Y.; Yang, M.R.; Zhang, S.; Zhao, D.; Duan, J.G.; Wang, W.D.; Yan, L. Iron and sulfur oxidation pathways of Acidithiobacillus ferrooxidans. *World J. Microbiol. Biotechnol.* **2019**, *35*, 12. [CrossRef] [PubMed]
2. Moinier, D.; Byrne, D.; Amouric, A.; Bonnefoy, V. The Global Redox Responding RegB/RegA Signal Transduction System Regulates the Genes Involved in Ferrous Iron and Inorganic Sulfur Compound Oxidation of the Acidophilic *Acidithiobacillus ferrooxidans*. *Front. Microbiol.* **2017**, *8*, 16. [CrossRef] [PubMed]
3. Zhang, S.; Yan, L.; Xing, W.J.; Chen, P.; Zhang, Y.; Wang, W.D. *Acidithiobacillus ferrooxidans* and its potential application. *Extremophiles* **2018**, *22*, 563–579. [CrossRef]
4. Iakovleva, E.; Mäkilä, E.; Salonen, J.; Sitarz, M.; Wang, S.B.; Sillanpää, M. Acid mine drainage (AMD) treatment: Neutralization and toxic elements removal with unmodified and modified limestone. *Ecol. Eng.* **2014**, *81*, 30–40. [CrossRef]
5. Valdes, J.; Pedroso, I.; Quatrini, R.; Dodson, R.J.; Tettelin, H.; Blake, R.; Eisen, J.A.; Holmes, D.S. *Acidithiobacillus ferrooxidans* metabolism: From genome sequence to industrial applications. *BMC Genom.* **2008**, *9*, 24. [CrossRef]
6. Lorenzo-Tallafigo, J.; Iglesias-González, N.; Mazuelos, A.; Romero, R.; Carranza, F. An alternative approach to recover lead, silver and gold from black gossan (polymetallic ore). Study of biological oxidation and lead recovery stages. *J. Clean. Prod.* **2019**, *207*, 510–521. [CrossRef]
7. Nie, H.Y.; Yang, C.; Zhu, N.W.; Wu, P.X.; Zhang, T.; Zhang, Y.Q.; Xing, Y.J. Isolation of *Acidithiobacillus ferrooxidans* strain Z1 and its mechanism of bioleaching copper from waste printed circuit boards. *J. Chem. Technol. Biotechnol.* **2015**, *90*, 714–721. [CrossRef]
8. Yang, M.R.; Zhan, Y.; Zhang, S.; Wang, W.D.; Yan, L. Biological materials formed by *Acidithiobacillus ferrooxidans* and their potential applications. *3 Biotech* **2020**, *10*, 9. [CrossRef]
9. Rout, P.G.; Mohanty, A.K.; Pradhan, N.; Biswal, S.K.; Behera, S.K. Study on the Reaction Mechanism of Oxidative Microbial Desulfurization of Organic Sulfur-Rich Coal. *Geomicrobiol. J.* **2022**, *39*, 210–218. [CrossRef]
10. Lavalle, L.; Chiacchiarini, P.; Pogliani, C.; Donati, E. Isolation and characterization of acidophilic bacteria from Patagonia, Argentina. *Process Biochem.* **2005**, *40*, 1095–1099. [CrossRef]
11. Kai, M.; Yano, T.; Fukumori, Y.; Yamanaka, T. Cytochrome oxidase of an acidophilic iron-oxidizing bacterium, *Thiobacillus ferrooxidans*, functions at pH 3.5. *Biochem. Biophys. Res. Commun.* **1989**, *160*, 839–843. [CrossRef] [PubMed]
12. Rhoads, A.; Au, K.F. PacBio Sequencing and Its Applications. *Genom. Proteom. Bioinform.* **2015**, *13*, 278–289. [CrossRef] [PubMed]
13. Delcher, A.L.; Bratke, K.A.; Powers, E.C.; Salzberg, S.L. Identifying bacterial genes and endosymbiont DNA with Glimmer. *Bioinformatics* **2007**, *23*, 673–679. [CrossRef]
14. Besemer, J.; Borodovsky, M. GeneMark: Web software for gene finding in prokaryotes, eukaryotes and viruses. *Nucleic Acids Res.* **2005**, *33*, W451–W454. [CrossRef] [PubMed]
15. Bertelli, C.; Laird, M.R.; Williams, K.P.; Lau, B.Y.; Hoad, G.; Winsor, G.L.; Brinkman, F.S.L.; Simon Fraser Univ Res Comp, G. IslandViewer 4: Expanded prediction of genomic islands for larger-scale datasets. *Nucleic Acids Res.* **2017**, *45*, W30–W35. [CrossRef] [PubMed]
16. Fouts, D.E. Phage_Finder: Automated identification and classification of prophage regions in complete bacterial genome sequences. *Nucleic Acids Res.* **2006**, *34*, 5839–5851. [CrossRef] [PubMed]
17. Bland, C.; Ramsey, T.L.; Sabree, F.; Lowe, M.; Brown, K.; Kyrpides, N.C.; Hugenholtz, P. CRISPR Recognition Tool (CRT): A tool for automatic detection of clustered regularly interspaced palindromic repeats. *BMC Bioinform.* **2007**, *8*, 8. [CrossRef]
18. Cury, J.; Jove, T.; Touchon, M.; Neron, B.; Rocha, E.P.C. Identification and analysis of integrons and cassette arrays in bacterial genomes. *Nucleic Acids Res.* **2016**, *44*, 4539–4550. [CrossRef]
19. Chen, J.J.; Liu, Y.L.; Diep, P.; Mahadevan, R. Genomic Analysis of a Newly Isolated *Acidithiobacillus ferridurans* JAGS Strain Reveals Its Adaptation to Acid Mine Drainage. *Minerals* **2021**, *11*, 14. [CrossRef]
20. Akcil, A.; Ciftci, H.; Deveci, H. Role and contribution of pure and mixed cultures of mesophiles in bioleaching of a pyritic chalcopyrite concentrate. *Miner. Eng.* **2007**, *20*, 310–318. [CrossRef]
21. Gonzalez-Toril, E.; Llobet-Brossa, E.; Casamayor, E.O.; Amann, R.; Amils, R. Microbial ecology of an extreme acidic environment, the Tinto river. *Appl. Environ. Microbiol.* **2003**, *69*, 6959. [CrossRef]
22. Umanskii, A.B.; Klyushnikov, A.M. Bioleaching of low grade uranium ore containing pyrite using *A. ferrooxidans* and *A. thiooxidans*. *J. Radioanal. Nucl. Chem.* **2013**, *295*, 151–156. [CrossRef]
23. Zhang, Y.; Zhang, S.; Zhao, D.; Ni, Y.Q.; Wang, W.D.; Yan, L. Complete Genome Sequence of *Acidithiobacillus ferrooxidans* YNTRS-40, a Strain of the Ferrous Iron- and Sulfur-Oxidizing Acidophile. *Microorganisms* **2020**, *8*, 10. [CrossRef]
24. Hinger, I.; Ansorge, R.; Mussmann, M.; Romano, S. Phylogenomic Analyses of Members of the Widespread Marine Heterotrophic Genus *Pseudovibrio* Suggest Distinct Evolutionary Trajectories and a Novel Genus, Polycladidibacter gen. nov. *Appl. Environ. Microbiol.* **2020**, *86*, 17. [CrossRef]
25. Hemme, C.L.; Green, S.J.; Rishishwar, L.; Prakash, O.; Pettenato, A.; Chakraborty, R.; Deutschbauer, A.M.; Van Nostrand, J.D.; Wu, L.Y.; He, Z.L.; et al. Lateral Gene Transfer in a Heavy Metal-Contaminated-Groundwater Microbial Community. *mBio* **2016**, *7*, 14. [CrossRef] [PubMed]
26. Acosta, M.; Beard, S.; Ponce, J.; Vera, M.; Mobarec, J.C.; Jerez, C.A. Identification of putative sulfurtransferase genes in the extremophilic *Acidithiobacillus ferrooxidans* ATCC 23270 genome: Structural and functional characterization of the proteins. *Omics* **2005**, *9*, 13–29. [CrossRef] [PubMed]

27. Mealman, T.D.; Blackburn, N.J.; McEvoy, M.M. Metal export by CusCFBA, the periplasmic Cu(I)/Ag(I) transport system of Escherichia coli. *Curr. Top. Membr.* **2012**, *69*, 163–196.
28. Chacon, K.N.; Perkins, J.; Mathe, Z.; Alwan, K.; Ho, E.N.; Ucisik, M.N.; Merz, K.M.; Blackburn, N.J. Trapping intermediates in metal transfer reactions of the CusCBAF export pump of *Escherichia coli*. *Commun. Biol.* **2018**, *1*, 11. [CrossRef]
29. Almarcegui, R.J.; Navarro, C.A.; Paradela, A.; Albar, J.P.; von Bernath, D.; Jerez, C.A. Response to copper of *Acidithiobacillus ferrooxidans* ATCC 23270 grown in elemental sulfur. *Res. Microbiol.* **2014**, *165*, 761–772. [CrossRef]
30. Wenbin, N.; Dejuan, Z.; Feifan, L.; Lei, Y.; Peng, C.; Xiaoxuan, Y.; Hongyu, L.; Nan, W.B.; Dejuan, L.Z.; Feifan, Y.; et al. Quorum-sensing system in *Acidithiobacillus ferrooxidans* involved in its resistance to Cu^{2+}. *Lett. Appl. Microbiol.* **2011**, *53*, 84–91. [CrossRef]
31. Popa, O.; Hazkani-Covo, E.; Landan, G.; Martin, W.; Dagan, T. Directed networks reveal genomic barriers and DNA repair bypasses to lateral gene transfer among prokaryotes. *Genome Res.* **2011**, *21*, 599–609. [CrossRef] [PubMed]
32. Polz, M.F.; Alm, E.J.; Hanage, W.P. Horizontal gene transfer and the evolution of bacterial and archaeal population structure. *Trends Genet.* **2013**, *29*, 170–175. [CrossRef]
33. Coutinho, T.J.D.; Franco, G.R.; Lobo, F.P. Homology-Independent Metrics for Comparative Genomics. *Comp. Struct. Biotechnol. J.* **2015**, *13*, 352–357. [CrossRef] [PubMed]
34. Dominguez-Mirazo, M.; Jin, R.; Weitz, J.S. Functional and comparative genomic analysis of integrated prophage-like sequences in "candidatus liberibacter asiaticus". *mSphere* **2019**, *4*, 409–419. [CrossRef] [PubMed]
35. Cady, K.C.; Bondy-Denomy, J.; Heussler, G.E.; Davidson, A.R.; O'Toole, G.A. The CRISPR/Cas Adaptive Immune System of Pseudomonas aeruginosa Mediates Resistance to Naturally Occurring and Engineered Phages. *J. Bacteriol.* **2012**, *194*, 5728–5738. [CrossRef] [PubMed]
36. Dopson, M.; Holmes, D.S. Metal resistance in acidophilic microorganisms and its significance for biotechnologies. *Appl. Microbiol. Biotechnol.* **2014**, *98*, 8133–8144. [CrossRef] [PubMed]
37. Nies, D.H. Efflux-mediated heavy metal resistance in prokaryotes. *Fems Microbiol. Rev.* **2003**, *27*, 313–339. [CrossRef]
38. Hemme, C.L.; Deng, Y.; Gentry, T.J.; Fields, M.W.; Wu, L.Y.; Barua, S.; Barry, K.; Tringe, S.G.; Watson, D.B.; He, Z.L.; et al. Metagenomic insights into evolution of a heavy metal-contaminated groundwater microbial community. *ISME J.* **2010**, *4*, 660–672. [CrossRef]
39. Hallberg, K.B.; Gonzalez-Toril, E.; Johnson, D.B. *Acidithiobacillus ferrivorans*, sp nov.; facultatively anaerobic, psychrotolerant iron-, and sulfur-oxidizing acidophiles isolated from metal mine-impacted environments. *Extremophiles* **2010**, *14*, 9–19. [CrossRef]
40. Bonnefoy, V.; Holmes, D.S. Genomic insights into microbial iron oxidation and iron uptake strategies in extremely acidic environments. *Environ. Microbiol.* **2012**, *14*, 1597–1611. [CrossRef]
41. Ponce, J.S.; Moinier, D.; Byrne, D.; Amouric, A.; Bonnefoy, V. Acidithiobacillus ferrooxidans oxidizes ferrous iron before sulfur likely through transcriptional regulation by the global redox responding RegBA signal transducing system. *Hydrometallurgy* **2012**, *127*, 187–194. [CrossRef]
42. Johnson, D.B.; Hallberg, K.B. Carbon, Iron and Sulfur Metabolism in Acidophilic Micro-Organisms. In *Advances in Microbial Physiology*; Poole, R.K., Ed.; Academic Press Ltd-Elsevier Science Ltd: London, UK, 2009; Volume 54, pp. 201–255.
43. Bird, L.J.; Bonnefoy, V.; Newman, D.K. Bioenergetic challenges of microbial iron metabolisms. *Trends Microbiol.* **2011**, *19*, 330–340. [CrossRef] [PubMed]
44. Yarzabal, A.; Appia-Ayme, C.; Ratouchniak, J.; Bonnefoy, V. Regulation of the expression of the *Acidithiobacillus ferrooxidans* rus operon encoding two cytochromes c, a cytochrome oxidase and rusticyanin. *Microbiology* **2004**, *150*, 2113–2123. [CrossRef] [PubMed]
45. Amouric, A.; Appia-Ayme, C.; Yarzabal, A.; Bonnefoy, V. Regulation of the iron and sulfur oxidation pathwayways in the acidophilic *A. Ferrooxidans*. *Adv. Mater. Res.* **2009**, *71–73*, 163–166. [CrossRef]
46. Kucera, J.; Bouchal, P.; Lochman, J.; Potesil, D.; Janiczek, O.; Zdrahal, Z.; Mandl, M. Ferrous iron oxidation by sulfur-oxidizing *Acidithiobacillus ferrooxidans* and analysis of the process at the levels of transcription and protein synthesis. *Antonie Van Leeuwenhoek* **2013**, *103*, 905–919. [CrossRef]
47. Wakai, S.; Tsujita, M.; Kikumoto, M.; Manchur, M.A.; Kanao, T.; Kamimura, K. Purification and characterization of sulfide: Quinone oxidoreductase from an acidophilic iron-oxidizing bacterium, acidithiobacillus ferrooxidans. *Biosci. Biotechnol. Biochem.* **2007**, *71*, 2735–2742. [CrossRef]
48. Liu, Y.D.; Ji, J.J.; Yu, R.L.; Qiu, G.Z. Expression, Purification and Molecular Modeling of Another HdrC from *Acidithiobacillus ferrooxidans* Which Binds Only One 4Fe-4S Cluster. *Curr. Microbiol.* **2012**, *65*, 416–423. [CrossRef]
49. Offeddu, F.G.; Cama, J.; Soler, J.M.; Dávila, G.; McDowell, A.; Craciunescu, T. Processes affecting the efficiency of limestone in passive treatments for AMD: Column experiments. *J. Environ. Chem. Eng.* **2015**, *3*, 304–316. [CrossRef]
50. Nazari, B.; Jorjani, E.; Hani, H.; Manfi, Z.; Riahi, A. Formation of jarosite and its effect on important ions for *A. ferrooxidan*s bacteria. *Trans. Nonferrous Met. Soc. China* **2014**, *24*, 1152–1160. [CrossRef]
51. Li, W.B.; Feng, Q.Y.; Liang, H.Q.; Chen, D.; Li, X.D. Passive treatment test of acid mine drainage from an abandoned coal mine in Kaili Guizhou, China. *Water Sci. Technol.* **2021**, *84*, 1981–1996.
52. Konishi, Y.; Asai, S.; Yoshida, N. Growth Kinetics of *Thiobacillus thiooxidans* on the Surface of Elemental Sulfur. *Appl. Environ. Microbiol.* **1995**, *61*, 3617–3622. [CrossRef]

53. Knickerbocker, C.; Nordstrom, D.K.; Southam, G. The role of "blebbing" in overcoming the hydrophobic barrier during biooxidation of elemental sulfur by *Thiobacillus thiooxidans*. *Chem. Geol.* **2000**, *169*, 425–433. [CrossRef]
54. Kuang, J.L.; Huang, L.N.; Chen, L.X.; Hua, Z.S.; Li, S.J.; Hu, M.; Li, J.T.; Shu, W.S. Contemporary environmental variation determines microbial diversity patterns in acid mine drainage. *ISME J.* **2013**, *7*, 1038–1050. [CrossRef] [PubMed]
55. Cardona, I.C.; Marquez, M.A. Biodesulfurization of two Colombian coals with native microorganisms. *Fuel Process. Technol.* **2009**, *90*, 1099–1106. [CrossRef]
56. Yang, X.; Wang, S.; Liu, Y.; Zhang, Y. Identification and characterization of *Acidithiobacillus ferrooxidans* YY2 and its application in the biodesulfurization of coal. *Can. J. Microbiol.* **2015**, *61*, 65–71. [CrossRef]
57. Yang, X.P.; Wang, S.M.; Liu, Y.J.; Liang, Y. A Comparative Study of the Biodesulfurization Efficiency of *Acidithiobacillus ferrooxidans* LY01 Cells Domesticated with Ferrous Iron and Pyrite. *Geomicrobiol. J.* **2016**, *33*, 488–493. [CrossRef]
58. Newman, D.K. Feasting on Minerals. *Science* **2010**, *327*, 793–794. [CrossRef]
59. Liu, F.W.; Lei, Y.S.; Shi, J.; Zhou, L.X.; Wu, Z.H.; Dong, Y.; Bi, W.L. Effect of microbial nutrients supply on coal bio-desulfurization. *J. Hazard. Mater.* **2020**, *384*, 10. [CrossRef]
60. Arslan, V. The application of combined lignite cleaning processes, bacterial leaching and flotation, for reducing higher ash and sulfur contents. *Int. J. Coal Prep. Util.* **2022**, *42*, 2114–2126. [CrossRef]
61. Silva, R.A.; Park, J.; Ilyas, S.; Borja, D.; Zhao, H.B.; Urik, M.; Rastegar, S.O.; Kim, H. Biodegradation mechanism of arsenopyrite mine tailing with *Acidithiobacillus ferrooxidans* and influence of ferric supplements. *Int. Biodeterior. Biodegrad.* **2020**, *153*, 6. [CrossRef]
62. Schippers, A. Sand, Bacterial leaching of metal sulfides proceeds by two indirect mechanisms via thiosulfate or via polysulfides and sulfur. *Appl. Environ. Microbiol.* **1999**, *65*, 319–321. [CrossRef] [PubMed]
63. Chen, Z.H.; Huang, X.Y.; He, H.; Tang, J.L.; Tao, X.X.; Huang, H.Z.; Haider, R.; Ali, M.I.; Jamal, A.; Huang, Z.X. Bioleaching Coal Gangue with a Mixed Culture of *Acidithiobacillus ferrooxidans* and *Acidithiobacillus thiooxidans*. *Minerals* **2021**, *11*, 11. [CrossRef]

Review

Progress of Mine Land Reclamation and Ecological Restoration Research Based on Bibliometric Analysis

Ya Shao [1], Qinxue Xu [2],* and Xi Wei [1]

[1] College of Earth Sciences, Guilin University of Technology, Guilin 541004, China; yshao@glut.edu.cn (Y.S.); 1020210012@glut.edu.cn (X.W.)

[2] College of Environmental Science and Engineering, Guilin University of Technology, Guilin 541004, China

* Correspondence: xqx@glut.edu.cn

Abstract: The mining of mineral resources has caused serious damage to land and significant pressure on ecological environment. During the repairing of damaged land and degraded ecosystems, there have been many pieces of literature related to land reclamation and ecological restoration (LRER) that have emerged. To understand the progress and prospect of LRER research, it is necessary to sort out such pieces of literature, analyze the current research status, and forecast the future research directions. Here, Bibliometrix R-package was used to analyze 2357 articles, which were derived from the core database of Web of Science, to explore the development of LRER from 1990 to 2022. The results are as follows. (1) The annual scientific output results show that both the number of articles published on LRER and the number of articles annually cited were increasing gradually from 1990 to 2022. (2) High-frequency keyword analysis indicates that heavy metal (Cd, Pb) pollution remediation is a research hotspot. The cluster analysis (CA) and multiple correspondence analysis (MCA) show that there are two clusters in the current research of LRER, in which one surrounds heavy metal pollution and the other focuses on ecological restoration of mining areas. The two clusters correspond to the remediation and ecological restoration (rehabilitation) stages of stepwise ecological restoration, respectively. Thematic evolution analysis shows that, for more than 30 years, mine drainage and heavy metal pollution treatment, soil reconstruction (soil profile reconstruction, soil improvement), and vegetation restoration have been the focus of research. (3) Future research should focus on the relationship between mine ecological restoration and carbon sequestration and the relationship between ecological restoration and biodiversity in mine areas. In addition, LRER technology exchange, international cooperation, and industrialization are also main directions of development. Generally, in this study, metrology software (Bibliometrix R-package 3.1.4) from the literature was used to sort out the relevant literature on LRER over the past 30 years so as to provide reference for future research on LRER.

Keywords: mine; land reclamation and ecological restoration (LRER); research status; research directions; Web of Science; Bibliometrix

1. Introduction

The mining industry is a large contributor to the global economy and has been developing since the industrial revolution [1]. The mining of metal minerals, non-metallic minerals, and organic minerals leads to many ecological and environmental problems, for example, land excavation and occupation, surface subsidence, soil erosion, desertification, land pollution, and biodiversity loss [2,3]. Open-pit mining can cause drastic disturbances to regional ecosystem and soil properties [4], resulting in a significant loss of soil nutrients (soil organic carbon, total nitrogen) [5]. Compared with open-pit mining, underground mining inevitably causes a large amount of land subsidence [6]. For example, underground coal mining with high ground-water level can cause many environmental problems, of which the most serious are subsidence and waterlogging [7]. In addition, mining is a significant source of soil heavy metal pollution [8].

In recent years, the United Nations (UN) Sustainable Development Goals (SDGs) for 2030 call for restoration of degraded terrestrial ecosystems (Goal 15) to "protect, restore and promote sustainable use of terrestrial ecosystems, . . . halt and reverse land degradation and halt biodiversity loss" [9]. The Convention on Biological Diversity (2016) called for the "restoration of degraded natural and semi-natural ecosystems, . . . as a contribution to . . . adapting to the effects of climate change, combating desertification and land degradation" [10]. In addition, the United Nations General Assembly has declared 2021–2030 as the Decade of Ecosystem Restoration [11]. A series of development goals and initiatives of the United Nations have put forward that it is urgent to restore various ecosystems, including mine ecosystems, to protect biodiversity and improve ecosystem stability and sustainability.

During the repairing of damaged land and degraded ecosystems, there are many pieces of research literature that have emerged, involving a lot of relevant terms, for example, ecological restoration, ecosystem restoration, mitigation hierarchy, eco-compensation (biodiversity, ecosystems), reclamation, rehabilitation, remediation, repurposing, revegetation, etc. [12,13]. According to Mine closure and reclamation—Vocabulary (ISO 20305:2020(E)—2020), reclamation (rehabilitation) is defined as "reinstating of disturbed land, associated with a mine or a mine feature to be safe, stable, non-polluting and consistent with the agreed post mining land use" [14]. The Society for Ecological Restoration's international standards (SER Standards), second edition, defines reclamation as "the process of making severely degraded land fit for cultivation or a state suitable for some human use" [13]. For ecological restoration, SER Standards have been proposed four times, and the latest one is that "ecological restoration is the process of assisting the recovery of an ecosystem that has been degraded, damaged, or destroyed" [13,15]. Classic ecological terminology regards rehabilitation, reclamation, and restoration as terms with similar goals [15]. Usually, reclamation is often used in the USA and UK, restoration is used in the UK sometimes, and rehabilitation is often used in Australia and Canada [16]. Remediation aims to remove degradation to achieve safe, stable, and non-polluting landscapes, and it is a precondition for ecological restoration, reclamation, or rehabilitation after mining [12]. Some scholars also believe that, except for restoration, reclamation, and rehabilitation, it is necessary to add a term "ecological reclamation" and define it [17]. From the above literature, it can be seen that there are many terms related to mine restorative practices, and their use in the academic community is quite chaotic. Although the terminology is different, the work content is quite similar or the same. In recent years, land reclamation and ecological restoration are often used side by side in many international academic conferences, for example, the first international symposium on LRER was held in Beijing, China, 2014, the second international symposium on LRER was held in Xi'an, Shaanxi, 2017, and the third international symposium on LRER was held in Xuzhou, Jiangsu, 2021. The convening of three international conferences indicates a trend towards gradually unifying terminology in this field. LRER is so important that it has become one of the academic research focuses. However, due to the large amount of terms in this field, the literature on LRER lacks systematic induction and sorting. How have scholars progressed in research on LRER so far? There should be more information to be obtained. Hence, relevant methods, such as the bibliometric method, are needed for literature analysis. Using bibliometrics for science mapping, we can answer three general types of research questions (the knowledge base, the research front, and the social network of scientific collaborations) [18].

Therefore, to clarify the development of existing research on LRER and to better grasp the future trend, in this study, the Bibliometrix R-package was used to systematically summarize and sort out the literature on LRER included in the core database of Web of Science between 1990 and 2022. The objectives of this study are as follows:

(1) To render a review of the research on LRER from 1990 to 2022 (dataset, sources, authors, and documents).

(2) To research the collaboration network feature among countries/institutions in the field.

(3) To analyze the current research status and explore future research directions of LRER.

2. Materials and Methods

The Bibliometrix R-package (http://www.bibliometrix.org (accessed on 1 January 2023)) provides a set of tools for quantitative research in bibliometrics and scientometrics [18]. Biblioshiny helps users perform relevant bibliometric and visual analysis on an interactive web interface and reduce the difficulty of literature analysis operations [19]. The Web of Science has the world's largest set of comprehensive academic resources with the most disciplines, covering more than 12,000 academic journals in natural sciences, engineering, biomedicine, social sciences, arts, humanities, and so on [20]. The Web of Science core database was used as the data source for retrieval, and the retrieval terms used were TS = ("ecological restoration" or "ecosystem restoration" or "reclamation" or "restoration" or "rehabilitation" or "revegetation" or "remediation" or "mitigation hierarchy" or "repurpose") and TS = ("mining industry" or "mining area" or "mining site" or "mine site" or "mined land"). The time span of the retrieval was set as 1990–2022. Literature types were limited to "Article", "Proceeding paper", "Review Article", "Early Access", and "Data Paper". The search language was English. After eliminating reduplicative and irrelevant data, a total of 2357 documents on LRER were obtained. The download data were converted to R data frame.

After data collection and conversion, the articles were analyzed using the Bibliometrix. Firstly, we analyzed the dataset, authors, sources, and documents on LRER, including annual scientific production, average citation per year, corresponding author's country, most relevant affiliations, most relevant sources, globally most cited documents, and high-frequency keywords, so as to give an overview of the research in that field from 1990 to 2022. Secondly, we analyzed cooperation between countries and institutions to find out the feature of a collaboration network. Finally, the conceptual structure, including topic dendrogram and thematic evolution, was analyzed to obtain the current research topics and future research directions for LRER (Figure 1).
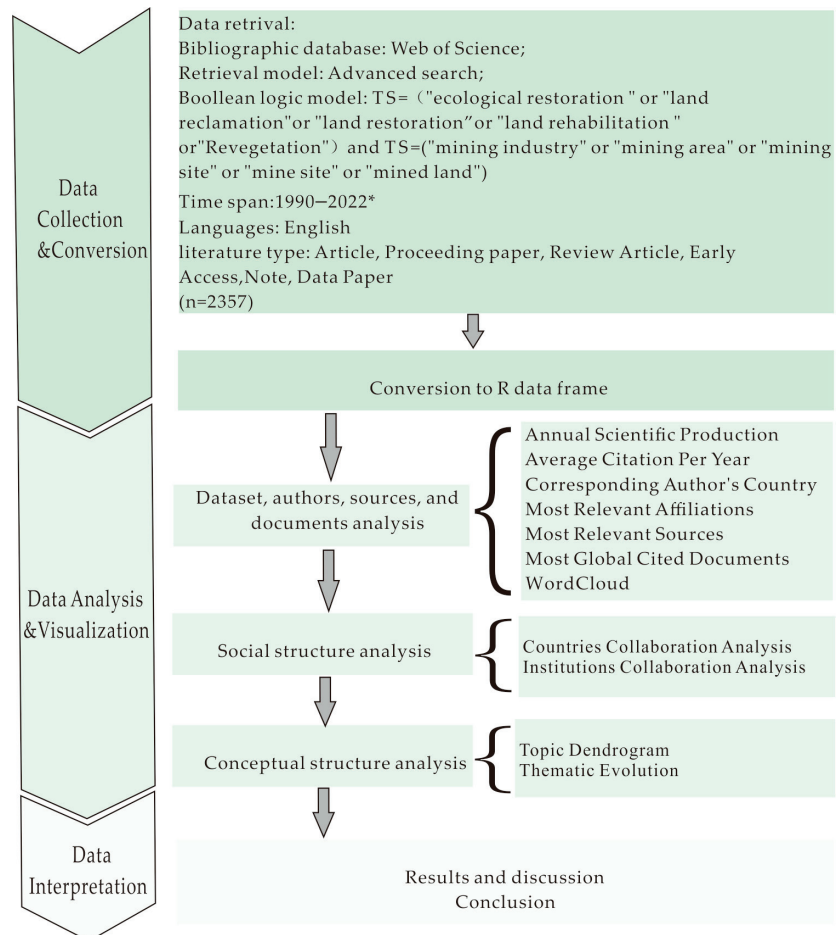
Figure 1. Technical flow of the Bibliometrics approach (* as of 15 January 2023).

3. Results and Analysis

3.1. Analysis of the Annual Scientific Production on LRER

The research progress on LRER can be obtained by counting the number of documents published each year. From 1990 to 2022, the number of papers published on LRER showed an increasing trend year on year (Figure 2), indicating that LRER attracted more and more attention of scholars. From 1990 to 2000, the total number of published relevant papers was 124, with an annual average number less than 20, accounting for only 7.47% of the total number. The annual growth of papers was low and slow, indicating, at that stage, the research on LRER was still in its infancy. Subsequently, between 2001 and 2014, published relevant papers increased significantly, with an average annual number of about 50, indicating that LRER research was closely related to socio-economic development during that period and more and more scholars paid attention to it. After 2015, the number of published relevant papers on LRER continued to increase significantly. In particular, the number of papers published in 2021 and 2022 reached 255 and 261, respectively. It can be seen that LRER has become a hotspot of current research.
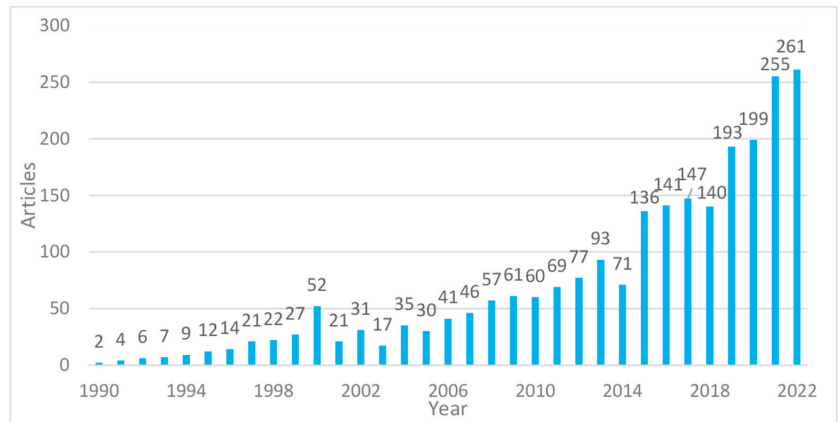
Figure 2. Numbers of relevant papers published each year from 1990 to 2022.

3.2. Analysis of Literature Citations on LRER

3.2.1. Annual Citation Rate

The annual average citation rate of pieces of literature on LRER is gradually increasing (Figure 3). The citation rate in 1990–2000 was very low (<1), indicating that the research was still in the initial stage of exploration and did not yet receive widespread attention of researchers. The average citation frequencies during 2001–2015 and 2009–2022 were 1.51 and 2.39, respectively. It peaked in 2018 (3.41). From 2018 to 2020, the citation frequency of the literature remained at a historical high level. In general, the number of citations has been increasing over time, indicating that the influence of LRER is increasing.
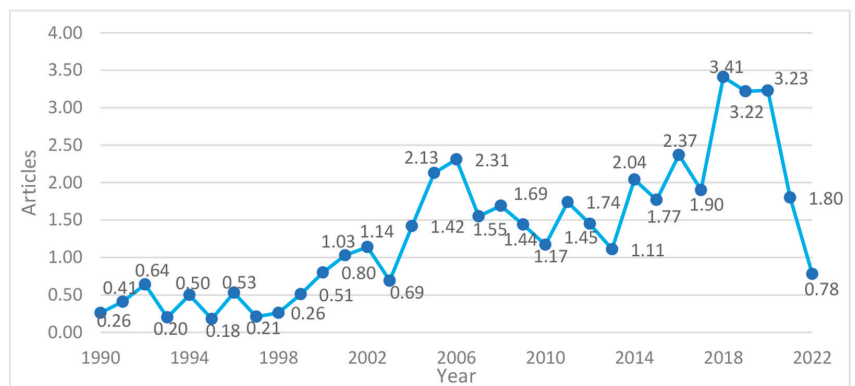
Figure 3. Average total citation rates per year on LRER from 1990 to 2022.

3.2.2. Analysis of Highly Cited Articles

Table 1 shows the top 10 most cited publications on LRER from 1990 to 2022. Among the literature related to LRER published from 1990 to 2022, the most frequently cited article in the world is the one titled Heavy Metal Removal Mechanism of Acid Mine Drainage in Wetlands: a Critical Review, published in Minerals Engineering by AS Sheoran and V. Sheoran [21] of Jai Jai Narain Vyas University, with 474 citations worldwide. Since about 1985, passive treatment has been used more and more frequently as a method for treating acid mine drainage [22]. In that article, the latest progress of passive treatment systems in constructed wetlands was reviewed, and suggestions were made for new trends in the development of passive treatment technology. The article further promoted the development of passive treatment technology for acid mine drainage. The second most

frequently cited article is Metal Contamination of Soils and Crops Affected by the Chenzhou Lead/Zinc Mine Spill (Hunan, China), published in Science of the Total Environment by Hongyu Liu et al. [23] of Hunan University, with 473 citations worldwide. The article showed that frequent mining activities caused heavy metal contamination in large areas of farmlands. The article pointed out that the heavy metal accumulation effect was not entirely depending on total element concentrations in soil. The article has important reference value for the research on remediation of heavy metal pollution in mines. The third most frequently cited article is Arsenic and Heavy Metal Pollution of Soil, Water and Sediments in a Semi-Arid Climate Mining Area in Mexico, with 296 citations worldwide [24]. The article assessed the impact of mining on environment and identified the main factors involved in the dispersion of arsenic and heavy metals under semi-arid conditions. It is of great significance to control arsenic and heavy metal pollution under semi-arid conditions.

Table 1. Top 10 most cited publications on LRER from 1990 to 2022.

Rank	Paper	DOI	Year	Journal	TC
1	SHEORAN AS, 2006, MINER ENG	10.1016/j.mineng.2005.08.006	2006	Minerals Engineering	474
2	LIU HY, 2005, SCI TOTAL ENVIRON	10.1016/j.scitotenv.2004.07.030	2005	Science of the Total Environment	473
3	RAZO I, 2004, WATER AIR SOIL POLL	10.1023/B:WATE.0000015350.14520.c1	2004	Water Air and Soil Pollution	296
4	LI MS, 2007, ENVIRON POLLUT	10.1016/j.envpol.2006.08.006	2007	Environmental Pollution	264
5	LI MS, 2006, SCI TOTAL ENVIRON	10.1016/j.scitotenv.2005.05.003	2014	Science of the Total Environment	264
6	YU HY, 2016, ENVIRON POLLUT	10.1016/j.envpol.2015.11.021	2006	Environmental Pollution	197
7	QIAO JT, 2018, CHEMOSPHERE	10.1016/j.chemosphere.2017.12.081	2018	Chemosphere	192
8	SHRESTHA RK, 2011, GEODERMA	10.1016/j.geoderma.2010.12.015	2011	Geoderma	173
9	RIOS CA, 2008, J HAZARD MATER	10.1016/j.jhazmat.2007.11.123	2008	Journal of Hazardous Materials	170
10	MACINTOSH DJ, 2002, ESTUAR COAST SHELF S	10.1006/ecss.2001.0896	2002	Estuarine Coastal and Shelf Science	169

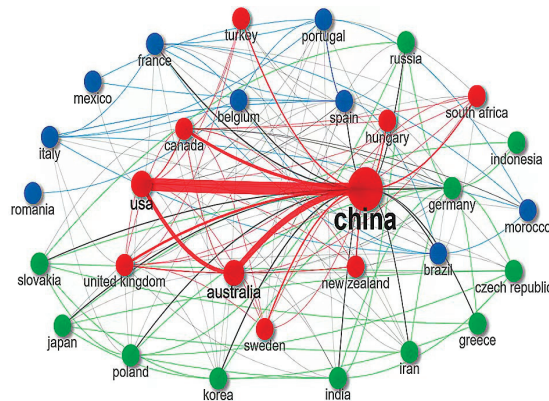*3.3. Main Countries/Regions Conducting Research on LRER*

According to our statistic (Table 2), the ten countries with the most publications on LRER are China, Australia, the USA, Canada, Germany, Poland, India, Spain, Brazil, and the UK. The publications of the top five countries accounted for 28.26%, 10.82%, 9.63%, 6.07%, and 3.52%, respectively, indicating those countries made the greatest contributions to the research on LRER. For example, in China, there are many studies on LRER in coal mining areas, and the research areas are mainly concentrated in ecologically fragile areas in Northwest China [4,25–44] and high water level areas in Eastern China [6,45–52]. The research focuses include reclamation of open-pit coal mines [8,38,39,53–58], reclamation of coal mining subsidence sites [7,51,59–77], and ecological restoration of coal gangue hills [78–80]. The research objects of LRER in the USA are extensive, from restoration of open pit coal mines to reclamation of various production and construction projects, and the research focuses are acid mine drainage treatment [81–83], soil reconstruction, and vegetation restoration [84,85]. Australia is in the top three countries with land areas impacted by mining, and it was a leader in land rehabilitation in the field of theory, application, demonstration, and communication late last century [86–88].

Additionally, the numbers of single-country publications (SCP) and multiple-country publications (MCP) were used to determine the level of international cooperation. China has the highest number of articles (666), the highest MCP (564), and the highest SCP (102). The collaboration network of 50 countries (Figure 4) publishing articles on LRER was drawn to demonstrate the status and level of cooperation between countries. The radius of the circle is used to reflect the number of articles published by each country, and

the thickness of the lines between countries is used to indicate the degree of cooperation between countries. Clearly, there is more collaboration among China, the USA, Australia, Canada, and the UK, especially between China and the USA and between China and Australia. As countries attach importance to the issue of LRER, promoting national and regional cooperative research has become a consensus.

Table 2. Top 10 countries in terms of the literature numbers on LRER.

Rank	Country	Number of Articles	Single-Country Publications (SCP)	Multiple-Country Publications (MCP)
1	China	666	564	102
2	Australia	255	189	66
3	USA	227	204	23
4	Canada	143	118	25
5	Germany	83	68	15
6	Poland	75	69	6
7	India	73	66	7
8	Spain	69	50	19
9	Brazil	64	49	15
10	UK	50	38	12

Figure 4. Collaboration network of countries publishing articles on LRER.

*3.4. Main Institutions Conducting Research on LRER*

The top ten LRER research institutions were determined according to their publication quantities (Table 3), and they are China Univ Min and Technol, Univ Queensland, China Univ Geosci, Univ Western Australia, Curtin Univ, China Univ Min and Technol Beijing, Univ Chinese Acad Sci, Key Lab Land Consolidat and Rehabil, Univ Cagliari, and Univ Quebec Abitibi Temiscamingue.

China Univ Min and Technol published 133 articles in that field, followed by the Univ Queensland with 98 articles, and China Univ Geosci with 84 articles. Among the top ten research institutions, five are from China and three are from Australia, indicating China and Australia attach great importance to LRER research.

The collaboration network of 50 institutions is shown in Figure 5. It can be seen that institutional cooperation is mainly carried out within the same country, for example, the cooperation between Univ Western Australia and Curtin Univ happened in Australia. The two research institutions of LRER, China Univ Min and Technol and China Univ Geosci, have more cooperation with other research institutions in China. Compared with the level of institutional cooperation within the same countries, the level of international institutional cooperation is still low.

Table 3. Top 10 research institutions related to LRER.

Rank	Research Institution	Country	Number of Articles
1	The China Univ Min and Technol	China	133
2	Univ Queensland	Australia	98
3	China Univ Geosci	China	84
4	Univ Western Australia	Australia	70
5	Curtin Univ	Australia	46
6	China Univ Min and Technol Beijing	China	42
7	Univ Chinese Acad Sci	China	36
8	Key Lab Land Consolidat and Rehabil	China	33
9	Univ Cagliari	Italy	27
10	Univ Quebec Abitibi Temiscamingue	Canada	27
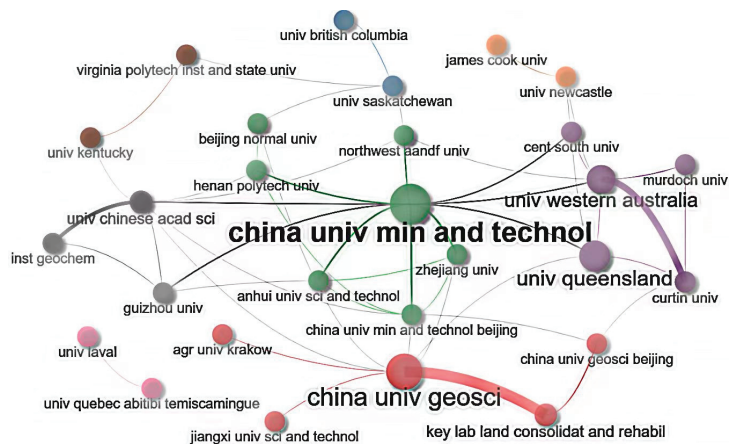
Figure 5. Collaboration network of main institutions on LRER.

3.5. Research Categories on LRER

A bibliometric analysis was carried out on the literature disciplines of LRER research with the data from Web of Science to explore the main research areas. It can be seen that the field of ecological restoration involves multiple disciplines (Figure 6), including environmental science, engineering environment, water resource, etc. Among the research disciplines related to LRER, environmental science is the principal category, accounting for 46.6% of the total, followed by engineering environment (13.9%), water resources (10.7%), mining mineral proceedings (10.6%), ecology (10.4%), geosciences multidisciplinary (10.4%), soil science (8.9%), green sustainable science technology (5.45%), and environmental studies (5.3%). There are also other categories involved, such as geochemistry geophysics, remote sensing, plant science, and public environmental occupational health; however, none of their percentages are higher than 5%. The most attention is paid to environmental science and engineering environment, and in these two disciplines there are the most extensive publications. The key issues are related to soil and water pollution by heavy metals in mining areas, especially the pollution of heavy metals such as Cd and Pb, heavy metal phytoremediation, and vegetation reconstruction. Water resource is concerned in terms of the discharge and treatment of acidic water containing heavy metals in mining areas and the pollution of river water. The discipline of ecology focuses on topics such as mining damage to ecosystems, impacts on ecosystem services, biodiversity conservation, and ecosystem spontaneous succession.
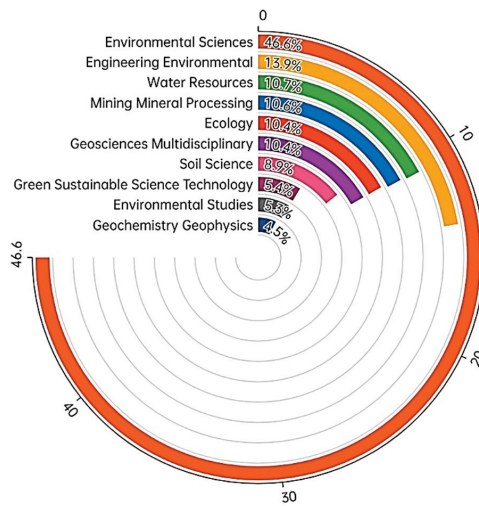
Figure 6. Main research categories on LRER.

3.6. Main Journals on LRER

The most abundant journals that publish research articles on LRER are shown in Table 4. The top ten journals are from The Netherlands, USA, Germany, UK, and Switzerland. The main journals according to the number of LRER articles are Science of the Total Environment, Environmental Science and Pollution Research, and Restoration Ecology. The journal with the most published articles is Science of the Total Environment, which has a JCR division of Q1 in 2022 and an impact factor of 10.753. It published 74 articles related to LRER in total from 1990 to 2022. The second is Environmental Science and Pollution Research, which has a JCR division of Q2 and an impact factor of 5.190. It published 53 articles related to LRER in total from 1990 to 2022. The third is Restoration Ecology, which has a JCR division of Q2 and an impact factor of 4.181. It published 51 articles related to LRER in total from 1990 to 2022.

Table 4. Top 10 journals in terms of the literature quantity on LRER.

Rank	Journal	Country	Journal Citation Report (JCR)	Impact Factor (If)	Articles
1	Science of the Total Environment	The Netherlands	Q1	10.753	74
2	Environmental Science and Pollution Research	Germany	Q2	5.190	53
3	Restoration Ecology	United States	Q2	4.181	51
4	Ecological Engineering	The Netherlands	Q2	4.379	46
5	Journal of Cleaner Production	United States	Q1	11.072	44
6	Environmental Earth Sciences	Germany	Q2	3.119	41
7	Journal of Environmental Management	England	Q1	8.910	41
8	Sustainability	Switzerland	Q2	3.889	41
9	Chemosphere	England	Q1	8.943	36
10	Remote Sensing	Switzerland	Q1	5.349	29

3.7. Hot Research Topics and Trends on LRER

3.7.1. High-Frequency Keyword Analysis

Keywords are a high-level summary of research contents [89]. The cloud map of the top 50 keywords related to LRER is shown in Figure 7. The larger the keyword font in the figure, the higher the frequency of occurrence. As seen from Figure 7, the high-frequency keywords
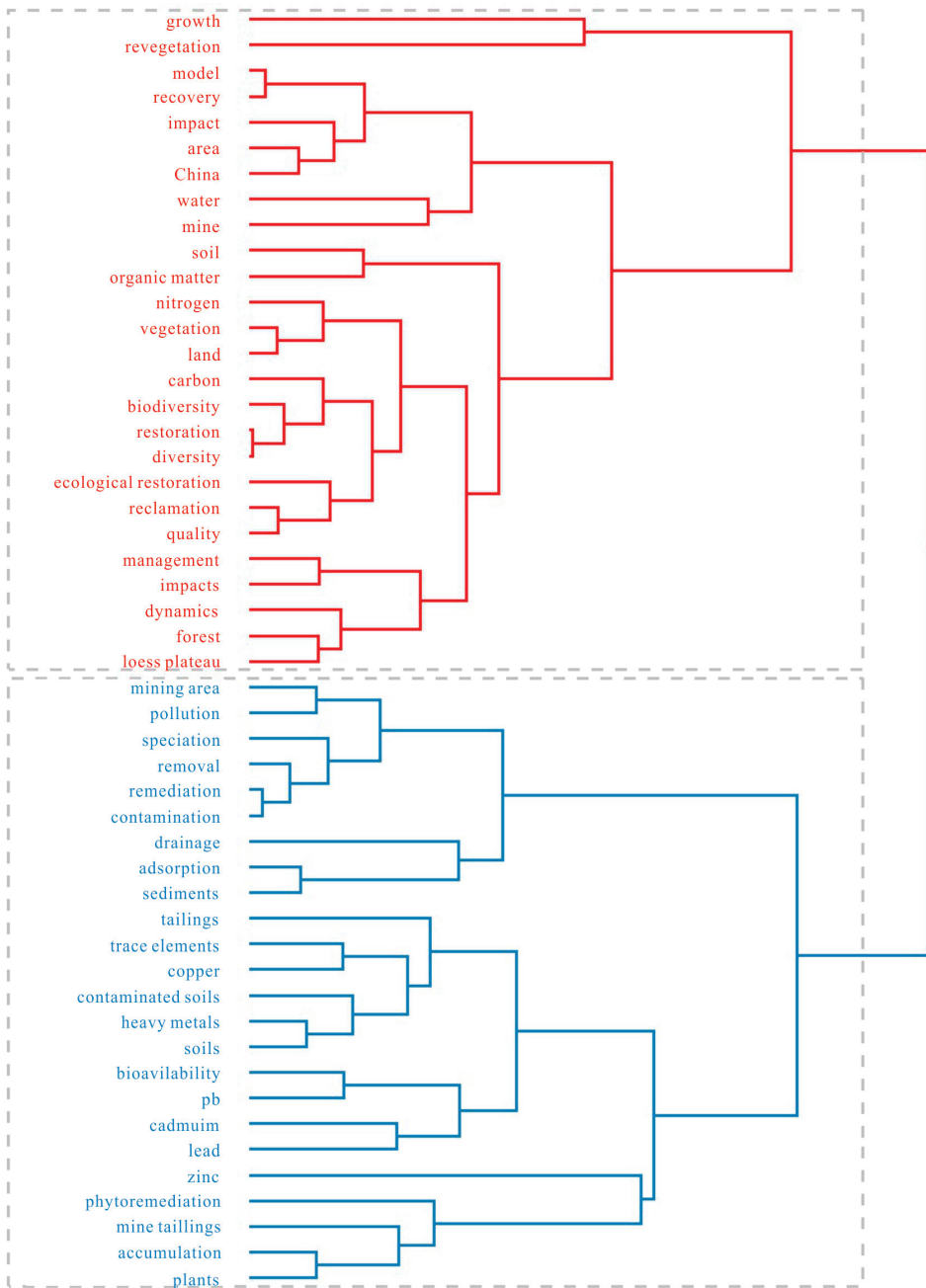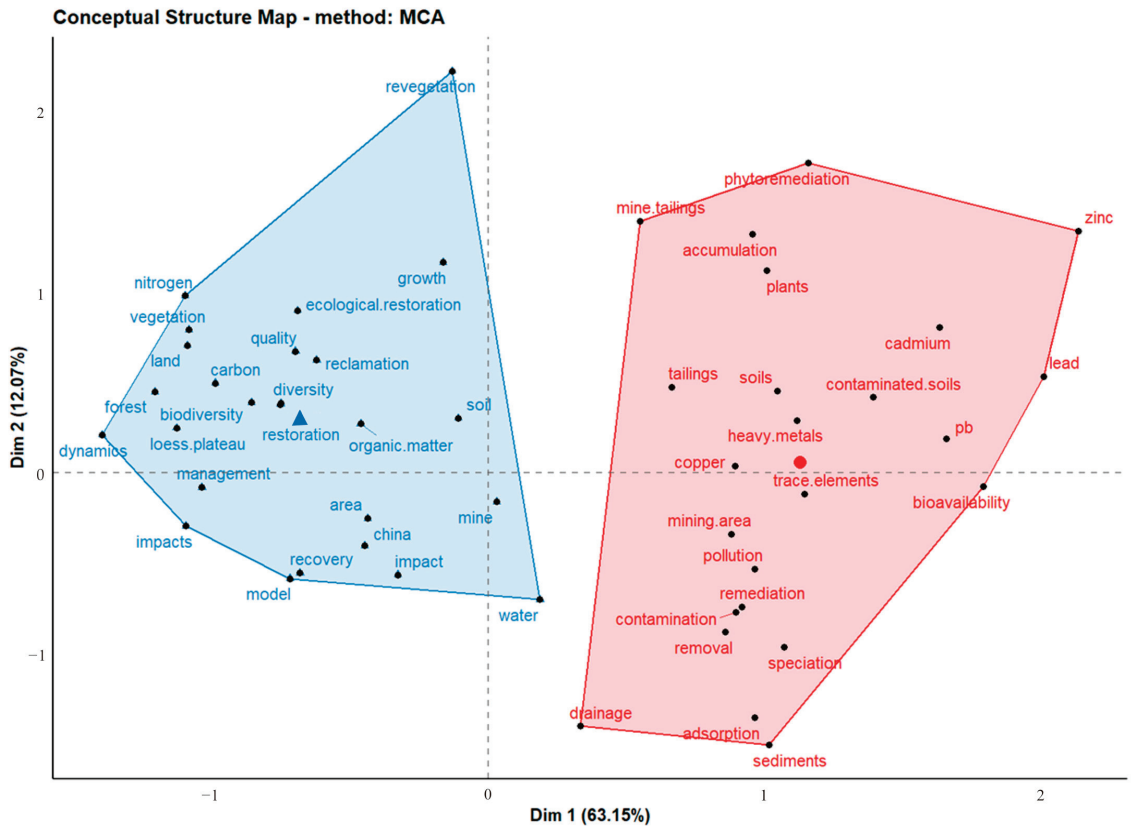
that appear include "heavy-metals", "mining area", "soil", "remediation", "accumulation", "reclamation", "restoration", "water", "growth", "pollution", "cadmium", "vegetation", "diversity", and so on. As it shows, the scope of research on LRER is very wide. For a long time, the discharge of mineral acidic wastewater has often led to heavy metal pollution [21], especially Cd and Pb pollution. Remediation aims to remove degradation to achieve safe, stable, and nonpolluting landscapes, and it is a pre-requisite for ecological restoration, reclamation, or rehabilitation after mining [12]. Soil occupies an important position in the ecosystem because it provides the environment with places where various plants, soil, animals, and microorganisms grow. Soil heavy metal pollution remediation is the key to LRER, and it is also a current research hotspot. Vegetation cover provides a cost-effective and environmentally sustainable method for stabilizing the bare area and minimizing the pollution problem, and the growth of plants (biomass, growth rates, and biomass of nodules) is the focus of research [90–92]. The objective of LRER is to assist the recovery of the ecosystem, thus terms such as accumulation, vegetation, and growth are also high-frequency keywords on LRER.

Figure 7. Cloud map of high-frequency keywords on LRER from 1990 to 2022.

3.7.2. Cluster Analysis (CA) and Multiple Correspondence Analysis (MCA) of High-Frequency Keywords

CA is one of the main methods for analyzing multivariate data [93]. The CA results of high-frequency keywords are shown in Figure 8. In this study, keywords are clustered into two categories. The first is mainly related to "heavy metals", "soil amendments", "mine tails", "biochar", "toxicity", etc. This type of research focuses on heavy metal pollution in metal mine wasteland and tailings, especially the remediation of heavy metal pollution in soil by biochar, which is a current research hotspot [94,95]. The second is mainly related to "organic matter", "organic carbon", "nitrogen", "vegetation", "succession", "quality", "diversity", etc. This type of research focuses on soil organic carbon, nitrogen, natural succession, vegetation reconstruction, biodiversity, etc. Since the major problems of land after mining include physical properties (structure, stability, moisture), nutrition (macronutrients, micronutrients), and toxicity (pH, heavy metals, salinity) [96,97], research on LRER is also mainly conducted on those aspects.

MCA is an unsupervised learning algorithm for visualizing the patterns of large and multidimensional categorical data [98]. The results of MCA on keywords are shown in Figure 9, where there are two clusters on the figure, one is centered on heavy metals, and the other is centered on restoration. CA and MCA of high-frequency keywords show that, currently, there are two clusters in LRER research, one is heavy metal pollution caused by mining, and the other is ecological restoration in mining areas, especially soil reconstruction and vegetation restoration.

Figure 8. Dendrogram of keywords on LRER from 1990 to 2022.

Figure 9. Word map of keywords on LRER from 1990 to 2022.

3.7.3. Thematic Evolution Analysis

In the past 30 years, the research direction on LRER has had both continuity and development. Figure 10 shows the chronological order of the evolution of various themes. Connections between keywords are indicated by gray lines connected to various rectangular colored shapes. Before 2000, the research on LRER was in its infancy, and researchers began to explore topics such as reclamation, rehabilitation, and acid rock drainage (acid mine drainage) treatment. From 2001 to 2014, the contents of LRER research were gradually enriched, mainly involving land reclamation, mine site rehabilitation, mine site restoration, the impact of mining and reclamation on soil physical and chemical properties (especially bulk density), and heavy metals pollution, especially mercury (Hg) and arsenic (As) contamination. The research on LRER from 2015 to 2020 mainly focused on reclamation, mine site restoration, phytoremediation, heavy metals, reforestation, etc. In the past two years, the research on LRER has focused on heavy metals and their pollution, arbuscular mycorrhizal fungi microbial restoration, mine vegetation restoration, and coal gangue ecological restoration. Overall, for more than 30 years, mine acid wastewater treatment and heavy metal pollution control, soil reconstruction (soil profile reconstruction, soil improvement), and vegetation restoration have been the key topics of research.
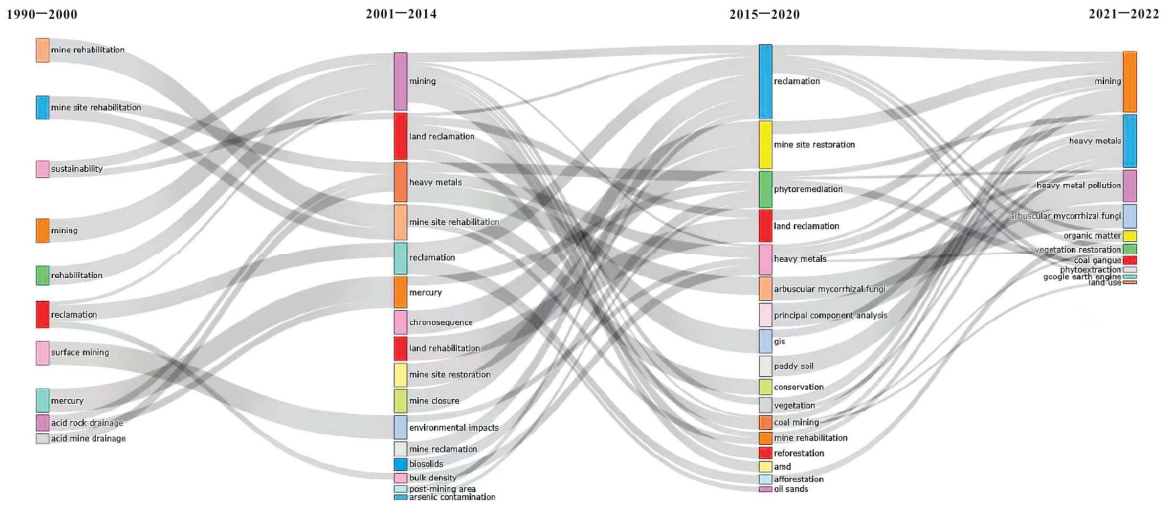
Figure 10. Thematic evolution on LRER.

4. Discussion

Before 2004, there were few studies on LRER. From 2005 to 2014, the number of relevant publications increased steadily. A big increase of relevant articles occurred from 2015 to 2022, especially in 2021 and 2022. A series of actions, such as UN SDGs for 2030, the Convention on Biological Diversity, and the UN Decade of Ecosystem Restoration 2021–2030, have greatly promoted research on LRER. In addition, the three consecutive International Symposiums on LRER held in 2014, 2017, and 2021 promoted academic exchanges and strongly promoted international cooperation in LRER [99].

LRER is closely related to the development and utilization of mineral resources. Therefore, countries that contributed more publications on LRER are also those that have rich mineral resources and pay more attention to ecological and environmental issues, such as China, Australia, USA, Canada, and Germany. In recent years, the number of articles published by Chinese scholars gradually increased. Since 2012, China has put the construction of ecological civilization in a prominent position. China's adherence to the green development strategy and strict laws and regulations (such as the Land Reclamation Regulations, the Implementation Measures for Land Reclamation Regulations) have made ecological and environmental protection a hard constraint for mine development. As a result, the number of research institutions on LRER in China has also increased. The field of LRER involves categories such as environmental science, engineering environment, water resources, mining mineral proceeding, ecology, etc., showing a trend of multidisciplinary development. There are many kinds of periodicals that publish articles about land reclamation and ecology, mainly focusing on environmental science and ecology, earth science, and engineering technology, which are related to the research content and direction of LRER.

For the heavy metal pollution in metal mine wasteland and tailings, the remediation of heavy metal pollution in soil by biochar is a current research hotspot [94,95]. For energy mines, such as coal mines, more attention is paid to terrain remodeling [100], soil profile reconstruction and improvement [4,101], revegetation [102–104], dynamic reclamation methods for subsidence band [105], and biodiversity [106], and that is why more articles on LRER are published in popular journals of environment and ecology. The CA and MCA of high-frequency keywords show that the current LRER research has two clusters, one is around heavy metal pollution (Cd, Pb, etc.), and the other is around ecological restoration in mining areas, including soil reconstruction and vegetation restoration. Renee E. Young et al. [12] put forward the idea of stepwise ecological restoration in 2022. The idea of stepwise ecological restoration is to use three restorative modes for different levels of

ecosystem degradation, i.e., environmental remediation for seriously degraded ecosystems, ecological rehabilitation for moderately degraded ecosystems, and ecological (even natural) restoration for slightly degraded ecosystems. It can be seen that current LRER research is in different stages of stepwise ecological restoration, i.e., remediation stage and ecological restoration (rehabilitation) stage. The analysis results of high-frequency keywords are consistent with the theory of stepwise ecological restoration [12]. From this perspective, it is also necessary to carry out stepwise ecological restoration based on targets and end goals for post-mining recovery of ecosystems with different degrees of degradation [107].

Thematic evolution analysis shows that mine acid wastewater treatment and heavy metal pollution control, soil reconstruction (soil profile reconstruction, soil improvement), and vegetation restoration have been the focus of research for more than 30 years. Judging from the three consecutive international conferences on LRER held in 2014, 2017, and 2021, soil reconstruction and landform remodeling, solid waste and acidic water treatment, reclamation and ecological restoration of coal mining subsidence, open-pit mine reclamation and ecological restoration, and restoration of contaminated land are also hot topics. The UN SDGs for 2030, the Convention on Biological Diversity, the UN Decade of Ecosystem Restoration 2021–2030, and other international initiatives have brought opportunities and challenges to the field of LRER. For mine ecosystems, as one of the degraded ecosystems, the future LRER should not only focus on traditional hotspots such as soil reconstruction and landform remodeling, solid waste and acid water treatment, mining subsidence and ecological restoration, open pit mine reclamation and ecological restoration, and polluted land restoration, but also focus on the relationship between LRER and carbon sequestration and the relationship between LRER and biodiversity. In addition, from the analysis of the national cooperation network and institutional cooperation network of LRER, it can be seen that the international cooperation is mainly concentrated among countries such as China, the USA, and Australia; the current international cooperation among other countries is not so frequent, and institutional cooperation is mainly carried out within the same country. Therefore, the technical exchanges and international cooperation should be strengthened. A series of ecological restoration goals and initiatives of the UN also require the cooperation of all countries.

Insufficiencies and recommendations. Articles retrieved through the core database of Web of Science in this study are only a subset of the research field of LRER. For example, some articles published in international conferences on LRER and national reclamation societies (societies of ecological restoration) of different countries are included by EI and ISTP, but not by SCI. In addition, setting the search language to English also blocks articles published in other languages. For example, there are many articles written by experts on reclamation in China, and some articles are written in Chinese, which are missed in the search. Therefore, future bibliometric research should include articles from different databases and languages for more comprehensive analysis.

5. Conclusions

In this study, an R runtime environment was set up and the Bibliometrix software packages (version 3.1.4) were used to systematically summarize and sort out the literature on LRER. The trends in publications, major research journals, institutions, countries, research hotspots, and themes were analyzed, and the future research directions were discussed.

The annual scientific output results show that the number of articles published on LRER and the number of annual average citations increased gradually from 1990 to 2022. China, Australia, the USA, Canada, and Germany made the greatest contribution to the research on LRER.

There is more collaboration among China, the USA, Australia, Canada, and the UK, especially between China and the USA as well as between China and Australia. The technical exchanges and international cooperation should be strengthened. There are five Chinese institutions ranking top ten on LRER research. China attaches great importance to LRER research. The field shows the interdisciplinary development trend of environmental

sciences, engineering environment, mining resources, proceedings, and ecology. The top five prolific journals are Science of the Total Environment, Environmental Science and Pollution Research, Restoration Ecology, Ecological Engineering, and Journal of Cleaner Production. The globally most cited articles focus on passive treatment of contaminated acid wastewater, phytostabilization of mine tailings, and biochar on mine tailings.

Currently, there are two major concerns of LRER, one is heavy metal pollution caused by mining, and the other is ecological restoration in mining areas, especially soil reconstruction and vegetation restoration. Those two major concerns of LRER correspond to different stages of stepwise ecological restoration, i.e., remediation stage and ecological restoration (rehabilitation) stage. The mine acid wastewater treatment, heavy metal pollution control, soil reconstruction (soil profile reconstruction, soil improvement), and vegetation restoration are the focus of research. In addition to traditional reclamation hotspots, future LRER should also focus on the relationship between LRER and carbon sequestration as well as the relationship between LRER and biodiversity. In addition, technology exchanges, international cooperation, and industrialization of LRER should be strengthened in the future.

We try to sort out the research status quo, dig out the research hotspots, forecast the future research trends, and provide references for future research on LRER.

Abbreviations

CA	Cluster analysis
LRER	Land reclamation and ecological restoration
MCA	Multiple correspondence analysis
MCP	Multiple-country publications
SCP	Single-country publications
SDGs	Sustainable Development Goals

References

1. PwC. Mine 2022: A Critical Transition. Available online: https://www.pwc.com/mine (accessed on 27 January 2023).
2. Zhang, L.; Hu, Z.; Yang, D.; Li, H.; Liu, B.; Gao, H.; Cao, C.; Zhou, Y.; Li, J.; Li, S. Land Use Dynamic Evolution and Driving Factors of Typical Open-Pit Coal Mines in Inner Mongolia. *Int. J. Environ. Res. Public Health* **2022**, *19*, 9723. [CrossRef]
3. Sonter, L.J.; Moran, C.J.; Barrett, D.J.; Soares, B.S. Processes of land use change in mining regions. *J. Clean. Prod.* **2014**, *84*, 494–501. [CrossRef]
4. Liu, X.Y.; Bai, Z.K.; Zhou, W.; Cao, Y.G.; Zhang, G.J. Changes in soil properties in the soil profile after mining and reclamation in an opencast coal mine on the Loess Plateau, China. *Ecol. Eng.* **2017**, *98*, 228–239. [CrossRef]
5. Wang, J.M.; Yang, R.X.; Bai, Z.K. Spatial variability and sampling optimization of soil organic carbon and total nitrogen for Minesoils of the Loess Plateau using geostatistics. *Ecol. Eng.* **2015**, *82*, 159–164. [CrossRef]
6. Hu, Z.Q.; Xiao, W. Optimization of concurrent mining and reclamation plans for single coal seam: A case study in northern Anhui, China. *Environ. Earth Sci* **2013**, *68*, 1247–1254. [CrossRef]

7. He, T.T.; Xiao, W.; Zhao, Y.L.; Deng, X.Y.; Hu, Z.Q. Identification of waterlogging in Eastern China induced by mining subsidence: A case study of Google Earth Engine time-series analysis applied to the Huainan coal field. *Remote Sens. Environ.* **2020**, *242*, 111742. [CrossRef]

8. Liu, X.; Shi, H.; Bai, Z.; Zhou, W.; Liu, K.; Wang, M.; He, Y. Heavy metal concentrations of soils near the large opencast coal mine pits in China. *Chemosphere* **2020**, *244*, 125360. [CrossRef]

9. United Nations. UN Sustainable Development Goals. Available online: https://sdgs.un.org/goals (accessed on 27 January 2023).

10. McNeely, J.A. The Convention on Biological Diversity. In *Encyclopedia of the Anthropocene*; Dellasala, D.A., Goldstein, M.I., Eds.; Elsevier: Oxford, UK, 2018; pp. 321–326.

11. United Nations. The Decade on Ecosystem Restoration. Available online: https://www.decadeonrestoration.org/about-un-decade (accessed on 27 January 2023).

12. Young, R.E.; Gann, G.D.; Walder, B.; Liu, J.; Cui, W.; Newton, V.; Nelson, C.R.; Tashe, N.; Jasper, D.; Silveira, F.A.O.; et al. International principles and standards for the ecological restoration and recovery of mine sites. *Restor. Ecol.* **2022**, *30*, e13771. [CrossRef]

13. Gann, G.D.; McDonald, T.; Walder, B.; Aronson, J.; Nelson, C.R.; Jonson, J.; Hallett, J.G.; Eisenberg, C.; Guariguata, M.R.; Liu, J.G.; et al. International principles and standards for the practice of ecological restoration. Second edition. *Restor. Ecol.* **2019**, *27*, S3–S46. [CrossRef]

14. *BS ISO 20305-2020*; Mine Closure and Reclamation. Vocabulary. ISO: Geneva, Switzerland, 2020.

15. Society for Ecological Restoration International Science & Policy Working Group. The SER International Primer on Ecological Restoration. Available online: https://www.ser-rrc.org/resource/the-ser-international-primer-on/ (accessed on 27 January 2023).

16. Hu, Z.Q. *Land Reclamation and Ecological Restoration*; China University of Mining and Technology Press: Xuzhou, China, 2008.

17. Gerwing, T.G.; Hawkes, V.C.; Gann, G.D.; Murphy, S.D. Restoration, reclamation, and rehabilitation: On the need for, and positing a definition of, ecological reclamation. *Restor. Ecol.* **2022**, *30*, 13461. [CrossRef]

18. Aria, M.; Cuccurullo, C. bibliometrix: An R-tool for comprehensive science mapping analysis. *J. Informetr.* **2017**, *11*, 959–975. [CrossRef]

19. Xie, H.; Zhang, Y.; Wu, Z.; Lv, T. A Bibliometric Analysis on Land Degradation: Current Status, Development, and Future Directions. *Land* **2020**, *9*, 28. [CrossRef]

20. Liu, Z.; Ye, C.; Chen, R.; Zhao, S.X. Where are the frontiers of sustainability research? An overview based on Web of Science Database in 2013–2019. *Habitat. Int.* **2021**, *116*, 102419. [CrossRef]

21. Sheoran, A.S.; Sheoran, V. Heavy metal removal mechanism of acid mine drainage in wetlands: A critical review. *Miner. Eng.* **2006**, *19*, 105–116. [CrossRef]

22. Rose, A.W. Passive Treatment of Acid Mine Drainage (Wetlands). In *Water Encyclopedia*; John Wiley & Sons, Inc.: Hoboken, NJ, USA, 2005; pp. 423–426.

23. Liu, H.; Probst, A.; Liao, B. Metal contamination of soils and crops affected by the Chenzhou lead/zinc mine spill (Hunan, China). *Sci. Total Environ.* **2005**, *339*, 153–166. [CrossRef]

24. Razo, I.; Carrizales, L.; Castro, J.; Diaz-Barriga, F.; Monroy, M. Arsenic and heavymetal pollution of soil, water and sediments in a semi-arid climate mining area in Mexico. *Water Air Soil Pollut.* **2004**, *152*, 129–152. [CrossRef]

25. Bao, N.S.; Ye, B.Y.; Bai, Z.K. Rehabilitation of Vegetation Mapping of ATB Opencast Coal-Mine Based on GIS and RS. *Sens. Lett.* **2012**, *10*, 387–393. [CrossRef]

26. Cao, Y.G.; Wang, J.M.; Bai, Z.K.; Zhou, W.; Zhao, Z.Q.; Ding, X.; Li, Y.N. Differentiation and mechanisms on physical properties of reconstructed soils on open-cast mine dump of loess area. *Environ. Earth Sci.* **2015**, *74*, 6367–6380. [CrossRef]

27. Cao, Y.G.; Zhou, W.; Bai, Z.K.; Wang, J.M.; Zhang, X.R. Differentiations in nutrients of reconstructed soils on open-cast mine dump of loess area. *Fresenius Environ. Bull.* **2016**, *25*, 2331–2342.

28. Feng, Y.; Wang, J.M.; Bai, Z.K.; Reading, L. Effects of surface coal mining and land reclamation on soil properties: A review. *Earth-Sci. Rev.* **2019**, *191*, 12–25. [CrossRef]

29. Gao, L.; Miao, Z.W.; Bai, Z.K.; Zhou, X.Y.; Zhao, J.K.; Zhu, Y.M. A case study of ecological restoration at the Xiaoyi Bauxite Mine, Shanxi Province, China. *Ecol. Eng.* **1998**, *11*, 221–229. [CrossRef]

30. Guan, Y.J.; Wang, J.; Zhou, W.; Bai, Z.K.; Cao, Y.G. Identification of land reclamation stages based on succession characteristics of rehabilitated vegetation in the Pingshuo opencast coal mine. *J. Environ. Manag.* **2022**, *305*, 114352. [CrossRef]

31. Guan, Y.J.; Zhou, W.; Bai, Z.K.; Cao, Y.G.; Huang, Y.H.; Huang, H.Y. Soil nutrient variations among different land use types after reclamation in the Pingshuo opencast coal mine on the Loess Plateau, China. *Catena* **2020**, *188*, 104427. [CrossRef]

32. Huang, Y.H.; Cao, Y.G.; Pietrzykowski, M.; Zhou, W.; Bai, Z.K. Spatial distribution characteristics of reconstructed soil bulk density of opencast coal-mine in the loess area of China. *Catena* **2021**, *199*, 105116. [CrossRef]

33. Huang, Y.H.; Kuang, X.Y.; Cao, Y.G.; Bai, Z.K. The soil chemical properties of reclaimed land in an arid grassland dump in an opencast mining area in China. *RSC Adv.* **2018**, *8*, 41499–41508. [CrossRef]

34. Hui, J.W.; Bai, Z.K.; Ye, B.Y.; Wang, Z.H. Remote Sensing Monitoring and Evaluation of Vegetation Restoration in Grassland Mining Areas-A Case Study of the Shengli Mining Area in Xilinhot City, China. *Land* **2021**, *10*, 743. [CrossRef]

35. Wang, J.M.; Jiao, Z.Z.; Bai, Z.K. Changes in carbon sink value based on RS and GIS in the Heidaigou opencast coal mine. *Environ. Earth Sci.* **2014**, *71*, 863–871. [CrossRef]

36. Wang, J.M.; Wang, H.D.; Cao, Y.G.; Bai, Z.K.; Qin, Q. Effects of soil and topographic factors on vegetation restoration in opencast coal mine dumps located in a loess area. *Sci. Rep.* **2016**, *6*, 22058. [CrossRef]

37. Wang, J.M.; Zhang, M.; Bai, Z.K.; Guo, L.L. Multi-fractal characteristics of the particle distribution of reconstructed soils and the relationship between soil properties and multi-fractal parameters in an opencast coal-mine dump in a loess area. *Environ. Earth Sci.* **2015**, *73*, 4749–4762. [CrossRef]

38. Wang, S.F.; Cao, Y.G.; Geng, B.J.; Yang, K.; Bai, Z.K. Succession law and model of reconstructed soil quality in an open-pit coal mine dump of the loess area, China. *J. Environ. Manag.* **2022**, *312*, 114923. [CrossRef]

39. Wang, S.F.; Cao, Y.G.; Pietrzykowski, M.; Zhou, W.; Bai, Z.K. Research on the influence of vegetation restoration in loess open-pit coal mines of China: Influencing factors and mechanism. *Ecol. Eng.* **2022**, *177*, 106549. [CrossRef]

40. Yang, K.; Wang, S.F.; Cao, Y.G.; Li, S.P.; Zhou, W.X.; Liu, S.H.; Bai, Z.K. Ecological Restoration of a Loess Open-Cast Mining Area in China: Perspective from an Ecological Security Pattern. *Forests* **2022**, *13*, 269. [CrossRef]

41. Yuan, Y.; Zhao, Z.Q.; Niu, S.Y.; Bai, Z.K. The reclaimed coal mine ecosystem diverges from the surrounding ecosystem and reaches a new self-sustaining state after 20-23 years of succession in the Loess Plateau area, China. *Sci. Total Environ.* **2020**, *727*, 138739. [CrossRef]

42. Zhang, L.; Wang, J.M.; Bai, Z.K.; Lv, C.J. Effects of vegetation on runoff and soil erosion on reclaimed land in an opencast coal-mine dump in a loess area. *Catena* **2015**, *128*, 44–53. [CrossRef]

43. Zhang, X.R.; Cao, Y.G.; Bai, Z.K.; Wang, J.M.; Zhou, W.; Ding, X. Relationships between vegetation coverage and soil properties on the reclaimed dump of opencast coal mine in loess plateau, China. *Fresenius Environ. Bull.* **2016**, *25*, 4767–4776.

44. Zhao, Z.Q.; Shahrour, I.; Bai, Z.K.; Fan, W.X.; Feng, L.R.; Li, H.F. Soils development in opencast coal mine spoils reclaimed for 1–13 years in the West-Northern Loess Plateau of China. *EUR J. Soil. Biol.* **2013**, *55*, 40–46. [CrossRef]

45. Cui, X.Q.; Peng, S.P.; Lines, L.R.; Zhu, G.W.; Hu, Z.Q.; Cui, F. Understanding the Capability of an Ecosystem Nature-Restoration in Coal Mined Area. *Sci. Rep.* **2019**, *9*, 19690. [CrossRef]

46. Duo, L.H.; Hu, Z.Q. Soil Quality Change after Reclaiming Subsidence Land with Yellow River Sediments. *Sustainability* **2018**, *10*, 4310. [CrossRef]

47. Feng, Z.J.; Hu, Z.Q.; Li, G.S.; Zhang, Y.H.; Zhang, X.; Zhang, H. Improving mine reclamation efficiency for farmland sustainable use: Insights from optimizing mining scheme. *J. Clean. Prod.* **2022**, *379*, 134615. [CrossRef]

48. Han, J.Z.; Hu, Z.Q.; Mao, Z.; Li, G.S.; Liu, S.G.; Yuan, D.Z.; Guo, J.X. How to Account for Changes in Carbon Storage from Coal Mining and Reclamation in Eastern China? Taking Yanzhou Coalfield as an Example to Simulate and Estimate. *Remote Sens.* **2022**, *14*, 2014. [CrossRef]

49. Hu, Z.Q.; Fu, Y.H.; Xiao, W.; Zhao, Y.L.; Wei, T.T. Ecological restoration plan for abandoned underground coal mine site in Eastern China. *Int. J. Min. Reclam. Environ.* **2015**, *29*, 316–330. [CrossRef]

50. Hu, Z.Q.; Wang, X.T.; McSweeney, K.; Li, Y. Restoring subsided coal mined land to farmland using optimized placement of Yellow River sediment to amend soil. *Land Degrad. Dev.* **2022**, *33*, 1029–1042. [CrossRef]

51. Li, G.S.; Hu, Z.Q.; Yuan, D.Z.; Li, P.Y.; Feng, Z.J.; He, Y.B.; Wang, W.J. A new approach to increased land reclamation rate in a coal mining subsidence area: A case-study of Guqiao Coal Mine, China. *Land Degrad. Dev.* **2022**, *33*, 866–880. [CrossRef]

52. Ren, H.; Xiao, W.; Zhao, Y.L.; Hu, Z.Q. Land damage assessment using maize aboveground biomass estimated from unmanned aerial vehicle in high groundwater level regions affected by underground coal mining. *Environ. Sci. Pollut. Res.* **2020**, *27*, 21666–21679. [CrossRef]

53. Zhu, Q.; Hu, Z.Q.; Liu, X.R.; Wu, Y.J. Topsoil alternatives selection for surface coal-mined land reclamation in Inner Mongolia, China: An experimental study. *Int. J. Min. Reclam. Environ.* **2021**, *35*, 421–434. [CrossRef]

54. Du, W.F.; Chen, L.; He, Y.L.; Wang, Q.M.; Gao, P.Q.; Li, Q.S. Spatial and Temporal Distribution of Groundwater in Open-Pit Coal Mining: A Case Study from Baorixile Coal Mine, Hailaer Basin, China. *Geofluids* **2022**, *2022*, 8753217. [CrossRef]

55. Hu, Z.Q.; Zhu, Q.; Liu, X.R.; Li, Y. Preparation of topsoil alternatives for open-pit coal mines in the Hulunbuir grassland area, China. *Appl. Soil Ecol.* **2020**, *147*, 103431. [CrossRef]

56. Liu, X.Y.; Zhou, W.; Bai, Z.K. Vegetation coverage change and stability in large open-pit coal mine dumps in China during 1990–2015. *Ecol. Eng.* **2016**, *95*, 447–451. [CrossRef]

57. Wang, S.G.; Huang, J.; Yu, H.C.; Ji, C.N. Recognition of Landscape Key Areas in a Coal Mine Area of a Semi-Arid Steppe in China: A Case Study of Yimin Open-Pit Coal Mine. *Sustainability* **2020**, *12*, 2239. [CrossRef]

58. Zhang, L.J.; Zhai, Z.H.; Zhou, Y.; Liu, S.A.; Wang, L.W. The Landscape Pattern Evolution of Typical Open-Pit Coal Mines Based on Land Use in Inner Mongolia of China during 20 Years. *Sustainability* **2022**, *14*, 9590. [CrossRef]

59. Bi, Y.L.; Xiao, L.; Guo, C.; Christie, P. Revegetation type drives rhizosphere arbuscular mycorrhizal fungi and soil organic carbon fractions in the mining subsidence area of northwest China. *Catena* **2020**, *195*, 104791. [CrossRef]

60. Chen, Y.; Hu, Z.Q.; Li, P.Y.; Li, G.S.; Yuan, D.Z.; Guo, J.X. Assessment and Effect of Mining Subsidence on Farmland in Coal-Crop Overlapped Areas: A Case of Shandong Province, China. *Agriculture* **2022**, *12*, 1235. [CrossRef]

61. Gu, Y.Y.; Zhou, D.W.; Zhang, D.M.; Wu, K.; Zhou, B.H. Study on subsidence monitoring technology using terrestrial 3D laser scanning without a target in a mining area: An example of Wangjiata coal mine, China. *Bull. Eng. Geol. Environ.* **2020**, *79*, 3575–3583. [CrossRef]

62. He, T.T.; Xiao, W.; Zhao, Y.L.; Chen, W.Q.; Deng, X.Y.; Zhang, J.Y. Continues monitoring of subsidence water in mining area from the eastern plain in China from 1986 to 2018 using Landsat imagery and Google Earth Engine. *J. Clean. Prod.* **2021**, *279*, 123610. [CrossRef]

63. Hu, T.H.; Chang, J.; Liu, X.X.; Feng, S.S. Integrated methods for determining restoration priorities of coal mining subsidence areas based on green infrastructure: -A case study in the Xuzhou urban area, of China. *Ecol. Indic.* **2018**, *94*, 164–174. [CrossRef]

64. Hu, Z.Q.; Xu, X.L.; Zhao, Y.L. Dynamic monitoring of land subsidence in mining area from multi-source remote-sensing data—A case study at Yanzhou, China. *Int. J. Remote Sens.* **2012**, *33*, 5528–5545. [CrossRef]

65. Jing, Z.R.; Wang, J.M.; Zhu, Y.C.; Feng, Y. Effects of land subsidence resulted from coal mining on soil nutrient distributions in a loess area of China. *J. Clean. Prod.* **2018**, *177*, 350–361. [CrossRef]

66. Li, L.; Li, T.L.; Meng, H.S.; Xie, Y.H.; Zhang, J.; Hong, J.P. Effects of Seven-Year Fertilization Reclamation on Bacterial Community in a Coal Mining Subsidence Area in Shanxi, China. *Int. J. Environ. Res. Public Health* **2021**, *18*, 12504. [CrossRef]

67. Qiu, L.; Bi, Y.L.; Jiang, B.; Wang, Z.G.; Zhang, Y.X.; Zhakypbek, Y. Arbuscular mycorrhizal fungi ameliorate the chemical properties and enzyme activities of rhizosphere soil in reclaimed mining subsidence in northwestern China. *J. Arid. Land* **2019**, *11*, 135–147. [CrossRef]

68. Sun, J.F.; Yuan, X.Z.; Liu, H.; Liu, G.D.; Zhang, G.X. Emergy evaluation of a swamp dike-pond complex: A new ecological restoration mode of coal-mining subsidence areas in China. *Ecol. Indic.* **2019**, *107*, 105660. [CrossRef]

69. Wang, J.M.; Wang, P.; Qin, Q.; Wang, H.D. The effects of land subsidence and rehabilitation on soil hydraulic properties in a mining area in the Loess Plateau of China. *Catena* **2017**, *159*, 51–59. [CrossRef]

70. Xiao, L.; Bi, Y.L.; Du, S.Z.; Wang, Y.; Guo, C. Effects of re-vegetation type and arbuscular mycorrhizal fungal inoculation on soil enzyme activities and microbial biomass in coal mining subsidence areas of Northern China. *Catena* **2019**, *177*, 202–209. [CrossRef]

71. Xie, K.; Zhang, Y.Q.; Yi, Q.T.; Yan, J.P. Optimal resource utilization and ecological restoration of aquatic zones in the coal mining subsidence areas of the Huaibei Plain in Anhui Province, China. *Desalin. Water Treat.* **2013**, *51*, 4019–4027. [CrossRef]

72. Zeng, F.X.; Wu, K.; He, Q.; Diao, X.P.; Li, L. Model Establishment for Ponding in Coal Mining Subsidence Areas and its Prediction: Case Study of Northern Jining, China. *Geotech. Geol. Eng.* **2017**, *35*, 83–89. [CrossRef]

73. Zhang, Q.; Ma, J.; Yang, Y.J.; Luo, Z.B.; Wang, Y.F.; Chen, F. Mining Subsidence-Induced Microtopographic Effects Alter the Interaction of Soil Bacteria in the Sandy Pasture, China. *Front. Environ. Sci.* **2021**, *9*, 656708. [CrossRef]

74. Zhang, Y.X.; Bi, Y.L.; Shen, H.H.; Zhang, L.J. Arbuscular Mycorrhizal Fungi Enhance Sea Buckthorn Growth in Coal Mining Subsidence Areas in Northwest China. *J. Microbiol. Biotechnol.* **2020**, *30*, 848–855. [CrossRef]

75. Zhang, Y.X.; Du, L.Z.; Liu, J. Identifying the reuse patterns of coal mining subsidence areas: A case-study of Jixi City (China). *Land Degrad. Dev.* **2021**, *32*, 4858–4870. [CrossRef]

76. Zhong, S.Q.; Wei, C.F.; Liu, B.; Zhang, W.H.; Du, J.; Zhang, S.C. Restoration technologies of damaged paddy in hilly post-mining and subsidence-stable area of Southwest China. *Int. J. Agric. Biol. Eng.* **2015**, *8*, 46–57. [CrossRef]

77. Zhu, M.; Bazail, N.A.; Li, X.L.; Huang, M.N.; Mohammad, T.; Lei, M.; Wang, H. Research on wetland ecological restoration of coal mining subsidence area in suzhou, China. *Fresenius Environ. Bull.* **2017**, *26*, 5177–5183.

78. Du, T.; Wang, D.M.; Bai, Y.J.; Zhang, Z.Z. Optimizing the formulation of coal gangue planting substrate using wastes: The sustainability of coal mine ecological restoration. *Ecol. Eng.* **2020**, *143*, 105669. [CrossRef]

79. Hao, J.; Guo, D.G.; Li, H.Y.; Meng, W.Q. Ecological restoration status index for evaluating the restored coal gangue pile: A chronosequence study based on the plant-soil system in the shanxi mining area, China. *Appl. Ecol. Environ. Res.* **2019**, *17*, 11587–11604. [CrossRef]

80. Wang, J.M.; Li, X.F.; Bai, Z.K.; Huang, L.B. The effects of coal gangue and fly ash on the hydraulic properties and water content distribution in reconstructed soil profiles of coal-mined land with a high groundwater table. *Hydrol. Process.* **2017**, *31*, 687–697. [CrossRef]

81. Skousen, J.; Zipper, C.E.; Rose, A.; Ziemkiewicz, P.F.; Nairn, R.; McDonald, L.M.; Kleinmann, R.L. Review of Passive Systems for Acid Mine Drainage Treatment. *Mine Water Environ.* **2017**, *36*, 133–153. [CrossRef]

82. Neff, A.N.; DeNicola, D.M.; Maltman, C. Passive treatment for acid mine drainage partially restores microbial community structure in different stream habitatsina. *Water* **2021**, *13*, 3300. [CrossRef]

83. Ramos-Perez, D.; Alcantara-Hernandez, R.J.; Romero, F.M.; Gonzalez-Chavez, J.L. Changes in the prokaryotic diversity in response to hydrochemical variations during an acid mine drainage passive treatment. *Sci. Total Environ.* **2022**, *842*, 156629. [CrossRef] [PubMed]

84. Bodapati, V.S.; Wells, L.G. Automated system to improve levelness of reconstructed soil. *Appl. Eng. Agric.* **2012**, *28*, 187–195. [CrossRef]

85. Trippe, K.M.; Manning, V.A.; Reardon, C.L.; Klein, A.M.; Weidman, C.; Ducey, T.F.; Novak, J.M.; Watts, D.W.; Rushmiller, H.; Spokas, K.A.; et al. Phytostabilization of acidic mine tailings with biochar, biosolids, lime, and locally-sourced microbial inoculum: Do amendment mixtures influence plant growth, tailing chemistry, and microbial composition? *Appl. Soil Ecol.* **2021**, *165*, 103962. [CrossRef]

86. Maus, V.; Giljum, S.; Gutschlhofer, J.; da Silva, D.M.; Probst, M.; Gass, S.L.B.; Luckeneder, S.; Lieber, M.; McCallum, I. A global-scale data set of mining areas. *Sci. Data* **2020**, *7*, 289. [CrossRef]

87. Cummings, J. The mining industry and land rehabilitation in Australia—Once were leaders? *J. Clean. Prod.* **2014**, *84*, 39–40. [CrossRef]

88. Dixon, K.; MacDonald, V.; D'Agui, H. Advances in mining restoration. *Restor. Ecol.* **2022**, *30*, e13776. [CrossRef]

89. Abafe, E.A.; Bahta, Y.T.; Jordaan, H. Exploring biblioshiny for historical assessment of global research on sustainable use of water in agriculture. *Sustainability* **2022**, *14*, 10651. [CrossRef]

90. Tordoff, G.M.; Baker, A.J.M.; Willis, A.J. Current approaches to the revegetation and reclamation of metalliferous mine wastes. *Chemosphere* **2000**, *41*, 219–228. [CrossRef] [PubMed]

91. Wong, M.H. Ecological restoration of mine degraded soils, with emphasis on metal contaminated soils. *Chemosphere* **2003**, *50*, 775–780. [CrossRef] [PubMed]

92. Ye, Z.H.; Yang, Z.Y.; Chan, G.Y.S.; Wong, M.H. Growth response of Sesbania rostrata and S-cannabina to sludge-amended lead/zinc mine tailings—A greenhouse study. *Environ. Int.* **2001**, *26*, 449–455. [CrossRef] [PubMed]

93. Kettenring, J.R. The Practice of Cluster Analysis. *J. Classif.* **2006**, *23*, 3–30. [CrossRef]

94. Beesley, L.; Inneh, O.S.; Norton, G.J.; Moreno-Jimenez, E.; Pardo, T.; Clemente, R.; Dawson, J.J.C. Assessing the influence of compost and biochar amendments on the mobility and toxicity of metals and arsenic in a naturally contaminated mine soil. *Environ. Pollut.* **2014**, *186*, 195–202. [CrossRef]

95. Fellet, G.; Marchiol, L.; Delle Vedove, G.; Peressotti, A. Application of biochar on mine tailings: Effects and perspectives for land reclamation. *Chemosphere* **2011**, *83*, 1262–1267. [CrossRef]

96. Bradshaw, A.D. The reconstruction of ecosystems. *J. Appl. Ecol.* **1983**, *20*, 1–17. [CrossRef]

97. Bradshaw, A.D. Restoration of mined lands—Using natural processes. *Ecol. Eng.* **1997**, *8*, 255–269. [CrossRef]

98. Murtagh, F. Multiple correspondence analysis and related methods. *Psychometrika* **2007**, *72*, 275–277. [CrossRef]

99. Chinese Ecological Restoration Network; China University of Mining and Technology(Beijing); China University of Mining and Technology. The 3rd International Symposium on Land Reclamation and Ecological Restoration. Available online: http://enislrer3.er-china.com/ (accessed on 27 January 2023).

100. Liu, H.; Zhang, M.; Su, L.J.; Chen, X.X.; Liu, C.F.; Sun, A.G. A boundary model of terrain reconstruction in a coal-mining subsidence waterlogged area. *Environ. Earth Sci.* **2021**, *80*, 187. [CrossRef]

101. Abdelrhman, A.A.; Gao, L.L.; Li, S.P.; Lu, J.J.; Song, X.J.; Zhang, M.N.; Zheng, F.J.; Wu, H.J.; Wu, X.P. Long-term application of organic wastes improves soil carbon and structural properties in dryland affected by coal mining activity. *Sustainability* **2021**, *13*, 5686. [CrossRef]

102. Vieira, C.K.; Borges, L.G.D.; Bortolini, J.G.; Soares, C.; Giongo, A.; Sturmer, S.L. Does a decrease in microbial biomass alter mycorrhizal attributes and soil quality indicators in coal mining areas under revegetation process? *Sci. Total Environ.* **2022**, *802*, 149843. [CrossRef] [PubMed]

103. Roy, R.; Sultana, S.; Wang, J.X.; Mostofa, M.G.; Sarker, T.; Shah, M.M.R.; Hossain, M.S. Revegetation of coal mine degraded arid areas: The role of a native woody species under optimum water and nutrient resources. *Environ. Res.* **2022**, *204*, 111921. [CrossRef]

104. Du, H.D.; Wang, S.M.; Nie, W.J.; Song, S.J. Soil Properties and Bacterial Community Dynamics in a Coal Mining Subsidence Area: Active Versus Passive Revegetation. *J. Soil Sci. Plant Nutr.* **2021**, *21*, 2573–2585. [CrossRef]

105. Chen, Q.J.; Hang, M.R. Dynamic reclamation methods for subsidence land in the mining area with high underground water level. *Open Geosci.* **2018**, *10*, 639–646. [CrossRef]

106. Bi, Y.L.; Guo, Y.; Christie, P. Mining subsidence area reconstruction with N-2-fixing plants promotes arbuscular mycorrhizal fungal biodiversity and microbial biomass C:N:P stoichiometry of cyanobacterial biocrusts. *Forest Ecol. Manag.* **2022**, *503*, 119763. [CrossRef]

107. Lima, A.T.; Mitchell, K.; O'Connell, D.W.; Verhoeven, J.; Van Cappellen, P. The legacy of surface mining: Remediation, restoration, reclamation and rehabilitation. *Environ. Sci. Policy* **2016**, *66*, 227–233. [CrossRef]

Article

Mapping the Reality of Hg-Free Artisanal Small-Scale Gold Mining

Tatiane Marin [1],*, Jacopo Seccatore [2] and Yingchao Cheng [3]

[1] Department of Metallurgy and Materials Engineering, Federico Santa María Technical University, Santiago 8940897, Chile

[2] Metallurgy and Mining Engineering Department, Universidad Catolica del Norte, Antofagasta 1270398, Chile; jacopo.seccatore@ucn.cl

[3] Global Resource Sustainability Research Section, Material Cycles Division, National Institute for Environmental Studies, 16-2 Onogawa, Tsukuba 305-8506, Japan; cheng.yingchao.6r@kyoto-u.ac.jp

* Correspondence: tatiane.marin@usm.cl; Tel.: +56-9-7547-0503

Abstract: Artisanal gold mining (AGM) is a very important topic, of which the environmental and social impact has been widely studied. However, there are few studies on operational efficiency, financial analysis, and the lack of mine planning. The purpose of this work was to investigate whether AGM operation without mercury is sustainable. The following parameters were analyzed in the case study: the general situation, interaction with the company that owns the area, production, drilling and blasting, loading and transport, freight to the centralized plant, workforce, materials and supplies, geological control planning and the relationship with the processing plant. Even without the mercury variable, AGM was found to be unsustainable. The lack of planning and operational inefficiency did not allow for continuous operation. The results of this research provide guidance on the future steps the current government and society should take to achieve sustainable AGM.

Keywords: mining sustainability; artisanal small-scale gold mining; Hg-free

1. Introduction

The concept of "sustainable mining operations" is based on the efficiency of operations and rigorous mine planning and adherence to the plan to ensure maximum efficiency.

In most cases, small-scale mining (SSM) fails to employ proper mine planning. The core of mine planning lies in the knowledge of the mineral body that depends on geological research, which is in turn based on expensive exploratory drilling campaigns. The lack of capital access within SSM constrains the implementation of the aforementioned procedure.

The main subjects addressed by scholars regarding artisanal and small-scale mining encompass the formalization of operation, followed by assessing environmental and health impacts, the relationship between small mining and communities, conflict between small and large mining, and case studies in different countries [1–13].

Projects that analyze technical aspects of operations integrated with the environmental impacts are novel and scarce [14–16].

In the last two years, a recurring theme in studies has been the impact of the pandemic on the mineral economy and its social impact [17–20].

Formalization is still a very important topic worldwide, especially in places far from urban centers that are difficult to control, such as the Amazon [21–23].

Each country in Latin America has different bottlenecks. For example, in Colombia, although mining is seen as an economic growth import, small-scale mining is controlled by violent national groups [24].

Many Latin American governments believe that the centralization of purchasing minerals and constructing more efficient processing plants is the solution for increasing the

formalization of activities. With these new mechanisms, small-scale miners have obtained a greater revenue from the production and sale of minerals [25,26].

This research was conducted in a mercury-free AGM region, in order to determine whether Hg-free AGM operation is sustainable.

1.1. Artisanal Mining in Chile

In Chile, most operations are formalized; therefore, the topics addressed differ from those of other countries. ENAMI, a government mining company founded in 1960, focuses on small- and medium-scale mining, encouraging the formalization of and reduction in environmental impacts.

The Atacama region still faces problems of formalization and environmental impacts due to mercury use. Nevertheless, this is not a scientific issue, because the solutions are already well defined. The regional government declared its intention to invest CLP 792 million in the construction of three Hg-free concentration plants in the provinces of Chañaral, Copiapó and Huasco in northern Chile [27].

Environmental impact has been the subject of a few recent peer-reviewed publications on small-scale mining in Chile. However, in the last three years, only four articles were published relating to technical aspects [28–31].

As established earlier, SSM is affected by a lack of planning, but also by high operating costs (OPEX, due to scale effects) and a high variability in income [32].

Operational health and safety are also one of the most critical issues in small mining. It is common to read news of accidents related to a lack of technical knowledge and the non-application of good practices, which are consolidated in the mining sector in medium and large companies. The main causes are related to landslides, a lack of geo-mechanical studies and the improper handling of explosives [33–35].

Veiga and Fadina [36] analyzed the relationship between miners and mineral processors. According to them, a successful system for eliminating mercury use is having a central plant, and the miners sell their ore to processing plants instead of processing it themselves: they make more profit than when they use mercury for amalgamation.

1.2. The Support of Public Agencies for Small-Scale Mining in Chile

Figure 1 shows the complex network of public agencies and their contribution to the small-scale mining sector in Chile (for any substance, not only Au). In Chile, artisanal mining is considered a subset of small-scale mining. Such support includes financial help, access to loans and technical assistance. The most important contribution, in terms of environmental protection, is the fact that the ores (or ore concentrates) are bought and processed in centralized plants that operate with industrial standards and do not involve pollutants such as cyanide or Hg. This was the same condition observed by Veiga and Fadina [36], but with the distinction of the processing plants belonging to a public company instead of a private one.

ENAMI

Of the public agencies indicated in Figure 1, the only one dedicated to small- and medium-sized companies is ENAMI, which promotes and sustains small- and medium-sized mining companies [37].

i.   ENAMI buys the minerals from miners

ENAMI buys both run-of-mine (ROM) ores and concentrated minerals, with the minerals of interest being copper, gold and silver, whether major or minor. The material is processed in controlled and clean plants (therefore, no Hg or other pollutants are involved) and sold by ENAMI itself. In 2020, 1557 small miners were registered to sell their minerals to this agency [38].

The purchase value at which ENAMI buys from the mines is a function of (a) the main mineral grade; (b) the type of processing ENAMI executes; (c) the international value of the mineral being processed; (d) the dollar exchange rate with the Chilean Peso; (e) penalties

for contaminants and moisture content; and (f) added value for secondary minerals. A table of all the values mentioned above is published monthly on the ENAMI website.
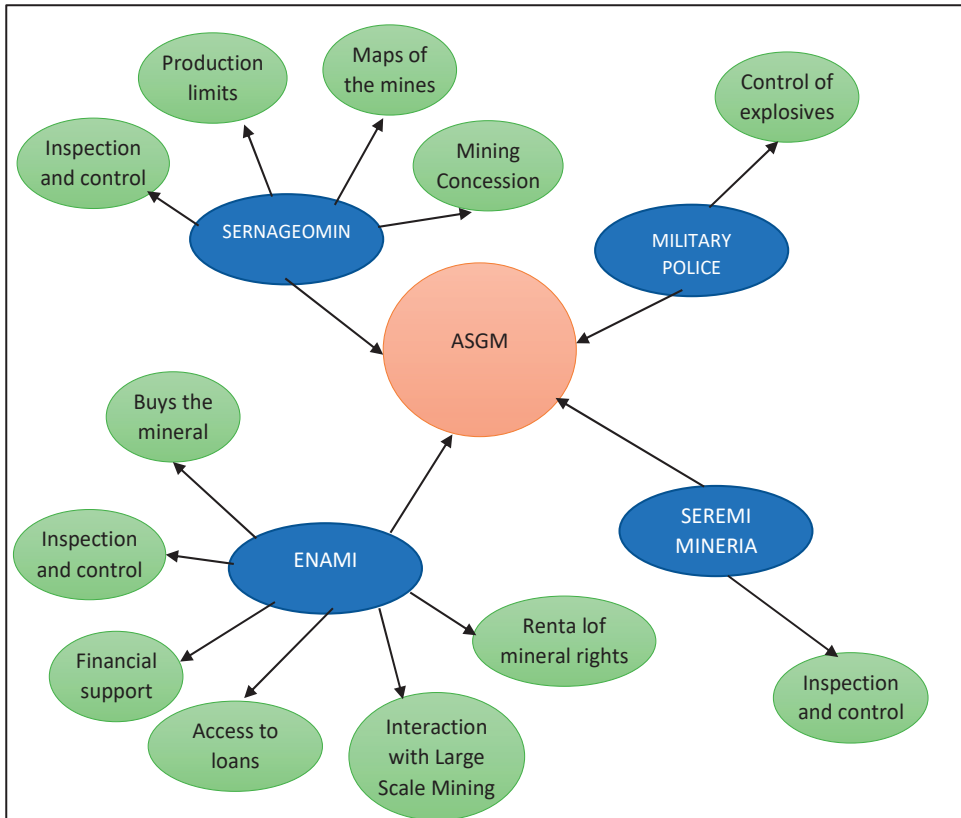
Figure 1. Map of the role of government agencies in small-scale mining in Chile.

ii.   Non-refundable financial support

The types of financial support mechanisms are:

- Development of the Competitive Capacities Program: The objective of the program is to incorporate and develop technical and business management capacities. The maximum amount is USD 2500 for individual projects and USD 20,000 for projects of associated miners. The nomination options are fostering innovation, technological transfer and training.
- Recognition of resources and/or reserves and mine planning: This involves financing exploratory drilling or reconnaissance tunnels for the preparation of a mining project. To apply for this financing mechanism, it is necessary to wait for a national competition managed by ENAMI.
- Technical assistance: This is specialized consultancy for the development of mining projects, including the study of the entire mineral production chain, from topographic surveys to the sale of ores.
- District Studies Program: This involves bidding for geological studies of areas predefined by ENAMI. The maximum annual amount is USD 150,000 per mining district. In this case, the benefit to small-scale miners is having access to maps to help postulate other development instruments.

- Production Support Program: This attends to the specific technical requirements of the miners, such as equipment repair, mining works or the purchase of materials. The maximum amount is USD 5000 per project.

iii. Loans

The value of loans is deducted from the sale of material to ENAMI. The grace period, discount rate and payment period vary according to the program.

- Support for safe production: This is a loan to adapt the mine closure plan, ground support, ventilation, emergency exits, and other works related to occupational hygiene and safety; payment for consultancy in management and risk prevention; quality; and the environment. The maximum amount is USD 30,000 per project. The payment period is 5 years, with a grace period of up to 1 year. The method of payment sales discounts at the rate of 1 USD/ton of mineral sold to ENAMI. There is no warranty, and the interest rate is fixed by ENAMI.
- Mine Reactivation Program: This is a program for putting an inactive mine back into production. The amount per project is USD 35,000. The return period is up to 2 years.
- Credits for the operation: This is a loan to stabilize cash flow and finance the purchase of minor equipment and other materials. The maximum amount is USD 50,000, with a payment term of up to one year and a grace period of three months. The interest rate is set semi-annually, and the commission is 2.5%.
- Credit for mine development: This is funding for open-pit or underground development to access the orebody. The maximum amount is USD 300,000, with a term of up to 5 years and a grace period of 1 year. The interest rate is set semi-annually. In this case, it is necessary to present real guarantees. The loan is released gradually as the progress of the project is monitored.
- Credit for investments: This is a loan for the purchase and renovation of equipment, innovations, the construction of access roads, environmental care and working capital, among other activities related to mining work. There is a term of up to 5 years with a grace period of 1 year. The interest rate is defined every six months and the commission is 2.5%. In this case, it is necessary to present real guarantees. The project will determine the value and the loan is released gradually as the progress of the project is monitored.
- Emergency credit: This is a loan to solve unforeseen situations caused by natural catastrophes. There are limits of USD 25,000 if raw minerals are sold and USD 50,000 if mineral products are sold. There are terms of up to 1 year, with a grace period of 3 months. The interest rate is set semi-annually, and the commission is 2.5%.

Other roles of ENAMI are:

- Supervising miners who have some type of promotion or active credit.
- Interaction with big-scale mining companies: the rental of areas belonging to large companies.
- Leasing properties: the lease of mining prospects from ENAMI to small-scale miners.

2. Materials and Methodology

2.1. Study Population

This field study collected sample data from the mining area of Chancón (see Figure 2). This area has already been the focus of previous small-scale mining studies [30,38].

Mines in the Chancón sector (see their distribution in Figure 3) are all underground, in hard rock and operate utilizing drilling and blasting methods.

When cataloging the mines for census purposes, public agencies cited a previously encountered difficulty in identifying the mines due to the local custom of changing the tunnel name whenever a new mine owner assumes the mine. In order to minimize this problem, the local government agency for mining (called "SEREMI Mineria") created a project to identify the tunnels with standardized plaques at the entrance to each mine (Figure 4) and location signs along the way (Figure 5).

Figure 2. Location of the field study area in Chile. The blue star indicates the location of the Chancón district.
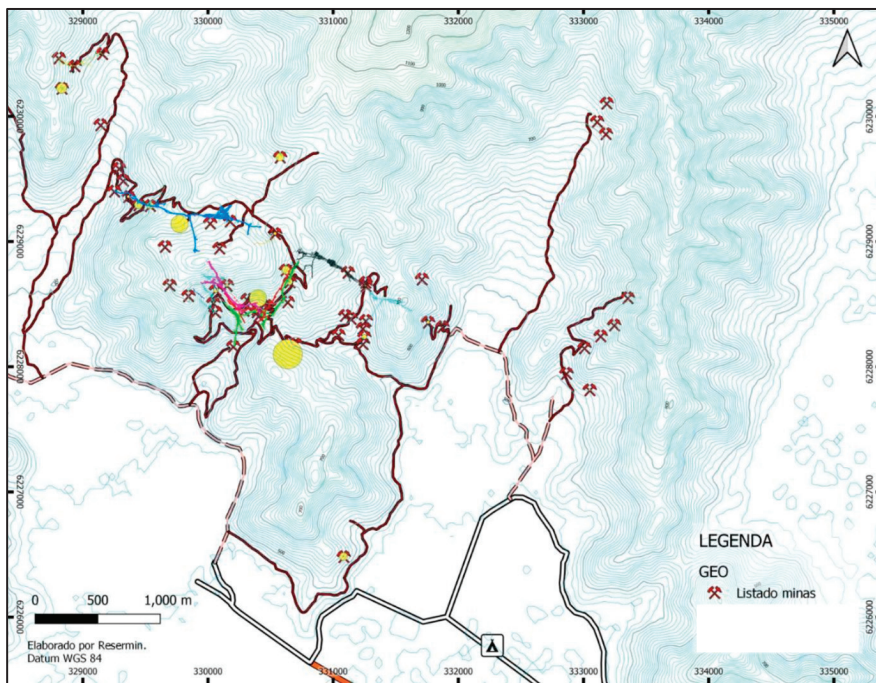

Figure 3. Distribution of the mines in the Chancón district. The legend is in Spanish. "Listado minas" = list of mines.

Figure 4. A currently abandoned mine with its identification plate (upper right).

Figure 5. Sign along the road indicating the paths toward the mines.

2.2. Methodology

The first phase of the study was to catalog the mines currently in operation in the Chancón sector. The indicators were collected in situ, starting with a visit to the tunnel and an interview with the miner in charge of the operation. The questions were adapted for the area from the general questionnaire previously developed by Seccatore et al. [39].

The number of mines operating in the area varied significantly over time, mainly as a function of the gold price and the organization of the company. In 2012, the regional government cataloged 158 tunnels, of which 129 were classified as irregular (active or not), 24 were abandoned, and only 5 were active [40]. In 2014, ENAMI identified 40 active

mines [41]. At the time of the field survey (2019–2023), approximately 30 mines were in operation, and it was possible to visit 23 of them, of which only 19 fed our database, as four of the miners failed to answer many of the questions or did so in an untrustworthy way. None of the visits made it possible to complete the questionnaire, especially the questions about cost per item, such as explosives, diesel, water, maintenance, labor, etc. In the area, costs were associated with the cost per meter of the tunnel advanced. By disregarding the section of the tunnel, which is irregular and varied from time to time, it was impossible to calculate the cost per ton of mineral, the stripping ratio or mineral dilution.

3. Results

The area of Chancón is peculiar with regard to the organizational models among small-scale miners. The legal concessions in the region only belonged to three different companies, which will be referred to as Company A, Company B and Company C, for confidentiality. Company C owned approximately 80% of the concessions, land and property.

In the case of negotiations with Company C, the area was divided into three-dimensional "cubes", and each cube was leased to an "owner". These owners paid a fee to Company C, depending on the mineral grade sold to ENAMI, as shown in Table 1.

Table 1. Discount rates paid to Company C as a function of the mineral grade of the ROM.

Mineral Grade	Discount
0.00–5.00 g/t	22%
5.01–6.00 g/t	27%
6.01–7.00 g/t	33%
>7.01 g/t	38%

Daily production varied significantly, from 2 to 40 tons per day. Figure 6 shows the production distribution of the 19 mines visited.
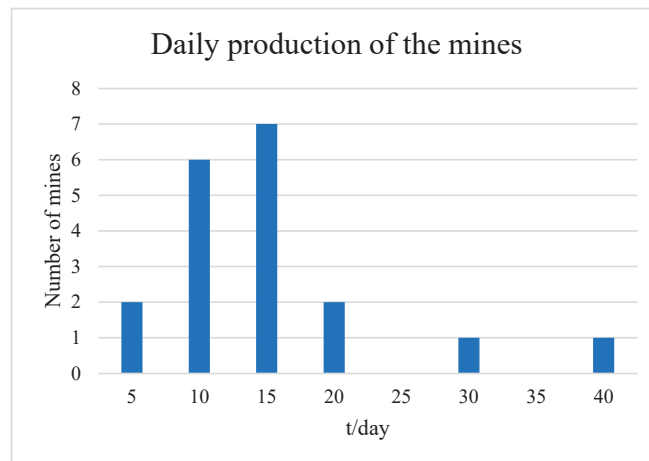
Figure 6. Number of mines associated with their daily production.

The mineral ROM grades of the mines were between 1.8 g/t and 5.0 g/t, with an average of 3.7 g/t. As discussed before, the sections of the tunnels were irregular, and so the dilution and stripping ratio influenced the inconsistencies of the grade sampled in the whole ROM. A common practice was to blend the material to keep it at about 5 g/t, to avoid the higher discounts imposed by Company C.

Mine operations were composed of drilling and blasting, loading and transport to the mine stockpile and then transport from the stockpile to the ENAMI plant. The miners

did not see potential value for the waste rock, so this was randomly deposited on the mountain slopes of that region. The workforce, inputs, geological control, planning and other observations are detailed below.

3.1. Drilling and Blasting

This was an operation that can be considered as the standard for the whole of the Chancón area. It consisted of an emulsion 1″ per 8″ cartridge as a primer for a column charge of ANFO (ammonium nitrate/fuel oil). The emulsion is initiated by a fire cap and safety fuse. Hole distributions on the tunnel face and their 3D inclination depend purely on the sentiment of the driller. Figure 7 (manual drilling) and Figure 8 (explosives ignited by the fuse and fire cap) show examples of the drilling and blasting activity.

Figure 7. Rock drilling.

Figure 8. Explosives handling (incorrect and dangerous).

The mines visited were being operated by a drilling team with a manual jackleg drill and one set of air compressors with a diesel generator per drill. Even in mines with only one drilling crew, the number of drills was 2–3 for maintenance backup purposes.

The advance per blast was between 1.0 and 1.8 m, with an average of 1.5 m. The efficiency of advancing after a tunnel blast was a key indicator in tunneling science; it is the ratio between the drilled length (pull) and the actual pull obtained. It is commonly lower than 100%, and only excellent blasting in very competent rock achieves the full efficiency. This indicates how much work (drilling) and material (explosives) were wasted in the incomplete advance of the drilled length. In economic terms, this was loss in the investment: drilling and charging 1.0 m and obtaining a 0.9 m advance meant that 10% of the investment to advance the 1.0 m was lost. In previous studies on rock blasting in a mine within the region [31], actual measurements of the pull efficiency were performed. In the

case of the present work, for practical reasons, it was impossible to perform measurements in all the mines. Therefore, miners were directly asked for their average efficiency. Due to lack of technical knowledge, the miners had some confusion regarding this aspect; therefore, our interviews obtained "perceived" pull efficiency (see Figure 9). This shows that the miners did not consider the pull efficiency to be an important concept, as they did not understand it. Most miners thought that they obtained all that they drilled, which was hardly the case using the rudimentary techniques of fire fuse and manual ignition. Some even considered their efficiency to be superior to 100%, a clear physical impossibility.
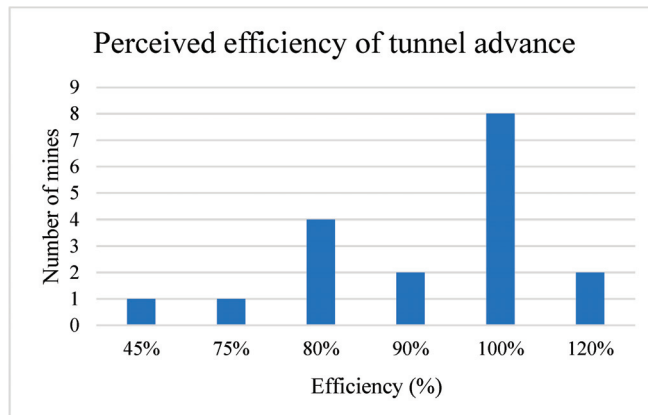
Figure 9. The efficiency of tunnel advance according to miners' perceptions.

An indicator of the operation inefficiency was the frequent use of secondary breaking, whether manual (with a sledgehammer) or with explosives and/or hydraulic hammers, as shown in Figure 10.

Figure 10. Secondary breaking of fragments.

3.2. Loading and Hauling to the Mine Stockpile

This operation was extremely variable: from 100% manual operations, up to the use of 3 ton capacity transport equipment.

In most of the mines visited, the equipment was owned, but cases of equipment being rented or shared by more than one mine were also registered. Figures 11 and 12 show examples of the hauling equipment used in the area.

Figure 11. Manual hauling equipment.

Figure 12. Hauling equipment.

3.3. Transport from the Mine Stockpile to the Plant

To deliver the material from the mine to the ENAMI processing plant, the miners needed to pay for transporting the ore on large trucks to the plant (Figure 13). The transport fee ranged between 2 and 4 USD per ton, depending on the distance from each specific mine to the plant. The closest plant was within the area of Chancón. There was another ENAMI plant about 250 km to the north; the transport fee was USD 18 per ton, and miners sent their ore there only when the mineral grade was very high.

Figure 13. Hauling truck from the mine to the plant.

3.4. Workforce

This was different to other areas of artisanal mining, where the work was remunerated by participation in production (as documented in [42]); the remuneration in Chancón was a monthly salary. There were also day labor contracts for occasional jobs or to increase production when extracting high-grade ores.

Across the region, there was still the antique figure of the "chanqueiro". A chanqueiro is a skilled miner who can visually appreciate fragments of the ROM and assess which of them are rich in ore. The chanqueiro manually selects the rocks in the ore pile that will be sent to the processing plant. Whoever transports the ROM also performs this visual separation of the mineral.

Work shifts varied for each mine: the most common was from Monday to Friday, with a 7–8 h shift and occasionally part-time on Saturday. Only one of the mines visited adopted the 5 × 5-day shift system employed in large-scale mining. This shift system comprises 5 days of work and 5 days off. In large-scale mining, the production never stops, as the size of the workforce allows for alternating teams to cover any days off. In this case, the workforce of these mines is limited; hence, for the 5 days off, the mine does not operate. The owner declared that he prefers not to have two teams taking alternate turns, as he believes that it is better for each operator to be responsible for the equipment that they use.

In general, a team of miners consisted of one driller, one drilling assistant and a hauling machine operator. The driller and the machine operator were trained and, generally, did not take turns.

The presence of female operatives was almost non-existent in the operation and management of the mines. Only one woman was observed as an active miner, specializing in the use of loading–hauling equipment. In addition to her, another woman worked as a prospector. Generally speaking, female presence was associated with being caregivers or cooks, whose husbands are mine managers or mine watchmen.

3.5. Materials and Supplies

In the case of materials and supplies, the owners knew their consumption over a period but did not document cost control or expenses.

- The operation consumed around 200 L of water per day. The sources were local spring water, mine drainage water, water brought in from the city or water from a reservoir.

- Potable water for human consumption was about 20 L per operator per day.
- Diesel consumption varied between 250 and 3000 L per month. This wide range was due to the fact that some mines employed used equipment bought from large-scale mines.
- Oil consumption for equipment lubrication was not registered by the miners, as equipment maintenance was only carried out inconsistently.
- There was no electricity beamline. Two mines had solar-powered systems for their office and cafeteria.

3.6. Geological Control and Mine Planning

Geological control was performed visually at the tunnel face, by color or the presence of accessory minerals that the miners generally associated with the presence of gold. A common practice was to use the drill bar to drill up to 12 m and observe the color of the flush water. The miners called this "exploratory drilling".

Regarding the identification of the veins at the surface, the miners observed veins on the outcrops and attempted to visually project the visible veins to the location of the veins in the other mines. This operation was extremely imprecise. In the field, cases were observed in which a tunnel had to drastically detour from its axis because the vein was 5 to 10 m away from the estimated location. In other cases, advances of between 30 and 50 m have been observed without "reaching" the vein. The associated costs of advances per meter are documented by Seccatore et al. [30], and the chances of finding a vein and the associated economical risk of losing the investment for tunnel advance in the case of "missing" the vein are extensively documented, calculated and discussed by Espinoza et al. [38].

Without geological knowledge, it is impossible to perform mine planning. The miners relied on a general idea of the direction of the next tunnel advance depending on the visually determined direction of the vein. A monthly limit of ores that can be sold to ENAMI exists, which is determined by SERNAGEOMIN, depending on the available equipment in the mine.

3.7. Economic Analyses

As described in the methodology section, despite the detailed questionnaire, miners could not define every separated item of cost. Instead, they considered the cost per meter of tunnel advanced. The cost reported was 350,000 CPL/m for a tunnel with a section of 2.5 m × 2.5 m. The actual tunnel contour was irregular, but, for the sake of simplicity in the calculation, it was considered a square. The average rock density was 2.7 t/m^3. The cost per mass of ROM was calculated using Equation (1), and the result was 20,741 CLP/t.

$$Cost/mass = \frac{Cost/meters}{\rho \times A} \tag{1}$$

Cost/mass: cost per mass of ROM (CLP/t).
Cost/meters: cost by extraction meters (CLP/m).
ρ: density (t/m^3).
The income was calculated using the following equations:

$$INC = ROM \times P \tag{2}$$

INC: income (CLP).
ROM: run-of-mine (t).
P: ROM price at the mine (USD/t).
The price of the mineral is what ENAMI pays, minus the transportation cost of the mineral from the mine to the plant and the fee that the miners must pay to the actual owner of the mine.

$$P = V_E - f - t_o \tag{3}$$

V_E: amount paid by ENAMI.
F: mine-to-plant freight.
t_o: mine owner's fee (Table 1).
ENAMI payments are subjected to different reductions, varying from taxes to penalties related to the quality of the mineral sent to the plant.

$$V_E = P_R - reductions \tag{4}$$

V_E: amount paid by ENAMI.
P_R: reference price for calculating fees.
Reductions: taxes, fees, moisture and contaminant penalty and loan payment.

$$V_E = P_R - t_{SM} \times P_R - f_{RM} \times P_R \tag{5}$$

$$V_E = P_R \times (1 - (t_{SM} + f_{RM})) \tag{6}$$

t_{SM}: taxes for small-scale mining in Chile.
f_{RM}: Rancagua miners association fee (ASOMIN).

$$P_R = g_R \times (V_B + (g_R - g_B) \times V_S) - d_{con} \times V_S \tag{7}$$

P_R: reference price for calculating fees.
g_R: ROM grade.
V_B: mineral base value of ENAMI.
g_B: base grade of ENAMI.
V_S: mineral **scale value** of ENAMI (discount based on the base grade).
d_{Con}: **fee** for minerals to be concentrated on ENAMI.

$$P = ((g_R \times (V_B + (g_R - g_B) \times V_S) - d_{con} \times V_S) \times (1 - (t_{SM} + f_{RM} + f_{ower})) - f \tag{8}$$

g_R: variable g/t.
V_B: CLP 119,342.
g_B: 5 g/t.
V_S: CLP 31,957.
d_{Con}: 15%.
t_{SM}: 4%.
f_{RM}: 0.2%.
f_{ower}: 22%.
The results for differences in grades, costs and production rates are presented in Tables 2 and 3. The production rates considered here are the most frequent rates indicated in Figure 6. The costs indicated here do not consider the investments necessary for waste excavation nor equipment purchase, maintenance or rental.

Table 2. Net cash provided by the grade and cost for 200 t/month.

Grade (g/t)	INCOME (CLP)	Cost CLP/t					
		10,000	15,000	20,000	25,000	30,000	35,000
2	18,664	1,732,712	732,712	(267,288)	(1,267,288)	(2,267,288)	(3,267,288)
3	42,248	6,449,602	5,449,602	4,449,602	3,449,602	2,449,602	1,449,602
4	65,832	11,166,492	10,166,492	9,166,492	8,166,492	7,166,492	6,166,492
5	89,417	15,883,383	14,883,383	13,883,383	12,883,383	11,883,383	10,883,383

Scenario 1—Net Cash Provided by Operating Activities for: 200 t/Month (CLP/Month)

Table 3. Net cash provided by the grade and cost for 300 t/month.

Scenario 2—Net Cash Provided by Operating Activities: 300 t/Month (CLP/Month)							
Grade (g/t)	INCOME (CLP)	Cost/t					
		10,000	15,000	20,000	25,000	30,000	35,000
2	18,664	2,599,068	1,099,068	(400,932)	(1,900,932)	(3,400,932)	(4,900,932)
3	42,248	9,674,404	8,174,404	6,674,404	5,174,404	3,674,404	2,174,404
4	65,832	16,749,739	15,249,739	13,749,739	12,249,739	10,749,739	9,249,739
5	89,417	23,825,074	22,325,074	20,825,074	19,325,074	17,825,074	16,325,074

It was reported by the miners that it is necessary to develop up to 100 m in waste rock until the mineral vein is reached. The cost of mere development in waste to encounter the vein can reach CLP 35,000,000. Realistically, for Chancón, a reserve of about 193k oz Au was plausible. This corresponds to 10 months of production for scenario 1 and 7 months for scenario 2. These values are shown in Tables 2 and 3; conditions with a mineral grade below 3 g/t and OPEX above 25,000 CLP/t are unfeasible. We show these values in Tables 2 and 3 with a lighter tone for didactic purposes.

3.8. Accidents

Table 4 summarizes the accidents in Chancón documented by the public media. It is plausible that the number of accidents that were not fatal is higher, as they may not have been communicated outside the mine, therefore not having mediatic coverage.

Table 4. Accidents in Chancón reported by the public media.

Year	Type of Accident	Number of Miners Involved	Fatal	Source
2022	Fall from height	1	Yes	2022 [42]
2022	Rockfall	1	No	2022 [43]
2020	Rockfall	1	Yes	2020 [44]
2016	Premature detonation of explosives	3	No	2016 [45]

Figure 14 and Table 5 summarize the fatal accidents in the whole mining industry in Chile as reported by Sernageomin [46]. Table 5 details the accidents in the mining industry over the last few months, before the redaction of this article.
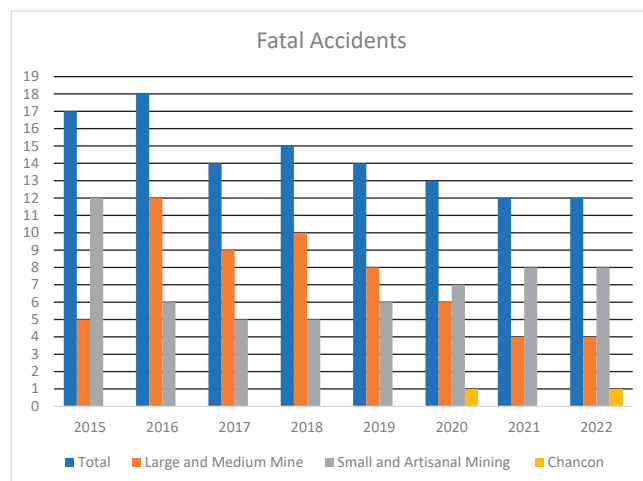
Figure 14. Mining fatal accidents, 2015–2022.

Table 5. Fatal accidents during mining operations in the second quartile of 2023 (Sernageomin).

Month	Type of Accident	Mine Type	Number of Miners Involved	Number of Deaths
January	Getting crushed	Large	1	1
February	Fall from height	Small-Scale	1	1
February	Rockfall	Artisanal	2	1
March	Vehicle out of control	Exploration	1	1
April	Fall from height	Medium	3	1

Figure 15 shows the total number of accidents, both fatal and non-fatal, in the Chilean mining industry between 2019 and 2022.
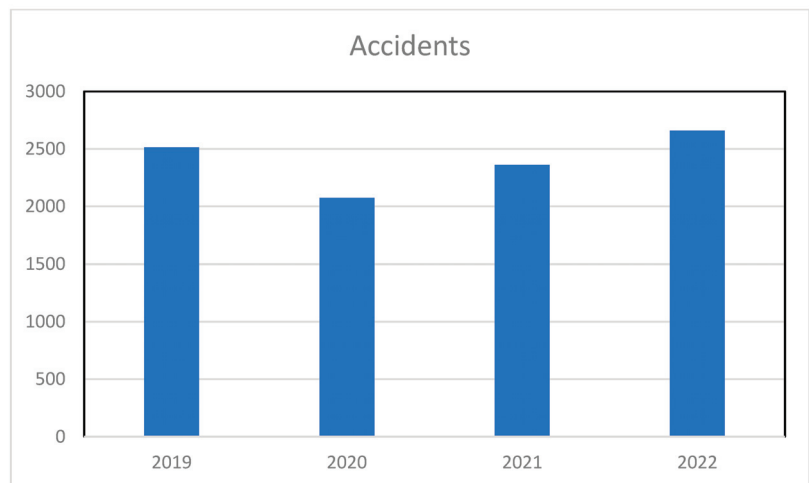
Figure 15. Total mining accidents, 2019–2022.

3.9. Further Observations

- Of the mines, 60% had some type of funding from ENAMI. The range of funding was between CLP 5,000,000 and CLP 75,000,000.
- The government is present in the region: at least every six months, an agency visits each mine. In the case of mines with active financing, visits from the funding agency may take place on a monthly basis.
- In general, miners had only one work front available, which did not allow for operational flexibility and generated periods of pure cost, extracting only waste rock.

  The main problems that miners identified were:

- The time taken to analyze the samples of the material sent to ENAMI. The miners used these results as a control tool to know what mineral grade was present in the ore they extracted. Therefore, they would know if they were excavating in the right direction or not. The average time to obtain the grade was 30 days; therefore, when the result arrived, the area had already been mined.
- There is a systematic positive difference between the grade of the sample collected by the miners and sent for analysis and the grade of the lot sent to the processing plant and estimated by ENAMI. This is because the miners sampled the vein and, as mentioned, did not contemplate the concept of excavation dilution due to the size of the tunnel.
- The monthly production limit established by SERNAGEOMIN "strangled" cashflow, which was already compromised by all the other reductions documented above.

3.10. Issues with the Processing Plant

The biggest challenge observed was the reconciliation between the grades of the samples collected by the grades of the lot delivered to the plant. Miners sampled the "richest area" samples and did not consider the operational dilution, so the lot grade was systematically lower than that of the samples. The difference between the analyses, reported by the miners, was 100–400%.

Furthermore, if the grade of the lot was lower than the cut-off grade, miners lost the amount they paid for freight. The current cut-off grade at Chancón is 2 g/t. There is a rule according to which lots between 1 and 2 g/t are stored for 1 month: if the miner manages to deliver a lot that is sufficient to be blended to a grade greater than 2 g/t, then the miner receives the value of the low-grade lot. Otherwise, the material stays within the plant.

An alternative solution which was encountered was to send the material to a gravitational pre-concentration plant, located about 300 km to the north of Chancón. This is a private plant which carries out a pre-concentration, from the mill to the flotation cells, and sells the concentrate to ENAMI (Figures 16–19). This reduced the grade variability. Miners could follow the lot processing, and the amount of transported material was reduced by at least 80%, which can be visually observed by the difference between the lots in Figures 16 and 19. The advantage was that the plant was completely mercury- and cyanide-free. The disadvantage was that it generated flotation waste which, despite being an inert material, needed to be deposited in a tailings dam.

Figure 16. Stockpiles of the initial lot that would be processed. Each pile belonged to a different miner.

Figure 17. Crusher and mill at the plant.

Figure 18. Flotation cells.

Figure 19. End-of-process material that would be sold to ENAMI. Each stack belonged to a different miner.

4. Discussion

The area of study is unique to South American artisanal mining sites. Even within Chile, many artisanal miners still process their own ore, amalgamating it with mercury, especially in the north. They are called "pirquineros", and the common process is milling the ore in what are known as "Chilean mills" or "trapiches", which consist of a stone basin in which the material is deposited and two stone wheels, which rotate around an axis to mill the material. Mercury is usually added directly into the trapiche. This is well documented in many works, such as [47–54]. As such, artisanal gold mining (AGM) is generally associated with Hg pollution, as stated in the introduction, within studies across the world. Therefore, previous initiatives have focused on the elimination of Hg in Au processing. Table 6 reports a selected list of initiatives aimed at the reduction in or elimination of Hg pollution.

Over time, initiatives moved from purely technological approaches to a more heuristic approach, including a broader vision of the framework.

Regarding the attempts made in Table 6 (and as mentioned in the introduction), one of the most prolific authors working and publishing in this field eventually came to an unfortunate conclusion: "those approaches have not resulted in mercury reduction or elimination" [36]. It is in that study that the authors came to the proposed solution from the experience of "over 40 years of intensive research and field projects across 35 countries":

centralized, clean and modern processing plants where the miners' ores are processed for them. "The miners mine while the processors process".

Table 6. A selected list of initiatives which attempted to reduce or eliminate Hg from Au processing.

Source	Place	Solution Proposed	Type of Solution
[55]	Latin America	Gravity concentration Flotation Electro-leaching Cyanidation NaCl electrolytic process Retort for Hg recovery Law enforcement Technical assistance Training artisanal miners	Technological Policy Strategic
[6]	Transversal	Construction of a training center for miners	Policy
[55]	Indonesia, Ecuador, Colombia	Mill leaching	Technological
[56]	Mozambique	Adopt clean technologies that obey the criteria of being economically beneficial, simple and expedient	Technological
[12]	Transversal	Mercury removal technology, miner education on mercury hazards, economic gains and policy	Policy
[57]	Colombia	Capacity building, education and the presence of trainers prior to introducing a new approach	Strategic
[58]	Ecuador–Peru	Gold isolation via centrifugal and magnetic removal of gangue materials	Strategic
[59]	Transversal	Incentivize gravity concentration	Technological–Policy

This conclusion formed the basis of this study: a clean centralized processing plant with no Hg involved. Having eliminated Hg, is it currently a sustainable operation?

The authors' findings indicated that no, it is not.

Albeit simplified, the general perception of sustainability or sustainable development is based on three concepts, or "pillars": social, economic and environmental factors (see the discussion by Purvis et al. [60]). Considering these three concepts, the following considerations can be made for the Chancón district:

- Economic point of view: The miners did not have a constant income; they had only one producing front and advances in the hope of finding ores. The system was to work as much as possible on the mineral with all the equipment and people available and, when operating in waste rock, work gradually, according to how much was possible to invest. Generally, the earnings from ore extraction were spent or saved and not used as working capital to invest in waste rock extraction. There was no planning for managing the sterile–mineral ratio (stripping ratio). If it were not for the support of ENAMI, many miners would not be able to sustain their operating costs.
- Social point of view: Even though the operation produced a small economy and socially impacted miners' families and the surroundings (e.g., maintaining the presence of a school), this impact was not constant. There was no real development in the region, as there was no increase in or development of new schools, good medical care, clean water, sanitation, etc. This was due to the precarious income described above.

- Environmental point of view: As stated, Hg was not used in the area. Nevertheless, Hg is not the only environmental externality of a mining operation. Waste rock was simply deposited on the slopes of surrounding hills, creating a geotechnical hazard in the form of slope instability (also considering Chilean seismicity) and the potential for acid drainage. The mines were not closed, but simply abandoned, leaving a panorama of empty holes on hillsides, with many dangers associated with abandoned tunnels. There was no concern for material and equipment management. Machinery which did not work was set aside to rust or be used as a source of scrap materials. Used tires, diesel and motor oil were thrown away (one of the authors of this study needed some used tires for another project and found four at the side of the first bend of the road).
- To parallel the list in Table 6 (of proposed solutions for the Hg issue adopted in the past), the authors prepared a list of issues encountered, proposed solutions and classifications of solution types for this Hg-free alternative (Table 7).

Table 7. Issues versus solutions for Chancón artisanal and small-scale Hg-free mining.

Issue Encountered	Solution Proposed	Type of Solution
High discount rates paid to Company C (the company that owned 80% of the concessions). The discounts are determined according to a rigid table with pre-fixed ranges of values of mineral grades (0.1 g/t above the limit value of the range, and the discount rate rises to the upper range).	Negotiate new rates with the company. Negotiate a continuous discount curve based on the grade and not a discrete set of values.	Economic Note: The government could help in the negotiation.
Waste rock: currently, it is dumped with no criterion or control on the slopes of hills.	Adopt a circular economy concept to give economical value to waste rock, e.g., for road pavement or construction material. Transform an environmental passive externality into an economic asset. Within the concept of the zero-waste operation.	Technological Market Note: The government could create projects for material use and valorization, together with entities such as universities.
Drilling and blasting. The drilling mesh, selection of the number of holes and their distribution is aleatorial. Hole ignition is still made by a safety fuse.	Create rules for a blasting plan (drill plan, charge per hole, initiation sequence) for each type of rock, and train miners in its implementation and realization. Adopt modern techniques (such as shock-tube initiation and employ delays). These solutions were discussed by Seccatore et al. [30,39]	Technological Training
Lack of geological control and mine planning.	Carry out studies for small-scale geological characterization (with auditable samples). Create auditable geological models. Implement a mine planning cycle for small-scale mining (thoroughly discussed in [14,61]).	Technology Transfer Economic Policies Note: Central and local governments and local agencies play a central role in helping public or private financing of these initiatives
Issues with the ENAMI processing plant: its technological efficiency and real recovery rate.	Public investment for upgrading the ENAMI plant. Promotion of investment to build competitive private plants with state-of-the-art technology and higher recovery. Build gravimetric concentration plants close to the mines to transport concentrate only.	Policy Technological Economic

From the list of proposed solutions, only a few are purely technological; they go hand-in-hand with policy making and economic investment.

5. Conclusions

Most academic studies on AGM are focused on mercury use and its environmental and social impacts. They are mainly focused on people's health, including both the miners and the people around mines. Another much-studied aspect is the formalization of operations: as anyone would agree, it is necessary to be familiar with the operations in order to do something about them. Little is discussed about operational efficiency and mine planning, which was the focus of this study.

This work was carried out in a Hg-free AGM region to answer the following question: Are Hg-free AGM operations sustainable? The focus was to analyze sustainability in the context of the following main pillars: social, economic, and environmental factors.

It can be concluded that, for an AGM operation to be sustainable, there are many other requirements besides eliminating mercury. It is necessary to act on the three pillars of sustainability simultaneously and implement a mine planning cycle with geological knowledge, constant improvement, and operational efficiency.

With mining planning, it will be possible to respect the sterile–mineral relation (stripping ratio). The waste rock can be extracted at the necessary pace to make mineralized fronts available. The operation could continue steadily, in a similar manner to a standard medium or large mining company.

In this study, we performed a transversal diagnosis of mining operations. Based on the results exposed here, it is possible to implement simple operational improvements, plan mineral exploration and, by employing a geological model, create a mining plan, thus achieving sustainable operations.

Author Contributions: Conceptualization, T.M. and J.S.; methodology, T.M. and J.S.; validation, T.M., J.S. and Y.C.; formal analysis, T.M.; investigation, T.M. and J.S; resources, T.M. and J.S.; data curation, T.M. and J.S; writing—original draft preparation, T.M.; writing—review and editing, T.M., J.S. and Y.C.; visualization, J.S.; supervision, J.S.; project administration, T.M.; funding acquisition, T.M. and J.S. All authors have read and agreed to the published version of the manuscript.

Informed Consent Statement: Informed consent was obtained from all subjects involved in the study.

Data Availability Statement: Data is unavailable due to privacy.

Conflicts of Interest: The authors declare no conflict of interest.

References

1. Cano, Á.; Kunz, N.C. Large-scale and small-scale mining in Peru: Exploring the interface. *Resour. Policy* **2022**, *76*, 102530. [CrossRef]
2. CASM. Map of Artisanal and Small-Scale Miners around the World, Communities and Small-Scale Mining (CASM). 2012. Available online: http://www.artisanalmining.org/casm/minersmap (accessed on 20 August 2019).
3. Cossa, H.; Scheidegger, R.; Leuenberger, A.; Ammann, P.; Munguambe, K.; Utzinger, J.; Macete, E.; Winkler, M.S. Health studies in the context of artisanal and small-scale mining: A scoping review. *Int. J. Environ. Res. Public Health* **2021**, *18*, 1555.
4. Estrela, A.M.; Hilson, M.H. Cooperatives as a Centre Piece for Formalizing Small-Scale Mining in Sub-Saharan Africa: Rationale, Benefits and Limitations. In *Routledge Handbook of the Extractive Industries and Sustainable Development*; Routledge: London, UK, 2022.
5. Hilson, G. 'Formalization bubbles': A blueprint for sustainable artisanal and small-scale mining (ASM) in sub-Saharan Africa. *Extr. Ind. Soc.* **2020**, *7*, 1624–1638. [CrossRef]
6. Hinton, J.J.; Veiga, M.M.; Veiga, A.T.C. Clean artisanal gold mining: A utopian approach? *J. Clean. Prod.* **2003**, *11*, 99–115.
7. McDaniels, J.; Chouinard, R.; Veiga, M.M. Appraising the Global Mercury Project: An adaptive management approach to combating mercury pollution in small-scale gold mining. *Int. J. Environ. Pollut.* **2010**, *41*, 242. [CrossRef]
8. MMSD. Artisanal and Small-Scale Mining. In *Final Report on Mining, Minerals and Sustainable Development*; International Institute for Environment and Development and World Business Council for Sustainable Development: London, UK, 2002; Chapter 13.

9.   Purnomo, M.; Utomo, M.R.; Pertiwi, V.A.; Laili, F.; Pariasa, I.I.; Riyanto, S.; Andriatmoko, N.D.; Handono, S.Y. Resistance to mining and adaptation of Indonesia farmer's household to economic vulnerability of small scale sand mining activities. *Local Environ.* **2021**, *26*, 1498–1511.

10. Sousa, R.N.; Veiga, M.M.; Meech, J.; Jokinen, J.; Sousa, A.J. A simplified matrix of environmental impacts to support an intervention program in a small-scale mining site. *J. Clean. Prod.* **2011**, *19*, 580–587. [CrossRef]

11. Urkidi, L. A local environmental movement against gold mining: Pascua–Lama in Chile. *Ecol. Econ.* **2010**, *70*, 219–227.

12. Veiga, M.M.; Angeloci-Santos, G.; Meech, J.A. Review of barriers to reduce mercury use in artisanal gold mining. *Extr. Ind. Soc.* **2014**, *1*, 351–361. [CrossRef]

13. Velásquez, J.R.; Schwartz, M.; Phipps, L.M.; Restrepo-Baena, O.J.; Lucena, J.; Smits, K.M. A review of the environmental and health implications of recycling mine tailings for construction purposes in artisanal and small-scale mining communities. *Extr. Ind. Soc.* **2022**, *9*, 101019. [CrossRef]

14. Marin, T.; Seccatore, J.; De Tomi, G.; Veiga, M. Economic feasibility of responsible small-scale gold mining. *J. Clean. Prod.* **2016**, *129*, 531–536. [CrossRef]

15. Massaro, L.; de Theije, M. Understanding small-scale gold mining practices: An anthropological study on technological innovation in the Vale do Rio Peixoto (Mato Grosso, Brazil). *J. Clean. Prod.* **2018**, *204*, 618–635.

16. Teschner, B.; Smith, N.M.; Borrillo-Hutter, T.; John, Z.Q.; Wong, T.E. How efficient are they really? A simple testing method of small-scale gold miners' gravity separation systems. *Miner. Eng.* **2017**, *105*, 44–51. [CrossRef]

17. Calvimontes, J.; Massaro, L.; Araujo, C.; Moraes, R.; Mello, J.; Ferreira, L.; de Theije, M. Small-scale gold mining and the COVID-19 pandemic: Conflict and cooperation in the Brazilian Amazon. *Extr. Ind. Soc.* **2020**, *7*, 1347–1350. [CrossRef]

18. Hilson, G.; Van Bockstael, S.; Sauerwein, T.; Hilson, A.; McQuilken, J. Artisanal and small-scale mining, and COVID-19 in sub-Saharan Africa: A preliminary analysis. *World Dev.* **2021**, *139*, 105315. [CrossRef]

19. Perks, R.; Schneck, N. COVID-19 in artisanal and small-scale mining communities: Preliminary results from a global rapid data collection exercise. *Environ. Sci. Policy* **2021**, *121*, 37–41. [CrossRef]

20. Pijpers, R.J.; Luning, S. We have so many challenges: Small-scale mining, COVID-19 and constant interruptions in West Africa. *Anthropol. Today* **2021**, *37*, 10–14.

21. Springer, S.K.; Peregovich, B.G.; Schmidt, M. Capability of social life cycle assessment for analyzing the artisanal small-scale gold mining sector—Case study in the Amazonian rainforest in Brazil. *Int. J. Life Cycle Assess.* **2020**, *25*, 2274–2289. [CrossRef]

22. Ulmer, G. The Earth Is Hungry: Amerindian Worlds and the Perils of Gold Mining in the Peruvian Amazon. *J. Lat. Am. Caribb. Anthropol.* **2020**, *25*, 324–339. [CrossRef]

23. Siqueira-Gay, J.; Sánchez, L.E. The outbreak of illegal gold mining in the Brazilian Amazon boosts deforestation. *Reg. Environ. Chang.* **2021**, *21*, 28. [CrossRef]

24. Kaufmann, C.; Côte, M. Frames of extractivism: Small-scale goldmining formalization and state violence in Colombia. *Political Geogr.* **2021**, *91*, 102496. [CrossRef]

25. IIMP—El Instituto de Ingenieros de Minas del Perú. Colombia y Peru Buscan Centralizar Compra de Oro Para Combatir Crime e Informalidad. 2021. Available online: https://iimp.org.pe/raiz/colombia-y-peru-buscan-centralizar-compra-de-oro-para-combatir-crimen-e-informalidad (accessed on 17 January 2022). (In Spanish).

26. DW; El Oro De Los Latinoamericanos: ¿Qué Tanto Se Conserva En Los Bancos Centrales? 2022. Available online: https://www.dw.com/es/el-oro-de-los-latinoamericanos-qu%C3%A9-tanto-se-conserva-en-los-bancos-centrales/a-56776949 (accessed on 15 July 2022). (In Spanish).

27. MCH. Invertirán $792 Millones Para Modernizar Plantas de Procesamiento de Oro Libre de Mercurio en Atacama. 2021. Available online: https://www.mch.cl/2021/02/15/invertiran-792-millones-para-modernizar-plantas-de-procesamiento-de-oro-libre-de-mercurio-en-atacama/# (accessed on 10 May 2022). (In Spanish).

28. Faúndez, P.I.; Marquardt, C.; Jara, J.J.; Guzmán, J.I. Valuation and Prioritization of Early-Stage Exploration Projects: A Case Study of Cu–Ag and Au-Mineralized Systems in the Tiltil Mining District, Chile. *Nat. Resour. Res.* **2020**, *29*, 2989–3014. [CrossRef]

29. Poveda-Bautista, R.; Gonzalez-Urango, H.; Ramírez-Olivares, E.; Diego-Mas, J.-A. Engaging Stakeholders in Extraction Problems of the Chilean Mining Industry through a Combined Social Network Analysis-Analytic Network Process Approach. *Complexity* **2022**, *2022*, 9096744. [CrossRef]

30. Seccatore, J.; Gonzalez, P.; Herrera, M. Peculiarities of drilling and blasting in underground small-scale mines. *REM-Int. Eng. J.* **2020**, *73*, 387–394. [CrossRef]

31. Tripodi, E.E.M.; Rueda, J.A.G.; Céspedes, C.A.; Vega, J.D.; Gómez, C.C. Characterization and geostatistical modelling of contaminants and added value metals from an abandoned Cu–Au tailing dam in Taltal (Chile). *J. South Am. Earth Sci.* **2019**, *93*, 183–202. [CrossRef]

32. Reinoso, F.; Rodrigo, P. Formulación de Instrumentos de Fomento a la Innovación em Pequeña Minería. Tesis Para Optar al Grado de Magíster em Gestión Políticas Públicas. Ph.D. Thesis, Universidade de Chile, Facultad de Ciencias Físicas y Matemáticas, Departamento de Ingeniería Industrial, Santiago, Chile, 2013. (In Spanish).

33. BBCL—BioBio Chile. 2022. Available online: https://www.biobiochile.cl/noticias/nacional/region-de-ohiggins/2022/03/24/rescatan-a-minero-que-quedo-atrapado-tras-derrumbe-en-el-maiten-de-chacon-de-rancagua.shtml (accessed on 7 October 2022). (In Spanish).

34. MIREME. Ministério dos Recursos Minerais e Energia, Republica de Mocambique. 2022. Available online: https://www.mireme.gov.mz/index.php?option=com_content&view=article&id=2:ministra-dos-recursos-minerais-inteira-se-do-acidente-na-mina-de-ouro-em-nampula&catid=9:comunicados&Itemid=101 (accessed on 10 May 2022). (In Portuguese)

35. NYTIMES. Mining Disasters. 2022. Available online: https://www.nytimes.com/topic/subject/mining-disasters (accessed on 2 May 2022).

36. Veiga, M.M.; Fadina, O. A review of the failed attempts to curb mercury use at artisanal gold mines and a proposed solution. *Extr. Ind. Soc.* **2020**, *7*, 1135–1146. [CrossRef]

37. ENAMI—Empresa Nacional de Mineria. 2023. Available online: www.enami.cl (accessed on 8 February 2023). (In Spanish).

38. Espinoza, C.; Seccatore, J.; Herrera, M. Chilean artisanal mining: A gambling scenario. *REM-Int. Eng. J.* **2020**, *73*, 241–246. [CrossRef]

39. Seccatore, J.; Magny, L.; De Tomi, G. Technical and operational aspects of tunnel rounds in artisanal underground mining. *REM Rev. Esc. Minas* **2014**, *67*, 303–310. [CrossRef]

40. SERNAGEOMIN. *Atlas de Faenas Mineras, Regiones de Valparaíso, del Libertador General Bernardo O´Higgins y Metropolitana de Santiago (Versión Actualizada)*; Servicio Nacional de Geología y Minería, Mapas y Estadísticas de Faenas Mineras de Chile: Santiago, Chile, 2012; No 9; 177p. (In Spanish)

41. ENAMI. *Estudio Geológico Distrital Enami Chancon*; Propriedade ENAMI: Santiago, Chile, 2014; 112p. (In Spanish)

42. El Rancaguino. Fallece Trabajador en Mina don Hector Ubicada en Chancon. 2022. Available online: https://www.elrancaguino.cl/2022/10/28/fallece-trabajador-en-mina-don-hector-ubicada-en-chancon/ (accessed on 11 July 2023). (In Spanish).

43. Portal Minero. Tras Estar Atrapado Por Mas de Seis Horas Fue Rescatado Minero En Chancon. 2022. Available online: https://www.portalminero.com/wp/tras-estar-atrapado-por-mas-de-seis-horas-fue-rescatado-minero-en-chancon/ (accessed on 11 July 2023). (In Spanish).

44. El Tipografo. Trabajador Minero Fallece en Chan-Con. 2020. Available online: https://eltipografo.cl/2020/05/trabajador-minero-fallece-en-chancon (accessed on 11 July 2023). (In Spanish).

45. Revista Tecnicos Mineros. Trabajadores Resultan Lesionados en Faenas Mineras de Chan-Con. 2016. Available online: https://www.revistatecnicosmineros.com/2016/12/trabajadores-resultan-lesionados-en-faenas-mineras-de-chancon/ (accessed on 11 July 2023). (In Spanish).

46. Sernageomin. Estadísticas de Accidentabilidad. Industria Extractiva Minera. Servicio Nacional de Geología y Minería. 2023. Available online: https://www.sernageomin.cl/accidentabilidad-minera/ (accessed on 11 July 2023). (In Spanish).

47. Castro, S.H.; Sánchez, M. Environmental viewpoint on small-scale copper, gold and silver mining in Chile. *J. Clean. Prod.* **2003**, *11*, 207–213. [CrossRef]

48. Ghorbani, Y.; Kuan, S.H. A review of sustainable development in the Chilean mining sector: Past, present and future. *Int. J. Min. Reclam. Environ.* **2017**, *31*, 137–165. [CrossRef]

49. Higueras, P.; Oyarzun, R.; Oyarzún, J.; Maturana, H.; Lillo, J.; Morata, D. Environmental assessment of copper–gold–mercury mining in the Andacollo and Punitaqui districts, northern Chile. *Appl. Geochem.* **2004**, *19*, 1855–1864. [CrossRef]

50. Higueras, P.; Oyarzun, R.; Lillo, J.; Oyarzún, J.; Maturana, H. Atmospheric mercury data for the Coquimbo region, Chile: Influence of mineral deposits and metal recovery practices. *Atmos. Environ.* **2005**, *39*, 7587–7596. [CrossRef]

51. Higueras, P.; Oyarzun, R.; Kotnik, J.; Esbrí, J.M.; Martínez-Coronado, A.; Horvat, M.; López-Berdonces, M.A.; Llanos, W.; Vaselli, O.; Nisi, B.; et al. A compilation of field surveys on gaseous elemental mercury (GEM) from contrasting environmental settings in Europe, South America, South Africa and China: Separating fads from facts. *Environ. Geochem. Health* **2014**, *36*, 713–734. [CrossRef] [PubMed]

52. Oyarzún, J.; Castillo, D.; Maturana, H.; Kretschmer, N.; Soto, G.; Amezaga, J.M.; Rötting, T.S.; Younger, P.L.; Oyarzún, R. Abandoned tailings deposits, acid drainage and alluvial sediments geochemistry, in the arid Elqui River Basin, North-Central Chile. *J. Geochem. Explor.* **2012**, *115*, 47–58. [CrossRef]

53. Rector, J.L. *The History of Chile*, 2nd ed.; Greenwood: Santa Barbara, CA, USA, 2019; ISBN 9781440863738.

54. Veiga, M.M.; Nunes, D.; Klein, B.; Shandro, J.A.; Velasquez, P.C.; Sousa, R.N. Mill leaching: A viable substitute for mercury amalgamation in the artisanal gold mining sector? *J. Clean. Prod.* **2009**, *17*, 1373–1381. [CrossRef]

55. Veiga, M.M. *Introducing New Technologies for Abatement of Global Mercury Pollution in Latin America*; CETEM/CNPq: Rio de Janeiro, Brazil, 1997; p. 94.

56. Drace, K.; Kiefer, A.M.; Veiga, M.M.; Williams, M.K.; Ascari, B.; Knapper, K.A.; Logan, K.M.; Breslin, V.M.; Skidmore, A.; Bolt, D.A.; et al. Mercury-free, small-scale artisanal gold mining in Mozambique: Utilization of magnets to isolate gold at clean tech mine. *J. Clean. Prod.* **2012**, *32*, 88–95. [CrossRef]

57. García, O.; Veiga, M.M.; Cordy, P.; Suescún, O.E.; Molina, J.M.; Roeser, M. Artisanal gold mining in Antioquia, Colombia: A successful case of mercury reduction. *J. Clean. Prod.* **2015**, *90*, 244–252. [CrossRef]

58. Veiga, M.M.; Angeloci, G.; Ñiquen, W.; Seccatore, J. Reducing mercury pollution by training Peruvian artisanal gold miners. *J. Clean. Prod.* **2015**, *94*, 268–277. [CrossRef]

59. Zolnikov, T.R.; Ortiz, D.R. A systematic review on the management and treatment of mercury in artisanal gold mining. *Sci. Total Environ.* **2018**, *633*, 816–824. [CrossRef]

60. Purvis, B.; Mao, Y.; Robinson, D. Three pillars of sustainability: In search of conceptual origins. *Sustain. Sci.* **2019**, *14*, 681–695. [CrossRef]

61. Seccatore, J.; Marin, T.; De Tomi, G.; Veiga, M. A practical approach for the management of resources and reserves in Small-Scale Mining. *J. Clean. Prod.* **2014**, *84*, 803–808. [CrossRef]

Article

An Adaptive Modeling-Based Aeromagnetic Maneuver Noise Suppression Method and Its Application in Mine Detection

Fengyi Bi, Ping Yu, Jian Jiao *, Longran Zhou, Xiangcheng Zeng and Shuai Zhou

Department of Solid Earth Geophysics, College of Geo-Exploration Science and Technology, Chaoyang Campus, Jilin University; Changchun 130012, China; bify20@mails.jlu.edu.cn (F.B.)
* Correspondence: jiaojian001@jlu.edu.cn

Abstract: Aeromagnetic measurement plays an important role in mineral exploration, but unmanned aerial vehicles generate maneuvering noise during aerial flight, which negatively impacts the accuracy of aeromagnetic measurement data. Therefore, aeromagnetic compensation is an indispensable step in aeromagnetic data processing. The multicollinearity of variables in the aeromagnetic compensation model based on linear regression affects its accuracy, resulting in a large difference in the compensation effect of the same group of compensation coefficients in different directions. In order to obtain high-quality aeromagnetic data, this study proposes an adaptive model-based method for suppressing aeromagnetic maneuvering noise. First, due to the fact that the variables that cause multiple collinearity in the compensation model are related to the flight heading, the model variables are adaptively assigned to each heading based on the characteristics of the variable data for different headings. The compensation model is optimized and improved, and the impact of multiple collinearity is thus suppressed. In adaptive modeling, variables with greater significance and smaller multicollinearity are automatically allocated to build the optimal heading model, and then high-precision compensation coefficients are obtained. This algorithm was applied to the data collected by a certain unmanned aerial vehicle aeromagnetic measurement platform in Ma'anshan and compared with traditional methods. The experimental results show that the adaptive modeling-based aeromagnetic compensation algorithm is superior to traditional algorithms, with fewer errors and a higher improvement ratio. Hence, the method can effectively solve the ill-conditioned problem of a model affected by multicollinearity and further improve its compensation accuracy and robustness. Moreover, the feasibility and value of this algorithm were verified in actual mineral resource detection.

Keywords: aeromagnetic compensation; unmanned aerial vehicles (UAVs); adaptive; linear regression; multicollinearity

1. Introduction

Aeromagnetic detection is an effective method for finding metal deposits. In recent years, many scholars [1–3] have conducted research using aeromagnetic data for robust and low-cost identification of polymetallic minerals. Therefore, improving the quality of aeromagnetic data can lead to more effective mineral resource exploration. The process of processing and interpreting aeromagnetic data is mainly divided into two aspects: one is aeromagnetic compensation, and the other is aeromagnetic data interpretation [4]. This study mainly focuses on the research of aeromagnetic compensation; the interpretation of aeromagnetic data will be carried out in subsequent research. During aircraft flight, magnetic sensors record the required aeromagnetic data and the magnetic interference generated by the aircraft. In order to obtain high-quality aeromagnetic data, it is necessary to carry out aeromagnetic compensation research [5].

The earliest research was the mathematical model (T-L model) established by Tolles and Lawson for magnetic interference and aircraft attitude [6]. Based on this research,

Leliak designed a compensation model to solve for the compensation coefficient in order to eliminate magnetic interference [7]. Bickel proposed an effective method to solve for the compensation coefficient using a small signal approximation [8] with strict requirements for compensation actions. Leach proposed a ridge regression (RR) algorithm to solve the multicollinearity problem in the T-L compensation model [9], overcoming the poor robustness possible from the least squares (LS) method. Wu used principal component analysis (PCA) to eliminate multicollinearity to some extent through linear dimensionality reduction [10]. Ren [11] proposed a truncated singular value decomposition (TSVD) algorithm to further remove redundancy in the data and improve compensation accuracy on the basis of PCA. Inaba designed a compensation coefficient solution method based on FIR filtering [12]. Zhao [13] proposed a multimodel aeromagnetic compensation method, which removed model variables that contribute significantly to multicollinearity. Although this method somewhat limits the influence of multicollinearity, the only factor it considers when constructing multiple models is the VIF value of the variable, ignoring the impact of variable significance on the model. Zhao [14] proposed a fast processing method for aeromagnetic compensation based on fluxgate estimation, and its effectiveness was verified through simulation. Zhang [15] used fuzzy adaptive Kalman filtering to estimate compensation coefficients, which is relatively lenient and easy to implement. Pan [16] derived parameter estimation and compensation formulas for the unsteady geomagnetic field and modified the T-L model. Through simulation, it has been proven that the improved model has a good compensatory effect on magnetic interference. Xu [17] established a binary classification network for magnetic anomaly detection and a regression network for geomagnetic noise suppression and applied deep learning to magnetic anomaly detection and noise elimination. Zhang [18] analyzed the sway interference of aircraft not considered in the T-L model and used a one-dimensional convolutional neural network to eliminate the influence of tail beam sway. Zhou [19] conducted numerical simulation experiments on magnetic interference in aeromagnetic data based on unmanned aerial vehicles and, for the first time, proposed the radial basis function (RBF) artificial neural network (ANN) algorithm to compensate for aeromagnetic data. Feng [20] proposed an improved geomagnetic gradient compensation method, which improves the compensation accuracy by modeling the geomagnetic gradient and subtracting the estimated geomagnetic gradient from the measured data. Chen [21] designed a compensation method that combines an inertial navigation system and fluxgate magnetometer based on the errors existing in the fluxgate magnetometer and then verified the effectiveness of the algorithm through experiments.

Most methods consider a figure-of-merit (FOM) flight as a whole to solve for compensation coefficients, with little consideration for the impact of the scale of flight heading and attitude changes. Meanwhile, due to the fact that the T-L model consists of cosine functions and their derivatives, the variables between the models are not independent, which inevitably leads to multicollinearity [22]. Due to the ill-conditioned nature of the model, the accuracy of the solved compensation coefficient is not high, thus affecting the quality of the aeromagnetic data. Therefore, this study is based on the principle that the variables that cause multicollinearity in the compensation model are different in different directions. It introduces an adaptive strategy idea that reduces the correlation between coefficient matrix variables and increases the significance of variables on magnetic interference to model the four directions of FOM flight separately in order to weaken the multicollinearity of the model and improve the compensation accuracy. This will be verified through compensation flight and line flight experiments. Interpretation of the aeromagnetic data will be carried out in subsequent research.

This study first analyzes the causes and properties of aeromagnetic maneuvering noise and establishes a magnetic compensation model using mathematical modeling. Subsequently, the compensation method for adaptive modeling and the method for evaluating compensation results proposed in this article are described in detail. Through compensating flight experiments, the effectiveness of the adaptive modeling compensation method was verified by comparing it with the traditional T-L model compensation method. Finally,

a line flight experiment was conducted to obtain clearer magnetic anomalies, providing support for subsequent inversion and interpretation research.

In the flight test of the survey line, a 1:10,000 aeromagnetic method was carried out in a certain survey area in Ma'anshan to delineate the range of aeromagnetic anomalies, providing further research data and a basis for the peripheral and deep exploration of old mines in this area. The experimental measurement area is located in the middle section of the Ningwu Mesozoic fault basin, and the geological overview of the area is shown in the inner circle of Figure 1. The area mainly develops a set of sedimentary facies and a set of volcanic rock facies strata, and the folding structures in the area can be divided into basement folds and volcanic rock series folds [23]. The regional fault structure is very developed and is mainly a series of vertical, horizontal, and oblique faults formed during the Yanshan period, dividing the region into several diamond-shaped fault blocks that restrict the distribution of volcanic intrusion activities and related minerals in the region. The geological conditions in the Ningwu Basin are favorable for mineralization, with iron ore as the main metal mineral, followed by copper and gold, which are very rich in mineral resources.
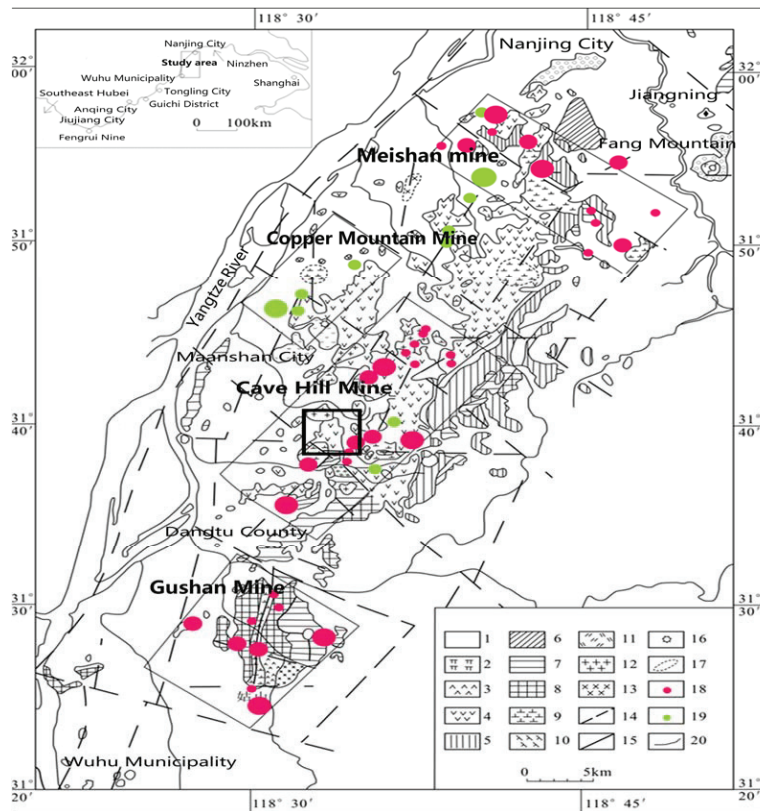
Figure 1. Geological and mineral resources diagram of the Ningwu Basin (cited from [24]). 1. Quaternary; 2. Niangniangshan Formation volcanic rocks; 3. Gushan Formation volcanic rocks; 4. Dawangshan Formation volcanic rocks; 5. Longwangshan Formation volcanic rocks; 6. Upper Jurassic; 7. Middle and Lower Jurassic; 8. Triassic; 9. Gabbro-diorite porphyrite; 10. Andesitic porphyrite, crude porphyry, trachyte porphyry; 11. Monzonite and quartz diorite; 12. Granite; 13. Gabbro; 14. Inferred fault; 15. Measured fault; 16. Volcano; 17. Concealed speculation according to geological drilling; 18. Iron deposit; 19. Copper deposit; 20. Ore field boundary.

2. Compensation Model and Method

There are multiple steps in aeromagnetic data processing, as shown in Figure 2. After the aeromagnetic measurement is completed, the measured data are imported into the corresponding database for a series of calibration and aeromagnetic compensation processes. After leveling, magnetic data interpretation technology is used to locate the geometric locations of underground minerals [25]. This study mainly focuses on the aeromagnetic compensation process in aeromagnetic data processing. Aeromagnetic compensation technology is mainly divided into three parts: construction of the compensation model, calculation of compensation coefficients, and compensation flight. Firstly, a magnetic interference compensation model is established, and then magnetic interference and other aeromagnetic data are obtained through the compensation flight, which are incorporated into the compensation model. The compensation coefficients are calculated through the compensation algorithm, thereby achieving the purpose of aeromagnetic compensation.
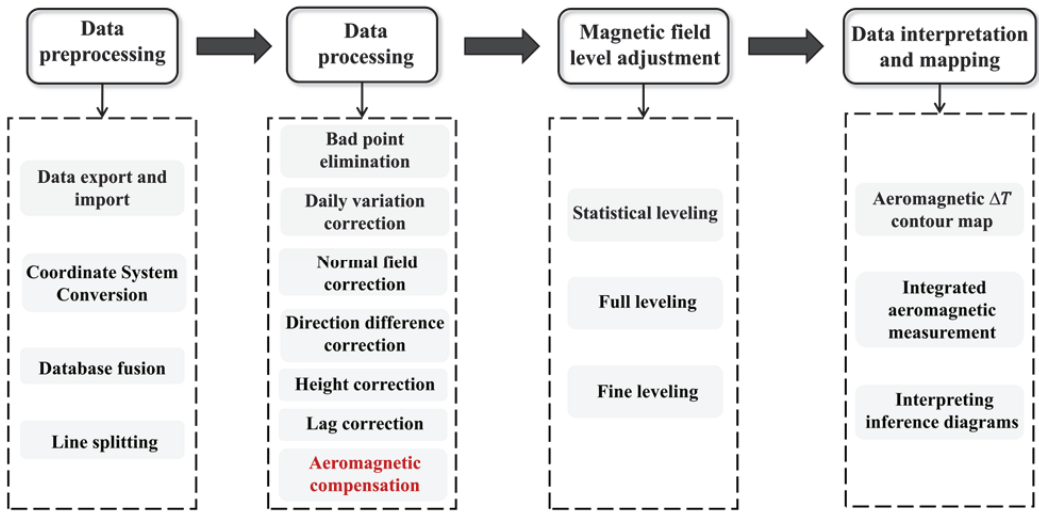
Figure 2. Aeromagnetic data processing flowchart.

2.1. T-L Model

Aircraft maneuvering noise includes three primary parts [6]: the constant magnetic field (H_p) generated by the residual magnetization of ferromagnetic objects in the aircraft, the induced magnetic field (H_i) generated by the magnetization of ferromagnetic objects in the aircraft by the Earth's magnetic field, and the eddy current magnetic field (H_{ec}) generated by the cutting of the Earth's magnetic field by soft magnetic objects in the aircraft, which can be expressed as follows:

$$H_p = c_1 cos\alpha + c_2 cos\beta + c_3 cos\gamma \tag{1}$$

$$H_i = T\left(c_4 cos^2\alpha + c_5 cos\alpha cos\beta + c_6 cos\alpha cos\gamma + c_7 cos^2\beta + c_8 cos\beta cos\gamma + c_9 cos^2\gamma\right) \tag{2}$$

$$H_{ec} = T(c_{10} cos\alpha cos'\alpha + c_{11} cos\beta cos'\alpha + c_{12} cos\gamma cos'\alpha + c_{13} cos\alpha cos'\gamma + c_{14} cos\beta cos'\gamma + c_{15} cos\gamma cos'\gamma + c_{16} cos\alpha cos'\beta + c_{17} cos\beta cos'\beta + c_{18} cos\gamma cos'\beta), \tag{3}$$

where $c_1, c_2, \ldots, c_{18}$ are compensation coefficients; $cos'\alpha$, $cos'\beta$, $and\ cos'\gamma$ are the derivatives of $cos\alpha$, $cos\beta$, and $cos\gamma$, respectively, and T is the Earth's magnetic field. $cos\alpha$, $cos\beta$,

and $cos\gamma$ are the directional cosines of the geomagnetic field in three directions in the aircraft coordinate system and can be calculated based on the aircraft attitude (λ, ψ, η).

As shown in Figure 3, x_b, y_b, z_b is the coordinate axis of the aircraft coordinate system, x_g, y_g, z_g is the coordinate axis of the local coordinate system, and the origin coincides. α, β, γ is the angle between T and x_b, y_b, z_b. Let ϕ and θ represent the magnetic dip angle and heading angle. Let λ, ψ, and η be the respective pitch, roll, and yaw angles.
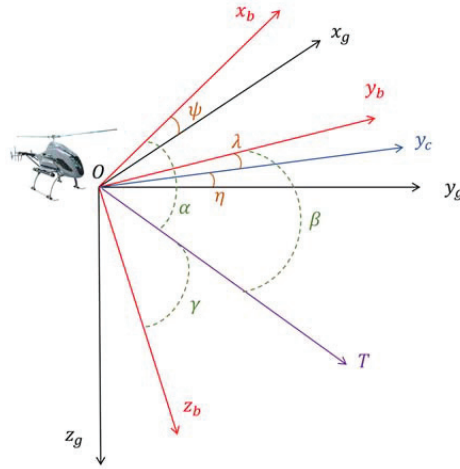
Figure 3. Coordinate system and aircraft attitude.

Then, $cos\alpha$, $cos\beta$, $and\ cos\gamma$ can be represented as follows:
For pitches:
$$cos\alpha = cos\phi\ sin\theta$$
$$cos\beta = cos\phi\ cos\theta\ cos\lambda + sin\phi\ sin\lambda \quad (4)$$
$$cos\gamma = sin\phi\ cos\lambda - cos\phi\ cos\theta\ sin\lambda.$$

For rolls:
$$cos\alpha = cos\phi\ sin\theta\ cos\psi + sin\phi\ sin\psi$$
$$cos\beta = cos\phi\ cos\theta \quad (5)$$
$$cos\gamma = sin\phi\ cos\psi - cos\phi\ sin\theta\ sin\psi.$$

For yaws:
$$cos\alpha = cos\phi\ sin\theta\ cos\eta - cos\phi\ cos\theta\ sin\eta$$
$$cos\beta = cos\phi\ cos\theta\ cos\eta + cos\phi\ sin\theta\ sin\eta \quad (6)$$
$$cos\gamma = sin\phi.$$

For flat:
$$cos\alpha = cos\phi\ sin\theta$$
$$cos\beta = cos\phi\ cos\theta \quad (7)$$
$$cos\gamma = sin\phi.$$

The total magnetic interference field can be expressed as follows:

$$H_t = H_p + H_i + H_{ec}$$
$$= c_1x_1 + c_2x_2 + c_3x_3 + c_4x_4 + c_5x_5 + c_6x_6$$
$$+ c_7x_7 + c_8x_8 + c_9x_9 + c_{10}x_{10} + c_{11}x_{11} + c_{12}x_{12} \quad (8)$$
$$+ c_{13}x_{13} + c_{14}x_{14} + c_{15}x_{15} + c_{16}x_{16} + c_{17}x_{17} + c_{18}x_{18},$$

where x_i is composed of $cos\alpha$, $cos\beta$, and $cos\gamma$ and $cos'\alpha$, $cos'\beta$, $and\ cos'\gamma$ in Equations (1)–(3).

The magnetic interference compensation model is simplified as follows:

$$XC = H_t \tag{9}$$

where C is composed of column vectors $C_i (i = 1, 2, \ldots, 18)$ and H_t is a column vector.

2.2. Adaptive Compensation Method

Zhao's analysis [13] shows that the variables that lead to the multicollinearity of the T-L model are related to the flight heading. On this basis, we further consider the impact of variable significance on the model through adaptive methods.

Figure 4 shows the implementation process. First, two compensatory flights were performed. In the data processing stage, two flight data sets were preprocessed separately, the four headings were identified, and the heading data were obtained. Subsequently, in the calibration phase, the variables are adaptively assigned based on the characteristics of the calibration flight data ($X_{cal}, H_{t,cal}$), an optimal heading model is constructed, and the compensation coefficients are calculated. As shown in the orange part of Figure 4, the standard of adaptive variable allocation is to repeatedly exclude the variable with the largest variance inflation factor (VIF) value until the multicollinearity of the remaining variable is small and then conduct a t-test to repeatedly eliminate the variable with less significance until the variable of the heading model is constructed with greater significance and less contribution to multicollinearity. Based on these variables, the heading model is constructed. The model was used to compensate for aeromagnetic interference and obtain the compensation coefficients (C_{cal}). The compensation coefficient is calculated using the least squares method (LS) and the ridge regression method (RR):

$$X_{cal}C_{cal} = H_{t,cal} \tag{10}$$
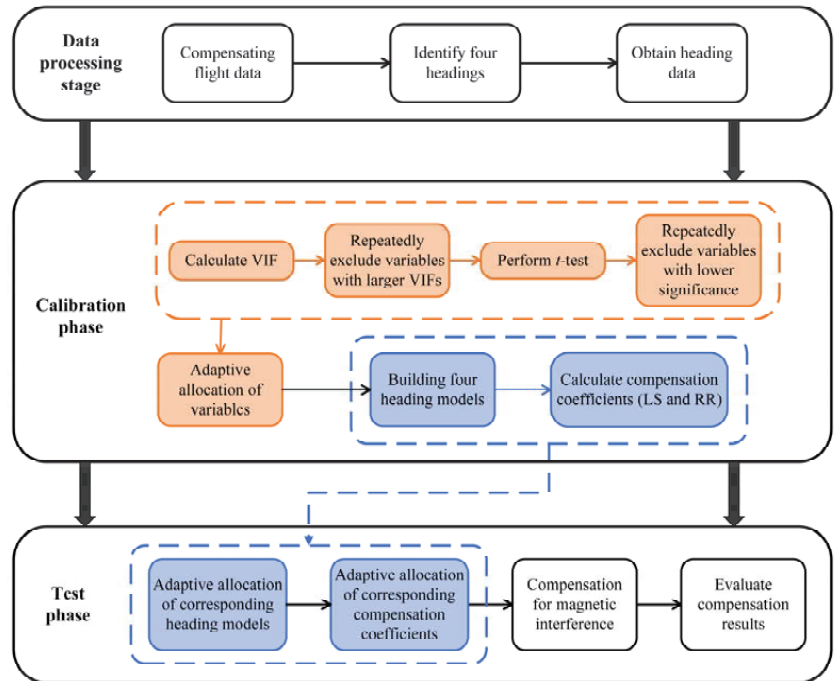
Figure 4. Flowchart of the aeromagnetic compensation method based on adaptive modeling.

During the testing phase, by identifying the current heading of the test flight data $(X_{test}, H_{t,test})$, as shown in the blue part of Figure 4, the corresponding heading models and compensation coefficients are automatically assigned, and the magnetic interference is compensated as follows:

$$\overline{H_{t,test}} = X_{test}C_{cal} \tag{11}$$

The magnetic interference after compensation is $\overline{H_{t,test}} - H_{t,test}$. Finally, the compensation results are evaluated.

The VIF quantifies the severity of multicollinearity in regression models, with larger values indicating a high degree of collinearity in the model. The VIF of the ith regression coefficient is defined as follows: $VIF_i = \frac{1}{1-R_i^2}$, where R_i^2 is the R^2 value between an independent variable X_i and the remaining independent variables in the linear regression model.

The t-test can be used to test the significance of the regression coefficient and whether the corresponding explanatory variable has a significant impact on the dependent variable, i.e., whether the T-L model variable X_i has a significant impact on the magnetic interference H_t.

The null hypothesis H_{j0} corresponds to $b_j = 0$, and the alternative H_{j1} corresponds to $b_j \neq 0$, where $j = 1, 2, \ldots, a$; b_j is the jth regression coefficient, and a is the number of variables X in the compensation model.

The T-statistic is the following:

$$T_j = \frac{\hat{b}_j}{\hat{\sigma}\sqrt{C_{jj}}} \sim t(n - a - 1) \tag{12}$$

where $n - a - 1$ is the degree of freedom, n is the number of samples, and $\hat{\sigma}\sqrt{C_{jj}}$ is the standard deviation of the jth regression coefficient.

The rejection region is the following:

$$|T_j| \geq t_{\frac{\alpha}{2}}(n - a - 1) \tag{13}$$

where α is the significance level.

The variable p of the T-statistic is its significance probability. If , the original assumption is accepted, and the explanatory variable has no significant impact on the dependent variable; if $p < \alpha$, the null hypothesis is rejected and the alternative solution is accepted, indicating that the variable X_i corresponding to the jth regression coefficient b_j has a significant impact.

The multicollinearity of the model directly leads to the ill condition of the regression equation, increasing the confidence interval of the solution, affecting its sensitivity to noise, and therefore reducing the quality of aeromagnetic compensation [26]. Effective variables are automatically allocated through adaptive modeling, and the multicollinearity of the T-L model can be effectively weakened by reducing the strong and insignificant variables of multicollinearity.

The compensation coefficient solution in this study mainly uses LS and RR. The LS solution of the T-L equation is the following:

$$C_{LS} = \left(X^T X\right)^{-1} X^T H_{t,} \tag{14}$$

When a strong correlation exists between variables, due to the singularity of $X^T X$, the LS solution variance will be large, leading to deviations, which in turn affect the compensation accuracy [27]. RR improves the stability and reliability of the compensation model by abandoning the unbiased nature of LS and obtaining regression coefficients at the cost of some information loss and reduced accuracy. It has good results in repairing and

fitting ill-conditioned data. RR adds an identity matrix to the coefficient matrix to improve stability. The solution is expressed as follows:

$$C_{RR} = \left(X^T X + \mu I \right)^{-1} X^T H_t \tag{15}$$

where μ is a ridge parameter, and I is the identity matrix. Numerous scholars have conducted research on the optimal selection of μ, such as using a combination of nonlinear programming models and Kibria's method to select μ, which can enable the estimator to achieve high performance [28].

Hardwick [29] suggested using the standard deviation (STD) and improvement ratio (IR) of the signal to evaluate data quality improvement. The STD can provide a good performance evaluation for the compensation system without being misunderstood and can better reflect the performance of the airborne magnetic measurement system. The larger the IR value, the higher the accuracy of compensation. The STD and IR are defined as follows:

$$STD = \sqrt{\frac{1}{n} \sum_{i=1}^{n} (x_i - \mu)^2} \tag{16}$$

$$IR = \frac{STD_u}{STD_c} \tag{17}$$

where μ is the arithmetic mean of the variable, and STD_u and STD_c are the respective standard deviations of the uncompensated and compensated data.

3. Compensation Flight Experiment

3.1. Compensation Flight

To validate the method proposed in this research, the study refers to a FOM flight experiment designed by Leliak [7]. This experiment obtains the magnetic interference data generated during the flight process by flying in a specific way and brings it into the magnetic interference compensation model. The compensation parameters are solved through compensation algorithms. Compensation parameters are applied to another set of flight data for compensation processing. As shown in Figure 5a, the FOM flight includes maneuvers in four directions: north, east, south, and west. Each direction undergoes $\pm 5°$ yaw, $\pm 5°$ pitch, and $\pm 10°$ roll attitude maneuvers, with a duration of 5–10 s for each attitude and a 5 s flat between each group of attitudes. The actual FOM flight paths for flights A and B are shown in Figure 5b; a square represents the beginning of the flight, and a diamond represents the end of the flight. The magnetic interference data measured by the optical pumping magnetometer installed on the aircraft during the flight are shown in Figure 6.

3.2. Adaptive Modeling

Fight A is used as a calibration flight, and flight B is used as a test flight. Taking the north heading of flight A as an example, the method in Section 2.2 is used to establish a heading model adaptively.

Firstly, the correlations between variables are analyzed in the T-L model. Here, a thermodynamic diagram (Figure 7) is used to display the correlation between variables visually. The numbers on the graph represent the correlation coefficient matrix, and different colors represent varying degrees of correlation. The closer the correlation coefficient is to 0, the lighter the color is, and the more irrelevant the variables are. The closer the correlation coefficient is to 1 or -1, the darker the color and the higher the degree of linear relationship between variables. Therefore, it can be seen that there is a high correlation between the compensation model variables X, indicating the existence of severe multicollinearity in the T-L model.
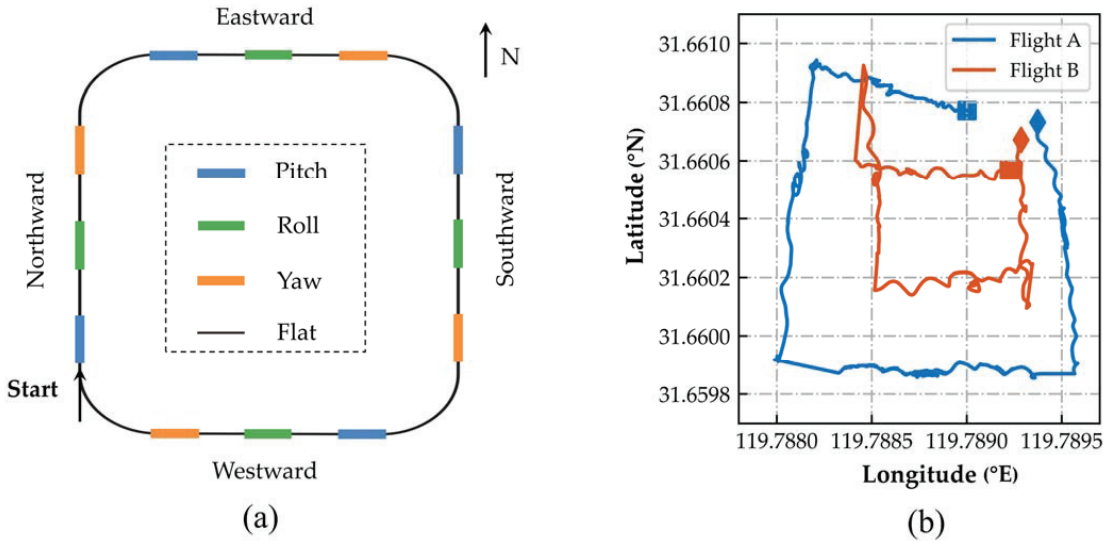
Figure 5. (**a**) FOM flight schematic; (**b**) actual trajectory map of the FOM flight.
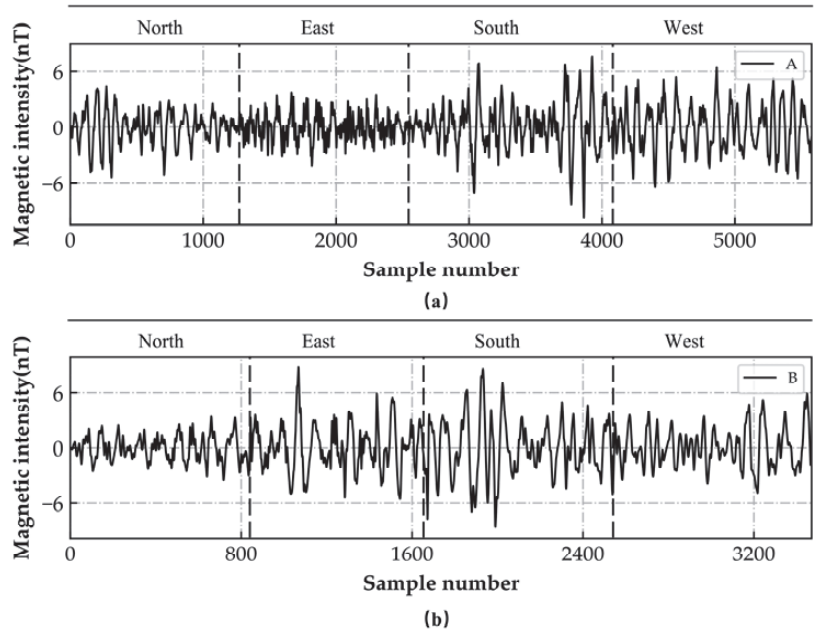

Figure 6. Magnetic interference during flight. (**a**) Flight A; (**b**) Flight B.
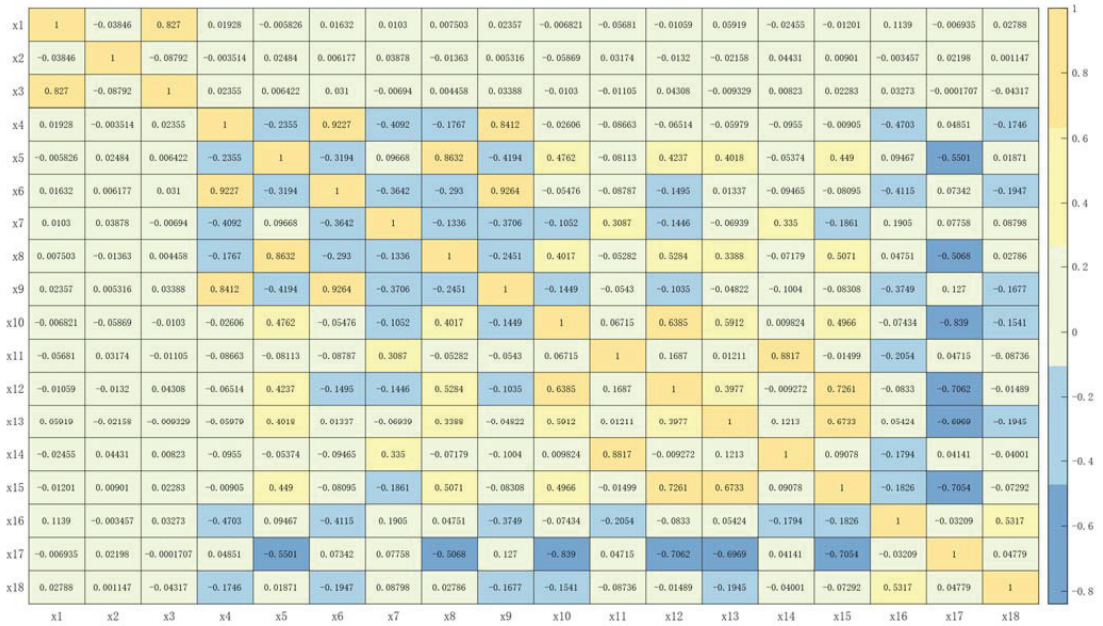
Figure 7. Thermal diagram of the correlation coefficient matrix of the north heading variable for flight A.

Therefore, in order to eliminate multicollinearity in the model, it is necessary to adaptively allocate effective variables based on the VIF and t-test and then establish a heading model. Table 1 shows the process of adaptive allocation of variables in the north direction of flight A. In model 1, all the variables are input, and their VIFs are listed. The largest is for X_6, which is *cosαcosγ*. That means X_6 makes the largest contribution to the multicollinearity of the model and should be excluded. Subsequently, model 2 was established with 17 input variables, excluding X_{11}, which has the largest VIF. This operation was performed in sequence until the VIF of all variables in the final model 4 decreased, and the multicollinearity was weak (green column, Table 1). Then, on this basis, the variables were allocated according to the *p*-value of the t-test, similar to the VIF-based variable allocation process above. Using the remaining variables, model 5 excluded the variable with the highest *p*-value, in sequence, until the *p*-values of all variables approached 0. In model 7 $[X_1, X_2, X_3, X_5, X_7, X_8, X_9, X_{10}, X_{13}, X_{15}, X_{16}, X_{17}, X_{18}]$ (orange column, Table 1), the variables have small multicollinearity and high significance, which can suppress the impact of multicollinearity on magnetic interference compensation.

Finally, after obtaining the adaptively assigned heading model, fitting tests need to be conducted to verify its effectiveness and accuracy further. The residual histogram of the regression model and the normal probability diagram (P-P diagram) of the regression standardized residual are used to test whether the residual follows a normal distribution. If the residual histogram is concentrated near the centerline and presents a normal distribution, and the P-P diagram is approximately a straight line that conforms to a normal distribution, then the regression model meets the assumption of the residual distribution, and the fitting effect is good. On the contrary, the model may have systemic bias, homoscedasticity, or heteroscedasticity. As shown in Figure 8, the residual error of the model meets the normal distribution, indicating that the confidence interval is stable, the regression coefficient solution accuracy is higher, and a heading model with strong regression ability can be obtained.

Table 1. Process of adaptive allocation of variables for flight A north heading.

Variable	VIF				P		
	Model 1	Model 2	Model 3	Model 4	Model 5	Model 6	Model 7
X1	3.7026	3.6942	3.6826	3.5521	2.54×10^{-82}	2.74×10^{-82}	1.01×10^{-84}
X2	1.0531	1.0513	1.0513	1.0430	0.00×10^{0}	0.00×10^{0}	0.00×10^{0}
X3	3.7073	3.6989	3.6980	3.5858	2.59×10^{-75}	2.73×10^{-75}	6.51×10^{-78}
X4	17.1471	10.2101	10.2068	——	——	——	——
X5	17.3934	9.9203	9.8983	7.3872	5.87×10^{-10}	6.48×10^{-10}	1.29×10^{-11}
X6	63.3209	——	——	——	——	——	——
X7	3.8956	2.5798	2.5678	2.3076	1.75×10^{-05}	$1.10 \times$	1.67×10^{-05}
X8	16.9119	8.5958	8.5825	6.8657	2.52×10^{-08}	2.50×10^{-08}	1.97×10^{-09}
X9	42.0086	11.4980	11.4965	1.9235	6.10×10^{-07}	3.24×10^{-07}	5.49×10^{-08}
X10	5.3301	5.2683	5.0892	4.9592	4.50×10^{-03}	5.30×10^{-04}	7.86×10^{-04}
X11	19.5990	19.4916	——	——	——	——	——
X12	11.0102	10.9935	4.1326	4.0829	5.18×10^{-01}	——	——
X13	5.4917	5.1444	4.7143	4.2271	1.76×10^{-01}	7.30×10^{-02}	2.27×10^{-02}
X14	17.4016	17.2145	1.7951	1.7671	2.40×10^{-01}	2.32×10^{-01}	——
X15	12.1846	11.6172	5.9216	5.6138	2.09×10^{-04}	5.17×10^{-07}	5.06×10^{-07}
X16	3.2808	3.2048	3.0031	2.9681	3.63×10^{-04}	2.14×10^{-04}	3.08×10^{-05}
X17	6.5936	6.5046	6.4299	6.4131	1.64×10^{-06}	$1.92 \times$	3.78×10^{-06}
X18	1.8687	1.8573	1.8510	1.8507	3.79×10^{-02}	3.44×10^{-02}	1.74×10^{-02}
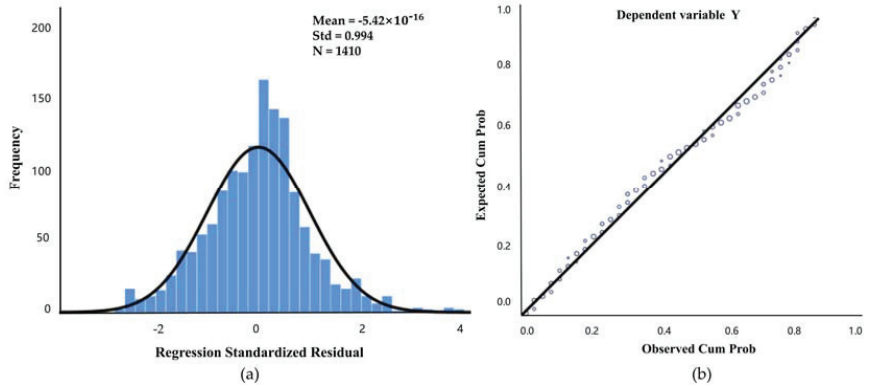
Figure 8. (a) Residual histogram of the regression model; (b) normalized P-P plot of the regression normalization residuals.

3.3. Magnetic Interference Compensation

In the previous section, a heading model with strong regression ability was obtained, and then flight B was compensated after solving for the compensation coefficient. Figure 9 shows the compensation results of the T-L model using the LS and RR algorithms for flight B, and Figure 10 shows the results of the adaptive established heading model. Taking the north heading as an example, when compensated using the LS algorithm, the T-L model reduces the STD from 1.297 to 0.219, and the IR is 5.922. The heading model lowers the STD to 0.182, and the IR is 7.126. Using the RR algorithm for compensation, the T-L model reduces the STD from 1.297 to 0.166, and the IR is 7.813. The heading model lowers the STD to 0.126, and the IR is 10.294. It can be seen that the IR of the heading model is higher than that of the T-L model, which can effectively weaken the influence of multicollinearity and achieve high-precision aeromagnetic compensation. The fitting ability of RR is stronger than that of LS, with higher compensation accuracy and stronger stability.
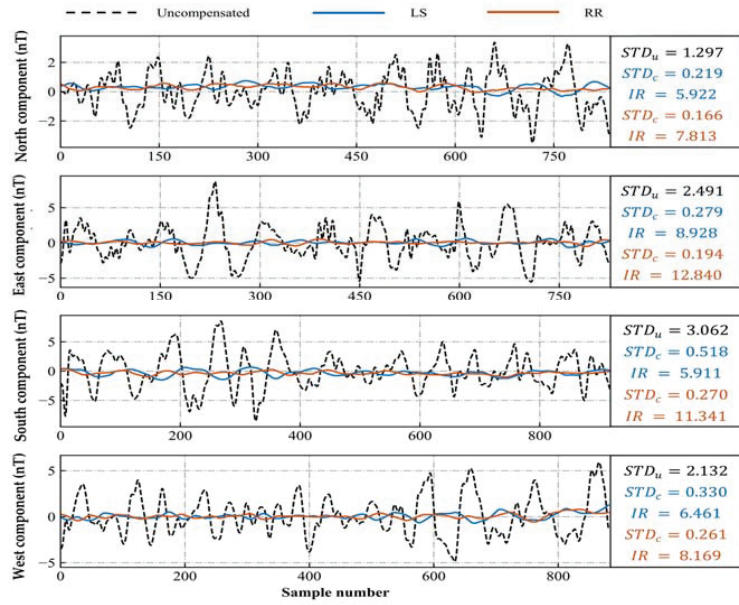
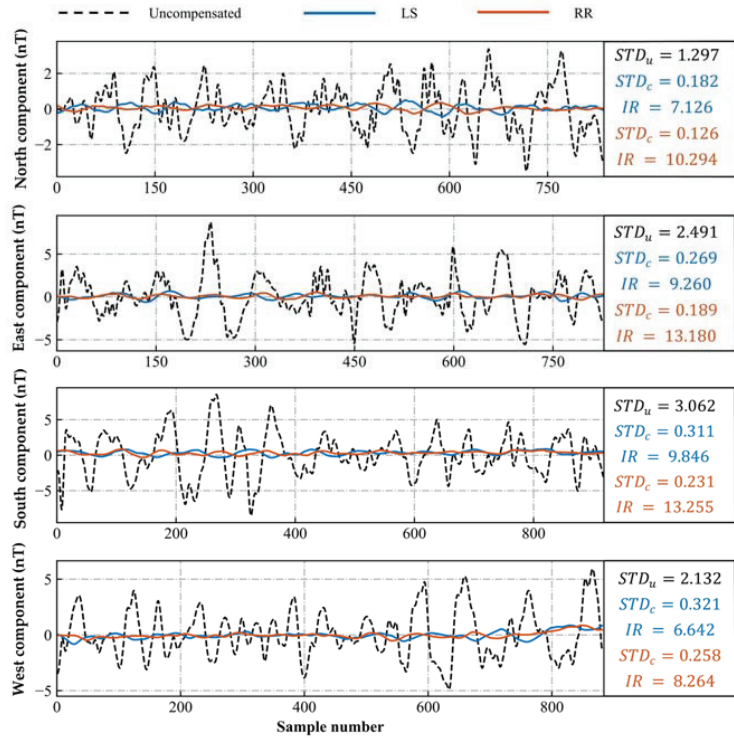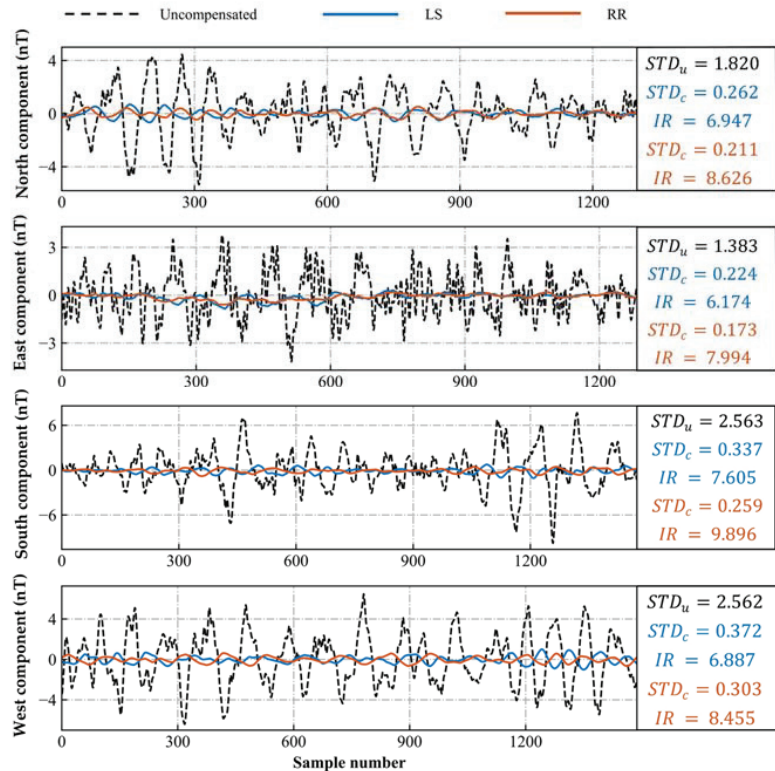**Figure 9.** Compensation results of the T-L model for four headings of flight B.

Figure 10. Compensation results of the heading model for four headings of flight B.

Similarly, flight B is used as a calibration flight, flight A as a test flight, and magnetic compensation is performed using the adaptive modeling-based aeromagnetic compensation algorithm. Figures 11 and 12 show the compensation results of flight A using the LS and RR algorithms for the T-L and heading models, respectively. Compared to LS, RR reduces the compensated STD and increases the IR. RR is different from LS unbiased estimation, as its estimated partial regression coefficients are often closer to the real situation and have better fitting ability. When using the RR algorithm for compensation, the heading model compensates for a smaller STD and a larger IR than the T-L model. This shows that the adaptive modeling algorithm reduces the multicollinearity between variables in the T-L model, improves the performance of the regression algorithm, and improves the accuracy of aeromagnetic compensation. Similarly, when using the LS algorithm, the compensation effect of the heading model is better than that of the T-L model. The above experiments show that the heading model obtained through adaptive variable allocation has a higher regression ability than the traditional T-L model, and the compensated magnetic interference has less error and a higher improvement ratio. This shows that the method effectively solves the ill-conditioned problem of the model caused by multicollinearity, thus improving the compensation accuracy and confirming the effectiveness of our proposed algorithm.

Figure 11. Compensation results of the T-L model for four headings of flight A.
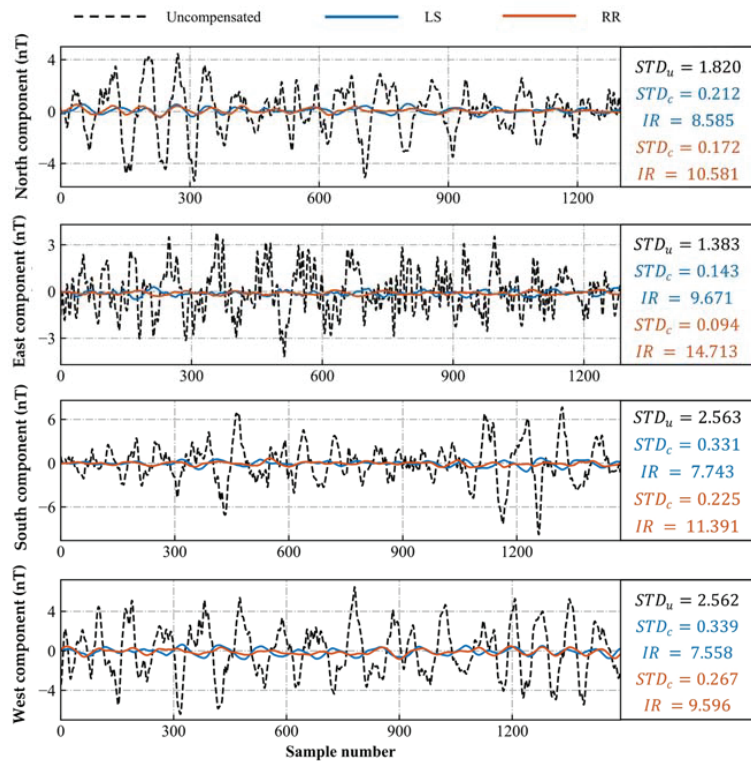
Figure 12. Compensation results of the heading model for four headings of flight A.

4. Line Flight Experiment

According to existing data, the structure and stratigraphy in the study area include NEE-trending and NE-trending structures [23]. A total of 32 north-south survey lines are arranged at intervals of 100 m to consider two different geological bodies. The measurement area is 8.99 km^2, the flight direction angles are 0° and 180°, and the average flight altitude is 164 m. Satellite remote sensing images of the survey area are shown in Figure 13a, while the plane section of the original total magnetic anomaly is shown in Figure 13b. Line 160 (north heading) and Line 170 (south heading) were selected as examples, and adaptive model methods were used as compensation algorithms.

The compensation results of the measuring line are shown in Figure 14. It can be seen that the compensated signal is smoother than the original signal because the adaptive modeling compensation method eliminates the aeromagnetic maneuvering noise, so the obvious sawtooth interference in the measurement line is compensated. Applying this algorithm to all line data, according to the magnetic anomaly map of the original data (Figure 15a), it can be seen that there are some obvious magnetic anomaly areas. Some local anomalies correspond to known mineral deposits in the region. However, there are many serrations, ellipses, protrusions, and other forms of high-frequency anomalies distributed throughout the entire anomalous area. Part of these are caused by maneuvering noise during the aeromagnetic measurement process, which can affect the resolution of the magnetic anomaly map and increase the inaccuracy in subsequent inversions. As shown in the circular part of Figure 15b, the method proposed in this article was used for compensation processing to eliminate high-frequency anomalies in the region, especially in the southwestern region where the local anomaly shape is more pronounced. The range of

magnetic anomalies is made clearer and smoother, providing better data for subsequent data inversion and interpretation combined with geological data.
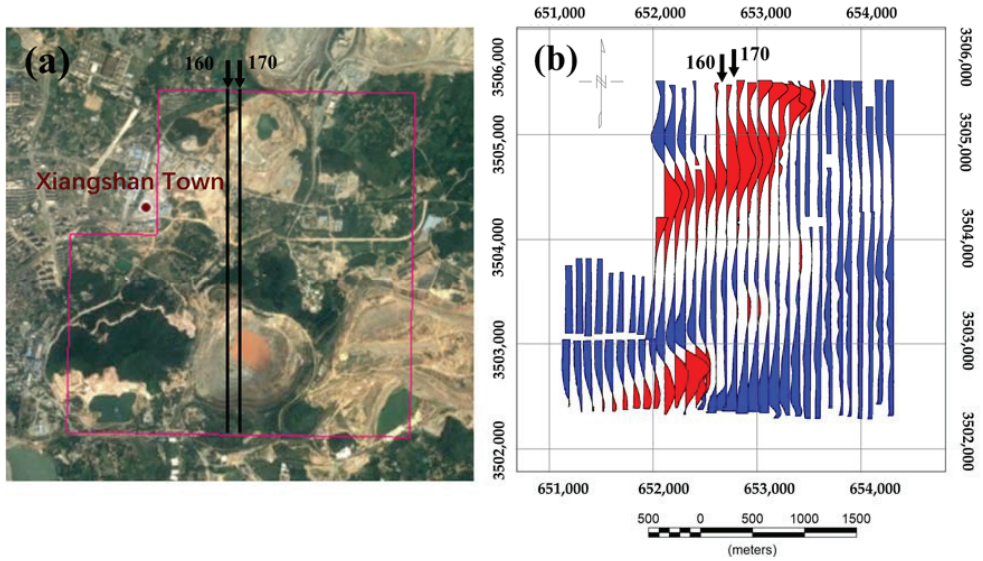
Figure 13. (**a**) Satellite remote sensing images of the survey area; the 160 and 170 measuring lines are the two required lines for this experiment; (**b**) original magnetic anomaly plane section.
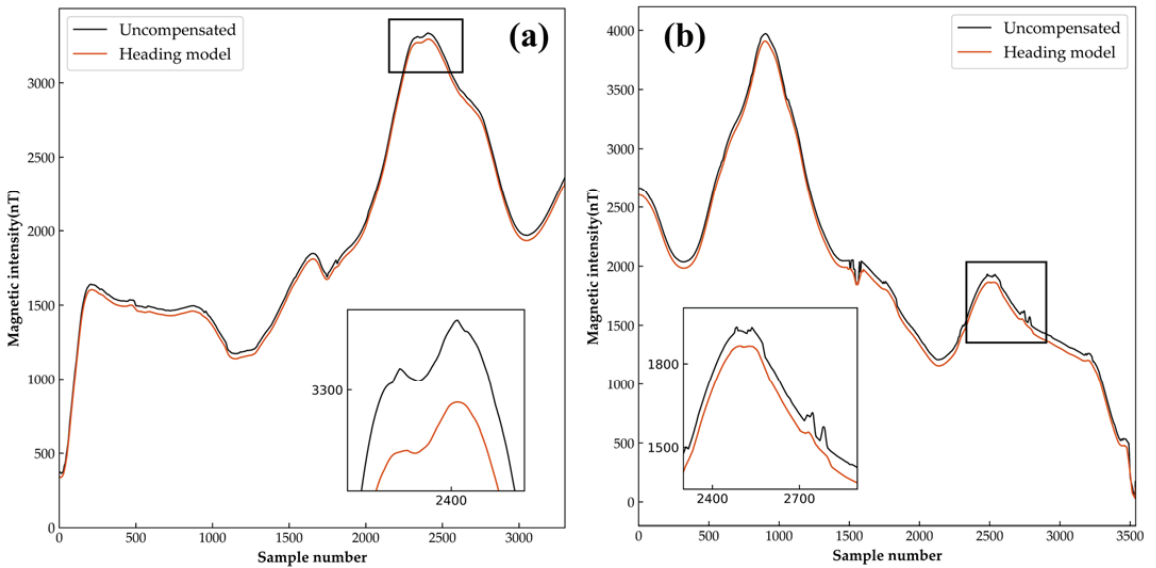
Figure 14. (**a**) Flight compensation results of the north direction line; (**b**) flight compensation results of the south direction line.
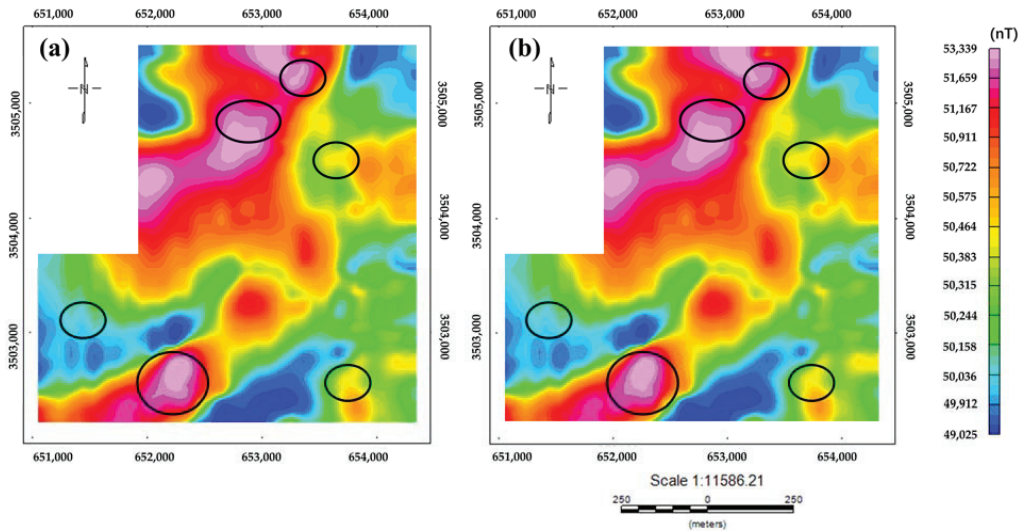
Figure 15. (**a**) The original magnetic anomaly; (**b**) the compensated magnetic anomaly.

5. Discussion

There has been extensive research on high-precision solutions for aviation magnetic compensation models based on linear regression. However, few studies have considered the effects of flight heading and attitude changes on FOM flights. Due to differences in the variables that cause multicollinearity in the compensation model under different heading conditions, this research adaptively modeled FOM flight for different headings. When modeling, the correlation and significance of the variables were considered through the VIF value of variables and the *p*-value of the t-test to reduce the compensation model's multicollinearity and improve the impact of variables on magnetic interference, thereby achieving higher compensation accuracy. Through experiments, it was proven that in using the same compensation algorithm, the compensation results through adaptive modeling are more accurate than those of traditional T-L models, verifying the effectiveness of this method. However, this method cannot completely eliminate all magnetic interference, as the multicollinearity of the compensation model not only comes from model variables and aircraft headings but also from the dependence of the UAV flight on control and real-time meteorological factors, which can lead to unstable flight attitude and result in abnormal data noise and multicollinearity of the model. Therefore, in order to improve compensation accuracy, it is necessary to have a more accurate grasp of drone flight.

Due to the high computational resources involved in adaptive modeling and compensation coefficient calculation, its running time is 0.784 s, which is longer than the T-L model's running time of 0.392 s. Therefore, further consideration must be given to computational complexity and real-time performance in practical applications.

6. Conclusions

The aeromagnetic compensation model has multicollinearity issues, which will lead to significant bias in the estimation of magnetic interference compensation, reducing interpretability and stability. This research decouples the magnetic interference of the aeromagnetic detection platform through independent modeling and numerical analysis of multiple directions and proposes a new adaptive modeling compensation method. By adaptively assigning variables with high significance and low multicollinearity, different heading models are established that effectively solve the problem of ill-conditioned models on multiple headings. Through FOM flight experiments, it was shown that the magnetic

interference compensation effect (IR = 10.294) generated by the aircraft after directional adaptive modeling is better than the traditional T-L model method (IR = 7.813), which verifies the effectiveness of the method. In addition, clear and smooth magnetic anomalies were obtained in the line flight experiment, providing a better data basis for subsequent inversion and interpretation research.

Author Contributions: P.Y., J.J., F.B.: Conceptualization, Methodology, Software; J.J., L.Z.: Resources Data curation; F.B.: Writing—Original draft preparation; F.B., X.Z.: Visualization; J.J., F.B., S.Z.: Writing—Reviewing and Editing. All authors have read and agreed to the published version of the manuscript.

Data Availability Statement: Data available on request due to restrictions eg privacy or ethical. The data presented in this study are available on request from the corresponding author. The data are not publicly available due to the data is provided by a classified project.

Conflicts of Interest: The authors declare no conflict of interest.

References

1. Aali, A.A.; Shirazy, A.; Shirazi, A.; Pour, A.B.; Hezarkhani, A.; Maghsoudi, A.; Hashim, M.; Khakmardan, S. Fusion of Remote Sensing, Magnetometric, and Geological Data to Identify Polymetallic Mineral Potential Zones in Chakchak Region, Yazd, Iran. *Remote Sens.* **2022**, *14*, 6018. [CrossRef]
2. Shabani, A.; Ziaii, M.; Monfared, M.S.; Shirazy, A.; Shirazi, A. Multi-Dimensional Data Fusion for Mineral Prospectivity Mapping (MPM) Using Fuzzy-AHP Decision-Making Method, Kodegan-Basiran Region, East Iran. *Minerals* **2022**, *12*, 1629. [CrossRef]
3. Jiang, D.; Zeng, Z.; Zhou, S.; Guan, Y.; Lin, T. Integration of an Aeromagnetic Measurement System Based on an Unmanned Aerial Vehicle Platform and Its Application in the Exploration of the Ma'anshan Magnetite Deposit. *IEEE Access* **2020**, *8*, 189576–189586. [CrossRef]
4. Noriega, G. Performance measures in aeromagnetic compensation. *Leading Edge* **2011**, *30*, 1122–1127. [CrossRef]
5. Walter, C.; Braun, A.; Fotopoulos, G. Characterizing electromagnetic interference signals for unmanned aerial vehicle geophysical surveys UAV electromagnetic interference. *Geophys. J. Soc. Explor. Geophys.* **2021**, *86*, J21–J32.
6. Tolles, W.E.; Lawson, J.D. *Magnetic Compensation of MAD Equipped Aircraft*; Airborne Instruments Lab. Inc.: Mineola, NY, USA, 1950; p. 201.
7. Leliak, P. Identification and evaluation of magnetic-field sources of magnetic airborne detector equipped aircraft. *IRE Trans. Aerosp. Navig. Electr.* **1961**, *3*, 95–105. [CrossRef]
8. Bickel, S.H. Small Signal Compensation of Magnetic Fields Resulting from Aircraft Maneuvers. *IEEE Trans. AES* **1979**, *15*, 518–525. [CrossRef]
9. Leach, B.W. Aeromagnetic compensation as a linear regression problem. In *Information Linkage between Applied Mathematics and Industry II*; Academic Press: London, UK, 1980; pp. 139–161.
10. Wu, P.L.; Zhang, Q.Y. Aeromagnetic compensation algorithm based on principal component analysis. *J. Sens.* **2018**, *2018*, 7. [CrossRef]
11. Ren, K.X. *Research on Magnetic Interference Compensation and Simulation Technology for Aviation Platforms*; Harbin Institute of Technology: Harbin, China, 2016.
12. Inaba, T.; Shima, A.; Konishi, M. Magnetic noise compensation using FIR model parameter estimation method. *Electron. Commun. Jpn.* **2002**, *85*, 1–11. [CrossRef]
13. Zhao, G.; Han, Q.; Peng, X. An Aeromagnetic Compensation Method Based on a Multimodel for Mitigating Multicollinearity. *Sensors* **2019**, *19*, 2931. [CrossRef]
14. Zhao, X.; Zheng, X.C.; Jiao, J. Fast Processing Method of Aeromagnetic Compensation Basedon Fluxgate Estimation. *J. Jilin Univ.* **2019**, *49*, 857–864.
15. Zhang, Y.; Zhao, Y.X.; Chang, S. An aeromagnetic compensation algorithm for aircraft based on fuzzy adaptive kalman filter. *J. Appl. Math.* **2014**, *2014*, 405671. [CrossRef]
16. Pan, X.; Zhang, Q. An aeromagnetic compensation method considering geomagnetic gradient changes. *Sensors and Microsystems* **2020**, *39*, 4.
17. Xu, X.; Huang, L.; Liu, X. DeepMAD: Deep Learning for Magnetic Anomaly Detection and Denoising. *IEEE Access* **2020**, *99*, 121257–121266. [CrossRef]
18. Zhang, D.K. Analysis of Aeromagnetic Swing Noise and Corresponding Compensation Method. *IEEE Trans. Geosci. Remote Sens.* **2021**, *60*, 1–10. [CrossRef]
19. Zhou, S.; Yang, C.; Su, Z. An Aeromagnetic Compensation Algorithm Based on Radial Basis Function Artificial Neural Network. *Appl. Sci.* **2022**, *13*, 136. [CrossRef]

20. Feng, Y.; Zhang, Q.; Zheng, Y.; Qu, X.; Wu, F.; Fang, G. An Improved Aeromagnetic Compensation Method Robust to Geomagnetic Gradient. *Appl. Sci.* **2022**, *12*, 1490. [CrossRef]
21. Chen, B.; Zhang, K.; Yan, B.; Zhu, W. The Conjunctive Compensation Method Based on Inertial Navigation System and Fluxgate Magnetometer. *Appl. Sci.* **2023**, *13*, 5138. [CrossRef]
22. Yu, P.; Zhao, X.; Jiao, J. An improved neural network method for aeromagnetic compensation. *Meas. Sci. Technol.* **2021**, *32*, 045106. [CrossRef]
23. Jiang, Y.; Zhang, Z.; Du, Y.; Luo, G.; Zhang, Y.; Zheng, Z.; Ren, C. Mineralogical characteristics and genetic significance of the Hemushan iron deposit in the southern section of Ningwu. *Depos. Geol.* **2015**, *34*, 163–178.
24. Liu, Y.; Ma, M.; Shen, X. Analysis of the Tectonic Construction Characteristics and Metallogenic Control of Mineral Fields in the Ningwu Area. *Adv. Geosci.* **2018**, *8*, 640.
25. Yu, P.; Zhao, X.; Jiao, J. An Aeromagnetic Compensation Algorithm Based on a Deep Autoencoder. *IEEE Geosci. Remote Sens. Lett.* **2020**, *19*, 1–5. [CrossRef]
26. Gamey, T.J.; Doll, W.E.; Beard, L.P. Analysis of Correlated Noise in Airborne Magnetic Gradients for Unexploded Ordnance Detection. *J. Environ. Eng. Geophys.* **2004**, *9*, 115–125. [CrossRef]
27. Zhang, N.; Lin, C. Modeling and Compensation of Aircraft Background Magnetic Interference Based on Improved Ridge Estimation. *Syst. Eng. Electron. Technol.* **2012**, *34*, 5.
28. Hefnawy, A.E.; Farag, A. A combined nonlinear programming model and Kibria method for choosing ridge parameter regression. *Commun. Stat.-Simul. Comput.* **2014**, *43*, 1442–1470. [CrossRef]
29. Hardwick, C.D. Important design considerations for inboard airborne magnetic gradiometers. *Geophysics* **1984**, *49*, 2004–2018. [CrossRef]

The Stability of Dams with Different Stoping Elevations in the Tongling Valley-Type Tailings Impoundment: A Case Study in Yunnan China

Yiwen Pan [1,2], Jianping Chen [1,2,*], Xiaohuan Zuo [3], Cheng Zhang [1,2] and Shuangshuang Wu [1,2]

[1] School of Earth Sciences and Resources, China University of Geosciences, Beijing 100083, China; panyw@email.cugb.edu.cn (Y.P.); 3001210074@email.cugb.edu.cn (C.Z.); wss0805@163.com (S.W.)
[2] Beijing Key Laboratory of Development and Research for Land Resources Information, Beijing 100083, China
[3] School of Emergency Management and Safety Engineering, China University of Mining and Technology Beijing 100083, China; zxh180329@163.com
* Correspondence: 3s@cugb.edu.cn

Abstract: Significant interest has been focused on recovery rates, recovery options, and recovery utilization when tailings impoundments are re-mined. However, the stability of the tailings dams during the recovery process is also a severe issue. Based on engineering geological surveys and laboratory tests, the evolution of the Tongling tailings impoundment's instability characteristics under different recovery heights and diverse working conditions was analyzed by numerical simulation. Firstly, with the help of 2D software, the position of the tailings dam infiltration line and the alteration of the dam safety factor during the stoping process were calculated. Secondly, 3Dmine (2017) software was used to create the 3D surface structure of the tailings impoundment, and then a 3D numerical analysis model was established by means of Midas GTS NX software. The numerical simulation of seepage and stress analyses were conducted based on the model. Consequently, the evolution of the stability characteristics of tailings dam under different operating conditions was calculated. The research demonstrates that the dry beach length of the tailings pond gradually reduces with a decrease in the extraction height, resulting in a lower infiltration line. Under flood conditions, the saturation line has partial overflow due to the poor seepage discharge capacity of the dam. The total displacement of the dam body is inversely proportional to the retrieval height. The more extreme the analyzed working conditions, the more the safety factor will be reduced. Additionally, the plastic variation area of the dam body will be more comprehensive, which will increase the risk of a dam collapse.

Keywords: tailings impoundment stoping; dam stability; displacement field; stress fields; different working conditions; numerical simulation

1. Introduction

Tailings impoundments are usually used to accumulate various types of mineral wastes generated in the process of mining and beneficiation, and are essential facilities for mine safety production [1–4]. The treatment and management of tailings present significant global environmental and economic challenges. Inadequate management of tailings impoundments can result in severe environmental pollution and disasters [5]. In Europe, research primarily focuses on tailings impoundment management and pollution control [6]. Researchers are actively working on innovative techniques, including mechanochemical activation methods, to enhance resource recovery rates and reduce waste production [7]. Additionally, various safety monitoring measures have been implemented to prevent pollution from tailings impoundments, particularly heavy metal contamination [8]. In the Americas, research is centered on assessing the environmental impacts of tailings impoundments. For instance, studies have revealed that tailings impoundment leakage can have

profound effects on downstream lake systems [9,10]. The research direction in Africa is significantly different from that in Europe and the United States. Africa is rich in diamond, platinum group, and other metal resources, which produce a large amount of such metals every year, providing opportunities for carbon remediation methods such as alkalinity production and mineral carbonation. How to reduce the impact of tailings on the environment and human beings is an important research topic in Africa [11,12].

Tailings impoundments pose potential hazards. Yin et al. summarized the characteristics of tailings ponds in China, which are numerous in number, multifarious in types, and occupy an extensive land area [5]. Edraki et al. reported that numerous tailings dams have collapsed over the years, bringing catastrophic damage to the economy, residents' lives, and ecosystems downstream of the tailings impoundments [6]. A tailings impoundment failure would not only destroy mine infrastructure, but the spilled tailings would also lead to serious damage to the surrounding ecological environment [7–10]. Secondary disasters such as landslides, floods, and debris flows will occur if a tailings dam fails [11–13]. Luino et al. presented that in 1985, a tailings pond collapsed near Stava in northern Italy, killing 286 people [14]. On 8 September 2008, a particularly serious tailings dam burst occurred in Shanxi, China, resulting in 281 deaths and significant economic losses to the residents of the mine and downstream [15], which was reported by Gomes et al. In November 2015, the Fundão tailings pond in Brazil collapsed, releasing over 50 million cubic meters of tailings. Villages downstream were washed away, and the surrounding ecosystem was destroyed. Agurto Detzel et al. informed that in November of the same year, the Samarco tailings pond in Brazil was destabilized, leaking over 30 million cubic meters of tailings [16]. On 25 January 2019, the tailings pond failed catastrophically in Brumadinho, Brazil, killing 363 people and causing serious environmental pollution [17], which was reported by Silva Rotta et al.

A large quantity of existing tailings impoundments is out of use in China, which have outstanding potential problems. The basic flood discharge facilities of the abandoned tailings impoundments cannot be checked and maintained in time, which will lead to the tailings impoundments becoming dangerous reservoirs and increasing the risk of a tailings dam breach. Meanwhile, the tailings contain a variety of complex heavy metal ions, and the heavy metal pollution of tailings is a severe environmental problem [18–20]. Tailings contain a variety of helpful components that can be recycled [21–23]. If tailings impoundments can be reasonably remined, it not only enables the rational recycling of resources but also dramatically reduces or even eliminates the risk of tailings pond collapse and reduces the tailings pond failure rate [24–27]. Furthermore, reclaiming abandoned tailings impoundments brings certain economic benefits to mines and protects the ecological environment [28–30]. Tailings generally have high water content and high compressibility [31,32]. It is a significant potential threat to mine safety and production [33], which was proposed by Wei et al. Unlike ordinary reservoirs, tailings impoundments contain various chemical substances produced in the mineral processing process [34,35]. Moreover, the diameter of the tailings is small, the mechanical properties are poor, and the shear strength is low [36–38]. In the process of the continuous accumulation of tailings, tailing materials will produce chemical siltation, biological siltation, and physical siltation, resulting in a reduction in the consolidation and drainage capacity of tailings ponds, which will make them more susceptible to dam failure [39–41]. Additionally, Zhang et al. summarized that as the tailings dam body is raised, the risk of dam failure increases [42]. External factors such as heavy rainfall, flooding, and earthquakes can also exacerbate tailings impoundment accidents during the operation of tailings impoundments. Previous studies have found that tailings dam reservoir levels, tailings reservoir drainage systems, foundation stability, seepage effects, seismic liquefaction, the depth of the infiltration line, the flooding of the dam, and the length of the dam's dry bank are the most critical factors directly affecting the safe operation of tailings ponds [43–45]. Therefore, based on the above research results, it is of great theoretical significance and practical value to carry out seepage analyses, flooding

analyses, and seismic analyses for the safe operation of tailings dams. Designing reasonable mining plans for the tailings ponds is also necessary.

There are few studies on the stability analysis of the dam body during tailing reservoir mining. However, tailing pond mining is a dynamic process. In the process of mining, the dam will reduce the load slowly, and the height of the dam body will decrease gradually. The combined effect of these can cause changes in the dry beach length and the buried depth of the infiltration line, which will affect the stability of the dam. Since the Tongling tailings impoundment is adjacent to an open-pit stope, the dam's stability is directly related to the safety production of the whole mine. The Tongling tailings impoundment is a valley-type tailings impoundment. In a valley-type tailings impoundment, two-dimensional analysis cannot fully evaluate the displacement field and stress field variation characteristics in the three directions of the tailings dam. The main purpose of this research is to analyze the stability characteristics of the Tongling tailings impoundment under different recovery heights and diverse working conditions. The instability characteristics of the dam body are calculated under different working conditions (such as strong rainfall, floods, and earthquakes) by a combination of 2D and 3D numerical simulation analysis. As a result, the Tongling tailings impoundment retreatment plan has not yet been implemented in the actual engineering. It is essential to design a reasonable mining plan for the tailing pond. This analysis makes it possible to identify the main factors affecting the stability of the dam in advance, and it is helpful in taking the appropriate protective measures in later engineering practice. The stoping of the tailings impoundment is of great significance to the ecological environment and the safe production of mines. Moreover, the research can provide a corresponding reference for later engineering practice.

2. Materials and Methods

2.1. Study Area

This research paper focuses on valley-type tailings impoundments. Valley-type tailings impoundments are a preferred safe storage method for tailings, mainly established in regions with rugged natural landscapes or numerous mountains, such as South America, North America, Asia, and some areas of Africa. Based on a comprehensive analysis of similar tailings impoundments around the world, we found that most of the disasters caused by this type of tailings dam are due to intense precipitation and earthquake events. Typically, valley-type tailings impoundments are located in low-lying areas at the mouth of a valley, resulting in a relatively large catchment area but with limited flood regulation capacity. Therefore, in the regions we have studied, the primary considerations for the stability of tailings impoundments are various extreme conditions, such as intense precipitation, floods, and earthquakes.

The Tongling tailings impoundment has been out of service for many years (Figure 1). An open-pit mine has been opened near the tailings pond, which is located within the open pit boundary (Figure 2). In order to ensure the safety of the open pit, the Tongling tailings pond now needs to be written off and progressively re-mined. After recovery, the tailings will be transferred to another tailings pond in the mine. After the mining is completed, all tailings facilities will be dismantled, eventually restoring the original gully landform.
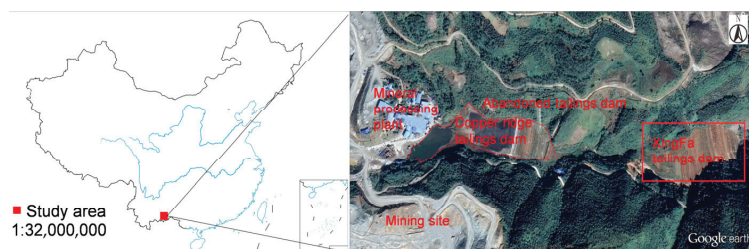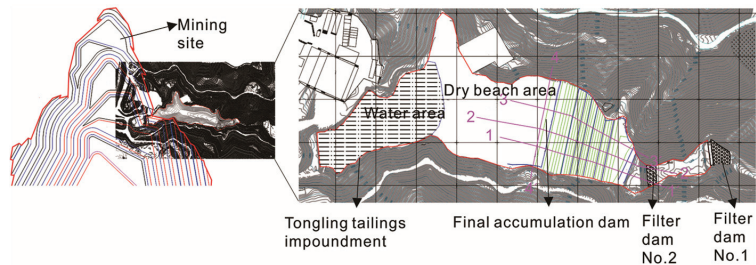

Figure 1. Overview of the study area.

Figure 2. Engineering geological map of the tailings dam (1–4 are section lines).

The initial dam is stacked from an elevation of 1220.0 m. The current tailings elevation is 1255 m, and the stacking dam height is 35 m. Approximately 486,500 m^3 of tailings have been stockpiled in the impoundment. There are 27 sub-dams in total. The average slope ratio of the dam is 1:3.0. Moreover, the total storage capacity of impoundment is 540,000 m^3. By reviewing China's tailings pond design code, the design grade of the tailings impoundment is fourth class. The tailings impoundment has been used to 1255 m, with 2 m remaining to the design final accumulation elevation of 1257 m. The Tongling tailings impoundment covers an area of approximately 0.038 km^2, with a dry beach length of approximately 170 m and a water area length of about 120 m.

2.2. Re-Mining Process of the Tailings Dam

Before analyzing and calculating the tailings pond, a detailed survey was launched on site, and samples were brought back for relevant physical and mechanical property analysis. The main components of the tailings are silty clay, silt, and silt sand.

The analysis shows that the materials in the tailings impoundment have a high water content, low strength, and slow percolation under natural conditions.

Combined with the buried depth of the infiltration obtained from the engineering surveys, the tailings impoundment materials are divided into two parts by the infiltration line. These are the unsaturated tailings above the infiltration line and saturated tailings below the infiltration line. In accordance with the current status of the mine and the physical and mechanical properties of the tailings, the unsaturated tailings above the infiltration line in the dry beach area will be recovered by a combination of water gun flushing and a floating sand pumping vessel. In contrast, the saturated tailings below the infiltration line will be recovered by a floating sand pumping vessel.

There are four main stages of the tailings dam recovery process, namely, the current tailings accumulation elevation (1255 m), recovery to half of the dam (1238 m), recovery to the top of the initial dam (1220 m), and recovery to half of the initial dam (1210 m). The subsequent analysis is based on these four stages.

2.3. Stability Analysis Model and Material Parameters

(1)   Analysis model

In order to make the results of the subsequent numerical simulation analysis more representative of the overall stability of the tailings pond, the most unfavorable profile for the subsequent analysis was selected, that is, the maximum longitudinal section along the tailings pond trench (as shown in Figure 3). The profile model has a height of 70 m and a length of 360 m. The tailings deposition pattern is coarse at the top and fine at the bottom, and the tailings particle size is coarse before the dam and fine at the end of the dam. The structure of the tailings is heterogeneous and anisotropic. According to the geotechnical engineering investigation report of the tailings pond (Project No.: 15ZG389-PMN-51-0007) and the drilling lithological data, the analysis section was divided into six material zones: silty sand tailing, silty soil tailing, tail silty clay, initial dam, filter dam, and dam foundation (Figure 3).
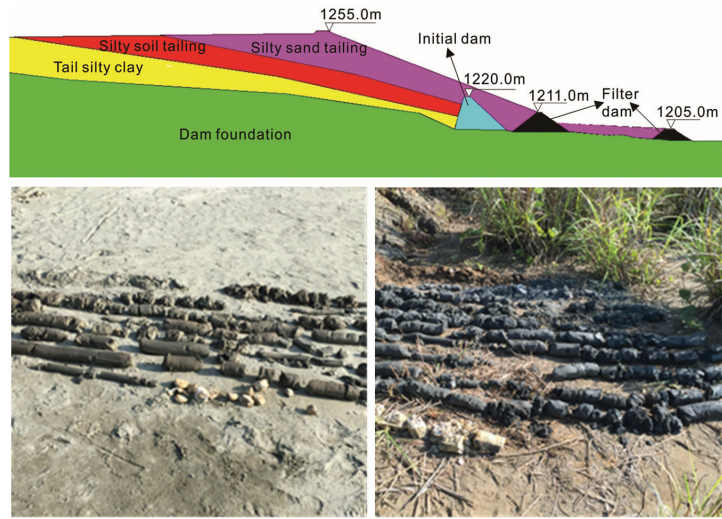
Figure 3. 2-2′ Section material division diagram and rock core photograph.

(2)   Calculation parameters

In order to ensure that the simulation calculation results are consistent with the actual situation of the mine and to ensure calculation accuracy, it is necessary to select the calculation parameters accurately. A detailed survey of the tailings impoundment was conducted, and multiple representative sampling points were set in the tailings impoundment. A large number of samples (approximately 130 kg) were retrieved. The samples were then processed in strict accordance with the relevant geotechnical test protocols (Figure 4). Soil mechanical tests were launched, such as density tests, tailings consolidation tests, permeability tests, direct shear tests, etc., as shown in Figure 3. After processing the measured data, the simulation calculation parameters of the tailings pond were obtained. In order to ensure the reliability of the data during the tests, multiple parallel tests were carried out for each test. The results are summarized in Table 1. The values of the material parameters for the two-dimensional and three-dimensional analyses are taken strictly from Table 1.

Figure 4. The samples and experiments: (**a**–**c**) site sampling; (**d**–**g**) laboratory test.

Materials	Wet Unit Weight γ (KN/m^3)	Modulus of Compressibility E_s	Saturated Unit Weight γ (KN/m^3)	Internal Friction Angle (°)	Cohesive Forces C (KPa)	Osmotic Coefficient (cm/s)
silty sand tailing	21.5	8.41	22.1	28.9	8.1	4.15×10^{-4}
silty soil tailing	18.8	4.04	18.4	18.5	10.0	4.1×10^{-5}
tail silty clay	18.7	3.76	19.0	13.5	12.6	4.5×10^{-5}
initial dam	23.0	3.73	23.0	32.0	120.0	1.0×10^{-6}
filter dam	20.5	–	21.0	30.0	10.0	1.0×10^{-3}
dam foundation	25.6	–	26.0	60.0	100.0	5.2×10^{-5}

2.4. The Basic Principles of Seepage Calculation

2.4.1. Darcy's Law

In 1856, Darcy determined the relationship between seepage velocity (V) and hydraulic slope ($\Delta H/L$) by launching a large number of penetration experiments. Afterwards, the famous Darcy's law was proposed. This law shows that the velocity of water is not only related to the hydraulic gradient but also to the permeability of the soil [46]. Darcy's law is given by Equation (1)

$$V = \frac{Q}{A} = -k\frac{\Delta H}{L} = kJ \tag{1}$$

where V is the flow rate, Q is the flow rate, and A is the section area, which corresponds to the cross-sectional area of the sand column in the experiment. k is the permeability coefficient. ΔH is the head loss, i.e., the difference in head between the upstream and downstream overflow sections. L is the length of the percolation path, and J is the hydraulic gradient. The formula is only proposed for the case of laminar flow. In the operation of the tail mine, the vast majority of seepage is a part of the laminar flow, to which the formula can be applied.

Under rainfall and flood conditions, the shear strength of the tailings will gradually decrease and seepage will gradually cause slip damage to the dam [47]. The initial shear stress of the tailings can be obtained by Equation (2)

$$\tau_c = 0.00821\gamma RS^{0.040}\left(\frac{\rho_d - \rho}{\rho}\right)^{0.323} \tag{2}$$

where ρ_d is the dry density of the tailings, S is the percentage of clay content, ρ is the density of clear water, and R is the hydraulic radius.

2.4.2. 3D Seepage Field and Stress Field Coupling Principle

(1) The fundamental differential equation for the calculation of 3D steady seepage.

The fundamental differential equation for calculating three-dimensional steady seepage is expressed as Equation (3) [48]

$$\frac{\partial}{\partial x}\left(k_x\frac{\partial h}{\partial x}\right) + \frac{\partial}{\partial y}\left(k_y\frac{\partial h}{\partial y}\right) + \frac{\partial}{\partial z}\left(k_z\frac{\partial h}{\partial z}\right) = 0 \tag{3}$$

where h is the head function, and k_x, k_y, k_z are the permeability coefficients in the x, y, z directions, respectively. The following two types of boundary conditions need to be satisfied for a steady seepage field.

The water head is the first type of boundary condition and is obtained using Equation (4).

$$\text{h}|\Gamma_1 = h(x,y,z) \tag{4}$$

The flow rate is the second type of boundary condition, is equal to zero, and can be obtained using Equation (5).

$$k_x \frac{\partial h}{\partial x} \cos(n, x) + k_y \frac{\partial h}{\partial y} \cos(n, y) + k_z \frac{\partial h}{\partial z} \cos(n, z)|\Gamma_2 = 0 \tag{5}$$

Since the free surface of the seepage is the flow surface, there is no inflow or outflow of flow, so the seepage free surface also needs to satisfy the following conditions, which are given by Equation (6).

$$h = z \tag{6}$$

Γ_1 and Γ_2 constitute the full boundary conditions in the 3D space, and the seepage field inside the tailings dam body can be obtained by solving the finite element equations.

(2) Coupling principle of 3D seepage field and stress field.

In MIDAS/GTS, pore water pressure is calculated through seepage analysis to determine fluid permeability. The effect of seepage on stress is mainly realized by applying osmotic force to the soil in seepage. The total stress is divided into effective stress and pore water pressure [49,50]. Since water cannot withstand shear stress, the mechanical effect of effective shear stress is the same as total shear stress, so the total stress expression is assumed as Equation (7).

$$\begin{cases} \sigma_{xx} = \sigma_{xx}' + u_w \\ \sigma_{yy} = \sigma_{yy}' + u_w \\ \sigma_{zz} = \sigma_{zz}' + u_w \\ \tau_{xy} = \tau_{xy}' \\ \tau_{yz} = \tau_{yz}' \\ \tau_{zx} = \tau_{zx}' \end{cases} \tag{7}$$

In the formula, σ_{xx}, σ_{yy}, σ_{zz}, σ_{xy}, σ_{yz}, σ_{zx} are the stress components of a certain point in space, KPa. σ_{xx}', σ_{yy}', σ_{zz}', σ_{xy}', σ_{yz}', σ_{zx}' are the effective stress components at a point in space, KPa. u_w is the pore water pressure, KPa.

The pore water pressure can be divided into steady pore water pressure and excess pore water pressure, which is given by Equation (8)

$$u_w = P_{steady} + P_{excess} \tag{8}$$

where P_{steady} is the steady pore water pressure, KPa. P_{excess} is the excess pore water pressure, KPa. Equation (9) can be obtained from Hooke's law.

$$\left(\dot{\varepsilon}_x^e, \dot{\varepsilon}_y^e, \dot{\varepsilon}_z^e, \dot{\gamma}_{xy}^e, \dot{\gamma}_{yz}^e, \dot{\gamma}_{zx}^e \right)^T = \frac{1}{E} \begin{pmatrix} 1 & -v & -v & 0 & 0 & 0 \\ -v & 1 & -v & 0 & 0 & 0 \\ -v & -v & 1 & 0 & 0 & 0 \\ 0 & 0 & 0 & 2+2v & 0 & 0 \\ 0 & 0 & 0 & 0 & 2+2v & 0 \\ 0 & 0 & 0 & 0 & 0 & 2+2v \end{pmatrix} \begin{pmatrix} \dot{\sigma}_{xx}' \\ \dot{\sigma}_{yy}' \\ \dot{\sigma}_{zz}' \\ \dot{\sigma}_{xy}' \\ \dot{\sigma}_{yz}' \\ \dot{\sigma}_{zx}' \end{pmatrix} \tag{9}$$

E is Elastic Modulus, MPa. v is the Poisson's ratio of the material. ε_x, ε_y, ε_z, γ_{xy}, γ_{yz}, γ_{zx} are the line and tangential strains at any point in space.

In Formula (7), the steady pore water pressure is determined by the height of the underground water level, and its derivative is zero. Equation (10) can be obtained.

$$\dot{u}_w = \dot{P}_{excess} \tag{10}$$

According to Formulas (7) and (10), Formula (9) can be solved. The stress and strain state of any point in the tailings dam can be obtained by solving Formula (11).

$$
\begin{pmatrix} \dot{\varepsilon}_x^e \\ \dot{\varepsilon}_y^e \\ \dot{\varepsilon}_z^e \\ \dot{\gamma}_{xy}^e \\ \dot{\gamma}_{yz}^e \\ \dot{\gamma}_{zx}^e \end{pmatrix} = \frac{1}{E} \begin{pmatrix} 1 & -v & -v & 0 & 0 & 0 \\ -v & 1 & -v & 0 & 0 & 0 \\ -v & -v & 1 & 0 & 0 & 0 \\ 0 & 0 & 0 & 2+2v & 0 & 0 \\ 0 & 0 & 0 & 0 & 2+2v & 0 \\ 0 & 0 & 0 & 0 & 0 & 2+2v \end{pmatrix} \begin{pmatrix} \dot{\sigma}_x - \dot{P}_{excess} \\ \dot{\sigma}_y - \dot{P}_{excess} \\ \dot{\sigma}_z - \dot{P}_{excess} \\ \dot{\tau}_{xy} \\ \dot{\tau}_{yz} \\ \dot{\tau}_{xz} \end{pmatrix} \tag{11}
$$

2.5. Two-Dimensional Seepage Analysis of the Tailings Dam

2.5.1. Analysis of Dam Infiltration Lines at Different Elevations

The height of the tailings dam and the length of the dry beach in tailings impoundment design are related to the infiltration line, which is the lifeline directly related to the safety of the tailings dam. In the process of mining tailings, with the change of the dam height, the dry beach length is also changed, thus affecting the position of the infiltration line. The variation of the infiltration line under different stoping elevations was analyzed, and the seepage characteristics of the tailings pond under various working conditions, which can provide a reference for subsequent stability calculations, was also determined.

The infiltration line is generally obtained by field measurements, and the defective part of the field measurement is acquired by seepage calculations. The numerical simulation is performed using two-dimensional software based on the infiltration lines actually measured in the field. During the calculations, it was assumed that the upstream water level of the tailings pond and the downstream water level remained constant for a short period, therefore, the seepage analysis was performed as a steady flow. In order to make the calculation results closer to reality, the calculation result is modified according to the survey data of the field infiltration line.

2.5.2. Two-Dimensional Stability Analysis of Dams

Based on the above infiltration line analysis results, the limit equilibrium method was used [51,52] to analyze the effects of different elevations and working conditions on the stability of the dam body during the stoping process of the tailings impoundment. The different recovery heights are equivalent to the four different recovery heights in the infiltration line analysis. Southwest China is an earthquake-prone region, therefore, earthquake influence should be considered in dam stability analyses. (According to the engineering survey data, the earthquake fortification intensity of the area is 6 degrees, and the design basic acceleration of ground motion value of the site is 0.05 g.)

The stability analysis takes into account three main operating conditions: ① The steady infiltration pressure at the normal reservoir level, the self-weight of the dam, and the pore water pressure in the foundation of the dam (normal working conditions); ② The self-weight, the pore water pressure in the dam foundation, and the potential for stable infiltration pressure at the design flood level (flood working conditions); ③ The infiltration pressure at the normal reservoir level, the self-weight of the dam, the pore water pressure in the dam and foundation, and seismic loading (special working conditions).
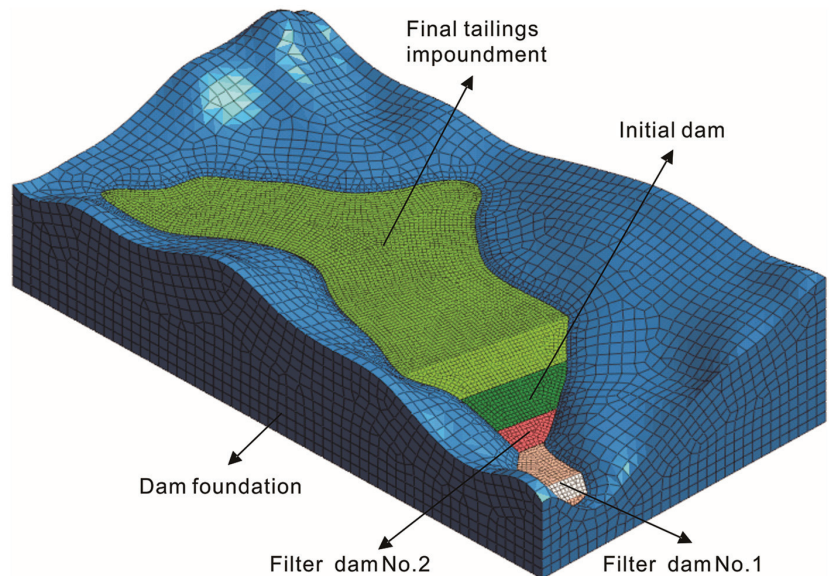
2.6. 3D Stability Analysis of the Tailings Dam under Different Working Conditions

The stability analysis was conducted at different elevations by means of a two-dimensional analysis. However, the stress and displacement changes within the tailings impoundment during the operation cannot be derived from the two-dimensional analysis. Therefore, in order to further determine the variation of the stress and displacement fields in the tailings pond, a three-dimensional analysis of the tailings pond was launched. 3Dmine software was used to create the 3D surface structure of the tailings impoundment, and then

a 3D numerical analysis model was established by means of Midas GTS NX software 2023 v1.1. There are two main approaches: ① If the object of the analysis object is regular, the terrain conditions are relatively simple, and the terrain fluctuation is not large, the object profile can be analyzed directly for lateral stretching to generate 3D entities; ② When the object of the analysis is located in complex terrain, the terrain is significantly undulating, and the object of the analysis is irregular. Firstly, it is necessary to generate a realistic ground surface with 3Dmine software and then couple it with Midas GTS NX numerical simulation software to generate a more realistic 3D entity for analysis. A combination of two three-dimensional analyses was used to make the analysis more comprehensive. The Midas GTS NX numerical simulation software was selected to carry out the analysis.

2.6.1. Three-Dimensional Static Analysis of the Tailings Impoundment

Four different stoping heights were selected to conduct a three-dimensional static analysis of the tailings impoundment. The overall displacement variation of the tailings impoundment in the process of mining was analyzed. The tailings dam model has a length of 690 m, a width of 370 m, and a height of 90 m. The grid cell size is 5 m, and the model has 97,328 cells and 54,654 nodes. Figure 5 presents the calculation model.

Figure 5. Calculation model diagram.

2.6.2. Three-Dimensional Stability Analysis of the Tailings Impoundment under Different Working Conditions

(1) Establishment of the 3D model

Due to the low depression in the middle of the tailings impoundment, the surrounding terrain fluctuates wildly. In the three-dimensional analysis, due to avoiding software focus on the surrounding high and steep mountains, the accuracy of the tailings pond area cannot be guaranteed. The dam body at the highest elevation of the tailings impoundment (1255.0 m) was selected as the analysis model, and a 3D solid was generated from the calculated profile. The model has a length of 360 m, a width of 80 m, and a height of 80 m. The grid cell size is 5 m, and the model has 13,472 cells and 15,283 nodes (Figure 6).
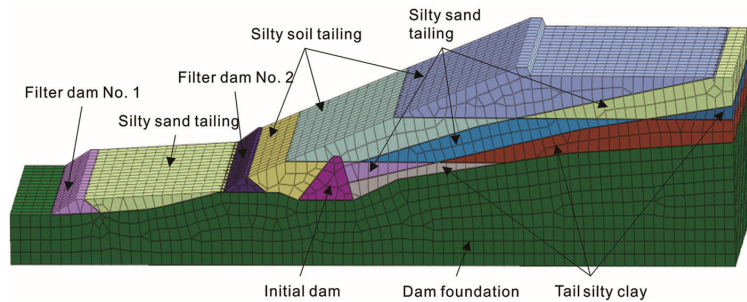
Figure 6. Three-dimensional stability calculation model of the dam.

The MIDAS GTS NX software has a variety of constitutive models, and the Mohr–Coulomb constitutive model was chosen. Choosing an appropriate constitutive model for numerical simulation analysis of tailings impoundment is crucial. This is because, under normal conditions, the stress and strain interactions among tailings are complex, with nonlinear, elasto-plastic, dilatant, and anisotropic physical properties being common. The rationality of the selection of the constitutive model is directly related to the accuracy of the numerical simulation calculations. However, current research does not yet provide a constitutive model for tailings soil that accurately reflects all conditions; most existing models apply only to tailings soil under certain specific conditions. With the deepening of research on finite element technology, research on the constitutive models of geotechnical bodies has greatly improved, and the accuracy of analysis and calculation has also become higher.

This study chose the Mohr–Coulomb model for numerical analysis. The main advantages and disadvantages of this model can be summarized as follows:

(1) The main advantages of the Mohr–Coulomb model are:

(a) Accuracy: the Mohr–Coulomb constitutive model is an empirical clay behavior model, which can be understood as a mixture of perfectly plastic behavior and linear elasto-plasticity. Hence, it is more accurate than linear elastic models in describing the nonlinear behavior of soil;

(b) Applicability: the Mohr–Coulomb model applies to various soil conditions (dry, wet, saturated, etc.) and soil types (sand, clay, etc.), making it broadly applicable in practical engineering. In this study, the tailings consist primarily of clay tailings and sand tailings. Hence, the Mohr–Coulomb model can effectively reflect the dam's stability under intense rainfall and flooding;

(c) Completeness: the Mohr–Coulomb theory considers both normal stress and shear stress, thus evaluating material resistance to damage more comprehensively;

(2) The main disadvantages of the Mohr–Coulomb model are:

(a) Parameter selection: choosing the Mohr–Coulomb parameters is essential but can sometimes pose difficulties. The accuracy of the parameter selection directly influences the analysis results' accuracy;

(b) Practical problems: the Mohr–Coulomb model might not suit all types of soil. For instance, the Mohr–Coulomb model may not accurately predict the behavior of highly plastic clay or very soft soils.

In this study, the tailings and dam body did not involve highly plastic clay and soft soil. The tailings soil body was mainly composed of powdery clay tailings and sand tailings. Therefore, based on the actual situation of the tailings impoundment and considering the applicability and disadvantages of the Mohr–Coulomb model, this study chooses this model to more accurately reflect the constitutive behavior of the studied subject.

The strength reduction method (SRM) was selected as the stability analysis method of the 3D model.

(2)　The calculation conditions of the 3D model

Four analysis conditions were comprehensively considered according to the actual conditions and the two-dimensional analysis conditions: ① Working condition 1 is the normal water level; ② Working condition 2 is the flood level; ③ Working condition 3 is a combination of flooding and heavy rainfall (special working condition I); ④ Working condition 4 is a combination of flooding and an earthquake (special working condition II). The earthquake fortification intensity and the design basic acceleration of ground motion value are consistent with the two-dimensional analysis.

The values of each material parameter are shown in Table 1. The calculated values of the safety factors for different operating conditions are summarized in Table 2.

Table 2. Safety factors under different working conditions.

Working Condition	Calculated Safety Factor	Minimum Safety Coefficient Allowed by Code	Whether Safety Requirements Are Met
Normal	1.4630	1.45	Yes
Flooding	1.4375	1.1~1.2	Yes
Special I	1.3625	1.05~1.10	Yes
Special II	1.3373	1.05	Yes

In analyzing and comparing the research materials on the stability of valley-type tailings dams from other regions, it has been found that floods, rainfall, and earthquakes are the primary factors affecting the stability of such reservoirs. Due to their unique terrain and geological conditions, as well as hydrological and meteorological conditions and ecological environment, valley-type tailings dams present a high safety risk. Floods may lead to scouring and landslides of the dam, and inadequate spillway facilities or blockages may trigger overtopping due to floods. Rainwater infiltration leads to the rise of the saturation line, which in turn decreases the stability and strength of the dam and increases the risk of landslides. Earthquakes can cause geological disasters and landslides or collapses of the dam, threatening the safety of the tailings dam.

The safety of tailings dams mainly depends on whether the safety factor is reduced, whether the displacement amount is large, and whether the penetration range of equivalent plastic area is expanded. By comparing the results of 3D stability and the critical safety factor, it is clear that the overall dam displacement decreased with the recovery height in the static analysis. Under the different analysis conditions, the dams are subject to small displacements, and the strains all occur on the outer slope of the tailings dam. Under flood and heavy rainfall conditions, the silty sand tailing becomes saturated, increasing the dam's self-weight and leading to a lack of slip resistance. A saturated silty sand tailing will have low strength and poor consolidation and will liquefy during seismic events. Therefore, there is a certain zone of plastic deformation inside the reservoir under seismic conditions, which occurs from the top of the initial dam to the middle of the stacked dam.

3. Results

3.1. Variation of the Infiltration Line of the Tailings Dam

By performing seepage calculations on the tailings dam body, the variation law of the infiltration line of the dam in the process of mining is observed. Figures 7 and 8 show the results of the infiltration line calculations for tailings dam with different mining heights.

In Figures 7 and 8, a presents the tailings dam elevation, b presents the initial dam, c presents filter dam no. 2, d presents the saturation line, e presents filter dam no. 1, f presents the tailings dry beach.

From the above calculations, it can be seen that the calculated infiltration line is substantially similar to the field exploration infiltration line. Since the calculation of the infiltration line combines different working conditions, it more comprehensively reflects the stability of the tailings. The dam elevation has a significant influence on the buried depth of the saturation line. The infiltration line is significantly higher under flood conditions

indicating that flooding has a more significant impact on the stability of the tailings dam. Under flood conditions, the tailing sands gradually saturate. Under the action of seepage, the pore water pressure within the soil decreases, and the shear strength subsequently decreases, which can cause infiltration damage to the tailing dam body.
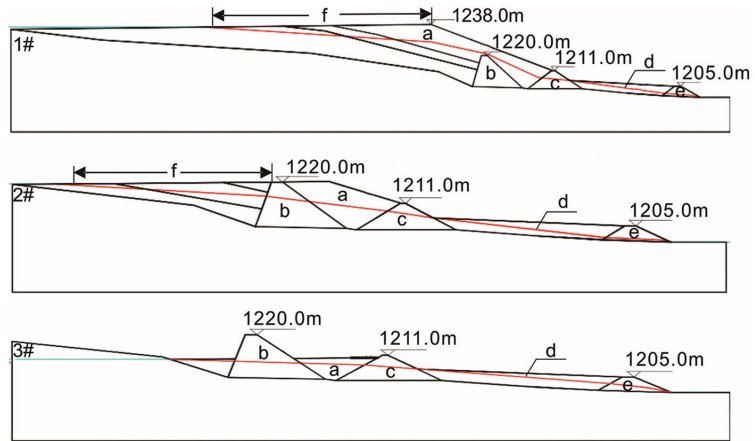
Figure 7. Seepage calculation (normal working conditions): 1# the dam elevation is 1238 m, 2# the dam elevation is 1220 m, 3# the dam elevation is 1211 m.
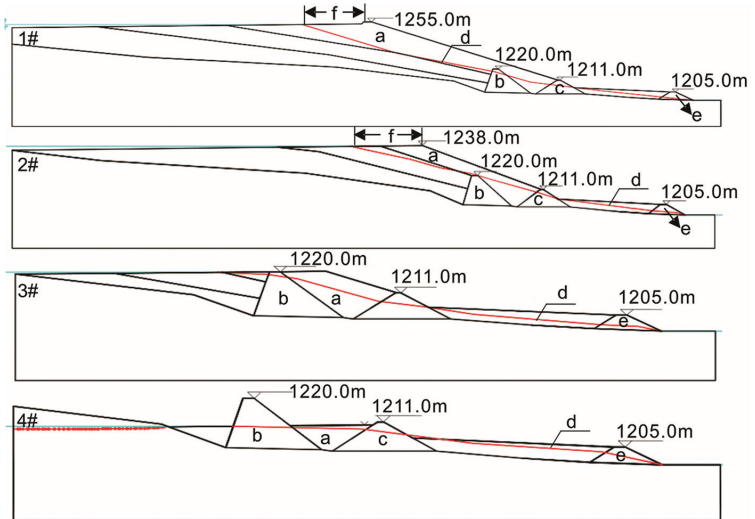
Figure 8. Seepage calculation (flooding conditions): 1# the dam elevation is 1255 m, 2# the dam elevation is 1238 m, 3# the dam elevation is 1220 m, 4# the dam elevation is 1211 m.

With the advancement of the re-mining process, the elevation of the tailings dam gradually decreases, the infiltration line is reduced, and the length of the dry beach is also shortened. This is due to the gradual reduction in tailings and industrial waste in the impoundment during the recovery process, influenced by the deposition pattern of tailing sand in the reservoir area. The particles of the tailings deposit on the beach successively change from coarse to fine going from the near to the far end. As a result, the permeability of the infiltration line from the beginning to the end changes from small to large.

3.2. Two-Dimensional Stability

Due to the limited space available, the safety factors for the different operating conditions in the recovery process are summarized in Table 3. The calculated values are compared with the minimum permissible safety factors required by the code.

Table 3. Calculation results of dam stability.

Tailings Dam Elevation (m)	Working Conditions	Calculated Safety Factor	Circle Arc Sliding Radius (m)	Minimum Safety Factor Allowed by Code
	Normal	1.238	134.574	1.15
1255	Flooding	1.195	133.400	1.05
	Special	1.174	132.651	1.00
	Normal	1.670	140.594	1.15
1238	Flooding	1.621	140.594	1.05
	Special	1.596	140.594	1.00
	Normal	1.910	60.384	1.15
1220	Flooding	1.864	60.384	1.05
	Special	1.835	30.491	1.00
	Normal	3.202	28.258	1.15
1210	Flooding	3.131	28.258	1.05
	Special	3.020	28.258	1.00

The accumulation elevation of the tailings pond gradually decreases during the recovery process, the accumulation in the dam gradually reduces, and the total self-weight of the tailings pond decreases. The infiltration line is directly proportional to the recovery and accumulation elevations in the previous section. Under each working condition, the safety factor is inversely proportional to the accumulation elevation, and the safety factor gradually rises with the elevation reduction. The overall relationship between the safety factor value of the three operating conditions is normal working conditions > flood working conditions > special (earthquake) working conditions (Figure 9).
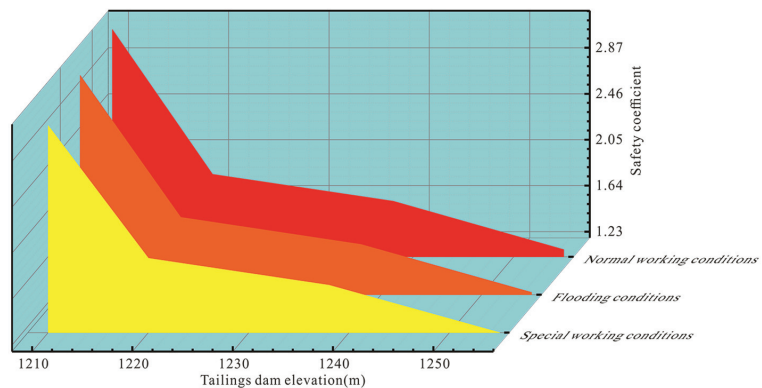
Figure 9. Change of dam safety coefficient.

3.3. Three-Dimensional Stability

3.3.1. Statical Analysis Results

At the elevation stage of 1255 m–1238 m, the minimum principal stress, the maximum principal stress, and the maximum shear stress are all positive values (Figure 10). There is both tensile and compressive stress at this stage, which is mainly concentrated in the tailings reservoir area. The maximum shear stress decreases in a laminar pattern from

bottom to top in the reservoir area, indicating that the shear stress is mainly influenced by self-weight.
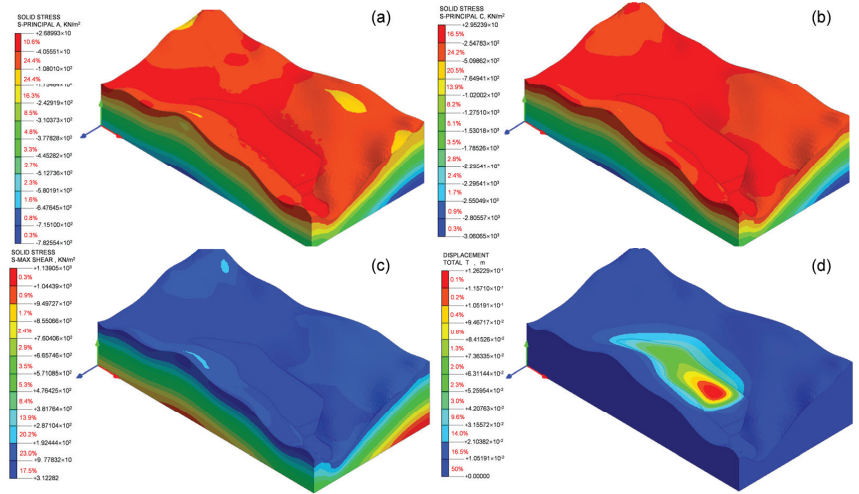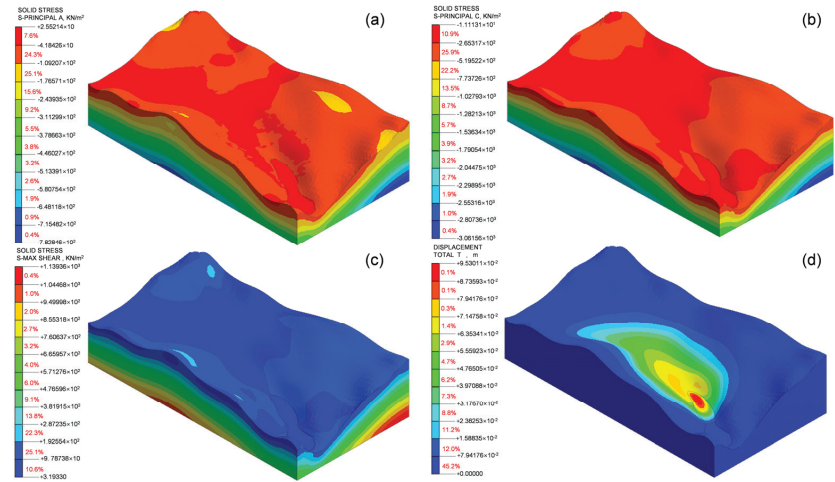

Figure 10. The calculation of 1255 m–1238 m: (**a**) the minimum principal stress cloud atlas, (**b**) the maximum principal stress cloud atlas, (**c**) the maximum shear stress cloud atlas, (**d**) the excursion cloud atlas.

When mining to the crest of the initial dam, the minimum principal stress and the maximum shear stress are positive, and the maximum principal stress is negative, indicating that there is tensile stress in the reservoir area. The maximum shear stress decreases in a laminar pattern from bottom to top in the reservoir area, indicating that the shear stress is mainly influenced by self-weight. After mining, small displacement changes will occur in the dam, mainly occurring in the position of the tailings impoundment (Figure 11).
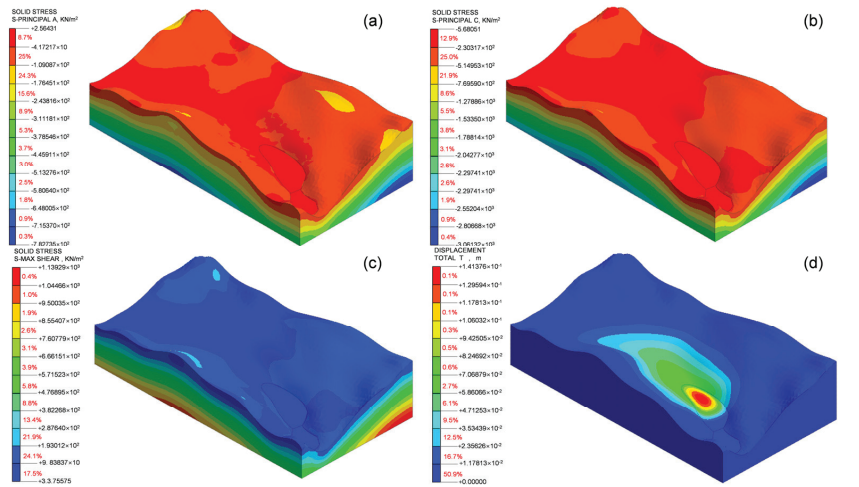
Figure 11. The calculation of 1238 m–1220 m: (**a**) the minimum principal stress cloud atlas, (**b**) the maximum principal stress cloud atlas, (**c**) the maximum shear stress cloud atlas, (**d**) the excursion cloud atlas.

At the elevation stage of 1220 m–1211 m, the maximum shear stress is in the upper part of the dam, where the shear stress is minimal and gradually increases in the direction of the ground in a laminar pattern (Figure 12). The shear stress is mainly influenced by self-weight. After stoping, the displacement is 0.095 m, which may be caused by the fact that the actual flushing production cannot be determined by the water gun flushing method.

Figure 12. The calculation of 1220 m–1211 m: (**a**) the minimum principal stress cloud atlas, (**b**) the maximum principal stress cloud atlas, (**c**) the maximum shear stress cloud atlas, (**d**) the excursion cloud atlas.

During the mining process, the tailings dam gradually decreases from 1255 m to 1211 m, and the displacement mainly occurs in the middle of the tailings dam. The displacement decreases from 0.126 m to 0.095 m, the total displacement is small, and the tailings dam foundation can remain stable during the whole mining process. The tailings pond is mainly affected by compressive stresses generated by self-weight. Although there is a certain displacement, considering that the actual construction method of the reservoir is hydraulic mining, the displacement is negligible.

3.3.2. 3D stability Analysis Results under Diverse Analysis Conditions

(1) Normal working conditions

Under normal conditions, the safety factor value of the strength reduction calculation is 1.4630. The total displacement is mainly at the dam top. The amount is 0.443 m, which is slightly larger than the static analysis. The maximum shear strain and the equivalent plastic strain under these conditions are found to be in approximately the same location. The maximum shear stress and equivalent plastic strain diagrams reveal that the main strain is at the back end of filter dam no. 2, where the deformation is small (Figure 13).
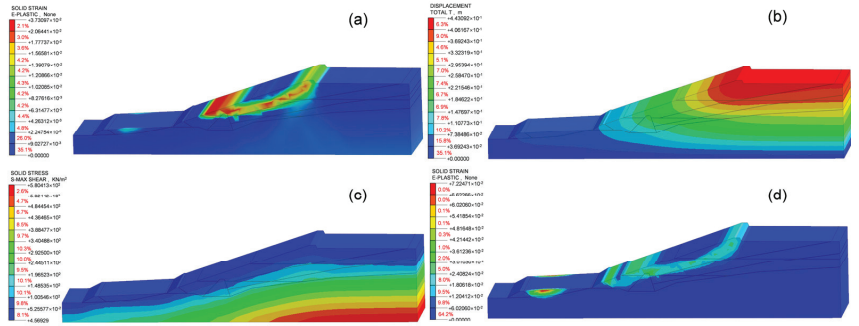
(2) Flooding conditions

Under flooding conditions, the safety factor value of the strength reduction calculation is 1.4375. The value of the safety factor is lower than the normal working conditions, and the total displacement is about 0.305 m. According to the equivalent plastic strain cloud atlas, it was found that there is a particular plastic deformation zone on the front slope of the dam, and that the excessive region of the equivalent plastic strain becomes more prominent, which may lead to slip failure (Figure 14).
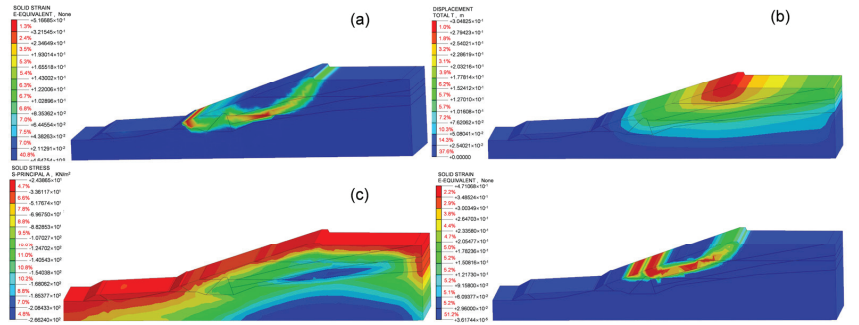
(3) Special working conditions I: flood + heavy rainfall

The safety factor value of the strength reduction calculation is 1.3625 under the special working conditions I. The total displacement mainly occurs at the top of the dam. The amount of the displacement is 0.268 m. The equivalent plastic strain zone mainly occurs at

filtration dam no. 2 and in the lower area of the dam crest, where the strain zone is larger, and the safety factor is reduced (Figure 15).

Figure 13. (**a**) The safety factor cloud atlas, (**b**) the excursion cloud atlas, (**c**) the maximum shear stress cloud atlas, (**d**) the equivalent plastic strain cloud atlas.
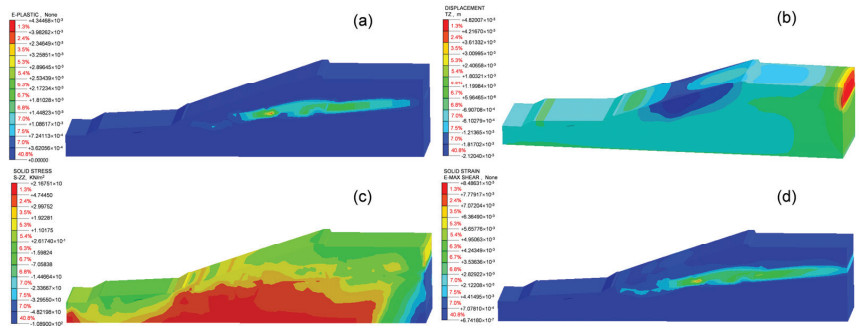

Figure 14. (**a**) The safety factor cloud atlas, (**b**) the excursion cloud atlas, (**c**) the maximum principal stress cloud atlas, (**d**) the Equivalent plastic strain cloud atlas.
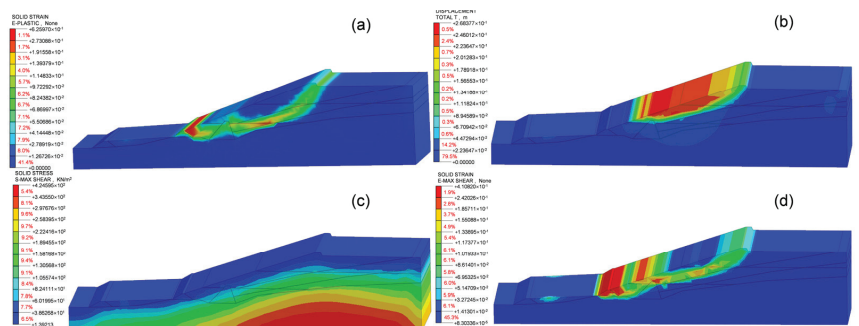
Figure 15. (**a**) The safety factor cloud atlas, (**b**) the excursion cloud atlas, (**c**) the maximum shear stress cloud atlas, (**d**) the Equivalent plastic strain cloud atlas.

(4) Special working conditions II: flood + earthquake

The safety factor value of the strength reduction calculation is 1.3373 under special working conditions II. Under earthquake conditions, the shear stress in the dam changes, and a partial plastic deformation zone is generated inside the dam. The deformation zone runs from the initial dam position to the tail of the dam body, and the penetration area is expanded (Figure 16).

Figure 16. (**a**) The safety factor cloud atlas, (**b**) the maximum principal stress cloud atlas, (**c**) the maximum shear stress cloud atlas, (**d**) the Equivalent plastic strain cloud atlas.

4. Discussion

Research on tailings dam re-mining at home and abroad has mainly focused on the replacement of re-mining methods, re-mining equipment, reclamation technology, and the use of tailings to fill the void area. A comprehensive analysis of the tailings pond around the stability evolution characteristics of the tailings dam during the re-mining process is presented to ensure the stability of the tailings dam and the safety of the staff during the re-mining process. A seepage analysis model at different elevations was established, and seepage and infiltration line change patterns from an actual 3D ground surface were analyzed. Four typical retrieval elevations were selected, and various analytical conditions were considered by means of 2D and 3D numerical simulations. The research reveals the pattern of the interaction between the recovery elevation and the analyzed working conditions. The results provide a deeper insight into the changes in the stress field, seepage field, and displacement field of the tailings impoundment during the recovery process, which may help us carry out dam safety monitoring and early warning and forecasting and provide a theoretical basis for the actual construction of the mine.

In the two-dimensional numerical simulation, the dam body was simplified, and the physical and mechanical parameters were somewhat modified according to the engineering survey data. The infiltration line calculated by the two-dimensional software has also been amended. The surrounding geological environment of the tailings impoundment was simplified in the 3D morphing, and the boundary conditions were set slightly differently from the actual situation, which may lead to some specific errors. In future studies, it should be modified and modeled according to the current situation.

Tailings impoundment retrieval is a dynamic process, and only four typical retrieval heights were analyzed, failing to take any one height into account to calculate its stability. Therefore, a dynamic simulation of the whole retrieval process should be achieved in our subsequent study.

5. Conclusions

A combination of field investigation, laboratory tests, seepage theory analysis, and numerical simulation was used to study the stability of dams with different stoping elevations in the Tongling valley-type tailings impoundment. Based on the actual situation of the mining area and the calculation, the following conclusions can be drawn.

(1) In the stoping process, different elevations significantly influence the burial depth of the saturation line. The lower the retrieval height, the deeper the infiltration line is buried, which is beneficial to the dam's stability. However, at the same elevation, a small portion of the infiltration line will overflow under flood conditions, mainly because the tailings pond has been out of service for many years and the relevant drainage facilities have not been repaired and unclogged for many years, resulting in the poor drainage capacity of the dam, which leads to an apparent uplift of the infiltration line under flood

conditions. Therefore, before mining the tailings pond in the current project, the drainage facilities should undergo maintenance, and the drainage device should be dredged to ensure the stability of the tailings dam during the mining process.

(2) The recovery of tailings ponds is a slow load-shedding process. In the limit equilibrium analysis, the safety factor increases with the decrease in mining height. The coefficient of the safety of the dam under different working conditions is greater than the minimum value allowed by the code, and the dam is always in a steady condition during the retrieval process. In the three-dimensional static analysis, the higher the dam elevation, the greater the overall displacement of the tailings pond and the more detrimental it is to the stability of the dam.

(3) The more extreme the analysis, the less safe the dam. Under extreme working conditions, the shear stress inside the dam will switch, the shear strength of the dam will be reduced, and the safety coefficient will decrease too. The equivalent plastic zone will also expand through the scope. There is an apparent continuous slip surface within the tailings dam, particularly under seismic conditions. However, under the various working conditions, the tailing pond is able to meet the requirements for dam body stability and fulfill the conditions for safe production.

(4) The method developed in the study centers around numerical simulation, which allows the researchers to assess the potential risks and outcomes related to the stability of tailings dams during the recovery process. The use of 2D software assists in determining the position of the tailings dam infiltration line and the changes in the dam safety factor during the stoping process. The study also incorporates 3D mapping of the tailings impoundment with 3Dmine software, enabling a more comprehensive 3D numerical analysis model established through Midas GTS NX software. Combining these processes provides them with a clear visual and numerical representation of the impoundment's state. This technology-supported approach has many potential applications around the world, especially in regions where tailings dam failure could pose significant environmental and human risks. Therefore, this study presents not only a promising avenue for the management and recovery of tailings impoundments but also highlights the pressing need to incorporate technology into our environmental management strategies.

Author Contributions: Conceptualization, Y.P. and J.C.; methodology, Y.P.; software, Y.P.; validation, Y.P., J.C. and X.Z.; formal analysis, Y.P.; investigation, Y.P.; resources, X.Z.; data curation, Y.P.; writing—original draft preparation, Y.P.; writing—review and editing, Y.P., J.C., C.Z., X.Z. and S.W.; visualization, Y.P.; supervision, Y.P., J.C., C.Z., X.Z. and S.W.; project administration, J.C.; funding acquisition, J.C. All authors have read and agreed to the published version of the manuscript.

Data Availability Statement: Not applicable.

Conflicts of Interest: The author declare no conflict of interest.

References

1. Dong, L.; Deng, S.; Wang, F. Some developments and new insights for environmental sustainability and disaster control of tailings dam. *J. Clean. Prod.* **2020**, *269*, 122270. [CrossRef]
2. Hatje, V.; Pedreira, R.M.; de Rezende, C.E.; Schettini, C.A.F.; de Souza, G.C.; Marin, D.C.; Hackspacher, P.C. The environmental impacts of one of the largest tailing dam failures worldwide. *Sci. Rep.* **2017**, *7*, 10706. [CrossRef] [PubMed]
3. Tian, S.; Chen, J.-h. Multi-hierarchical fuzzy judgment and nested dominance relation of rough set theory-based environmental risk evaluation for tailings reservoirs. *J. Cent. S. Univ.* **2015**, *22*, 4797–4806. [CrossRef]
4. Yang, Y.; Wei, Z.; Cao, G.; Yang, Y.; Wang, H.; Zhuang, S.; Lu, T. A case study on utilizing geotextile tubes for tailings dams construction in China. *Geotext. Geomembr.* **2019**, *47*, 187–192. [CrossRef]

5. Yin, G.; Li, G.; Wei, Z.; Wan, L.; Shui, G.; Jing, X. Stability analysis of a copper tailings dam via laboratory model tests: A Chinese case study. *Miner. Eng.* **2011**, *24*, 122–130. [CrossRef]

6. Edraki, M.; Baumgartl, T.; Manlapig, E.; Bradshaw, D.; Franks, D.M.; Moran, C.J. Designing mine tailings for better environmental, social and economic outcomes: A review of alternative approaches. *J. Clean. Prod.* **2014**, *84*, 411–420. [CrossRef]

7. He, Y.; Li, B.-b.; Zhang, K.-n.; Li, Z.; Chen, Y.-g.; Ye, W.-m. Experimental and numerical study on heavy metal contaminant migration and retention behavior of engineered barrier in tailings pond. *Environ. Pollut.* **2019**, *252*, 1010–1018. [CrossRef]

8. He, Z.-b.; Liao, T.; Liu, Y.-g.; Xiao, Y.; Li, T.-t.; Wang, H. Influence of sulfur addition/solids content ratio on removal of heavy metals from mine tailings by bioleaching. *J. Cent. S. Univ.* **2012**, *19*, 3540–3545. [CrossRef]

9. Salam, S.; Xiao, M.; Khosravifar, A.; Ziotopoulou, K. Seismic stability of coal tailings dams with spatially variable and liquefiable coal tailings using pore pressure plasticity models. *Comput. Geotech.* **2021**, *132*, 104017. [CrossRef]

10. Zhang, Z.; Zhang, S. A new method of coal fine particles humidification and agglomeration: Synergistic dust suppression with composition of soap solution. *Process Saf. Environ. Prot.* **2022**, *159*, 146–156. [CrossRef]

11. Tian, S.; Dai, X.; Wang, G.; Lu, Y.; Chen, J. Formation and evolution characteristics of dam breach and tailings flow from dam failure: An experimental study. *Nat. Hazards* **2021**, *107*, 1621–1638. [CrossRef]

12. Wu, T.; Qin, J. Experimental study of a tailings impoundment dam failure due to overtopping. *Mine Water Environ.* **2018**, *37*, 272–280. [CrossRef]

13. Xu, W.-b.; Liu, B.; Wu, W.-l. Strength and deformation behaviors of cemented tailings backfill under triaxial compression. *J. Cent. S. Univ.* **2020**, *27*, 3531–3543. [CrossRef]

14. Luino, F.; De Graff, J.V. The Stava mudflow of 19 July 1985 (Northern Italy): A disaster that effective regulation might have prevented. *Nat. Hazards Earth Syst. Sci.* **2012**, *12*, 1029–1044. [CrossRef]

15. de Oliveira Gomes, L.E.; Correa, L.B.; Sá, F.; Neto, R.R.; Bernardino, A.F. The impacts of the Samarco mine tailing spill on the Rio Doce estuary, Eastern Brazil. *Mar. Pollut. Bull.* **2017**, *120*, 28–36. [CrossRef]

16. Agurto-Detzel, H.; Bianchi, M.; Assumpção, M.; Schimmel, M.; Collaço, B.; Ciardelli, C.; Barbosa, J.R.; Calhau, J. The tailings dam failure of 5 November 2015 in SE Brazil and its preceding seismic sequence. *Geophys. Res. Lett.* **2016**, *43*, 4929–4936. [CrossRef]

17. Rotta, L.H.S.; Alcântara, E.; Park, E.; Negri, R.G.; Lin, Y.N.; Bernardo, N.; Mendes, T.S.G.; Souza Filho, C.R. The 2019 Brumadinho tailings dam collapse: Possible cause and impacts of the worst human and environmental disaster in Brazil. *Int. J. Appl. Earth Obs. Geoinf.* **2020**, *90*, 102119.

18. Beauchemin, S.; Langley, S.; MacKinnon, T. Geochemical properties of 40-year old forested pyrrhotite tailings and impact of organic acids on metal cycling. *Appl. Geochem.* **2019**, *110*, 104437. [CrossRef]

19. Chen, T.; Lei, C.; Yan, B.; Li, L.-l.; Xu, D.-m.; Ying, G.-G. Spatial distribution and environmental implications of heavy metals in typical lead (Pb)-zinc (Zn) mine tailings impoundments in Guangdong Province, South China. *Environ. Sci. Pollut. Res.* **2018**, *25*, 36702–36711. [CrossRef]

20. Ouyang, J.; Liu, Z.; Zhang, L.; Wang, Y.; Zhou, L. Analysis of influencing factors of heavy metals pollution in farmland-rice system around a uranium tailings dam. *Process Saf. Environ. Prot.* **2020**, *139*, 124–132. [CrossRef]

21. Dinis, M.d.L.; Fiúza, A.; Futuro, A.; Leite, A.; Martins, D.; Figueiredo, J.; Góis, J.; Vila, M.C. Characterization of a mine legacy site: An approach for environmental management and metals recovery. *Environ. Sci. Pollut. Res.* **2020**, *27*, 10103–10114. [CrossRef]

22. Hu, W.; Xin, C.; Li, Y.; Zheng, Y.; Van Asch, T.; McSaveney, M. Instrumented flume tests on the failure and fluidization of tailings dams induced by rainfall infiltration. *Eng. Geol.* **2021**, *294*, 106401. [CrossRef]

23. Mohamed, M.H.; Wilson, L.D.; Headley, J.V.; Peru, K.M. Novel materials for environmental remediation of tailing pond waters containing naphthenic acids. *Process Saf. Environ. Prot.* **2008**, *86*, 237–243. [CrossRef]

24. Vasile, A.; Milăşan, A.R.; Andrei, A.E.; Turcu, R.N.; Drăgoescu, M.F.; Axinte, S.; Mihaly, M. An integrated value chain to iron-containing mine tailings capitalization by a combined process of magnetic separation, microwave digestion and microemulsion–assisted extraction. *Process Saf. Environ. Prot.* **2021**, *154*, 118–130. [CrossRef]

25. Wang, G.; Tian, S.; Hu, B.; Xu, Z.; Chen, J.; Kong, X. Evolution pattern of tailings flow from dam failure and the buffering effect of debris blocking dams. *Water* **2019**, *11*, 2388. [CrossRef]

26. Wei, Z.-a.; Yang, Y.-h.; Zhao, H.-j.; Chen, Y.-l. Stability of tailings dam of Xiaodae tailings pond. *J. Northeast. Univ. (Nat. Sci.)* **2016**, *37*, 589.

27. Yu, G.; Song, C.; Pan, Y.; Li, L.; Li, R.; Lu, S. Review of new progress in tailing dam safety in foreign research and current state with development trent in China. *Chin. J. Rock Mech. Eng.* **2014**, *33*, 3238–3248.

28. Gao, H.-Y.; Xu, Z.-M.; Wang, K.; Ren, Z.; Yang, K.; Tang, Y.-J.; Tian, L.; Chen, J.-P. Evaluation of the impact of karst depression-type impoundments on the underlying karst water systems in the Gejiu mining district, southern Yunnan, China. *Bull. Eng. Geol. Environ.* **2019**, *78*, 4673–4688. [CrossRef]

29. Mackay, I.; Videla, A.; Brito-Parada, P. The link between particle size and froth stability-Implications for reprocessing of flotation tailings. *J. Clean. Prod.* **2020**, *242*, 118436. [CrossRef]

30. Martín-Moreno, C.; Martin Duque, J.F.; Nicolau Ibarra, J.M.; Muñoz-Martín, A.; Zapico, I. Waste dump erosional landform stability–a critical issue for mountain mining. *Earth Surf. Process. Landf.* **2018**, *43*, 1431–1450. [CrossRef]

31. Chen, X.; Jing, X.; Chen, Y.; Pan, C.; Wang, W. Tailings dam break: The influence of slurry with different concentrations downstream. *Front. Earth Sci.* **2021**, *9*, 726336. [CrossRef]

32. Hancock, G. A method for assessing the long-term integrity of tailings dams. *Sci. Total Environ.* **2021**, *779*, 146083. [CrossRef] [PubMed]

33. Wei, Z.; Yin, G.; Li, G.; Wang, J.-G.; Wan, L.; Shen, L. Reinforced terraced fields method for fine tailings disposal. *Miner. Eng.* **2009**, *22*, 1053–1059. [CrossRef]

34. Agapito, L.A.; Bareither, C.A. Application of a one-dimensional large-strain consolidation model to a full-scale tailings storage facility. *Miner. Eng.* **2018**, *119*, 38–48. [CrossRef]

35. Li, S.; Liang, H.; Li, H.; Ma, J.; Li, B. Minimum Void Ratio Model Established from Tailings and Determination of Optimal Void Ratio. *Geofluids* **2021**, *2021*, 8619121. [CrossRef]

36. Bi, Q.; Li, C.-h.; Chen, J.-x. Effect of fine particle content on mechanical properties of tailings under high confining pressure. *Arab. J. Geosci.* **2021**, *14*, 942. [CrossRef]

37. Chen, Q.; Zhang, C.; Yang, C.; Ma, C.; Pan, Z. Effect of fine-grained dipping interlayers on mechanical behavior of tailings using discrete element method. *Eng. Anal. Bound. Elem.* **2019**, *104*, 288–299. [CrossRef]

38. Li, W.; Coop, M. Mechanical behaviour of Panzhihua iron tailings. *Can. Geotech. J.* **2019**, *56*, 420–435. [CrossRef]

39. Li, Q.-m.; Yuan, H.-n.; Zhong, M.-h. Safety assessment of waste rock dump built on existing tailings ponds. *J. Cent. S. Univ.* **2015**, *22*, 2707–2718. [CrossRef]

40. Rico, M.; Benito, G.; Salgueiro, A.; Díez-Herrero, A.; Pereira, H. Reported tailings dam failures: A review of the European incidents in the worldwide context. *J. Hazard. Mater.* **2008**, *152*, 846–852. [CrossRef]

41. Wang, S.; Mei, G.; Xie, X.; Cui, Y. Analysis on Influence of Tailing Pond Construction on Stability of Surrounding Loose Waste Dump. In Proceedings of the IOP Conference Series: Earth and Environmental Science, Tianjin, China, 24–26 April 2020; p. 012104.

42. Zhang, C.; Chen, Q.; Pan, Z.; Ma, C. Mechanical behavior and particle breakage of tailings under high confining pressure. *Eng. Geol.* **2020**, *265*, 105419. [CrossRef]

43. Deng, Z.; Wu, S.; Fan, Z.; Yan, Z.; Wu, J. Research on the overtopping-induced breaching mechanism of tailings dam and its numerical simulation. *Adv. Civ. Eng.* **2019**, *2019*, 3264342. [CrossRef]

44. Gui, R.; He, G. The Effects of Internal Erosion on the Physical and Mechanical Properties of Tailings under Heavy Rainfall Infiltration. *Appl. Sci.* **2021**, *11*, 9496. [CrossRef]

45. Naeini, M.; Akhtarpour, A. Numerical analysis of seismic stability of a high centerline tailings dam. *Soil Dyn. Earthq. Eng.* **2018**, *107*, 179–194. [CrossRef]

46. Liu, Y.; Zhao, X.; Wu, S. Analysis of Static Liquefaction and Numerical Simulation for tailings pond under high depositing rates. *Chin. J. Rock Mech. Eng.* **2014**, *33*, 1158–1168.

47. Marsooli, R.; Wu, W. 3-D finite-volume model of dam-break flow over uneven beds based on VOF method. *Adv. Water Resour.* **2014**, *70*, 104–117. [CrossRef]

48. Mao, C. *Computational Analysis and Control of Seepage Flow*; China Water Conservancy and Hydropower Publishing House: Beijing, China, 2002.

49. Lu, R.-L.; Sun, D.-P.; Wei, W.; Zhou, J.-j. Numerical simulation of seepage field in the tailing dam with draining seepage system. In Proceedings of the 2013 Fourth International Conference on Digital Manufacturing & Automation, Shinan, China, 29–30 June 2013; pp. 858–861.

50. Junrui, C.; Yanqing, W. Research on multiple-level fracture network model for coupled seepage and stress fields in rock mass. *Chin. J. Rock Mech. Eng.* **2000**, *19*, 712–717.

51. Özer, A.T.; Bromwell, L.G. Stability assessment of an earth dam on silt/clay tailings foundation: A case study. *Eng. Geol.* **2012**, *151*, 89–99. [CrossRef]

52. Tang, G.-p.; Zhao, L.-h.; Li, L.; Yang, F. Stability charts of slopes under typical conditions developed by upper bound limit analysis. *Comput. Geotech.* **2015**, *65*, 233–240. [CrossRef]

Article

Quantification of Vegetation Phenological Disturbance Characteristics in Open-Pit Coal Mines of Arid and Semi-Arid Regions Using Harmonized Landsat 8 and Sentinel-2

Bing Wang [1,2], Peixian Li [1,2,*] and Xiaoya Zhu [1,2]

[1] Key Laboratory of Mine Ecological Effects and Systematic Restoration, Ministry of Natural Resources, Beijing 100081, China; wangbing@student.cumtb.edu.cn (B.W.); xyzhu@student.cumtb.edu.cn (X.Z.)
[2] College of Geoscience and Surveying Engineering, China University of Mining and Technology (Beijing), Beijing 100083, China
* Correspondence: lipx@cumtb.edu.cn

Abstract: Open-pit mining activities inevitably affect the surrounding ecological environment. Therefore, it is crucial to clarify the disturbance characteristics of open-pit mining activities on the surrounding vegetation and scientifically implement ecological restoration projects. This study investigates the impact of open-pit coal mining in arid and semi-arid regions on surrounding vegetation from a vegetation phenology perspective. Initially, we construct a high-frequency time series of vegetation indices by Harmonized Landsat 8 and Sentinel-2 surface reflectance dataset (HLS). These time series are then fitted using the Double Logistic and Asymmetric Gaussian methods. Subsequently, we quantify three pivotal phenological phases: Start of Season (SOS), End of Season (EOS), and Length of Season (LOS) from the fitted time series. Finally, utilizing mine boundaries as spatial units, we create a buffer zone of 100 m increments to statistically analyze changes in phenological phases. The results reveal an exponential variation in vegetation phenological metrics with increasing distance from the mining areas of Heidaigou-Haerwusu (HDG-HEWS), Mengxiang (MX), and Xingda (XD) in northwest China. Then, we propose a method to identify the disturbance range. HDG-HEWS, MX, and XD mining areas exhibit disturbance ranges of 1485.39 m, 1571.47 m, and 671.92 m for SOS, and 816.72 m, 824.73 m, and 468.92 m for EOS, respectively. Mineral dust is one of the primary factors for the difference in the disturbance range. The HDG-HEWS mining area exhibits the most significant disruption to vegetation phenological metrics, resulting in a delay of 6.4 ± 3.4 days in SOS, an advancement of 4.3 ± 3.9 days in the EOS, and a shortening of 6.7 ± 3.5 days in the LOS. Furthermore, the overlapping disturbance zones of the two mining areas exacerbate the impact on phenological metrics, with disturbance intensities for SOS, EOS, and LOS being 1.38, 1.20, and 1.33 times those caused by a single mining area. These research results are expected to provide a reference for the formulation of dust suppression measures and ecological restoration plans for open-pit mining areas.

Keywords: mining disturbance; vegetation phenology; cumulative effects; mine dust pollution

1. Introduction

Coal plays a crucial role in the economic and social development of nations [1]. In 2021, global coal consumption increased by 6.3% compared to the previous year, accounting for 26.9% of the primary energy consumption structure [2]. Driven by energy demands, China's coal production has maintained an upward trend in recent years. Although the intensive coal mining has met the needs of economic growth, it has also triggered a series of ecological and environmental issues, including land desertification, vegetation degradation, and environmental pollution [3,4]. Particularly in the arid and semi-arid regions of northwestern China, mining activities have caused detrimental effects on the local vegetation that relies on groundwater for survival due to groundwater depletion and the disruption of hydrogeological structures caused by mining [5], and the inherent

vulnerability of the geological environment makes the local ecosystem more sensitive to external disturbances [6]. Therefore, it is essential to clarify the impact of mining activities on the surrounding environment to carry out targeted ecological restoration and optimize landscape patterns. Remote sensing technology offers a practical solution for monitoring vegetation disturbance in mining areas. Yang et al. constructed multi-temporal mining disturbance templates using a long-term Landsat NDVI time series from 1984 to 2015 and identified disturbed pixels through the coefficient of variation and maximum value methods [7]. Yang et al. utilized the LandTrendr algorithm to monitor vegetation changes and historical dynamic characteristics around mining areas [8]. Although these analyses establish continuous vegetation monitoring information, the limited monitoring frequency hampers the representation of intra-annual vegetation dynamic disturbance effects under continuous mining influences. Some scholars have employed indicators such as fraction vegetation cover [9], remote sensing ecological index [10], and landscape ecological health index [11] to quantify the impact of mining activities on the ecological environment. However, these indicators can only depict the external characteristics of surface vegetation at a certain moment and do not reflect growth conditions of vegetation. Recent research suggests that vegetation phenology can serve as a quantifiable indicator of disturbances caused by mining activities in the surrounding environment [12,13], as vegetation phenological metrics can characterize the phased changes in vegetation growth stages. Notably, mining activities not only physically damage vegetation during excavation and transportation but can also cause vertical groundwater leakage, which may lead to vegetation degradation within and around the mining area, subsequently affecting vegetation phenology [14,15]. Hence, this study quantifies the range and intensity of mining disturbance through the response of vegetation phenology around the mining area.

Lieth defined phenology as the study of recurring life cycle stages of plants and animals [16]. Vegetation phenology refers to specific life cycle events of individual plants and serves as a sensitive indicator of terrestrial ecosystem responses to climate fluctuations and human activities [17,18]. Investigating vegetation phenology requires frequent monitoring of the vegetation growth status to accurately capture key stages of vegetation growth. The spatiotemporal development of land surface vegetation from a satellite sensor perspective is referred to as Land Surface Phenology (LSP) [19]. LSP metrics utilize spectral information from remote sensing imagery to explain intra- and inter-annual variations in vegetation, including the onset, end, peak, and duration of the growing season. The datasets produced by Advanced Very High Resolution Radiometer (AVHRR) and Moderate-resolution Imaging Spectroradiometer (MODIS) are suitable for large-scale and single landscape LSP monitoring, but their coarse spatial resolution limits the study of heterogeneous landscape LSP [20,21]. Landsat 8 imagery with 30 m spatial resolution can satisfy small-scale vegetation change monitoring, yet its 16-day temporal resolution constrains the detection of rapidly changing vegetation phenological events. Since 2017, the Sentinel satellite constellation has provided optical imagery with a revisit cycle of 5 days and spatial resolutions ranging from 10 to 60 m, improving the quality of LSP observations. Nonetheless, frequent cloud cover remains a challenge for optical imagery-based vegetation phenology detection [22]. In recent years, NASA's Harmonized Landsat 8 and Sentinel-2 (HLS) project has supplied near-daily surface reflectance products globally [23], showing significant potential for LSP monitoring. Notably, Minkyu Moon et al. performed a comparative assessment of vegetation index time series derived from HLS dataset, daily 3 m spatial resolution commercial PlanetScope imagery, and PhenoCam imagery, which demonstrated a remarkable consistency [24]. Thus, in this study, the HLS dataset was employed to construct a 2022 vegetation index time series for the mining areas.

Mining activities cause spatiotemporal differences in the surrounding vegetation condition and accumulate effects over time, consequently exacerbating the impact on natural ecosystems and biodiversity [25]. Some scholars utilize NDVI or remote sensing ecological indices to quantify the long-term cumulative ecological effects of specific mining areas, finding that the cumulative ecosystem service value decreases to varying intensities around

the mining area as mining activities continue [26,27]. At present, research on the cumulative disturbance effects between mining areas is relatively scarce. Our study involves a quantitative analysis of the phenological response intensity of neighboring mining areas, which will facilitate a more targeted delineation of ecological management zones.

The dynamic and externality of mining activities result in continuous disturbances with vegetation growth within a certain range. Particularly in ecologically vulnerable arid and semi-arid regions of Northwestern China, it is imperative to elucidate the environmental quality and spatial patterns around mining areas to provide theoretical guidance for ecological restoration schemes. Therefore, this study focuses on how to quantify the disturbance characteristics of surface coal mining through vegetation phenology. The primary objectives encompass three aspects: (1) to reveal the distance and intensity of the disturbance to the surrounding vegetation phenology by mining activities; (2) to explore the cumulative effect of disturbances between mining areas; and (3) to analyze the quantitative effects of mining dust on vegetation phenology.

2. Study Area and Materials

2.1. Study Area

We selected four clustered mining areas in the eastern part of Zhungeer City, Inner Mongolia Autonomous Region, China, as the study area (Figure 1a,b), with geographical coordinates ranging from 111°12′ to 111°24′E and 39°41′ to 39°49′N. Located in the northern portion of the Ordos Loess Plateau, this region features a characteristic eroded hilly topography and is part of the Yellow River basin, constituting a primary tributary of the Yellow River [28]. The study area is situated within the semi-arid continental monsoon climate zone falling within the middle temperate zone. It undergoes dry and blustery springs, short yet intense hot summers, gentle and enjoyable autumns, and cold and generally snowless winters. Based on their spatial characteristics, the four mining areas are categorized into three study units: Heidaigou-Haerwusu, Mengxiang, and Xingda open-pit mining areas (Figure 1c). The study area is endowed with abundant mineral resources, as indicated by the annual production capacities of 6.9, 1.8, and 1.2 million tons, respectively, based on the national energy statistics by the end of 2019.

The process of open-pit mining involves the extensive removal of rock and soil layers, leading to the disruption of the natural landscape pattern (Figure 1d,e) and posing a significant threat to the ecological environment in the vicinity of the mining area [29]. The vegetation in this region is predominantly composed of natural grasslands, and the climatic conditions and geological features are generally uniform across the mining areas. Therefore, the study area is suitable for investigating the quantitative impact of open-pit mining activities on the phenology of surrounding vegetation.

2.2. Data Acquisition and Preprocessing

The temporal variation in the Normalized Vegetation Index (NDVI) is closely related to the vegetation growth condition, and thus, it is widely used for phenological characterization [30,31]. The NDVI is calculated by spectrally computing data from the red band, sensitive to chlorophyll content, and the near-infrared band, responsive to variations in the internal leaf structure. The high-frequency NDVI time series in this study was computed using the HLS v1.5 dataset, sourced from the Landsat 8 Operational Land Imager (OLI) and Sentinel 2 Multi Spectral Instrument (MSI) sensors. NASA performed a series of processing steps on this dataset including atmospheric correction, spatial registration, BRDF correction, bandpass adjustment, and resampling, resulting in uniform projection onto the Military Grid Reference System [32]. Initially, we utilized a Python web crawler to acquire the HLS dataset for MGWR tiles 49TDE, 49TEE, 49SDD, and 49SED [33]. Subsequently, these tiles underwent preprocessing involving mosaicking and cropping. Furthermore, the quality information band FMASK, generated using the Fmask 4.2 algorithm, is employed to delete pixels affected by cloud cover, snow, and cloud shadows. Ultimately, this process yielded a total of 189 NDVI images covering the study area, including 46 Landsat 8 NDVI images

and 143 Sentinel-2 NDVI images (Figure 2). For duplicate dates, Landsat 8 and Sentinel-2 images were mosaic using the maximum value to obtain the corresponding daily image.
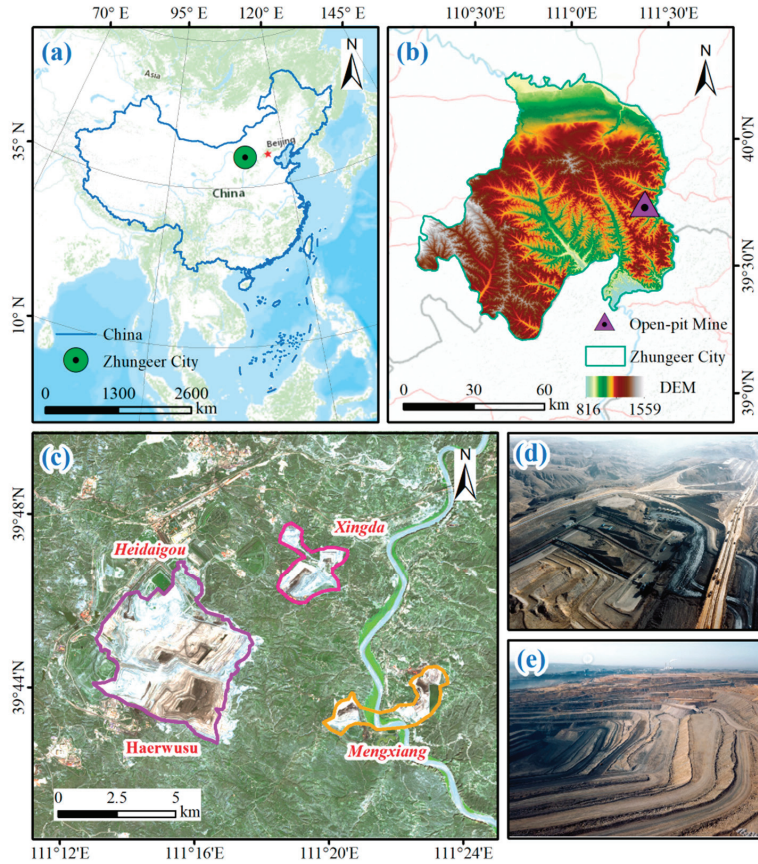
Figure 1. Geographic location of the study area. (**a**) Zhungeer City in China; (**b**) Shendong open-pit mines location; (**c**) image of the open-pit mines in 2022; (**d**,**e**) unmanned aerial vehicle photos of the Heidaigou mining area.
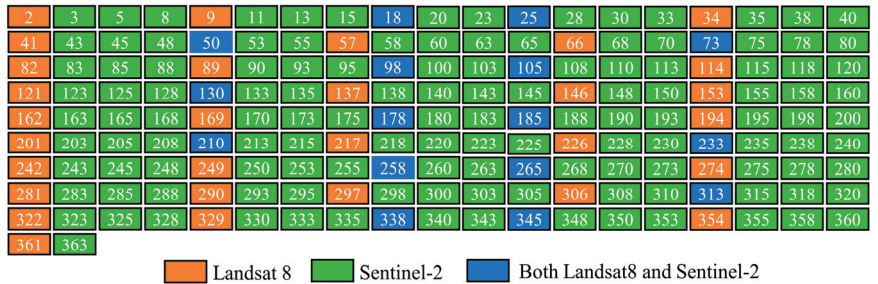
Figure 2. Date distribution of NDVI images in the study area.

This study focuses on the extent of ecological disruption caused by mining disturbances in the surrounding environment. The phenological changes of farmland vegetation are more sensitive to seasonal drought than grassland and forest land [34]. However, the agricultural growth processes are influenced by human activities, while there are significant

differences in the forest and grassland phenological phases [35]. Therefore, we used the global 10 m land use type data (https://livingatlas.arcgis.com/ (accessed on 10 March 2023)) to mask agricultural and forested areas. Through visual interpretation and validation on Google Earth, we rectified classification errors and formed a high-quality thematic map of grassland patches in the study area. In addition, the high-quality 1 km monthly PM2.5 and PM10 dataset for China (https://data.tpdc.ac.cn/ (accessed on 25 April 2023)) and the 1 km monthly precipitation dataset for China (https://data.tpdc.ac.cn/ (accessed on 25 April 2023)) were used to investigate the driving mechanisms of vegetation phenology in areas disturbed by dust and precipitation. To address data scale discrepancies between the mineral dust and phenological metrics, the data resolution of PM2.5 and PM10 were downscaled to 30 m using the bilinear interpolation method.

3. Methodology

The overall process of this study is shown in Figure 3, which is divided into three parts: constructing an NDVI spatiotemporal cube, developing a disturbance identification model for mining areas, and analyzing the cumulative effects of open-pit mining and the impact of mineral dust on vegetation phenological metrics. (1) The grassland NDVI spatiotemporal cube was initially constructed from the HLS dataset, subsequently polluted pixels were removed using the "Fmask" quality band, and pixels of grassland were extracted using the land use type. (2) The pixel-wise NDVI time series were fitted through the utilization of the Double Logistic and Asymmetric Gaussian algorithm, followed by the extraction of vegetation phenology metrics using the dynamic threshold method, then we developed a disturbance identification model for open-pit mining by counting the changes in phenological metrics in the gradual buffer zone. (3) Identify the disturbance ranges of all mining areas and create a rectangular array of mining areas for two mining areas with overlapping disturbance ranges to quantitatively analyze the change characteristics of phenological metrics. A correlation analysis was performed between the pixels within the superimposed disturbance range and the mine dust data (PM2.5, PM10).

3.1. Data Smoothing

A time series curve of the vegetation index calculated from remote sensing image bands is not always a regular curve, and the mining activities in the study area continuously affect the surrounding vegetation, resulting in a fluctuation in the vegetation index value within a certain range. The time series fitting methods enable a more objective approximation of the dynamic growth trajectory of vegetation, effectively reducing the impact of data noise [36]. Double Logistic (DL) and Asymmetric Gaussian (AG) are widely used in the reconstruction of vegetation index time series for several scenarios [37]. In this study, these two filtering algorithms with superior performance are utilized to reconstruct the NDVI time series of the study area's 2022 HLS dataset. Furthermore, both methods are employed to perform the consistency tests of subsequent phenological metrics calculation and disturbance range identification.

3.1.1. Double Logistic

Beck et al. developed the DL algorithm based on approximating the Sigmoid function to the cumulative distribution function and the accumulation characteristics of vegetation green coverage over time [38]. Specifically, a positive sigmoid logistic function is employed to fit the phases of vegetation growth and greening, while a negative sigmoid logistic function is used to fit the phases of vegetation senescence and leaf fall. The general expression of the DL is

$$f_{dl}(t) = v1 + v2 \times \frac{1}{1 + \exp\left[\frac{m1-t}{m2}\right]} - \frac{1}{1 + \exp\left[\frac{m3-t}{m4}\right]} \tag{1}$$

where $f_{dl}(t)$ represents the smoothed NDVI value at time t. The linear parameters $v1$ and $v2$ correspond to the background value and amplitude of NDVI over the entire year. The nonlinear parameters $m1$ and $m2$ represent the phase and slope of the vegetation greening period, respectively, while $m3$ and $m4$ represent the phase and slope of the vegetation senescence period, respectively.
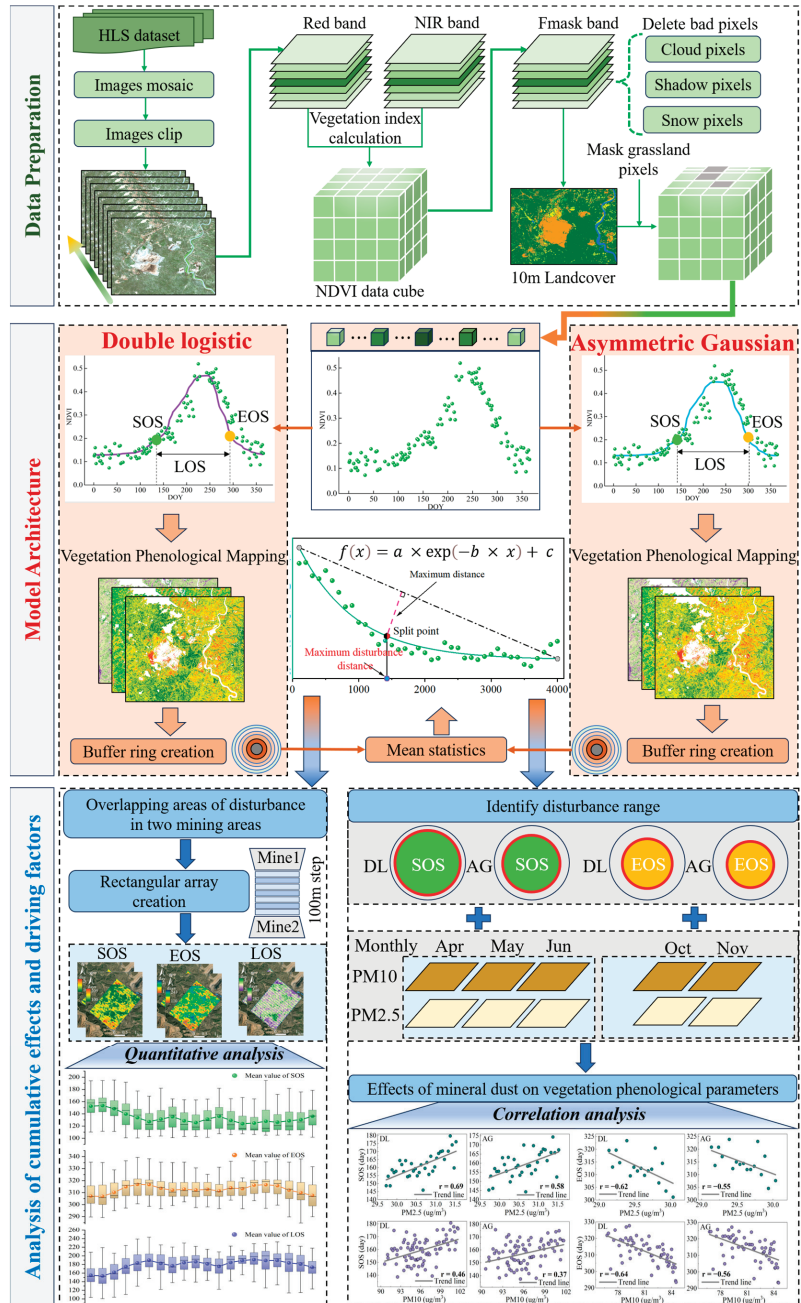

Figure 3. Overview of methodology.

3.1.2. Asymmetric Gaussian

The AG function is divided according to the maximum (minimum) value of the fitted time series, the local functions are, respectively, fitted by exponential functions, then the NDVI time series is reconstructed by smooth connection [39]. The general expression for AG function is

$$
f_{ag}(t) = \begin{cases} v1 + v2 \times \exp\left[-\left(\frac{t-m1}{m2}\right)^{m3}\right], & t > m1 \\ v3 + v4 \times \exp\left[-\left(\frac{m1-t}{m4}\right)^{m5}\right], & t < m1 \end{cases} \tag{2}
$$

where $f_{ag}(t)$ represents the smoothed NDVI value at time t. The intervals $(v1, v2)$ and $(v3, v4)$ are the minimum and the magnitude of change for $f_{ag}(t)$ within their respective segments. $m1$ signifies the independent time corresponding to the maximum or minimum in the time series, while $m2$ and $m4$, respectively, denote the width and flatness of the right and left parts of the function. The linear parameters are denoted as $(v1, v2, v3, v4)$ and the nonlinear parameters as $(m1, m2, m3, m4, m5)$.

To ensure consistency between the fitted function and actual observed NDVI, it is necessary to constrain the nonlinear parameters of the aforementioned model within a defined range. The linear parameters in the model are determined via the least squares method, while the nonlinear parameters are computed using the Levenberg–Marquardt method. The DL and AG fitting methods are implemented in Python language.

3.2. Extraction of Vegetation Phenological Metrics

Vegetation phenological metrics extraction methods include the maximum derivative method, threshold extraction, and change detection, among others. The study area is situated in a typical arid and semi-arid region with sparse vegetation, and the extent of the mining activity's impact on surrounding vegetation NDVI remains uncertain. Thus, the simple and effective dynamic threshold extraction method was chosen to calculate the phenological metrics of each pixel. We mainly focus on three phenological metrics, namely start of the growing season (SOS), end of the growing season (EOS), and length of growing season (LOS).

The SOS, EOS, and LOS were calculated using the following formula:

$$
\text{SOS} = f^{-1}\left\{\text{threshold} \times \left[\max f(t) - \min f_{left}(t)\right] + \min f_{left}(t)\right\} \tag{3}
$$

$$
\text{EOS} = f^{-1}\left\{\text{threshold} \times \left[\max f(t) - \min f_{right}(t)\right] + \min f_{right}(t)\right\} \tag{4}
$$

$$
\text{LOS} = \text{EOS} - \text{SOS} \tag{5}
$$

where the critical threshold is set to 0.2 based on previous research [40,41], $f^{-1}(*)$ is the corresponding time when the NDVI value is $*$, $f(t)$ signifies the NDVI value at time t as determined by the DL or AG, $f_{left}(t)$ denotes the fitting sequence of the left part, and $f_{right}(t)$ indicates the fitting sequence of the right part.
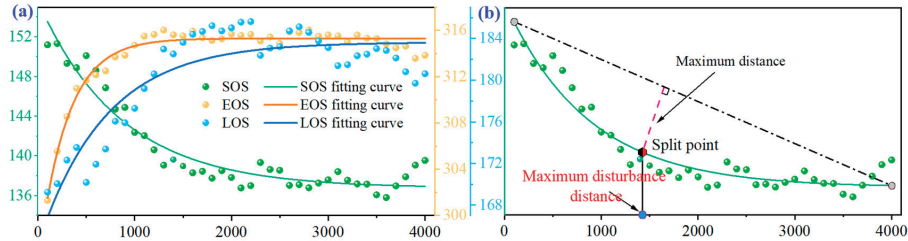
3.3. Identification Method of Disturbance Range in a Single Mining Area

According to the first law of geography, as objects get closer, their correlation increases. Hence, we first quantified the disturbance characteristics of the surrounding vegetation by open-pit mining through a buffer zone analysis, then explored the disturbance rules of distance and vegetation phenology metrics, and finally determined the disturbance distance. Specifically, 40 buffer rings with a step length of 100 m were created within 4 km of the mining area boundary in 2022, and the average vegetation phenology in each buffer ring was counted. We found that the mean value of SOS for three mining areas exhibit exponential decrease with increasing distance from the mining zones, while EOS

and LOS exhibit exponential growth trends (Figure 4a), consistent with the findings by SUN et al. [12]. The general equation for the vegetation phenology fitting function is as follows:

$$f(x) = a \times \exp(-b \times x) + c \qquad (6)$$

where x represents the distance from the mining area. a signifies the maximum divergence within the buffer ring mean sequence (SOS: $a > 0$; EOS and LOS: $a < 0$), and b denotes the rate of variation within the phenological mean sequence. c denotes the horizontal asymptotic of the exponential function value.

Figure 4. Schematic diagram of disturbance range identification. (**a**) Variation characteristics of phenological metrics with distance from mining area; (**b**) Identification of maximum disturbance range in a single mining area.

Furthermore, various human activities within the 4 km buffer zone also exert a certain degree of influence on vegetation phenology, which leads to oscillatory characteristics in the mean sequence of the buffer ring. Leveraging the principles akin to the Douglas–Peuker algorithm, we first construct a line segment that connects the endpoints of the fitted exponential function. Subsequently, we identify the point along this fitted curve that corresponds to the maximum distance to the aforementioned line segment. This point denotes which is the disturbance segmentation point, and its corresponding abscissa represents the maximum disturbance range of a single mining area (Figure 4b). This method overcomes the drawback of not being able to determine the maximum disturbance point caused by the absence of inflection points in exponential functions. Different vegetation index time series models result in differences in fitting sequences. In order to balance the model differences, the ultimate disturbance range for phenological metrics is determined by calculating the average of the disturbance points using both the DL and AG methods.

4. Results

4.1. Cross Validation of Phenological Metrics Extraction Results

Figure 5 illustrates the high similarity in the extracted vegetation phenological parameters of the study area using both DL and AG, and the similarity of SOS is significantly higher than that of EOS and LOS. To be specific, the R^2 for SOS, EOS, and LOS are 0.92, 0.75, and 0.86, respectively, with corresponding RMSE values of 5.81, 5.53, and 9.68, respectively. This further emphasizes the consistency of the results obtained via the DL and AG algorithms' extraction. The DL and AG algorithms exhibit inherent differences in constructing NDVI time series leading to variations in the phenological metric results, but our study focused more on the consistency of the phenology metric variations. The phenological metric histograms generated by both methods demonstrate highly similar trends, making them suitable for studying vegetation phenological disturbance characteristics in the vicinity of mining areas.
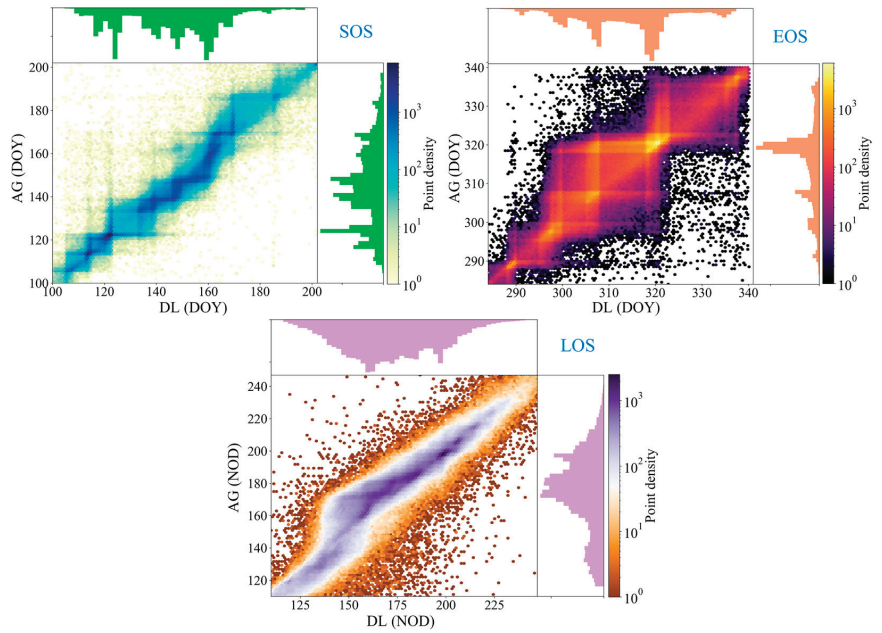
Figure 5. Comparison of phenological metric extraction results using DL and AG. Note: DOY: date of year; NOD: number of days.

4.2. Phenological Metrics Mapping

The spatial distribution of the three phenological metrics in the study area differs to varying intensities (Figure 6). Phenological metrics were characterized by a gradual lagging of the SOS, advancing of the EOS, and shortening of the LOS from west to east. The spatial mapping of phenological metrics using both the DL and AG fitting methods exhibits a high degree of consistency. The phenological metrics within a certain range of the three open-pit mining areas display similar spatial patterns. Subsequently, the means of the phenological metrics were computed for the entire region and within a 1000 m distance from the mining boundaries (Table 1). The results from both DL and AG fitting methods consistently revealed a delayed SOS and shortened LOS, while EOS showed no significant variation. The mean values of SOS within a 1000 m radius from the mining boundaries for the HDG-HEWS, MX, and XD mining areas lagged behind the entire region by 7.1, 10.5, and 1.0 days, respectively.

Table 1. Means of phenological metrics within 1 km of open-pit mines and the entire area.

| | SOS (Days) | | EOS (Days) | | LOS (Days) | |
	DL	AG	DL	AG	DL	AG
Entire region	145.0	143.9	313.3	315.4	170.6	174.2
HDG-HEWS	152.1	151.3	313.9	316.3	166.2	169.9
MX	155.5	154.8	314.3	314.8	163.1	166.8
XD	146.0	145.4	311.9	314.3	167.9	171.0
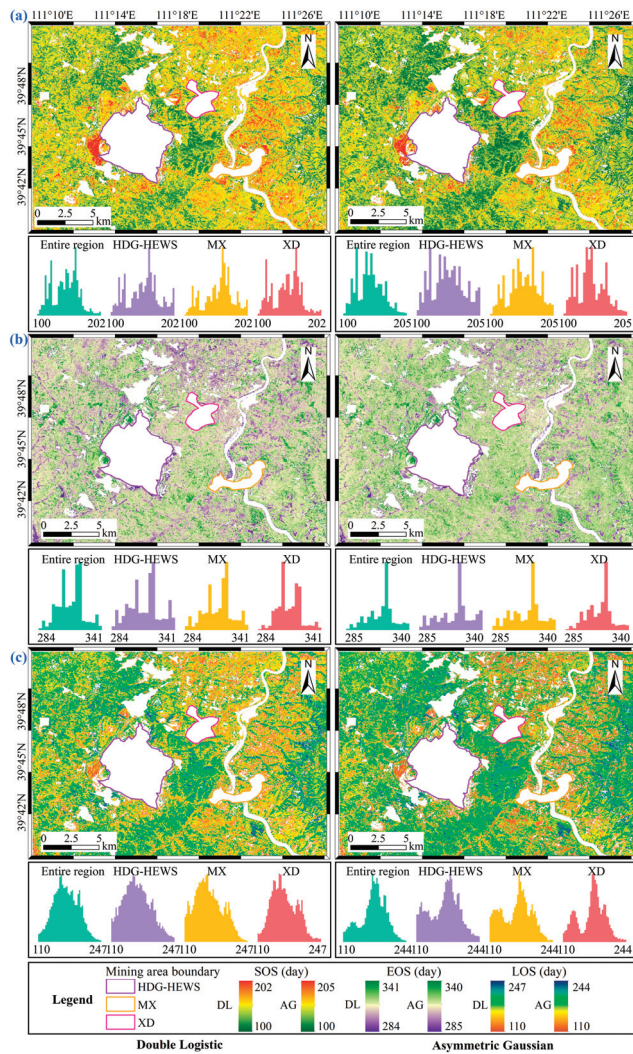
Figure 6. Spatial distribution of phenological metrics. (**a**) SOS; (**b**) EOS; (**c**) LOS.

4.3. Disturbance Distance and Intensity of Vegetation Phenology from Open-Pit Mining Activities

The mean sequences of phenological metrics in the 100 m buffer ring were fitted by exponential functions (Figure 7), which showed highly similar variation characteristics on both the DL and AG methods. Open-pit mining activities disrupt the surrounding vegetation growth to varying degrees. According to the proposed disturbance identification method, the disturbance range was extracted (Table 2). Disturbance ranges of the SOS and LOS in the three open-pit mining areas were greater than the EOS, and the disturbance range showed MX > HDG-HEWS > XD. The maximum disturbance distance of the LOS to the surrounding vegetation in the MX mining area was 1625.53 m, which shortened the vegetation phenological growth cycle by 3.1 ± 2.2 days. Although the disturbance distance was not the farthest, the degree of disturbance to the surrounding vegetation by HDG-HEWS was significantly higher than that of the other mining areas. Overall, the mean SOS of the HDG-HEWS mining area lagged by 2.8 and 4.4 days, respectively, the mean

EOS was advanced by 2.5 and 3.1 days, and the average LOS was shortened by 3.6 and 4.2 days compared to the MX and XD mining areas.
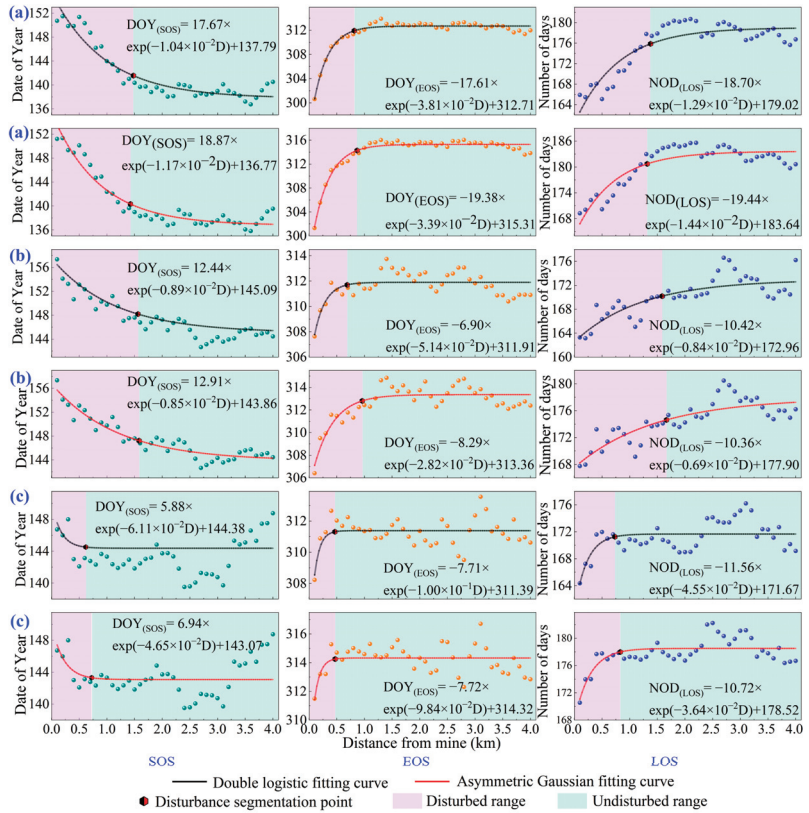
Figure 7. Changes in phenological metrics within the disturbance range of the mining area. (**a**) HDG-HEWS mining area; (**b**) MX mining area; (**c**) XD mining area.

Table 2. Disturbance range and degree of mining area from different phenological metrics.

Mining Area	HDG-HEWS		MX		XD	
	Smax (m)	Δt (Days)	Smax (m)	Δt (Days)	Smax (m)	Δt (Days)
SOS	1485.39	6.4 ± 3.4	1571.47	3.6 ± 2.7	671.92	2.0 ± 1.4
EOS	816.72	4.3 ± 3.9	824.73	1.8 ± 1.6	468.92	1.2 ± 1.0
LOS	1377.28	6.7 ± 3.5	1625.53	3.1 ± 2.2	781.23	2.5 ± 2.6

Smax: Maximum disturbance distance. Δt: Time difference of phenological metrics within the disturbance range.

Furthermore, we observed a significant exponential relationship in the calculated mean disturbance range for the HDG-HEWS mining area, whereas the exponential characteristics in the XD mining area were not pronounced (Figure 7). Beyond the 1800 m buffer zone of the XD mining area, the fluctuations in the disturbance characteristics of the mean value of the regional phenological metrics indicate influences on its vegetation phenology from external conditions in addition to the mining area itself. Hence, apart from focusing on the identification of disturbance ranges for single open-pit mining, this study also gives special attention to whether the overlapping regions of disturbance ranges accumulate effects on vegetation phenology.

4.4. Cumulative Effect of Mining Disturbance

Several 100 m step rectangular arrays were created in the direction from the HDG-HEWS to the XD mining area. The spatial distribution of vegetation phenological metrics on the rectangular arrays reveals (Figure 8) varying degrees of exacerbation in the SOS lag, EOS advancement, and LOS shortening in the central region. The histogram distribution of phenological metrics was calculated for each rectangular array, and the results indicated that the disturbance characteristics of phenological metrics were more significant in the rectangular array area from 700 m to 1300 m. The cumulative disturbance effects of the SOS and LOS were greater than that of the EOS. Specifically, the cumulative effects of the disturbance resulted in the overlapping areas of the SOS lagging by 6.3 ± 5.9 days, the EOS advancing by 1.2 ± 1.0 days, and the LOS shortening by 6.8 ± 4.8 days. The disturbance degrees for the SOS, EOS, and LOS were 1.38, 1.20, and 1.33 times the degree of disturbance in a single mining area, respectively.
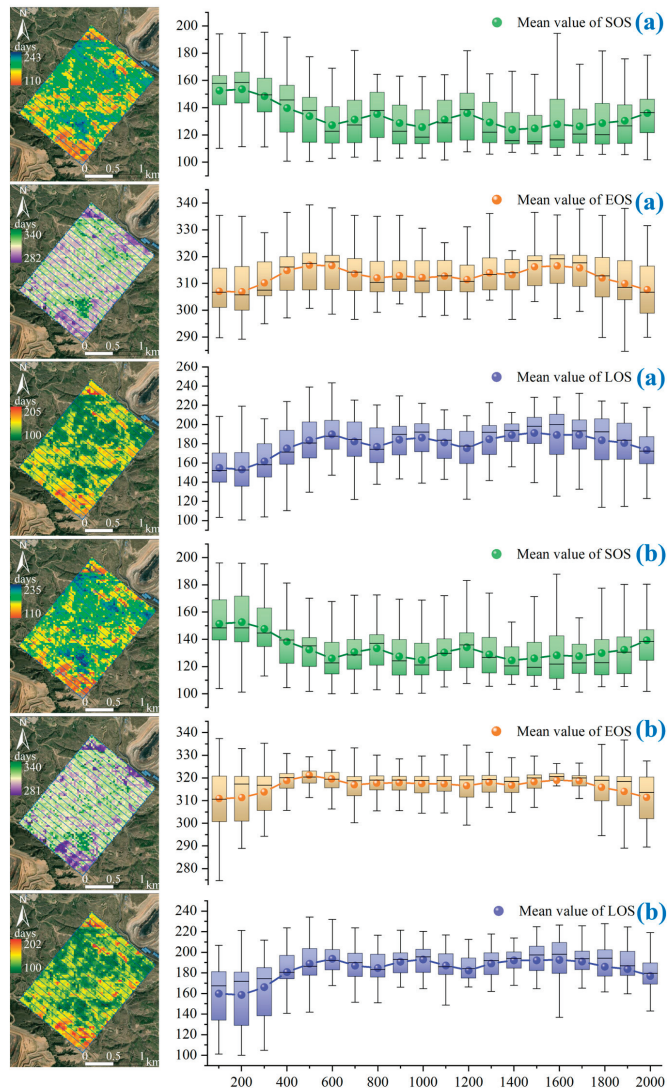
Figure 8. Changes in vegetation phenology in disturbed overlapping areas. (**a**) DL; (**b**) AG.

5. Discussion

5.1. Effects of Mineral Dust on Vegetation Phenology

A substantial volume of dust was generated in the open-pit mining area during the blasting of the rock mass, stripping of the rock and soil, and transportation. Affected by the wind flow, the dust particles will cover the vegetation, causing a rise in leaf temperature and consequent dehydration, which hinders the photosynthetic activity of plants [42]. The dust in open-pit mines is small particle dust, including PM10 and PM2.5 with aerodynamic diameters less than 10 μm and 2.5 μm [43]. According to the Ambient Air Quality Standards (GB 3095-2012), the annual average concentration limits for PM2.5 and PM10 are 35 μg/m^3 and 70 μg/m^3, respectively. Within the vegetation disturbance range of the study area, PM2.5 remains below the critical concentration (29.1~31.8 μg/m^3), while PM10 is significantly higher than the critical concentration. The disturbed pixel concentration for PM10 exceeds the critical concentration by 20~32 μg/m^3. PM10 is the primary air quality pollutant in this region [44]. Therefore, monthly cumulative dust data and vegetation phenological metrics were utilized for the pixel-level response analysis. The PM2.5 and PM10 data were divided into equal concentration gradients, and the mean phenological metrics for each gradient were calculated for the subsequent Pearson correlation analysis. Correlation analysis between the monthly PM2.5 and PM10 data of open-pit coal mining during April–June and October–November and the vegetation phenology within the disturbance range (Figure 9) reveals that as the concentration of PM2.5 and PM10 levels rise, the SOS date gradually lags behind, and the EOS date gradually advances. Additionally, there is a strong negative correlation between the EOS and the concentrations of both PM2.5 and PM10. However, the correlation between the SOS and PM10 concentration is not significant, which may be caused by rainfall. The study area has ample rainfall during the spring and summer, with average precipitation ranging from 57.6 to 63.1 mm between April and June, whereas from 11.8 to 15.6 mm between October and November. Rainfall can to some extent mitigate larger particulate matter like PM10, but it faces difficulty in mitigating PM2.5 [45]. Drought is considered a key factor in controlling the SOS and EOS in arid and semi-arid regions, and arid soil conditions make the phenological growth period of grassland vegetation more sensitive to precipitation [46,47]. In winter, continuous drought and a lack of rainfall in the study area hinder the implementation of dust inhibitors, leading to a prolonged dust pollution duration and accumulation of PM10 on the surface of vegetation leaves. As a result, this postpones the onset of the SOS for the vegetation.

5.2. Analysis of Key Factors within the Mining Disturbance Area

The production capacities of the three open-pit mines of HDG-HEWS (69 million tons/year), MX (1.8 million tons/year), and XD (1.2 million tons/year) are directly proportional to their impact on vegetation phenological metrics. The greater the mining intensity, the more significant the threat to the surrounding vegetation. However, even though HDG-HEWS has a significantly higher production capacity than the other mining areas, the disturbance ranges on phenological metrics were not consistently the largest. Previous research supports this conclusion. Sun et al. analyzed the disturbance range of mining areas at different latitudes, indicating a weak correlation between the open-pit coal mining intensity and disturbance range, and topography and climate factors also affect the disturbance range to some extent [12]. Since 2011, the HDG-HEWS open-pit mining area has prioritized ecological construction, afforestation, and road dust suppression projects. These measures have improved the ecological environment of the abandoned dump site, slowed down the diffusion and accumulation of dust to the surrounding environment, and shortened the mining disturbance distance. The MX and XD mining areas began production in 2017 and 2022, respectively, the production scales are smaller than that of the HDG-HEWS mining area, and only ecological restoration projects have been carried out for some waste dump sites. Hence, there should be targeted implementation of necessary dust control measures and ecological restoration projects to reduce the disturbance range to vegetation caused by open-pit mining. Especially, the MX mining area's disturbance

zone encompasses villages and cultivated land. We suggest prioritizing dust monitoring and prevention, enabling concurrent mining production and ecological restoration for harmonious regional green development.
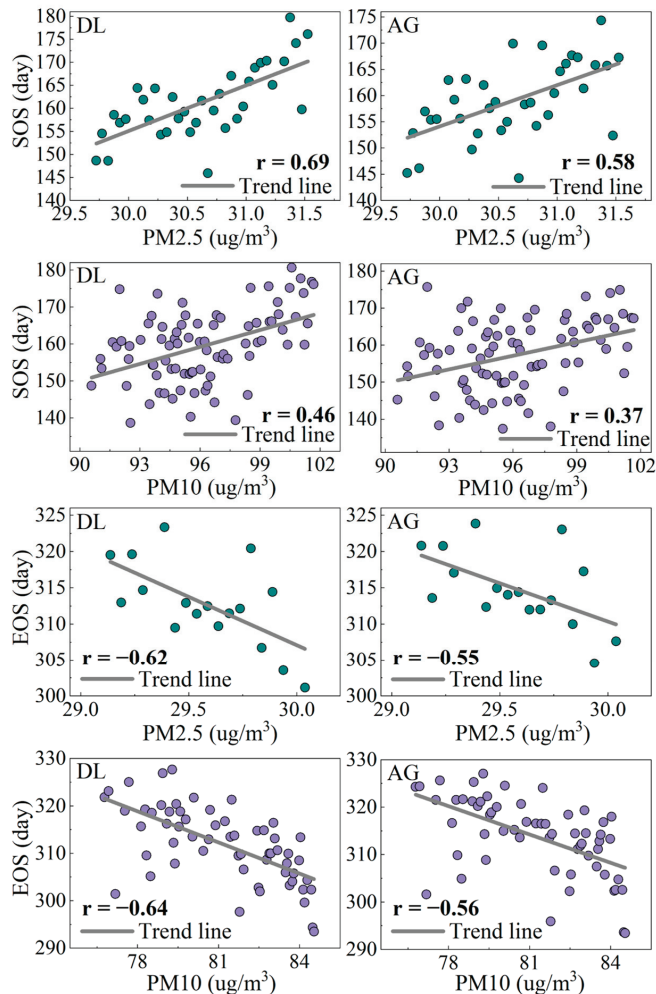
Figure 9. Correlation analysis of phenological metrics between mineral dust and vegetation.

5.3. Advantages of the HLS Dataset in Studying Vegetation Phenology in Mining Areas

Extracting vegetation phenology by integrating multi-source remote sensing data is a highly effective approach, especially for LSP derivation of seasonal vegetation with a small greenness amplitude in arid and semi-arid regions [26,48]. Despite existing studies showing that image super-resolution using deep learning can provide high spatiotemporal resolution data, the current fusion cost is expensive, and the accuracy of fusion results still needs to be measured [49]. Therefore, NASA's harmonized Landsat 8 and Sentinel-2 dataset is considered the preferred choice for extracting LSP. This study successfully utilized the HLS dataset to capture grassland LSP in arid and semi-arid regions, confirming the dataset's applicability in mining-scale scenarios. The reliability of LSP derivation depends on the vegetation index time series [50]. To build a high-frequency NDVI time series, Sun et al. used three years of Sentinel-2 MSI data [12], which makes it difficult to adapt to phenological extraction in mining scenarios and apply the results to ecological restoration

planning for the subsequent year. Due to the dynamic nature of mining activities and variations in annual climate conditions, NDVI differences on the same day may occur, potentially causing deviations in Sun et al.'s phenological metric extraction results compared to the actual phenological phases. Therefore, we believe that the HLS dataset can be effectively applied to LSP extraction in small-scale scenarios in arid and semi-arid regions.

5.4. Limitations and Future Work

Based on the perspective of phenology, this study scientifically analyzed the disturbance range and threat degree of open-pit mining in arid and semi-arid areas to the surrounding vegetation. The limitations of this study mainly exist in the following aspects: The research object is the global buffer zone of the mining area; the landscape pattern of open-pit mining varies in different directions. Future research should concentrate on understanding the cumulative disturbance effects and characteristics of the mining area under different scenarios. Secondly, the study unit was grassland phenology in a broad sense; however, the phenological responses of different grassland vegetation types to mining area disturbances might not be consistent. In the future, integrating unmanned aerial vehicle imagery and on-site investigations will be essential to acquire more refined grassland classification products. Furthermore, the research method we proposed is suitable for identifying the disturbance range of a single open-pit mining area, but when disturbed by other human projects (e.g., a city and another mine), the vegetation phenology metrics are superimposed and disturbed, which makes the modeling sequence oscillate, resulting in an underestimated determination of the distance of disturbance. Establishing a mining disturbance range identification model in complex scenarios is the focus of future research.

6. Conclusions

This study focuses on the disturbance characteristics of the surrounding vegetation caused by open-pit coal mining in arid and semi-arid areas from the perspective of vegetation phenology. We observed that open-pit mining leads to delayed greening, advanced senescence, and shortened vegetation growth cycles. As the distance from the mining area increases, phenological metrics exhibit exponential changes. This paper proposes a simple and effective method to identify the disturbance range of a single open-pit coal mine mining. Open-pit mining activities have significant differences for the disturbance range of vegetation growth at different stages, and the disturbance range of the vegetation senescence phase is smaller than other phenological metrics. The maximum disturbance distances of vegetation phenological metrics caused by HDG-HEWS, MX, and XD open-pit mining are 1485.39 m, 1625.53 m, and 781.23 m, respectively. Accumulated deposition of PM10 and PM2.5 from mine dust affects vegetation photosynthesis and threatens normal vegetation growth. With the expansion of the mining area production scale and intensity, the disturbance range of vegetation phenology does not show a significant alteration, but the degree of disruption is intensified. Notably, the overlapping disturbance zones of adjacent mining areas will also increase the disturbance degree of vegetation phenology, with disturbance degrees for the SOS, EOS, and LOS being 1.38, 1.20, and 1.33 times that of a single mining area. In conclusion, our research findings can serve as a pertinent reference for coal mining enterprises to implement targeted ecological restoration plans, while also offering novel insights into identifying the range and degree of disturbance to the surrounding vegetation caused by open-pit mining activities.

Author Contributions: B.W. proposed the research methodology, designed and performed the experiments, and wrote the manuscript. P.L. helped in manuscript review, editing and acquired the funding. X.Z. made great contributions to the methodology and analysis. All authors have read and agreed to the published version of the manuscript.

References

1. Jie, D.; Xu, X.; Guo, F. The Future of Coal Supply in China Based on Non-Fossil Energy Development and Carbon Price Strategies. *Energy* **2021**, *220*, 119644. [CrossRef]
2. Statistical Review of World Energy 2022. Available online: https://www.bp.com/en/global/corporate/energy-economics/statistical-review-of-world-energy.html (accessed on 16 April 2023).
3. Guan, Y.; Wang, J.; Zhou, W.; Bai, Z.; Cao, Y. Identification of Land Reclamation Stages Based on Succession Characteristics of Rehabilitated Vegetation in the Pingshuo Opencast Coal Mine. *J. Environ. Manag.* **2022**, *305*, 114352. [CrossRef] [PubMed]
4. Odell, S.D.; Bebbington, A.; Frey, K.E. Mining and Climate Change: A Review and Framework for Analysis. *Extr. Ind. Soc.* **2018**, *5*, 201–214. [CrossRef]
5. Shen, Z.; Zhang, Q.; Chen, D.; Singh, V.P. Varying Effects of Mining Development on Ecological Conditions and Groundwater Storage in Dry Region in Inner Mongolia of China. *J. Hydrol.* **2021**, *597*, 125759. [CrossRef]
6. Li, P.; Wang, B.; Chen, P.; Zhang, Y.; Zhao, S. Vulnerability Assessment of the Eco-Geo-Environment of Mining Cities in Arid and Semi-Arid Areas: A Case Study from Zhungeer, China. *Ecol. Indic.* **2023**, *152*, 110364. [CrossRef]
7. Yang, Z.; Li, J.; Zipper, C.E.; Shen, Y.; Miao, H.; Donovan, P.F. Identification of the Disturbance and Trajectory Types in Mining Areas Using Multitemporal Remote Sensing Images. *Sci. Total Environ.* **2018**, *644*, 916–927. [CrossRef]
8. Yang, Y.; Erskine, P.D.; Lechner, A.M.; Mulligan, D.; Zhang, S.; Wang, Z. Detecting the Dynamics of Vegetation Disturbance and Recovery in Surface Mining Area via Landsat Imagery and LandTrendr Algorithm. *J. Clean. Prod.* **2018**, *178*, 353–362. [CrossRef]
9. Zhang, C.; Zheng, H.; Li, J.; Qin, T.; Guo, J.; Du, M. A Method for Identifying the Spatial Range of Mining Disturbance Based on Contribution Quantification and Significance Test. *Int. J. Environ. Res. Public Health* **2022**, *19*, 5176. [CrossRef]
10. Xu, F.; Li, H.; Li, Y. Ecological Environment Quality Evaluation and Evolution Analysis of a Rare Earth Mining Area under Different Disturbance Conditions. *Environ. Geochem Health* **2021**, *43*, 2243–2256. [CrossRef] [PubMed]
11. Wu, Z.; Lei, S.; Lu, Q.; Bian, Z.; Ge, S. Spatial Distribution of the Impact of Surface Mining on the Landscape Ecological Health of Semi-Arid Grasslands. *Ecol. Indic.* **2020**, *111*, 105996. [CrossRef]
12. Sun, X.; Yuan, L.; Liu, M.; Liang, S.; Li, D.; Liu, L. Quantitative Estimation for the Impact of Mining Activities on Vegetation Phenology and Identifying Its Controlling Factors from Sentinel-2 Time Series. *Int. J. Appl. Earth Obs. Geoinf.* **2022**, *111*, 102814. [CrossRef]
13. Liu, Y.; Wang, L.; Lu, Y.; Zou, Q.; Yang, L.; He, Y.; Gao, W.; Li, Q. Identification and Optimization Methods for Delineating Ecological Red Lines in Sichuan Province of Southwest China. *Ecol. Indic.* **2023**, *146*, 109786. [CrossRef]
14. Yang, Y.; Erskine, P.D.; Zhang, S.; Wang, Y.; Bian, Z.; Lei, S. Effects of Underground Mining on Vegetation and Environmental Patterns in a Semi-Arid Watershed with Implications for Resilience Management. *Environ. Earth Sci* **2018**, *77*, 605. [CrossRef]
15. Liu, S.; Li, W.; Wang, Q. Zoning Method for Environmental Engineering Geological Patterns in Underground Coal Mining Areas. *Sci. Total Environ.* **2018**, *634*, 1064–1076. [CrossRef]
16. Lieth, H. Purposes of a Phenology Book. In *Phenology and Seasonality Modeling*; Lieth, H., Ed.; Ecological Studies; Springer: Berlin/Heidelberg, Germany, 1974; Volume 8, pp. 3–19, ISBN 978-3-642-51865-2.
17. Verhegghen, A.; Bontemps, S.; Defourny, P. A Global NDVI and EVI Reference Data Set for Land-Surface Phenology Using 13 Years of Daily SPOT-VEGETATION Observations. *Int. J. Remote Sens.* **2014**, *35*, 2440–2471. [CrossRef]
18. Buyantuyev, A.; Wu, J. Urbanization Diversifies Land Surface Phenology in Arid Environments: Interactions among Vegetation, Climatic Variation, and Land Use Pattern in the Phoenix Metropolitan Region, USA. *Landsc. Urban Plan.* **2012**, *105*, 149–159. [CrossRef]
19. De Beurs, K.M.; Henebry, G.M. Spatio-Temporal Statistical Methods for Modelling Land Surface Phenology. In *Phenological Research*; Hudson, I.L., Keatley, M.R., Eds.; Springer: Dordrecht, The Netherlands, 2010; pp. 177–208, ISBN 978-90-481-3334-5.
20. Moody, A.; Johnson, D.M. Land-Surface Phenologies from AVHRR Using the Discrete Fourier Transform. *Remote Sens. Environ.* **2001**, *75*, 305–323. [CrossRef]
21. Ganguly, S.; Friedl, M.A.; Tan, B.; Zhang, X.; Verma, M. Land Surface Phenology from MODIS: Characterization of the Collection 5 Global Land Cover Dynamics Product. *Remote Sens. Environ.* **2010**, *114*, 1805–1816. [CrossRef]

22. Zeng, L.; Wardlow, B.D.; Xiang, D.; Hu, S.; Li, D. A Review of Vegetation Phenological Metrics Extraction Using Time-Series, Multispectral Satellite Data. *Remote Sens. Environ.* **2020**, *237*, 111511. [CrossRef]
23. Griffiths, P.; Nendel, C.; Pickert, J.; Hostert, P. Towards National-Scale Characterization of Grassland Use Intensity from Integrated Sentinel-2 and Landsat Time Series. *Remote Sens. Environ.* **2020**, *238*, 111124. [CrossRef]
24. Moon, M.; Richardson, A.D.; Friedl, M.A. Multiscale Assessment of Land Surface Phenology from Harmonized Landsat 8 and Sentinel-2, PlanetScope, and PhenoCam Imagery. *Remote Sens. Environ.* **2021**, *266*, 112716. [CrossRef]
25. Li, H.; Xie, M.; Wang, H.; Li, S.; Xu, M. Spatial Heterogeneity of Vegetation Response to Mining Activities in Resource Regions of Northwestern China. *Remote Sens.* **2020**, *12*, 3247. [CrossRef]
26. Peng, D.; Wang, Y.; Xian, G.; Huete, A.R.; Huang, W.; Shen, M.; Wang, F.; Yu, L.; Liu, L.; Xie, Q.; et al. Investigation of Land Surface Phenology Detections in Shrublands Using Multiple Scale Satellite Data. *Remote Sens. Environ.* **2021**, *252*, 112133. [CrossRef]
27. Li, J.; Liang, J.; Wu, Y.; Yin, S.; Yang, Z.; Hu, Z. Quantitative Evaluation of Ecological Cumulative Effect in Mining Area Using a Pixel-Based Time Series Model of Ecosystem Service Value. *Ecol. Indic.* **2021**, *120*, 106873. [CrossRef]
28. Zhao, Y.; Wang, Y.; Zhang, Z.; Zhou, Y.; Huang, H.; Chang, M. The Evolution of Landscape Patterns and Its Ecological Effects of Open-Pit Mining: A Case Study in the Heidaigou Mining Area, China. *Int. J. Environ. Res. Public Health* **2023**, *20*, 4394. [CrossRef] [PubMed]
29. Xiao, W.; Deng, X.; He, T.; Guo, J. Using POI and Time Series Landsat Data to Identify and Rebuilt Surface Mining, Vegetation Disturbance and Land Reclamation Process Based on Google Earth Engine. *J. Environ. Manag.* **2023**, *327*, 116920. [CrossRef] [PubMed]
30. Peng, D.; Wu, C.; Li, C.; Zhang, X.; Liu, Z.; Ye, H.; Luo, S.; Liu, X.; Hu, Y.; Fang, B. Spring Green-up Phenology Products Derived from MODIS NDVI and EVI: Intercomparison, Interpretation and Validation Using National Phenology Network and AmeriFlux Observations. *Ecol. Indic.* **2017**, *77*, 323–336. [CrossRef]
31. Kariyeva, J.; Van Leeuwen, W. Environmental Drivers of NDVI-Based Vegetation Phenology in Central Asia. *Remote Sens.* **2011**, *3*, 203–246. [CrossRef]
32. Claverie, M.; Ju, J.; Masek, J.G.; Dungan, J.L.; Vermote, E.F.; Roger, J.-C.; Skakun, S.V.; Justice, C. The Harmonized Landsat and Sentinel-2 Surface Reflectance Data Set. *Remote Sens. Environ.* **2018**, *219*, 145–161. [CrossRef]
33. Zhang, J.; Zou, T.; Lai, Y. Novel Method for Industrial Sewage Outfall Detection: Water Pollution Monitoring Based on Web Crawler and Remote Sensing Interpretation Techniques. *J. Clean. Prod.* **2021**, *312*, 127640. [CrossRef]
34. Ge, C.; Sun, S.; Yao, R.; Sun, P.; Li, M.; Bian, Y. Long-Term Vegetation Phenology Changes and Response to Multi-Scale Meteorological Drought on the Loess Plateau, China. *J. Hydrol.* **2022**, *614*, 128605. [CrossRef]
35. Zhou, X.; Geng, X.; Yin, G.; Hänninen, H.; Hao, F.; Zhang, X.; Fu, Y.H. Legacy Effect of Spring Phenology on Vegetation Growth in Temperate China. *Agric. For. Meteorol.* **2020**, *281*, 107845. [CrossRef]
36. Zhang, X. Reconstruction of a Complete Global Time Series of Daily Vegetation Index Trajectory from Long-Term AVHRR Data. *Remote Sens. Environ.* **2015**, *156*, 457–472. [CrossRef]
37. Zhao, Y.; Lee, C.K.F.; Wang, Z.; Wang, J.; Gu, Y.; Xie, J.; Law, Y.K.; Song, G.; Bonebrake, T.C.; Yang, X.; et al. Evaluating Fine-Scale Phenology from PlanetScope Satellites with Ground Observations across Temperate Forests in Eastern North America. *Remote Sens. Environ.* **2022**, *283*, 113310. [CrossRef]
38. Beck, P.S.A.; Atzberger, C.; Høgda, K.A.; Johansen, B.; Skidmore, A.K. Improved Monitoring of Vegetation Dynamics at Very High Latitudes: A New Method Using MODIS NDVI. *Remote Sens. Environ.* **2006**, *100*, 321–334. [CrossRef]
39. Jonsson, P.; Eklundh, L. Seasonality Extraction by Function Fitting to Time-Series of Satellite Sensor Data. *IEEE Trans. Geosci. Remote Sens.* **2002**, *40*, 1824–1832. [CrossRef]
40. Xu, L.; Niu, B.; Zhang, X.; He, Y. Dynamic Threshold of Carbon Phenology in Two Cold Temperate Grasslands in China. *Remote Sens.* **2021**, *13*, 574. [CrossRef]
41. Shang, R.; Liu, R.; Xu, M.; Liu, Y.; Zuo, L.; Ge, Q. The Relationship between Threshold-Based and Inflexion-Based Approaches for Extraction of Land Surface Phenology. *Remote Sens. Environ.* **2017**, *199*, 167–170. [CrossRef]
42. Wang, Z.; Zhou, W.; Jiskani, I.M.; Ding, X.; Luo, H. Dust Pollution in Cold Region Surface Mines and Its Prevention and Control. *Environ. Pollut.* **2022**, *292*, 118293. [CrossRef]
43. Entwistle, J.A.; Hursthouse, A.S.; Marinho Reis, P.A.; Stewart, A.G. Metalliferous Mine Dust: Human Health Impacts and the Potential Determinants of Disease in Mining Communities. *Curr. Pollut. Rep* **2019**, *5*, 67–83. [CrossRef]
44. Trechera, P.; Moreno, T.; Córdoba, P.; Moreno, N.; Zhuang, X.; Li, B.; Li, J.; Shangguan, Y.; Dominguez, A.O.; Kelly, F.; et al. Comprehensive Evaluation of Potential Coal Mine Dust Emissions in an Open-Pit Coal Mine in Northwest China. *Int. J. Coal Geol.* **2021**, *235*, 103677. [CrossRef]
45. Liu, Z.; Shen, L.; Yan, C.; Du, J.; Li, Y.; Zhao, H. Analysis of the Influence of Precipitation and Wind on PM2.5 and PM10 in the Atmosphere. *Adv. Meteorol.* **2020**, *2020*, 5039613. [CrossRef]
46. Kang, W.; Wang, T.; Liu, S. The Response of Vegetation Phenology and Productivity to Drought in Semi-Arid Regions of Northern China. *Remote Sens.* **2018**, *10*, 727. [CrossRef]
47. Yuan, M.; Zhao, L.; Lin, A.; Wang, L.; Li, Q.; She, D.; Qu, S. Impacts of Preseason Drought on Vegetation Spring Phenology across the Northeast China Transect. *Sci. Total Environ.* **2020**, *738*, 140297. [CrossRef]
48. Zhan, Y.; Ma, C.; Yan, Y.; Zhu, J.; Ji, Y.; Ma, C.; Luo, Y. Spatial Differentiation Characteristics of Vegetation Greening Rates and Climate Attribution in China's Arid and Semi-Arid Regions. *Glob. Ecol. Conserv.* **2023**, *46*, e02563. [CrossRef]

49. Wang, Z.; Chen, J.; Hoi, S.C.H. Deep Learning for Image Super-Resolution: A Survey. *IEEE Trans. Pattern Anal. Mach. Intell.* **2021**, *43*, 3365–3387. [CrossRef]

50. Tian, J.; Zhu, X.; Chen, J.; Wang, C.; Shen, M.; Yang, W.; Tan, X.; Xu, S.; Li, Z. Improving the Accuracy of Spring Phenology Detection by Optimally Smoothing Satellite Vegetation Index Time Series Based on Local Cloud Frequency. *ISPRS J. Photogramm. Remote Sens.* **2021**, *180*, 29–44. [CrossRef]

Technical Note

Three-Dimensional Resistivity and Chargeability Tomography with Expanding Gradient and Pole–Dipole Arrays in a Polymetallic Mine, China

Meng Wang [1,2,3], **Junlu Wang** [4,*], **Pinrong Lin** [5] **and Xiaohong Meng** [1]

[1] School of Geophysics and Information Technology, China University of Geosciences, Beijing 100083, China; wangmeng@mail.cgs.gov.cn (M.W.); mxh@cugb.edu.cn (X.M.)
[2] China Aero Geophysical Survey and Remote Sensing Center for Natural Resources, Beijing 100083, China
[3] National Engineering Research Center of Offshore Oil and Gas Exploration, Beijing 100028, China
[4] Development and Research Center, China Geology Survey, Beijing 100037, China
[5] Institute of Geophysical and Geochemical Exploration, Chinese Academy of Geological Sciences, Langfang 065000, China; linpinrong@igge.cn
* Correspondence: wjunlu@mail.cgs.gov.cn; Tel.: +86-137-8546-5866

Abstract: Three-dimensional resistivity/chargeability tomography based on distributed data acquisition technology is likely to provide abundant information for mineral exploration. To realize true 3D tomography, establishing transmitter sources with different injection directions and collecting vector signals at receiver points is necessary. We implemented 3D resistivity/ chargeability tomography to search for new ore bodies in the deep and peripheral areas of Huaniushan, China. A distributed data acquisition system was used to form a vector receiver array in the survey area. First, by using the expanding gradient array composed of 11 pairs of transmitter electrodes, we quickly obtained the 3D distributions of the resistivity and chargeability of the whole area. Based on the electrical structure and geological setting, a NE-striking potential area for mineral exploration was determined. Next, a pole–dipole array was employed to depict the locations and shapes of the potential ore bodies in detail. The results showed that the inversion data for the two arrays corresponded well with the known geological setting and that the ore veins controlled by boreholes were located in the low-resistivity and high-chargeability zone. These results provided data for future mineral evaluation. Further research showed that true 3D tomography has obvious advantages over quasi-3D tomography. The expanding gradient array, characterized by a good signal strength and field efficiency, was suitable for the target determination in the early exploration stage. The pole–dipole array with high spatial resolution can be used for detailed investigations. Choosing a reasonable data acquisition scheme is helpful to improve the spatial resolution and economic efficiency.

Keywords: resistivity; induced polarization; 3D tomography; mining

1. Introduction

Direct current (DC) resistivity and induced polarization (IP) methods have been increasingly used in mineral exploration [1–4], hydrocarbon surveys [5,6], engineering investigations [7,8] and hydrogeophysical prospecting [9,10]. The resistivity and chargeability parameters, which reflect the resistive and capacitive characteristics of subsurface media, respectively, can be obtained by observing the time-domain responses of the Earth to the injected current signals. Compared with the DC resistivity method, the IP method is especially effective at mapping sulfide minerals [11,12]. With the increasing demand for mineral resources, exploration directions are developing towards complex geological and topographic conditions. Greater demands are being placed on data acquisition and interpretation technology as the exploration environments are more challenging.
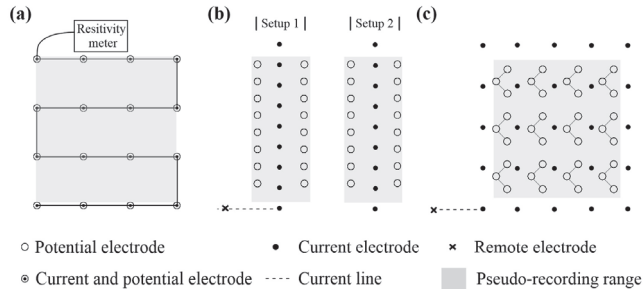
In traditional two-dimensional (2D) data acquisition, the transmitter electrodes and receiver electrodes lie along the same line. This method has been successfully applied in

relatively simple geological settings [13,14]. However, in areas with complex geological settings, such as complex changes in electrical parameters and target shapes caused by folds or magma intrusions, the information obtained by 2D data acquisition technology is insufficient [15]. Interpreting the real three-dimensional (3D) electrical structure is difficult and can result in drawing the wrong conclusions when using these data for interpretation in 2D inversion algorithms [16]. In addition, due to the non-uniform arrangement of particle pores and fractures in the rock, electrical anisotropy is possible [17]. The currents flowing through an anisotropic body deviate from the original injection direction, which leads to interpretation deviation for the observational data [18]. With the development of instruments and 3D inversion technology [19–21], the DC/IP method has developed from 2D profile acquisition to 3D acquisition.

Early 3D cases have been mostly realized using 2D multi-electrode systems. The first approach is to a use multi-branch layout of multicore cables to implement the 3D electrode array (Figure 1a) [7,20]. However, the 3D layout of the 2D instrument is not always suitable for high-precision and deep, large-scale surveys. The second approach is to combine several common 2D profiles and use a 3D inversion algorithm to investigate a large area [2,22–24]. Some classical 2D arrays were specially modified for 3D data acquisition, such as double offset pole–dipole array (Figure 1b) [25,26]. However, the 2D combination method mainly reflects the electrical structure along the receiver lines, which is a quasi-3D technique [27]. Webb et al. [28] collected not only the electric field component in the line direction but also the transverse direction when using a pole–dipole array to implement 3D data acquisition. His experiment showed that collecting 'between the lines' provided critical information.

Obtaining true 3D tomography of complex geological bodies requires using a series of current sources with different injection locations and collecting potential signals in two orthogonal directions at the receiver points [29]. With the development of distributed acquisition systems, we can set up many independent two-channel receivers into a bi-directional receiver array [1,30,31]. Bournas et al. [32] and Sun et al. [33] carried out 3D data acquisition using a pole–L-shaped-dipole array (Figure 1c). Wang et al. [4] and Gong et al. [34] proposed using an expanding gradient–L-shaped-dipole array. Distributed true 3D acquisition technology is suitable for large-scale and high-precision mineral exploration. As the receiver array covers a large area and n-spacing could be set very large, distributed true 3D acquisition technology can detect the deep buried target body. As there are a large number of receiver electrode locations, it can improve the horizontal resolution. Common electrode array configurations include pole–pole, pole–dipole, dipole–dipole and gradient array configurations, which have different signal strengths, detection depths, spatial resolutions and operating complexities [27,30]. The spatial resolution of the pole–pole array is poor. The dipole-dipole array has a good spatial resolution, but its signal strength is small, especially when the n-spacing is too large, which limits the exploration depth [29,35]. The vertical resolution of the gradient array is poor, but it has a good signal strength and the electrical structure of the subsurface media can be quickly obtained through a small number of transmitter sources [4,30]. The spatial resolution and signal strength of the pole–dipole array are between those of the dipole–dipole and gradient arrays [25]. Therefore, the trade-offs among the signal-to-noise ratio, exploration depth, spatial resolution and work efficiency must be considered when selecting the array type [36].

In this paper, we describe the 3D resistivity and chargeability tomography obtained in Huaniushan, Gansu Province, China. By using a distributed electromagnetic (DEM) system, a vector receiver array was deployed. We used expanding gradient and pole–dipole arrays to implement 3D data acquisition. Then, the 3D resistivity and chargeability data were inverted to generate a 3D geoelectric model. Our work had two purposes. One goal was to search for continuous resources in the deep and peripheral parts of a mining area. The other aim was to compare the quality and efficiency of these arrays (including the combinations of partial data) to seek a reasonable acquisition scheme.
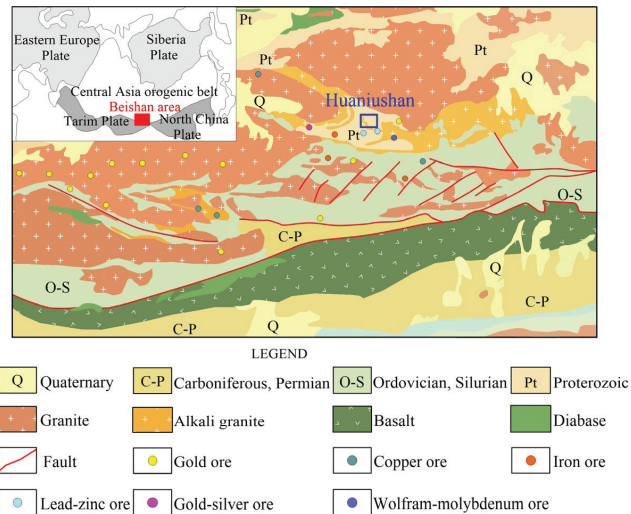
○ Potential electrode   • Current electrode   × Remote electrode

⊙ Current and potential electrode   ---- Current line   ▨ Pseudo-recording range

Figure 1. Schematic diagram of the different 3D observation configurations. (**a**) The S-shaped electrodes arrangement using a multi-branch layout of multicore cables (after Loke, et al. [20]). (**b**) The double offset pole–dipole array (after White et al. [22]). (**c**) The pole–L-shaped-dipole array using distributed acquisition systems (after Sun, et al. [33]).

2. Tectonic and Geological Setting

2.1. Tectonic Setting

The Beishan area, situated at the convergence of the Tarim plate, North China plate and Central Asia orogenic belt, represents a multi-cycle composite orogenic belt and is a multi-cycle composite orogenic belt [37]. The Huaniushan Au–Ag–Pb–Zn deposit is located in the western part of the Beishan area. Its geotectonic location belongs to the Dunhuang landmass in the northeast of the Tarim plate (Figure 2). The Dunhuang landmass is mainly composed of the hypo-metamorphic rocks of the Archaean Dunhuang Group. In the Mesoproterozoic period, the ancient land began to break apart and developed a set of shallow marine carbonaceous clastic and carbonate rock formations with a small number of intermediate basic volcanic rocks. The regional structure is controlled by an ENE-trending deep fault.

LEGEND

Q	Quaternary	C-P	Carboniferous, Permian	O-S	Ordovician, Silurian	Pt	Proterozoic

Granite   Alkali granite   Basalt   Diabase

Fault   Gold ore   Copper ore   Iron ore

Lead-zinc ore   Gold-silver ore   Wolfram-molybdenum ore

Figure 2. The regional geological map of Huaniushan in the Beishan area. The tectonic setting of the Beishan area is located at the junction of the Tarim plate, North China plate and the Central Asia orogenic belt [38,39].

The laser ablation inductively coupled plasma mass spectrometry (LA-ICP-MS) zircon dating of basalt showed that the crystallization age was 1071 Ma ± 5 Ma, and the strata related to mineralization mainly composed the Pingtoushan Formation of Jixianian Sys-

tem [40]. As shown in Figure 3, the third and fourth lithologic members of the Pingtoushan Formation were exposed in the NE-trending study area. The third lithologic member (Jxp^c) was a set of shallow marine carbonate and argillaceous rock formations and was mainly composed of marble and phyllite, which were divided into three sections. The upper part of the third lithologic member was the main ore-bearing horizon of the Pb–Zn mine. The fourth lithologic member (Jxp^d) was a set of shallow marine carbonaceous argillaceous rock formations, which mainly consisted of phyllite, slate and hornfels. The magmatic activity in the study area was intense and frequent, including late Mesoproterozoic submarine volcanic eruptions and early to middle Indosinian and Variscan magmatic intrusions [41].
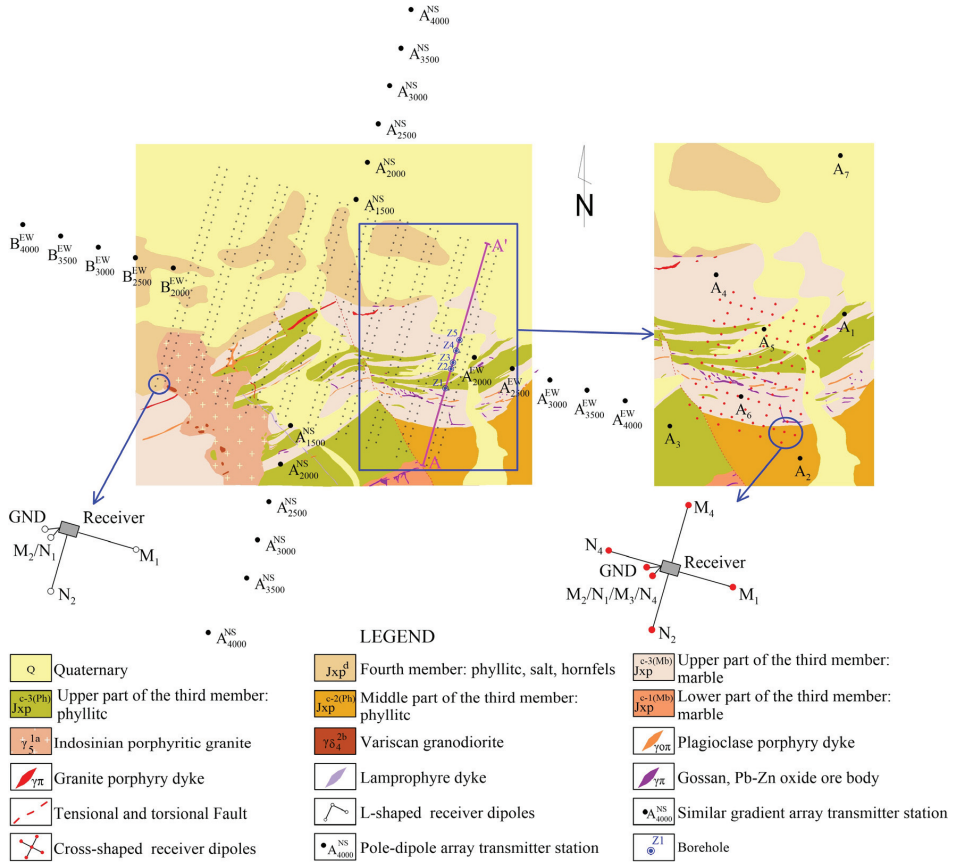
Figure 3. Geological and array arrangement map [39]. Data collection in the study area was conducted using the expanding gradient array (**the left image**). Data collection in the blue-boxed area was carried out using the pole–dipole array (**the right image**).

Since the 1960s, 221 ore bodies have been delineated, eight of which have reserves of more than 10,000 tons. Ninety percent of ore bodies are located in the contact zone between clastic rocks and carbonate rocks of the Pingtoushan Formation. The thicknesses of the ore veins typically range from 0.5 to 0.9 m, but the larger veins reach up to 16.5 m [41]. Despite the significant mineral resource potential in this area, the current reserves are insufficient, necessitating the discovery of new ore bodies in deep or peripheral areas. Therefore, finding new ore bodies in deep or peripheral areas is urgent.

2.2. Geophysical Setting

A total of 1098 rock (ore) specimens were collected from the boreholes and surface of the study area. In the laboratory, the resistivity and chargeability of these samples were measured using the four-electrode measuring method. Table 1 shows that the range of the resistivity values within the different samples of the same kind of rock was very large. The average resistivity of magmatic rock was higher than that of metamorphic rock. The resistivity of carbonaceous rock was, as expected, lower than that of non-carbonaceous rock. Mineralization led to a decrease in resistivity. The average resistivity of lead–zinc ore was lower than the resistivity of marble and quartzite. Based on the chargeability of these samples, it was evident that lead–zinc ore demonstrated a high chargeability. This established a foundation of physical properties for utilizing resistivity and chargeability imaging methods to investigate lead–zinc deposits. Carbon-bearing rocks, which are characterized by a high chargeability and low resistivity, had similar characteristics to lead–zinc ore and was an interference factor in our study. In practical situations, due to factors such as the ore body size and grade, the apparent chargeability observed in lead–zinc mines is often smaller than the apparent chargeability observed in carbon-bearing rocks. Based on this characteristic, combined with the actual geological conditions, it is often possible to distinguish to some extent between ore bodies and carbon-bearing rocks.

Table 1. Electrical parameters of the rock samples in the survey area.

Lithology	Number	Resistivity (Ω·m)			Chargeability (%)		
		Maximum	Minimum	Average	Maximum	Minimum	Average
Marble	272	15,649	1	1478	76.4	0.1	1.8
Phyllite	112	11,083	33	1443	47.4	0.1	1.9
Granite	103	38,243	10	3394	71.8	0.1	1.1
Carbonaceous marble	2	165	84	118	54.4	24.9	36.8
Carbonaceous phyllite	105	1550	16	79	92.4	29.8	68.9
Mineralized marble	166	6284	1	83	100.0	0.1	3.6
Mineralized phyllite	161	9750	8	453	91.6	0.1	8.1
Mineralized granite	5	3150	736	1684	3.1	0.4	1.2
Hornstone	47	6129	471	2884	58.3	0.1	0.7
Phyllitic slate	10	34,456	3483	12,417	8.96	1.26	5.49
Gray-black limestone	15	2334	23	1196	32	57.5	42.7
Pb–Zn ore	100	4145	1	25	94.8	0.3	68.4

3. Data Acquisition and Processing

A distributed electromagnetic (DEM) system was used to collect 3D data. The DEM consisted of a transmitter (1600 V, 100 Amp) and many multi-channel receivers (two, three and eight channels) (Figure 4). The DEM can be used to collect full waveform data. Some authors argue that this system is capable of detection at a great depth [4,31].

3.1. Expanding Central Gradient Array

To quickly obtain the underground electrical characteristics of the whole study area, an expanding gradient array, which was characterized by a good signal strength and an efficient operational approach, was used first. Using the adjoint equation method, the sensitivity distribution of the gradient array was calculated [42]. Figure 5a shows that the observed signals contained more deep electrical information with the increase in the transmitting electrodes distance. In the study area, the 3D receiving array was arranged with a 200 m line spacing and 50 m station interval. At each receiver point, two channels of receivers were used to form L-shaped receiver dipoles (Figure 3), and the time-domain full waveform potential difference signals in two orthogonal directions were recorded. A total of eleven pairs of transmitter electrodes were arranged, six of which were nearly in the N–S direction, with electrode distances (AB) of 1500 m, 2000 m, 2500 m, 3000 m, 3500 m and 4000 m. Five pairs were nearly in the E–W direction, with AB values of 2000 m, 2500 m,

3000 m, 3500 m and 4000 m. The transmitter cycle was 16 s. Before data acquisition, all the transmitter electrodes were buried in deep pits and sprinkled with salty water to reduce the grounding resistivity. During the survey, we first deployed 4000 m transmitter wires in each direction and gradually shortened the wires to achieve other layouts for the transmitter dipoles. Compared with the pole–dipole array, moving the transmitter wires required less time with the expanding gradient array, and every group of vector receiver dipoles could record signals with a greater amplitude strength. Another advantage of the expanding gradient array was that the high-sensitivity zone below the receiver electrodes did not indicate an obvious offset. Therefore, in the field, we could draw apparent resistivity and chargeability maps to quickly analyze the electrical characteristics of the study area.


Figure 4. The receivers of the DEM system.
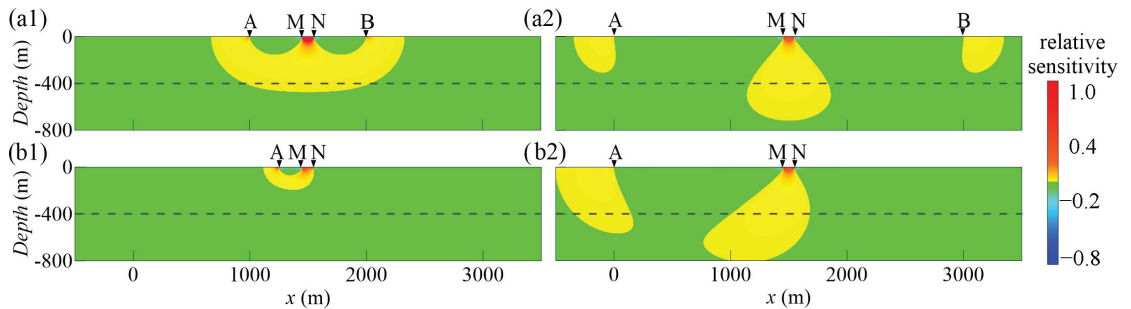
Figure 5. Sensitivity distribution of the different arrays. (**a**) Gradient array with AB = 1 km (**a1**) and AB = 3 km (**a2**); (**b**) pole–dipole array with AM = 0.2 km (**b1**) and AM = 1.5 km (**b2**).

In the conventional time-domain DC/IP method, the apparent resistivity is computed by employing the geometric factor, and the apparent chargeability is determined as the ratio of the secondary voltage to the primary voltage [43]. Based on the full waveform data, it was possible to calculate the decoupled percent frequency effect (PFE) coefficients and decoupled phases using a multi-parameter extraction algorithm [44]. Another advantage of utilizing full waveform data was the ability to suppress noise by excluding individual erroneous data points and addressing multiple superpositions [45].

Figure 6 shows the apparent resistivity and chargeability data of the expanding gradient array with different transmitter electrode distances. Longitudinally, the apparent resistivity characteristics of the 2 km transmitter electrode distances were similar to those of 4 km, but there were obvious differences in the local positions. Two main factors contributed to these differences. First, the positions of the transmitter electrodes differed, which meant that the data of the expanding gradient array contained the electrical information of the transmitter electrode locations. Second, the data with longer transmitter electrode distances contained more information about the deep electric structure. Horizontally, there were some variations in the apparent resistivity measured in different observation directions

from the diverse current injection directions. These variations reflected the electrical differences between 'along the lines' and 'between the lines'. As the nearly N–S direction was more perpendicular to the strike of the geology, the apparent resistivity data obtained from the nearly N–S-trending transmitter and receiver was more consistent with the distribution of the lithologies and stratigraphy in the area. As shown in Figure 6, the low-resistivity zone in the northwestern part of the survey area corresponded to the carbonaceous argillaceous rock formations of the fourth lithologic member. The high-resistivity zone was attributed to the carbonate and argillaceous rock formations of the third lithologic member.
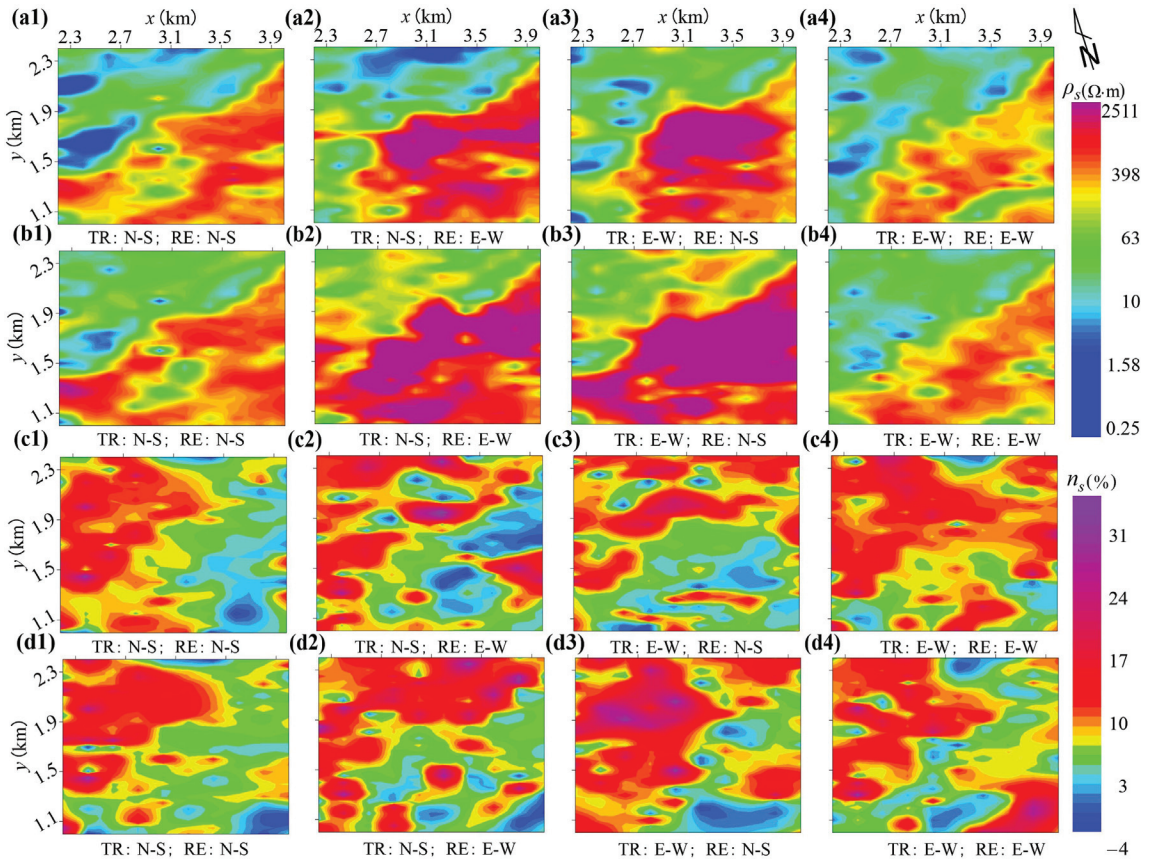
Figure 6. Apparent resistivity data from the expanding gradient array with AB = 2 km (**a1**–**a4**) and 4 km (**b1**–**b4**). Subfigures (**c1**–**c4**) and (**d1**–**d4**) display the apparent chargeability data for AB = 2 km and AB = 4 km, respectively. The transmitter–receiver directions are marked at the bottom of the figure panels. TR: current injection direction. RE: receiving direction.

3.2. Pole–Dipole Array

According to the 3D inversion results of the expanding gradient array, the zone of interest with the characteristics of low resistivity and high chargeability was selected for the 3D tomography with the pole–dipole array (blue frame in Figure 3). The 3D receiver array was arranged with a 50 m line spacing and a 50 m station interval. Four-channel receivers at each location were used to form cross-shaped receiver dipoles (Figure 3). There were seven transmitting sources inside and outside the potential zone, among which electrodes A_1 through A_4 were located near the four corners outside the receiver array. Electrodes A_5 and A_6 were placed in the middle of the receiver array to increase the shallow spatial resolution,

and electrode A_7 was located in the north, 550 m from the nearest receiver electrode, to improve the deep spatial resolution. The infinite transmitter electrode for all seven sources was placed 5 km from the receiver array.

As shown in Figure 7, the apparent resistivity and chargeability values of the stations were set at the midpoint of receiver electrodes M and N. However, in theory, the high-sensitivity zone below the receiver electrodes was offset to the transmitter electrode, as illustrated in Figure 5b. In addition, the apparent resistivity map of the pole–dipole array did not reflect information from the same depth. The above reasons led to the difference between the panels shown in Figure 6. Although there were differences, all of them could reflect the NE-trending banded anomaly in the eastern area.
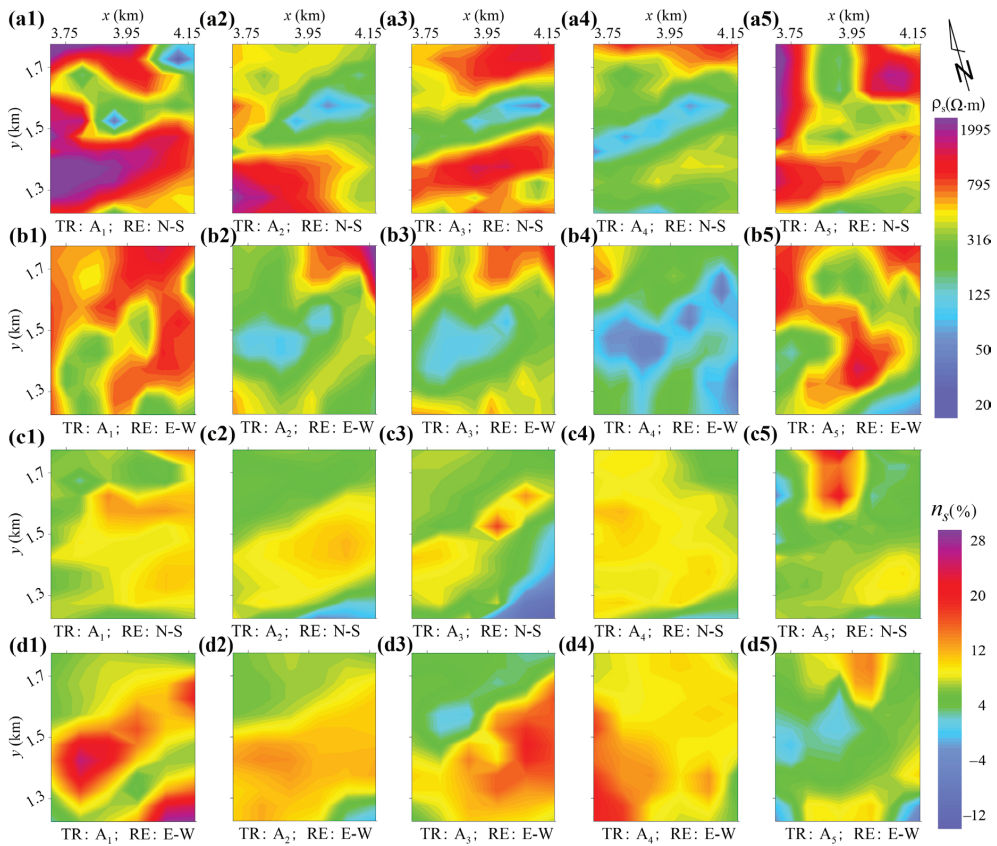
Figure 7. Apparent resistivity and apparent chargeability data from the pole–dipole array for five transmitter electrodes: A_1 (**a1,b1,c1,d1**); A_2 (**a2,b2,c2,d2**); A_3 (**a3,b3,c3,d3**); A_4 (**a4,b4,c4,d4**); and A_5 (**a5,b5,c5,d5**). TR: transmitter electrode. RE: receiving direction.

3.3. D Inversion

The finite element method (FEM) was used to implement forward modeling [46]. Since the maximum elevation difference of the survey area was less than 20 m, the influence of the surface topography was not considered in the mesh generation. The investigated domain was discretized into a set of hexahedral elements. We used the incomplete Cholesky conjugate gradient (ICCG) algorithm to solve a large sparse linear equation [47].

For the resistivity inversion problem, we minimized the following target functional based on the regularization method.

$$\Theta(m) = \Theta_d + \lambda\Theta_m = \|d(\boldsymbol{m}) - d_{obs}\|^2 + \lambda\left\|W_m\left(\boldsymbol{m} - \boldsymbol{m}_{ref}\right)\right\|^2, \tag{1}$$

where Θ_d and Θ_m are the data constraint item and model constraint item, respectively, λ is the regularization factor, $\boldsymbol{m}$ is the forward response of the current model, d_{obs} is the observed data and W_m is the model weighting matrix containing the derivatives of the model in three orthogonal directions. The iteration format of Equation (1) is as follows.

$$\left(\boldsymbol{J}^T\boldsymbol{J} + \lambda\boldsymbol{W}^T\boldsymbol{W}\right)\Delta\boldsymbol{m}_{k+1} = \boldsymbol{J}^T(d_{obs} - d(\boldsymbol{m}_k)) - \lambda\boldsymbol{W}^T\boldsymbol{W}\left(\boldsymbol{m}_k - \boldsymbol{m}_{ref}\right), \tag{2}$$

$$\boldsymbol{m}_{k+1} = \boldsymbol{m}_k + \Delta\boldsymbol{m}_{k+1}, \tag{3}$$

where $\boldsymbol{J}$ is the Jacobian matrix. The regularization factor λ was updated by decreasing it step by step. The natural logarithm conductivity method was used to avoid negative resistivity values [48]. The conjugate gradient method was employed for the rapid inversion of the resistivity.

For the chargeability inversion problem, the linearization of the data equations was used in our algorithm. The approximate relationship between the apparent chargeability of the sounding point and the model chargeability is shown as follows [48,49].

$$\eta_{ai} = \sum_{j=1}^M J_{ij}\eta_j = -\sum_{j=i}^M \frac{\partial ln(\varphi)}{\partial ln(\sigma_j)}\eta_j, \tag{4}$$

where $\boldsymbol{J}$ is the negative value of the Jacobian matrix in the resistivity inversion, which was calculated; φ is the apparent resistivity; and η_j is the model chargeability. Since Equation (4) was similar to Equations (2) and (3), we could easily implement the chargeability inversion. Instead of the natural logarithm chargeability method, a hard constraint was used to keep the chargeability within a reasonable range.

Mesh generation is a trade-off between the inversion accuracy and speed. In the horizontal direction, the actual electrode coordinates were used for the grid generation, and a node was inserted between two adjacent electrodes. In the vertical direction, the layer thickness increased with the number of layers at a specific scale factor. The thickness of the first layer was one-third of the minimum electrode distance and the scale factor was 1.12. The maximum depth of the inversion model was approximately 540 m. To suppress the boundary effect, we expanded the mesh by 10 elements. A uniform half-space with the average value of the observed apparent resistivity was used as the initial model. The initial regularization parameter was 0.1 and decreased with the number of iterations.

4. Results and Interpretation
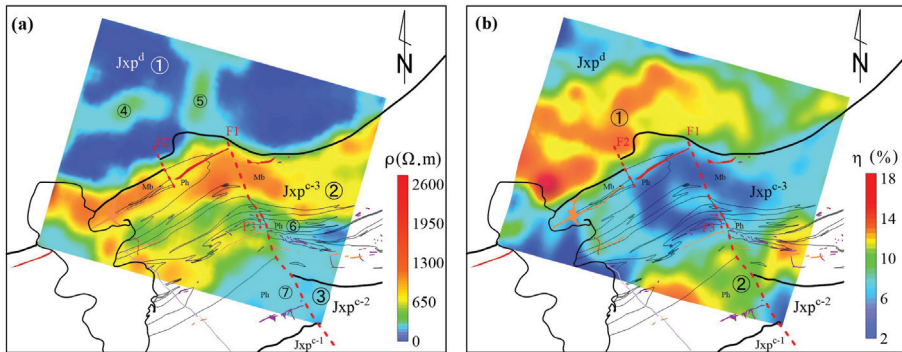
4.1. Expanding Gradient Array

In the inversion of expanding the gradient array data, the total number of model grids was 105,222. The 3D inversion was performed using the L-shaped dipoles array data of all 11 transmitters. After five iterations, the fitting error of the inverted resistivity was 16.4% and that of chargeability was 7.2%. The effective depth was 500 m.

Figure 8 shows the 3D models of the inversion results. The shallow inversion results agreed well with the distributions of the lithologies. To further analyze the results, deep slices were extracted at 80 m (Figure 9). As shown in Figures 8a and 9a, a NE-striking border between the third (Jxp^c) and fourth lithologic members (Jxp^d) cut through the whole survey area. The carbonaceous rocks of the Jxp^d, which were covered by the Quaternary system, were characterized by low resistivity (zone ①). The local high-resistivity zones ④ and ⑤ were related to exposed slate. The carbonate rock formation of the Jxp^c showed a moderate- to high-resistivity area overall (zone ②). The local high- and low-resistivity anomalies were

related to lithological changes, such as the NE-trending low-resistivity belt (zone ⑥ and ⑦) in the Jxp^{c-3}, which roughly coincided with phyllite. The argillaceous rock formations in the Jxp^{c-2} showed a low-resistance zone (zone ③). A change in the orientation of the high-resistivity belt occurred near the F1 fault. As shown in Figures 8b and 9b, two high-chargeability belts (zone ① and ②) were clear. Figure 8c shows the 3D morphology of the low-resistance and high-chargeability bodies. The anomaly in the northwestern area represented the reaction of carbonaceous rocks in the fourth lithologic member. The anomaly in the southeastern area was related to mineralization.
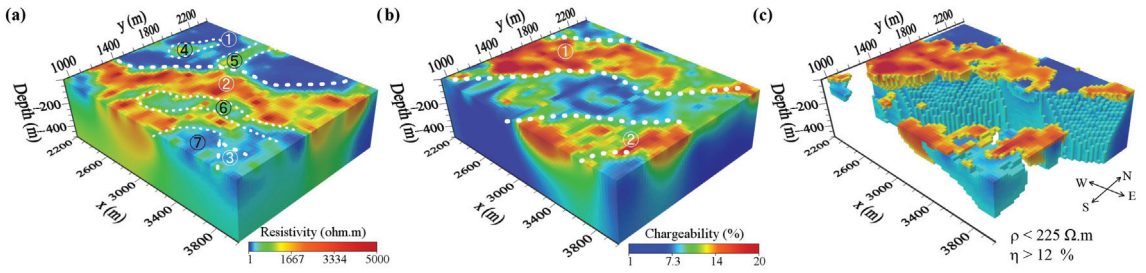
Figure 8. 3D inversion results from the expanding gradient array. (**a**) 3D distribution of the resistivity; (**b**) 3D distribution of the chargeability; (**c**) 3D morphology of the low-resistivity and high-chargeability bodies. In panel c, the low-resistivity bodies (less than 225 Ω·m) are displayed in cool colors, consistent with the color bar in panel a. The high-chargeability bodies (greater than 12%) are displayed in warm colors, consistent with the color bar in panel b. Zone ①–⑦ represent resistivity anomalies.

Figure 9. The inversion results of the expanding gradient array presented as a horizontal slice along the depth of 80 m, where (**a**) represents the resistivity and (**b**) represents the chargeability deep slices along z = 80 m. Zone ①–⑦ represent chargeability anomalies.

Figure 10a shows the geological structure along line AA′, in which the black lines and the red polygons represent the drilling paths and ore bodies, respectively. An ore vein with a thickness of 4.41 m was revealed at 506.59 m in the Z6 borehole. Figure 8b,c shows the inversion results for line AA′. The 3D DC inversion results largely agreed with the geological profile. The shape of the low-resistivity zone at 950 to 1200 m was interpreted as the middle part of the third lithologic member. The range of the fourth lithologic member exposed on the surface at 2300 to 2400 m was consistent with the shallow low-resistivity zone in the resistivity profile, which extended deeper towards the south. The locations of the low-resistivity and high-chargeability bodies were consistent with those of the known ore veins.
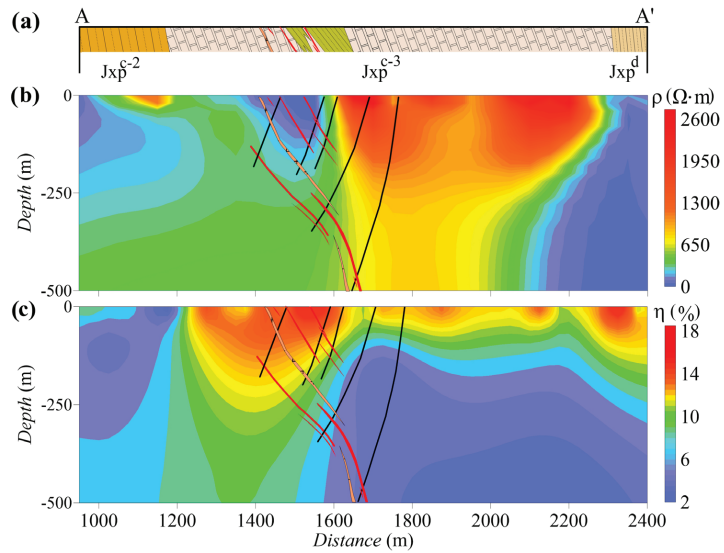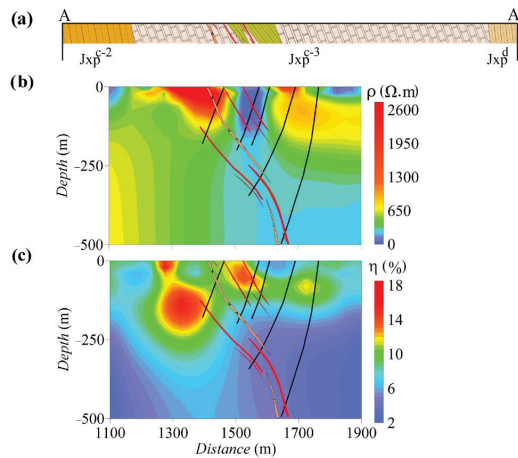
Figure 10. Slices of the 3D inversion results from the expanding gradient array along line AA′. (**a**) Geological profile of line AA′ (after Yang et al., 2010a [39]); (**b**) resistivity profile; (**c**) chargeability profile. The section along line AA′ (magenta line) is shown in Figure 3.

4.2. Pole–Dipole Array

In the inversion of the pole–dipole array data, the total number of model grids was 30,420. The 3D inversion was performed using the cross-shaped dipoles array data of all seven transmitters. After six iterations, the fitting error of the inverted resistivity was 15.8% and that of the chargeability was 8.6%. Figures 11 and 12 show the 3D electrical structure and slices along line AA′, respectively. As shown in Figure 12c, the chargeability profile revealed three anomalies. At 1450 to 1600 m, the known ore veins showed an anomalous low-resistivity and high-chargeability zone, which was similar to those shown in Figure 10. The high-chargeability zone at 1250 to 1450 m also showed relatively low-resistivity characteristics and was located in the extension direction of the known veins. Therefore, this area was inferred to be favorable for mineralization, which could be used for drilling verification. The high-resistivity and high-polarization zone at 1650 to 1800 m may have been caused by wall rock alteration.
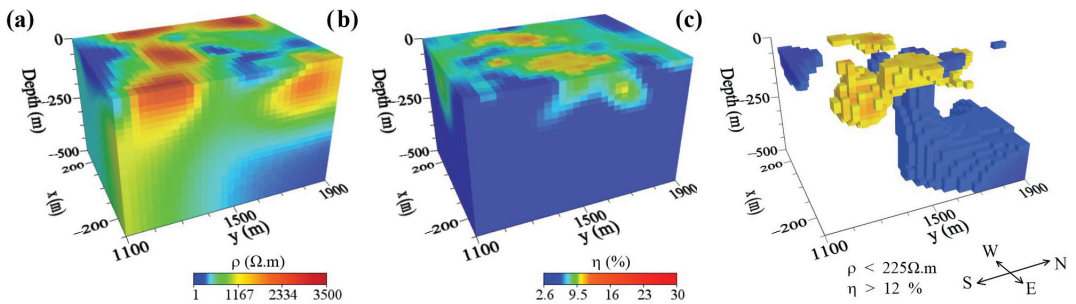
Figure 11. 3D inversion results from the pole–dipole array. (**a**) 3D distribution of the resistivity; (**b**) 3D distribution of the chargeability; (**c**) 3D morphology of the low-resistance and high-chargeability bodies. In panel c, the low-resistivity bodies (less than 225 Ω·m) are displayed in cool colors, consistent with the color bar in panel a. The high-chargeability bodies (greater than 12%) are displayed in warm colors, consistent with the color bar in panel b.

Figure 12. Slices of the 3D inversion results with a pole–dipole array along line AA′. (**a**) Geological profile; (**b**) resistivity profile; (**c**) chargeability profile.

5. Discussion

5.1. Comparison between the Expanding Gradient Array and Pole–Dipole Array

Although the inversion results from the expanding gradient array data showed electrical structures similar to those from the pole–dipole array data, the details differed obviously. As shown in Figure 10c, the high-chargeability zones at 1250 to 1450 m and 1650 to 1800 m extended to the surface, which was different from the result in Figure 12c. As shown in Figure 5, when the transmitter–receiver separation was small, the high-sensitivity zone was concentrated in the shallow part. With the increase in the separation, the sensitivity of the deep part increased. For the expanding gradient array, since the minimum AB reached 1000 m, the shallow resistivity in the inversion results was affected by the depth. Accordingly, the pole–dipole array with the smaller separation had the higher resolution in the shallow part. In addition, with the same separation, the pole–dipole array was more sensitive to the deep part, as shown in Figure 5. Figure 12b describes the more detailed resistivity characteristics in the deep part than Figure 10b, which indicated that the former had a greater detection depth.

However, the disadvantages of pole–dipole arrays are also obvious. In our work, seven transmitter electrodes were used to cover an area of only 0.3 km^2. Therefore, many transmitter sources were needed to achieve the larger-scale high-resolution survey. In addition, the signal level was very small for a large transmitter–receiver separation, which reduced the signal-to-noise ratio of the observed data and may not have even yielded effective data. In our work, when the transmitter electrode A_7 was used to inject the current, the amplitudes of the signals recorded at several points in the southern area were less than the minimum detectable value for the DEM receiver.

Although the vertical resolution of the expanding gradient array was poor, a small number of transmitter sources could be used to investigate a large area. Therefore, the expanding gradient array was suitable for seeking targets in the early exploration stage. In the target zone, a pole–dipole array could be used for detailed investigation. In this stage, by moving the receivers outside into the target area, arranging a denser receiver array was easy.

5.2. Comparison between True 3D and Quasi-3D

Theoretically, when the transmitter sources are dense enough, a high-resolution geoelectric model can be obtained. Any combination of arrays can be used for joint inversion. However, a reasonable work layout is the trade-off among spatial resolution, detection depth and work efficiency. The results shown in Figures 8–12 were calculated using all the

vector observational data generated by all the transmitters. To compare the results of true 3D tomography and quasi-3D tomography, the data for the different transmitter–receiver relations were combined for inversion, which contributed to the design of a reasonable and efficient acquisition scheme. Taking the resistivity as an example, we performed a comparative analysis of the 3D model and line AA′ slices. The model grid and inversion parameters shown in Figures 13 and 14 were the same as those shown in Figures 8–11, respectively.
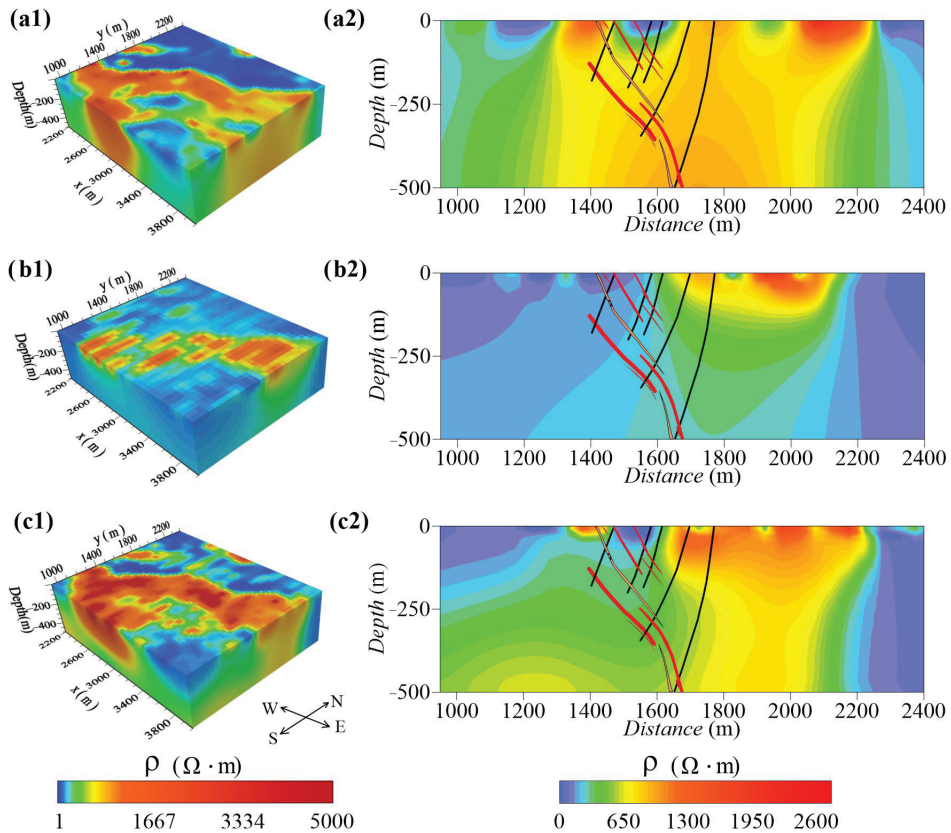
Figure 13. Inversion results using different data combinations with an expanding gradient array. (**a1**) is the 3D distribution of the resistivity with the nearly N–S-trending transmitter and nearly N–S-trending receiver. (**b1**) is the 3D distribution of the resistivity with the nearly E–W-trending transmitter and nearly E–W-trending receiver. (**c1**) is a 3D resistivity model obtained by combining the data used in Figures 13a and 13b for inversion. (**a2**), (**b2**) and (**c2**) are the slices of (**a1**), (**b1**) and (**c1**) along line AA′, respectively.

For the expanding gradient array, we mainly focused on the difference in the current injection direction. As shown in Figure 13a, the inversion results with the nearly N–S-trending transmitter and nearly N–S-trending receiver mostly reflected the longitudinal information and a lack the transverse information. Although the shallow resistivity characteristics shown in left panel of Figure 13a agreed well with the geological structure, the slice (right panel of Figure 13a) showed a lower vertical resolution, with only the features in the top 150 m being imaged. The inversion results with the nearly E–W-trending transmitter and nearly E–W-trending receiver mainly reflected the transverse information. Figure 13a,b displays the resistivity characteristics along a single direction, that is, quasi-3D tomography

(Figure 13c). The data used in Figure 13a,b were combined to invert the resistivity model, including 'along the lines' and 'between the lines' information. Compared with those shown in Figure 13a,b, the resistivity model shown in Figure 13c was more consistent with the geological structure. In the profile, the low-resistivity anomaly caused by the ore veins showed further downward stretching. The vertical and horizontal resolutions were further improved by using the inversion of all the sounding points from all the transmitter sources (Figure 8).
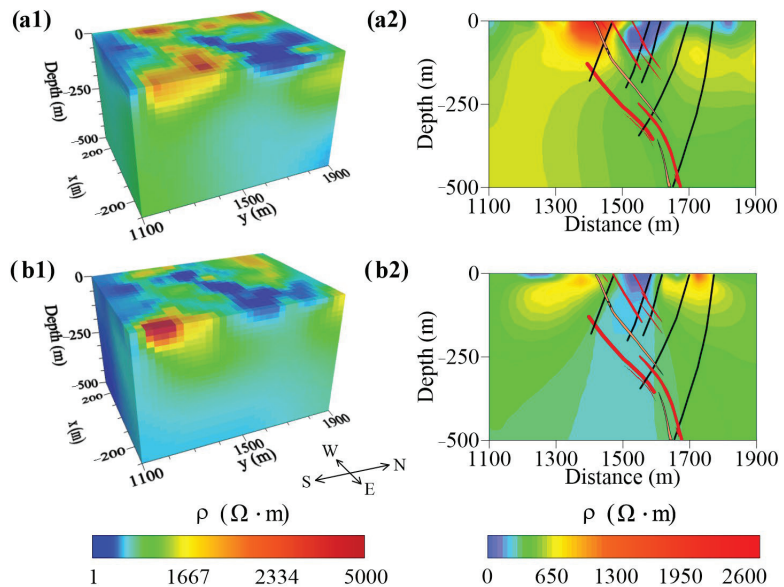
Figure 14. Inversion results using different data combinations with the pole–dipole array. (**a1**) and (**b1**) are the resistivity inversion results of the nearly S–N-trending and E–W-trending data, respectively. (**a2**) and (**b2**) are the slices of (**a1**) and (**b1**) along line AA′, respectively.

For the pole–dipole array, the differences caused by the receiver direction were analyzed. We inverted the data received along the nearly N–S and E–W directions independently (Figure 14). The inversion results using the data measured along the nearly N–S-trend were more consistent with the geological setting than those of the nearly E–W-trend. At depths of 1700 to 1900 m, the inversion results of the nearly E–W-trending data did not well depict the low-resistivity anomaly caused by the fourth lithologic member. Compared with the inversion results from single-direction data, the electrical structure described by the vector data was more detailed and better corresponded to the geological structure.

The inversion results of both arrays showed that true 3D acquisition had obvious advantages over quasi-3D acquisition. The vector observation data based on multi-directional transmitters can be used for the high-resolution tomography of real geoelectric models. Arranging L-shaped or cross-shaped vector receiver arrays to record data is advisable. In addition, because the data of the vertical trend showed a better detection effect, larger density dipoles can be arranged in this direction.

6. Conclusions

In our case, a distributed acquisition system was used to implement 3D resistivity and chargeability tomography to search for new deep and peripheral ore bodies of Huaniushan, China. We used expanding gradient and pole–dipole arrays to implement 3D data acquisition. Based on the Gauss–Newton algorithm, the 3D resistivity and chargeability data were inverted to generate a 3D geoelectric model. The conclusions are as follows.

(1) By using DC/IP 3D tomography technology, we obtained a high-resolution geoelectric model of underground media. The inversion results from the two arrays showed good agreement with the distribution of the geological formations, fault locations and borehole data. The NE-striking low-resistivity and high-chargeability body delineated in the southeast was related to mineralization, which provided data for further mineral evaluation.

(2) The true 3D data acquisition technology had obvious advantages over the quasi-3D approach. To realize true 3D tomography, establishing transmitter sources with different injection directions and collecting vector signals at sounding points was necessary. Using L-shaped or cross-shaped dipole arrays for data acquisition was reasonable.

(3) While the true 3D inversion in this study demonstrated better results compared to the pseudo 3D inversion, isotropic inversion algorithms may not be suitable for situations with pronounced anisotropy, leading to the inversion of data misfit. The next step involves the development of a 3D inversion algorithm that incorporates anisotropic resistivity to obtain a more accurate 3D resistivity model reflective of the actual geological conditions.

(4) When designing an acquisition scheme, the spatial resolution, signal-to-noise ratio, maximum detection depth and field efficiency should be considered comprehensively. Although the vertical resolution of the expanding array was poor, its signal strength and field efficiency were good, and this method could be used to determine the target in the early exploration stage. The pole–dipole array had a high spatial resolution, but it needed densely spaced transmitters, which was more suitable for detailed investigation. To improve the cost/benefit ratio, a large spacing could be used along the strike of the geological structures.

Conflicts of Interest: The authors declare no conflicts of interest.

References

1. Gharibi, M.; Killin, K.; Mcgill, D.; Henderson, W.B.; Retallick, T. Full 3D acquisition and modelling with the Quantec 3D system The Hidden Hill Deposit Case Study. *ASEG Ext. Abstr.* **2012**, *1*, 1–4. [CrossRef]
2. Ali, M.A.; Mewafy, F.M.; Qian, W.; Alshehri, F.; Ahmed, M.S.; Saleem, H.A. Saleem. Integration of electrical resistivity tomography and induced polarization for characterization and mapping of (Pb-Zn-Ag) sulfide deposits. *Minerals* **2023**, *13*, 986. [CrossRef]
3. Han, M.H.; Shin, S.W.; Park, S.; Cho, S.J.; Kim, J.H. Induced polarization imaging applied to exploration for low-sulfidation epithermal Au-Ag deposits, Seongsan mineralized district, South Korea. *J. Geophys. Eng.* **2016**, *13*, 817–823. [CrossRef]
4. Wang, J.L.; Lin, P.R.; Wang, M.; Li, D.; Li, J.H. Three-dimensional tomography using high-power induced polarization with the similar central gradient array. *Appl. Geophys.* **2017**, *14*, 291–300. [CrossRef]
5. Burtman, V.; Gribenko, A.; Zhdanov, M.S. Induced polarization in hydrocarbon-saturated sands and sandstones: Experimental study and general effective medium modelling. In Proceedings of the 79th SEG Annual Meeting Expanded Abstracts, Houston, TX, USA, 25–30 October 2009; pp. 774–778.
6. Veeken, P.; Legeydo, P.J.; Davidenko, Y.; Kudryavceva, E.; Ivanov, S.; Chuvaev, A. Benefits of the induced polarization geoelectric method to hydrocarbon exploration. *Geophysics* **2009**, *74*, B47–B59. [CrossRef]
7. Santarato, G.; Ranieri, G.; Occhi, M.; Morelli, G.; Fischanger, F.; Gualerzi, D. Three-dimensional electrical resistivity tomography to control the injection of expanding resins for the treatment and stabilization of foundation soils. *Eng. Geol.* **2011**, *119*, 18–30. [CrossRef]
8. Rossi, M.; Olsson, P.I.; Johanson, S.; Fiandaca, G.; Bergdahl, D.P.; Dahlin, T. Mapping geological structures in bedrock via large-scale direct current resistivity and time-domain induced polarization tomography. *Near Surf. Geophys.* **2017**, *15*, 657–667. [CrossRef]

9. Vacquier, V.; Holmes, C.R.; Kintzinger, P.R.; Lavergne, M. Prospecting for ground water by induced electrical polarization. *Geophysics* **1957**, *22*, 660–687. [CrossRef]
10. Johnson, T.C.; Versteeg, R.J.; Ward, A.; Day-Lewis, F.D.; André, R. Improved hydrogeophysical characterization and monitoring through parallel modeling and inversion of time-domain resistivity and induced-polarization data. *Geophysics* **2010**, *75*, WA27–WA41. [CrossRef]
11. Bleil, D.F. Induced Polarization: A Method of Geophysical Prospecting. *Geophysics* **1953**, *18*, 636–661. [CrossRef]
12. James, R. *Overvoltage Research and Geophysical Applications*; Pergamon Press: London, UK, 1959.
13. Santos, F.A.M.; Afonso, A.R.A. Detection and 2D modelling of cavities using pole-dipole array. *Environ. Geol.* **2005**, *48*, 108–116. [CrossRef]
14. Nyquist, J.E.; Peake, J.S.; Roth, M.J.S. Comparison of an optimized resistivity array with dipole-dipole soundings in karst terrain. *Geophysics* **2007**, *72*, F139–F144. [CrossRef]
15. Spitzer, K. The three-dimensional DC sensitivity for surface and subsurface sources. *Geophys. J. Int.* **1998**, *134*, 736–746. [CrossRef]
16. Rutley, A.; Oldenburg, D.W.; Shekhtman, R. 2D and 3D IP/Resistivity inversion for the interpretation of Isa-Style Targets. *Explor. Geophys.* **2001**, *32*, 156–159. [CrossRef]
17. Mir, R.; Perrouty, S.; Astic, T.; Bérubé, C.L.; Smith, R.S. Structural complexity inferred from anisotropic resistivity: Example from airborne EM and compilation of historical resistivity/IP data from the gold-rich Canadian Malartic district, Québec, Canada. *Geophysics* **2019**, *84*, B153–B167. [CrossRef]
18. Asten, M.W. The influence of electrical anisotropy on Mise A La Masse surveys. *Geophys. Prospect.* **1974**, *22*, 238–245. [CrossRef]
19. Sasaki, Y. 3D resistivity inversion using the finite-element method. *Geophysics* **1994**, *59*, 1839–1848. [CrossRef]
20. Loke, M.H.; Barker, R.D. Practical techniques for 3D resistivity surveys and data inversion. *Geophys. Prospect.* **1996**, *44*, 499–523. [CrossRef]
21. Li, Y.; Oldenburg, D.W. 3D inversion of induced polarization data. *Geophysics* **2000**, *65*, 1931–1945. [CrossRef]
22. White, R.M.S.; Collins, S.; Denne, R.; Hee, R.; Brown, P. A new survey design for 3D IP inversion modelling at copper hill. *Explor. Geophys.* **2001**, *32*, 152–155. [CrossRef]
23. Neyamadpour, A.; Taib, S.; Wan Abdullah, W.A.T. An application of three-dimensional electrical resistivity imaging for the detection of an underground waste-water system. *Stud. Geophys. Geod.* **2009**, *53*, 389–402. [CrossRef]
24. Power, C.; Tsourlos, P.; Ramasamy, M.; Nivorlis, A.; Mkandawire, M. Combined dc resistivity and induced polarization (DC-IP) for mapping the internal composition of a mine waste rock pile in nova scotia, Canada. *J. Appl. Geophys.* **2018**, *150*, 40–51. [CrossRef]
25. White, R.; Collins, S.; Loke, M. Resistivity and IP arrays, optimized for data collection and inversion. *Explor. Geophys.* **2003**, *34*, 229–232. [CrossRef]
26. Collins, S.; White, R. Case histories in the use of three-dimensional inversion of induced polarization and resistivity surveys. *ASEG Ext. Abstr.* **2003**, *2*, 1–4.
27. Neyamadpour, A. Field test to compare 3D imaging capabilities of three arrays in a site with high resistivity contrast regions. *Stud. Geophys. Geod.* **2011**, *55*, 755–769. [CrossRef]
28. Webb, D.; Rowston, P.; McNeill, G. A Comparison of 2D and 3D IP from Copper Hill NSW. In Proceedings of the ASEG 16th Geophysical Conference and Exhibition, Adelaide, Australia, 16–19 February 2003.
29. Eaton, P.; Anderson, B.; Queen, S.; Mackenzie, I.; Wynn, D. NEWDAS-the Newmont distributed IP data acquisition system. In Proceedings of the SEG International Exposition and Annual Meeting, SEG, Denver, CO, USA, 17–22 October 2010.
30. Goldie, M.A. A comparison between conventional and distributed acquisition induced polarization surveys for gold exploration in Nevada. *Lead. Edge* **2007**, *26*, 180–183. [CrossRef]
31. Zheng, C.L.; Liu, X.Z.; Lin, P.R.; Sun, F.W.; Li, Y.; Li, J.H.; Wang, J.L. Design and realization of the distributed electromagnetic instrument system. *Chin. J. Geophys.* **2019**, *62*, 3772–3784.
32. Bournas, N.; Hearst, R.; Clements, E.; Clements, E. Silver Queen, a new stockwork porphyry discovery using the Titan24 DCIP and MT. In Proceedings of the 2012 SEG Annual Meeting, Las Vegas, NV, USA, 4–9 November 2012.
33. Sun, J.J.; Li, Y.G.; Nabighian, M. Lithology differentiation based on inversion of full waveform induced polarization data from Newmont Distributed IP Data Acquisition System (NEWDAS). In Proceedings of the SEG International Exposition and Annual Meeting, Las Vegas, NV, USA, 4–9 November 2012.
34. Gong, S.P.; Yang, Y.B.; Lin, P.R.; Wu, W.L.; Zheng, C.J.; Shi, F.S.; Wu, X.P.; Weng, A.H.; Zhang, G.Z.; Gu, G.W.; et al. Three-dimensional electrical exploration methods for the mapping of polymetallic targets in gansu province, China. *Geophys. Prospect.* **2019**, *67*, 1929–1947. [CrossRef]
35. Zhang, G.; Lyu, Q.T.; Lin, P.R.; Zhang, G.B. Electrode array and data density effects in 3d induced polarization tomography and applications for mineral exploration. *Arab. J. Geosci.* **2019**, *12*, 221. [CrossRef]
36. Friedel, S. Resolution, stability and efficiency of resistivity tomography estimated from a generalized inverse approach. *Geophys. J. R. Astron. Soc.* **2010**, *153*, 305–316. [CrossRef]
37. Qi, Q.J.; Wang, Y.H.; Feng, M.X.; Yang, J.G.; Yu, J.Y.; Wang, L.; Wang, X.H. Geochronology, geochemistry and tectonic significance of dike swarms in Beishan, Gansu. *Acta Geol. Sin.* **2016**, *90*, 131–132. [CrossRef]
38. Liu, D.C.; Qiu, J.T.; Tian, F.; Sun, Y. Application of airborne hyper-spectrum remote sensing to mapping of ore-control faults: A case study of the Heishishan-Huaniushan fault. *Geol. Explor.* **2015**, *51*, 0366–0375.

39. Yang, J.G.; Zhai, J.Y.; Yang, H.W.; Wang, X.H.; Xie, C.L.; Wang, X.A.; Ren, B.C. Metallotectonics and Prospection of the Huaniushan Exhalogene Gold Silver Lead Zinc Deposit in Beishan, Gansu Province. *Geotecton. Metallog.* **2010**, *34*, 246–254.
40. Yang, J.G.; Zhai, J.Y.; Yang, H.W.; Wang, C.F.; Xie, C.L.; Wang, X.H.; Lei, Y.X. LA-ICP-MS zircon U-Pb dating of basalt and its geological significance in Huaniushan Pb-Zn deposit, Beishan area, Gansu, China. *Geol. Bull. China* **2010**, *29*, 1017–1023.
41. Yang, J.G.; Ren, Y.X.; Wang, X.H.; Ren, B.C.; Zhai, J.Y.; Wang, X.A. *Metallogenic Regularity and Prospecting Prediction of Huaniushan Gold Silver Polymetallic Ore Field, Beishan*; Geological Press: Beijing, China, 2011.
42. McGillivray, P.R.; Oldenburg, D.W. Methods for calculating Frechet derivatives and sensitivities for the non-linear inverse problem: A comparative study. *Geophys. Prospect.* **1990**, *38*, 499–524. [CrossRef]
43. Sumner, J.S. *Principles of Induced Polarization for Geophysical Exploration*; Elsevier Scientific Publishing Company: Amsterdam, The Netherlands, 1976.
44. Wang, J.L.; Lin, P.R.; Wang, M.; Li, J.H. A multiple parameter extraction and electromagnetic coupling correction technique for time domain induced polarisation full waveform data. *Explor. Geophys.* **2019**, *50*, 113–123. [CrossRef]
45. Paine, J.; Copeland, A. Reduction of noise in induced polarization data using full time-series data. *Explor. Geophys.* **2003**, *34*, 225–228. [CrossRef]
46. Karaoulis, M.; Revil, A.; Tsourlos, P.; Werkema, D.D.; Minsley, B.J. IP4DI: A software for time-lapse 2D/3D DC-resistivity and induced polarization tomography. *Comput. Geosci.* **2013**, *54*, 164–170. [CrossRef]
47. Poole, E.L.; Ortega, J.M. Multicolor iccg methods for vector computers. *SIAM J. Numer. Anal.* **1987**, *24*, 1394–1418. [CrossRef]
48. Oldenburg, D.W.; Li, Y. Inversion of induced polarization data. *Geophysics* **1994**, *59*, 1327. [CrossRef]
49. Seigel, H.O. Mathematical formulation and type curves for induced polarization. *Geophysics* **1959**, *24*, 547–565. [CrossRef]

minerals

The Effect of Wetting–Drying Cycles on the Deterioration of the Physical and Mechanical Properties of Cemented Paste Backfill in Open-Pit Coal Mines

Tao Chen [1,2,3], **Jisen Shu** [1,2,3,*], **Liu Han** [1,2], **Zhaowan Tan** [3] and **Jinxing Lyu** [1,4]

[1] School of Mines, China University of Mining and Technology, Xuzhou 221116, China; chentao2020@cumt.edu.cn (T.C.); hanliucumt@163.com (L.H.); lvjinxing@xju.edu.cn (J.L.)
[2] Key Laboratory of Coal Resources and Safe Mining, Xuzhou 221116, China
[3] Yunnan·Top Field-Mining Sci & Tech., Ltd., Kunming 650200, China; 13908761211@139.com
[4] School of Geology and Mines, Xinjiang University, Urumqi 830047, China
[*] Correspondence: jsshu888@cumt.edu.cn

Abstract: To promote the sustainable exploitation of open-pit coal resources, waste is used as backfill material to realize the comprehensive utilization of solid waste mine resources. We proposed a mining method that is a combination of the highwall mining and filling mining methods. Cemented paste backfill (CPB) samples were prepared with high-clay-mineral-content marl particles as aggregate and normal Portland cement, sulfoaluminate cement and gypsum as cementing materials. The physical and mechanical properties and microstructural evolution of CPB with different binder ratios under wetting–drying cycles were measured. The results showed that the CPB with 0–3 wetting–drying cycles underwent shear and tensile coalescence, and that with 4–10 cycles underwent shear coalescence. The unconfined compressive strength (UCS) and elastic modulus (EM) decreased exponentially with increasing number of wetting–drying cycles but decreased exponentially and cubically with increasing porosity, respectively. The EM is more sensitive to gypsum content than the UCS. CPB deterioration was divided into an initial deterioration stage and a secondary deterioration stage. The evolution curve of the total damage variable presents an 'S' shape, with an initial damage stage, an accelerated damage expansion stage, a decelerated damage expansion stage and an end damage stage. The research results provide a basis for improving the recovery rate of resources under highwall conditions, and the extensive utilization of stripping materials, and promote the coordinated development of coal resource exploitation and environmental protection.

Keywords: highwall filling mining; cemented paste backfill; wetting–drying cycle; bond strength; damage evolution

1. Introduction

In recent years, the proportion of open-pit mining in the world's mining industry has been increasing, resulting in a large amount of waste and causing a series of environmental problems, such as the spontaneous combustion of coal gangue [1], release of excessive soil heavy metals [2], ecological damage [3], acid mine drainage (AMD) [4], collapse of mining areas [5] and other issues. Over the past decades, many scientists from the United States, Canada, Australia and other countries have been working on coal waste management and environmental issues in depth [6]. For example, the establishment of coal-based solid waste dams and coal slurry impounds [7], coal-based solid waste as construction materials (cement [8], road base materials [9], asphalt [10], environmental brick [11], coal waste-derived soil-like substrate [12], microbiological liquefaction of lignite and mechanochemical oxidative modification for the treatment of solid waste resources [13,14], backfilled roadways [15], AMD industrial extraction of metal elements [16] and dewatering for landfill [17], etc.

After high-intensity mining, open-pit coal mines leave a considerable amount of coal resources within the mining boundary. Due to the previous lack of coal mining theory and poor mining technologies, coal resources have been wasted [18]. At this time, waste is backfilled to the stope and adit, which not only improves the recovery rate of coal resources but also realizes the comprehensive utilization of solid waste mine resources as CPB [19]. However, in the process of coal mining, in the complex geological environment, rainfall easily infiltrates into the interior of the mining chamber along fault fracture zones and slope steps [20]. At the same time, groundwater easily infiltrates the adit along fractures after coal mining [21]. The exposure of CPB to air and water cause it to repeatedly undergo wetting–drying cycles [22], so the CPB is degraded by the water–rock chemical reaction [23], as shown in Figure 1. Therefore, it is necessary to study the solid waste utilization method of open-pit coal mines and CPB performance under wetting–drying cycles.
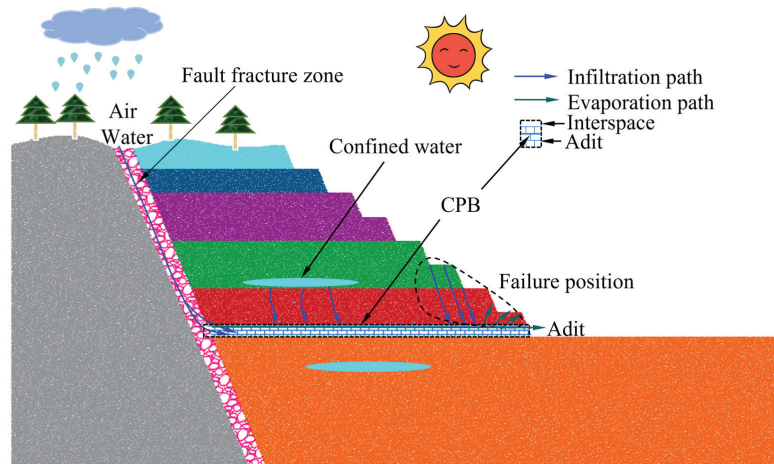
Figure 1. Wetting–drying cycle diagram of CPB under an open-pit coal mine slope.

Most of the striped rock layers in open-pit coal mines belong to geological soft rock, often containing a large amount of expansive clay minerals, which easily soften, expand and disintegrate in water [24]. Currently, with CPB with waste as the aggregate, clay minerals and their influence on its performance need to be considered [25]. Previous studies on backfill materials containing clay minerals under wetting–drying cycles mainly focused on the effect of gypsum on backfill. Aldaood et al. [26] showed that, under wetting–drying cycles, the higher the gypsum content, the greater the crack propagation and the smaller the unconfined compressive strength (UCS) of the soil sample. Durgun [27] found that polypropylene reduces the negative effects of wetting–drying cycles on gypsum-containing basalt pumice, reducing the loss of flexural strength to less than 7%. Li et al. [28] believed that extending the curing period of gypsum-treated soil samples from 7 days to 21 days could reduce the formation of vertical cracks during soaking. Ying et al. [29] indicated that wetting–drying cycles softened gypsum-treated soil and that seawater was more likely to cause macropore development than deionized distilled water. Although these studies have increased the understanding of the effect of wetting–drying cycles on gypsum-treated soil, there has been no relevant experimental study on the effect of CPB containing clay minerals, and the degree and mechanism of deterioration need further study.

Studies have shown that wetting–drying cycles have a significant effect on the water physical and mechanical properties of rocks [30]. With the increase in the number of wetting–drying cycles, the water absorption and porosity of rock [31,32], the crack propagation radius decreases [33], and the mechanical properties, such as UCS, EM, cohesion and internal friction angle, gradually decrease [34,35]. The dissolution and loss of soluble minerals and increased permeability are the key factors for the deterioration effect of a

wetting–drying cycle [36]. However, for soft rock with a high clay mineral content, the expansion/contraction behavior of clay mineral particles is more serious [37,38]. Although CPB and rock have some similar characteristics, because CPB is a prefabricated material, its particle size composition and cementing material composition are very different from rock. Therefore, clay minerals and cementing materials are important to study to understand the effect of wetting–drying cycles on CPB with waste as an aggregate. At present, the mechanism of the physical and mechanical properties of CPB under this condition is not clear, and the test method can be further explored.

Many scholars have studied CPB damage evolution. Aldhafeeri and Fall [39] examined the relationship between sulfide-containing CPB reactivity and mechanical damage. Fu et al. [40] established a damage evolution model of CPB with a layered structure and introduced the concepts of initial damage, load damage and total damage. Wang et al. [41] and Zhou et al. [42] established a damage model based on the acoustic emission ringing count rate and studied the variation in damage variables and the fractal dimension during CPB damage. Yin et al. [43] proposed a CPB segmented damage constitutive model considering fiber content. Zhang et al. [44] established a CPB damage model considering initial pore damage. The above studies focused on only mechanical damage and did not involve wetting–drying cycle damage. Therefore, it is necessary to consider the establishment of a CPB damage model under wetting–drying cycles.

In view of the existing technical defects and knowledge shortcomings, we propose a method of solid waste utilization in open-pit coal mines. The water absorption crack development, dynamic evolution law of porosity, mechanical property and failure characteristics, damage evolution law and scanning electron microscopy (SEM) structure deterioration analysis of CPB with marl as aggregate under wetting–drying cycles are studied. The purpose of this work is to improve the recovery efficiency of coal resources, realize solid waste utilization, clarify the deterioration effect and damage degree of the wetting–drying cycle on CPB and promote the coordinated development of coal resource exploitation and environmental protection.

2. Materials and Methods

2.1. CPB Preparation Process

While mining coal resources in open-pit coal mines, a large amount of waste is produced, mainly the soil–rock mixture of the stripped coal seam roof and overlying strata. Therefore, this study was conducted in the context of CPB filling mining in the Puyang open-pit coal mine, China. The coal mine uses marl as the raw material of the CPB aggregate. Through grading screening, marl is broken and divided into five particle size ranging from 0–0.3 mm, 0.3–0.6 mm, 0.6–1.18 mm, 1.18–2.36 mm and 2.36–4.75 mm, as shown. To ensure the uniformity of the prepared CPB sample, Talbot continuous grading theory was used to remix the aggregate particles to meet the following relationships [45]:

$$\frac{M\left(r < \overline{d}_i\right)}{M_0} = \left(\frac{\overline{d}_i}{d_{\max}}\right)^{3-\text{FD}} \tag{1}$$

where $M\left(r < \overline{d}_i\right)$ refers to the cumulative mass of rock and soil particle sizes greater than d_i; M_0 is the total mass of rock and soil particle sizes; $\overline{d} = \frac{d_i + d_{i+1}}{2} (d_i > d_{i+1}, i = 1, 2, \ldots)$ is the average value between the two particle sizes; $d_{\max}$ is the maximum rock particle size; and FD is the fractal dimension.

Three groups (No. 1–3) of particle size screening tests were carried out on marl particles of 100.00 g each. The mass of marl particles in each particle size range was calculated using Equation (1) (see Table A1). No. 4 is the average of Nos. 1–3, and the aggregate is configured with the particle mass in No. 4. Marl is a transitional rock between carbonate rock and clay rock, and its mineral composition is very important for the analysis of the CPB deterioration mechanism in subsequent wetting–drying cycles. Therefore, a

X'Pert Pro MPD (see Table A2 for detailed parameters) was used to analyze the whole rock and clay composition of the marl powder, as shown in Figure 2.
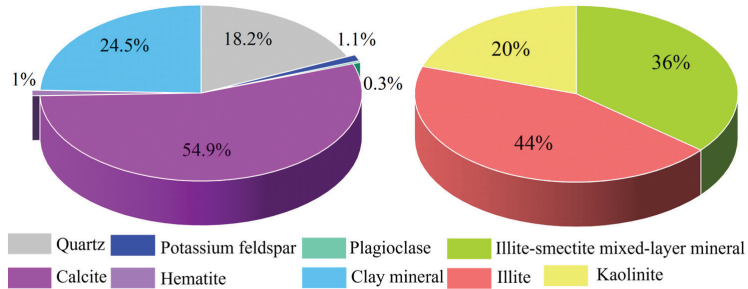

Figure 2. Mineral composition of marl minerals and clay minerals.

In this study, normal Portland cement, sulfoaluminate cement and gypsum were selected as cementing materials for the marl particles. Their basic physical properties and main component contents are shown in Tables A3–A6. Since CPB has difficulty in meeting the requirements of early strength with Portland cement alone, other reagents are often added [46]. Therefore, four different composite cementing materials were set up, and the mass ratios of normal Portland cement:sulfoaluminate cement:gypsum were 10:0:0, 8:0:2, 8:1:1, and 8:2:0. At room temperature, standard samples (50 mm in diameter and 100 mm in height) were prepared by cementing material and marl aggregate with a cement–sand ratio of 1:4.23 and a slurry concentration of 76%. A sample was placed at a temperature of 20 ± 5 °C for 24 h until solidified; then, it was numbered, demolded and placed in a SHBY-40A cement standard curing box with a temperature of 22 °C and a humidity of 95% for 28 days. The sample preparation process is shown in Figure 3.
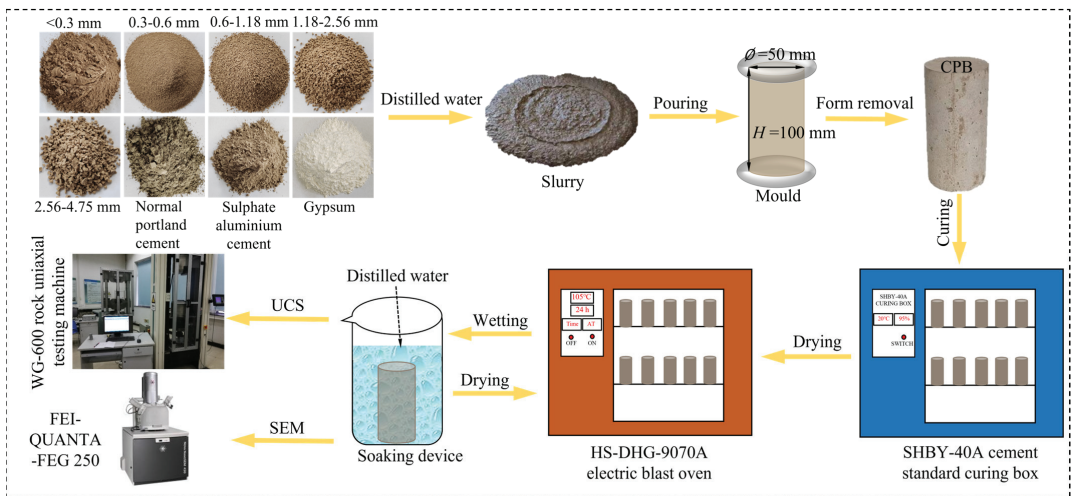

Figure 3. CPB sample preparation and wetting–drying cycle test process.

2.2. Experimental Process

2.2.1. Wetting–Drying Cycle Test

To study the effect of wetting–drying cycles on the water physical and mechanical properties of CPB, 48 samples were divided into 8 groups in the experimental design scheme. A wetting–drying cycle determination test, wetting–drying cycle test and UCS test were carried out, in that order. The specific scheme of each test is shown in Table 1. Before

the wetting–drying cycle test, all CPB samples that had been cured for 28 days were placed in an electric blast oven at 105 °C (see Table A7 for detailed parameters) for a 24 h drying treatment and then sealed with a preservative film.

Table 1. Experimental scheme design.

Sample Number	Test Classification	Normal Portland Cement:Sulphoaluminate Cement:Gypsum	Wetting–Drying Cycles	Number of Samples
WD-1~3	Wetting–drying cycle time determination test	8:1:1	1	3
RU1~4	Wetting–drying cycle test	10:0:0	10	1
RU2~4		8:0:2	10	1
RU3~4		8:2:0	10	1
RU1-1~3	Wetting–drying cycle test; UCS test	10:0:0	5	3
RU2-1~4		8:0:2	5	3
RU3-1~4		8:2:0	5	3
RU4-0~10-1~3		8:1:1	0~10	33

To determine the wetting–drying cycle time, a preliminary test was performed using the method of Ma et al. [22] to obtain the time it took the CPB to reach saturation and then fully dry. The dry CPB samples without wetting–drying cycles were designated as experiencing 0 cycles. First, three initial CPB samples (WD-1~3) were immersed in deionized distilled water with a pH value of 7 at room temperature by the free immersion method and then dried in an electric blast oven at 105 °C. The CPB samples were weighed every 5 min during immersion and every 1 h during drying. When the mass of the CPB sample remained unchanged, it was considered that the CPB sample had reached a saturated or dry state, and the curve of the water content of the CPB sample with time is shown in Appendix C. According to the wetting–drying cycle time to determine the test results, the control standard times were determined: 105 °C drying for 10 h and room temperature soaking for 45 min. A CPB sample was immersed in water at room temperature for 45 min for a wetting cycle; the sample was then dried in an oven at 105 °C for 10 h and then cooled to room temperature, to complete a wetting–drying cycle. The CPB samples were subjected to 10 wetting–drying cycles, and then immediately sealed with an impervious film.

2.2.2. UCS Test

According to the sample number in Table 1, the UCS test of the WG-600 rock uniaxial testing machine was carried out on CPB samples of different composite cementing materials under wetting–drying cycles, as shown in Figure 3. The samples were numbered RU1-1~3, RU1-2~3, RU3-1~3 and RU4-0~10-1~3 in the first wetting–drying cycle test and subsequent UCS test. Before testing, the CPB samples were processed to ensure that the deviation of the parallelism of the two ends was not greater than 0.1 mm and that the diameter deviation was not greater than 0.2 mm. Three samples from each group were tested and loaded at a displacement rate of 0.50 mm/s until failure. According to the test data, a smooth stress–strain curve was drawn, and the USC and strain were obtained. The slope was solved in the relatively straight area of the curve to obtain the EM.

2.2.3. SEM Test

The water absorption, compactness and bond strength of CPB samples are determined by the distribution of microcracks, pores and hydration products with different contents of composite cementing materials under wetting–drying cycles. The microstructure of CPB samples was scanned by an FEI-QUANTA-FEG 250 scanning electron microscope under different resolution conditions, and the corresponding parameters are shown in Table A8.

2.3. Methodology

2.3.1. Highwall Filling Mining Method

Highwall mining originated in the United States and subsequently became an important means of mining open-pit coal in the United States, Australia, Indonesia and other countries [47–49]. Due to the large number of coal pillars set up in the highwall mining process [50,51], the recovery rate of highwall coal resources has not been considerably improved. Currently, nonpillar mining technology by using waste as the filling aggregate has great advantages. In this study, the highwall filling mining method (Figure 4a) is proposed for the first time. It is based on the technology of mining the overlying coal seam under the highwall of the continuous shearer [52]. The filling process system is integrated, and the waste is used as the aggregate to form CPB, which completes the filling of the adit formed by the continuous shearer mining, thereby controlling the movement of the slope rock layer. The main process is as follows: the continuous shearer mining forms a series of adits in the overlying coal seam under the highwall by means of sequential skip mining, and then the wastes (coal gangue, soil–rock mixture, etc.) produced by the stripping of the working side are transported to the crushing station through the mining truck, and the wastes are broken into aggregate particles of appropriate particle size and then transported to the batching station through the belt conveyor to mix with cement materials and water to form CPB slurry. The filling pump station transports the CPB slurry to the adit through the pipeline for filling and then recovers and fills the coal pillar after the filling of the adit is completed. The specific implementation method is described in a patent [53]. Finally, the stripping–mining–transportation–filling/dumping–reclamation integrated collaborative operation is realized, as shown in Figure 4b. Through technological and conceptual innovation, green mining with zero ecological damage is achieved, which improves the recovery rate of coal resources, realizes solid waste utilization and greatly reduces the damage to the ecological environment. This mining technology was first applied to the Puyang open-pit coal mine in China.
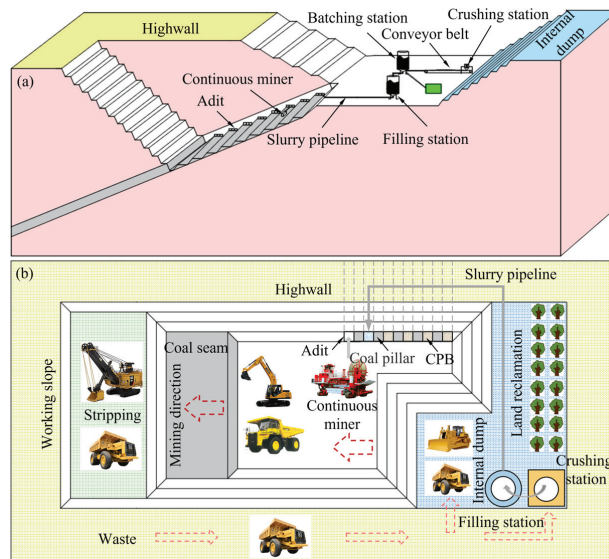

Figure 4. Schematic diagram of highwall backfill mining (**a**,**b**).

2.3.2. Porosity Calculation

Porosity is an important index with which to measure CPB and reflects the density of the CPB [54]. By testing the mass and size of the CPB during the wetting–drying cycles, the porosity φ_t of the t wetting–drying cycle can be calculated using Equation (2):

$$\varphi_t = \frac{4(m_{wt} - m_{dt})}{\pi \phi^2 H \rho_w} \tag{2}$$

where m_{wt} is the mass of the CPB sample after water absorption (g); m_{dt} is the mass of the CPB sample after drying (g); ϕ is the diameter of the CPB sample (cm); H is the height of the CPB sample (cm); and ρ_w is the density of deionized distilled water (g/cm^3), which is 1 g/cm^3.

2.3.3. Deterioration Degree of CPB

Previous studies have shown that wetting–drying cycles have different degrees of influence on CPB. To further analyze the influence of the number of wetting–drying cycles on the deterioration of the UCS and EM of CPB samples, Equations (3) and (4) were used to calculate the following:

$$D_\sigma = \frac{\sigma_t - \sigma_{t+1}}{\sigma_t} \times 100\% \tag{3}$$

$$D_E = \frac{E_t - E_{t+1}}{E_t} \times 100\% \tag{4}$$

where D_σ and D_E are the deterioration degrees of UCS and EM, respectively; σ_t and E_t are the UCS (MPa) and EM (GPa) of wetting–drying cycle t; and σ_{t+1} and E_{t+1} are the UCS (MPa) and EM (GPa) of wetting–drying cycle $t + 1$.

2.3.4. Damage Model of CPB

Under the combined action of the wetting–drying cycles and load, the CPB damage variable can be expressed by the generalized damage variable D (Xu et al., 2017) obtained by the equivalent strain principle [55]:

$$D = D_w + D_L - D_w D_L \tag{5}$$

where D is the damage variable under the coupling of the wetting–drying cycle and load; D_W is the damage variable under the wetting–drying cycles; and D_L is the damage variable under load.

The change in microstructure leads to a change in the macroscopic mechanical properties. Therefore, the damage variable of the damaged part of the sample after wetting–drying cycles can be defined with the macroscopic mechanical properties EM of CPB, namely,

$$D_w = 1 - E_t / E_0 \tag{6}$$

where E_0 is the EM of CPB with 0 wetting–drying cycles.

Assuming that the CPB strength obeys a Weibull distribution, the damage variables of the CPB under the load [56] are

$$D_L = \int_0^\varepsilon Q(x)\,\mathrm{d}x = 1 - \exp\left[-(\varepsilon/\xi)^m\right] \tag{7}$$

where $Q(x)$ is the probability density function; ε is the strain value of CPB; and m and ξ are parameters that characterize the physical and mechanical properties of CPB, which can be determined by the peak strength σ_p on the stress–strain curve and its corresponding peak strain ε_p.

Bringing Equations (6) and (7) into Equation (5),

$$D = 1 - \frac{E_t}{E_0} \exp\left[-(\varepsilon/\xi)^m\right] \tag{8}$$

According to Hooker's theorem, in the case of one-dimensional elasticity, the basic relationship of the damage constitutive can be obtained according to the Lemaitre strain equivalence principle [57]:

$$\sigma = E_t \varepsilon (1 - D_L) \tag{9}$$

where σ is the stress of the CPB.

Taking Equation (7) into Equation (9), the CPB damage constitutive model equation under the coupling of the wetting–drying cycle and load can be obtained as follows:

$$\sigma = E_t \varepsilon \exp\left[-(\varepsilon/\xi)^m\right] \tag{10}$$

The derivative of Equation (10) is

$$\frac{\partial \sigma}{\partial \varepsilon} = E_t \left(1 + m(-\varepsilon/\xi)^m\right) \exp\left[-(\varepsilon/\xi)^m\right] \tag{11}$$

According to the geometric control equation, when $\varepsilon = \varepsilon_p$, $\sigma = \sigma_p$; when $\varepsilon = \varepsilon_p$, $\partial \sigma / \partial \varepsilon = 0$; and

$$\begin{cases} \sigma_p = E_t \varepsilon_p \exp\left[-(\varepsilon_p/\xi)^m\right] \\ E_t \left(1 - m(\varepsilon_p/\xi)^m\right) \exp\left[-(\varepsilon_p/\xi)^m\right] = 0 \end{cases} \tag{12}$$

The parameters m and ξ can be obtained from Equation (12):

$$m = \frac{1}{\ln\left(E_t \varepsilon_p / \sigma_p\right)} \tag{13}$$

$$\xi = \varepsilon_p / \left(m^{-1}\right)^{m^{-1}} \tag{14}$$

The damage evolution equation and damage constitutive model equation of CPB are obtained by bringing Equations (13) and (14) into Equations (8) and (10), respectively:

$$D = 1 - \frac{E_t}{E_0} \exp\left[-\frac{1}{m}(\varepsilon/\varepsilon_p)^m\right] \tag{15}$$

$$\sigma = E_t \varepsilon \exp\left[-\frac{1}{m}(\varepsilon/\varepsilon_p)^m\right] \tag{16}$$

2.3.5. Data Processing Statistics

This study used OriginPro2021 to visualize the data and Microsoft Excel 2019 to perform statistical analysis. The mean $\overline{X}$ (Equation (17)) and standard deviation S (Equation (18)) were used to analyze the porosity, UCS and EM of the CPB samples after each wetting–drying cycle. The calculation equations are as follows:

$$\overline{X} = \frac{1}{N} \sum_{i=1}^{N} X_i \tag{17}$$

$$S = \sqrt{\frac{\sum_{i=1}^{N} \left(X_i - \overline{X}\right)^2}{N-1}} \tag{18}$$

where X_i refers to the porosity, UCS and EM of a CPB sample in the same group, and N refers to the number of the three CPB samples in the same group.

3. Results

3.1. Water Physical

3.1.1. Crack Propagation Law

The CPB samples with a composite cementing material ratio of 8:1:1 were subjected to 10 wetting–drying cycles. For the zero–two wetting–drying cycle CPB samples, the surface of the samples remained intact, and no visible microcracks were found, as shown in Figure 5a–c. In the process of three~four wetting–drying cycles, a few pinnate microcracks formed on the upper surface of the samples, and the range of microcracks was small, as shown in Figure 5d,e. Starting from the fifth cycle, pinnate microcracks and other microcracks appeared in the upper and middle parts of the sample surface, as shown in Figure 5f. During the sixth cycle, V-type microcracks appeared on the upper part of the sample, the crack length increased and the microcracks gradually expanded, as shown in Figure 5g. During the seventh and eighth cycles, crack microcracks and V-type microcracks were generated in the upper and middle parts of the samples, and the range of microcracks gradually expanded, as shown in Figure 5h,i. During the 9th and 10th cycles, microcracks and cracks appeared on the surface of the samples, the microcracks gradually expanded into Y-type cracks and axial cracks and the crack length and range increased, as shown in Figure 5j,k. According to the change in cracks, the crack propagation of CPB samples in the wetting–drying cycles can be divided into several stages: fine crack formation stage—V-type, pinnate microcrack development stage—crack microcrack formation stage—Y-type crack propagation stage.
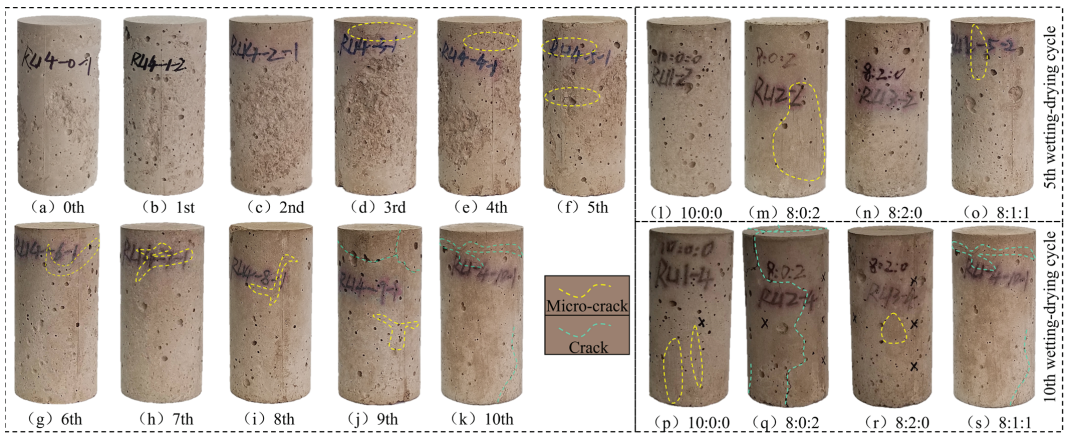

Figure 5. Effect of wetting–drying cycles on CPB surface crack propagation.

Figure 5l–s shows that the surface crack propagation trends of CPB samples with different cementation contents are significantly different. In the process of five wetting–drying cycles, samples RU1-2 and RU3-2 (which did not contain gypsum) still maintained surface integrity, and no visible microcracks were found. However, many microcracks appeared on the surface of the RU2-2 and RU4-5-2 samples. Linear cracks appeared in the middle and lower parts of sample RU2-2, and pinnate microcracks appeared in the upper part of sample RU4-5-2. In the process of 10 wetting–drying cycles, samples RU1-4 and RU3-4 with composite cementing material ratios of 10:0:0 and 8:2:0 exhibited a few visible microcracks, and the microcracks were linear. The surfaces of samples RU2-4 and RU4-10-2 with composite cementing material ratios of 8:0:2 and 8:1:1 showed many cracks, and the crack propagation and development degree of sample RU2-4 were significantly more serious than those of sample RU4-10-2. The top crack of sample RU2-4 shows a cross

type, and the crack propagates across the whole surface of the sample. The upper surface of sample RU4-10-2 shows a Y-type crack, and the lower part shows a linear crack.

3.1.2. Variation in Porosity

The porosity curves of CPB samples with four different cementation ratios were obtained by a wetting–drying cycle test. The initial porosity of all samples was approximately 12.91~14.39%, as shown in Figure 6. Figure 6a shows that the porosity change processes of samples WD-1, WD-2 and WD-3 were almost the same, and the porosity rate increased rapidly in the first wetting–drying cycle test. The porosity of the three samples was basically in equilibrium after the fourth wetting–drying cycle. The porosity after the fourth wetting–drying cycle is plotted in Figure 6c. The porosity was between 25.88% and 27.65%, and the average porosity was 26.81%. From Figure 6b, the porosity change trends of samples RU1-4 and RU3-4 were basically consistent. The porosity of the samples with four different cementation contents increased with the number of wetting–drying cycles and finally reached a stable porosity [31]. Among them, the porosity change rates of samples RU1-4 and RU3-4 were basically the same, and the porosity change rate of sample RU4-10-1 was basically the same as that of sample WD-3, but the porosity change rate of sample RU2-4 was more complex than that of the other three samples. The equilibrium porosity histogram of Figure 6d shows that the porosity of the four samples followed the order of RU2-4 > RU4-10-1 > RU3-4 > RU1-4.
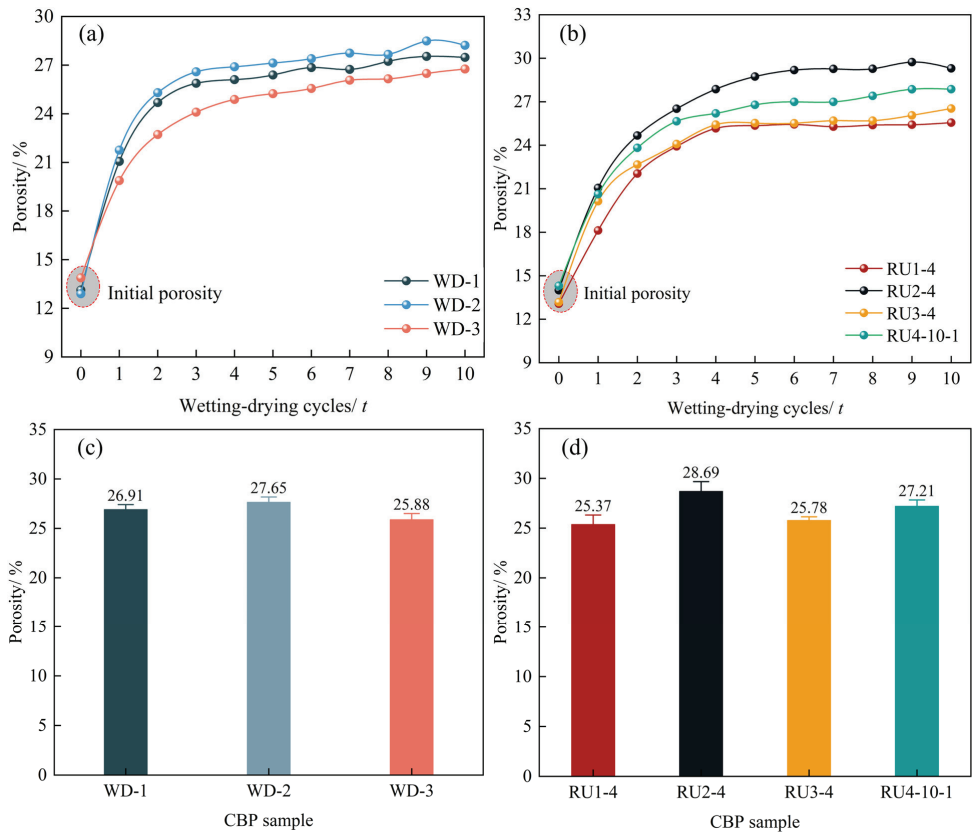

Figure 6. Changes in porosity of (**a**) samples WD-1, 2, 3 and (**b**) samples RU1, 2,3-4 and RU4-10-1 with with wetting-drying cycles; average values of porosity of (**c**) samples WD-1, 2, 3 and (**d**) samples RU1, 2,3-4 and RU4-10-1 after the fourth wetting-drying cycle.

3.2. Variation in Mechanical Properties

3.2.1. Stress–Strain Curve

Figure 7a–c shows the CPB stress–strain curve for 0–10 wetting–drying cycles. The results show that, with the increase in the number of wetting–drying cycles, the original pore compaction stage of CPB increased, the peak stress decreased and the peak strain increased. In the process of 0–10 wetting–drying cycles, the stress–strain curve shows an S-type shape; the CPB had high compressibility and plastic–elastic-plastic characteristics. With 0–3 wetting–drying cycles, the CPB cementation strength was high, the surface of the sample remained intact and the internal pores and microcracks were underdeveloped. As shown in Figure 5, the original pore compaction stage was shortened, the change rate of the stress–strain curve was fast and the peak stress changed greatly, but the peak strain was not much different. In the process of 4–10 wetting–drying cycles, the pores and voids in the sample increased, resulting in a weak CPB cementation ability, low strength, gentle stress–strain curve slope, a small change in the peak stress and a large change in the peak strain.
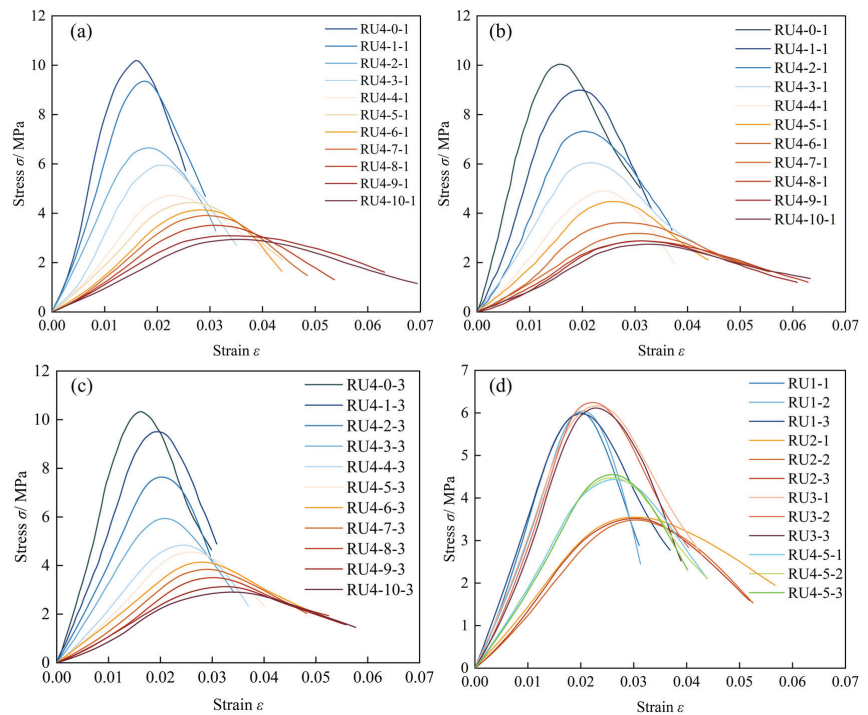
Figure 7. Stress-strain curves of (**a**) RU4-0~10-1, (**b**) RU4-0~10-2, (**c**) RU4-0~10-3, (**d**) RU1-1~3, RU2-1~3, RU3-1~3, RU4-5-1~3 under different wetting-drying cycles.

Figure 7d shows the stress–strain curves of CPB samples with different composite binders after five wetting–drying cycles. The cementation strength of samples RU1 and RU3 was significantly greater than that of samples RU2 and RU4. Among them, the peak strength of RU1 and RU3 was approximately 6.00 MPa. The strength of the CPB samples with the four different composite cementing materials followed the order of RU1 ≈ RU3 > RU4 > RU2, indicating that CPB samples with only normal Portland cement or mixed with sulphoaluminate cement have better anti-degradation performance during wetting–drying cycles. However, the cementation performance of the samples mixed with gypsum is poor. The greater the amount of incorporation, the worse the performance of the sample after the wetting–drying cycle, and the more serious the deterioration of the sample.

The peak strain of samples RU1 and RU3 was significantly smaller than that of RU2 and RU4, and RU2 > RU4, suggesting ductile failure [58]. From the original pore compaction stage, the order of the compression time was RU2 > RU4 > RU3 > RU1. RU2 > RU4 because, for sulfate cement in the early stages, the higher the heat of hydration [59], the more dry shrinkage and bubbles, so that the addition of sulfate cement to normal Portland cement increases the initial porosity. RU3 > RU1, because gypsum also forms more small bubbles in the early hardening process, and in the subsequent wetting–drying cycle, gypsum and clay minerals react with water to hydrate, resulting in an increase in pores in the sample [60].

3.2.2. Failure Mode and Characteristics

In 1960, Griggs performed a statistical analysis to classify rock uniaxial compression failure. According to the strain corresponding to the peak stress in the stress–strain curve, rock deformation can be divided into brittle failure, brittle–ductile transition failure and ductile failure [58]. Figure 7 shows that the strain value of the CPB sample to reach the peak stress is between 1.5% and 3.5%. If there is a relatively complete stress–strain curve, the CPB sample is judged to be in ductile failure. This is consistent with the results of Zhao et al. [61]. Bobet and Einstein [62] carried out uniaxial compression tests on prefractured gypsum samples and proposed a mechanism of crack coalescence under uniaxial compression: the mechanism of shear coalescence is usually characterized by a crack propagation path with twists and turns, rough crack edges, and more broken particles in the sample; the tensile penetration shows that there are no broken solid particles on the crack surface, and the crack edge is relatively smooth. Shear and tensile coalescence conforms to failure between the two. Combined with Figure 8, it was found that there are fewer main cracks in samples RU4-0, RU4-1, RU1 and RU3, and that there are fewer secondary cracks around the main cracks. The edge of a crack is relatively regular, but there is local falling debris. Therefore, it was determined that the penetration form of these CPB cracks is shear and tensile penetration. The main cracks of RU2 and RU4-2~RU4-9 are more numerous, and the crack propagation path, with more secondary cracks, is more tortuous and prone to form debris and cause debris falls, which indicates that the crack coalescence form of these samples is shear coalescence. This shows that the crack propagation of CPB is not only affected by the particle size distribution and mechanical damage but also related to the properties of the cementing materials and wetting–drying cycle damage.

The uniaxial compression failure mode of CPB with a composite cementing material ratio of 8:1:1 under 0–10 wetting–drying cycles is shown in Figure 8. The number of wetting–drying cycles had a significant effect on the damage morphology of the CPB. In the CPB that was not affected by the wetting–drying cycling, the main crack gradually expanded along the loading direction, and the two main cracks were obviously parallel to the axial stress direction, accompanied by more secondary cracks. When the compression energy reached the critical value, the local surface of the sample exhibited a spalling phenomenon and, finally, the main crack penetrated the sample instability failure, as shown in Figure 8 (RU4-0). The angle between the main crack and the axial stress direction of the sample with one wetting–drying cycle gradually increased, the secondary cracks were smaller and small debris appeared in localized places at the end, as shown in Figure 8 (RU-1). After two–four wetting–drying cycles of the sample, the main crack direction was diagonal across the sample, and the number of main cracks gradually increased. The surface of the sample exhibited a small amount of large pieces of falling debris and more broken small pieces. The end of the sample damage was more seriously damaged, and the sample exhibited obvious shear failure, as shown in Figure 8 (RU4-2~RU4-4). After five–six wetting–drying cycles of the samples, the main crack direction and the axial stress direction were approximately 45°, there were fewer secondary cracks, the lateral expansion of the samples under pressure was obvious and only a small number of debris falls occurred, since the samples exhibited significant shear failure, as shown in Figure 8 (RU4-5 and RU4-6). After seven–nine wetting–drying cycles of the sample, the main crack directions were roughly the two diagonal directions of the samples, the main crack development was

good and there were more secondary cracks and microcracks. However, after the failure of the sample, there were only small pieces of falling debris, and the sample showed obvious shear failure, as shown in Figure 8 (RU4-7~RU4-9).
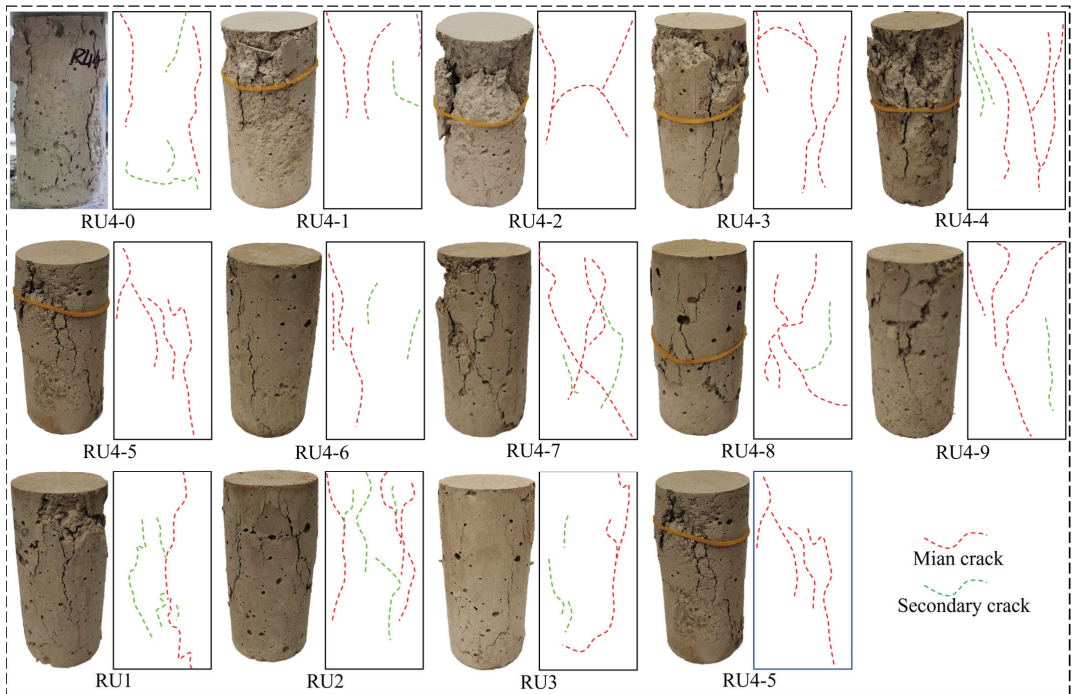
**Figure 8.** Failure characteristics of CPB samples (RU4-0~9 and RU1~3).

The uniaxial compression failure modes of CPB with different composite binder ratios under five wetting–drying cycles are shown in Figure 8. For sample RU1, with a composite cementing material ratio of 10:0:0, under axial stress loading, a main crack began to gradually expand along the loading direction, accompanied by many secondary cracks. The direction of the secondary crack was roughly parallel to the direction of the axial stress. As the stress value continued to increase, a small piece of debris spalled off at the end of the sample, and the main crack eventually penetrated the entire sample until the entire sample was destabilized. In the process of axial stress loading, sample RU2 with a ratio of 8:0:2 of the composite cementing material produced multiple main cracks and gradually penetrated the middle and lower sides of the sample; the secondary cracks were more developed. The lateral expansion of the sample was obvious, and only a small amount of debris fell, showing ∧-type shear failure. Sample RU3, with a composite cementing material ratio of 8:2:0, produced only one main crack after the sample was destroyed. The main crack gradually expanded from top to bottom, and some secondary cracks were generated locally. The failure characteristics of RU4-5 with a composite cementing material ratio of 8:1:1 are analyzed in Figure 8.

3.2.3. Variation in Cementation Strength

(1)   Effects of wetting–drying cycles on UCS and EM

The UCS and EM changes in CPB under different numbers of wetting–drying cycles are shown in Figure 9a,b. The wetting–drying cycling had a significant effect on the UCS and EM. As the number of wetting–drying cycles increased, the UCS and EM decreased exponentially. In zero–five wetting–drying cycles, the UCS decreased by 0.91 MPa, 2.9 MPa,

4.21 MPa, 5.58 MPa and 5.84 MPa, respectively, and the EM decreased by 0.28 GPa, 0.45 GPa, 0.59 GPa, 0.72 GPa and 0.76 GPa, respectively. For zero–four cycles, the wetting–drying cycles had a significant effect on the UCS and EM, and the EM changed the most after the first wetting–drying cycle. The degree of deterioration of CPB by a wetting–drying cycle first increased and then decreased and then increased and decreased, gradually reaching a stable trend. The degradation degree of the UCS under two–four wetting–drying cycles was 21.47%, 18.05% and 22.87%, respectively, and the average degradation degree was 20.80%. Among them, the degradation degree due to the fourth cycle was the largest observed, the rest of the degradation degrees were below 9.27% and the average degradation degree of the UCS under five–ten wetting–drying cycles was 7.53%. This shows that two–four wetting–drying cycles had a great influence on the UCS, among which the fourth wetting–drying cycle had the greatest degree of deterioration, and the five–ten wetting–drying cycles had a relatively stable degree of deterioration. The degree of deterioration of the EM for two–four wetting–drying cycles was 28.12%, 23.89%, 25.71% and 32.50%, respectively, and the average degree of deterioration was 27.56%. Among them, the fourth wetting–drying cycle had the greatest degree of EM deterioration, and the remaining degrees of deterioration were below 13.37%, indicating that zero–four wetting–drying cycles had a significant impact on the deterioration of the EM, and the average degree of deterioration of the EM was greater than that of the UCS, indicating that the EM was more sensitive to wetting–drying cycles than the UCS.
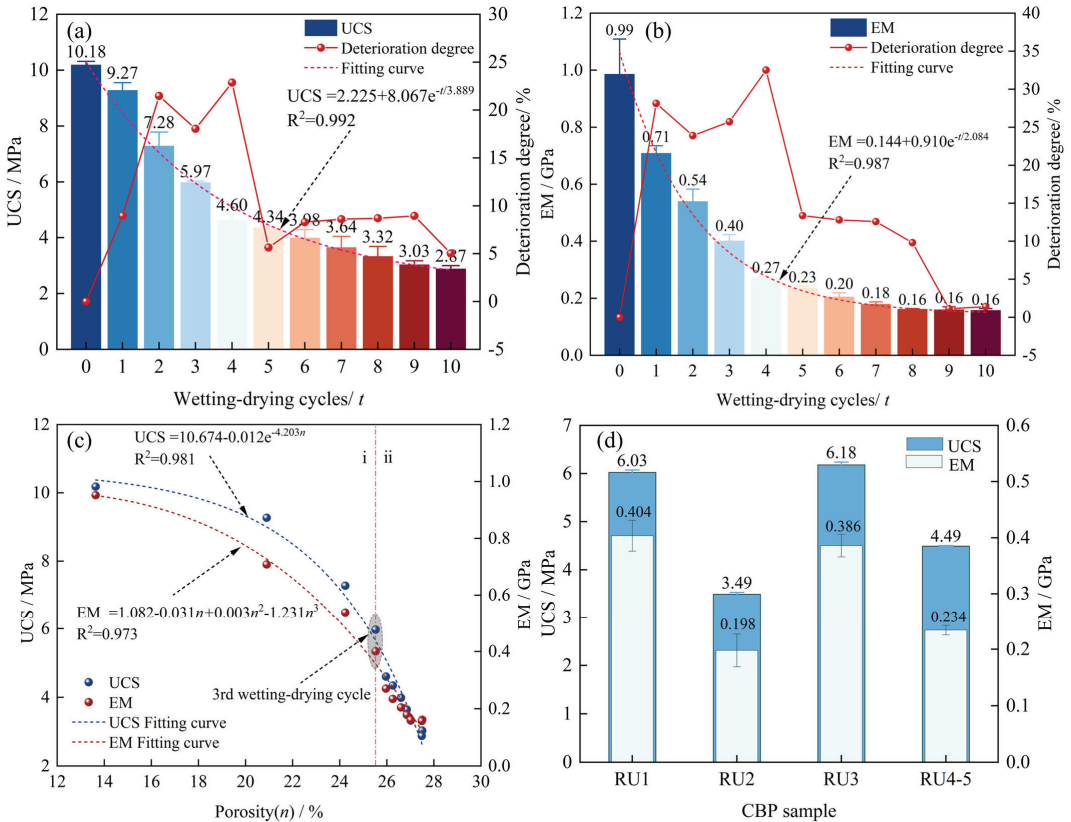
Figure 9. (**a**,**b**) The changes in and deterioration degrees of UCS and EM with wetting–drying cycles, respectively. (**c**) The relationship between UCS, EM and porosity. (**d**) Effect of different cementing materials on CPB strength.

(2)   Variation in UCS and EM with porosity

To further analyze the relationship between UCS and EM and porosity, Figure 9c was drawn. The UCS decreased exponentially with increasing porosity n. However, the EM decreased in the form of a quadratic function with increasing porosity n. According to the rate of change in the UCS and EM curves with porosity, these curves were roughly divided into an initial deterioration stage i and a secondary deterioration stage ii. In the initial deterioration stage i, UCS and EM decreased slowly with increasing porosity, indicating that the porosity had little effect on the UCS and EM at this stage. In the secondary deterioration stage ii, with the increase in porosity, the change rate of the UCS and EM curves was accelerated, indicating that the porosity had a significant effect on the UCS and EM.

(3)   The change in CPB bond strength of different composite cementing materials

Figure 9d shows that the CPB bond strengths of composite cementitious materials with different contents after five wetting–drying cycles were quite different. The average UCS results of RU1 and RU3 were 6.03 MPa and 6.18 MPa, respectively. The average UCS results of RU2 and RU4-5 were 3.49 MPa and 4.49 MPa, respectively. The average UCS results of RU1 and RU3 (6.11 MPa) were higher than the 75.07% and 36.08% of RU2 and RU4-5, respectively. The average EM results of RU1 and RU3 (0.395 GPa) were higher than those of RU2 and RU4-5 by 99.49% and 68.80%, respectively. The UCS and EM of the RU1 and RU3 series of samples with ratios of 10:0:0 and 8:2:0 were similar and higher, and the UCS and EM of the RU2 and RU4 series of samples with ratios of 8:0:2 and 8:1:1 were lower. The CPB strength of the four composite cementing materials followed the order of RU1 ≈ RU3 > RU4-5 > RU2.

3.3. Damage Evolution

According to the experimental data of the stress–strain curves of CPB samples under different numbers of wetting–drying cycles in the UCS test, the strain values (peak strain) corresponding to UCS, EM and UCS were obtained. The physical and mechanical parameters m and $1/m$ of CPB samples were obtained by substituting them into Equation (13), and the CPB damage constitutive equation was calculated, as shown in Table 2.

Table 2. Parameter value and equation of the damage constitutive model for marl paste samples.

Sample Number	EM/MPa	UCS/MPa	Strain ε	m	$1/m$	Damage Constitutive Equation
RU4-0-1	1009.16	10.225	0.0159	2.223	0.450	$\sigma = 1009.16\varepsilon \exp\left(-0.450(\varepsilon/0.0159)^{2.223}\right)$
RU4-2-1	469.73	6.666	0.0182	4.069	0.246	$\sigma = 496.73\varepsilon \exp\left(-0.246(\varepsilon/0.0182)^{4.069}\right)$
RU4-4-1	286.97	4.723	0.0228	3.055	0.327	$\sigma = 286.97\varepsilon \exp\left(-0.327(\varepsilon/0.0228)^{3.055}\right)$
RU4-6-1	203.61	4.149	0.0284	3.073	0.325	$\sigma = 203.61\varepsilon \exp\left(-0.325(\varepsilon/0.0284)^{3.073}\right)$
RU4-8-1	160.52	3.519	0.0314	2.781	0.360	$\sigma = 160.52\varepsilon \exp\left(-0.360(\varepsilon/0.0314)^{2.781}\right)$
RU4-10-1	112.66	2.951	0.0359	3.185	0.314	$\sigma = 112.66\varepsilon \exp\left(-0.314(\varepsilon/0.0359)^{3.185}\right)$

The parameters in Table 2 were brought into Equation (15) to obtain the damage variable evolution curves of CPB samples under different wetting–drying cycles, as shown in Figure 10. There were significant differences in D_W for different wetting–drying cycles. As the number of wetting–drying cycles increased, D_W increased. In general, compared with CPB samples without wetting–drying cycles, the influence of the first three wetting–drying cycles were the largest for D_W, and the values were between 0 and 0.562. The D_W variation during four–ten wetting–drying cycles was relatively small, and its value was between 0.716 and 0.888. The damage accumulation of the CPB sample gradually slowed, namely, the axial strain gradually increased. The damage variable of the CPB sam-

ple reached one in a large strain range. The evolution curve of the total damage variable showed an S shape and was divided into four stages (taking CPB samples without wetting–drying cycles as an example). The initial damage stage I: there were microcracks in the CPB at this stage, and the microcracks gradually closed under uniaxial loading. In a small strain range, the CPB remains. Accelerated damage propagation stage II: in this stage, with the increase in the load, the microcracks inside the CPB developed rapidly, resulting in the dislocation and connection of pores and cavities; the total damage value increased rapidly, and the CPB peak strength was reached. Damage decelerated propagation stage III: the microcracks and voids inside the CPB were connected, so that the CPB gradually lost its bearing capacity, and the total damage value gradually approached one. End of damage stage IV: the CPB internal cracks broke through to the surface, and the CPB completely lost its bearing capacity, so the total damage value remained unchanged at one.
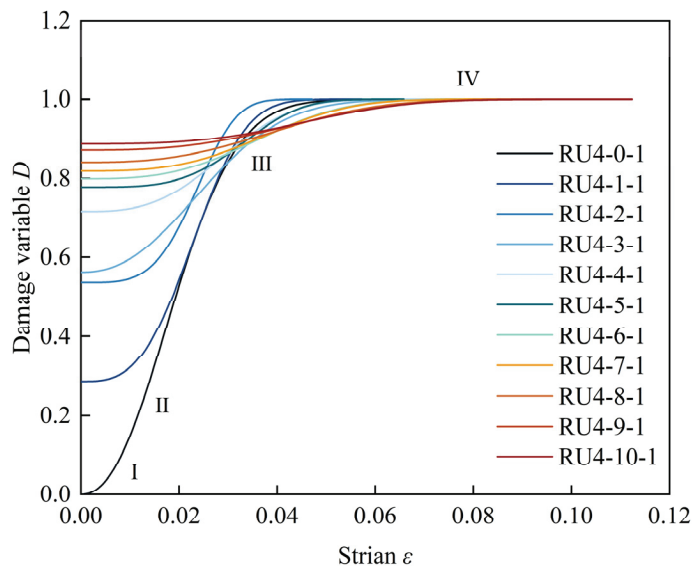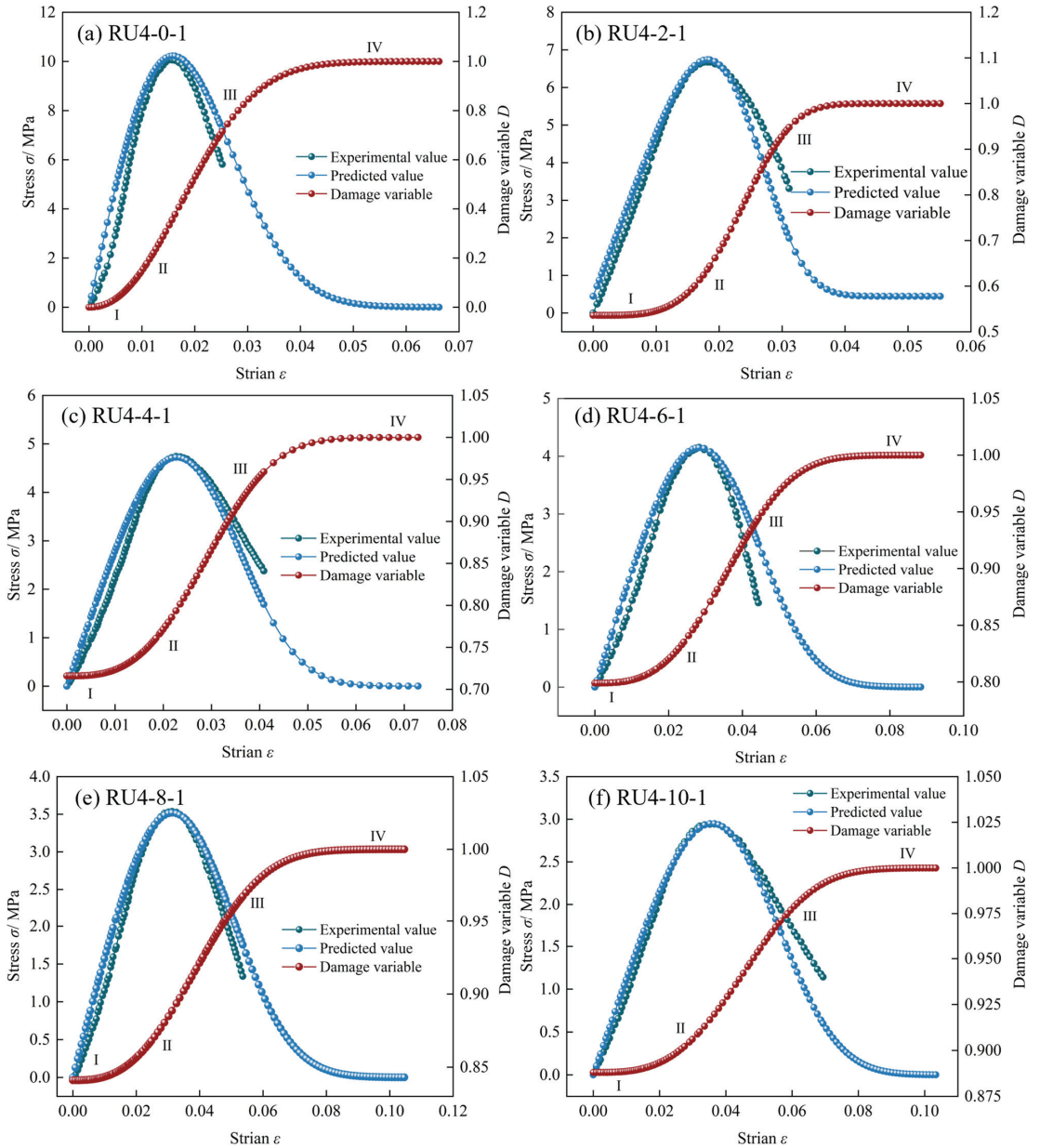

Figure 10. Damage variable curve of CPB samples.

The parameters in Table 2 were brought into Equation (16) to obtain the damage constitutive equation of CPB under different wetting–drying cycles. According to the damage constitutive equation, the theoretical prediction curve and the measured curve were drawn, as shown in Figure 11. It can be seen from the figure that the theoretical prediction curve is in good agreement with the measured curve, which indicates that the established damage constitutive model is reasonable and reliable and can provide a reference for the CPB filling design of open-pit mines.

3.4. Deterioration Mechanism of the Microstructure

For CPB samples under zero–four wetting–drying cycles, small pores developed, and the overall structure was relatively dense. The internal hydration products of the CPB were analyzed. As the number of wetting–drying cycles increased, the number of ettringite grains with longer needle bar lengths increased, and the remaining hydration products remained basically unchanged. Compared with CPB samples without wetting–drying cycles, small particles fell off of the surface of the CPB internal cement during the second and fourth wetting–drying cycles, as shown in Figure 12a–c. For the CPB samples that underwent 8 and 10 cycles, the surface voids of the cement were more developed, the traces of large particles falling off were obvious, many small cracks appeared and the structure of the cement was seriously damaged, but the cement still maintained a large structure.

Large cracks appeared along the edge of the aggregate, the connection between the cement and the aggregate was poor and the whole sample was in a loose state. The number of internal ettringite was small, and the calcium silicate hydrate (C-S-H) distribution gradually changed from a network distribution to a coral and cluster distribution. The spherical contour of aluminum glue gradually became obvious, the internal macropores were well connected and the porosity was relatively large, as shown in Figure 12d–f.

Figure 11. Stress-strain test and theoretical curve and damage variable curve of CPB samples. I is initial damage stage, II is accelerated damage propagation stage, III is damage decelerated propagation stage and IV is end of damage stage (**a**–**f**).
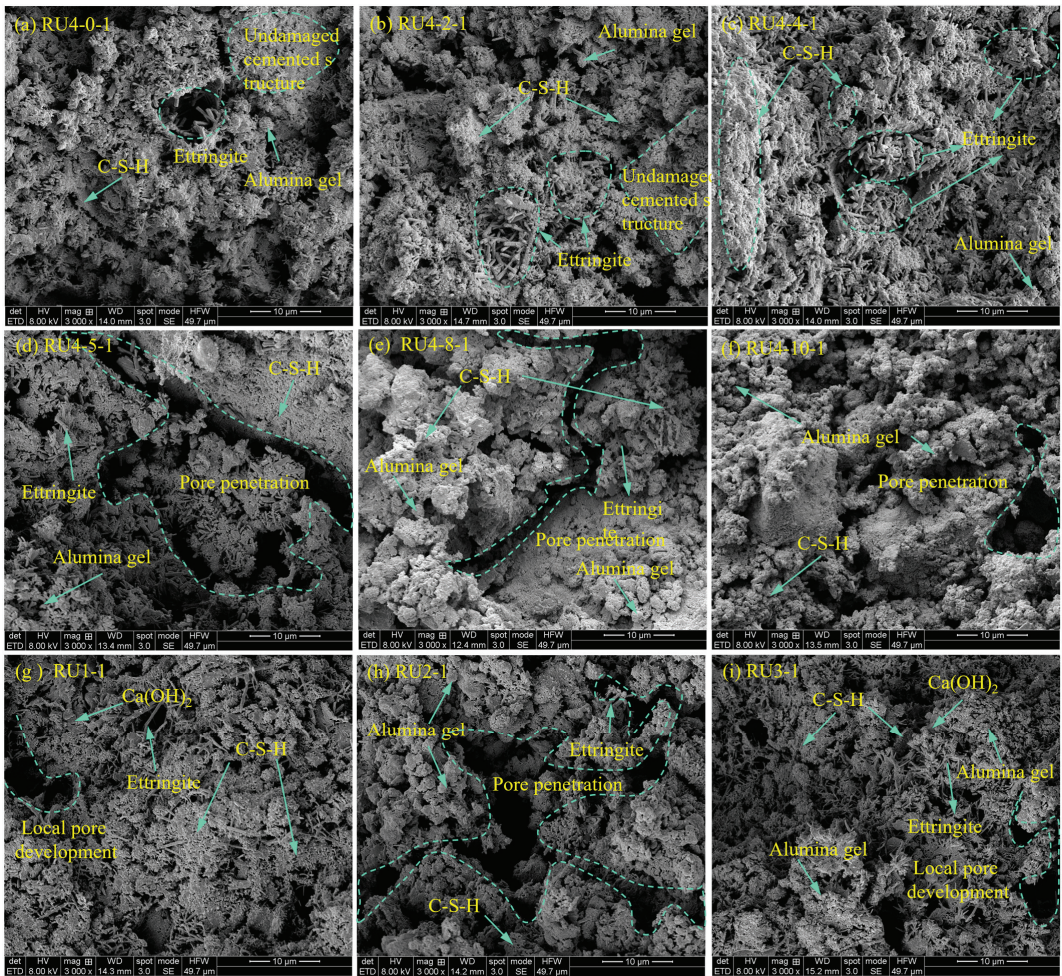
Figure 12. SEM images of CPB samples.

From the comparison of the density of CPB samples, RU1-1 and RU3-1 were denser, followed by RU4-5-1, and RU2-1 was the worst. Regarding the development of microcracks on the surface of the cement, RU2-1 and RU4-5-1 developed well, and RU1-1 and RU3-1 had a low degree of microcrack propagation. The damage degrees of the cement followed the order of RU2-1 > RU4-5-1 > RU1-1, RU3-1. Comparing the quantity and structure of the hydration products, the quantity of ettringite followed the order of RU1-1, RU3-1 > RU4-5-1 > RU2-1. For RU2-1 > RU4-5-1 > RU1-1, RU3-1, RU2-1 and RU4-5-1, the macropores gradually penetrated, whereas for RU1-1 and RU3-1, local pores penetrated, as shown in Figure 12d,g,h.

4. Discussion

The common methods for recovering coal resources in the highwall of open-pit coal mines include continuous miner highwall mining [52], timeliness slope theory [63], steep end-slope mining [64] and filling roadway mining [65]. Timeliness slope theory and steep end-slope mining technology further increase the mining angle of the slope and complete the coal mining of the limit mining angle of the highwall within a certain period but cannot solve the problem of coal mining under the highwall [66]. The filling roadway mining

technology of highwall roadways overcomes the limit of steep end-slope mining technology, but it is restricted according to the relevant national regulations and mining costs [67]. At present, continuous miner highwall mining is used to mine near-horizontal and gently inclined coal seams in the highwall, and many coal pillars are retained, making the recovery rate of the coal resources less than 50% [51]. Therefore, based on the technology of continuous highwall mining of the overlying coal seam under the highwall, the waste is used as CPB aggregate to backfill the adit (Figure 4a) to realize the utilization of solid waste and the recovery of coal resources with maximum efficiency. To better realize the concept of ecological restoration during mining and reclamation [68], in the integrated collaborative operation of stripping–mining–transportation–filling/dumping–reclamation in open-pit mines (Figure 4b), it is necessary to emphasize the coordination, cooperation and synchronization among various mining processes and reclamation processes. The synergistic attributes and the synergistic effects generated reflect the spatiotemporal relationship among the stripping, mining, transportation, filling, dumping and reclamation projects in open-pit mines. An orderly design considering time, space and level is established, and unified planning and parallel operation are carried out to form a process system of collaborative mining of the same open-pit mine, the coordinated disposal of solid waste and common reclamation.

A wetting–drying cycle had a significant effect on the physical and macroscopic mechanical properties of CPB. In a wetting–drying cycle, CPB samples produced a certain number of microcracks and cracks, as shown in Figure 5a–k. This was because there was no water bonding on the surface of a CPB sample, but there was a temperature difference between the inside and outside of the sample, resulting in thermal expansion and contraction. The surface of the sample lost water quickly, and the surface tension was less than the internal tension. Under the combined action of gravity and tension at the bottom of the sample, many microcracks were generated. With the increase in the number of wetting–drying cycles, the position of microcracks on the surface of CPB samples was continuously damaged by wetting–drying cycles, resulting in the water–rock chemical reaction of clay minerals and gypsum on the surface, so that microcracks gradually expanded into cracks [26]. The main reason for the cracks in Figure 5l–s was that the greater the proportion of gypsum in the CPB samples, the greater the promoting effect of temperature on the formation of ettringite [69]. The greater the number of wetting–drying cycles, the higher the probability of expansion of the ettringite in the sample, which caused the internal stress in the CPB samples to expand and crack the original skeleton of the sample, resulting in expansion cracking [70,71]. With the development of microcracks and cracks on the surface of CPB samples, gypsum aggravates the propagation of cracks, which is extremely unfavorable to the integrity of the samples.

According to past research on cementing materials under wetting–drying cycles, the main reasons for the deterioration of CPB in stage i are the loss of small particles from the CPB skeleton, the water–rock chemical reactions of clay minerals and the development of microcracks and cavities. CPB is formed by the consolidation and demolding of particles with different sizes as aggregates under the hydration reaction of composite cementitious materials. Among them, particles with particle sizes less than 0.3 mm account for 13.93%, which form noncritical cements with composite cementing materials [22] and fill the spaces between larger particles. During a drying–wetting cycle, these noncritical cements are destroyed, and small particles are detached from the cements [72] and are transported to the distilled water through pores and microcrack channels, resulting in noncritical cements. A loose, weak cementation ability can also be observed in Figure 12a–c. According to the mineral composition analysis of marl, it contains 24.50% clay minerals, and these clay minerals include illite (44%), illite–smectite mixed-layer minerals (36%) and kaolinite (20%), as shown in Figure 2. Illite and illite–smectite mixed-layer minerals are highly hydrophilic minerals [24]. During the immersion process, it was found that the color of the distilled water mixture gradually turned pale yellow after immersion, which was speculated to be caused by the loss of the water–rock chemical reaction from illite and illite–smectite

mixed-layer minerals to distilled water [32]. This phenomenon caused the disintegration of illite and illite–smectite mixed-layer minerals, a loss of connection between clay particles or between clay particles and noncritical cements [37], the expansion of noncritical cements and an increase in noncritical cement pores [29]. Under the action of wetting–drying cycles, the clay particles repeatedly underwent expansion–contraction or even disintegration (the process mechanism is shown in Figure 13), until they detached from the cement. Under the action of water gravity, the water carried small particles, such as detached clay particles, flowing from the pores and initial microcracks [73], resulting in the loss of some fine aggregate particles inside the CPB before the four wetting–drying cycles. In addition to the weakening of the cementation ability of the noncritical cements, the microcracks and voids generated inside the CPB during the consolidation and demolding process still dominated the mechanical failure performance of the first three wetting–drying cycles [31,60].

(a) Dry clay grains   (b) Soaked clay grains   (c) Dried clay grains
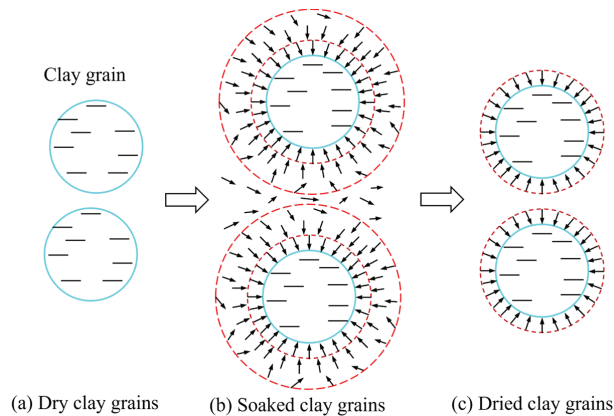
Figure 13. Clay grain expansion process of cement.

In the degradation stage (stage ii), the loss of small particles, clay minerals and cements in the CPB decreased, and its UCS and EM decreased rapidly. Because cement is the main component of CPB, it is mainly the hydration product of the composite binder [74]. As the number of wetting–drying cycles increases, the hydration products in the cement at the critical steady state frequently undergo a water absorption–dehydration process, and these hydration products are easily converted at a certain [75]. When the ettringite growth reaches a certain level, at temperatures above 65 °C, some of the ettringite will decompose to form delayed ettringite [76]. When the temperature reaches 95 °C, the ettringite will disappear quickly and become difficult to observe [69]. Some other ettringite absorbs a large amount of water molecules, causing repulsion between the particles, resulting in expansion [77] and causing the cement in the critical stable state to be destroyed (Figure 12d–f), resulting in an increase in the number of internal cracks in the CPB and the gradual development of microcracks. Finally, although the number of wetting–drying cycles increased, the UCS and EM basically remained stable, indicating that the key cements and aggregates in the CPB form a relatively stable skeleton [22] and are not easily affected by wetting–drying cycles.

CPB with composite cementitious ordinary Portland cement and sulfoaluminate cement has better resistance to the deterioration of wetting–drying cycles, while CPB with gypsum has poor water resistance (Figure 5l–s) (Durgun, 2020), and the more gypsum that is added, the less stable the strength of CPB (Figure 9d). From the variation in UCS and EM, EM is more sensitive to gypsum incorporation than UCS. Although some hydration products in CPB with normal Portland cement and sulfoaluminate cement are degraded, they still maintain a relatively complete cementation structure, so they can maintain a higher UCS and EM. However, too much ettringite may be generated in CPB with too much added gypsum [78], which accelerates the development of pores and microcracks

and destroys the bonding structure (Figure 12g–i), resulting in a weakened resistance to deformation and decreased compression resistance.

There were significant differences in D_W between different wetting–drying cycles, and D_W increased with an increasing number of wetting–drying cycles [79]. With the increase in axial strain, the total damage variable evolution curve of CPB presented an 'S' shape, and Song et al. [80] and Wang et al. [41]) also obtained this conclusion. CPB deformation to failure is a progressive damage process [81].

Based on the above, for the CPB backfill of open-pit coal mines with frequent groundwater activities and frequent rainfall, especially backfill with aggregates with a high clay mineral content, it is necessary to strengthen waterproofing and drainage measures. The upper bench of the adit is also protected by a flood dam, and flood protection is provided at the adit entrance to ensure that surface precipitation does not enter the adit and affect the stability of the coal pillar, the filling body and the roof of the adit. The exposed areas of the filled adit are protected by sprayed concrete to minimize the deterioration of the filling body wetting–drying cycles weathering. Carefully consider the amount of gypsum added, and pay attention to CPB softening in water to prevent slope failure due to the deterioration of the physical and mechanical properties of the CPB and weak layer sliding.

5. Conclusions

(1) The highwall filling mining method and the stripping–mining–transportation–filling/dumping–reclamation integrated operation scheme are proposed to achieve solid waste utilization and improve the recovery rate of coal resources in an open-pit coal mine.

(2) The wetting–drying cycles and added gypsum accelerated the development of microcracks and cracks on the CPB surface. The higher the gypsum content, the further developed the microcracks and cracks on the surface of the CPB after five wetting–drying cycles, which was not conducive to the strength stability of CPB, and EM was more sensitive to gypsum incorporation than UCS.

(3) With the increase in the number of wetting–drying cycles, the porosity increased gradually and tended to be stable after four cycles. The tested CPB showed ductile failure. The crack coalescence form of the CPB during the 0–3 wetting–drying cycles was shear and tensile coalescence, and that during the 4–10 cycles was shear coalescence. Both UCS and EM decreased exponentially with the increase in the number of wetting–drying cycles, but they decreased exponentially and cubically, respectively, with the increase in porosity.

(4) The initial degradation stage of the CPB was caused by the loss of small particulate matter from the skeleton, the water–rock chemical reaction of clay minerals and the development of original microcracks and cavities. The main reason for the secondary deterioration stage was the destruction of the cement in the critical stable state formed by the hydration products.

(5) With the increase in the number of wetting–drying cycles, the initial damage degree of the CPB increased continuously. The damage to the CPB during the zero–three wetting–drying cycles was the largest observed, and the evolution curve of the total damage variable showed an 'S' shape. The proposed damage constitutive model of CPB is reasonable and reliable and can provide a reference for CPB filling design in open-pit coal mines.

Author Contributions: Conceptualization, T.C.; Methodology, T.C.; Software, J.L.; Validation, J.S.; Formal analysis, J.S.; Investigation, Z.T.; Resources, Z.T.; Data curation, L.H.; Writing—original draft, L.H.; Writing—review & editing, J.L.; Visualization, Z.T.; Supervision, L.H.; Funding acquisition, J.S. All authors have read and agreed to the published version of the manuscript.

Appendix A

Table A1. Physical properties of marl after crushing.

Numbering	Particle Size Distribution (mm)					Fractal Dimension FD	Match Index R^2
	<0.300	0.300–0.600	0.600–1.180	1.180–2.360	2.360–4.750		
1	13.93	7.04	11.44	11.62	55.97	2.40	0.947
2	11.40	13.18	14.56	10.48	50.38	2.34	0.986
3	12.41	9.73	13.87	11.56	52.43	2.36	0.979
4#	11.34	11.32	12.16	18.87	46.31	2.37	1.000

Table A2. Key parameters of X'Pert Pro MPD.

Model	X'Pert Pro MPD
Manufacturer	Nalytical, Netherlands
X-ray tube	Copper target
Maximum power	2.2 kW
Maximum tube voltage	60 kV
Maximum tube current	55 mA
Diffraction angle	1°~160°

Appendix B

Table A3. Chemical composition statistics of marl (%).

Sample	CaO	SiO_2	Al_2O_3	Fe_2O_3	MgO	K_2O	TiO_2	SO_3	Other
Marl	39.78	33.23	14.76	5.90	2.50	2.22	0.70	0.62	0.29

Table A4. Chemical composition statistics of normal Portland cement (%).

Sample	CaO	SiO_2	Al_2O_3	SO_3	Fe_2O_3	MgO	Ignition Loss
Normal portland cement	49.70	22.60	9.87	3.84	3.50	2.06	8.43

Table A5. Statistics of chemical composition of sulphate aluminum cement (%).

Sample	CaO	Al_2O_3	SO_3	SiO_2	Fe_2O_3	MgO	TiO_2	Ignition Loss
Sulphatealuminium cement	45.30	18.40	12.50	7.23	4.30	1.35	0.87	10.05

Table A6. Chemical composition statistics of gypsum (%).

Sample	SO_3	CaO	Al_2O_3	SiO_2	Fe_2O_3	SrO
gypsum	59.92	39.76	0.13	0.11	0.04	0.04

Table A7. Key parameters of electric blast drying oven.

Model	HS-DHG-9070A
Power supply voltage	AC220V $\pm$ 10%, 50 Hz $\pm$ 1 Hz
Heating power	1050 W
Working temperature	Room temperature~200 °C
Temperature control accuracy	$\pm$0.1 °C
Timing device	0~9999 h

Table A8. Key parameters of Scanning Electron Microscope.

Model	FEI-QUANTA-FEG 250
Resolution	1.04 nm
Magnification	15~300,000
Accelerating voltage	0.2~30 kV
Searching current	0.3–22 nA

Appendix C
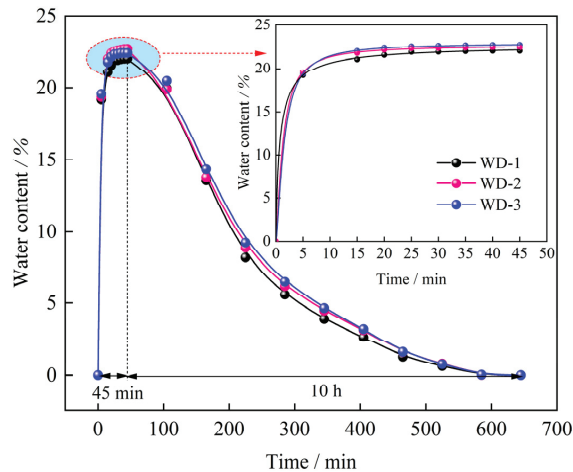
Figure A1. Variation in the water content of marl paste samples with time.

References

1. Li, M.; Zhang, J.; Li, A.; Zhou, N. Reutilisation of coal gangue and fly ash as underground backfill materials for surface subsidence control. *J. Clean. Prod.* **2020**, *254*, 120113. [CrossRef]
2. Cheng, W.; Lei, S.; Bian, Z.; Zhao, Y.; Li, Y.; Gan, Y. Geographic distribution of heavy metals and identification of their sources in soils near large, open-pit coal mines using positive matrix factorization. *J. Hazard. Mater.* **2020**, *387*, 121666. [CrossRef]
3. Li, J.; Yan, X.; Cao, Z.; Yang, Z.; Liang, J.; Ma, T.; Liu, Q. Identification of successional trajectory over 30 Years and evaluation of reclamation effect in coal waste dumps of surface coal mine. *J. Clean. Prod.* **2020**, *269*, 122161. [CrossRef]
4. Rodríguez-Galán, M.; Baena-Moreno, F.M.; Vázquez, S.; Arroyo-Torralvo, F.; Vilches, L.F.; Zhang, Z. Remediation of acid mine drainage. *Environ. Chem. Lett.* **2019**, *17*, 1529–1538. [CrossRef]
5. Porsani, J.L.; de Jesus, F.A.N.; Stangari, M.C. GPR Survey on an Iron Mining Area after the Collapse of the Tailings Dam I at the Córrego do Feijão Mine in Brumadinho-MG, Brazil. *Remote. Sens.* **2019**, *11*, 860. [CrossRef]
6. Weiler, J.; Firpo, B.A.; Schneider, I.A. Technosol as an integrated management tool for turning urban and coal mining waste into a resource. *Miner. Eng.* **2020**, *147*, 106179. [CrossRef]
7. Pappas, D.M.; Vallejo, L.E. The settlement and degradation of nondurable shales associated with coal mine waste embankments. *Int. J. Rock Mech. Min. Sci.* **1997**, *34*, 241. [CrossRef]
8. Karimaei, M.; Dabbaghi, F.; Sadeghi-Nik, A.; Dehestani, M. Mechanical performance of green concrete produced with untreated coal waste aggregates. *Constr. Build. Mater.* **2020**, *233*, 117264. [CrossRef]

9. Kua, T.-A.; Arulrajah, A.; Horpibulsuk, S.; Du, Y.-J.; Shen, S.-L. Strength assessment of spent coffee grounds-geopolymer cement utilizing slag and fly ash precursors. *Constr. Build. Mater.* **2016**, *115*, 565–575. [CrossRef]

10. Amir, M.; Morteza, R. Application of coal waste powder as filler in hot mix asphalt. *Constr. Build. Mater.* **2014**, *66*, 476–483. [CrossRef]

11. Taha, Y.; Benzaazoua, M.; Hakkou, R.; Mansori, M. Coal mine wastes recycling for coal recovery and eco-friendly bricks production. *Miner. Eng.* **2017**, *107*, 123–138. [CrossRef]

12. Weiler, J.; Firpo, B.; Schneider, I. Coal waste derived soil-like substrate: An opportunity for coal waste in a sustainable mineral scenario. *J. Clean. Prod.* **2018**, *174*, 739–745. [CrossRef]

13. Sobolczyk-Bednarek, J.; Choińska-Pulit, A.; Łaba, W. Biosolubilization of low-rank coal by the newly isolated strain *Streptomyces fulvissimus* K59. *Fuel* **2021**, *301*, 121082. [CrossRef]

14. Skripkina, T.; Bychkov, A.; Tikhova, V.; Smolyakov, B.; Lomovsky, O. Mechanochemically oxidized brown coal and the effect of its application in polluted water. *Environ. Technol. Innov.* **2018**, *11*, 74–82. [CrossRef]

15. Mo, S.; Canbulat, I.; Zhang, C.; Oh, J.; Shen, B.; Hagan, P. Numerical investigation into the effect of backfilling on coal pillar strength in highwall mining. *Int. J. Min. Sci. Technol.* **2018**, *28*, 281–286. [CrossRef]

16. Anwar, R.; Ahmed, M.; Seats, P.; Huang, Q.; Lin, L.-S. Prospect of utilizing coal mine drainage sludge as an iron source for value-creating applications. *Rev. Environ. Sci. Bio./Technol.* **2021**, *20*, 679–695. [CrossRef]

17. Kefeni, K.K.; Msagati, T.M.; Maree, J.P.; Mamba, B.B. Metals and sulphate removal from acid mine drainage in two steps via ferrite sludge and barium sulphate formation. *Miner. Eng.* **2015**, *81*, 79–87. [CrossRef]

18. Yuan, L.; Zhang, T.; Zhao, Y.; Ren, B.; Hao, X.; Xu, C. Precise coordinated mining of coal and associated resources: A case of environmental coordinated mining of coal and associated rare metal in Ordos basin. *Zhongguo Kuangye Daxue Xuebao/J. China Univ. Min. Technol.* **2017**, *46*, 449–459. [CrossRef]

19. El Kamash, W.; El Naggar, H.; Nagaratnam, S. Novel adaptation of Marston's stress solution for inclined backfilled stopes. *Alex. Eng. J.* **2022**, *61*, 8221–8239. [CrossRef]

20. Chen, T.; Shu, J.; Han, L.; Tian, G.; Yang, G.; Lv, J. Modeling the effects of topography and slope gradient of an artificially formed slope on runoff, sediment yield, water and soil loss of sandy soil. *Catena* **2022**, *212*, 106060. [CrossRef]

21. Eang, K.E.; Igarashi, T.; Kondo, M.; Nakatani, T.; Tabelin, C.B.; Fujinaga, R. Groundwater monitoring of an open-pit limestone quarry: Water-rock interaction and mixing estimation within the rock layers by geochemical and statistical analyses. *Int. J. Min. Sci. Technol.* **2018**, *28*, 849–857. [CrossRef]

22. Ma, D.; Kong, S.; Li, Z.; Zhang, Q.; Wang, Z.; Zhou, Z. Effect of wetting-drying cycle on hydraulic and mechanical properties of cemented paste backfill of the recycled solid wastes. *Chemosphere* **2021**, *282*, 131163. [CrossRef]

23. Jiang, X.; Li, C.; Zhou, J.-Q.; Zhang, Z.; Yao, W.; Chen, W.; Liu, H.-B. Salt-induced structure damage and permeability enhancement of Three Gorges Reservoir sandstone under wetting-drying cycles. *Int. J. Rock Mech. Min. Sci. Géoméch. Abstr.* **2022**, *153*, 105100. [CrossRef]

24. Kühnel, R.A.; Van der Gaast, S.J.; Broekmans, M.A.; Theng, B.K. Wetting-induced layer contraction in illite and mica-family relatives. *Appl. Clay Sci.* **2017**, *135*, 226–233. [CrossRef]

25. Cheng, Q.; Guo, Y.; Dong, C.; Xu, J.; Lai, W.; Du, B. Mechanical Properties of Clay Based Cemented Paste Backfill for Coal Recovery from Deep Mines. *Energies* **2021**, *14*, 5764. [CrossRef]

26. Aldaood, A.; Bouasker, M.; Al-Mukhtar, M. Impact of wetting–drying cycles on the microstructure and mechanical properties of lime-stabilized gypseous soils. *Eng. Geol.* **2014**, *174*, 11–21. [CrossRef]

27. Durgun, M.Y. Effect of wetting-drying cycles on gypsum plasters containing ground basaltic pumice and polypropylene fibers. *J. Build. Eng.* **2020**, *32*, 101801. [CrossRef]

28. Li, W.; Yi, Y.; Puppala, A.J. Effects of curing environment and period on performance of lime-GGBS-treated gypseous soil. *Transp. Geotech.* **2022**, *37*, 100848. [CrossRef]

29. Ying, Z.; Benahmed, N.; Cui, Y.-J.; Duc, M. Wetting-drying cycle effect on the compressibility of lime-treated soil accounting for wetting fluid nature and aggregate size. *Eng. Geol.* **2022**, *307*, 106778. [CrossRef]

30. Zhou, W.; Cheng, J.; Zhang, G.; Li, H.; Cheng, Y.; Ma, G.; Ji, X. Effects of wetting–drying cycles on the breakage characteristics of slate rock grains. *Rock Mech. Rock Eng.* **2021**, *54*, 6323–6337. [CrossRef]

31. Cantón, Y.; Solé-Benet, A.; Queralt, I.; Pini, R. Weathering of a gypsum-calcareous mudstone under semi-arid environment at Tabernas, SE Spain: Laboratory and field-based experimental approaches. *Catena* **2001**, *44*, 111–132. [CrossRef]

32. Jiang, X.; Huang, Q.; Zhang, Z.; Vallejo, L.E.; Chen, X.; Zhao, W.; Deng, H.; Liu, X.; Song, D.; Chen, Z. Influence of Clay Content on Crack Evolution of Clay–Sand Mixture. *Front. Earth Sci.* **2022**, *10*, 915478. [CrossRef]

33. Hua, W.; Dong, S.; Li, Y.; Xu, J.; Wang, Q. The influence of cyclic wetting and drying on the fracture toughness of sandstone. *Int. J. Rock Mech. Min. Sci. Géoméch. Abstr.* **2015**, *78*, 331–335. [CrossRef]

34. Gu, D.; Liu, H.; Gao, X.; Huang, D.; Zhang, W. Influence of Cyclic Wetting–Drying on the Shear Strength of Limestone with a Soft Interlayer. *Rock Mech. Rock Eng.* **2021**, *54*, 4369–4378. [CrossRef]

35. Li, X.; Peng, K.; Peng, J.; Hou, D. Experimental investigation of cyclic wetting-drying effect on mechanical behavior of a medium-grained sandstone. *Eng. Geol.* **2021**, *293*, 106335. [CrossRef]

36. Wang, J.; Fu, J.; Song, W.; Zhang, Y.; Wu, S. Acoustic emission characteristics and damage evolution process of layered cemented tailings backfill under uniaxial compression. *Constr. Build. Mater.* **2021**, *295*, 123663. [CrossRef]

37. Yang, Y.-L.; Zhang, T.; Liu, S.-Y.; Luo, J.-H. Mechanical Properties and Deterioration Mechanism of Remolded Carbonaceous Mudstone Exposed to Wetting–Drying Cycles. *Rock Mech. Rock Eng.* **2022**, *55*, 3769–3780. [CrossRef]
38. Zhang, Z.; Han, L.; Wei, S.; Chen, L.; Liu, G.; Zhang, L. Disintegration law of strongly weathered purple mudstone on the surface of the drawdown area under conditions of Three Gorges Reservoir operation. *Eng. Geol.* **2020**, *270*, 105584. [CrossRef]
39. Aldhafeeri, Z.; Fall, M. Time and damage induced changes in the chemical reactivity of cemented paste backfill. *J. Environ. Chem. Eng.* **2016**, *4*, 4038–4049. [CrossRef]
40. Fu, J.; Wang, J.; Song, W. Damage constitutive model and strength criterion of cemented paste backfill based on layered effect considerations. *J. Mater. Res. Technol.* **2020**, *9*, 6073–6084. [CrossRef]
41. Wang, J.; Zhang, C.; Fu, J.; Song, W.; Zhang, Y. Effect of water saturation on mechanical characteristics and damage behavior of cemented paste backfill. *J. Mater. Res. Technol.* **2021**, *15*, 6624–6639. [CrossRef]
42. Zhou, Y.; Yan, Y.; Zhao, K.; Yu, X.; Song, Y.; Wang, J.; Suo, T. Study of the effect of loading modes on the acoustic emission fractal and damage characteristics of cemented paste backfill. *Constr. Build. Mater.* **2021**, *277*, 122311. [CrossRef]
43. Yin, S.; Hou, Y.; Chen, X.; Zhang, M.; Du, H.; Gao, C. Mechanical behavior, failure pattern and damage evolution of fiber-reinforced cemented sulfur tailings backfill under uniaxial loading. *Constr. Build. Mater.* **2022**, *332*, 127248. [CrossRef]
44. Zhang, C.; Wang, J.; Song, W.; Fu, J. Pore structure, mechanical behavior and damage evolution of cemented paste backfill. *J. Mater. Res. Technol.* **2022**, *17*, 2864–2874. [CrossRef]
45. Wu, J.; Feng, M.; Mao, X.; Xu, J.; Zhang, W.; Ni, X.; Han, G. Particle size distribution of aggregate effects on mechanical and structural properties of cemented rockfill: Experiments and modeling. *Constr. Build. Mater.* **2018**, *193*, 295–311. [CrossRef]
46. Zhou, N.; Zhang, J.; Ouyang, S.; Deng, X.; Dong, C.; Du, E. Feasibility study and performance optimization of sand-based cemented paste backfill materials. *J. Clean. Prod.* **2020**, *259*, 120798. [CrossRef]
47. Mark, C.; Agioutantis, Z. Analysis of coal pillar stability (ACPS): A new generation of pillar design software. *Int. J. Min. Sci. Technol.* **2019**, *29*, 87–91. [CrossRef]
48. Verma, C.P.; Porathur, J.L.; Thote, N.R.; Roy, P.P.; Karekal, S. Empirical Approaches for Design of Web Pillars in Highwall Mining: Review and Analysis. *Geotech. Geol. Eng.* **2014**, *32*, 587–599. [CrossRef]
49. Porathur, J.L.; Karekal, S.; Palroy, P. Web pillar design approach for Highwall Mining extraction. *Int. J. Rock Mech. Min. Sci. Géoméch. Abstr.* **2013**, *64*, 73–83. [CrossRef]
50. Jiang, J.; Lu, Y.; Wang, D.; Han, X. Slope stability calculation method for highwall mining with open-cut mines. *Sci. Rep.* **2022**, *12*, 209. [CrossRef]
51. Ross, C.; Conover, D.; Baine, J. Highwall mining of thick, steeply dipping coal—A case study in geotechnical design and recovery optimization. *Int. J. Min. Sci. Technol.* **2019**, *29*, 777–780. [CrossRef]
52. Adhikary, D.; Shen, B.; Fama, M. A study of highwall mining panel stability. *Int. J. Rock Mech. Min.* **2002**, *39*, 643–659. [CrossRef]
53. Chen, T.; Han, L.; Shu, J. A Filling Mining Method for an End Slope Large-Dip-Angle Thick Coal Seam of a Strip Mine. China Patent No CN202110708279, 25 June 2022.
54. Ke, X.; Zhou, X.; Wang, X.; Wang, T.; Hou, H.; Zhou, M. Effect of tailings fineness on the pore structure development of cemented paste backfill. *Constr. Build. Mater.* **2016**, *126*, 345–350. [CrossRef]
55. Xu, X.; Gao, F.; Zhang, Z. Thermo-mechanical coupling damage constitutive model of rock based on the Hoek–Brown strength criterion. *Int. J. Damage Mech.* **2017**, *27*, 1213–1230. [CrossRef]
56. Han, T.; Shi, J.; Cao, X. Fracturing and Damage to Sandstone Under Coupling Effects of Chemical Corrosion and Freeze–Thaw Cycles. *Rock Mech. Rock Eng.* **2016**, *49*, 4245–4255. [CrossRef]
57. Zhao, Y.; Ran, H.; Feng, G.; Guo, Y.; Fan, Y. Damage evolution and failure characteristics of cemented gangue backfill body with different height-width ratios under uniaxial compression. *Caikuang Yu Anquan Gongcheng Xuebao/J. Min. Saf. Eng.* **2022**, *39*, 674–682. [CrossRef]
58. Wu, X.; Liu, J.; Liu, X.; Zhao, K.; Zhang, Y. Study on the coupled relationship between AE accumulative ring-down count and damage constitutive model of rock. *Caikuang Yu Anquan Gongcheng Xuebao/J. Min. Saf. Eng.* **2015**, *32*, 28–34. [CrossRef]
59. Quennoz, A.; Scrivener, K.L. Interactions between alite and C3A-gypsum hydrations in model cements. *Cem. Concr. Res.* **2013**, *44*, 46–54. [CrossRef]
60. Huan, C.; Zhu, C.; Liu, L.; Wang, M.; Zhao, Y.; Zhang, B.; Zhang, X. Pore Structure Characteristics and Its Effect on Mechanical Performance of Cemented Paste Backfill. *Front. Mater.* **2021**, *8*, 700917. [CrossRef]
61. Zhao, K.; Wu, J.; Yan, Y.; Zhou, Y.; Yang, J.; He, Z. Multi-scale characteristics of crack evolution of cemented tailings backfill. *Yanshilixue Yu Gongcheng Xuebao/Chin. J. Rock Mech. Eng.* **2022**, *41*, 1626–1636. [CrossRef]
62. Bobet, A.; Einstein, H. Fracture coalescence in rock-type materials under uniaxial and biaxial compression. *Int. J. Rock Mech. Min. Sci. Géoméch. Abstr.* **1998**, *35*, 863–888. [CrossRef]
63. Cai, Q.; Zhou, W.; Che, Z.; Liu, Y.; Peng, H. Research on the mining method and stripping ratio of steep end-slope min-ing in surface coal mines with flat coal deposit. *Zhongguo Kuangye Daxue Xuebao/J. China Univ. Min. Technol.* **2007**, *36*, 743–747.
64. Cai, Q.; Zhou, W.; Shu, J.; Liu, Y.; Peng, H. Analysis and application on end-slope timeliness of internal dumping under flat dipping ore body in large surface coal mine. *Zhongguo Kuangye Daxue Xuebao/J. China Univ. Min. Technol.* **2008**, *37*, 740–744.
65. Zhang, Q.; Zhang, J.; Chen, Y.; Ntigurirwa, J.D.; Xia, K. Moving set-up room theory of weakening the mining pressure caused by the backfilling body in solid backfilling mining. *Energy Sci. Eng.* **2020**, *8*, 898–909. [CrossRef]

66. Shang, T.; Han, L.; Shu, J.; Chen, S. Slope structure and stress development rule under mining mode of land saving and ecological detraction. *Meitan Xuebao/J. China Coal Soc.* **2019**, *44*, 3644–3654. [CrossRef]

67. Wang, F.; Zhang, C. Reasonable coal pillar design and remote control mining technology for highwall residual coal resources. *R. Soc. Open Sci.* **2019**, *6*, 181817. [CrossRef]

68. Hu, Z.; Xiao, W.; Zhao, Y. Re-discussion on coal mine eco-environment concurrent mining and reclamation. *Meitan Xuebao/J. China Coal Soc.* **2020**, *45*, 351–359. [CrossRef]

69. Ramlochan, T.; Thomas, M.; Hooton, R. The effect of pozzolans and slag on the expansion of mortars cured at elevated temperature: Part II: Microstructural and microchemical investigations. *Cem. Concr. Res.* **2004**, *34*, 1341–1356. [CrossRef]

70. Ogawa, K.; Roy, D. C4A3S hydration, ettringite formation, and its expansion mechanism: II. Microstructural observation of expansion. *Cem. Concr. Res.* **1982**, *12*, 101–109. [CrossRef]

71. Calvo, J.G.; Carballosa, P.; Pedrosa, F.; Revuelta, D. Microstructural phenomena involved in the expansive performance of cement pastes based on type K expansive agent. *Cem. Concr. Res.* **2022**, *158*, 106856. [CrossRef]

72. Bian, X.; Zhang, W.; Li, X.; Shi, X.; Deng, Y.; Peng, J. Changes in strength, hydraulic conductivity and microstructure of superabsorbent polymer stabilized soil subjected to wetting–drying cycles. *Acta Geotech.* **2022**, *17*, 5043–5057. [CrossRef]

73. Yang, J.; Wang, L.; Li, X.; Zhao, G. Research on micro-fracture mechanism of mudstone after wet-dry cycles. *Yanshilixue Yu Gongcheng Xuebao/Chin. J. Rock Mech. Eng.* **2014**, *33*, 3606–3612. [CrossRef]

74. Bull, A.J.; Fall, M. Curing temperature dependency of the release of arsenic from cemented paste backfill made with Portland cement. *J. Environ. Manag.* **2020**, *269*, 110772. [CrossRef]

75. Damidot, D.; Glasser, F. Thermodynamic investigation of the CaO Al_2O_3 $CaSO_4$ H_2O system at 50 °C and 85 °C. *Cem. Concr. Res.* **1992**, *22*, 1179–1191. [CrossRef]

76. Qian, J.; Yu, J.; Sun, H.; Ma, Y. Formation and Function of Ettringite in Cement Hydrates. *Kuei Suan Jen Hsueh Pao/J. Chin. Ceram. Soc.* **2017**, *45*, 1569–1581. [CrossRef]

77. Comboni, D.; Gatta, G.D.; Lotti, P.; Merlini, M.; Hanfland, M. Anisotropic compressional behavior of ettringite. *Cem. Concr. Res.* **2019**, *120*, 46–51. [CrossRef]

78. Bizzozero, J.; Gosselin, C.; Scrivener, K.L. Expansion mechanisms in calcium aluminate and sulfoaluminate systems with calcium sulfate. *Cem. Concr. Res.* **2014**, *56*, 190–202. [CrossRef]

79. Shi, Z.; Li, J.; Zhao, Y. Study on damage evolution and constitutive model of sandstone under the coupled effects of wetting-drying cycles and cyclic loading. *Eng. Fract. Mech.* **2021**, *253*, 107883. [CrossRef]

80. Song, X.; Hao, Y.; Wang, S.; Zhang, L.; Liu, W.; Li, J. Mechanical properties, crack evolution and damage characteristics of prefabricated fractured cemented paste backfill under uniaxial compression. *Constr. Build. Mater.* **2022**, *330*, 127251. [CrossRef]

81. Zhou, Y.; Yu, X.; Guo, Z.; Yan, Y.; Zhao, K.; Wang, J.; Zhu, S. On acoustic emission characteristics, initiation crack intensity, and damage evolution of cement-paste backfill under uniaxial compression. *Constr. Build. Mater.* **2021**, *269*, 121261. [CrossRef]

MDPI